Liqiu Wang
Editor

Advances in Transport Phenomena 2010

Springer

Liqiu Wang (Ed.)

Advances in Transport Phenomena 2010

Liqiu Wang (Ed.)

Advances in Transport Phenomena 2010

Springer

Prof. Liqiu Wang
Department of Mechanical Engineering
The University of Hong Kong
Pokfulam Road, Hong Kong
E-mail: lqwang@hku.hk
http://www3.hku.hk/mech/mechstaf/WangLQ.htm

ISBN 978-3-642-19465-8 e-ISBN 978-3-642-19466-5

DOI 10.1007/978-3-642-19466-5

Advances in Transport Phenomena ISSN 1868-8853

Library of Congress Control Number: 2011923889

Typeset & *Cover Design:* Scientific Publishing Services Pvt. Ltd., Chennai, India.

Printed in acid-free paper

9 8 7 6 5 4 3 2 1

springer.com

Preface

The term *transport phenomena* is used to describe processes in which mass, momentum, energy and entropy move about in matter. *Advances in Transport Phenomena* provide state-of-the-art expositions of major advances by theoretical, numerical and experimental studies from a molecular, microscopic, mesoscopic, macroscopic or megascopic point of view across the spectrum of transport phenomena, from scientific enquiries to practical applications. The annual review series intends to fill the information gap between regularly published journals and university-level textbooks by providing in-depth review articles over a broader scope than in journals. The authoritative articles, contributed by internationally-leading scientists and practitioners, establish the state of the art, disseminate the latest research discoveries, serve as a central source of reference for fundamentals and applications of transport phenomena, and provide potential textbooks to senior undergraduate and graduate students.

The series covers mass transfer, fluid mechanics, heat transfer and thermodynamics. The 2010 volume contains the four articles on the field synergy principle for convective heat transfer optimization, the lagging behavior of nonequilibrium transport, the microfluidics and the multiscale modelling of liquid suspensions of particles, respectively. The editorial board expresses its appreciation to the contributing authors and reviewers who have maintained the standard associated with *Advances in Transport Phenomena*. We also would like to acknowledge the efforts of the staff at Springer who have made the professional and attractive presentation of the volume.

Serial Editorial Board

Contents

Optimization Principles for Heat Convection 1
Zhi-Xin Li, Zeng-Yuan Guo

Nonequilibrium Transport: The Lagging Behavior 93
D.Y. Tzou, Jinliang Xu

Microfluidics: Fabrication, Droplets, Bubbles and Nanofluids Synthesis 171
Yuxiang Zhang, Liqiu Wang

Multi-scale Modelling of Liquid Suspensions of Micron Particles in the Presence of Nanoparticles 295
Chane-Yuan Yang, Yulong Ding

Author Index 333

List of Contributors

Numbers in parenthesis indicate the pages on which the authors' contribution begins.

Ding, Y.L.

Institute of Particle Science and Engineering, University of Leeds, Leeds LS2 9JT, UK (295)

Guo, Z.-Y.

Key Laboratory for Thermal Science and Power Engineering of Ministry of Education, Department of Engineering Mechanics, School of Aerospace, Tsinghua University, Beijing 100084, China (1)

Li, Z.-X.

Key Laboratory for Thermal Science and Power Engineering of Ministry of Education, Department of Engineering Mechanics, School of Aerospace, Tsinghua University, Beijing 100084, China (1)

Tzou, D.Y.

Department of Mechanical and Aerospace Engineering, University of Missouri, Columbia, MO 65211, USA (93)

Wang, L.Q.

Department of Mechanical Engineering, The University of Hong Kong, Pokfulam Road, Hong Kong (171)

Xu, J.L.

School of Renewable Energy, North China Electric Power University, Beijing 102206, China

Yang, C.-Y.

Institute of Particle Science and Engineering, University of Leeds, Leeds LS2 9JT, UK (295)

Zhang, Y.X.

Department of Mechanical Engineering, The University of Hong Kong, Pokfulam Road, Hong Kong (171)

Optimization Principles for Heat Convection

Zhi-Xin Li and Zeng-Yuan Guo

Abstract. Human being faces two key problems: world-wide energy shortage and global climate worming. To reduce energy consumption and carbon emission, it needs to develop high efficiency heat transfer devices. In view of the fact that the existing enhanced technologies are mostly developed according to the experiences on the one hand, and the heat transfer enhancement is normally accompanied by large additional pumping power induced by flow resistances on the other hand, in this chapter, the field synergy principle for convective heat transfer optimization is presented based on the revisit of physical mechanism of convective heat transfer. This principle indicates that the improvement of the synergy of velocity and temperature gradient fields will raise the convective heat transfer rate under the same other conditions. To describe the degree of the synergy between velocity and temperature gradient fields a non-dimensional parameter, named as synergy number, is defined, which represents the thermal performance of convective heat transfer. In order to explore the physical essence of the field synergy principle a new quantity of entransy is introduced, which describes the heat transfer ability of a body and dissipates during hear transfer. Since the entransy dissipation is the measure of the irreversibility of heat transfer process for the purpose of object heating the extremum entransy dissipation (EED) principle for heat transfer optimization is proposed, which states: for the prescribed heat flux boundary conditions, the least entransy dissipation rate in the domain leads to the minimum boundary temperature difference, or the largest entransy dissipation rate leads to the maximum heat flux with a prescribed boundary temperature difference. For volume-to-point problem optimization, the results indicate that the optimal distribution of thermal conductivity according to the EED principle leads to the lowest average domain temperature, which is lower than that with the minimum entropy generation (MEG) as the optimization criterion. This indicates that the EED principle is more preferable than the MEG principle for heat conduction optimization with the purpose of the domain temperature reduction. For convective heat transfer optimization, the field synergy equations for both laminar and

Zhi-Xin Li · Zeng-Yuan Guo
Key Laboratory for Thermal Science and Power Engineering of Ministry of Education, Department of Engineering Mechanics, School of Aerospace, Tsinghua University, Beijing 100084, China
e-mail: lizhx@tsinghua.edu.cn, demgzy@tsinghua.edu.cn

L.Q. Wang (Ed.): Advances in Transport Phenomena, ADVTRANS 2, pp. 1–91.
springerlink.com

turbulent convective heat transfer are derived by variational analysis for a given viscous dissipation (pumping power). The optimal flow fields for several tube flows were obtained by solving the field synergy equation. Consequently, some enhanced tubes, such as, alternation elliptical axis tube, discrete double inclined ribs tube, are developed, which may generate a velocity field close to the optimal one. Experimental and numerical studies of heat transfer performances for such enhanced tubes show that they have high heat transfer rate with low increased flow resistance. Finally, both the field synergy principle and the EED principle are extended to be applied for the heat exchanger optimization and mass convection optimization.

1 Introduction

At present, human being faces two key problems: world-wide energy shortage and global climate worming. Since the utilization of about 80% various kinds of energy are involved in heat transfer processes, to study enhanced heat transfer techniques with high energy efficiency becomes more and more important for reducing energy consumption and carbon emission.

Since convection heat transfer has broad applications in various engineering areas, a large amount of studies have been conducted in the past decades to get the heat transfer correlations and to improve heat transfer performance for different cases. However, the conventional way to investigate convection heat transfer has been to first classify convection as internal/external flow, forced/natural convection, boundary layer flow/elliptic flow, rotating flow/non-rotating flow, etc., then to determine the heat transfer coefficient, h, and the corresponding dimensionless parameter, Nusselt number, Nu, by both theoretical and experimental methods. The Nu can usually be expressed as various functions of the Reynolds number，Re, (or Grashof number, Gr) and Prandtl number, Pr, and heat transfer surface geometries [1,2]. However, there is no unified principle, which may generally describe the performance of different types of convection heat transfer, and consequently guide the enhancement and optimization of convection heat transfer.

Up to now, passive means have usually been used for single phase convective heat transfer enhancement [3,4], various heat transfer enhancement elements, especially rolled tubes, such as the spirally grooved tube [5,6] and the transverse grooved tube [7] have been widely used to improve heat transfer rates[8]. Tube inserts such as twisted-tape inserts [9,10] and coiled wire turbulence promoters [11], have also been used to enhance the heat transfer in tubes. However, the development of these enhancement elements has mostly been based on experience with heat transfer enhancement normally accompanied by large flow resistances [12]. This implies that the enhanced heat transfer does not always save energy.

To develop heat transfer technologies with high energy efficiency, Guo and his colleagues studied the optimization principle, which, unlike the heat transfer enhancement, refers to maximizing the heat transfer rate for a given pumping power. By analyzing the energy equation for two-dimensional laminar boundary

layer flow, Guo et al. [13,14] proposed the concept of field synergy (coordination), and then presented the field synergy principle for convective heat transfer, which indicates that the Nusselt number for convective heat transfer depends not only on the temperature difference, flow velocity and fluid properties, but also on the synergy of the flow and temperature fields. Tao [15] proved that this principle is also valid for elliptic flows of which most convective heat transfer problems are encountered in engineering. Thus, the field synergy principle provides a new approach for evaluating heat transfer performance of various existing enhancement techniques on the one hand, and can guide us to develop a series of novel enhanced techniques with high energy efficiency on the other hand [16-27].

But the field synergy principle can tell us how to improve the field synergy of flow and temperature fields qualitative only due to their strong coupling, and can not guide our quantitative design of heat transfer components and devices with the best field synergy degree.

In order to reveal the physical nature of the field synergy principle and to establish the field synergy equations, Guo et al. [28] and Cheng [29] introduced a physical quantity, entransy, by analogy between heat and electric transports, which can be used to define the efficiencies of heat transfer processes and to establish the extremum entransy dissipation principle for heat transfer optimization. The difference between the principles of minimum entropy production and the extremum entransy dissipation lies in their optimization objective. The former is the maximum heat-work conversion efficiency, called thermodynamic optimization, while the latter is the maximum heat transfer rate for given temperature difference or the minimum temperature difference for given heat flux. Several applications of the field synergy principle and the extremum entransy dissipation principle for developing energy-efficient heat transfer components and devices are demonstrated in references [16-19, 30-32].

2 Field Synergy Principle for Convective Heat Transfer

2.1 Convective Heat Transfer Mechanism

Guo [14] and Guo et al. [13,22] revisited the mechanism of convective heat transfer by considering an analog between convection and conduction. They regarded the convection heat transfer as the heat conduction with fluid motion. Consider a steady, 2-D boundary layer flow over a cold flat plate at zero incident angle, as shown in Fig.1(a). The energy equation is

$$\rho c_p \left(u \frac{\partial T}{\partial x} + v \frac{\partial T}{\partial y} \right) = \frac{\partial}{\partial y} \left(k \frac{\partial T}{\partial y} \right) \tag{1}$$

The energy equation for conduction with a heat source between two parallel plates at constant but different temperatures as shown in Fig.1(b) is

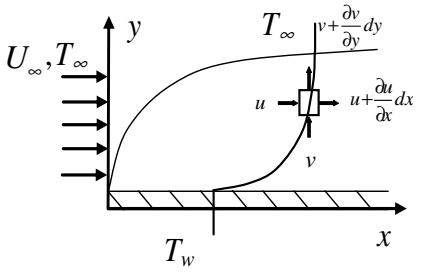

(a) Laminar boundary layer

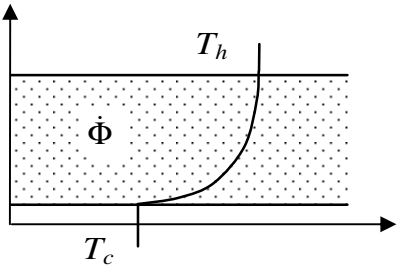

(b) conduction with a heat source

Fig. 1 Temperature profiles for (a) laminar boundary layer flow over a flat plate, and (b) conduction with a heat source between two parallel plates at different constant temperatures.

$$-q = \frac{\partial}{\partial y}\left(k\frac{\partial T}{\partial y}\right) \tag{2}$$

From Eqs. (1) and (2), it can be seen that the convection term in the energy equation for the boundary layer flow corresponds to the heat source term in the conduction equation.

The difference is that the ‘‘heat source’’ term in convection is a function of the fluid velocity. The presence of heat sources leads to an increased heat flux at the boundary for both the conduction and convection problems. The integral of Eq. (1) over the thickness of the thermal boundary layer is

$$\int_0^{\delta_{t,x}} \rho c_p (u\frac{\partial T}{\partial x} + v\frac{\partial T}{\partial y})dy = -k\frac{\partial T}{\partial y}\bigg|_w = q_w(x) \tag{3}$$

where δt is the thermal boundary layer thickness. The integral of the energy equation of heat conduction with heat source, Eq. (2), over the thickness between two plates, δ, we have

$$\int_0^{\delta} \dot{\Phi}(x, y)dy = -k\frac{\partial T}{\partial y}\bigg|_w = q_w(x) \tag{4}$$

On the left hand side of Eq. (4) is the sum of the heat source in the cross-section at x position between the two plates, the term on the right hand side is the surface heat flux at x. It is obvious that the larger the heat source, the larger the surface heat flux, the reason is that all the heat generated in the domain must be transferred from the cold plate. This is the concept of source induced enhancement.

On the left hand side of Eq.(3) is the sum of the convection source term in the boundary layer at x position, the right hand is the surface heat flux at x, which is the physical parameter to be enhanced or controlled. Same as heat conduction analyzed above, the larger the sum of the convective source term, the larger the heat transfer rate, which is also the source induced enhancement. For the case of fluid temperature higher than solid surface temperature, the heat transfer will be enhanced/weakened by the existed heat source/sink. For convection problems, the convection source term acts heat source/sink if the fluid temperature is higher/lower than the wall surface temperature. Therefore, we can conclude from Eq. (3) that the convection heat transfer can be enhanced by increasing the value of the integral of the convection terms (heat sources) over the thermal boundary layer.

The above results are based on the analysis on 2D boundary layer problem, which also hold for the more general convection problems. The energy equation of convective heat transfer is,

$$\rho c_p(u\frac{\partial T}{\partial x}+v\frac{\partial T}{\partial y}+w\frac{\partial T}{\partial z}) = \frac{\partial}{\partial x}(k\frac{\partial T}{\partial x})+\frac{\partial}{\partial y}(k\frac{\partial T}{\partial y})+\frac{\partial}{\partial z}(k\frac{\partial T}{\partial z})+\dot{\Phi} \tag{5}$$

where $\dot{\Phi}$ is the real heat source, for example, heat generated by viscous dissipation, or by chemical reaction, or by electric heating. Rearranging and integrating Eq.(5), where all source terms are positioned in the right hand side of Eq.(5), leads to

$$\int_0^{\delta_{t,x}} \left\{ \rho c_p(u\frac{\partial T}{\partial x}+v\frac{\partial T}{\partial y}+w\frac{\partial T}{\partial z}) - \left[\frac{\partial}{\partial x}(k\frac{\partial T}{\partial x})+\frac{\partial}{\partial y}(k\frac{\partial T}{\partial y})\right] - \dot{\Phi} \right\} dy = -k\frac{\partial T}{\partial y}\bigg|_w = q_w(x) \tag{6}$$

Heat source by convection

Heat source by conduction

Real heat source

The term in the right hand side of Eq.(6) is the surface heat flux, and the term in the left hand side is the sum of the heat sources in the boundary layer. With the concept of source induced enhancement, it is easy to understand why the convective heat transfer between hot fluid with heat sources and cold wall surface can be enhanced.

2.2 Field Synergy Principle

Based on the revisit of the convective heat transfer mechanism, Guo [14] presented the field synergy principle for convective heat transfer optimization. Eq. (3) can be rewritten with the convection term in vector form as:

$$\int_0^{\delta_{t,x}} \rho c_p (U \cdot \nabla T) dy = -k \left. \frac{\partial T}{\partial y} \right|_w = q_w(x) \tag{7}$$

From Eq. (7) it can be seen that for a certain flow rate and temperature difference between the wall and the incoming flow, the wall heat flux increases with the decrement of the included (intersection) angle between the velocity and temperature gradient/heat flow vectors. Eq. (7) is also valid for laminar duct flow if the upper limit of the integral is the duct radius. With the following dimensionless variables for the boundary layer flow,

$$\overline{U} = \frac{U}{U_\infty}, \quad \overline{\nabla T} = \frac{\nabla T}{(T_\infty - T_w)/\delta_t}, \quad \bar{y} = \frac{y}{\delta_t}, \quad T_\infty > T_w \tag{8}$$

Eq. (7) can be written in the dimensionless form,

$$\mathrm{Re}_x \, \mathrm{Pr} \int_0^1 (\overline{U} \cdot \overline{\nabla T}) d\bar{y} = \mathrm{Nu}_x \tag{9}$$

Eq. (9) gives us a more general insight on convective heat transfer. It can be seen that there are two ways to enhance heat transfer: (a) increasing Reynolds or/and Prandtl number; which is well known in the literatures; (b) increasing the value of the dimensionless integration. The vector dot product in the dimensionless integration in Eq. (9) can be expressed as

$$\overline{U} \cdot \overline{\nabla T} = \left|\overline{U}\right| \cdot \left|\overline{\nabla T}\right| \cos\beta \tag{10}$$

where β is the included angle, or called the synergy angle, between the velocity vector and the temperature gradient (heat flow vector). Eq. (10) shows that in the convection domain there are two vector fields, U and ∇T, or three scalar fields, $\left|\mathrm{U}\right|, \left|\nabla \mathrm{T}\right|$ and $\cos\beta$. Hence, the value of the integration or the strength of the convection heat transfer depends not only on the velocity, the temperature gradient, but also on their synergy. Thus, the principle of field synergy for the optimization of convective heat transfer may be stated as follows: For a given temperature difference and incoming fluid velocity, the better the synergy of velocity and temperature gradient/heat flow fields, the higher the convective heat transfer rate under the same other conditions. The synergy of the two vector fields or the three scalar fields implies that (a) the synergy angle between the velocity and the

temperature gradient/heat flow should be as small as possible, i.e., the velocity and the temperature gradient should be as parallel as possible; (b) the local values of the three scalar fields should all be simultaneously large, i.e., larger values of cosβ should correspond to larger values of the velocity and the temperature gradient; (c) the velocity and temperature profiles at each cross section should be as uniform as possible. Better synergy among such three scalar fields will lead to a larger value of the Nusselt number.

2.3 Field Synergy Number

As indicated above, the most favorable case is that a small synergy angle is accompanied by large velocity and temperature gradients. So the average synergy angle in the whole domain can not fully represent the degree of velocity and temperature field synergy, which should be described by the dimensionless parameter as follows:

$$\int_0^1 \bar{U} \cdot \nabla \bar{T} d\bar{y} = \frac{\mathrm{Nu}}{\mathrm{Re}\,\mathrm{Pr}} = \mathrm{Fc} \tag{11}$$

where the dimensionless quantity, Fc, is designated as the field synergy number, which stands for the dimensionless heat source strength (i.e., the dimensionless convection term) over the entire domain, and therefore, is the indication of the degree of synergy between the velocity and temperature gradient fields. Its value can be anywhere between zero and unity depending on the type of heat transfer surface. It is worthy to note that the difference between Fc and the Stanton number, St, although they have identical formulas relating to the Nusselt number. The Stanton number, St = Nu/RePr, is an alternate to Nusselt number only for expressing dimensionless heat transfer coefficient for convective heat transfer, while the field synergy number, Fc, reveals the relationship of Nu with the synergy of flow and temperature fields. To further illustrate the physical interpretation of Fc, let's assume that U and ∇T are uniform and the included angles, β, are equal to zero everywhere in the domain, then Fc = 1, and

$$\mathrm{Nu}_x = \mathrm{Re}_x \mathrm{Pr} \tag{12}$$

For this ideal case the velocity and temperature gradient fields are completely synergized and Nu reaches its maximum for the given flow rate and temperature difference. It should be noted that Fc is much smaller than unity for most practical cases of convective heat transfer, as shown in Fig.2.

Therefore, from the view point of field synergy, there is a large room open to the improvement of convective heat transfer performance.

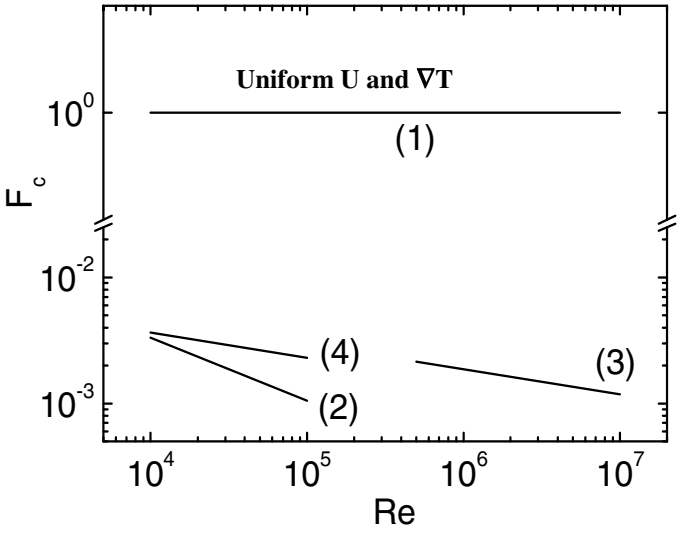

Fig. 2 Field synergy number for some cases of convective heat transfer. (1) Synergized flow; (2) Laminar boundary layer; (3) Turbulent boundary layer; (4) Turbulent flow in circular tube

2.4 Examples of Convection with Different Field Synergy Degrees

Consider a fully developed laminar flow in the channel composed of two parallel flat plates which are kept at different temperature, T_h and T_c, respectively as shown in Fig.3. If the flow is fully developed, the streamlines are parallel to the flat plates and the velocity profile no longer changes in the flow direction. The temperature profile along *y* direction is linear, same as that for the case of pure heat conduction. This implies that the fluid flow has no effect on the heat transfer rate.

For this convective heat transfer problem, the dot product of velocity vector and temperature gradient vector is equal to zero, that is, the velocity and heat flow fields are out of synergy completely.

Another typical convective heat transfer problem, shown in Fig.4, is the laminar convection with uniform velocity passing through two parallel porous plates. The two plates are kept at uniform temperatures, T_h and T_c, respectively. The fluid velocity is normal to the plates and the isotherms in between. Assume that the heat transfer between the porous plates and the fluid in the pores is intensive enough, the energy equation for the fluid between two plates can be simplified as,

$$\frac{d}{dy}\left(\rho V_w T\right) = \frac{d}{dy}\left(\frac{k}{c_p}\frac{dT}{dy}\right) \tag{13}$$

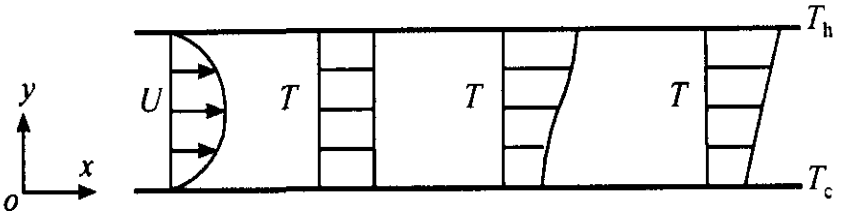

Fig. 3 Convective heat transfer between two parallel plates at different temperatures

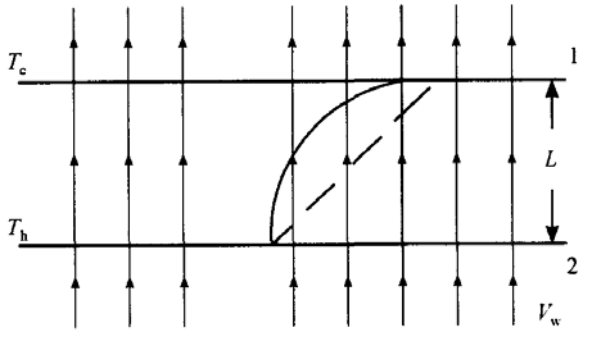

Fig. 4 Convection between two porous plates with different uniform temperatures

with the boundary of

$$T\big|_{y=0} = T_h;\ T\big|_{y=L} = T_c \tag{14}$$

The analytical solution of Eq.(13) gives,

$$\mathrm{Nu} = \frac{\mathrm{Re}\,\mathrm{Pr}}{1-\exp(-\mathrm{Re}\,\mathrm{Pr})} \tag{15}$$

For plate 1, V_w>0, the problem is a suction flow. Then, we have Nu>1 for RePr>0. Eq.(15) indicates that Nu almost equals to RePr for the cases of RePr>3. It means that the heat transfer rate tends to reach its maximum values as predicated by Eq.(12) for the fully synergized convection. Here, the Nusselt number is proportional to RePr, the reason is that the velocity and temperature gradient vectors are always parallel to each other.

For plate 2, V_w<0, it is a blowing flow. Then, we have Nu<1 for RePr>0. That is, the fluid motion does not enhance heat transfer, but weakens heat transfer. Nu<1 implies that the heat transfer rate is even lower than that of pure heat conduction.

If –RePr>3, we have Nu tends to zero, that is, the fluid motion plays the role of thermal insulation.

Zhao and Song [33] conducted an analytical and experimental study of forced convection in a saturated porous medium subjected to heating with a solid wall perpendicular to the flow direction as shown in Fig. 5(a). The heat transfer rate from the wall to the bulk fluid for such a heat transfer configuration had been shown to be described by the simple equation Nu = RePr at low Reynolds number region as shown in Fig.5(b). In this case the field synergy number, Fc = 1. Obviously, the complete synergy of the velocity and heat flow fields provides the most efficient heat transfer mode as compared with any other convective heat transfer situations.

The flow and heat transfer across a single circular cylinder with rectangular fins was numerically studied in [25]. To numerically simulate the flow field around the cylinder between two adjacent fins three-dimensional body fitted coordinates were adopted. The tube wall was kept at constant temperature and the fin surface temperature was assumed to be equal to the tube wall temperature. The flow across single cylinder was also simulated for comparison. Numerical results of isotherms and velocity vectors for flow over single smooth tube with U=0.02 m/s are presented in Fig. 6(a) and (b), from which it can be observed that over most part of the computational domain (except for upstream region where the isotherms are nearly vertical), the velocity and the local temperature gradient are nearly perpendicular each other, leading to a large field synergy angle. The synergy angle distribution is provided in Fig.6(c). The average synergy angle of the whole domain is 61.7degree.

For the finned tube at the oncoming flow velocity of 0.06 m/s, the fluid isotherms and the flow velocity at the middle plane between two adjacent fin surfaces are presented in Fig. 7(a) and (b). It can be clearly observed that the attachment of fin to the tube surface greatly changes the orientation of the isotherms as almost vertical so that the temperature gradient is in almost horizontal direction. The result is that the velocity and temperature gradient are almost parallel and thus in good synergy. The local synergy angle distribution is shown in Fig.7(c), and the average synergy angle is now reduced to 23.6 degree. Computational results further reveal that in the region of very low velocity (for the case studied, the oncoming flow velocity less than 0.08 m/s), the average finned tube heat transfer coefficient varies almost linearly with the flow velocity, once again showing a case where the local velocity and temperature gradient is almost parallel everywhere.

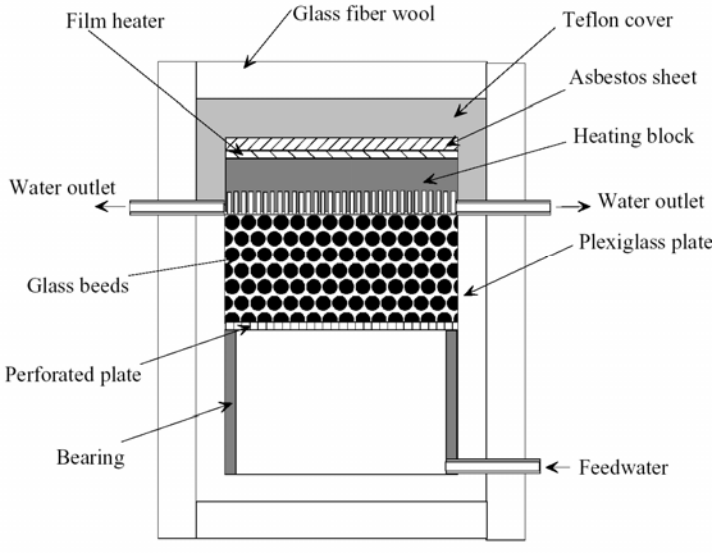

(a) test section

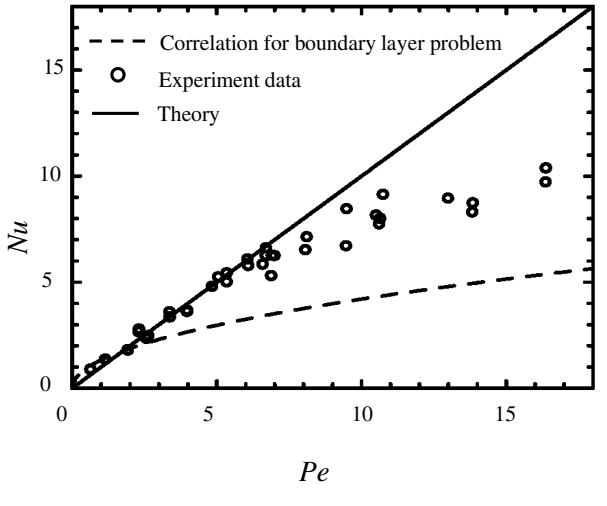

(b) Nu versus Pe for the wall

Fig. 5 Test section and Nu vs Pe for forced convection in a saturated porous medium

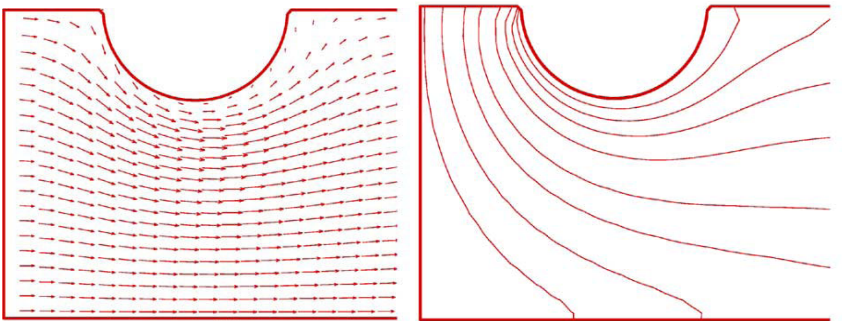

(a) velocity vectors (b) isotherms

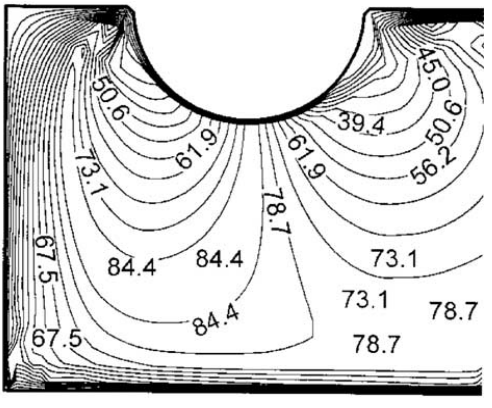

(c) synergy angle distribution

Fig. 6 Numerical results of velocity vectors, isotherms and in synergy angles for flow over single tube (U = 0.02 m/s)

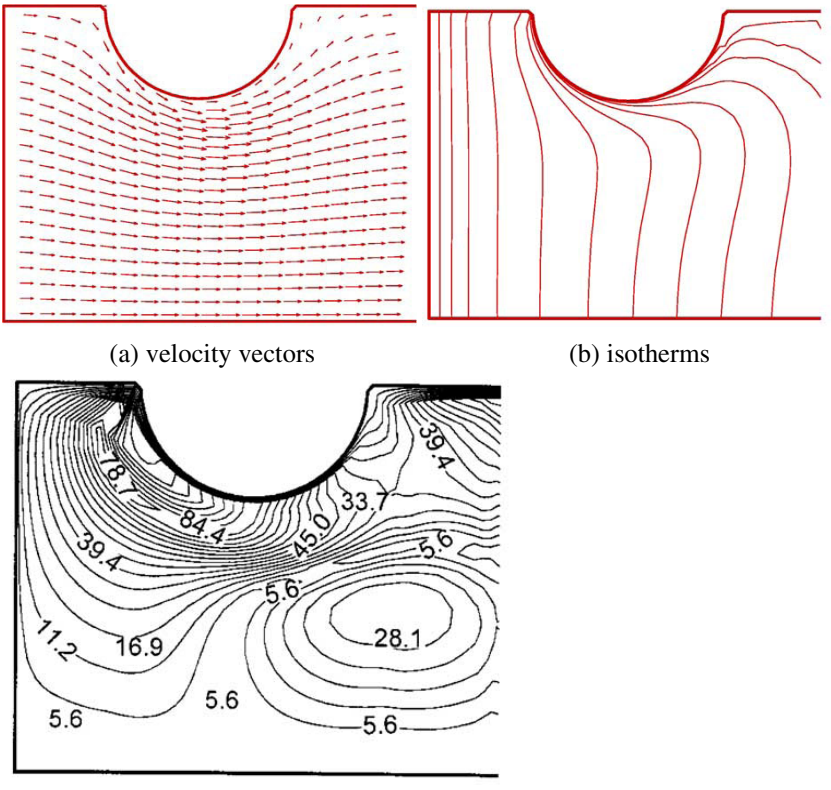

(a) velocity vectors (b) isotherms

(c) synergy angle distribution

Fig. 7 Velocity vectors, isothermals and synergy angle distributions for flow over finned tube (U = 0.06 m/s)

2.5 Ways to Improve Field Synergy Degree

It is seen from Eq.(9) that there are three ways to improve the field synergy for convective heat transfer. The first one is to vary the velocity distribution for a fixed flow rate in the duct flow, for example, by introducing vortices in a specially designed tube [19]. The second one is to improve the uniformity of the temperature profiles by the inserts composed of sparse metal filaments in circular tube [21]. The filaments are normal to the tube wall and thin enough to produce a slight additional increase in the pressure drop. Such kind of fins is neither for surface extension, nor for disturbance promotion, but for improvement of field synergy. The third one is to vary the synergy angles between velocity and temperature gradient vectors. For example, some parallel slotted fin surfaces are designed according to the principle of ‘‘front sparse and rear dense’’ to reduce the domain-averaged synergy angle of convective heat transfer.

3 Extremum Entransy Dissipation Principle

As mentioned in the above section, by improving the synergy of flow field and temperature gradient (heat flow) field, the convective heat transfer can be effectively enhanced for a given pumping power, and a little increment of the velocity component along heat flow direction will result in a profound augmentation of convective heat transfer, since the fluid flow is almost normal to the heat flow direction for the existing convection modes. Nevertheless, the field synergy principle gives us some principled measures for heat transfer optimization only, but not an approach for the quantitative analyses and design of heat transfer optimization. For example, it can not point out what kind of velocity field is the optimal one for maximum heat transfer rate at the prescribed oncoming flow rate and characteristic temperature difference. To find the optimal velocity field is an optimization problem of convective heat transfer.

3.1 Entransy

It is well known that, Fourier law, Newton cooling law and Stefen-Boltzmann law in heat transfer are used to describe the heat transfer rates in heat conduction, convection and radiation respectively. However there is no concept of heat transfer efficiency because thermal energy is conserved during transfer processes on the one hand, and the units of the input and output for enhanced heat transfer problems are not the same on the other hand. In heat transfer literatures, we have the concepts of fin efficiency and heat exchanger effectiveness, which can not be called the heat transfer efficiency, as they are defined as the ratio of actual heat transfer rate to maximum possible heat transfer rate, rather than the ratio of output to input heat flow rate.

Heat transfer is an irreversible, non-equilibrium process from the point of view of thermodynamics. Onsager [34, 35] set up the fundamental equations for non-equilibrium thermodynamic processes and derived the principle of the least dissipation of energy using variational theory. Prigogine [36] developed the principle of minimum entropy generation based on the idea that the entropy generation of a thermal system at steady-state should be the minimum. However, both of these principles do not deal with heat transfer optimization. Bejan [37, 38] developed entropy generation expressions for heat and fluid flows. He analyzed the least combined entropy generation induced by the heat transfer and the fluid viscosity as the objective function to optimize the geometry of heat transfer tubes and to find optimized parameters for heat exchangers and thermal systems. This type of investigation is called thermodynamic optimization because its objective is to minimize the total entropy generation due to flow and thermal resistance. For the volume-to-point heat conduction problem, Bejan [39, 40] developed a constructal theory network of conducting paths that determines the optimal distribution of a fixed amount of high conductivity material in a given volume such that the overall volume-to-point resistance is minimized. In view of the fact that there is lack of a fundamental quantity for heat transfer optimization, Guo et al. [28] presented a new

physical quantity, entransy, by analogy between electrical and thermal systems, which can be used to define the efficiencies of heat transfer processes and to optimize heat transfer processes. The two systems are analogous because Fourier's law for heat conduction is analogous to Ohm's law for electrical circuits. In the analogy, the heat flow corresponds to the electrical current, the thermal resistance to the electrical resistance, temperature to electric voltage, and heat capacity to capacitance. The analogies between the parameters for the two processes are listed in Table 1 from which shows that the thermal system lacks of the parameter corresponding to the electrical potential energy of a capacitor. An appropriate quantity, *G*, can be defined for a thermal system without volume variation as [28]

$$G = \frac{1}{2} Q_{vh} T \tag{16}$$

where $Q_{vh} = McT$ is the thermal energy stored in an object with constant volume which may be referred to as the thermal charge, *T* represents the thermal potential.

Table 1 Analogies between electrical and thermal parameters

Electrical charge stored in capacitor Q_{ve} / [C]	Electrical current (charge flux) I / [C]/[s]=A	Electrical resistance R_e / [Ω]	Capacitance $C_e=Q_{ve}/U_e$ / [F]
Thermal energy stored in an object $Q_{vh}= McT$ / [J]	Heat flow $\dot{Q}_h$ / [J/s]	Thermal resistance R_h / [s K/J]	Heat capacity $Mc= Q_{vh}/T$ / [J/K]
Electrical potential U_e / [V]	Electrical current density $\dot{q}_e$ / [C/m^{2}s]	Ohm's law $\dot{q}_e = -k_e \frac{dU_e}{dn}$	Electrical potential energy in a capacitor $E_e = 0.5 Q_e U_e$ / [J]
Thermal potential (temperature) $U_h=T$ / [K]	Heat flux $\dot{q}_h$ / [J/m^{2}s]	Fourier law $\dot{q}_h = -k_h \frac{dU_h}{dn}$	?

The physical meaning of entransy can be understood by considering a reversible heating process of an object with temperature of *T*. For a reversible heating process, the temperature difference between the object and the heat source and the heat added are infinitesimal, as shown in Fig. 8.

Continuous heating of the object implies an infinite number of heat sources that heat the object in turn. The temperature of these heat sources increases infinitesimally with each source giving an infinitesimal amount of heat to the object. The temperature represents the potential of the thermal energy because its heat transfer ability differs at different temperatures. Hence the ''potential energy" of the thermal energy increases in parallel with the increasing thermal energy

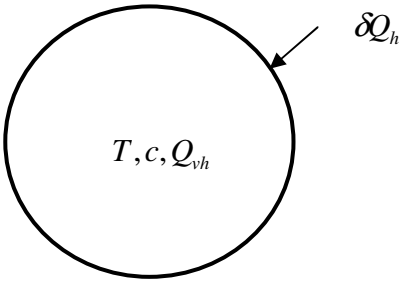

Fig. 8 Spheric thermal capacitor

(thermal charge) when heat is added. The word potential energy is quoted because its unit is J·K, not Joule. When an infinitesimal amount of heat is added to an object, the increment in ‘‘potential energy” of the thermal energy can be written as the product of the thermal charge and the thermal potential (temperature) differential,

$$dG = Q_{vh} dT \tag{17}$$

If absolute zero K is taken as the zero thermal potential, then the ‘‘potential energy” of the thermal energy in the object at temperature T is,

$$G = \int_0^T Q_{vh} dT = \int_0^T Mc_v T dT = \frac{1}{2} Mc_v T^2 \tag{18}$$

Hence, like an electric capacitor which stores electric charge and the resulting electric potential energy, an object can be regarded as a thermal capacitor which stores thermal energy/charge and the resulting thermal ‘‘potential energy”. If the object is put in contact with an infinite number of heat sinks that have infinitesimally lower temperatures, the total quantity of the ‘‘potential energy” of thermal energy which can be transferred out is $Q_{vh}T/2$. Hence the ‘‘potential energy” represents the heat transfer ability of an object.

This new concept is called entransy because it possesses both the nature of ‘‘energy” and the transfer ability. This has also been referred to as the heat transport potential capacity in an earlier paper by Guo et al.[41] Biot [42] introduced a concept of thermal potential in the 1950s in his derivation of the differential conduction equation using the variation method. The thermal potential plays a role similar with the ‘potential energy’ of thermal energy here, while the variational invariant is related to the concept of dissipation function. However, Biot did not further expand on the physical meaning of the thermal potential and its application to heat transfer optimization was not found later except in approximate solutions to anisotropic conduction problems.

3.2 Entransy Dissipation and Entransy Balance Equation

For heat conduction without heat source, the thermal energy conservation equation is,

$$\rho c_v \frac{\partial T}{\partial t} = -\nabla \cdot \boldsymbol{q} \tag{19}$$

where $\boldsymbol{q}$ is the heat flux. Meanwhile there is also an accompanying entransy flux through the medium, However, the entransy, unlike the thermal energy, is not conserved due to its dissipation during the heat transfer process. Eq.(19) multiplied by the temperature, T, changes to,

$$\rho c_v T \frac{\partial T}{\partial t} = -\nabla \cdot (\boldsymbol{q} T) + \boldsymbol{q} \cdot \nabla T \tag{20}$$

The term in the left hand side of Eq. (20) is the time variation of the entransy stored per unit volume. The first term in the right hand side is the entransy transfer associated with the heat transfer while the second term is the local rate of entransy dissipation. Then, we have the entransy dissipation function,

$$\varphi_{\mathrm{G}} = -\boldsymbol{q} \cdot \nabla T = k (\nabla T)^2 \tag{21}$$

where k is the thermal conductivity and ∇T is the temperature gradient. The physical meaning of the dissipation function is the entransy dissipation per unit time and per unit volume, which resembles the dissipation function for mechanical energy in fluid flow. The entransy balance equation, Eq.(20), can then be rewritten as,

$$\frac{dg_h}{dt} = -\nabla \cdot (\dot{g}_h) + \varphi_G \tag{22}$$

where g_h is the entransy density, or the entransy per unit volume, $\dot{g}_h$ is the entransy flux.

To understand the entransy dissipation in an irreversible heat transfer process, two simple heat transfer processes are discussed as follows. Consider one-dimensional steady-state heat conduction in a plate with thickness d as shown in Fig. 9, where the input heat flux is equal to the output heat flux, q_1=q_2. However, the input entransy flux is not equal to the output entransy flux due to dissipation during the heat transport. The entransy balance equation is,

$$qT_1 = qT_2 + \int_0^d \varphi_{\mathrm{G}} dx \tag{23}$$

where,

$$\int_0^d \varphi_G dx = -\int_0^d \boldsymbol{q} \cdot \nabla \boldsymbol{T} dx = q(T_1 - T_2) \tag{24}$$

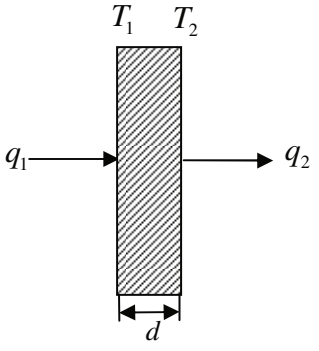

Fig. 9 1D steady heat conduction

Eq. (9) again shows that the input entransy flux is equal to the sum of the output entransy flux and the dissipated entransy per unit time and per unit volume. The entransy transfer efficiency is then,

$$\eta = \frac{\dot{g}_1 - \Phi_G}{\dot{g}_1} = \frac{qT_2}{qT_1} = \frac{T_2}{T_1} \tag{25}$$

Next discuss a transient heat conduction in a continuum. Consider two cubic objects with the same volume, mass, specific heat and thermal conductivity, as shown in Fig. 10. Their initial uniform temperatures are T_1 and T_2 with $T_1 > T_2$.

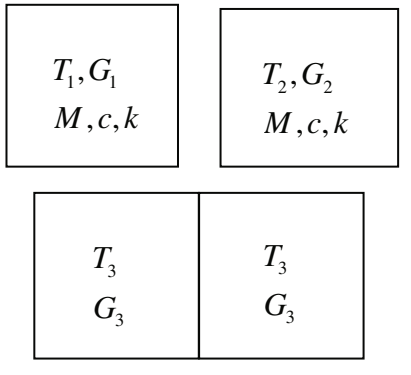

Fig. 10 Transient heat conduction between two objects

When the two objects are touched each other, heat will flow from the high temperature object to the lower temperature object. The internal resistances of the two objects induce entransy dissipation during the heat transfer process. After a sufficiently long time and if the two objects are thermally insulated from the environment, the two objects will come to an equilibrium temperature,

$$T_3 = \frac{T_1 + T_2}{2} \tag{26}$$

Before touching, the entransies in the two objects are,

$$G_1 = \frac{1}{2} Q_{h1} T_1 = \frac{1}{2} M c T_1^2 \tag{27}$$

$$G_2 = \frac{1}{2} Q_{h2} T_2 = \frac{1}{2} M c T_2^2 \tag{28}$$

After touching and equilibrium is achieved, the entransy of each object is,

$$G_3 = \frac{1}{2} Q_{h3} T_3 = \frac{1}{2} M c T_3^2 \tag{29}$$

The entransy dissipation can be obtained from the difference in entransy of two object systems at the initial and the equilibrium state,

$$\Phi_{\mathrm{G}} = G_1 + G_2 - 2G_3 = \frac{1}{4} M c \left(T_1 - T_2 \right)^2 \tag{30}$$

It is clear from Eq.(30) that the entransy dissipation is always larger than zero if the temperatures of the two objects before touching are not equal. Similar to the steady heat conduction, we have the entransy transfer efficiency from the initial state to the equilibrium state,

$$\eta = \frac{2G_3}{G_1 + G_2} = \frac{\left(T_1 + T_2 \right)^2}{2\left(T_1^2 + T_2^2 \right)} \tag{31}$$

For both the steady-state and transient cases the entransy transfer efficiency does not depend on the thermal conductivity as can be seen from Eqs. (25) and (31). However, larger temperature differences between the two objects in the transient heat conduction process result in more entransy dissipation and lower entransy transfer efficiency. Less time is needed for two objects with higher thermal conductivities to reach equilibrium when the entransy dissipation per unit time is larger. Hence, the entransy transfer efficiency between the two objects is not a function of the thermal conductivity.

3.3 Extremum Entransy Dissipation Principle

Following the definition of the entransy and the entransy dissipation in heat transfer process we will introduce the extremum entransy dissipation principle for heat transfer optimization in this section.

For simplicity consider the optimization of a steady state heat conduction problem. Cheng [29] and Cheng et al. [43] started from the differential form of the conduction equation to derive a variational statement of the heat conduction using the method of weighted residuals. They derived a minimum entransy dissipation principle for prescribed heat flux boundary conditions and a maximum entransy dissipation principle for prescribed temperature boundary conditions that are referred to as the extremum entransy dissipation principle (EED principle).

The minimum entransy dissipation principle states that for the prescribed heat flux boundary conditions, the minimum entransy dissipation rate in the domain leads to the minimum difference between the two boundary temperatures. This principle can be expressed as

$$\dot{Q}_t \delta \Delta T = \delta \iiint_V \frac{1}{2} k \left(\nabla T \right)^2 dV = 0 \tag{32}$$

where δ denotes the variation, ΔT is the temperature difference, and $\dot{Q}_t$ is the heat flow.

The maximum entransy dissipation principle states that the largest entransy dissipation rate in a domain with a prescribed temperature difference as the boundary condition leads to the maximum heat flux. This principle can be expressed as

$$\dot{Q}_t \delta \Delta T = \delta \iiint_V \frac{1}{2} k \left(\nabla T \right)^2 dV = 0 \tag{33}$$

Unlike the Biot's variational method, the present method works directly with the differential equation and boundary conditions. Furthermore, Biot's variational principle is a quasi-variational principle, as Finlayson [44,45] indicated, which applies only to the approximate solution, not necessarily to the exact solution of heat conduction. He also showed that the Euler equation developed from the theorem of minimum entropy production reduces to the heat conduction equation only when $k / T^2 = const$.

4 Optimization of Heat Conduction

4.1 Criterion of Uniform Temperature Gradient

Bejan [38, 39] developed the constructal theory of conducting paths to optimize the high conductivity material allocation so as to minimize the thermal resistance of the volume-to-point conduction, which seeks to effectively remove heat generated in a volume to a point on its surface. High conductivity material is embedded in the substrate to improve the thermal conduction. The problem is to optimize the allocation of a limited amount of high conductivity material so that the generated heat can be most effectively transported to the point to minimize the highest temperature in the domain. The material allocation in the volume-to-point conduction problem can also be optimized by using the extremum entransy dissipation principle to minimize the average temperature in the domain. Xia et al.[30], Cheng [29] and Cheng et al. [31] reported the bionic optimization of volume-to-point conduction based on the extremum entransy dissipation principle.

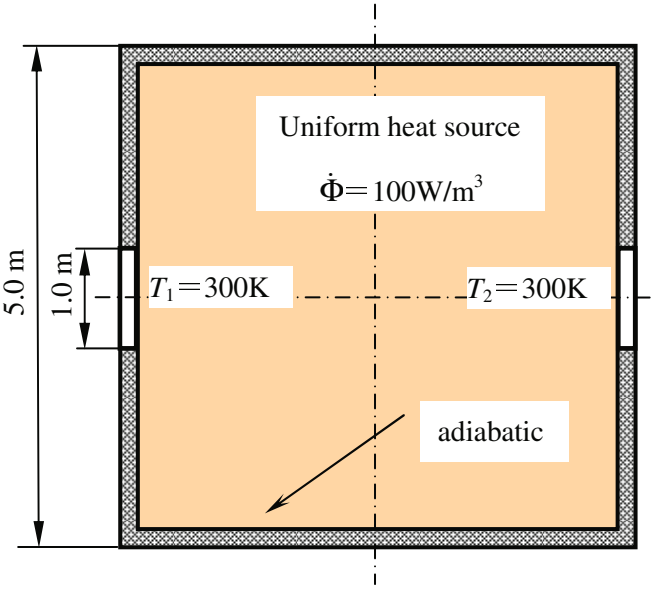

Fig. 11 Volume-to-point heat conduction problem

Fig.11 shows a typical volume-to-point heat conduction problem. In the square domain there is a uniform heat source, $\dot{\Phi}$ = 100W/m^3, the local material conductivity in the domain may vary continuously but the volume-averaged conductivity is kept at 1W/(m·K). Two small symmetric heat flow outlets with

uniform temperature of 300 K are located on the boundary with other boundaries adiabatic. The problem is to find the optimal thermal conductivity distribution which leads to a lowest average temperature in the domain.

The total heat flow rate through the two outlets is equal to the heat delivered from a uniform heat source in the domain per unit time,

$$Q_t = \iiint_V \dot{\Phi} dV \tag{34}$$

The average temperature in the domain is,

$$T_m = \frac{1}{Q_t} \iiint_V \dot{\Phi} T dV \tag{35}$$

According to the minimum entransy dissipation principle, Eq.(32) for the prescribed heat flow rate at the boundary (note: hear the heat flow rate is equal to the total heat source in the domain, the outlet temperature is fixed, we want to find the minimum average temperature of the domain, so as to obtain the minimum temperature difference for heat conduction), we have,

$$\delta \iiint_V \dot{\Phi} T dV = Q_t \delta T_m = \delta \iiint_V \frac{1}{2} k \left(\nabla T \right)^2 dV = 0 \tag{36}$$

with the constraint,

$$\iiint_V k dV = Const \tag{37}$$

For the above optimization problem, the following functional can be constructed,

$$J = \iiint_V \left[\frac{1}{2} k (\nabla T)^2 + \lambda_1 k \right] dV \tag{38}$$

where λ_1 is a Lagrange multiplier, which is a constant. By making the variation of the functional, *J*, with respect to temperature, equal to zero, then

$$\iint_A k \nabla T \delta T \cdot \mathbf{n} dA - \iiint_V \nabla \cdot \left(k \nabla T \right) \delta T dV = 0 \tag{39}$$

Due to the boundaries either adiabatic or isotherm, so,

$$\iint_A k \nabla T \delta T \cdot \mathbf{n} dA = 0 \tag{40}$$

For the case of the lowest average temperature,

$$\delta \iiint_V \dot{\Phi} T dV = \iiint_V \dot{\Phi} \delta T dV = 0 \tag{41}$$

By instituting Eq.(40) and Eq.41) into Eq.(39), we have,

$$\iiint_V \left(\nabla \cdot \left(k \nabla T \right) + \dot{\Phi} \right) \delta T dV = 0 \tag{42}$$

Therefore, we have the stagnation condition of the variation of the functional J with respect to temperature (steady heat conduction equation),

$$\nabla \cdot \left(k \nabla T \right) + \dot{\Phi} = 0 \tag{43}$$

Making the variation of the functional, J, with respect to thermal conductivity gives,

$$\left(\nabla T \right)^2 = -2\lambda_1 \tag{44}$$

This equation demonstrates that the temperature gradient in the domain should be uniform to minimize the entransy dissipation, and consequently to obtain the lowest average temperature in the domain. This is called the uniform temperature gradient criterion for heat conduction optimization. Using Fourier's law Eq. (43) can also be written as the constant ratio of the local heat flux to the local thermal conductivity over the domain for the best performance of volume-to-point heat conduction, This implies that the large conductivity should be put on the place where the heat flux is large.

4.2 Optimization of Volume-to-Point Problem

The volume-to-point problem, shown in Fig.11, can be optimized numerically by rearranging the local thermal conductivity according to the criterion of uniform temperature gradient obtained based on the extremum entransy dissipation principle. The numerical procedure for finding the optimum distribution of thermal conductivity is as follow.

(1) initially fill the domain with a uniformly distributed thermal conductivity,
(2) solve the differential conduction equation to obtain the temperature field and heat flux field,
(3) calculate the new thermal conductivity distribution using the following equation:

$$k_{n+1}(x,y,z)=\frac{\left|q_n(x,y,z)\right|}{\iiint_V \left|q_n(x,y,z)\right|dV}\cdot\iiint_V k_n(x,y,z)dV$$
$$=\frac{\left|-k_n(x,y,z)\nabla T\right|}{\iiint_V -k_n(x,y,z)\nabla T dV}\cdot\iiint_V k_n(x,y,z)dV \tag{45}$$

(4) return to step (2) to recalculate the temperature and heat flux fields until the following converging criterion is satisfied at each location,

$$\left(k_{n+1}(x,y,z)-k_n(x,y,z)\right)/k_{n+1}(x,y,z)<\varepsilon \tag{46}$$

where ε is a positive value that is much less than unity.

The temperature field before optimization (uniform thermal conductivity) is shown in Fig. 12, where the average temperature is 1005.1K. The optimized thermal conductivity distribution and temperature distribution are shown in Fig.13 and Fig.14 respectively. The larger thermal conductivity locates on the neighborhood of heat flow outlets, where the heat flux is larger. The average temperature after optimization is about 584.2 K. It is much lower than the value of 1005.1 K before optimization, and the temperature gradient in the domain is nearly uniform, as shown in Fig.14.

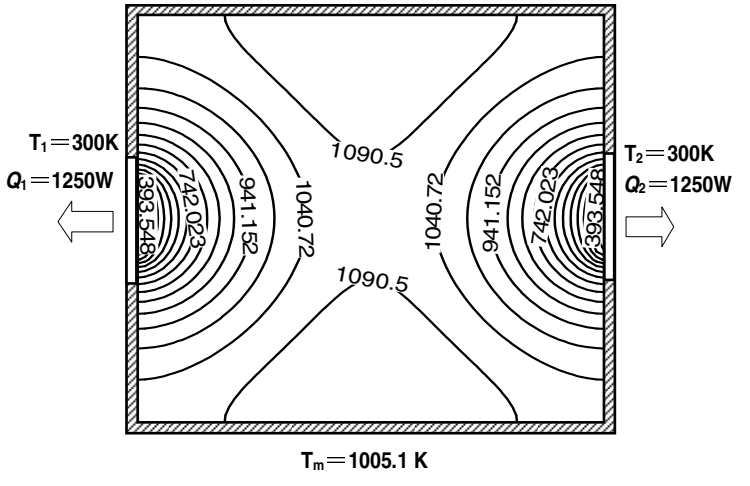

Fig. 12 Temperature distribution in the square domain with uniform thermal conductivity

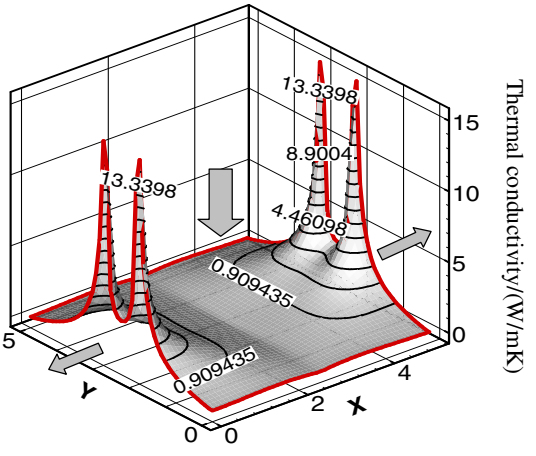

Fig. 13 Thermal conductivity distribution after optimization

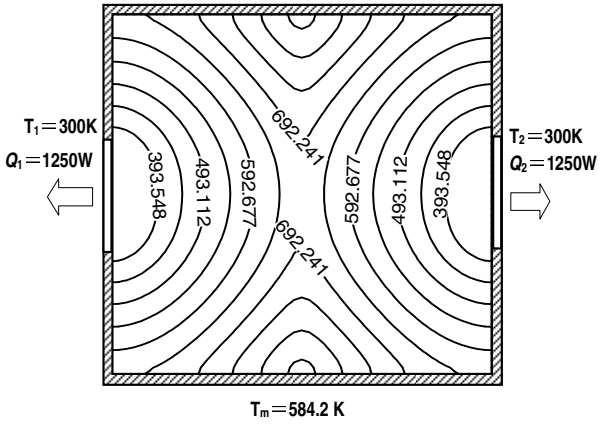

Fig. 14 Temperature distribution after optimization

In the following we discuss the optimization of a thermally asymmetric volume-to-point problem, that is, the two heat flow outlets are at different temperatures of 200 K and 300 K respectively, as shown in Fig.15. The other parameters are same as that in Fig.11. This problem was optimized numerically by performing the same procedure for symmetric problem. The optimal distribution of the thermal conductivity and temperature distribution are shown in Fig.16 and Fig.17 respectively.

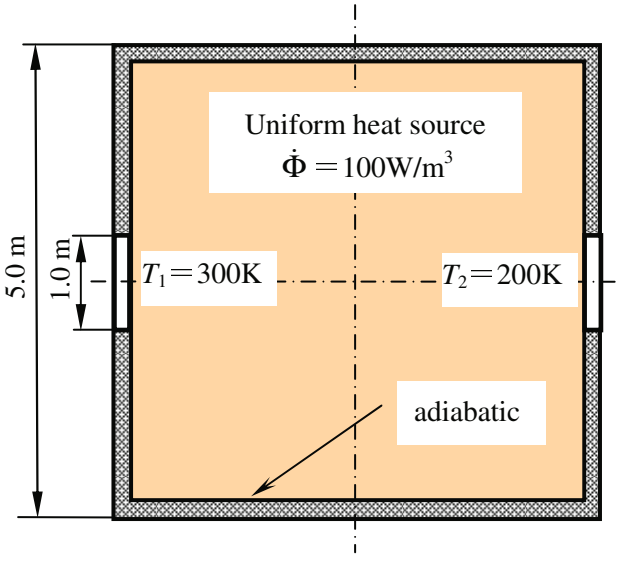

Fig. 15 Thermally asymmetric volume-to-point problem

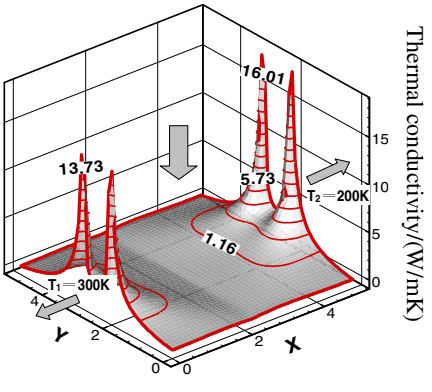

Fig. 16 Optimal thermal conductivity distribution of the thermally asymmetric volume-to-point problem

Fig.16 shows that the thermal conductivity is no longer distributed symmetrically and the heat flow rate at the low temperature outlet is relative larger. The average temperature after optimization is about 532.9 K, which is much lower than the value of 955.1 K before optimization. The temperature gradient in the

domain after optimization becomes uniform although the heat flow rates at two outlets are different, as shown in Fig.17.

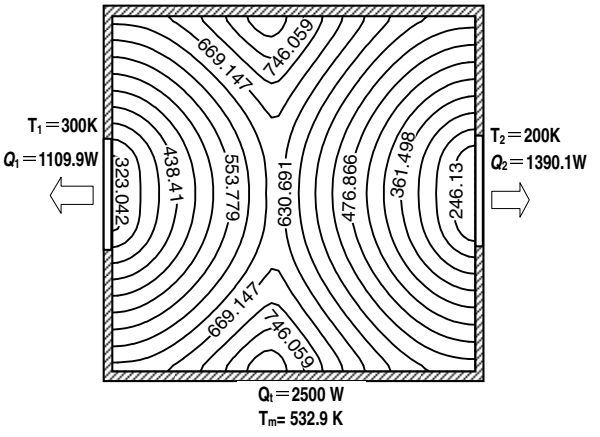

Fig. 17 Optimal temperature distribution of the thermally asymmetric volume-to-point problem

4.3 Comparison between EED Principle and MEG Principle

To further understand the difference between the extremum entransy dissipation (EED) principle and the minimum entropy generation (MEG) principle the optimization effects of heat conduction based on these two different principles are compared. For the symmetric volume-to-point problem shown in Fig. 11, the entropy generation rate during heat conduction equals to the difference between the entropy flow delivered from heat source and the entropy flow out from the two outlets,

$$\dot{S}_g = -\iiint_V \frac{\dot{\Phi}}{T} dV - \iint_A \frac{\boldsymbol{q}}{T} \cdot \mathbf{n} dA = \iint_{A_1} \frac{Q_1}{T_1} dA + \iint_{A_2} \frac{Q_2}{T_2} dA - Q_t \left(\frac{1}{T} \right)_m \tag{47}$$

where $\left(1/T\right)_m$ is the average value of $1/T$ in the domain. Because all the heat flow delivered from the heat source must goes through the isotherm boundary at 300 K, the total entropy flow through the two outlets is,

$$\iint_{A_1} \frac{Q_1}{T_1} dA + \iint_{A_2} \frac{Q_2}{T_2} dA = \dot{\Phi} V / T = const = 8.33 \text{ W/K} \tag{48}$$

The substitution of Eq.(48) into Eq.(47) yields

$$\dot{S}_g = const - Q_t\left(\frac{1}{T}\right)_m = 8.33 - 2500\left(\frac{1}{T}\right)_m \tag{49}$$

Eq.(16) indicates that the entropy generation is independent of the outlet temperature, and hence, the minimum entropy generation corresponds to the maximum average value of 1/T in the domain, which is approximately equal to the lowest average temperature, T, corresponding to the minimum entransy dissipation. Therefore, the optimal results given by EED principle and by MEG principle are close to each other for a symmetric volume-to-point problem.

For a thermally asymmetric volume-to-point problem, as shown in Fig.15, the entropy flows through the two outlets are different. Eq.(47) divided by the total heat flow leads to,

$$\frac{\dot{S}_g}{Q_t} = \iint_{A_1}\frac{1}{T_1}\frac{Q_1}{Q_t}dA + \iint_{A_2}\frac{1}{T_2}\frac{Q_2}{Q_t}dA - \left(\frac{1}{T}\right)_m \tag{50}$$

It can be seen in Eq.(50) that the entropy generation rate per unit heat flow depends not only on the average value of 1/T, but also on the difference in heat flow and consequently in temperature between two outlets. The entropy flow through the two outlets can be expressed as,

$$\iint_{A_1}\frac{Q_1}{T_1}dA + \iint_{A_2}\frac{Q_2}{T_2}dA = \iint_{A_1+A_2}\frac{Q_t}{T_1}dA + \iint_{A_2}Q_2\left(\frac{T_1-T_2}{T_2T_1}\right)dA \tag{51}$$

Substituting Eq.(18) into Eq.(50) gives

$$\frac{\dot{S}_g}{Q_t} = \iint_{A_1+A_2}\frac{Q_t}{T_1}dA + \iint_{A_2}Q_2\left(\frac{T_1-T_2}{T_2T_1}\right)dA - \left(\frac{1}{T}\right)_m \tag{52}$$

This implies that the minimum entropy generation rate corresponds no longer to the lowest average temperature in the domain, because the additional term $(T_1-T_2)/T_1T_2$ and Q_2 varies with the thermal conductivity distribution.

If $(T_1-T_2) \ll T_1T_2$, we then have

$$\iint_{A_1}\frac{Q_1}{T_1}dA + \iint_{A_2}\frac{Q_2}{T_2}dA \approx \iint_{A_1+A_2}\frac{Q_t}{T_1}dA = Const \tag{53}$$

so Eq.(17) can be simplified as

$$\dot{S}_g = Const - Q_t \left(\frac{1}{T} \right)_m \tag{54}$$

which is identified with Eq.(49).

To validate the above analysis, the numerical calculations for the optimization of volume-to-point problems are performed based on the MEG principle, and the results are compared with those given by the EED principle.

For the above optimization problem, we construct the following functional,

$$J = \frac{k(\nabla T)^2}{T^2} + \lambda_1 k + \lambda_2 \left[\nabla \cdot (k \nabla T) + \dot{\Phi} \right] \tag{55}$$

where λ_1 and λ_2 are the Lagrange multipliers, λ_1 is a constant. By making the variation of the functional, J, with respect to temperature and thermal conductivity, equal to zero, then

$$-\nabla \cdot (k \nabla \lambda_2) = \frac{2k(\nabla T)^2}{T^3} + \frac{2\dot{\Phi}}{T^2} \tag{56}$$

$$\frac{(\nabla T)^2}{T^2} + \lambda_1 - \nabla \lambda_2 \cdot \nabla T = 0 \tag{57}$$

The natural boundary conditions are: $\delta T = 0$, $\lambda_2 = 0$ for the case of isotherm boundary, and $\delta q = 0$, $k \nabla \lambda_2 = \frac{2k \nabla T}{T^2}$, for the constant heat flux boundary. Eq. (23) and the natural boundary conditions are used to identify the Lagrange multiplier λ_2, while Eq.(57) is the control equation of thermal conductivity for optimization.

The numerical procedure for finding the optimum distribution of thermal conductivity is as follow.

(1) initially fill the domain with a uniformly distributed thermal conductivity;
(2) solve the differential conduction equation to obtain the temperature field and heat flux field,

(3) solve Eq. (56) to obtain the distribution of λ_2 in the domain,
(4) solving thermal conductivity distribution based on the following equation,

$$k_{n+1}(x,y,z)=k_n(x,y,z)\left[\frac{(\nabla T)^2}{T^2}-\nabla\lambda_2\cdot\nabla T\right]\frac{\iiint_V k_0(x,y,z)dV}{\iiint_V k'_{n+1}(x,y,z)dV} \tag{58}$$

(5) return to step (2) to recalculate the temperature field, heat flux fields and λ_2 until the following converging criterion is satisfied at each location,

$$\left(k_{n+1}(x,y,z)-k_n(x,y,z)\right)/k_{n+1}(x,y,z)<\varepsilon \tag{59}$$

where ε is a positive value that is much less than unity.

For comparison, the optimal thermal conductivity distributions and the optimal temperature distributions for the symmetric volume-to-point problem based on the MEG principle and the EED principle are plotted in Fig.18 and Fig.19 respectively.

It is seen from Fig.18 and Fig.19 that though the optimal thermal conductivity distribution and temperature field based on two different optimization principles are similar, little difference can still be observed because of their different optimization objects, one is the lowest average temperature for EED principle and another is the maximum value of 1/*T* for MEG principle.

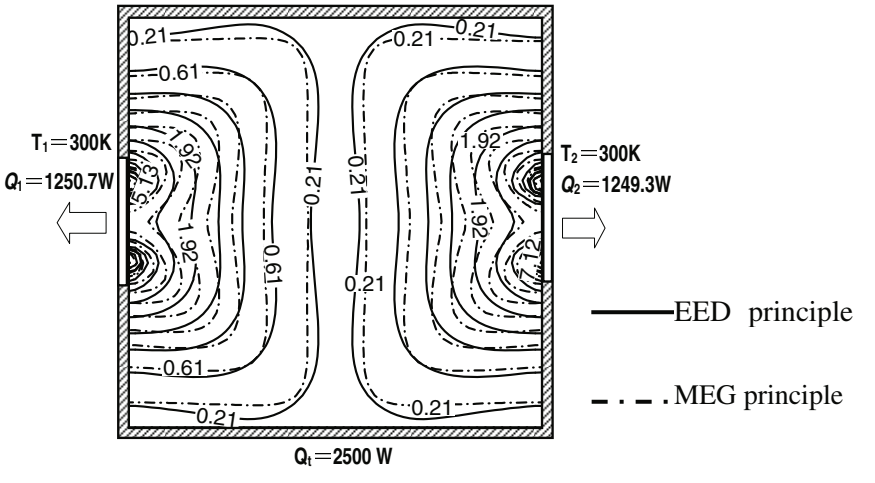

Fig. 18 The optimal thermal conductivity distribution

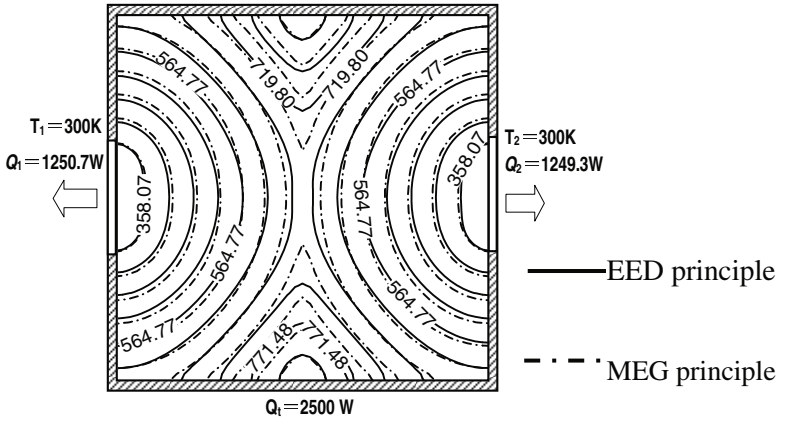

Fig. 19 The optimal temperature field

The average temperatures in the domain after optimization based on the MEG principle and EED principle are listed in table 2. It is seen that the difference of average temperature is very small.

Table 2 Domain average temperature after optimization for the symmetric problem

$T_1 = T_2 = 300K$	MEG principle	EED principle
Average temperature (K)	587.1	584.2

For the optimization of asymmetric volume-to-point problem, the optimal thermal conductivity distributions based on MEG principle and EED principle are shown in Fig.20 and Fig.21 respectively.

It can be seen from Fig.20 and Fig.21 that the results are much different from those of the symmetry case. Fig.20 shows that high thermal conductivity locates at the two outlets, and higher thermal conductivity is located at the higher temperature outlet. Fig.21 shows the result of high thermal conductivity locating at the two outlets, but higher thermal conductivity is located at the lower temperature outlet, which is opposite to the result given by the MEG principle.

The average temperatures in the domain of the asymmetric problem based on the MEG principle and EED principle are listed in Table 3. It is seen that the difference of average temperature becomes larger compared with the case of symmetric problem. Such difference in the domain average temperature increases rapidly with enlarging the increment of temperature difference between the two outlets, as shown in Fig.22.

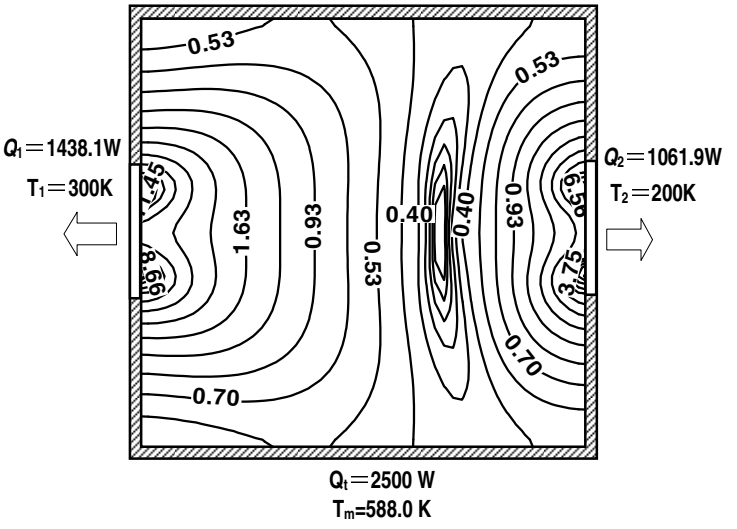

Fig. 20 Optimal thermal conductivity distribution obtained by MEG principle

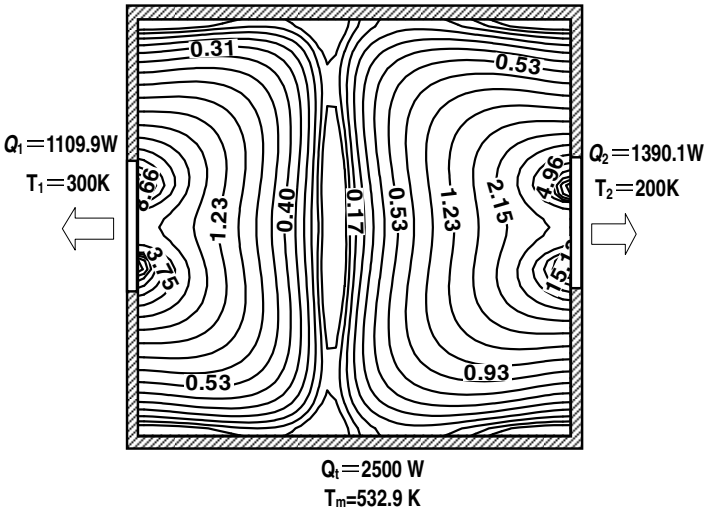

Fig. 21 Optimal thermal conductivity distribution obtained by EED principle

Table 3 Domain average temperature after optimization for the asymmetric problem

$T_1 = 300K, T_2 = 200K$	MEG principle	EED principle
Average temperature (K)	588.0	532.9

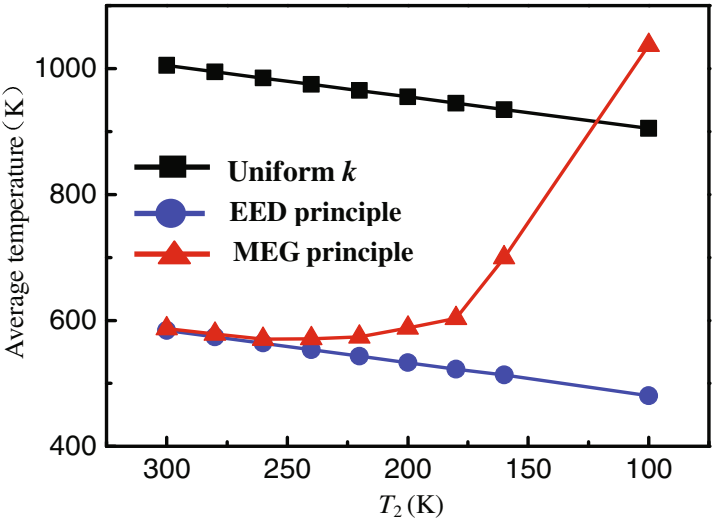

Fig. 22 The domain average temperatures before and after optimization based on the EED and MEG principles versus the lower outlet temperature

Fig.22 shows that the average temperatures are largely reduced after optimization according to either the EED or MEG principles for the case of $T_1 = T_2 = 300K$. However, the average temperatures after optimization according to the MEG principle do not decrease as T_2 is much less than T_1. This indicates that the EED principle is more preferable than the MEG principle for heat conduction optimization with the purpose of the reduction of the domain temperature.

5 Optimization of Convective Heat Transfer

Compared with heat conduction, the optimization of convective heat transfer is more complicated because two coupled irreversible processes, heat transfer and momentum transfer, occur simultaneously during heat convection. In the following we will hence focus on the optimization of heat convection with a goal to find the optimal velocity distribution for maximizing the heat transfer rate under the prescribed flow rate and the pumping power. This is a typical functional extremum problem.

5.1 Field Synergy Equation for Laminar Convection

Xia [46] and Meng [47] investigated such a functional problem in terms of variation principle and derived a field synergy equation which the optimal velocity

distribution should meet. According the extremum entransy dissipation principle the optimization criterion for heat convection is that the entransy dissipation rate in the whole domain Ω should be extremum,

$$\delta\Phi_{\mathrm{G}}=0 \tag{60}$$

where

$$\Phi_{\mathrm{G}}=\frac{1}{2}\int_{\Omega}k\left(\nabla T\right)^{2}\mathrm{d}V \tag{61}$$

There are some kinds of constraints for the heat convection optimization. The first is the fixed pumping power,

$$J_{\Phi}=\int_{\Omega}\Phi dV \tag{62}$$

where

$$\Phi=\mu\left[2\left(\frac{\partial u}{\partial x}\right)^{2}+2\left(\frac{\partial v}{\partial y}\right)^{2}+2\left(\frac{\partial w}{\partial z}\right)^{2}+\left(\frac{\partial u}{\partial y}+\frac{\partial v}{\partial x}\right)^{2}+\left(\frac{\partial u}{\partial z}+\frac{\partial w}{\partial x}\right)^{2}+\left(\frac{\partial v}{\partial z}+\frac{\partial w}{\partial y}\right)^{2}\right] \tag{63}$$

is the mechanical power dissipated by the fluid viscosity per unit volume and *u, v*, and *w* are the velocity components in *x, y, z*- axis respectively.

The second one is the boundary conditions,

$$\delta U\big|_{in}=0\text{, for prescribed flow rate} \tag{64}$$

$$\delta T\big|_{w}=0\text{, for the uniform wall temperature} \tag{65}$$

$$\text{or } \delta(k\nabla T)\big|_{w}=0 \text{ for the uniform heat flux} \tag{66}$$

The third includs the continuity equation,

$$\nabla\cdot\left(\rho U\right)=0 \tag{67}$$

and the energy equation,

$$\nabla\cdot\left(k\nabla T-\rho c_{p}UT\right)=0 \tag{68}$$

To get the optimal flow field, it needs to construct a Lagrange function which includes the optimization criterion and constraints as follow,

$$J = \int_{\Omega} \{ \frac{1}{2} k \left(\nabla T \right)^2 + \lambda_1 \Phi + A \left(k \nabla^2 T - \rho c_p U \cdot \nabla T \right) + \lambda_2 \nabla \cdot U \} dV \quad (69)$$

where A, λ_1, λ_2 are Lagrange multipliers, λ_1 is a constant, A and λ_2 are functions of *U, T*, and the position. Through the variation calculus of *J* with respect to temperature, *T,* and velocity, *U*, then we have,

$$\begin{aligned} &\int_{\Omega} \left(k \nabla^2 A + \rho c_p U \cdot \nabla A - k \nabla^2 T \right) \delta T dV \\ &+ \int_{\Gamma} \{ [k \nabla T - \left(k \nabla A + \rho c_p U A \right)] \delta T + A \delta \nabla T \} d\vec{S} = 0 \end{aligned} \quad (70)$$

and,

$$\int_{\Omega} \left(-2\lambda_1 \mu \nabla^2 U - \rho A \nabla T - \nabla \lambda_2 \right) \delta U dV + \int_{\Gamma} (2\lambda_1 P + \lambda_2) \delta U \cdot d\vec{S} = 0 \quad (71)$$

Due to the arbitrary value of δT and δU, the following governing equation and boundary conditions can be obtained,

$$-\rho c_p U \cdot \nabla A = k \nabla^2 A - k \nabla^2 T \quad (72)$$

$$\int_{\Gamma} \{ [k \nabla T - \left(k \nabla A + \rho c_p U A \right)] \delta T + A \delta \nabla T \} d\vec{S} = 0 \quad (73)$$

$$\mu \nabla^2 U + \frac{\rho}{2\lambda_1} A \nabla T + \frac{\nabla \lambda_2}{2\lambda_1} = 0 \quad (74)$$

$$\int_{\Gamma} (2\lambda_1 P + \lambda_2) \delta U \cdot d\vec{S} = 0 \quad (75)$$

According to the generalized variation principle [48], λ_2 in Eqs. (74) and (75) can be taken as follows,

$$\lambda_2 = -2\lambda_1 P \quad (76)$$

where *P* is the pressure. Then Eq. (74) can be rewritten as,

$$\mu \nabla^2 U - \rho U \cdot \nabla U - \nabla P + \left(C_{\Phi} A \nabla T + \rho U \cdot \nabla U \right) = 0 \quad (77)$$

Eq. (77) is similar to the momentum equation (Navier–Stokes equation), with an additional force,

$$F = (\rho c_p / 2\lambda_1) A\nabla T + \rho U \cdot \nabla U = C_\Phi A\nabla T + \rho U \cdot \nabla U \tag{78}$$

where constant $C_\Phi = \dfrac{\rho c_p}{2\lambda_1}$ is related to the given pumping power, and A satisfies Eq. (72) and boundary condition (73).

The velocity field satisfying Eq. (77) is the optimal velocity field which maximizes the heat transfer rate for heat convection. In other words, any deviation from such velocity field will deteriorate the heat transfer performance. Since the optimum velocity field corresponds to the largest field synergy number for convective heat transfer, Eq.(77) and the additional force in it are named as the field synergy equation and the synergy force respectively. The role of the synergy force is to promote the fluid to flow along the direction of the temperature gradient for the improvement of the field synergy degree.

It should be pointed out that the synergy force in the field synergy equation, which should be applied on the fluid from outside to form an optimal velocity field, is a complicated function of the velocity and temperature fields and can't be realized exactly in practice. However, the performance of heat transfer can be remarkably improved even though the flow field produced by an enhancement element is close only to the optimum velocity field.

5.2 Optimal Flow Patterns of Laminar Convection

5.2.1 Optimal Flow Pattern in Square Cavity

Consider the convection in a square cavity, as shown in Fig.23. The left and right side walls are isothermal at 300 K and 310 K respectively, the up and bottom walls are adiabatic. The natural convection occurs in the cavity. To enhance the heat transfer, in general, one can install a stirrer to produce a vortex flow in the square cavity. Meng [47] and Meng et al.[49] obtained the optimal flow patterns for the laminar convection in such a square cavity by solving the field synergy equation.

Different from the general governing equations, the synergy equation has multi-solutions depending on the initial flow fields. Fig. 24 shows the numerical results for C_Φ=-0.02 Pa/K^2.

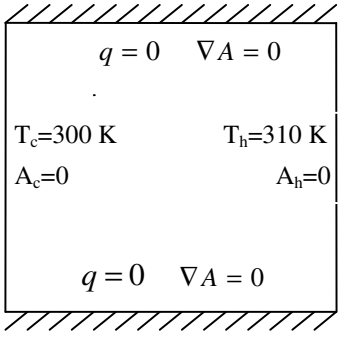

Fig. 23 Physical model of convection in a square cavity

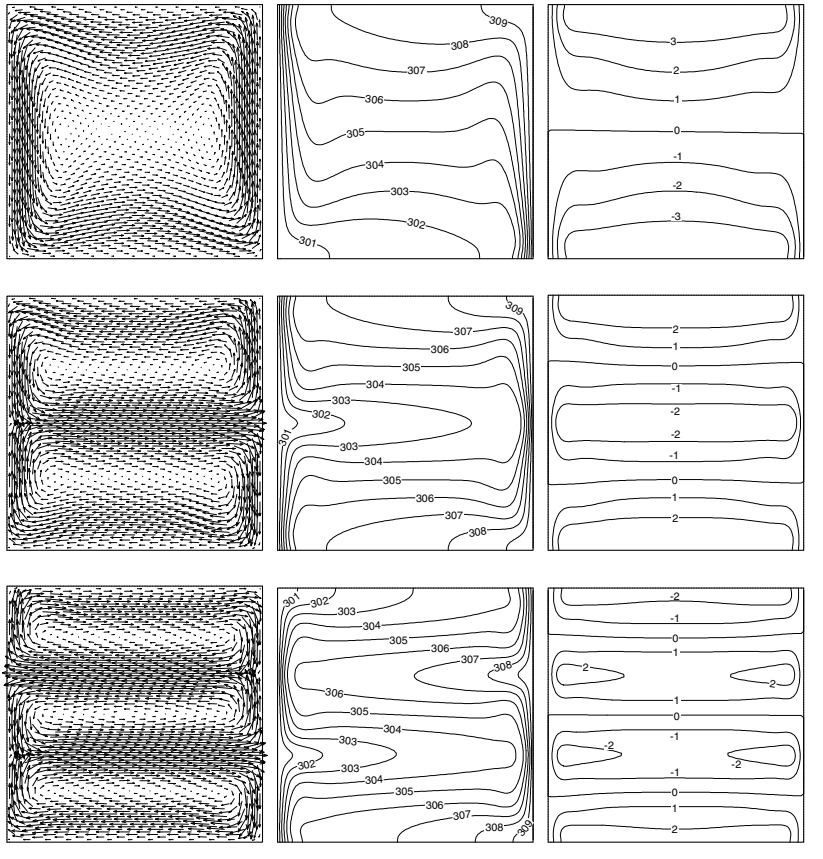

(a) velocity (b) temperature (c) Parameter A

Fig. 24 Multi solutions of the optimized velocity, temperature and parameter A for laminar convection in a square cavity ($C_{\Phi} = -0.02$ Pa/K^2)

The variations of Nusselt numbers with the viscous dissipation related parameter C_Φ for different vortex flow patterns are given in Fig.25. The Nusselt number is defined by,

$$\mathrm{Nu} = \frac{qL}{k\left(T_h - T_c\right)} \tag{79}$$

where q is the heat flux, L is the side length of the square, k is the fluid thermal conductivity. Fig.25 shows that the Nusselt numbers are different when the flow is of different number of vortex for the given mechanical work. The optimal flow field relates to the largest Nusselt number. If the viscous dissipation rate , J_Φ=3×10^{-5} W/m^3 is specified, for example, two vortex flow field is the optimal flow pattern, that is, the Nusselt number for the two vortex flow field is larger than that for other flow patterns. The vortex number of the optimal flow field increases with the increasing of given mechanical work input. The numerical results in Nusselt numbers are re-plotted in Fig. 26 to show that the optimal flow pattern is different for the different given mechanical work.

It should be noted once again that the optimal flow field obtained by solving the velocity field synergy equation is an idealized flow field. Some stirrers can be used to generate a flow field only close to the optimal flow field.

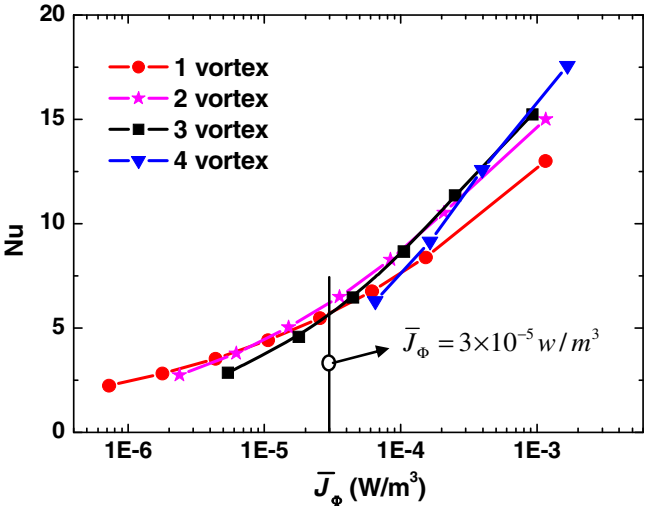

Fig. 25 Nusselt numbers versus viscous dissipation with vortex number as parameter

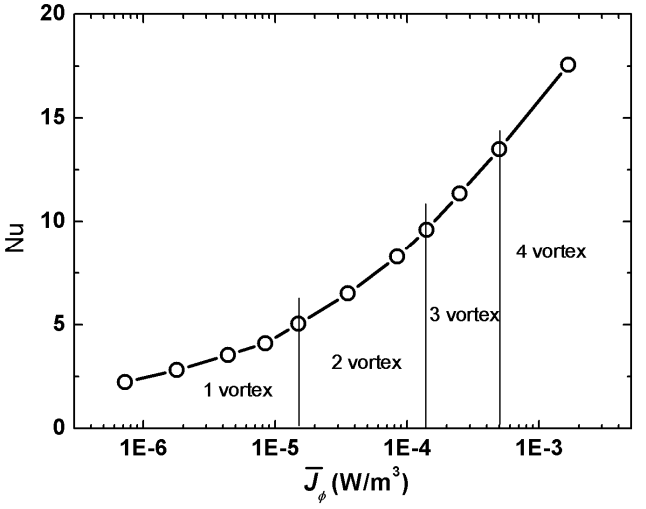

Fig. 26 Nusselt number versus viscous dissipation with the optimal flow patterns

5.2.2 Optimal Flow Pattern in Circular Tube

Circular tubes are commonly used as heat transfer elements in tube-shell heat exchangers. The optimal flow pattern of laminar convective heat transfer in circular tube was obtained by solving the field synergy equation under a certain flow and thermal boundary conditions [47, 49]. A straight isothermal circular tube with 20mm in diameter and 30mm in length is selected for numerical simulation with both the flow and heat transfer fully developed. The wall temperature is 310K and the average fluid temperature at the inlet is 300K.

Different values of C_{Φ} taken in the calculations result in different optimal flow patterns. The optimal flow behaves four longitudinal vortexes in the cross-section when C_{Φ} is small. The number of the longitudinal vortexes increases from four to eight for the optimal flow when C_{Φ} is larger than a certain value as demonstrated in Fig. 27. Compared to the fully-developed laminar convection heat transfer in circular tubes (fRe=64,Nu=3.66), the heat transfer rate (the Nusselt number) is increased by 313%, while the pumping power is increased by 17% only.

5.2.3 Optimal Flow Pattern in an Elliptical Tube

A straight elliptical tube with 15 mm in long axis and 10 mm in short axis is selected for numerical simulation to obtain the optimal flow pattern of laminar convection [47]. Both the flow and heat transfer are assumed to be fully developed and the tube wall is isothermal. The working fluid is water. The wall temperature is 310K, the

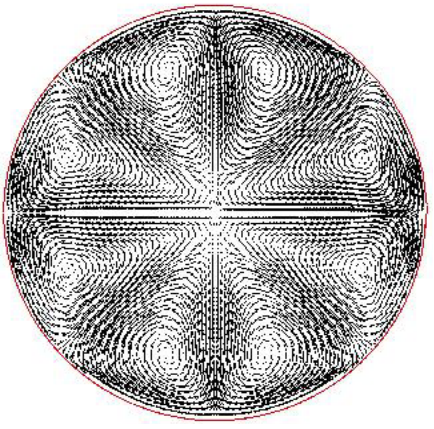

Fig. 27 Optimal flow field of laminar convection heat transfer in circular tube

Reynolds number is 400. Same as that in circular tube, the calculation for different given C_Φ results in different optimal flow patterns as shown in Fig.28.

Compared with the fully developed laminar convection in circular tube, for the 4 vortices flow pattern as shown in Fig.28 (a), the Nusselt number is three times increased for the optimized flow field, while the pumping power increases by 11.5% only. For the 8 vortices flow pattern shown in Fig.28(b), the Nusselt number is 4.5 times increased, while the pumping power increases by 21.9% only.

5.3 Field Synergy Equation for Turbulent Convection

Turbulent convection occurs more often in engineering compared with laminar convection. Based on the previous works, Chen [50] and Chen et al.[51] obtained the velocity field synergy equation for turbulent convection optimization by using the EED principle, in which the zero-equation turbulence model was adopted. For turbulent convection, the entransy dissipation is defined as,

$$\Phi_{\mathrm{G}} = k_{eff} \nabla T \cdot \nabla T \,. \tag{80}$$

where k_{eff} is the effective thermal conductivity, which contains the fluid thermal conductivity and turbulent thermal conductivity resulted from turbulent fluctuation. Similar to the analysis of laminar convection optimization, a Lagrange function can be constructed as,

$$J = \int_\Omega \left[k_{eff} \nabla T \cdot \nabla T + \lambda_1 \Phi + A\left(\nabla \cdot \left(k_{eff} \nabla T \right) - \rho c_p \vec{U} \cdot \nabla T \right) + \lambda_2 \nabla \cdot \vec{U} \right] dV \,, \tag{81}$$

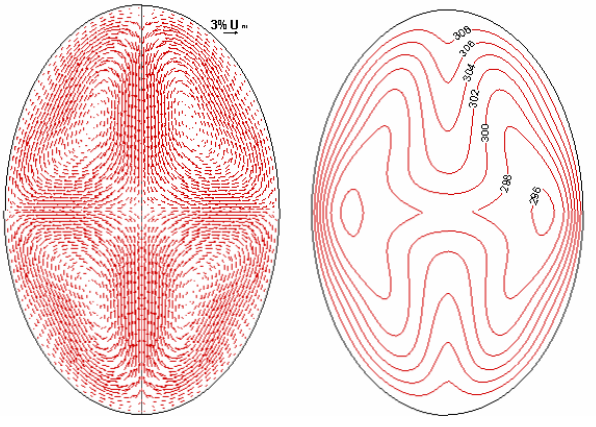

(a) Four vortices flow pattern and temperature field （C_{Φ} = -0.01 Pa/K^2)

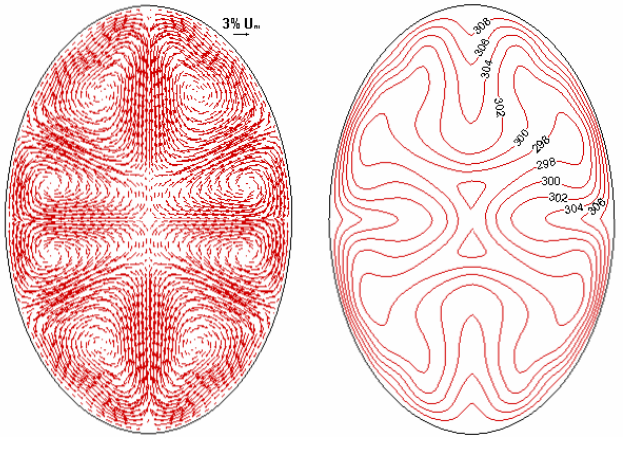

(b) Eight vortices flow pattern and temperature field （C_{Φ} = -0.02 Pa/K^2)

Fig. 28 Optimal flow and temperature fields for laminar convection heat transfer in an elliptical tube

where A, λ_1, λ_2 are Lagrange multipliers, λ_1 is required to be constant, *A* and λ_2 are functions of *U, T*, and the position. The viscous dissipation function is,

$$\Phi = \mu_{eff}\left[\begin{array}{l} 2\left(\frac{\partial u}{\partial x}\right)^2 + 2\left(\frac{\partial v}{\partial y}\right)^2 + 2\left(\frac{\partial w}{\partial z}\right)^2 \\ +\left(\frac{\partial u}{\partial y}+\frac{\partial v}{\partial x}\right)^2 + \left(\frac{\partial u}{\partial z}+\frac{\partial w}{\partial x}\right)^2 + \left(\frac{\partial v}{\partial z}+\frac{\partial w}{\partial y}\right)^2 \end{array}\right]. \tag{82}$$

where *u,v,w* are the time-averaged velocity components in *x,y,z* directions respectively. By the variation calculus of *J* with respect to temperature, *T,* there is,

$$-\rho c_p \boldsymbol{U}\cdot\nabla A = \nabla\cdot\left(k_{eff}\nabla A\right) - 2\nabla\cdot\left(k_{eff}\nabla T\right). \tag{83}$$

By the variation calculus of *J* with respect to *u,v, w,* there are,

$$\begin{aligned} &\frac{\rho c_p A}{2\lambda_1}\frac{\partial T}{\partial x} + \nabla\cdot\left(\mu_{eff}\nabla u\right) + \frac{1}{2\lambda_1}\frac{\partial \lambda_2}{\partial x} - \frac{\Gamma u}{2\lambda_1 \mathrm{Pr}_t}\left(\left|\nabla T\right|^2 + A\nabla\cdot\left(\nabla T\right)\right) - \frac{\Phi\Gamma u}{2\mu_{eff}} \\ &-\frac{A\Gamma}{2\lambda_1 \mathrm{Pr}_t}\frac{\partial T}{\partial x}\left[\frac{u}{l}\frac{\partial l}{\partial x} - \left(u\frac{\partial u}{\partial x}+v\frac{\partial v}{\partial x}+w\frac{\partial w}{\partial x}\right)\left|\overline{\boldsymbol{U}}\right|^{-2}u + \frac{\partial u}{\partial x}\right] \\ &-\frac{A\Gamma}{2\lambda_1 \mathrm{Pr}_t}\frac{\partial T}{\partial y}\left[\frac{u}{l}\frac{\partial l}{\partial y} - \left(u\frac{\partial u}{\partial y}+v\frac{\partial v}{\partial y}+w\frac{\partial w}{\partial y}\right)\left|\overline{\boldsymbol{U}}\right|^{-2}u + \frac{\partial u}{\partial y}\right] \\ &-\frac{A\Gamma}{2\lambda_1 \mathrm{Pr}_t}\frac{\partial T}{\partial z}\left[\frac{u}{l}\frac{\partial l}{\partial z} - \left(u\frac{\partial u}{\partial z}+v\frac{\partial v}{\partial z}+w\frac{\partial w}{\partial z}\right)\left|\overline{\boldsymbol{U}}\right|^{-2}u + \frac{\partial u}{\partial z}\right] \\ &+\left(\frac{\partial \mu_{eff}}{\partial x}\frac{\partial u}{\partial x} + \frac{\partial \mu_{eff}}{\partial y}\frac{\partial v}{\partial x} + \frac{\partial \mu_{eff}}{\partial z}\frac{\partial w}{\partial x}\right) \\ &+\frac{1}{2\lambda_1}\left[\frac{\partial}{\partial x}\left(\frac{A\Gamma u}{\mathrm{Pr}_t}\frac{\partial T}{\partial x}\right) + \frac{\partial}{\partial y}\left(\frac{A\Gamma u}{\mathrm{Pr}_t}\frac{\partial T}{\partial y}\right) + \frac{\partial}{\partial z}\left(\frac{A\Gamma u}{\mathrm{Pr}_t}\frac{\partial T}{\partial z}\right)\right] = 0 \end{aligned} \tag{84a}$$

$$\begin{aligned}
&\frac{\rho c_p A}{2\lambda_1}\frac{\partial T}{\partial y}+\nabla\cdot\left(\mu_{eff}\nabla v\right)+\frac{1}{2\lambda_1}\frac{\partial \lambda_2}{\partial y}-\frac{\Gamma v}{2\lambda_1 \mathrm{Pr}_t}\left(\left|\nabla T\right|^2+A\nabla\cdot\left(\nabla T\right)\right)-\frac{\Phi\Gamma v}{2\mu_{eff}}\\
&-\frac{A\Gamma}{2\lambda_1 \mathrm{Pr}_t}\frac{\partial T}{\partial x}\left[\frac{v}{l}\frac{\partial l}{\partial x}-\left(u\frac{\partial u}{\partial x}+v\frac{\partial v}{\partial x}+w\frac{\partial w}{\partial x}\right)\left|\overline{\boldsymbol{U}}\right|^{-2}v+\frac{\partial v}{\partial x}\right]\\
&-\frac{A\Gamma}{2\lambda_1 \mathrm{Pr}_t}\frac{\partial T}{\partial y}\left[\frac{v}{l}\frac{\partial l}{\partial y}-\left(u\frac{\partial u}{\partial y}+v\frac{\partial v}{\partial y}+w\frac{\partial w}{\partial y}\right)\left|\overline{\boldsymbol{U}}\right|^{-2}v+\frac{\partial v}{\partial y}\right]\\
&-\frac{A\Gamma}{2C_\Phi \mathrm{Pr}_t}\frac{\partial T}{\partial z}\left[\frac{v}{l}\frac{\partial l}{\partial z}-\left(u\frac{\partial u}{\partial z}+v\frac{\partial v}{\partial z}+w\frac{\partial w}{\partial z}\right)\left|\overline{\boldsymbol{U}}\right|^{-2}v+\frac{\partial v}{\partial z}\right]\\
&+\left(\frac{\partial \mu_{eff}}{\partial x}\frac{\partial u}{\partial y}+\frac{\partial \mu_{eff}}{\partial y}\frac{\partial v}{\partial y}+\frac{\partial \mu_{eff}}{\partial z}\frac{\partial w}{\partial y}\right)\\
&+\frac{1}{2\lambda_1}\left[\frac{\partial}{\partial x}\left(\frac{A\Gamma v}{\mathrm{Pr}_t}\frac{\partial T}{\partial x}\right)+\frac{\partial}{\partial y}\left(\frac{A\Gamma v}{\mathrm{Pr}_t}\frac{\partial T}{\partial y}\right)+\frac{\partial}{\partial z}\left(\frac{A\Gamma v}{\mathrm{Pr}_t}\frac{\partial T}{\partial z}\right)\right]=0
\end{aligned}\tag{84b}$$

$$\begin{aligned}
&\frac{\rho c_p A}{2\lambda_1}\frac{\partial T}{\partial z}+\nabla\cdot\left(\mu_{eff}\nabla w\right)+\frac{1}{2\lambda_1}\frac{\partial \lambda_2}{\partial z}-\frac{\Gamma w}{2\lambda_1 \mathrm{Pr}_t}\left(\left|\nabla T\right|^2+A\nabla\cdot\left(\nabla T\right)\right)-\frac{\Phi\Gamma w}{2\mu_{eff}}\\
&-\frac{A\Gamma}{2\lambda_1 \mathrm{Pr}_t}\frac{\partial T}{\partial x}\left[\frac{w}{l}\frac{\partial l}{\partial x}-\left(u\frac{\partial u}{\partial x}+v\frac{\partial v}{\partial x}+w\frac{\partial w}{\partial x}\right)\left|\overline{\boldsymbol{U}}\right|^{-2}w+\frac{\partial w}{\partial x}\right]\\
&-\frac{A\Gamma}{2\lambda_1 \mathrm{Pr}_t}\frac{\partial T}{\partial y}\left[\frac{w}{l}\frac{\partial l}{\partial y}-\left(u\frac{\partial u}{\partial y}+v\frac{\partial v}{\partial y}+w\frac{\partial w}{\partial y}\right)\left|\overline{\boldsymbol{U}}\right|^{-2}w+\frac{\partial w}{\partial y}\right]\\
&-\frac{A\Gamma}{2\lambda_1 \mathrm{Pr}_t}\frac{\partial T}{\partial z}\left[\frac{w}{l}\frac{\partial l}{\partial z}-\left(u\frac{\partial u}{\partial z}+v\frac{\partial v}{\partial z}+w\frac{\partial w}{\partial z}\right)\left|\overline{\boldsymbol{U}}\right|^{-2}w+\frac{\partial w}{\partial z}\right]\\
&+\left(\frac{\partial \mu_{eff}}{\partial x}\frac{\partial u}{\partial z}+\frac{\partial \mu_{eff}}{\partial y}\frac{\partial v}{\partial z}+\frac{\partial \mu_{eff}}{\partial z}\frac{\partial w}{\partial z}\right)\\
&+\frac{1}{2\lambda_1}\left[\frac{\partial}{\partial x}\left(\frac{A\Gamma w}{\mathrm{Pr}_t}\frac{\partial T}{\partial x}\right)+\frac{\partial}{\partial y}\left(\frac{A\Gamma w}{\mathrm{Pr}_t}\frac{\partial T}{\partial y}\right)+\frac{\partial}{\partial z}\left(\frac{A\Gamma w}{\mathrm{Pr}_t}\frac{\partial T}{\partial z}\right)\right]=0
\end{aligned}\tag{84c}$$

where, $\Gamma=0.03874\rho l\left|\vec{U}\right|^{-1}$, l is the distance to the wall surface, and,

$$\lambda_2=-2\lambda_1 P\,,\tag{85}$$

Similar to the analysis of laminar convection optimization, Eq. (83) is the governing equation for the parameter A, which is similar to the energy equation. Eq. (84a), Eq.(84b) and Eq.(84c) are the velocity synergy equations in *x,y,z* directions respectively. Compared to the momentum equation, an additional body force

(synergy force) appears in the field synergy equation. The components in of the synergy force in x,y,z directions are as follows,

$$
\begin{aligned}
F_x = {} & \rho \boldsymbol{U}\cdot\nabla u + \frac{\rho c_p A}{2\lambda_1}\frac{\partial T}{\partial x} - \frac{\Gamma u}{2\lambda_1 \mathrm{Pr}_t}\left(\left|\nabla T\right|^2 + A\nabla\cdot\left(\nabla T\right)\right) - \frac{\Phi\Gamma u}{2\mu_{eff}} \\
& - \frac{A\Gamma}{2\lambda_1 \mathrm{Pr}_t}\frac{\partial T}{\partial x}\left[\frac{u}{l}\frac{\partial l}{\partial x} - \left(u\frac{\partial u}{\partial x} + v\frac{\partial v}{\partial x} + w\frac{\partial w}{\partial x}\right)\left|\boldsymbol{U}\right|^{-2} u + \frac{\partial u}{\partial x}\right] \\
& - \frac{A\Gamma}{2\lambda_1 \mathrm{Pr}_t}\frac{\partial T}{\partial y}\left[\frac{u}{l}\frac{\partial l}{\partial y} - \left(u\frac{\partial u}{\partial y} + v\frac{\partial v}{\partial y} + w\frac{\partial w}{\partial y}\right)\left|\boldsymbol{U}\right|^{-2} u + \frac{\partial u}{\partial y}\right] \\
& - \frac{A\Gamma}{2\lambda_1 \mathrm{Pr}_t}\frac{\partial T}{\partial z}\left[\frac{u}{l}\frac{\partial l}{\partial z} - \left(u\frac{\partial u}{\partial z} + v\frac{\partial v}{\partial z} + w\frac{\partial w}{\partial z}\right)\left|\boldsymbol{U}\right|^{-2} u + \frac{\partial u}{\partial z}\right] \\
& + \left(\frac{\partial \mu_{eff}}{\partial x}\frac{\partial u}{\partial x} + \frac{\partial \mu_{eff}}{\partial y}\frac{\partial v}{\partial x} + \frac{\partial \mu_{eff}}{\partial z}\frac{\partial w}{\partial x}\right) \\
& + \frac{1}{2\lambda_1}\left[\frac{\partial}{\partial x}\left(\frac{A\Gamma u}{\mathrm{Pr}_t}\frac{\partial T}{\partial x}\right) + \frac{\partial}{\partial y}\left(\frac{A\Gamma u}{\mathrm{Pr}_t}\frac{\partial T}{\partial y}\right) + \frac{\partial}{\partial z}\left(\frac{A\Gamma u}{\mathrm{Pr}_t}\frac{\partial T}{\partial z}\right)\right]
\end{aligned}
\quad , \qquad (86a)
$$

$$
\begin{aligned}
F_y = {} & \rho \boldsymbol{U}\cdot\nabla v + \frac{\rho c_p A}{2\lambda_1}\frac{\partial T}{\partial x} - \frac{\Gamma v}{2\lambda_1 \mathrm{Pr}_t}\left(\left|\nabla T\right|^2 + A\nabla\cdot\left(\nabla T\right)\right) - \frac{\Phi\Gamma v}{2\mu_{eff}} \\
& - \frac{A\Gamma}{2\lambda_1 \mathrm{Pr}_t}\frac{\partial T}{\partial x}\left[\frac{v}{l}\frac{\partial l}{\partial x} - \left(u\frac{\partial u}{\partial x} + v\frac{\partial v}{\partial x} + w\frac{\partial w}{\partial x}\right)\left|\boldsymbol{U}\right|^{-2} v + \frac{\partial v}{\partial x}\right] \\
& - \frac{A\Gamma}{2\lambda_1 \mathrm{Pr}_t}\frac{\partial T}{\partial y}\left[\frac{v}{l}\frac{\partial l}{\partial y} - \left(u\frac{\partial u}{\partial y} + v\frac{\partial v}{\partial y} + w\frac{\partial w}{\partial y}\right)\left|\boldsymbol{U}\right|^{-2} v + \frac{\partial v}{\partial y}\right] \\
& - \frac{A\Gamma}{2\lambda_1 \mathrm{Pr}_t}\frac{\partial T}{\partial z}\left[\frac{v}{l}\frac{\partial l}{\partial z} - \left(u\frac{\partial u}{\partial z} + v\frac{\partial v}{\partial z} + w\frac{\partial w}{\partial z}\right)\left|\boldsymbol{U}\right|^{-2} v + \frac{\partial v}{\partial z}\right] \\
& + \left(\frac{\partial \mu_{eff}}{\partial x}\frac{\partial u}{\partial y} + \frac{\partial \mu_{eff}}{\partial y}\frac{\partial v}{\partial y} + \frac{\partial \mu_{eff}}{\partial z}\frac{\partial w}{\partial y}\right) \\
& + \frac{1}{2\lambda_1}\left[\frac{\partial}{\partial x}\left(\frac{A\Gamma v}{\mathrm{Pr}_t}\frac{\partial T}{\partial x}\right) + \frac{\partial}{\partial y}\left(\frac{A\Gamma v}{\mathrm{Pr}_t}\frac{\partial T}{\partial y}\right) + \frac{\partial}{\partial z}\left(\frac{A\Gamma v}{\mathrm{Pr}_t}\frac{\partial T}{\partial z}\right)\right]
\end{aligned}
\quad , \qquad (86b)
$$

$$
\begin{aligned}
F_z = {} & \rho \boldsymbol{U} \cdot \nabla w + \frac{\rho c_p A}{2\lambda_1} \frac{\partial T}{\partial y} - \frac{\Gamma w}{2\lambda_1 \mathrm{Pr}_t} \left(\left| \nabla T \right|^2 + A \nabla \cdot \left(\nabla T \right) \right) - \frac{\Phi \Gamma w}{2\mu_{eff}} \\
& - \frac{A\Gamma}{2\lambda_1 \mathrm{Pr}_t} \frac{\partial T}{\partial x} \left[\frac{w}{l} \frac{\partial l}{\partial x} - \left(u \frac{\partial u}{\partial x} + v \frac{\partial v}{\partial x} + w \frac{\partial w}{\partial x} \right) \left| \boldsymbol{U} \right|^{-2} w + \frac{\partial w}{\partial x} \right] \\
& - \frac{A\Gamma}{2\lambda_1 \mathrm{Pr}_t} \frac{\partial T}{\partial y} \left[\frac{w}{l} \frac{\partial l}{\partial y} - \left(u \frac{\partial u}{\partial y} + v \frac{\partial v}{\partial y} + w \frac{\partial w}{\partial y} \right) \left| \boldsymbol{U} \right|^{-2} w + \frac{\partial w}{\partial y} \right] \\
& - \frac{A\Gamma}{2\lambda_1 \mathrm{Pr}_t} \frac{\partial T}{\partial z} \left[\frac{w}{l} \frac{\partial l}{\partial z} - \left(u \frac{\partial u}{\partial z} + v \frac{\partial v}{\partial z} + w \frac{\partial w}{\partial z} \right) \left| \boldsymbol{U} \right|^{-2} w + \frac{\partial w}{\partial z} \right] \\
& + \left(\frac{\partial \mu_{eff}}{\partial x} \frac{\partial u}{\partial z} + \frac{\partial \mu_{eff}}{\partial y} \frac{\partial v}{\partial z} + \frac{\partial \mu_{eff}}{\partial z} \frac{\partial w}{\partial z} \right) \\
& + \frac{1}{2\lambda_1} \left[\frac{\partial}{\partial x} \left(\frac{A\Gamma w}{\mathrm{Pr}_t} \frac{\partial T}{\partial x} \right) + \frac{\partial}{\partial y} \left(\frac{A\Gamma w}{\mathrm{Pr}_t} \frac{\partial T}{\partial y} \right) + \frac{\partial}{\partial z} \left(\frac{A\Gamma w}{\mathrm{Pr}_t} \frac{\partial T}{\partial z} \right) \right]
\end{aligned}
\quad , \quad (86c)
$$

5.4 *Optimal Flow Pattern of Poiseuille Turbulent Convection*

In order to further illustrate the applicability of the velocity field synergy equation [50,51] in heat transfer optimization, we take the Poiseuille turbulent convection of water in a parallel plate channel as an example, where the height of the channel is 20 mm, the wall temperature of the plate is 350 K, the inlet temperature and the Reynolds number of water are 300 K and 20,000, respectively. Moreover, a repeated segment with the length of 2.5 mm was chosen in numerical simulation for simplicity.

For the usual case before optimization, the time-averaged velocity vector and the temperature gradient vector are nearly perpendicular to each other, leading to a small scalar product between them, i.e. a poor field synergy. Here, the turbulent convection seems a heat conduction process with an increased thermal conductivity from k to k_{eff}, compared to a laminar Poiseuille convection. In this case, the heat transfer rate is 1,782 W accompanying the pumping power of 4.61×10^{-3} W in the computational domain. The thicknesses of the laminar sub-layer and the transition sub-layer are 0.116 mm and 0.928 mm, respectively.

The optimized velocity and temperature fields near the upper wall for $\lambda_1 = -1.5 \times10^7$ K are shown in Fig. 29. There are several small counter-clockwise vortices near the upper wall. The heights of vortices perpendicular to the main flow direction are about 0.2 mm, and the distance between every two vortex centers is about 0.4 mm. Meanwhile, there are also several small clockwise vortices near the lower wall for symmetry. In this case, the heat transfer rate is 1,887 W, a 6 % improvement compared to that before optimization, and the pumping power is 5.65×10^{-3} W, a 23 % increment.

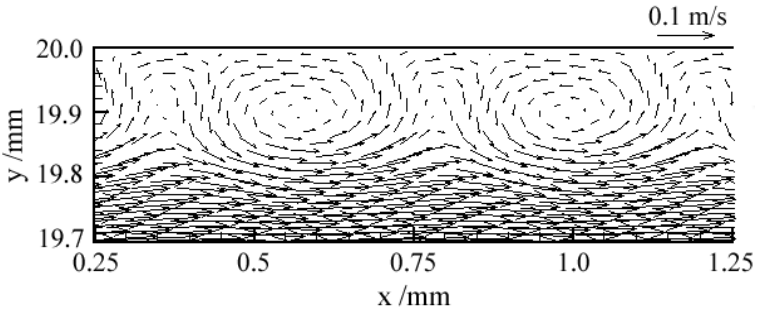

(a) Velocity vectors

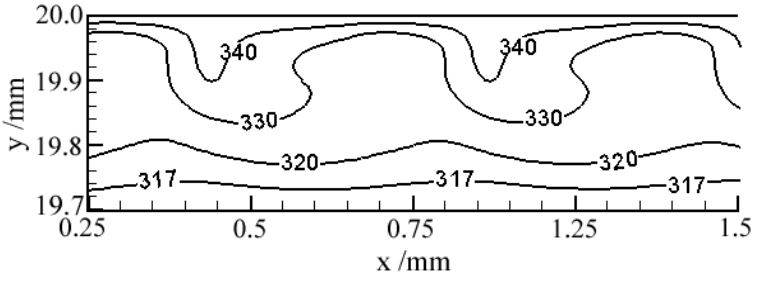

(b) Temperature contours

Fig. 29 Optimized velocity and temperature fields near the wall for a Poiseuille turbulent convection (λ_1 =-1.5 ×10^7 K, Re = 20,000)

For heat transfer in a turbulent convection between two parallel plates, the temperature gradients in the laminar sub-layer are two to three orders of magnitude larger than that far from the wall, which means that the thermal resistance in the laminar sub-layer is dominating. Hence, reducing the dominate resistance by vortices is the most effective way to improve heat transfer performance. Moreover, from the viewpoint of the field synergy principle, the field synergy number before optimization is small and the heat transfer rate is low. While with the optimized flow field as shown in Fig.29, in the upper right part of the vortex, the fluid flows towards the wall, leading to the velocity vectors are nearly parallel to the local temperature gradients in the same direction, and consequently the field synergy is largely improved in this area. In the lower left part of the vortex, the fluid flows away from the wall, and consequently the velocity vectors are nearly parallel to the local temperature gradients in the opposite direction, and hence the field synergy is reduced in this area. However, the magnitude of the temperature gradient in the upper right part is larger than that in the lower left part, so the overall field synergy around the entire vortex is improved and the heat transfer is enhanced.

For various values of λ_1, solving the field synergy equations obtains the optimal flow fields for different pumping power. Figs. 30(a)-(c) show the optimized

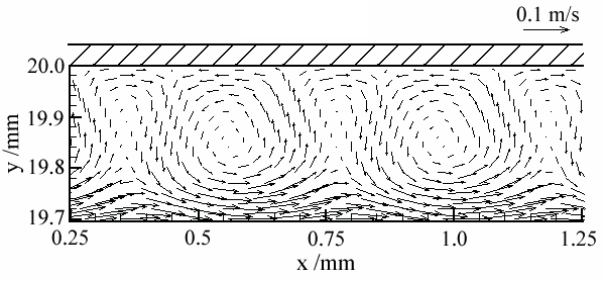

(a) $\lambda_1 = -1.3 \times 10^7$ K

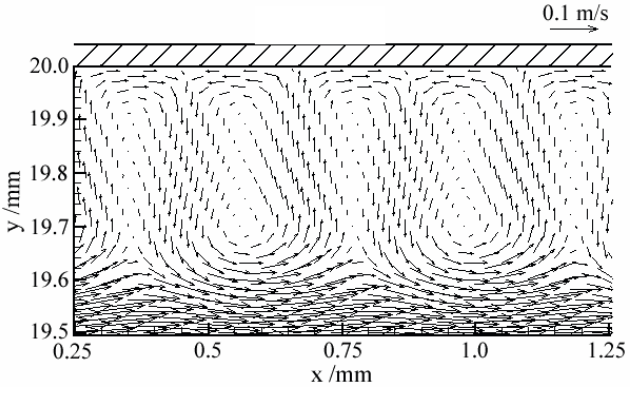

(b) $\lambda_1 = -1 \times 10^7$ K

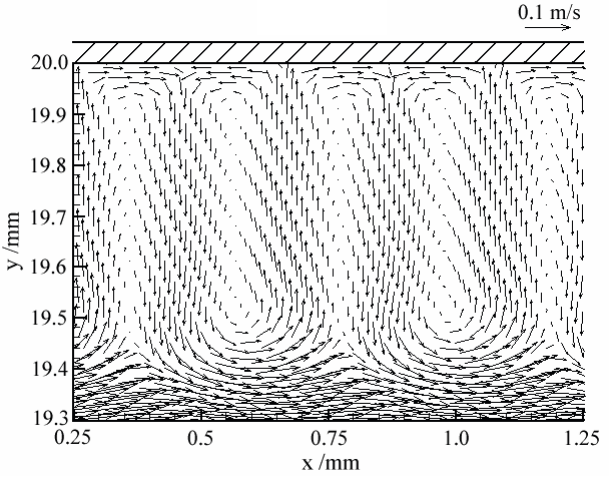

(c) $\lambda_1 = -5 \times 10^6$ K

Fig. 30 Optimized flow fields near the wall for various λ_1 (Re = 20,000)

velocity vectors near the upper wall for λ_1 = -1.3×10^7 K, -1×10^7 K and -0.5×10^6 K respectively. With increasing the value of λ_1, the heights of the vortex increase from 0.25 mm to 0.4 mm and to 0.6 mm respectively and consequently both the heat transfer and the pumping power increase. However, the normalized value of the increment of the pumping power is larger than those of heat transfer, especially for λ_1 larger than -1×10^7 K. Therefore, for λ_1 of about -1×10^7 K, the turbulent heat transfer can be effectively enhanced through the vortices. In this case, the vortex height is about half the transition layer thickness for the fluid flowing in a smooth parallel plate channel.

5.5 Physical Mechanism of Heat Transfer Performance of Micro-fin Tube

The micro-fin tube [52] is an effective facility for the heat transfer enhancement in turbulent convection, which usually consists of numerous helical fins with relatively small height on the inner surface. Webb [53] reported that the R-22 evaporation heat transfer coefficients in a micro-fin tube can be 3.1 times as high as that for a smooth tube, while the pressure drop increment is as low as 35 % only. The R-22 condensation heat transfer coefficient can be twice of that for a smooth tube with a pressure drop increment slightly less than that for evaporation. Meanwhile, Webb [53] also cautiously classified micro-fin tubes as internally finned tubes and discussed the enhanced heat transfer mechanisms of single-phase heat transfer. He pointed out that micro-fin tubes will both significantly enlarge the surface area and the roughness with flow separation. In addition, Al-Fahed et al. [54] experimentally studied the heat transfer and flow friction performance in a 15.9 mm outside diameter micro-fin tube with the Reynolds numbers ranging from 10,000 to 30,000, where the number, the heights and the helix angle of the helical fins are 70, 0.3 mm and 18^o, respectively. They found that the heat transfer enhancement ratios are between 1.2 and 1.8 and the friction factor ratios are between 1.3 and 1.8, whereas the heat transfer data showed a large discrepancy and the highest heat transfer enhancement occurred at a Reynolds number of 25,000 not 30,000. Wang et al. [55] studied the flow and heat transfer characteristics experimentally of 8 micro-fin tubes with the Reynolds numbers ranging from 2,500 to 40,000. Their results showed that the heat transfer enhancement is less than 20% for the Reynolds numbers below 6,000 but increases significantly between 6,000 and 13,000. And later Al-Fahed et al. [56] measured the laminar flow heat transfer and pressure drop in micro-fin tubes. They found that the heat transfer and pressure drop in micro-fin tubes were only slightly higher than those in plain tubes and hence recommended that micro-fin tubes not very suitable for laminar flow condition.

To study the heat transfer performance of micro-fin tube, Li [57] and Li et al. [58-60] carried out experimental and numerical investigations on a conventional micro-fin tube, shown in Fig. 31.

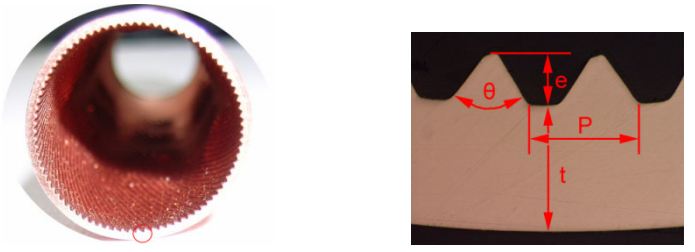

(a) Photograph (b) Micro-fin profile

Fig. 31 Illustration of the micro-fin tube

According to the Prandtl number dependence analysis, the vertical coordinates are in the form of $[Nu/(Pr_f/Pr_w)^{0.11}]/Pr^{0.56}$ and $[Nu/(Pr_f/Pr_w)^{0.11}]/Pr^{0.33}$ in Fig. 32 (a) and (b) for high and low Reynolds numbers, respectively. The solid line is the Gnielinski empirical correlation for water with the Prandtl number of 3.2. The dotted line is the Gnielinski empirical correlation for oil with the Prandtl number of 80. The filled and open symbols represent the Nusselt numbers with water and oil as the working fluids, respectively. Fig. 32 (a) shows that for flows with a low Prandtl number fluid (the filled symbols with water as the working fluid), the heat transfer is not enhanced until the Reynolds number larger than 10,000, which is defined as the critical Reynolds number for heat transfer enhancement, Re_{ceh}. For $Re < Re_{ceh}$, the difference between the Nusselt number of micro-fin tube and smooth tube is below 10 %. For $Re > Re_{ceh}$, the Nusselt number begins to increase markedly with the increasing Reynolds number and up to about 220 % of that for the smooth tube at Re > 30,000. For high Prandtl number fluid flows (the open symbols with oil as the working fluid), the critical Reynolds number is about 6,000. For Re < 6,000, the difference of the Nusselt number between a micro-fin tube and a smooth tube is below 10 %, while the heat transfer begins to be enhanced for Re > 6,000. In summary, for $Re < Re_{ceh}$, micro-fin tube behaves as a smooth tube as shown in Fig. 32, while for $Re > Re_{ceh}$, micro-fin tubes enhance heat transfer much. Moreover, the critical Reynolds numbers for heat transfer enhancement are different for fluids with different Prandtl numbers.

The existence of the critical Reynolds number for heat transfer enhancement, Re_{ceh}, is a interesting thing for micro-fin tubes, which is worth doing further discussion. In the wall bounded turbulence, there exists a very thin layer adjacent to the wall called viscous sub-layer, where the viscous force dominates the flow behavior. When the micro-fin is embedded in the viscous sub-layer, the flow is not influenced very much by the micro-fin, and the micro-fin tube behaves like a smooth tube. While when the micro-fin is higher than the viscous sub-layer, the micro-fin will generate turbulence and hence both the heat transfer rate and the flow resistance increase. Moreover, the thickness of the viscous sub-layer decreases with the increasing Reynolds number. For micro-fin tubes, increasing the Reynolds number reduces the viscous sub-layer, and thereafter the micro-fins begin to

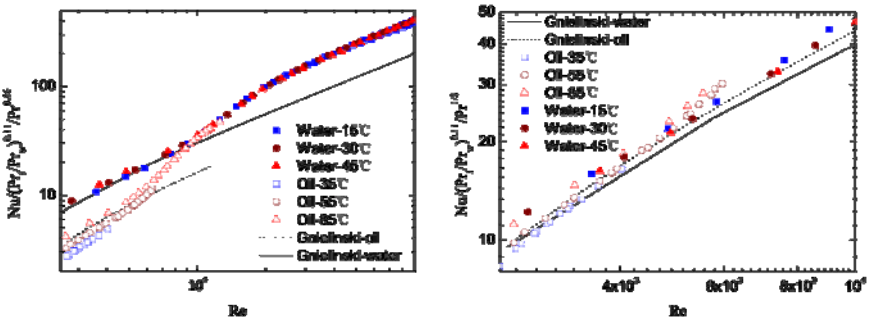

Fig. 32 Nusselt number of micro-fin tube

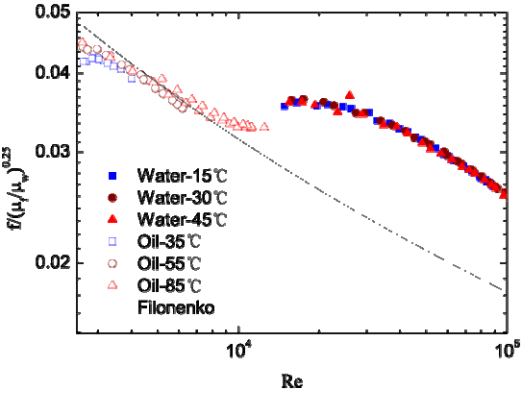

Fig. 33 Friction factor of micro-fin tube

take effect. It is the reason why a critical Reynolds number for heat transfer enhancement, $Re_{ceh,}$ exists. Especially, when the height of the micro-fin is 2-3 times of the sub-layer, the flow pattern in the tube is close to the optimal one as indicated in Fig.29 and Fig.30. This is why the micro-fin tube has the performance of high heat transfer coefficient with the relative low flow resistance. In addition, for different fluids with a wide Prandtl number range, though the velocity distribution near the tube wall is similar at the same Reynolds number, the temperature field is different, so the critical Reynolds number is not the same for working fluids with different Prandtl numbers.

The critical Reynolds number for heat transfer enhancement also explains the different Prandtl number dependence of the Nusselt number at high and low

Reynolds number regions. For $Re < Re_{ceh}$, the micro-fin tube is like a smooth tube and the Prandtl number dependence, n, is 0.3, and for $Re > Re_{ceh}$, heat transfer is enhanced in micro-fin tube and the Prandtl number dependence is n=0.56. Fig. 33 again shows the friction factor of the micro-fin tube, in which the effect of variable property has been taken into account. For Re < 10,000, the friction factor is almost the same as that in a smooth tube, while for Re > 10,000, the friction factor begins to increase and reaches 140~150 % of that in a smooth tube at Re=30,000.

6 Novel Enhanced Techniques

In the forgoing section, we introduced the EED principle for heat transfer optimization, which is valid for the conduction optimization of volume-to-point problem and in convective heat transfer optimization. Based on the EED principle, the velocity field synergy equations were derived for both laminar and turbulent convective heat transfer. In the following, two novel enhanced techniques based on the field synergy principle and EED principle will be discussed. Both of the enhanced techniques are of the feature that heat transfer is remarkably enhanced with lower flow resistance increment.

6.1 Alternating Elliptical Axis Tube

The alternating elliptical axis (AEA) tube, shown in Fig.34, is developed based on the principle of field synergy [47,61]. The tube consists of alternate segments whose cross-section is elliptical and its major axis direction is normal to that of the neighboring one. Between the alternate segments is a transition joint linking the neighboring alternate segments. Considering the junctions to the tube-bundle board and baffle board, the ends and several middle parts of the tube remained circular. The structure dimensions of the tube can influence its performance. The design of these dimensions has to accommodate the flow resistance, the heat transfer and the pressure-resistant ability. The reasonable data are as follows: the ratio of the major axis to the minor axis of the elliptical cross-section, A_0/B_0, is between 1.4 and 1.6; the ratio of the length of each alternate segment to the outer tube diameter, P/D, is from 2 to 3; and the length of the transition joint is about 0.3D–0.5D. The structure and dimensions of the AEA tube are shown in Fig. 35.

Fig. 34 The alternating elliptical axis tubes

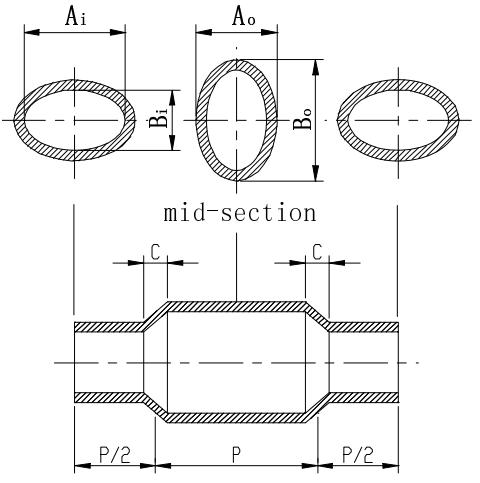

Fig. 35 Structure of the alternating elliptical axis tube

6.1.1 Experiment on Heat Transfer Performance of AEA Tube[17,47]

Experimental set-up. The schematic diagram of the experimental set-up is shown in Fig. 36. It is composed of the cold medium loop, hot medium loop, test section and the measure and control system. The effective length of the test tube with an annular structure is 2 m. The fluid outside the AEA tube is deionized water, and the fluid inside the AEA tube is deionized water or 22# lubricating oil. The flow rate outside the test tube is around 12 t/h, which is large enough to maintain a turbulent flow. The flow rate inside the test tube is less than 6 t/h. The maximum heating power is 15 kW for both heaters of the water and oil tanks. The self-stirring flow guarantees the medium temperature uniform inside the tanks. The refrigeration power of the refrigerator set is 10–15 kW. The temperature range is 5–65 ℃ for the cold medium and 10–95 ℃ for the hot medium. The flow rate, the inlet and outlet temperature and the pressure drop between the inlet and outlet for inner and outer flows are measured in the experiments for evaluating heat transfer performance.

The experiments are automatically controlled by a computer. Fig. 37 is the systematic block-diagram of the measurement and control system. Instructed by the ThermoCon software, the water and oil pumps, refrigerator and flow rate regulating valves are automatically controlled, the signals of temperature, the flow rate and the pressure drop are processed and transmitted to the computer and stored in a database. Based on the controlled objectives, such as flow rate, temperature, the computer adjusts the heating power and flow rate of the cold and hot working fluids instantly according to the programmed control algorithm. The self-adapting fuzzy algorithm used in the automatic control system guarantees that the experimental data are stable and reliable.

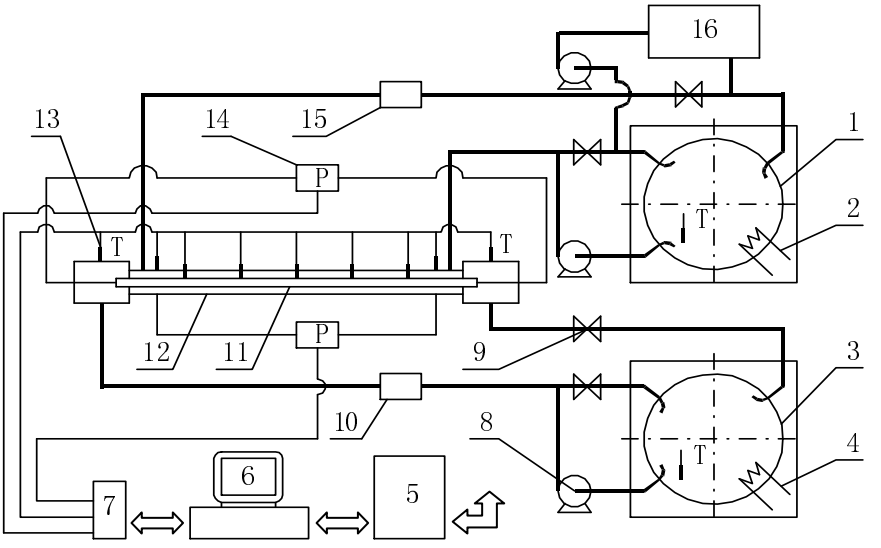

Fig. 36 Systematic diagram of the experimental apparatus
1、cold water tank 2、auxiliary heater 3、hot water / oil tank 4、heater
5、power supply 6、computer 7、data collector 8、pump 9、valve
10、mass flow meter 11、testing tube 12、test section 13、thermocouple
14、pressure meter 15、flow meter 16、refrigerator

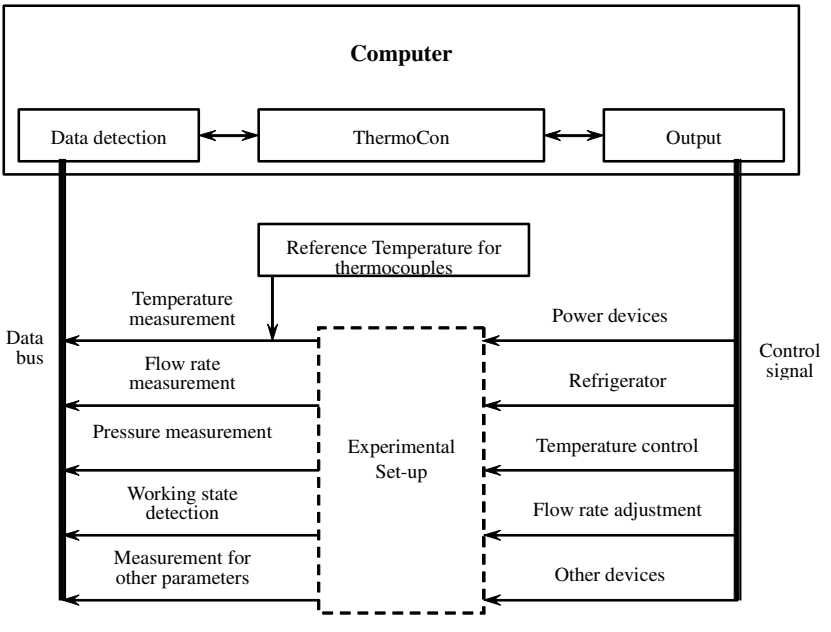

Fig. 37 Block-diagram of the measure and control system

Data Reduction. The first step is to determine the heat transfer relation outside the tube. From the measured fluid mass flow rate, $\dot{m}$, inside the tube, its temperature at inlet and outlet, T_{in} and T_{out}, its average flow velocity, $U_{\text{m,out,}}$ and the fluid temperature of outside tube at the inlet and outlet, t_{in} and t_{out}, the logarithmic average temperature difference of the test section and the heat flow rate inside the tube can be calculated with the measured parameters as follows,

$$\Delta T_m = \frac{\left(T_{in} - t_{out}\right) - \left(T_{out} - t_{in}\right)}{\ln \dfrac{T_{in} - t_{out}}{T_{out} - t_{in}}} \tag{87}$$

$$Q = \dot{m} c_p \left(T_{in} - T_{out}\right) \tag{88}$$

The overall heat transfer coefficient is determined as,

$$k = \frac{Q}{A_o \Delta T_m} \tag{89}$$

The overall heat transfer resistance from the hot fluid to the cold fluid is a series connection of the convection resistance inside the tube, resistance through the tube wall and the convection resistance outside the tube surface. Assume that the relationship between the Nu and $\text{Re}^{0.8}\text{Pr}^{0.4}$ is linear for the fluid outside the tube, the overall heat transfer resistance can be written as,

$$\frac{1}{k} = \frac{1}{h_o} + \frac{d_o}{\lambda_{wall}} \ln \frac{d_o}{d_i} + \frac{d_o}{d_i h_i} = \frac{1}{C}\left(\frac{d_o}{\lambda_{f,o}} \text{Re}^{0.8} \text{Pr}^{0.4} \right) + \frac{d_o}{\lambda_{wall}} \ln \frac{d_o}{d_i} + \frac{d_o}{d_i h_i} \tag{90}$$

where h_{i} is the heat transfer coefficient inside the tube, h_{o} is the heat transfer coefficient outside the tube, d_{i} is the internal diameter of the tube, d_{o} is the external diameter of the tube, $\lambda_{\text{f,o}}$ is the average thermal conductivity of fluid outside the tube, and λ_{wall} is the tube wall conductivity. In the experiments the flow rate and the heat transfer coefficient inside the tube are kept constant. It can be found from Eq. (90) that $(1/k)$ varies with $\text{Re}^{-0.8}\text{Pr}^{-0.4}$ linearly. Take $X = \dfrac{d_o}{\lambda_{f,o}} \text{Re}^{-0.8} \text{Pr}^{-0.4}$ as the x-axis and $Y = 1/k$ as the y-axis, we can obtain a linear relation between X and Y by changing the flow rate outside the tube. The constant C can be determined by curve fitting. Once C is obtained, it can be used to calculate the heat transfer coefficient outside the tube，

$$h_o = C\frac{\lambda_{f,o}}{d_o}\mathrm{Re}^{0.8}\,\mathrm{Pr}^{0.4} \tag{91}$$

The heat transfer performance inside the tube can be determined experimentally after the thermal resistance outside the tube is known. In such experiments the external flow rate is fixed at its maximum to reduce the external convection resistance. The fluid temperature difference between the inlet and outlet inside the tube depends then on the internal flow. Usually the fluid temperature difference of the inlet and outlet inside the tube is 10–40 times of that of the fluid temperature difference outside the tube. The overall heat transfer coefficient k can also be determined by Eqs. (87)–(89). Then the heat transfer coefficient inside the tube, h_i, is

$$\frac{1}{h_i} = \frac{d_i}{d_o}\left(\frac{1}{k} - \frac{1}{h_o} - \frac{d_o}{\lambda_{wall}}\ln\frac{d_o}{d_i}\right) \tag{92}$$

and Nu inside the tube is,

$$Nu = \frac{h_i d_i}{\lambda_{f,i}} \tag{93}$$

The copper tubes are used in experiments, which has very low thermal resistance (about 0.1–3% of the overall thermal resistance) and hence, its contribution to the data processing error can be negligible.

The frictional coefficient inside the tube is easy to be calculated, that is,

$$f = \frac{\Delta p}{\rho u^2/2}\cdot\frac{d_i}{L} \tag{94}$$

where Δp is the pressure drop over the tube length, L, u is the average flow velocity inside the tube; d_i is the internal tube diameter. Since the difference between the hydraulic diameter of the circular and elliptical tubes is not large (less 8%), and the Re has the same value for an equal flow rate, the circular tube diameter is taken as the hydraulic diameter for the sake of comparison and analysis.

Experimental results. The dimensions of the tested AEA tubes are listed in Table 4. Three AEA tubes are made from circular tube with 20 mm in diameter, 1.5 mm in wall thickness and 2m in effective length, but with different alternate segments which are 40, 50, 60 mm respectively. During the experiments, the fluid outside the AEA tube is deionized water, while the fluid inside the tube is either deionized water or 22# lubricating oil.

Table 4 Dimensions of the tested alternating elliptical axis tubes

No.	A_i (mm)	B_i (mm)	C (mm)	P (mm)
1	20.8	12.8	6	40
2	20.8	12.8	6	50
3	20.8	12.8	6	60

For experiments with the deionized water as the working fluid the temperature difference between hot and cold fluids is between 10 and 25 °C. The flow is turbulent due to the small viscosity of water. The Reynolds numbers are from 10^4 to 5×10^4 and the Prandtl numbers are from 2 to 7. The experimental results of the Nusselt number and frictional factors for three tested tubes are illustrated in Fig. 38. The difference in Nusselt number for different tubes is trivial shown in Fig. 38a, while the differences in friction factor for different tubes are apparent, as shown in Fig. 38b. The friction factor increases with decreasing alternate segment length because longer segment causes less variation in the flow pattern per unit length and leads to a less flow resistance.

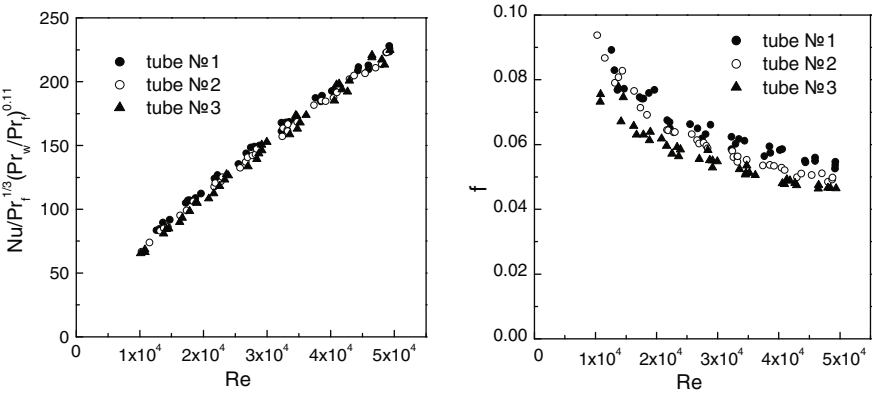

(a) Nusselt numbers (b) Frictional factors

Fig. 38 Experimental results of Nusselt numbers and frictional factors in alternating elliptical axis tubes with deionized water as the working fluid

The experimental results with the lubricating oil as the working fluid are shown in Fig. 39. In the experiments, the temperature difference between the hot and cold fluids is 10–30 °C. The viscosity of the oil ranges from 4.5×10^{-6} to 16×10^{-6} Pa.s, corresponding to the Reynolds numbers from 500 to 1.5×10^4, and the Prandtl numbers from 80 and 200. The segment length has similar effects on the Nusselt number and friction factor.

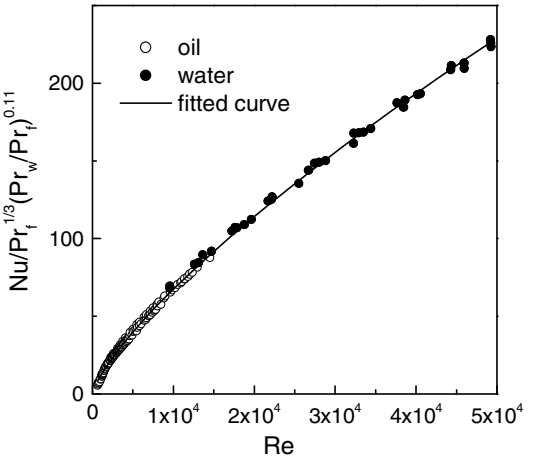

(a) Nusselt numbers

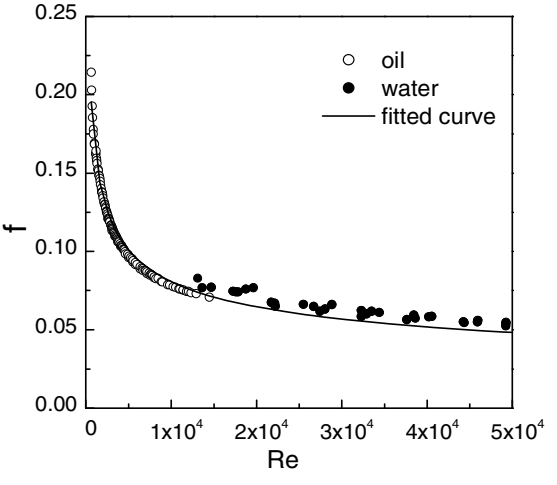

(b) Frictional factors

Fig. 39 Experimental results of Nusselt numbers and frictional factors in alternating elliptical axis tubes with 22# lubricating oil as the working fluid

For the AEA tubes, it is found that the experimental results of the Nusselt number and the friction factor can be correlated in a single expression for Reynolds numbers from 500 to 5×10^4. The correlations for tube 1 are,

$$Nu_e = 0.0615\,\mathrm{Re}^{0.76}\,\mathrm{Pr}_f^{\,1/3}\left(\frac{Pr_f}{Pr_w}\right)^{0.11} \tag{95}$$

$$f_e = 1.54\,\mathrm{Re}^{-0.32} \tag{96}$$

To illustrate the performance of the AEA tube, the ratios of the Nusselt number and friction factor of the AEA tubes to the smooth circular tube are depicted in Fig. 40. The entrance effect in the circular tube has been included. For 500 < Re < 2300, the heat transfer is enhanced by 100–500%, the flow resistance is increased by 100–350%. For 2300 < Re < 10^4, the heat transfer is increased by 60–200% and the flow resistance increment is 150–180%. The comparisons in Fig. 40 show that the AEA tube provides excellent heat transfer enhancement with less additional pressure drop for Re < 5×10^4.

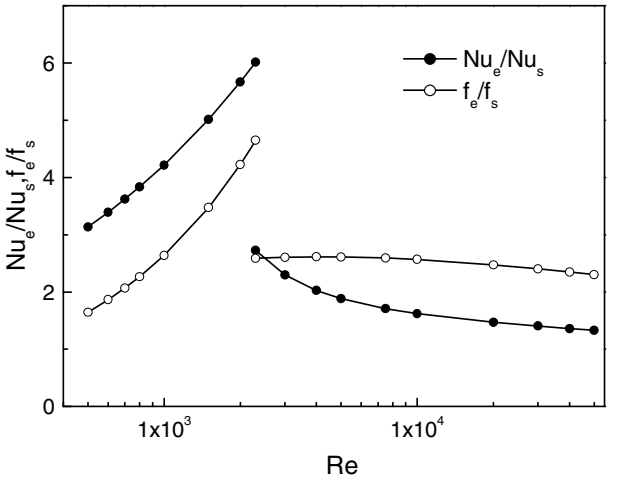

Fig. 40 Heat transfer enhancement and flow resistance increment of alternating elliptical axis tube compared to the circular tube

6.1.2 Numerical Analysis on Heat Transfer Performance of AEA Tube

To understand the mechanism of heat transfer enhancement/optimization of the AEA tube, Meng et al. [19] numerically analyzed the flow field and temperature distribution in AEA tubes subjected to the isothermal surface temperature. In the simulation, the flow and temperature fields are taken as fully developed and the numerical simulation was performed in two Reynolds number regions, one is low Re region of 500<Re<10^4, the other is high Re region of 10^4<Re<6 ×10^4. The working fluid is water with constant properties.

FLUENT6.0 is used for the numerical analysis. The local turbulences occur in the flow in the alternating elliptical axis tube even for Re<2300 because of the sharp variation of tube shape in the transition part. Hence, RNG k-ε model is used for the flow and heat transfer in the Re number range of 500-10^4. All the wall function of the turbulent model are obtained by using two-layer model with enhanced wall

functions supplied by Fluent6.0. The algorithm of SIMPLEC is selected to uncouple the pressure and velocity parameters. The QUICK format is applied for the divergence of both the momentum and energy equations. The grid mesh of the computed tube is shown in Fig.41.

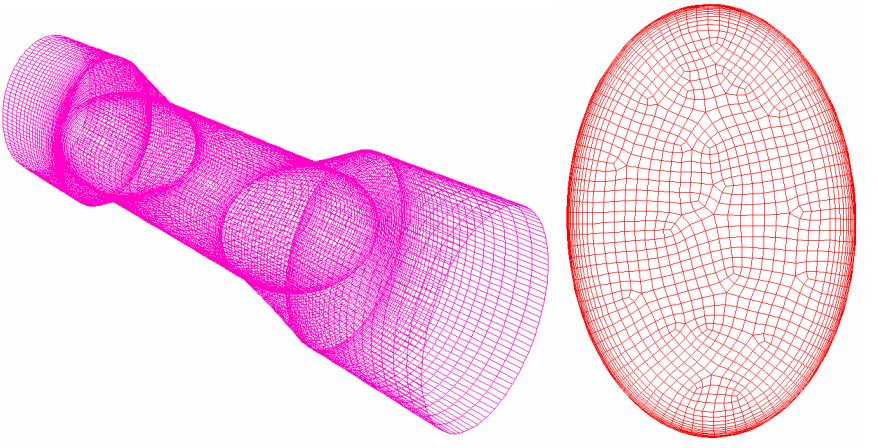

Fig. 41 Grid mesh for the alternating elliptical axis tube

The numerical results show that the multi-vortexes exist in the alternating elliptical axis tube. Four longitudinal vortexes appear for Re<2000, while there are eight longitudinal vortexes in the tube for Re>5000. Given in Figure 42 is the calculated flow field of the cross-section of the straight part of the elliptical tube for $Re=2\times10^4$, Pr = 7, T_w - T_m = 50 K, T_w = 350 K. In the cross-section, eight longitudinal vortices induced by the surface shape variation locate in the neighbor of the tube surface.

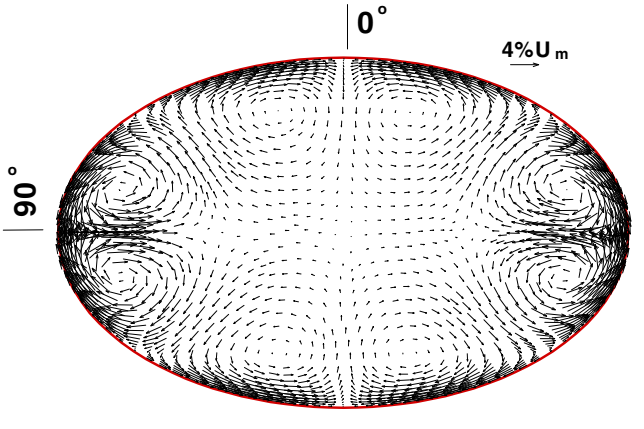

Fig. 42 Numerical results of the flow fields in the cross-section of the alternating elliptical tube ($Re=2\times10^4$)

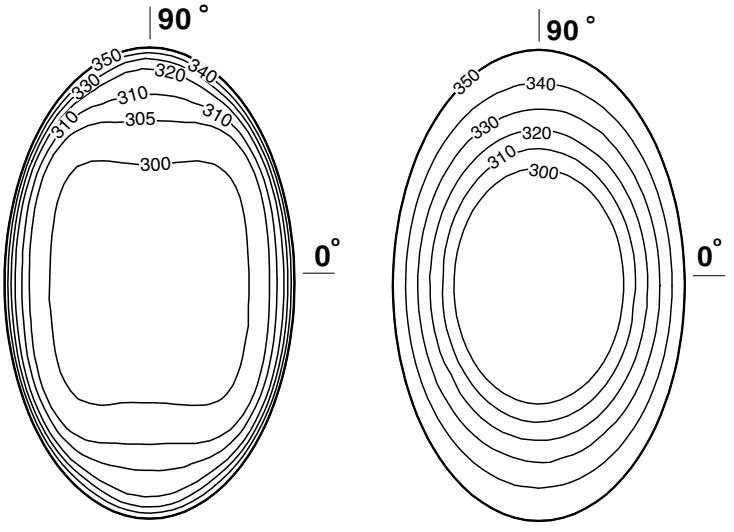

(a) Alternating elliptical axis tube (b) Straight elliptical axis tube

Fig. 43 Temperature field of the cross-section in the straight part of AEA-tube

Figure 43(a) shows the temperature distribution in the cross section of the straight part of the alternating elliptical axis tube. It can be found that the isothermals of the alternating elliptical axis tube are different from the ellipses as in the straight elliptical tube (see Fig. 43(b)). The isothermals near the AEA tube wall are much denser than those in the straight elliptical tube, which means the temperature gradient at the wall surface is significantly increased due to the improvement of the synergy between the flow and temperature fields, especially in the low Reynolds numbers region.

For comparison the local Nu distributions in circumferential direction of the alternating elliptical axis tube and the straight elliptical tube are given in Figure 44 for $Re=2\times10^4$ and Re=1,000. For the case of $Re=2\times10^4$, seen in Fig.44(a), the Nusselt numbers around $\varphi=60^o$ and 120^o are 70% higher and the Nusselt numbers around $\varphi=90^o$, which are slightly smaller than those for the straight elliptical tube. The average value of Nu along circumferential direction is 210.6, which is 35% higher than that for the straight elliptical tube. For the case of Re=1000 seen in Fig.44(b), it is found that the local Nusselt numbers along circumferential direction of AEA-tube may be as high as 8-16 times of that for the straight elliptical tube. This indicates that the heat transfer in the low Reynolds number region can be markedly enhanced.

Different from the existing enhanced tubes with twisted tape inserts or vortex generator inserts, the vortices are induced by the variation of original surface of the AEA tube. The velocity of the main flow does not change very much due to the small variation of the cross-sectional area along the axis and hence, the average

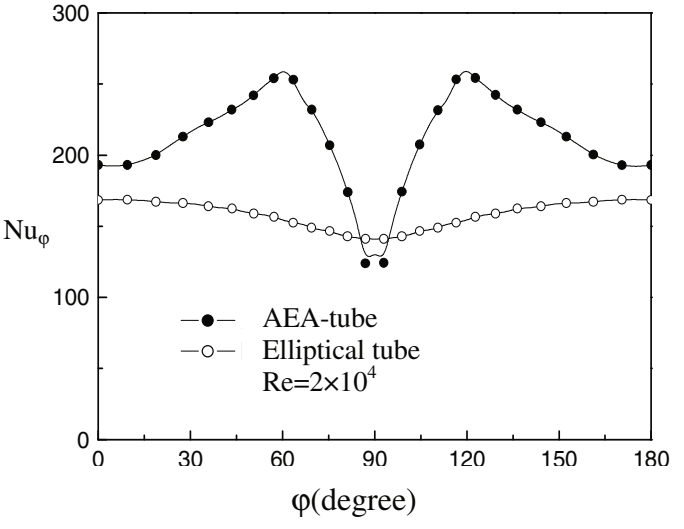

(a) $Re=2\times10^4$

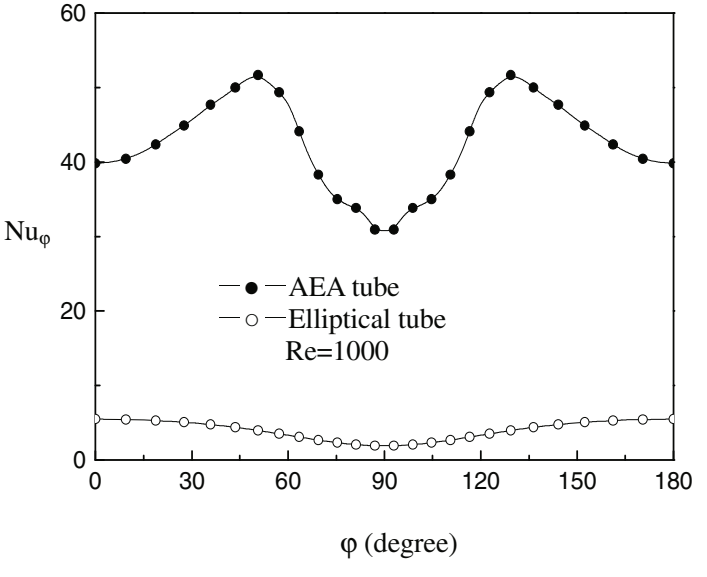

(b) Re=1000

Fig. 44 The Nusselt numbers of AEA-tube and straight elliptical tube along circumferential direction

velocity of the secondary flow is only about 2–4% of the main flow velocity. Therefore, the additional increment of flow resistance is small for the AEA tube compared to the straight pipe.

6.2 Discrete Double Inclined Ribs Tube

Based on the field synergy analysis for laminar convective heat transfer, a novel enhanced tube, discrete double inclined ribs tube (DDIR-tube) [62], was developed as shown in Fig.45. Multi-longitudinal vortexes flow can be induced by the periodical surface variation (discrete double-inclined ribs). The outer diameter of the DDIR-tube for experiment is 20 mm. There are three pairs of double-inclined ribs in the peripheral surface with 12 mm in pitch, 6 mm in rib length in axial direction, about 45 ° in inclined angle, and 0.85 mm in inner rib height.

Fig. 45 A photo of the DDIR-tubes

6.2.1 Experiment on Heat Transfer Performance of DDIR-Tube

The experiments on heat transfer coefficient and frictional factor of the DDIR-tube are performed on the experimental set-up described in the section of 6.1.1. Same as the experiments for AEA-tubes, the deionized water and 22# lubricating oil are used as the working fluids for the experiments and the experimental results for the DDIR-tube in high Re region and low Re region are shown in Figure 46 and Fig.47 respectively. For comparison the values of Nu and *f* in circular tube according to the conventional correlations are also plotted in Fig. 46 and Fig.47.

For $Re=10^4$-5×10^4, the average temperature difference between the fluids inside and outside the tube is about 10-15°C. It is seen from Fig.46 that the heat transfer in DDIR-tube is enhanced by 110%-130% and the flow resistance is increased by 220%-240% compared to the circular tube. For $Re=500$-1.5×10^4, the working fluid is 22# lubricating oil and the average temperature difference between the fluids inside and outside the tube is about 20-30°C. Under the experimental conditions, the dynamic viscosity of oil varies in the range of $(4.5\text{-}16)\times10^{-6}m^2/s$ and the Prandtl number varies in the range of 80-200. Figure 47 shows that the heat transfer in DDIR-tube in low Re region, especially for $Re<2000$, can be efficiently enhanced with low flow resistance increment compared to that in high Re region.

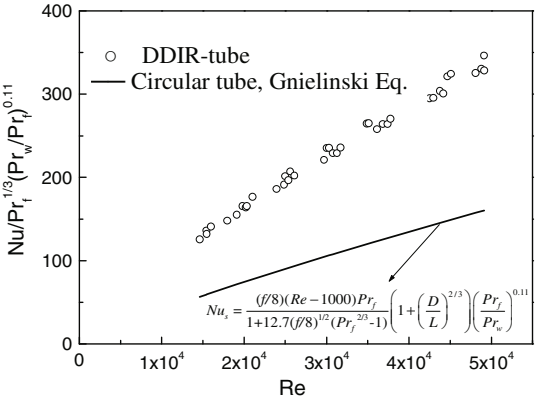

(a) Nusselt number

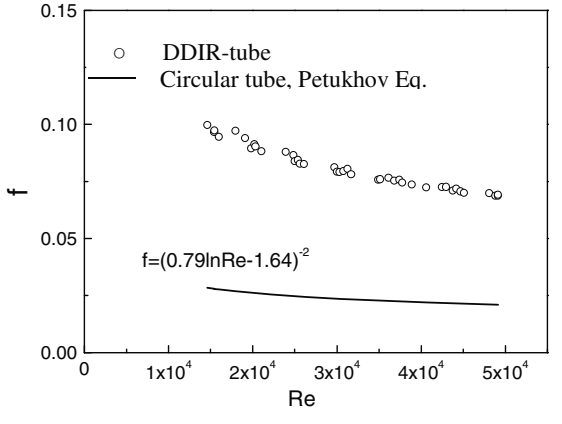

(b) Frictional factor

Fig. 46 The experimental results of Nusselt numbers and frictional factors for the DDIR-tube in high Reynolds number region

Same as for the AEA tubes, it is found that the experimental results of the Nusselt number of the tested DDIR-tube can be correlated in a single expression for Reynolds numbers from 500 to 5× 10^4 , as shown in Fig.48.

$$Nu_e = 0.0484\,\mathrm{Re}^{0.82}\,\mathrm{Pr}_f^{\,1/3}\left(\frac{Pr_f}{Pr_w}\right)^{0.11} \tag{97}$$

which is valid for Re=500-5×10^4, Pr=2-200, Pr_f/Pr_w=0.2-5.

Figure 49 shows the experimental results and the fitting curves of frictional factor for DDIR-tube. It is found that the experimental data of the frictional factor of

DDIR-tube have to be correlated in two expressions for Reynolds numbers from 500 to 5×10^4 as follows,

$$f_e = \begin{cases} 1/\left(14.3 - 45.5\,\mathrm{Re}^{-0.27}\right) & \mathrm{Re} = 10^4 - 5\times 10^4 \\ 6.3\,\mathrm{Re}^{-0.57} & \mathrm{Re} = 500 - 10^4 \end{cases} \tag{98}$$

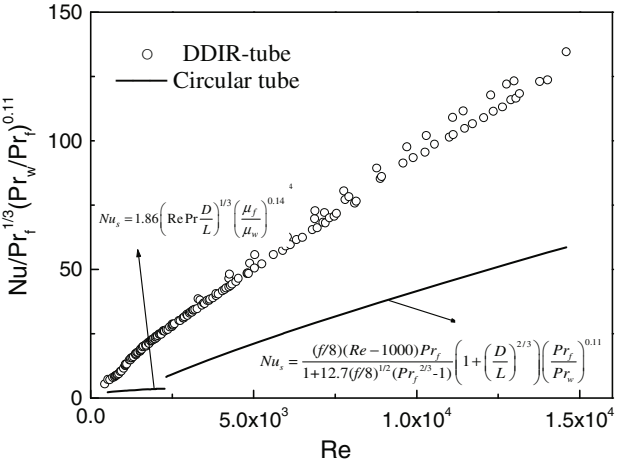

(a) Nusselt numbers

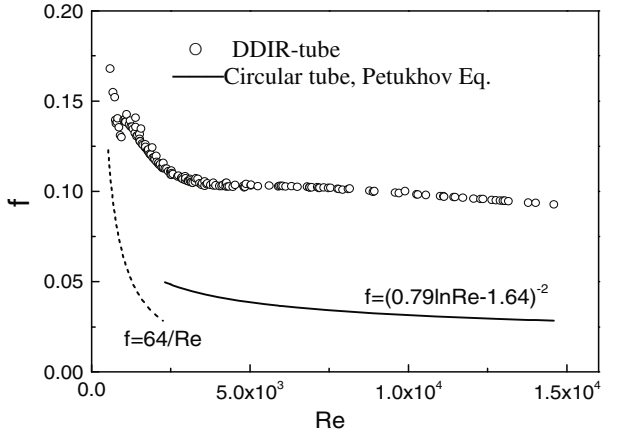

(b) Frictional factors

Fig. 47 The experimental results of Nusselt numbers and frictional factors for the DDIR-tube in low Reynolds number region

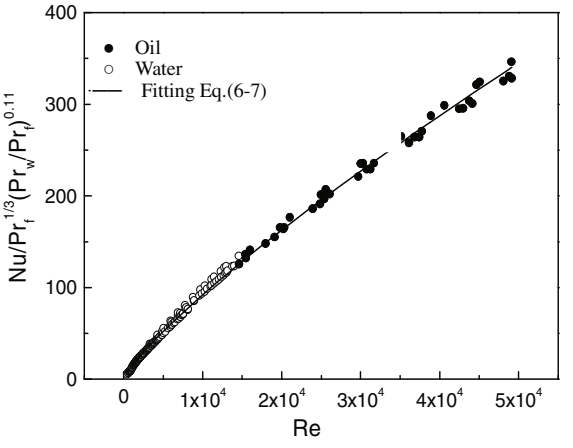

Fig. 48 The experimental data and the fitting curve of heat transfer in DDIR-tube

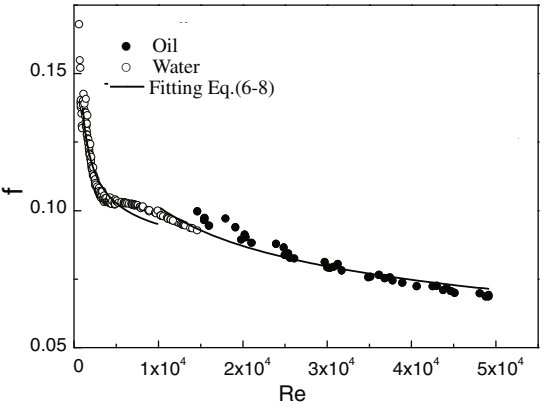

Fig. 49 The experimental data and the fitting curves of frictional factor in DDIR-tube

To illustrate the performance of the DDIR-tube, the ratios of the Nusselt number and the friction factor of the DDIR-tube to those of the smooth circular tube are depicted in Fig. 50, where the entrance effect in the circular tube has been included. For $500 < Re < 2300$, the heat transfer is enhanced by 350–750%, while the flow resistance increment is about 120–300%. For Reynolds numbers from 10^4 to 5×10^4, the heat transfer is enhanced by 130–240%, while the flow resistance increment is about 130–220%.

In summary, both the AEA tube and DDIR tube developed based on the field synergy principle and the EED principle have much better heat transfer performance with a low flow resistance increment in the low Re region.

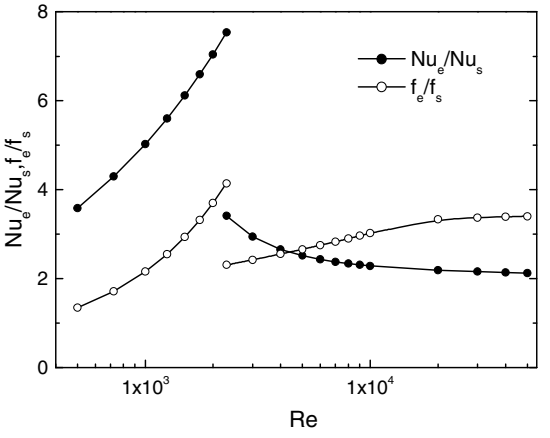

Fig. 50 Heat transfer enhancement and flow resistance increment of DDIR-tube compared to the circular tube

7 Field Synergy Principle for Heat Exchanger Optimization[63,64]

Heat exchangers are widely used in industries, and the improvement of thermal performances will raise the efficiency of energy utilization and minimize the equipment. The effectiveness, which represents the thermal performance of heat exchangers, can be improved from two levels. At the first one, heat transfer coefficient can be increased by enhanced heat transfer devices, such as ribs, inserts, turbulence generators, etc. At the second, the effectiveness of heat exchangers with the fixed heat transfer coefficient can be upgraded through the optimization of heat exchanger design, for example, using optimal flow arrangement. In this section, we will focus on the study of heat exchanger optimization.

7.1 Concept of Field Synergy of Heat Exchanger

It is known that the effectiveness of heat exchanger does not only depend on the heat transfer unit (NTU), but also on the flow arrangement (counterflow, parallelflow, crossflow etc.). However, we will exam the thermal performance of heat exchanger from the synergy of the temperature fields of hot and cold fluids in a heat exchanger.

Since the energy exchanges between fluids with different temperatures in a heat exchanger, the fluid temperatures vary along the flow path, forming hot and cold fluid temperature fields. The whole exchanger can be regarded as being made up of a number of sub elements and the average temperature of hot and cold fluids, $T(x,y,z)$ and $t(x,y,z)$, in each sub element are regarded as the local temperatures of

hot and cold fluid temperature fields respectively. The local temperature difference between hot and cold fluids in each sub element then forms a temperature difference field in the heat exchanger.

$$\theta(x, y, z) = T(x, y, z) - t(x, y, z) \tag{99}$$

For convective heat transfer, the field synergy refers to the synergy between the velocity field and the temperature gradient field of the fluid. The field synergy for a heat exchanger refers to the synergy between the temperature fields of hot and cold fluids. When they are of same function of space, but with different extra constant as follows,

$$T(x, y, z) = A + f(x, y, z) \tag{100}$$

$$t(x, y, z) = B + f(x, y, z) \tag{101}$$

their difference does not vary in space, that is, the local temperature difference becomes uniform in the entire heat exchanger

$$\theta(x, y, z) = T(x, y, z) - t(x, y, z) = A - B = Const \tag{102}$$

This implies that the temperature fields of hot and cold fluids are equivalent to the uniform temperature difference field in the heat exchanger. We can then define the uniformity factor of the temperature difference field as the field synergy factor of heat exchanger. For a two-dimensional heat exchanger, as shown in Fig. 51, the length is L and the width is W, the temperatures of the hot and cold fluids are $T(x,y)$ and $t(x,y)$ respectively. The field synergy factor is defined as,

$$\Phi = \frac{\int_0^W \int_0^L \left(T(x, y) - t(x, y)\right) dxdy}{\sqrt{WL \int_0^W \int_0^L \left(T(x, y) - t(x, y)\right)^2 dxdy}} \tag{103}$$

For a one-dimensional heat exchanger Eq.(103) reduces to

$$\Phi = \frac{\int \left(T(x) - t(x)\right) dx}{\sqrt{L \int_0^L \left(T(x, y) - t(x, y)\right)^2 dx}} \tag{104}$$

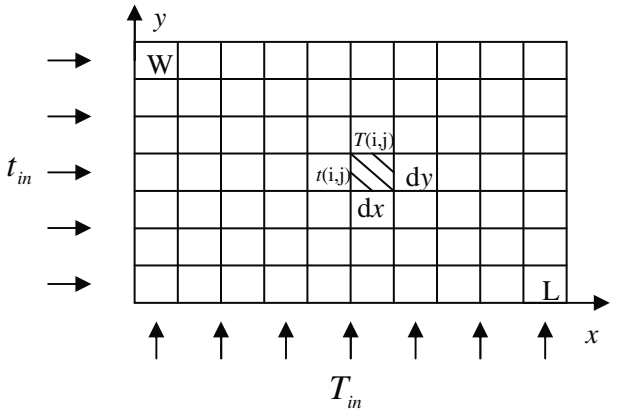

Fig. 51 Two-dimensional heat exchanger

7.2 Field Synergy Factors of Typical Heat Exchangers

The analytical expressions for the field synergy factor of heat exchangers with simple flow arrangement can be obtained through the solutions of energy equation [64, 65].

(a) parallel flow heat exchanger

For a single-pass parallel flow heat exchanger, as shown in Fig.52, the local heat transfer can be related to the change in enthalpy of the flowing streams:

$$dQ = (Gc)_{\min}\, dt(x) = -(Gc)_{\max}\, dT(x) = kPdx\big(T(x) - t(x)\big) \tag{105}$$

where, P is the perimeter of the tube cross-section, k is the constant overall heat transfer coefficient, $(Gc)_{\min}$ and $(Gc)_{\max}$ are the heat capacity rates of cold and hot fluids respectively. Rearranging Eq.(105) leads to

$$\frac{d\big(T(x) - t(x)\big)}{T(x) - t(x)} = -\left(\frac{1}{(Gc)_{\min}} + \frac{1}{(Gc)_{\max}}\right) kPdx \tag{106}$$

By using the inlet condition, $T(x) - t(x) = T_i - t_i$, we have the solution of Eq.(106),

$$T(x) - t(x) = (T_i - t_i)\exp\left(-\left(\frac{1}{(Gc)_{\min}} + \frac{1}{(Gc)_{\max}}\right) kPx\right) \tag{107}$$

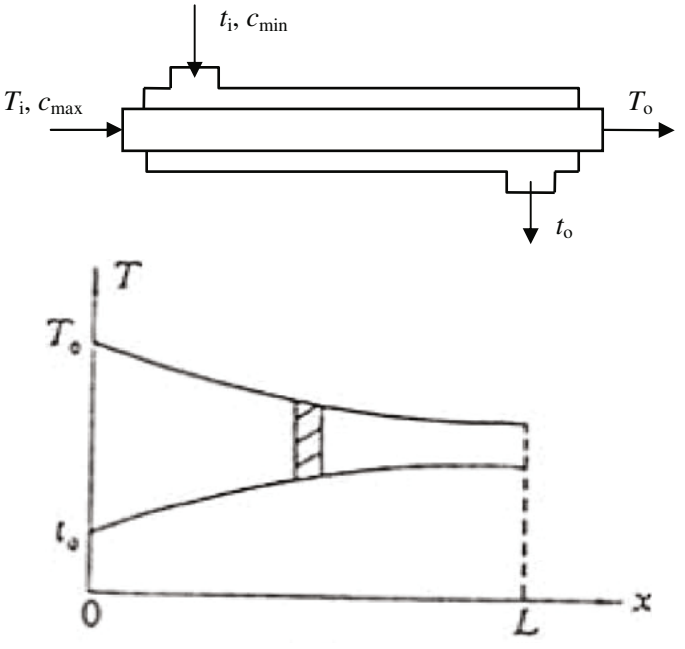

Fig. 52 Schematic of parallelflow heat exchanger

Substitution of Eq. (107) to Eq, (104) yields the field synergy factor for the single-pass parallel flow heat exchanger.

$$\Phi = \frac{\left(1-\exp\left(-2\left(1+c_r\right)Ntu\right)\right)/\left(\left(1+c_r\right)Ntu\right)}{\sqrt{\left(1-\exp\left(-2\left(1+c_r\right)Ntu\right)\right)/\left(2\left(1+c_r\right)Ntu\right)}} \tag{108}$$

where, $c_r = \left(Gc\right)_{\min}/\left(Gc\right)_{\max}$ is the heat capacity rate ratio,
$Ntu = kA/\left(Gc\right)_{\min}$ is the heat transfer unit.

(b) Counterflow heat exchanger

For a single-pass counterflow heat exchanger shown in Fig.53 the temperature difference field is more uniform than that in the parallel flow heat exchanger. Through similar derivation as for the parallel flow heat exchanger the field synergy factor of single-pass counterflow heat exchanger can be obtained

$$\Phi = \frac{\exp\left(Ntu\left(1-c_r\right)\right)-1}{\left(1-c_r\right)Ntu\sqrt{\dfrac{\exp\left(2Ntu\left(1-c_r\right)\right)-1}{2Ntu\left(1-c_r\right)}}} \tag{109}$$

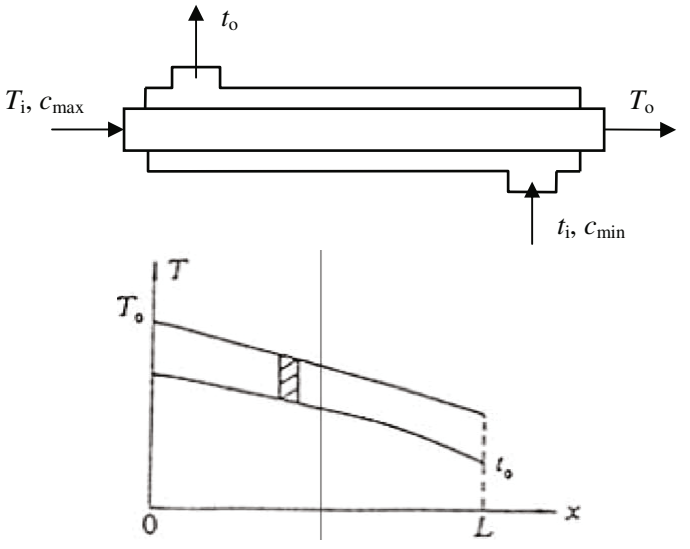

Fig. 53 Schematic of counterflow heat exchanger

(c) Mixed-unmixed crossflow heat exchanger

For a crossflow heat exchanger, shown in Fig. 54, the field synergy factor for mixed fluid of the larger capacity rate is

$$\Phi = 2\sqrt{\frac{1-\exp\left(-\left(1-\exp\left(-Ntu\right)\right)c_r\right)}{c_r Ntu\left(1+\exp\left(-Ntu\right)\right)\left(1+\exp\left(1-\exp\left(-Ntu\right)\right)c_r\right)}} \tag{110}$$

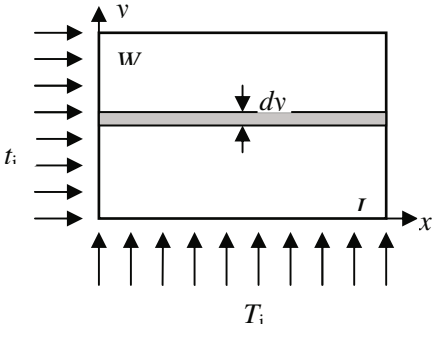

Fig. 54 Mixed-unmixed crossflow heat exchanger

The field synergy factor for mixed fluid of the smaller capacity rate is

$$\Phi = 2\frac{1-\exp(-(1-\exp(-c_r Ntu))/c_r)}{\sqrt{Ntu[1+\exp(-c_r Ntu)]\times[1-\exp(-2(1-\exp(-c_r Ntu))/c_r)]}} \quad (111)$$

The detailed derivation can be found in [64, 65].

In general, the field synergy factor of heat exchangers with complicated flow arrangements can be gained numerically only. Taking an unmixed-unmixed crossflow heat exchanger as an example, it can be divided into M×N sub elements shown in Fig.51. Based on the energy balance for each sub element,

$$(Gc)_c\left(t_o^{'}-t_i^{'}\right)dy=(Gc)_h\left(T_i^{'}-T_o^{'}\right)dx\approx k\left(T_i^{'}-t_i^{'}\right)dxdy \quad (112)$$

where $T_i^{'}$, $t_i^{'}$ are the inlet temperatures of the hot fluid and cold fluid, $T_o^{'}$, $t_o^{'}$ are the outlet temperatures. The field synergy number can then be calculated by using the discrete form of Eq.103,

$$\Phi=\frac{\sum_{i=1}^{N}\sum_{j=1}^{M}(T(i,j)-t(i,j))}{\sqrt{MN\sum_{i=1}^{N}\sum_{j=1}^{M}(T(i,j)-t(i,j))^2}} \quad (113)$$

7.3 Field Synergy Principle for Heat Exchanger Optimization

7.3.1 Field Synergy Principle for Heat Exchanger Optimization

In order to understand the relation between the effectiveness and the field synergy of heat exchangers, the synergy number of seven heat exchangers with different flow arrangements, shown in Fig.55, at different heat capacity rate ratio and heat transfer unit are numerically studied. The flow arrangements of the seven heat exchangers shown in Fig.55 are described in table 5. Fig.56 gives the effectiveness versus field synergy number for eleven heat exchangers including seven heat exchangers shown in Fig.55 and the other four heat exchangers with simple flow arrangements discussed in the last section. It can be seen from Fig.56 that the larger the field synergy number, the larger the effectiveness of heat exchanger. This indicates that improving the field synergy of heat exchanger can raise its effectiveness.

As well known, the counterflow heat exchanger has the largest effectiveness compared with other flow arrangements heat exchangers under the same given conditions. It seems that the flow arrangement determines the heat exchanger performance. However, this conclusion does not hold for multi-stream heat exchangers or heat exchangers with heat sink/source in fluids.

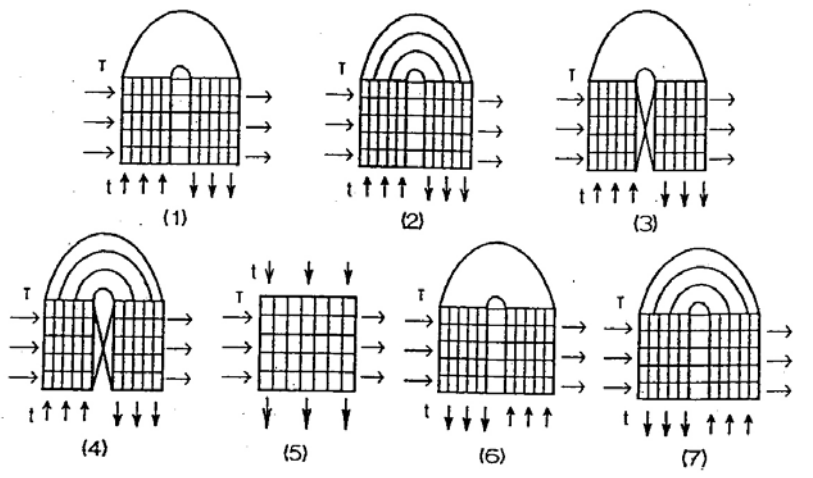

Fig. 55 Seven heat exchangers with different flow arrangements

Table 5 Description of the flow arrangements of the seven heat exchangers

1	Two pass parallel crossflow	Fluid1 unmixed in each pass and mixed between passes Fluid2 unmixed throughout, inverted order coupling
2		Fluid1 unmixed throughout, inverted order coupling Fluid2 unmixed throughout, inverted order coupling
3		Fluid1 unmixed in each pass and mixed between passes Fluid2 unmixed throughout, identical order coupling
4		Fluid1 unmixed throughout, inverted order coupling Fluid2 unmixed throughout, identical order coupling
5	crossflow	Both fluids unmixed
6	Two pass counter crossflow	Fluid1 unmixed in each pass and mixed between passes Fluid2 unmixed throughout, inverted order coupling
7		Fluid1 unmixed throughout, inverted order coupling Fluid2 unmixed throughout, inverted order coupling

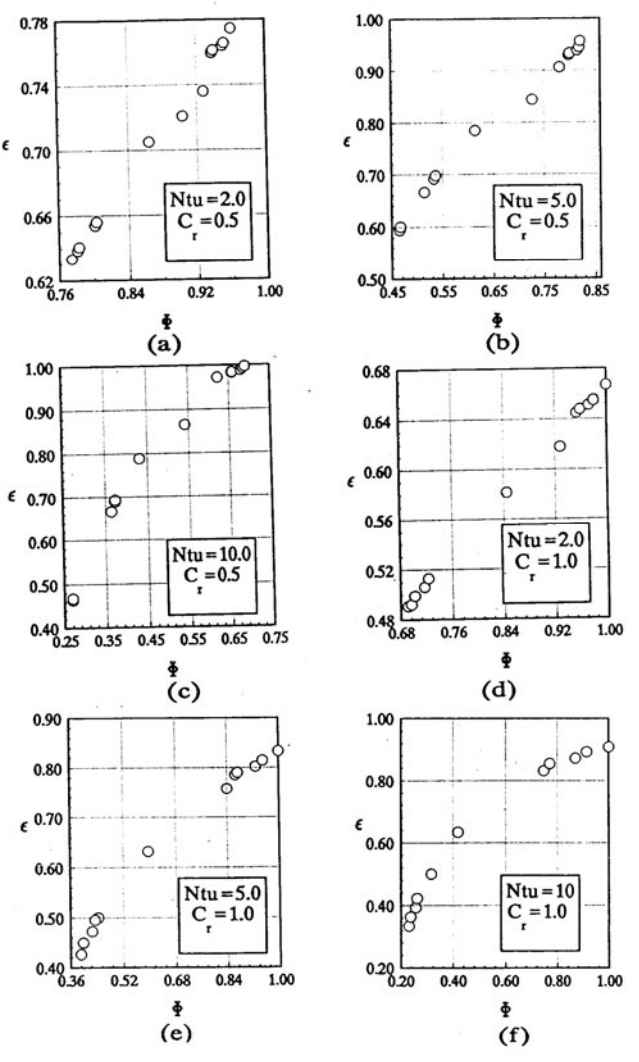

Fig. 56 Effectiveness versus field synergy number for eleven heat exchangers with different flow arrangements at different heat capacity rate ratio and heat transfer unit

The heat transfer equations for the parallelflow heat exchanger with heat sinks are,

$$-G_h c_h dT(x) = -G_c c_c dt(x) + Q_s(x) \tag{114}$$

$$kdx\big(T(x)-t(x)\big)=G_h c_h dT(x) \tag{115}$$

where G_h, G_c are the mass flow rates, c_h and c_c , the heat capacity, $T(x)$, $t(x)$, the local temperatures of hot and cold fluids respectively, $Q_s(x)$, heat flow rate delivered by the local heat sinks. Due to the presence of heat sinks in the cold fluid side, the temperature rise of the cold fluid in the parallel heat exchanger is suppressed, but the heat transfer rate increases due to the increase of the temperature difference between hot and cold fluids. If the intensity of the local heat sink is equal to the local heat transfer rate, the cold fluid temperature keeps constant, which resembles to a heat exchanger with the cold fluid being of infinite heat capacity rate. When the intensity of the heat sinks is larger than the local heat transfer rate, the cold fluid temperature will decreased and the consequent temperature difference between hot and cold fluids becomes more uniform along the flow direction, which resembles the evolution of the temperature difference in a counterflow heat exchanger. This phenomenon indicates that the effectiveness is dependent not only on the flow arrangement.

For comparison of the thermal performance of heat exchanger with the parallel flow and counter flow arrangements numerical calculations are carried out at parameters, Ntu = 1.0, cr = 0.5, $\eta = 3.24$, where η is the heat sink factor defined as,

$$\eta(x)=\frac{Q_s(x)}{(Gc)_{\min}(T_i-t_i)}. \tag{116}$$

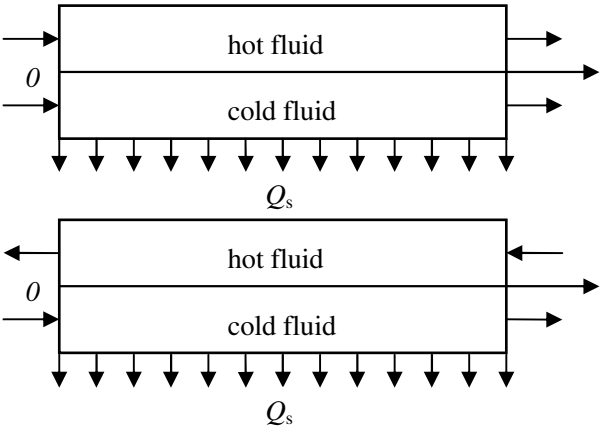

Fig. 57 Heat exchangers with heat sinks

The numerical results of temperature difference between hot and cold fluids for both the parallel flow and counterflow heat exchanger with heat sink are illustrated in Fig.58. It can be found that the temperature difference field in the parallelflow heat exchanger is more uniform than that in the counterflow heat exchanger. The field synergy number of the parallelflow heat exchanger equals to 1.00 higher than 0.85 for the counterflow heat exchanger. Correspondingly, the effectiveness of the parallelflow heat exchanger, 1.0, is larger than that of the counterflow heat exchanger, 0.991, which confirms that the criterion for heat exchanger performance is the field synergy number, rather than the flow arrangement of heat exchanger.

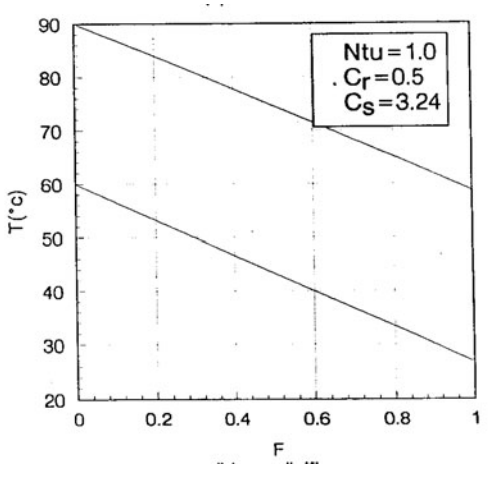

(a) parallelflow

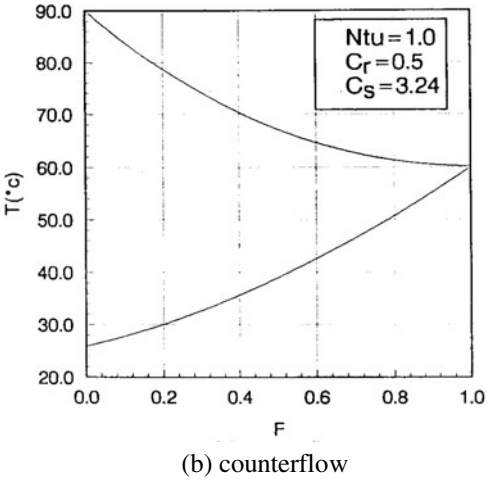

(b) counterflow

Fig. 58 Temperatures of hot and cold fluids in parallelflow/counterflow heat exchangers with heat sink (η=3.24)

In summary, the field synergy principle for heat exchanger optimization can be stated as: the more synergized the temperature fields of the hot and cold fluids is, the better thermal performance of heat exchanger has [64,65]. This principle is equivalent to the uniformity principle of temperature difference field in the earlier study, whose statement is that for given heat transfer unit and heat capacity rate ratio, the more uniform the temperature difference field is, the larger the effectiveness of the heat exchanger is [66,67] .

The field synergy principle is also suitable for multi-stream heat exchanger, the detail can be seen in references [63,64].

7.3.2 Optimization Method of Redistribution of Heat Exchange Area

For a crossflow heat exchanger with finned tube bundle, its field synergy can be improved by redistributing the heat transfer area. The numerical result of the normalized temperature difference field (TDF) for a two-dimensional crossflow heat exchanger is plotted in Fig. 59, from which the temperature difference on the diagonal and in the inlet region is larger than those on both sides of the diagonal and in the outlet region. The uniformity of TDF in the heat exchanger (on the other word, field synergy number), therefore, can be changed through the rearrangement of the heat exchange area to improve the performance of heat exchangers.

The log-mean temperature difference can be evaluated as usual from the discrete temperature difference by the expression [64,65]:

$$\Delta T_m = \frac{1}{MN}\sum_{i=1}^{M}\sum_{j=1}^{N} c(i,j)\left(T(i,j) - t(i,j)\right) \tag{117}$$

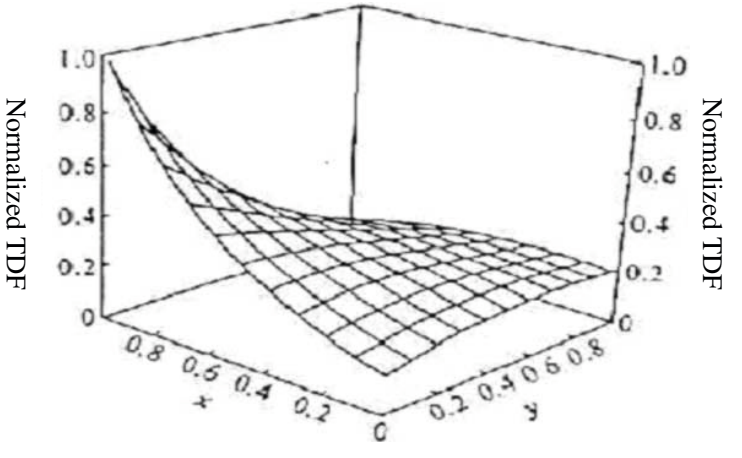

Fig. 59 TDF in crossflow heat exchanger for the uniform distribution of heat exchanger area

$$\sum_{i=1}^{M}\sum_{j=1}^{N} c(i,j)e\Delta x\Delta y = A \tag{118}$$

where $T(i,j)$-$t(i,j)$ is the local temperature difference between the hot and cold fluids in the subelement, M and N are the numbers of subelements in the length and width directions. The log-mean temperature difference equals to the arithmetic mean local temperature difference with a weight function of $c(i,j)$ when the heat transfer area is non-uniformly distributed. Based on Eqs. (117) and (118) and Δx, Δy are unchanged, the recurrence formula is derived for improving the field synergy/uniformity of TDF in the heat exchanger through the rearrangement of the heat transfer area [65],

$$c_{k+1}(i,j) = c_k(i,j)\frac{T_k(i,j) - t_k(i,j)}{\Delta T_{m,k}} \tag{119}$$

Combining Eq.(119) with the equations of energy conservation and known heat transfer rate, the field synergy factor, that is the uniformity factor of TDF, and the effectiveness for every recursion can be obtained numerically, and are shown in Fig. 60, where τ is the percentage increase in effectiveness compared to the case of uniform area distribution. Fig. 60 indicates that: (a) the TDF could be uniform and the effectiveness is consequently increased by rearranging the heat transfer area, (b) when C_r is unity the TDF of the crossflow heat exchanger could be fully uniform in an ideal distribution of heat transfer area, and the effectiveness of the crossflow heat exchanger becomes identical to that of the counterflow heat exchanger.

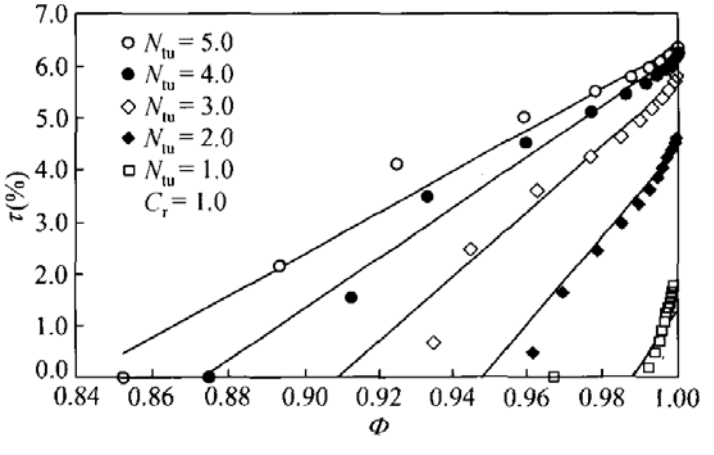

Fig. 60 Percentage increase in effectiveness versus the field synergy factor, Φ, for the redistribution of heat transfer area in crossflow heat exchanger(Cr=1.0)

If the heat transfer rate is fixed, the heat transfer area can be saved by redistributing the area shown in Fig.61, with the percentage of area saving defined as

$$\delta = \frac{A_1 - A_2}{A_1} \tag{120}$$

where, A_1, A_2 are the surface area of uniform distribution and non-uniform distribution.

As an example, the area redistribution can be realized by changing the density of the fins on the finned tubes. Fig.62 shows the crossflow heat exchanger consisting of four sub elements which is feasible in practice. The fin density in element A_e should be larger than in element A to improve the field synergy. The area saving percentages versus with the fin density ratio, $B=A_e/A$, are demonstrated at different values of C_r in Fig.63. It is seen that the optimal fin density ratio is between 3 and 4. For the case of fin density ratio equals to 2 and the heat capacity ratio is 0.4-0.6 the heat transfer area may be saved by 7-8%.[64]

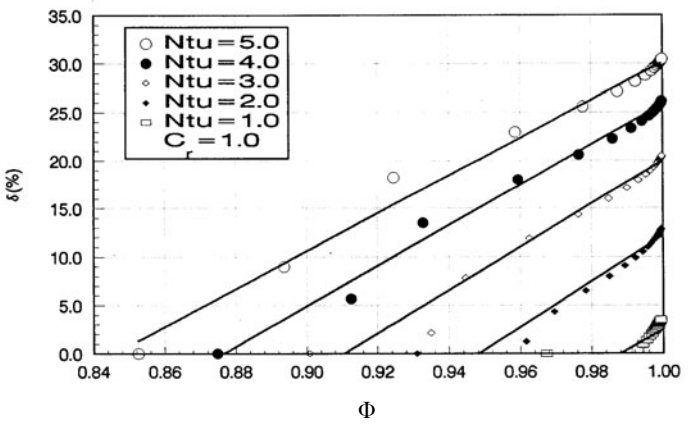

Fig. 61 Surface area saving by non-uniform distribution area for crossflow heat exchanger

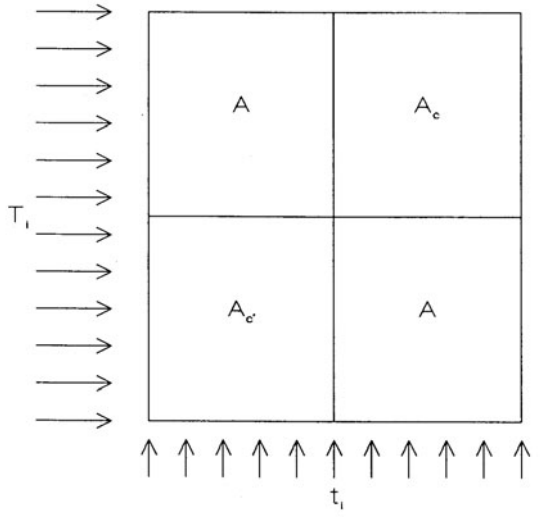

Fig. 62 Non-uniform surface area distribution

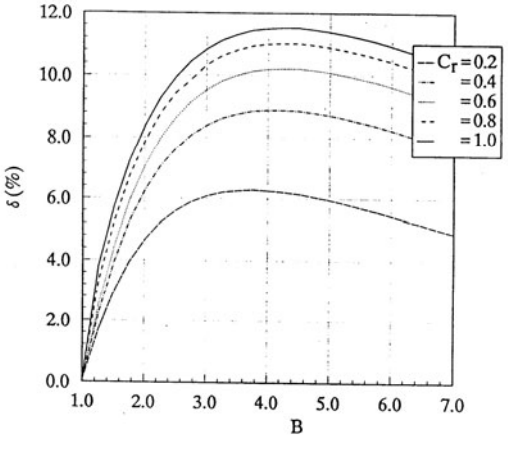

Fig. 63 Area saving percentage versus the fin density ratio with C_r as the parameter

8 Field Synergy Principle for Convective Mass Transfer

In view of the analogy between heat conduction governed by Fourier's law and mass diffusion governed by Fick's law, the field synergy principle and the extremum entransy dissipation principle for convective heat transfer have been extended to convective mass transfer processes by Chen [50] and Chen et al. [68]

8.1 Field Synergy Principle for Convective Mass Transfer

The 3D species concentration conservation equation for steady-state mass diffusion without mass sources can be written as,

$$\rho U \cdot \nabla Y = \nabla \cdot \left(\rho D \nabla Y \right) \tag{121}$$

where, ρ is density, U, velocity, ∇Y, species concentration gradient. Integrating the term on the right hand side of Eq.(121) over the mass transfer domain, Ω, and transforming the volume integral to surface integral by using Gaussian law, there is,

$$\int_{\Omega} \nabla \cdot \left(\rho D \nabla Y \right) dV = \int_{\Gamma} \vec{n} \cdot \left(\rho D \nabla Y \right) dS \tag{122}$$

For convective mass transfer process, the domain boundary can be divided into four parts: contaminant emitting surfaces, surfaces without mass transfer, air inlets and air outlets. Thus Eq. (122) can be written as

$$\begin{aligned} \int_{\Gamma} \vec{n} \cdot \left(\rho D \nabla Y \right) dS = & \int_{ms} \vec{n} \cdot \left(\rho D \nabla Y \right) dS + \int_{nms} \vec{n} \cdot \left(\rho D \nabla Y \right) dS \\ & + \int_{in} \vec{n} \cdot \left(\rho D \nabla Y \right) dS + \int_{out} \vec{n} \cdot \left(\rho D \nabla Y \right) dS \end{aligned} \tag{123}$$

The first term on the right hand side is the mass transfer between the contamination source surface and the air, which is the decontamination rate in convective mass transfer system. On surfaces without mass transfer, the contaminant concentration gradient is zero, so the second term on the right hand side is zero. The third and fourth terms are the axial diffusion of contaminants at the outlet and inlet, respectively, which may be neglected because the air velocity is high and the consequent contaminant concentration gradient is relatively small. Therefore, Eq. (123) can be simplified as,

$$\int_{\Omega} \rho U \cdot \nabla Y dV = \int_{ms} \vec{n} \cdot \left(\rho D \nabla Y \right) dS \tag{124}$$

Eq. (124) indicates that the integral of the fluid density times the dot product of the velocity vector and the concentration gradient over the entire domain equals to the overall decontamination rate in the ventilation system.

Define the equivalent length,

$$L = \frac{V}{S} \tag{125}$$

and the following dimensionless parameters,

$$\bar{U} = \frac{U}{U_{in}}, \quad \nabla \bar{Y} = \frac{\nabla Y}{(Y_{ms} - Y_{in})/L}, \quad d\bar{V} = \frac{dV}{V} \tag{126}$$

where, V is the volume of the convective mass transfer domain, S is the surface area emitting contaminants. Then, we have,

$$Sh = \mathrm{Re}\, Sc \int_{\Omega} \bar{U} \cdot \nabla \bar{Y} d\bar{V} \tag{127}$$

where Sh, Re and Sc represent the Sherwood number, the Reynolds number and the Schmidt number. Eq. (127) shows that the Sherwood number depends not only on the Reynolds number and the Schmidt number but also on the volume integration of $U \cdot \nabla Y$ in the mass transfer domain. The above integration is defined as the field synergy number of mass transfer,

$$Fc_m = \frac{Sh}{\mathrm{Re}\, Sc} = \int_{\Omega} \bar{U} \cdot \nabla \bar{Y} d\bar{V} \tag{128}$$

which represents the synergy between the velocity vector and the contaminant concentration gradient over the entire volume. Therefore, similar to convective heat transfer, we have the field synergy principle for convective mass transfer optimization, it states: the better the synergy of velocity and concentration gradient fields, the higher the convective mass transfer rate under the same other conditions. For decontamination ventilation, the fluid is air and the Schmidt number is constant. Hence, the various ways for increasing the overall strength of convective mass transfer can be classified into: (1) increasing the fresh air flow rates and the consequent Reynolds number and (2) increasing the field synergy number of mass transfer by changing ventilation arrangement. For a given fresh air flow rates, the Reynolds number is constant, so the convective mass transfer capability is influenced only by the mass transfer field synergy number.

8.2 Field Synergy Equation for Convective Mass Transfer Processes

Consider the analogy between heat and mass transfer, a new quantity of mass-entransy for a system can be defined as,

$$G_{vm} = \frac{1}{2} Q_{vm} Y \tag{129}$$

where, Q_{vm} is the total mass of a kind of species in the mixture, $Q_{vm} = \rho Y V$, its unit is, kg·(kg/kg). Y is the mass fraction of the species, its unit is kg/kg. The mass entransy of the species per unit volume is,

$$g_{vm} = \frac{1}{2}\rho Y^2 \tag{130}$$

Similarly, the mass-entransy dissipation function can be described as,

$$g_{\phi,m} = -q_m \cdot \nabla Y = \rho D\left|\nabla Y\right|^2 \tag{131}$$

For a steady, without mass source, laminar convective mass transfer process, the conservation equation for the species concentration is,

$$\rho U \cdot \nabla Y = \nabla \cdot \left(\rho D \nabla Y\right) \tag{132}$$

Multiplying Eq.(132) by Y, results in the mass-entransy equilibrium equation,

$$\rho U \cdot \nabla\left(\frac{Y^2}{2}\right) = \nabla \cdot \left(\rho D Y \nabla Y\right) - \rho D\left|\nabla Y\right|^2 \tag{133}$$

where the term on the left hand side of Eq.(133) is the mass-entransy transfer associated with fluid flow, the first term on the right hand side is the mass-entransy transfer associated with mass transfer, and the last term on the right hand side is the mass-entransy dissipation.

For a steady-state, constant property and incompressible convective mass transfer without mass sources, the optimal velocity field can be obtained by seeking the extremum of the mass-entransy dissipation for specific constraints, which is a typical variational problem. A Lagrange function can be constructed for a given set of constraints such as the continuity equation, species equation and given viscous dissipation,

$$\Pi = \iiint_{\Omega}\begin{bmatrix}\rho D\nabla Y \cdot \nabla Y + C_0\Phi \\ +A\left(\rho D\nabla \cdot \nabla Y - \rho U \cdot \nabla Y\right) + B\nabla \cdot \rho U\end{bmatrix} dV \tag{134}$$

where, A,B are functions of space, and the dimension of A is same as mass fraction, Y, C_0 is a constant, Φ is viscous dissipation. The variation of Eq.(134) with respect to Y leads to

$$-\rho U \cdot \nabla A = \rho D\nabla \cdot \left(\nabla A\right) - 2\rho D\nabla \cdot \left(\nabla Y\right) \tag{135}$$

For a given uniform concentration boundary, $A_b = 0$, and for a given uniform mass flux boundary,

$$\left(\partial A/\partial n\right)_b = 2\left(\partial Y/\partial n\right)_b. \tag{136}$$

The variation of Eq.(134) with respect to U , A and B leads to,

$$\mu\nabla^2 U + \frac{\rho}{2C_0} A\nabla Y + \frac{1}{2C_0}\nabla B = 0 \tag{137}$$

$$\rho U \cdot \nabla Y = \nabla \cdot \left(\rho D \nabla Y\right) \tag{138}$$

$$\nabla \cdot \rho U = 0 \tag{139}$$

There are four unknown variables, U, Y, A, B, in the Eqs.(135) and (137), species concentration equation, Eq.(138) and continuity equation, Eq.(139). Compared Eq.(137) with the momentum equation,

$$\rho U \cdot \nabla U = -\nabla P + \mu\nabla^2 U + F \tag{140}$$

we have,

$$B = -2C_0 P \tag{141}$$

$$F = C_{\Phi m} A\nabla Y + \rho U \cdot \nabla U \tag{142}$$

In which, $C_{\Phi m}$ is a constant related to the viscous dissipation in the domain, its dimension is Pa/(kg/kg)^2, and,

$$C_{\Phi m} = \frac{\rho}{2C_0} \tag{143}$$

Finally, we have the field synergy equation for convective mass transfer,

$$\rho U \cdot \nabla U = -\nabla P + \mu\nabla^2 U + \left(C_{\Phi m} A\nabla Y + \rho U \cdot \nabla U\right) \tag{144}$$

it is a momentum equation with an additional volume body force.

This additional body force can be divided into two parts, one is related to velocity, named as additional inertia force, $F_U = \rho U \cdot \nabla U$, and the other is related to the species concentration, named as additional concentration gradient force, $F_Y = C_{\Phi m} A\nabla Y$.

For the cases without the additional concentration gradient force, the field synergy equation for convective mass transfer can be simplified to,

$$0 = -\nabla P + \mu \nabla^2 U \tag{145}$$

As shown in Eq. (145), the additional body force counteracts the inertial force of the fluid flow. Its velocity distribution is of the minimum viscous dissipation relative to any other one for incompressible flow with the same velocity boundary [69]. If the additional concentration gradient force and the additional inertial force occur simultaneously in the fluid flow, the viscous dissipation becomes larger. The role of the additional concentration gradient force is to drive the fluid to flow along the direction of the mass flow, and then enhance the convective mass transfer. Therefore, the additional concentration gradient volume force may increase not only the viscous dissipation, but also enhance convective mass transfer. For various given values of $C_{\phi,m}$, different optimal velocity fields can be obtained in terms of solving the field synergy equation of Eq. (144).

8.3 Application

Indoor air quality (IAQ) is also a big problem for modern human beings. To improve the IAQ and to save energy, it needs to optimize the ventilating system so as to increase the ventilation efficiency. To illustrate the applicability of field synergy principle for the optimization of convective mass transfer, the decontamination quality was varied by changing the boundary conditions of the ventilation system, such as the intake air velocity and the ventilation arrangement. In addition, for a given set of boundary conditions, the field synergy equation for convective mass transfer was solved to vary the synergy of velocity and concentration gradient fields and to change the decontamination capability. In the simulation, all the flows were assumed to be laminar and steady.

8.3.1 Analysis of the Field Synergy

The two 2D ventilation configurations are shown in Fig. 64 and Fig.65. The dimensions of the rectangular cavity are L = 4 mm, H = 3 mm and $W_1 = W_2 = W_3 = W_4 = 0.2$ mm. Air enters the rectangular cavity from the top left corner horizontally in Fig. 64 and vertically in Fig.65. The outlet locates at the lower right corner. The inlet air has a zero contaminant mass fraction. The contaminant source with a contaminant mass fraction of 0.01 is placed on the bottom, while there is no mass transfer on the left, right and upper surfaces of the cavity.

The numerical results are shown in Fig.66 and Fig.67 for the vertical and horizontal ventilation configurations. With increasing the air inlet velocities, the overall decontamination rate increases non-linearly, while the field synergy number decreases. It is found from the two configurations in Fig.66 and Fig.67 that the field synergy of convective mass transfer in the vertical inlet configuration is much better than that in the horizontal inlet one. This is why the decontamination rate of

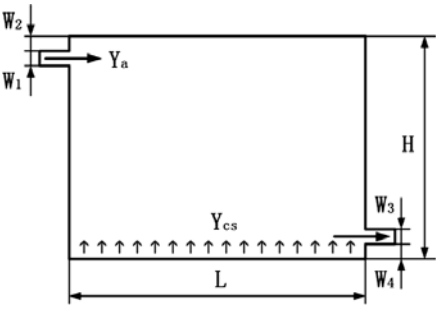

Fig. 64 Ventilation configuration with a horizontal inlet at the top left corner

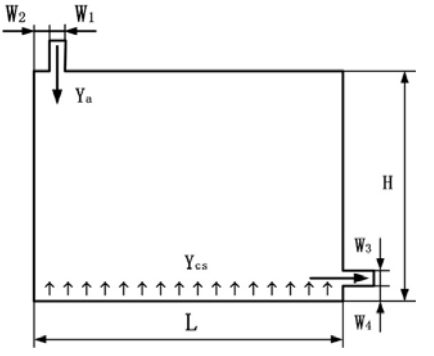

Fig. 65 Ventilation configuration with a vertical inlet at the top left corner

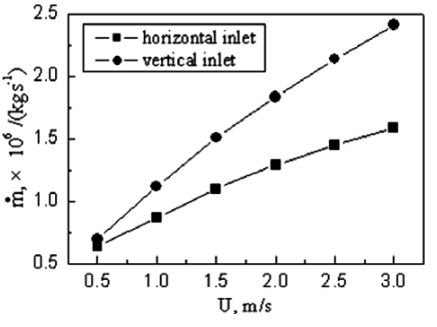

Fig. 66 Variation of decontamination rate horizontal and vertical inlets

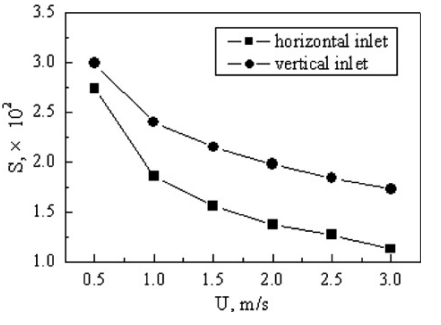

Fig. 67 Variation of field synergy numbers for for horizontal and vertical inlets

the vertical inlet configuration is larger than that of the horizontal inlet one for the same boundary condition.

8.3.2 Validation and Application of the Field Synergy Equation

The ventilation system with a horizontal inlet at the top left corner was selected to analyze how additional forces affect the velocity field and the decontamination rate. Numerical results for the velocity vectors and contaminant mass fraction contours for convective mass transfer without additional volume forces in the rectangular cavity at the intake velocity of 2 m/s are presented in Fig. 68. The entering air from the inlet creates a clockwise eddy in the cavity and the velocity vectors are parallel to the mass fraction contours in most of the computational domain, which leading to a worse field synergy. In this case the field synergy number is 1.37×10^{-2} and the overall decontamination rate is 1.29×10^{-6} kg /s.

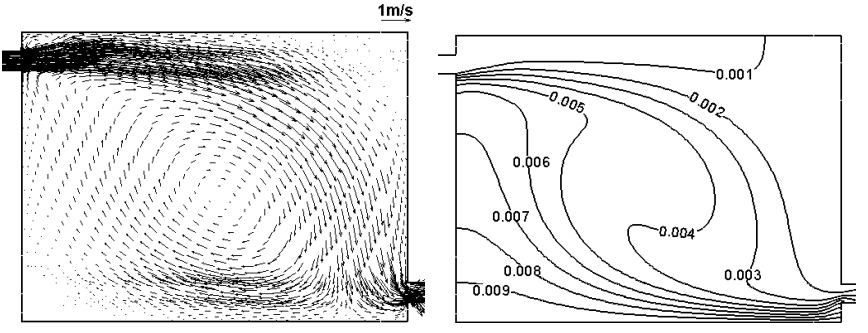

(a) velocity vectors (b) mass fraction contours

Fig. 68 Convective mass transfer without additional volume forces

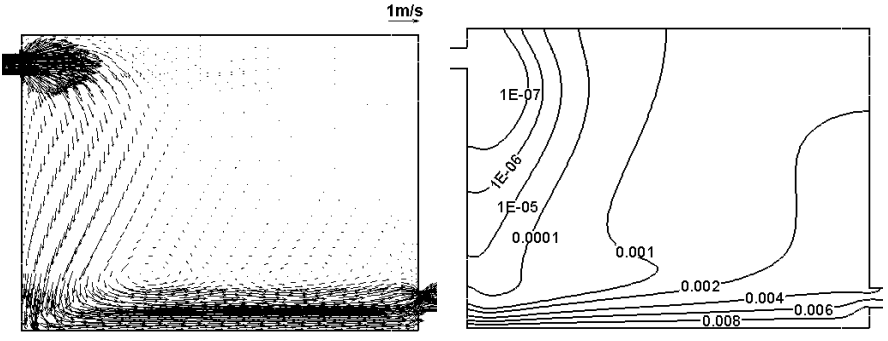

(a) velocity vectors (b) mass fraction contours

Fig. 69 Optimized results for the case of $C_{\phi,m} = -5 \times 10^5$

Fig.69 shows the numerical results for the velocity vectors and mass fraction contours in the cavity for the case of $C_{\phi,m} = -5 \times 10^5$. After entering the rectangle cavity from the inlet, the air is deflexed and flows down the left wall immediately, and then flows along the contaminant surface towards the outlet. The velocity vectors and the mass fraction contours are nearly perpendicular at the lower left corner of the cavity, leading to a much better field synergy. The field synergy number for this case is 3.34×10^{-2} with an overall decontamination rate of 3.15×10^{-6} kg/s, which are both 2.44 times the values before optimization.

9 Brief Summary

Based on the reexamination of the physical mechanism of heat convection, the concept of field synergy, which denotes the zero included angle between the local

velocity and temperature gradient vectors in the convection domain, is introduced. The field synergy principle is then proposed for the heat transfer optimization, which states: the better the synergy of velocity and temperature gradient fields, the higher the convective heat transfer rate for the given boundary conditions. The field synergy principle can not only explain the heat transfer enhancement mechanism of existing enhanced technologies, but also guide us to develop a series of new types of enhanced technologies.

In view of the fact that the field synergy principle is phenomenal only and can not be applied to the quantitative design of heat transfer optimization, the extremum entransy dissipation (EED) principle for heat transfer optimization are developed for optimizing heat transfer with the purpose of object heating, rather than doing work. The new quantity, entransy, describes the heat transfer ability of a body and the entransy dissipation during heat transfer process is the measure of its irreversibility. The EED principle can be stated as: for the prescribed heat flux boundary conditions, the least entransy dissipation rate in the domain leads to the minimum boundary temperature difference, or the largest entransy dissipation rate with a prescribed boundary temperature difference leads to the maximum heat flux.

When the EED principle is used to optimize the volume-to-point heat conduction problem, the optimal distribution of high conductivity leads to the lowest average domain temperature, which is lower than that with the minimum entropy generation (MEG) as the optimization criterion. This indicates that the EED principle is more preferable than the MEG principle for heat conduction optimization with the purpose of the reduction of the domain temperature.

When the EED principle is used to optimize the convective heat transfer problems, the field synergy equations are derived by variational analysis for both laminar and turbulent heat transfer at the given viscous dissipation (pumping power). By solving the field synergy equation, the optimal flow fields for several tube flows are achieved. Some enhanced tubes, such as the alternating elliptical axis tube and discrete double inclined ribs tube are developed, which may generate a velocity field close to the optimal one and augment heat transfer markedly with less increased flow resistance.

Unlike the heat transfer enhancement, heat transfer optimization refers to maximizing the heat transfer rate for a given pumping power. Both the field synergy principle and the EED principle are the optimization principle for heat transfer process.

Finally, both the field synergy principle and the extremum entransy dissipation principle are extended to be applied for the heat exchanger optimization and mass convection optimization.

Acknowledgement. This work was financially supported by the National Basic Research Program of China (G2000026301 & 2007CB206901). And the authors would like to thank the students for their contributions, they are Drs. Zhou S.Q., Wang S., Xia Z.Z., Meng J.A., Cheng X.G., Zhu H.Y., Li X.W., Chen Q. and Liu X.B.

References

1. Cebeci, T., Bradshaw, P.: Physical and Computational Aspects of Convection Heat Transfer. McGraw-Hill, New York (1980)
2. Warren, M., Hartnett, J.P., Schneider, P.T., et al.: Handbook of Heat Transfer, 3rd edn. McGraw-Hill, New York (1998)
3. Webb, R.L., Bergles, A.E.: Heat Transfer Enhancement: Second Generation Technology. Mechanical Engineering 115(6), 60–67 (1983)
4. Bergles, A.E.: Some Perspectives on Enhanced Heat Transfer Second Generation Heat Transfer Technology. ASME Journal of Heat Transfer 110, 1082–1096 (1988)
5. Withers, J.G.: Tube-Side Heat transfer and Pressure Drop for Tubes Having Helical Internal Ridging with Turbulent/Transitional Flow of Single-Phase Fluid. 1. Single-Helix Ridging. Heat Transfer Eng. 2(1), 48–61 (1980)
6. Withers, J.G.: Tube-Side Heat transfer and Pressure Drop for Tubes Having Helical Internal Ridging with Turbulent/Transitional Flow of Single-Phase Fluid. 2. Multiple-Helix Ridging. Heat Transfer Eng. 2(2), 43–50 (1980)
7. Kalinin, E.K., Dreitser, G.A., Yarkho, S.A., Kusminov, V.A.: The Experimental Study of the Heat Transfer Intensification under Conditions of Forced One- and Two-Phase Flow in Channels. In: Bergles, A.E., Webb, R.L. (eds.) Augmentation of Convective Heat and Mass Transfer, ASME, New York (1970)
8. Ravigururajan, T.S., Bergles, A.E.: Optimization of In-Tube Enhancement for Large Evaporators and Condensers. Energ. 21(5), 421–432 (1996)
9. Manglik, R.M., Bergles, A.E.: Heat Transfer and Pressure Drop Correlations for Twisted-Tape inserts in Isothermal Tubes: Part II- Transition and Turbulent Flows. Transactions of the ASME 115, 890–896 (1993)
10. Fujita, Y., Lopez, A.M.: Heat-transfer Enhancement of Twisted-tape Inserts in Turbulent Pipe Flows. Heat Transfer - Japanese Research 24(4), 378–396 (1995)
11. Kumar, P., Judd, R.L.: Heat Transfer with Coiled Wire Turbulence Promoters. Can. J. Chem. Eng. 48, 378–383 (1970)
12. Ravigurrurajan, T.S., Bergles, A.E.: Development and Verification of General Correlations for Pressure Drop and Heat Transfer in Single-Phase Turbulent Flow in Enhanced Tubes. Experimental Thermal and Fluid Science 13, 55–70 (1996)
13. Guo, Z.Y., Li, D.Y., Wang, B.X.: A novel concept for convective heat transfer enhancement. International Journal of Heat And Mass Transfer 41(14), 2221–2225 (1998)
14. Guo, Z.Y.: Mechanism and control of convective heat transfer - Coordination of velocity and heat flow fields. Chinese Science Bulletin 46(7), 596–599 (2001)
15. Tao, W.Q., Guo, Z.Y., Wang, B.X.: Field synergy principle for enhancing convective heat transfer-—its extension and numerical verifications. International Journal of Heat and Mass Transfer 45, 3849–3856 (2002)
16. Meng, J.A., Liang, X.G., Li, Z.X.: Field synergy optimization and enhanced heat transfer by multi-longitudinal vortexes flow in tube. Int. J. Heat and mass Transfer 48, 3331–3337 (2005)
17. Meng, J.A., Chen, Z.J., Li, Z.X., Guo, Z.Y.: Field-Coordination Analysis and Numerical Study on Turbulent Convective Heat Transfer Enhancement. J. of Enhanced Heat Transfer 12(1), 73–83 (2005)

18. Meng, J.A., Liang, X.G., Chen, Z.J., Li, Z.X.: Experimental study on convective heat transfer in alternating elliptical axis tubes. Experimental Thermal and Fluid Science 29(4), 457–465 (2005)
19. Meng, J.A., Liang, X.G., Li, Z.X., Guo, Z.Y.: Numerical study on low Reynolds number convection in alternate elliptical axis tube. Journal of Enhanced Heat Transfer 11(4), 307–313
20. Yu, J.C., Li, Z.X., Zhao, T.S.: An analytical study of pulsating laminar heat convection in a circular tube with constant heat flux. Int. J. Heat and mass Transfer 47(24), 5297–5301 (2004)
21. Wang, S., Guo, Z.Y., Li, Z.X.: Heat transfer enhancement by using metallic filament insert in channel flow. Int. J. Heat and Mass Transfer 44, 1373–1378 (2001)
22. Guo, Z.Y., Tao, W.Q., Shah, R.K.: The field synergy (coordination) principle and its applications in enhanceing single phase convective heat transfer. Int. J. Heat Mass Transfer 48(9), 1797–1807 (2005)
23. Chen, W.L., Guo, Z.Y., Chen, C.K.: A numerical study on the flow over a novel tube for heat-transfer enhancement with a linear Eddy-viscosity model. International Journal of Heat And Mass Transfer 47(14-16), 3431–3439 (2004)
24. Yang, L.J., Ren, J.X., Song, Y.Z., Min, J.C., Guo, Z.Y.: Convection heat transfer enhancement of air in a rectangular duct by application of a magnetic quadrupole field. International Journal of Engineering Science 42(5-6), 491–507 (2004)
25. Tao, W.Q., He, Y.L., Wang, Q.W., Qu, Z.G., Song, F.Q.: A unified analysis on enhancing single phase convective heat transfer with field synergy principle. International Journal of Heat and Mass Transfer 45, 4871–4879 (2002)
26. Zeng, M., Tao, W.Q.: Numerical Verifi cation of the Fıeld Synergy Principle for Turbulent Flow. Journal of Enhanced Heat Transfer 11(4), 451–457 (2004)
27. Zhou, J.J., Tao, W.Q.: Numerical simulation and field synergy analysis of heat transfer performance of radial slit fin surface. Progress in Computational Fluid Dynamics 6(7), 419–427 (2006)
28. Guo, Z.Y., Zhu, H.Y., Liang, X.G.: Entransy—A physical quantity describing heat transfer ability. International Journal of Heat and Mass Transfer 50, 2545–2556 (2007)
29. Cheng, X.G.: Entransy and its application in heat transfer optimization, Ph.D. thesis, Tsinghua University, Beijing (2004) (in Chinese)
30. Xia, Z.Z., Cheng, X.G., Li, Z.X., Guo, Z.Y.: Bionic optimization of heat transport paths for heat conduction problems. Journal of Enhanced Heat Transfer 11(2), 119–131 (2004)
31. Cheng, X.G., Li, Z.X., Guo, Z.Y.: Constructs of the highly effective heat transport paths by bionic optimization. Sciences in China (Series E) (3), 296–302 (2003)
32. Chen, Q., Ren, J.X., Meng, J.A.: Field synergy equation for turbulent heat transfer and its application. Int. J. Heat Mass Tran. 50(25-26), 5334–5339 (2007)
33. Zhao, T.S., Song, Y.J.: Forced convection in a porous medium heated by a permeable wall perpendicular to flow direction: analyses and measurements. Int. J. Heat Mass Transfer 44, 1031–1037 (2001)
34. Onsager, L.: Reciprocal relations in irreversible processes. II. Phys. Rev. 38(12), 2265–2279 (1931)
35. Onsager, L., Machlup, S.: Fluctuations and irreversible processes. Phys. Rev. 91(6), 1505–1512 (1953)
36. Prigogine: Introduction to Thermodynamics of Irreversible Processes, 3rd edn., pp. 76–77. Wiley, New York (1967)

37. Bejan, A.: Entropy Generation through Heat and Fluid Flow, pp. 118–134. Wiley, New York (1982)
38. Bejan, A.: Entropy Generation Minimization, pp. 47–112. CRC Press, Florida (1996)
39. Bejan, A.: Constructal-theory network of conducting paths for cooling a heat generation volume. Int. J. Heat Mass Transfer 40(4), 799–808 (1997)
40. Bejan, A.: Shape and Structure, from Engineering to Nature, pp. 52–81. Cambridge University Press, New York (2000)
41. Guo, Z.Y., Cheng, X.G., Xia, Z.Z.: Least dissipation principle of heat transport potential capacity and its application in heat conduction optimization. Chin. Sci. Bull. 48(4), 406–410 (2003) (in Chinese)
42. Biot, M.A.: Variational principle in irreversible thermodynamics with applications to viscoelasticity. Phys. Rev. 97(6), 1463–1469 (1955)
43. Cheng, X.G., Li, Z.X., Guo, Z.Y.: Variational principles in heat conduction. J. Eng. Thermophys. 25(3), 457–459 (2004) (in Chinese)
44. Finlayson, B.A., Scriven, L.E.: On the search for variational principles. Int. J. Heat Mass Transfer 10, 799–821 (1967)
45. Finlayson, B.A.: The Method of Weighted Residuals and Variational Principles, with Application in Fluid Mechanics. Heat and Mass Transfer, 347 (1972)
46. Xia, Z.Z.: Augmentation and optimization on heat conduction and convection processes, Ph.D. dissertation, Tsinghua University (2002)
47. Meng, J.A.: Enhanced heat transfer technology of longitudinal vortices based on field coordination principle and its application, Ph.D. dissertation, Tsinghua University (2004)
48. Qian, W.C.: The variational principle and general variational principle of viscous fluid mechanics. Appl. Math. Mech. 5(3), 305–322 (1984)
49. Meng, J.A., Guo, Z.Y.: Optimization for laminar convection heat transfer. In: 4th Kyoto-Seoul-Tsinghua University Thermal Engineering Conference, Kyoto, Japan (2004)
50. Chen, Q.: Irreversibility and Optimization of Convective Transport Processes, Ph.D. dissertation, Tsinghua University (2008)
51. Chen, Q., Ren, J.X., Meng, J.A.: Field synergy equation for turbulent heat transfer and its application. Int. J. Heat Mass Tran. 50(25-26), 5334–5339 (2007)
52. Fuji, K., Itoh, N., Innami, T., et al.: Heat transfer pipe. U.S. Patent, 4044797, assigned to Hitachi Ltd. (1977)
53. Webb, R.L.: Principles of enhanced heat transfer. Jone Wiley Sons, New York (1994)
54. Al-Fahed, S.F., Ayub, Z.H., Al-Marafie, A.M., et al.: Heat transfer and pressure drop in a tube with internal microfins under turbulent water flow condition. Exp. Thermal Fluid Sci. 7(3), 249–253 (1993)
55. Wang, C.C., Chiou, C.B., Lu, D.C.: Single-phase heat transfer and flow friction correlations for micro-fin tubes. Int. J. Heat Fluid Flow 17, 500–508 (1996)
56. Al-Fahed, S., Chamra, L.M., Chakroun, W.: Pressure drop and heat transfer comparison for both microfin tube and twisted-tape inserts in laminar flow. Exp. Thermal Fluid Sci. 18, 323–333 (1999)
57. Li, X.W.: Numerical and experimental study of the heat transfer enhancement in turbulent channel flow. Ph.D. dissertation, Tsinghua University (2008)
58. Li, X.W., Meng, J.A., Li, Z.X.: Enhancement mechanisms for single-phase turbulent heat transfer in micro-fin tubes. J. Enhanced Heat Transfer 15(3), 1–16 (2008)

59. Li, X.W., Meng, J.A.: Single-phase heat transfer characteristics of a micro-fin tube. In: Sixth International Conference on Enhanced, Compact and Ultra-Compact Heat Exchangers: Science, Engineering and Technology, Potsdam, Germany (September 2007)
60. Li, X.W., Meng, J.A., Li, Z.X.: Experimental study of single-phase pressure drop and heat transfer in a micro-fin tube. Experimental Thermal and Fluid Science 32(2), 641–648 (2007)
61. Meng, J. A.: Alternating elliptical axis heat transfer tube, Inventive patent of China, No. 00136122.8 (2000)
62. Meng, J.A., et al.: Heat transfer enhancement DDIR-tube, Inventive patent of China, no.: 03138077.8 (2003)
63. Guo, Z.Y., Wei, S., Cheng, X.G.: A novel method to improve the performance of heat exchanger - Temperature fields coordination of fluids. Chinese Science Bulletin 49(1), 111–114 (2004)
64. Li, Z.X., Guo, Z.Y.: Field synergy principle for convective heat transfer optimization. Science Press, Beijing (2010) (in Chinese)
65. Zhou, S.Q.: Uniformity principle of temperature difference field in heat exchanger and its application, Ph.D. dissertation, Tsinghua University (1995)
66. Guo, Z.Y., Zhou, S.Q., Li, Z.X., Chen, L.G.: Theoretical analysis and experimental confirmation of the uniformity principle of temperature difference field in heat exchanger. Int. J. Heat Mass Transfer 45(10), 2119–2127 (2002)
67. Guo, Z.Y., Li, Z.X., Zhou, S.Q., Xiong, D.X.: Principle of uniformity of temperature difference field in exchanger. Science in China(Series E) 39(1), 68–75 (1996)
68. Chen, Q., Ren, J.X., Guo, Z.Y.: Field synergy analysis and optimization of decontamination ventilation designs. International Journal of Heat and Mass Transfer 51, 873–881 (2008)
69. Batchelor, G.K.: An Introduction to Fluid Dynamics, Cambridge, p. 227 (1967)

Nonequilibrium Transport: The Lagging Behavior

D.Y. Tzou* and Jinliang Xu

Abstract. Lagging behavior describes the non-instantaneous response between heat flux and temperature gradient in nonequilibrium heat transport. Extending over to mass transport, mass flux is in place of the heat flux while density/concentration gradient is in place of the temperature gradient. The lagging behavior may occur during the ultrafast transient; in times comparable to the intrinsic times characterizing the nonequilibrium transition of thermodynamic states. For heat transport, such intrinsic times include the mean free time of energy carriers and the thermalization time for the energy carriers to come to thermal equilibrium. For mass transport involving different species, on the other hand, the intrinsic times include the finite time required for the effective interdiffusion among the participating substances, the finite time required for the chemical reactions to take place in forming the interfacial substance, or in some cases the finite times required for releasing or absorbing specific species. This chapter is dedicated to the lagging behavior during the ultrafast response in nonequilibrium heat/mass transport. The process is termed "ultrafast" because the time scales involved are comparable to the intrinsic time scales governing the various nonequilibrium processes in heat/mass transport. The essence of thermal lagging will be first illustrated by well known examples in microscale heat transport, with emphasis on the admissibility within the framework of nonequilibrium thermodynamics. Equivalence of the lagging behaviors in heat and mass transport then follows to stretch the lagging response over to the growth of the ultrathin

D.Y. Tzou
Department of Mechanical and Aerospace Engineering,
University of Missouri, Columbia, MO 65211, USA
e-mail: tzour@missouri.edu

Jinliang Xu
School of Renewable Energy
North China Electric Power University
Beijing 102206, China

* Corresponding author.

L.Q. Wang (Ed.): Advances in Transport Phenomena, ADVTRANS 2, pp. 93–170.
springerlink.com

film/interfacial compound, bioheat transfer, and multistage interdiffusion for drug delivery in tumor cells. In the full spectrum from the electron/phonon interactions in femto- to picoseconds, the heat exchange between blood and tissues and drug delivery in minutes to hours, to the ultrathin film/interfacial compound growth in days, the sources for lagging are identified and the analytical expressions for the phase lags are derived. A regime map based on the response time is established to characterize the alterations between wave and high-order diffusion as the phase lags of the various orders activate/diminish at certain time scales. The concept of thermal lagging, which is a nonequilibrium behavior in time, is extended to cover the nonlocal response in space in making contacts with ultrafast heat transport through the phonon gas with a finite mass. The correlation length and intrinsic times are linked together in describing the ultrafast thermal transport in small scales.

1 Introduction

Transport phenomena are nonequilibrium by nature, where the conservation laws join the constitutive equations in describing the transition of the thermodynamic state in a physical system. Nonequilibrium transition of the thermodynamic state is a direct consequence of the fast transient during the transport process and is closely ties to the pace at which the thermodynamic state varies as a result of the unbalanced heat or mass flow. The time-rate of change of temperature or mass density, for example, is a measure for the pace during the thermodynamic transition. Such a change with respect to time, termed time-rate of change, is an essential ingredient in nonequilibrium transport. If the time-rate of change of the thermophysical properties in transition of the thermodynamic state is small, the transport process can be assumed quasi-stationary, meaning that all thermodynamic properties would have sufficient time to well establish themselves before the thermodynamic state moves on to the next state. Fourier's law in conjunction with the conservation of energy (in heat transport) and Fick's law along with the conservation of mass (in mass transport) are known examples describing the quasi-stationary transition of thermodynamic states, giving rise to the transport equation of a diffusion type:

$$\frac{\partial^2 T}{\partial x^2}+\frac{\partial^2 T}{\partial y^2}+\frac{\partial^2 T}{\partial z^2}\equiv \nabla^2 T=\frac{1}{\alpha}\frac{\partial T}{\partial t} \tag{1}$$

where all physical properties are assumed constant and x, y, and z are the Cartesian coordinates, t is time, T is temperature (in heat transport) or density/concentration (mass transport), α is thermal/mass diffusivity, and ∇^2 the Laplacian operator. The right-hand side of Eq. (1) results from the time-rate of change of internal energy/mass density, as a result of unbalanced heat (or mass density) entering and leaving the representative volume describing the transport process. The balanced law based on the time-rate of change of internal energy, as an interpretation of the statement made by Fourier in 1822, distinguishes principles of heat transfer from

mechanical theories where such a balanced law is based on the dynamic inertia. There are several implications from Eq. (1). First, for a conductor with a characteristic dimension of L, the time-rate of change of temperature on the right-hand side, the transient term, will be as important as the conductive (steady-state) term on the left-hand side in times (t) comparable to the characteristic time of Fourier diffusion, $t \sim (L^2/\alpha)$. This can be readily seen by comparing the denominators involved in Eq. (1), $x \sim L^2 \cong \alpha t$, or $t \cong (L^2/\alpha)$. For abbreviation, the characteristic time of Fourier diffusion, L^2/α, is termed "diffusion time," which appears as the first time scale in the regime map to be constructed later in Fig. 10. As $t >> (L^2/\alpha)$, the right-hand side of Eq. (1) is vanishingly small and the effect of conduction dominates the transport process in steady state. As $t << (L^2/\alpha)$, or $L >> \sqrt{(\alpha t)}$, on the other hand, the left-hand side of Eq. (1) is vanishingly small and the lumped formulation prevails without the conduction effect. As recognized, the ratio of t to (L^2/α) is the well-known Fourier number defined in transient heat conduction. Second, the characteristic solution to Eq. (1) is

$$T \sim T_0(x,y,z)\exp\left[-\frac{t}{\left(L^2/\alpha\right)}\right], \quad \text{with } T_0 \text{ satisfying} \quad \nabla^2 T_0 + \frac{T_0}{L^2} = 0 \ . \tag{2}$$

For most solids with $\alpha \sim 10^{-5}$ m/s, the diffusion time (L^2/α) is of the range from 10^5 s (macroscale conductor with $L \sim 10^0$ m) to 10^{-13} s (microscale conductor with $L \sim 1$ nm). For ultrafast transient in the femtosecond (fs) domain, $t \sim 10^{-15}$ s and consequently $[t/(L^2/\alpha)] \sim 10^{-20} - 10^{-2}$ in the exponential function of Eq. (2), the diffusion based model would result in a negligible response since $T \sim T_0$. Recent experiments involving material interactions with femtosecond lasers, however, have shown quite a contrary. Not only a definite response has been observed in the samples irradiated by femtosecond lasers [1-7], the *clean cuts* resulting from ultrafast, ultraintense lasers have become a unique asset for producing nanoscale patterning and high-precision manufacturing [8-17]. Shown by the estimate on the order of magnitude above, the ultrafast interaction of materials with femtosecond lasers must have involved additional mechanisms that cannot be described by the classical Fourier's law [18-27]. Thermal response subjected to high-frequency (ω) excitations behaves the same way, with ω in place of the factor $[1/(L^2/\alpha)]$ in the exponent of Eq. (2). In ultrafast photonics with ω in the terahertz (10^{12}) domain, thermal effect may become pronounced even at regular times. As heating and consequently the thermal field is driven by a rapidly moving/varying source, obviously, additional mechanisms other than Fourier diffusion exist that are responsible for the temperature change.

The wave theory in heat propagation may be the first attempt in addressing the shortcomings of Fourier's law when used in describing the ultrafast transient in times comparable to the relaxation (mean free) time of energy carriers [28-33]:

$$\mathbf{q}(\mathbf{r},t) + \tau\frac{\partial \mathbf{q}}{\partial t}(\mathbf{r},t) = -k\nabla T(\mathbf{r},t) \tag{3}$$

where $\mathbf{q}$ is heat flux vector, τ is relaxation time, k is thermal conductivity, and $\mathbf{r} \equiv [x, y, z]$ is position vector. When combining with the energy equation,

$$-\nabla \bullet \mathbf{q}(\mathbf{r},t) = C\frac{\partial T}{\partial t}(\mathbf{r},t), \tag{4}$$

with C representing the volumetric heat capacity in W/(m^{3}K), Eq. (3) gives rise to the equation for thermal *waves*:

$$\nabla^2 T = \frac{1}{\alpha}\frac{\partial T}{\partial t} + \frac{1}{c^2}\frac{\partial^2 T}{\partial t^2}, \quad \text{with} \quad c = \sqrt{\frac{\alpha}{\tau}} \tag{5}$$

As compared to Eq. (1), Eq. (5) describes a thermal disturbance propagating at a finite speed c, which is a salient feature for heat transport taking place in times comparable to the relaxation time of energy carriers. In the limiting case of $\tau \to 0$, the wave speed (c) approaches infinity and Eq. (5) reduces to Eq. (1) for Fourier diffusion. The relaxation time is intrinsic by nature, since heat transport requires effective collisions to take place among energy carriers. The transport process described by Eq. (5) is thus termed ultrafast, since the process time (t) is of the same order of magnitude as the relaxation time. The relaxation time depends on the type of conductors. For metals with free electrons and phonons as energy carriers, the relaxation times for electron-to-electron collisions, electron-to-phonon collisions, and phonon-to-phonon collisions are of the order of 10 femtoseconds, 1 picosecond, and 10 picoseconds, respectively [5, 6]. Unlike Fourier diffusion where the heat affected zone extends to infinity as a result of the infinite speed of heat propagation, Eq. (5) implies a thermal wavefront at $r = ct$ that separates the heat affected zone ($r < ct$) from the thermally undisturbed zone ($r > ct$). Special features in the thermal wave model include the thermal shock formation [34-43] and thermal resonance subjected to high-frequency excitations [44, 45]. As the transient time enters the threshold of the relaxation time, the transport process becomes ultrafast and effect of thermal relaxation represented by the wave term in Eq. (5) needs to be accommodated in addition to Fourier diffusion.

Ultrafast transient often involves nonequilibrium processes that take place in an extremely small heat affected zone. For material processing by femtosecond lasers, for example, the depth of optical penetration is a mere few tens of nanometers, in which the various microstructural interactions are driven by the gigantic power (in tera- to petawatts) during the femtosecond transient. Effect of ultrafast transient in time thus tangles with the microstructural interaction effect in space, which is a platform for the full engagement of microscale heat transfer. This chapter starts with a quick review of several representative microscale heat conduction models, for the purpose of abridging the physical mechanisms that are known active during the nonequilibrium transport in microscale. Their applications and specific implications are emphasized during the review. Inheriting from different physical bases adopted in describing different behaviors in microscale, however, the mechanisms described in these models are somewhat

devious and may become confusing sometimes. Whether a known mechanism described in one model, such as the relaxation of internal energy, also exists in another model (such as the electron-phonon interactions or umklapp relaxation of phonons) could be dubious, making the selection of a most suitable model particularly difficult for inexperienced researchers. Guided by the same type of energy equations, even though the physical bases involved in the various microscale conduction models are philosophically different sometimes, the dual-phase-lag (DPL) model follows, pinpointing at their common features regardless of the different physical bases. The complicated microstructural interaction effects, in space, are lumped onto the resulting delayed response in time, with the two phase lags introduced in the DPL model describing the finite times required for the completion of the various physical processes in microscale. In view of the lagging behavior, in other words, the finite time required for recovering the momentum loss in the umklapp process in phonon scattering is equivalent to the relaxation time in the phonon-electron interactions (in metals) and the finite time required for achieving thermal equilibrium between electrons and phonons is equivalent to the relaxation time of internal energy. The sources for the delayed response may be different, but the same lagging behavior in time gives rise to a unified approach in describing the various microscale effects in space. Depending on the time scale in which the nonequilibrium transition takes place, high order effects in the lagging response may need to be considered to describe the physical phenomena in correspondence, which is the merit of establishing the regime map for characterizing the wave-diffusion duality in nonequilibrium transport. Analogy with mass transport in ultrathin film/interfacial compound layer growth is drawn to unify the same concept of phase lagging in describing nonequilibrium heat and mass transport. Debuting from the same origin of microscale heat transfer, the DPL model is the only model that has advanced itself to describe the complicated interactions among multiple carriers in biological systems. For both bioheat transfer (describing the nonequilibrium energy exchange between blood and tissue) and drug delivery in tumor cells (describing the rupture of liposome and effective absorption of antitumor drug), the phase lags resulting from the finite times required for accomplishing the biological processes in correspondence are derived to pinpoint the biological sources for delay. In spite of the intrinsically different physical processes, now stretching from engineering materials in femtoseconds to biological tissues in hours and days, the lagging behavior in time is shown to be a common feature that sheds light on a unified approach in describing the nonequilibrium transport in general.

2 Microscale Heat Conduction

The lagging behavior is originated from extracting the time constants governing the various heat transfer processes in microscale. As discussed earlier, a definite thermal effect observed in times comparable to the relaxation time of the energy carriers imply the existence of additional thermophysical mechanisms during the early-time transient. The effect of thermal relaxation described in Eq. (3) is simply one of the many possible mechanisms among others. This section review several

representative heat conduction models in microscale, for the purpose of establishing the concept of thermal lagging in addressing the various microstructural behaviors that are pronounced at short times. The relaxation behavior will be illustrated by the Cattaneo-Vernotte (CV) thermal wave model due to its simplest mathematical content. With the fundamental knowledge and mathematical tools thus developed, extension will be made to the phonon scattering model, the internal energy relaxation model, and the parabolic and hyperbolic two-step models to identify additional time constants for capturing more sophisticated physical phenomena in small scale. An in-depth review thus developed paves the way for a rigorous foundation in support of the dual-phase-lag model.

2.1 Cattaneo-Vernotte (CV) Thermal Waves

In times comparable to the relaxation time of the energy carriers, thermodynamic states are undergoing fast transition and the quasi-stationary assumption embedded in Fourier's law cannot be applied. Major developments in capturing the essential mechanisms in microscale heat conduction have been summarized in several review articles [31-33]. They include the evolution of the microscale heat conduction models, from the wave concept to the Jeffrey's type of heat equation, which have been examined in terms of thermal inertia, critical frequency in molecular dynamics, irreversible thermodynamics, Boltzmann transport equation, and the restrictions imposed by the theory of relativity. The physical context of microscale heat conduction has significantly stretched over Fourier's law and the *CV*-wave model, which by itself would be a sizable book for a complete inclusion and rigorous treatment. This chapter will take an alternate route in approaching the subject since thorough reviews are already in place. The emphasis will be placed on the special features behind every model reviewed, along with the mathematical methods required to unveil the physical insights of that model. Aiming toward extracting the fundamental behaviors, all thermophysical properties will be assumed constant unless stated otherwise. With the fundamental understanding thus developed, the temperature dependence of these properties can be reinstated for a more accurate description of the transport process, which however will require the use of extensive numerical methods due to the strong nonlinearity in the energy equations.

Resulting from Eq. (3), the *CV*-wave equation represented by Eq. (5) has many desirable properties. Most of all, for applications and in reality at least, the finite speed of heat propagation has resolved the long concern of the infinite speed of heat propagation assumed in Fourier's law. Estimated on the order of magnitude, accounting for the electron-to-phonon interactions with a relaxation time of 1 ps (10^{-12} s), thermal diffusivity (α) in the range from 10^{-6} – 10^{-4} (m^2/s) for most metals results in a thermal wave speed of $c \sim 10^3 - 10^5$ (m/s) according to Eq. (5). For semiconductors, insulators, and dielectrics in which free electrons are absent, the relaxation time for phonon-to-phonon interactions is lengthened to the order of 10 ps, which results in $c \sim 10^2 - 10^3$ (m/s) based on the thermal diffusivity in the range from 10^{-7} – 10^{-5} (m^2/s). Clearly, the presence of free electrons in metals does

expedite the thermal wave speed by approximately one order of magnitude. The relaxation time further shifts toward the value for the electron-to-electron collisions, approximately 10 fs, in metals with a higher density of free electrons. With the response time entering the femtosecond domain, the wave behavior will be pronounced and the thermal wave speed would increase by one to two orders of magnitude due to a smaller value of the relaxation time.

The time domain in which the thermal wave behavior becomes pronounced is the most important information for studying the wave behavior of heat propagation. Under a constant value of τ, Eq. (3) can be cast into a more useful form in weighing the contribution of the relaxation term:

$$\frac{\mathbf{q}}{1} + \frac{\partial \mathbf{q}}{\partial\left(\frac{t}{\tau}\right)} = -k\nabla T \,. \tag{6}$$

Since the numerators ($\mathbf{q}$ and $\Delta\mathbf{q}$) is of the same order of magnitude, the second term describing the thermal relaxation will be negligibly small as $(t/\tau) >> 1$, or in the time domain where $t >> \tau$. For heat transport dominated by phonon scattering with $\tau \sim 10$ ps, thermal waves will be active in times comparable to τ, and Fourier's law would be recovered as t lengthens to approximately $10^2\tau$ (nanoseconds). The picosecond transient is termed ultrafast because the process time is comparable to the relaxation time of phonons. For heat transport dominated by electron collisions such as that in metals, femtosecond transient is considered to be ultrafast and the relaxation behavior in the *electron gas* will diminish in transit to picoseconds, where the relaxation behavior from the electron-to-phonon interactions follows. Whether the wave behavior in heat propagation can be neglected or not thus depends on the process time of heat transport relative to the carrier-dependent relaxation time. The thermal wave theory yields indistinguishable results from Fourier's law in time $t \sim 10^2\tau$ where the thermal wavefront becomes extremely weak and temperature drop across the wavefront is negligibly small.

Equation (3) is in a special form of the evolution equation in nonequilibrium thermodynamics [46]. In view of the Taylor series expansion of a general function with discrete delays [18], alternatively,

$$\mathbf{q}(t+\tau) \cong \mathbf{q}(\mathbf{r},t) + \tau\frac{\partial \mathbf{q}}{\partial t}(\mathbf{r},t) + O(\tau^2) = -k\nabla T(\mathbf{r},t)\,, \tag{7}$$

the left hand side of Eq. (3) thus results from the first-order term in τ that approximates the heat flux at $(t + \tau)$ as $\tau << t$. This concept in terms of *lagging* will be used repeatedly in this chapter as the various microscale conduction models are revisited for revealing the essence of the lagging response in their frameworks. With $\tau > 0$, Eq. (7) presumes that heat flux (at $t + \tau$) flowing through a material volume occurs *later* than the temperature gradient (at t) established across the same material volume. Consequently, the cause of heat flow is presumed to be the temperature gradient while the heat flux is the effect. Due to

this assumption made beforehand, the *CV*-wave model can only capture a limited number of phenomena in microscale heat transfer.

Unlike Fourier's law, $\mathbf{q}(\mathbf{r}, t) = -k\nabla T(\mathbf{r}, t)$, where the heat flux vector at a certain location and time ($\mathbf{q}(\mathbf{r}, t)$) depends only on the temperature gradient (($\nabla T(\mathbf{r}, t)$) established at the same location and time, the relaxation behavior described by Eq. (3) implies a path-dependent process, which can be seen explicitly by integrating Eq. (3) with respect to time to give:

$$\mathbf{q}(\mathbf{r},t) = -\left(\frac{k}{\tau}\right)\exp\left(-\frac{t}{\tau}\right)\int_0^t \exp\left(\frac{t'}{\tau}\right)\left[\nabla T(\mathbf{r},t') + \tau\frac{\partial}{\partial t'}\left[\nabla T(\mathbf{r},t')\right]\right]dt' \quad (8)$$

where t' is the integral variable between 0 and t. At any instant during the process of heat transport, the heat flux vector not only depends on the end value of $\nabla T(\mathbf{r}, t')$ at $t' = t$, it also depends on the distribution of $\nabla T(\mathbf{r}, t')$ in the entire domain of $t' \in [0, t]$. Additional dependence on the time-rate of change of the temperature gradient further complicates the path dependency. Approaching the end value of $\nabla T(\mathbf{r}, t)$ in a time history, the heat flux vector "remembers" the entire course through which the end value has been developed. Such a memory fades with time, however, as reflected by the exponentially decaying function of time, $\exp(-t/\tau)$, in front of the integral.

The relaxation behavior shown by Eq. (3) results from the relaxation time approximation made in the estimate of the phonon-scattering term in the Boltzmann transport equation [18, 47]. As such, the time-rate of change of the phonon distribution function driven by phonon scattering is assumed to be the difference between the current and the initial values over one period of the relaxation time. In parallel, an equally important justification for any constitutive equation in heat transport is its admissibility within the framework of the second law of thermodynamics. For the *CV*-wave equation describing a finite speed of heat propagation; in times comparable to the mean free time (or the relation time) of the energy carriers, this has also been shown in the framework of the extended irreversible thermodynamics (EIT) [18, 48]. In addition to the physical properties such as temperature, pressure, and entropy defining a thermodynamic state during quasi-stationary transition, the heat flux vector also becomes an internal state variable in defining a transitional/nonequilibrium state in EIT. Since the heat flux vector is a *process* quantity pertinent to the transition between thermodynamic states, most importantly, such an extension involving the process variables (in additional to the internal variables defining a thermodynamic state in equilibrium) injects a strong path dependency in all the constitutive equations derived from EIT.

It is of paramount importance to note that all thermodynamic properties resulting from EIT are nonequilibrium by nature. The ways in which the nonequilibrium temperature evolves with time is described by the evolution equation describing the *dynamic* temperature, in the context of the gradient extension method in nonequilibrium thermodynamics [46]. Since Eqs. (3) and (5) apply in times comparable to the relaxation time of the energy carriers where the transition of thermodynamics is fast paced and highly dynamic, the nature of the temperature involved in Eq. (3) or Eq. (5) needs to be clarified. Let us first

distinguish the *dynamic* temperature, β, from *nonequilibrium* temperature, θ. The dynamic temperature evolves with time and is a function of the nonequilibrium temperature defined in the framework of EIT. As time elapses, the dynamic temperature recovers the nonequilibrium temperature and the dependence of the thermodynamic states on the process variables (such as heat flux in EIT) gradually diminishes. As time further lengthens, eventually, the thermodynamic state no longer depends on the process variable, the path-dependency disappears, and the nonequilibrium temperature recovers the equilibrium temperature. Mathematically, with τ being a positive time constant characterizing the ultrafast response as illustrated in Fig. 1, the dynamic temperature ($\beta(t)$) is higher than the nonequilibrium temperature ($\theta(t)$) at any instant in short times. As time elapses to ($t + \tau$), the dynamic temperature recovers the nonequilibrium temperature, which can be represented in general as

$$\beta(t+\tau) = \theta(t), \quad \tau > 0. \tag{9}$$

Under the same condition of $\tau << t$, parallel to that in Eq. (7), the Taylor series expansion of Eq. (9) containing the first-order term in τ gives

$$\beta(t+\tau) \cong \beta(t) + \tau \frac{d\beta}{dt}(t) = \theta(t). \tag{10}$$

The time constant, τ, is equivalent to the relaxation time due to its similar role played in Eq. (7). The process time (t) can be pushed toward the relation time (τ) by incorporating more high-order terms of τ Eq. (10), which will make $\beta(t)$ and

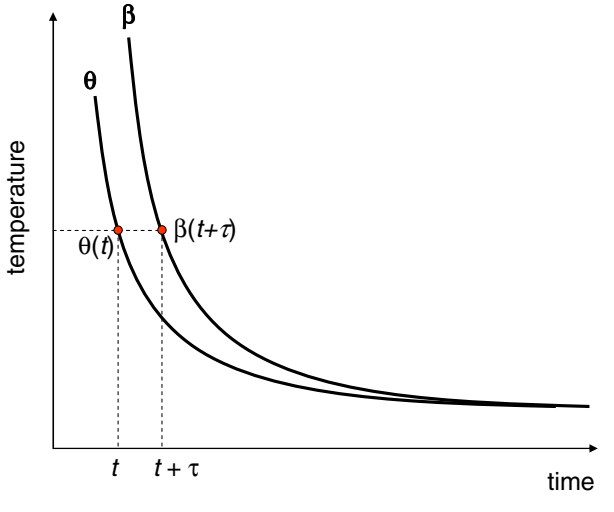

Fig. 1 Delayed response between dynamic temperature, $\beta(t)$, and nonequilibrium temperature, $\theta(t)$

$\theta(t)$ more distinct in the corresponding domain of time. Equation (10) is of the same form as the evolution equation used in the nonequilibrium irreversible thermodynamics, which displays the same path dependency as described by Eq. (8) with $\mathbf{q} \to \beta$ and $\nabla T \to \theta$. From a physical point of view, Eq. (10) describes the ways in which the dynamic temperature evolves into the nonequilibrium temperature as time lengthens. With an exponentially decaying behavior in time, as illustrated in Fig. 1, the two temperatures will merge after a certain instant of time and become indistinguishable afterwards. After the merger, the two temperatures will continue to move together toward the equilibrium temperature where the classical thermodynamics assuming quasi-stationary transition of thermodynamic states prevails.[1] It is customary to assume Fourier's law for the dynamic temperature [46], $\beta(t)$:

$$\mathbf{q} = -k\nabla\beta \,. \tag{11}$$

Taking the derivative of Eq. (11) with respect to time and substituting Eq. (10) (for $\dot{\beta}$) into the result,

$$\frac{\partial \mathbf{q}}{\partial t} = -k\nabla \overbrace{\frac{\partial \beta}{\partial t}}^{\text{Eq.(10): } \frac{1}{\tau}(\theta-\beta)} = -\frac{k}{\tau}\left(\nabla\theta - \overbrace{\nabla\beta}^{-\frac{\mathbf{q}}{k}}\right) \quad \Rightarrow \quad \mathbf{q} + \tau\frac{\partial \mathbf{q}}{\partial t} = -k\nabla\theta \tag{12}$$

Equation (12) has exactly the same form as Eq. (7) (or Eq. (3)) describing the *CV*-wave model, with the nonequilibrium temperature, θ, in place of T alleged in Eq. (7). The *CV*-wave model is thus admissible within the framework of nonequilibrium thermodynamics. Consequently, the temperature/gradient and heat flux vector posted earlier in Eq. (7) are nonequilibrium by nature. Both dynamic and nonequilibrium temperatures are semi-empirical because they are not directly measurable. Indirect means, such as the reflectivity change on a heated metal surface [49, 50], is often needed to relate them to the physical response based on solid state physics. Distinguishing from the equilibrium thermodynamics assuming quasi-stationary transition of thermodynamic states, the entropy

[1] The physical essence of the evolution equation shown by Eq. (10) can be revealed by the lumped capacitance formulation for a solid of temperature $T(t)$ that loses heat to the ambient (T_∞) due to convection: $C\cancel{V}\dfrac{\partial T}{\partial t} = -hA\left(T - T_\infty\right)$, or $\left(\dfrac{C\cancel{V}}{hA}\right)\dfrac{\partial T}{\partial t} + T = T_\infty$, where $\cancel{V}$ and A are the volume and surface area of the solid, respectively, and h is the heat transfer coefficient. With $(C\cancel{V}/hA)$ equivalent to τ, clearly, the lumped temperature of the solid (T) is equivalent to the dynamic temperature (β) and the ambient temperature (T_∞) is equivalent to the nonequilibrium temperature (θ). Equation (9) thus describes the lagging behavior between the immersed solid and the ambient temperatures before they come to thermal equilibrium.

production rate (Σ) results from nonequilibrium thermodynamics (Eq. (12)) is [18]:

$$\Sigma = -\mathbf{q}\bullet\left[k\nabla\theta + \tau\dot{\mathbf{q}}\right] = \overbrace{\Sigma_{eq}}^{-\mathbf{q}\bullet k\nabla\theta} - \tau\mathbf{q}\bullet\dot{\mathbf{q}} \geq 0 \tag{13}$$

While the equilibrium component (Σ_{eq}) depends only on the thermodynamic properties in the equilibrium state, the additional term led by τ results from the dependence on the process variable, the heat flux vector $\mathbf{q}$ in this case, in EIT. To assure a positive definite entropy production rate, i.e., $\Sigma \geq 0$, in the framework of EIT, note that one of the many possibilities for the bracketed quantity in Eq. (13) is

$$k\nabla\theta + \tau\dot{\mathbf{q}} = -\mathbf{q} \quad \Rightarrow \quad \Sigma = -\mathbf{q}\bullet\left[k\nabla\theta + \tau\dot{\mathbf{q}}\right] = \mathbf{q}\bullet\mathbf{q} \geq 0 \tag{14}$$

Once again, the first expression in Eq. (14) gives rise to Eq. (12), which justifies the validity of the *CV*-wave model in view of the second-law admissibility within the framework of EIT.

Mathematically, Eq. (5) is termed telegraph equation that already appears in mathematical physics. The same type of equation also appears as the equation of motion governing the wave propagation in Maxwell solids in viscoelasticity. A large amount of efforts, however, has been devoted over the past four decades to Eq. (5) under the various initial and boundary value problems pertinent to heat conduction, aiming toward the salient features of thermal wave propagation. Thorough reviews have appeared over time [18, 31-33, 40, 51], which categorize the nature of the vast publications according to their special emphases on thermal-wave interactions with boundaries, effects of apparent heating, and the various analytical and numerical techniques capturing the rapid changes in the vicinity of the wavefront.

With outstanding efforts addressing the wave theory of heat conduction in place, two unresolved issues in thermal wave propagation require our continued attention. First, the presumed heat flow driven by the temperature gradient gives rise to a sharp wavefront, which results in an *infinite* time-rate of change of temperature ($\partial T/\partial t$) and/or an *infinite* temperature gradient (∇T) across the wavefront. This situation is illustrated in Fig. 2, where the response curve for the *CV*-wave results from the solution to Eq. (5), which is typical for heat propagation in a semi-infinite solid without the interference from the boundary effect or internal heating. A sharp wavefront exists in the physical domain, at $x = ct$ with $c = \sqrt{(\alpha/\tau)}$, which separates the heat affected zone (in $x < ct$) from the thermally undisturbed zone ($x > ct$). The temperature level established by the *CV*-wave can be much higher than that by Fourier diffusion in the heat affected zone. On the contrary, Fourier diffusion always renders a higher temperature in the thermally undisturbed zone due to the instantaneous response assumed in Fourier's law. The sudden drop of temperature from the heat affected zone to the thermally undisturbed zone create a problem as the *CV*-wave approaches a physical boundary where the local temperature (obtained from the *CV*-wave equation) must satisfy a certain boundary condition. A sudden drop of temperature from a

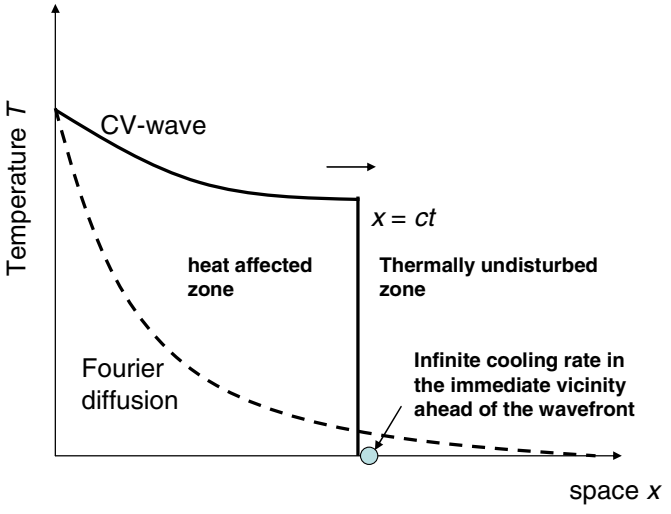

Fig. 2 A sharp wavefront at $x = ct$ and the infinite cooling rate in the immediate vicinity ahead of the wavefront

positive value in the heat affected zone (at $x = ct^-$) to zero in the thermally undisturbed zone ($x = ct^+$) implies an *infinite* cooling rate, i.e., $(\partial T/\partial t)_{x=ct^+} \to -\infty$, in the immediate vicinity ahead of the sharp wavefront. Such a singularity is preserved in every solution of the *CV*-waves, which not only makes it impossible to satisfy any boundary condition, but also produce an effect of temperature reversal due to the excessively large cooling rate. When reflected from a physical boundary maintained at zero degree Kevin, more specifically, the infinite cooling rate would render a temperature less than zero degree Kevin after the reflection, which violates the zeroth law of thermodynamics. An initial effort has been made to compensate such deficiency by introducing an auxiliary condition to enforce the satisfaction of the boundary conditions [52]. Such auxiliary conditions, in relation to the various types of boundary conditions encountered in heat conduction, remain to be critical in the continuous expansion of the wave theory in heat propagation.

Second, most successful experiments showing the wave behavior in heat propagation were carried out at low temperature in liquid helium and dielectric crystals [53-55]. It was believed that "… Slow speeds in ordinary materials at room temperature have never been measured and, even if they exist, they may be masked by diffusion arising from an effective thermal conductivity associated with modes of heat that have already relaxed…" [31]. Under some uncertainties due to the effects of impurities and imperfect lattice structures on the relaxation time, the wave speed calculated from $c = \sqrt{(\alpha/\tau)}$ is a mere one order of magnitude higher than those obtained at a temperature close to 4 degree Kelvin. For metals where most of heat is carried by electrons and their collisions with phonons, the

thermal wave speed is claimed to be close to the Fermi velocity (~ 10^6 m/s) [31, 49], which is nearly one order of magnitude larger than that calculated from the same formula. Evidently, different types of thermal waves activated in short time, a clear signature of such thermal waves, and consequently the determination of the thermal wave speed and the relaxation time are greatly needed for applications in material processing under normal conditions. The challenge remains to reside in the lack of fast instrumentation techniques to capture the ultrafast transient in times comparable to the relaxation time. For metals where the normalized temperature change can be calibrated in terms of the surface reflectivity change, the surface pumping and probing technique is exciting and promising [49]. For other materials where the number of free electrons is inadequate for effective heat transfer, slow materials with heterogeneous structures (such as an assembly of copper spheres, wicked structures with low volume fraction of solids, or rough carbon surfaces) have been used to match the speed of the thermal response with that of the infrared detectors [50]. There exist analytical efforts aiming toward permanent signatures of damage/phase change of materials induced by thermal waves that cannot be described Fourier's law. Preheating a sample of ferrous alloy to a temperature close to but still lower than its austenitizing temperature, for example, may drive the austenitizing (phase change) phenomena to occur due to the excessive temperature rise induced by the impingements of multiple thermal wavefronts, alleged temperature overshooting [18, 56]. Exaggerated temperature response due to the thermal resonance under high-frequency excitations [44, 45], the shock waves emanating from high-speed cutting/grinding tools [34-40], and the thermally induced fracture pattern around a rapidly moving heat source [36, 41] are additional examples that will place permanent marks on the sample that could be examined afterwards without relying on the fast instrumentation for the ultrafast response. Even though the phenomenon of temperature overshooting is somewhat controversial, the approach employing the creation of permanent marks by either phase change or cracking patterns may still be viable in verifying the existence of thermal waves. Should these phenomena induced by thermal waves be observed in the future, the thermal shock angle measured after the experiment can be used to calculate the thermal wave speed, and the resonance frequency in the temperature response can be used to calculate the relaxation time.

2.2 Phonon Scattering Model

Multiple relaxation times seem to exist in the phonon scattering model describing passage of heat waves in dielectric crystals [57]:

$$\mathbf{q} + \tau_R \frac{\partial \mathbf{q}}{\partial t} = -\left(\frac{\tau_R c^2 C}{3}\right)\nabla T + \left(\frac{\tau_R \tau_N c^2}{5}\right)\left[\nabla^2 \mathbf{q} + 2\nabla(\nabla \bullet \mathbf{q})\right] \tag{15}$$

where τ_R is the relaxation time describing the umklapp process in which momentum is temporarily lost from the phonon system, τ_N is the relaxation time for the normal (momentum conserving) processes, c is the mean phonon speed,

C is volumetric heat capacity, and the coefficient in front of ∇T could be viewed as effective thermal conductivity, $k = \tau_R c^2 C/3$. Equation (15) was derived from the linearized Boltzmann equation for the pure phonon field, under the condition of $\mathbf{q} = c^2\mathbf{p}$ with $\mathbf{p}$ being the momentum of the phonon gas. This condition holds in particular at low temperature. Along with Eq. (4), the energy equation, Eq. (15) needs to be solved for the heat flux vector ($\mathbf{q}$) and temperature (T). In steady state, $\nabla \bullet \mathbf{q} = 0$ from Eq. (4), Eq. (15) is reduced to

$$\mathbf{q} = -\left(\frac{\tau_R c^2 C}{3}\right)\nabla T + \left(\frac{\tau_R \tau_N c^2}{5}\right)\nabla^2 \mathbf{q} \quad \text{(steady state)}, \tag{16}$$

which differs from Fourier's law by the term containing $\nabla^2\mathbf{q}$. The phonon scattering model thus display a new type of constitutive equation, which does *not* recover Fourier's law in steady state.

The special structures of Eq. (15) in time will be tied to thermal lagging later. For the time being, a better focus will be made on the special behavior described by Eq. (16) in steady state. First, the coefficient $(\tau_R \tau_N c^2)/5$ can be rearranged into $(\tau_R c)(\tau_N c)/5$, which has a dimension of length squared. Symbolically, $(\tau_R c)(\tau_N c)/5 \sim l^2$, with l being the mean free path in phonon collisions. Equation (16) can thus be written as

$$\mathbf{q} = -k\nabla T + l^2 \nabla^2 \mathbf{q}. \tag{17}$$

This equation can be applied to study the radius (R) dependence of thermal conductivity of silicon nanowires [46, 58], which transits from a quadratic dependence ($\sim R^2$) under a larger radius to a linear dependence ($\sim R$) as the radius becomes smaller than a threshold value [59-61]. The nanowire is ideal to be modeled as a one-dimensional conductor due to its small aspect ratio, $2R << L$, with L being the length of the nanowire. As sketched in Fig. 3, a one dimensional heat flow is driven by a constant temperature gradient ($\Delta T/L$) established in the axial (x-) direction across L, $\mathbf{q} \equiv q\mathbf{e}_x$. The axial heat flux is not a function of x, as prescribed by the steady-state energy equation, $\partial q/\partial x = 0$, but it can vary in the r-direction due to backscattering of phonons from the nanowire surface. Consequently, The one-dimensional form of Eq. (17) is:

$$q = -k\left(\frac{\Delta T}{L}\right) + \frac{l^2}{r}\frac{\partial}{\partial r}\left(r\frac{\partial q}{\partial r}\right). \tag{18}$$

Boundary scattering of phonons, and hence the amount of heat they carry near the boundary, is less important for the nanowire with a larger radius due to the larger physical domain in support of heat conduction. Heat conduction; however, remains to be one-dimensional due to the large aspect ratio of the nanowire in place. Assuming no heat loss from the surface for this type of nanowires, Eq. (18) can be solved under the boundary conditions:

$$q(R) = 0, \quad q \text{ remains finite as } r \to 0. \tag{19}$$

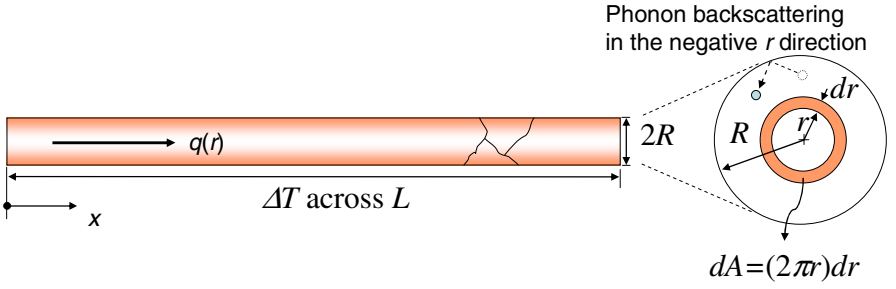

Fig. 3 One-dimensional heat flux in a nanowire whose intensity varies in the radial direction due to backscattering by the surface

A direct integration of Eq. (18) results in

$$q(r) = k\left(\frac{\Delta T}{L}\right)\left[\frac{I_0\left(\frac{r}{l}\right)}{I_0\left(\frac{R}{l}\right)} - 1\right] \tag{20}$$

where I_0 stands for the modified Bessel function of the first kind of order zero. Another solution Y_0 (Bessel function of the second kind of order zero) is eliminated because heat flux needs to remain finite at the origin ($r = 0$) ($Y_0(0) \to -\infty$). The effective thermal conductivity of the nanowire is calculated from the total amount of heat (Q) that integrates q over the entire cross section (A) of the nanowire

$$Q \equiv \int_0^R \overbrace{q(r)}^{\text{Eq. (20)}} \bullet (2\pi r)\, dr = -k_{\text{eff}} \overbrace{A}^{\pi R^2}\left(\frac{\Delta T}{L}\right), \quad \text{which gives} \quad k_{\text{eff}} = k\left[\frac{I_2(z)}{I_0(z)}\right] \quad \text{with} \quad z = \frac{R}{l} \tag{21}$$

For nanowires with a small aspect ratio, $z << 1$ or $R << l$, the Taylor series expansion applied to the ratio of the Bessel functions in Eq. (21) results in

$$k_{\text{eff}} \cong \frac{k}{8}\left(z^2 - \frac{z^4}{6} + \ldots\right), \quad \text{or} \quad k_{\text{eff}} \cong \left(\frac{k}{8}\right)\left(\frac{R}{l}\right)^2 + O\left(\frac{R}{l}\right)^4, \tag{22}$$

which shows that the effective thermal conductivity of the nanowire (of a larger radius) indeed increases with the radius squared. This is the R^2-dependece of the thermal conductivity observed in the experiments for nanowires of a radius greater than 37 nm [59-61].

As the radius of the silicon nanowire becomes smaller than 37 nm, exemplified by the case of R = 22 nm [59-61], effect of backscattering of phonons from the nanowire surface becomes more pronounced due to its interference with the axial heat flow in a smaller conductive domain. Heat flow through the slender nanowire resembles slip flow in microchannels [62], facilitating a direct extension of the

boundary slip to describe the heat flux at the surface of the nanowire. Inheriting the same condition for the Knudsen number between 10^{-3} and 10^{-1} [63], which measures the nanowire diameter relative to the mean free path of phonons in this analogy, this "slip" condition for the boundary heat flux can be expressed as

$$q = -sl\left(\frac{dq}{dr}\right) \quad \text{at} \quad r = R; \quad q \text{ remains finite as } r \to 0 \tag{23}$$

where a parameter s (nondimensional) is instated to describe the different surface conditions in phonon backscattering. Shown by Eq. (23), boundary heat flux replaces the slip velocity at the wall in this correlation. Going through exactly the same procedure, the axial heat flux and the effective thermal conductivity are

$$q(r) = k\left(\frac{\Delta T}{L}\right)\left[\frac{I_0\left(\frac{r}{l}\right)}{I_0\left(\frac{R}{l}\right) + sI_1\left(\frac{R}{l}\right)} - 1\right], \quad k_{\text{eff}} = \frac{k\left[zI_0(z) + (sz-2)I_1(z)\right]}{z\left[I_0(z) + sI_1(z)\right]} \tag{24}$$

For $z << 1$ or $R << l$, once again, the Taylor series expansion of Eq. (24) yields

$$k_{\text{eff}} \cong \frac{k}{2}\left[sz + \left(\frac{1-2s^2}{4}\right)z^2 + \ldots\right], \quad \text{which gives} \quad k_{\text{eff}} \cong \left(\frac{ks}{2}\right)\left(\frac{R}{l}\right) + O\left(\frac{R}{l}\right)^2 \tag{25}$$

As a result of the boundary-scattering of phonons at $r = R$, in a nanowire of a smaller radius with the "slip" condition (Eq. (23)) in place of the previous insulated boundary condition, the *linear dependence* of the thermal conductivity on the radius of the nanowire is nicely captured in Eq. (25). The effective thermal conductivity calculated from the Wiedemann-Franz law based on the electrical conductivity for thin wire is [64-66]

$$k_{\text{eff}} = k\left(\frac{1+p}{1-p}\right)\left(\frac{R}{l}\right), \tag{26}$$

with p being the specularity parameter varying from zero (for diffuse mode of phonon scattering) to one (for specular mode), depending on the surface roughness relative to the mean free path of phonons. Comparing Eqs. (25) and (26), the surface parameter (s) is related to the specularity parameter (p) by

$$s = 2\left(\frac{1+p}{1-p}\right). \tag{27}$$

In the case of specular scattering of phonons from the nanowire surface; $p \to 1$, the surface parameter s approaches infinity according to Eq. (27). The slope of boundary heat flux approaches zero in this case ($dq/dr \to 0$ at $r = R$) due to symmetry of phonon backscattering. In the case of $p \to 0$ for the diffuse mode of reflected phonons, the surface parameter s reduces to 2.

2.3 Internal-Energy Relaxation

Gurtin and Pipkin [67] constructed the heat flux, like the entropy, from the functional for the free energy in the weighted L_h^2 space. For the exponentially decaying functionals with time, for both the internal energy and the heat flux, their formulation was reduced to [31]

$$\begin{cases} e+\tau_e\dfrac{\partial e}{\partial t}=\left(\tau_e F_e+C\right)T+\tau_e C\dfrac{\partial T}{\partial t} \\ \mathbf{q}+\tau\dfrac{\partial \mathbf{q}}{\partial t}=-\tau_q F_q\nabla T \\ \dfrac{\partial e}{\partial t}=-\nabla\bullet\mathbf{q} \end{cases} \tag{28}$$

where e is the internal energy above its reference value at 0 K, and F_e and F_q are the initial values of the functionals characterizing the internal energy and the heat flux vector, respectively. The quantity F_e and F_q are viewed as additional material constants characterizing the fast transient process in Eq. (28). Distinguishing from others, the Gurtin-Pipkin model introduces two relaxation times for both the internal energy and the heat flux vector. The one characterizing thermal relaxation of the hat flux vector is the same as the *CV*-wave model, with (τF_q) takes the place of thermal conductivity (k). The one describing the relaxation behavior of the internal energy, however, is somewhat unique. Extending the same phenomenological description in terms of the first-order Taylor series expansion in τs, in parallel to Eq. (7), the first equation in Eq. (28) can be cast into the following form:

$$\overbrace{e+\tau_e\frac{\partial e}{\partial t}}^{\equiv e(t+\tau_e)}=\overbrace{\left(\tau_e F_e+C\right)}^{C_{\text{eff}}}\overbrace{\left[T+\overbrace{\left(\frac{\tau_e C}{\tau_e F_e+C}\right)}^{\tau_t}\frac{\partial T}{\partial t}\right]}^{\equiv T(t+\tau_t)} \quad\Rightarrow\quad e\left(t+\tau_e\right)\equiv C_{\text{eff}}T\left(t+\tau_t\right) \tag{29}$$

Equation (29) displays a non-instantaneous behavior between the internal energy and temperature, with two delay times, τ_e and τ_t, involved. The classical definition of the specific heat, $e = CT$, in particular, is no longer valid unless both delay times, τ_t and τ_e, are small in comparison with the process time, i.e., τ_t, $\tau_e << t$. Unlike the phonon scattering model, note that Eq. (28) does recover Fourier's law and specific heat in steady state. Equation (28) involves intrinsic coupling among the three variables, e, $\mathbf{q}$, and T, which need to be solved from the three coupled partial differential equations.

2.4 Phonon-Electron Interaction (Two-Step) Model

Nonequilibrium heat transport between electrons and phonons in metals, rather than modifying the constitutive equation, are described by the coupled energy equation in the phonon-electron interaction model [5, 6]:

$$\begin{cases} C_e \dfrac{\partial T_e}{\partial t} = k_e \nabla^2 T_e - \overbrace{G\left(T_e - T_l\right)}^{\text{phonon-electron coupling}} \\ C_l \dfrac{\partial T_l}{\partial t} = \underbrace{G\left(T_e - T_l\right)}_{\text{phonon-electron coupling}} \end{cases} \tag{30}$$

where the subscripts "*e*" and "*l*" denote electrons and phonons, respectively. Since heat capacity of electrons (C_e) is about two orders of magnitude smaller than that of phonons (C_l), the process described by Eq. (30) involves heating of electrons in the first step and heating of the lattices through the electron-to-phonon collisions in the second step. This is the reason that Eq. (30) is termed "two-step" model, which first appeared about five decades ago [68, 69]. It may be fair to say that rapid advances of femtosecond lasers since 1987 have provided strong impetus for the reactivation of the two-step model since the laser pulse (~ 100 fs) is of the same order of magnitude as the electron-to-phonon relaxation time.

Unlike the constitutive equation approach, the flavor of nonequilibrium heat transport is evident in the two-step model due to the explicit involvement of T_e and T_l. The energy exchange between electrons and phonons during the nonequilibrium stage are described the phonon-electron coupling terms, $G(T_e - T_l)$, with G (the phonon-electron coupling factor) being of the order of 10^{16} W/(m^{3}K) for most metals [5, 6]. As compared to the volumetric heat capacity (C) measured in J/(m^{3}K), the phonon-electron coupling factor differs from the volumetric heat capacity by a unit of time, measuring the *power* required to raise the temperature in a substance of a unit volume by one degree Kelvin. The magnitude of the resulting energy exchange (in terms of power) between electrons and phonons is proportional to their temperature difference, which is equal in magnitude but opposite in sense as described in Eq. (30). Equation (30) is targeted toward the phonon-electron interaction during the picosecond transient. It neglects the effect of conduction in the metal lattices. It also assumes Fourier's law for heat transport through electrons because the relaxation behavior of *electrons* of the order of 10 fs has already diminished during the picosecond transient targeted upon by Eq. (30). This can be clearly seen based on the comparison on the orders of magnitude as shown in Eq. (6).

Equation (30) will be explored in more detail later, in the context of thermal lagging, but it may be worthwhile for the time being to better illustrate the nonequilibrium feature behind it. Aiming toward the transient response between electrons and phonons, the simplest approach is to further neglect effect of conduction in the electron gas, $k_e = 0$ in Eq. (30). Electrons are assumed to start

with a temperature T_0, as $t = 0$, whereas phonons are assumed to have a zero initial temperature. Dropping the conduction term in the electron gas (by setting $k_e = 0$) and normalizing the resulting equation by introducing

$$\theta_{e,l} = \frac{T_{e,l}}{T_0}, \quad \beta = \frac{t}{\left(\frac{C_e}{G}\right)}, \quad C = \frac{C_e}{C_l}, \tag{31}$$

Eq. (30) and the initial conditions become

$$\frac{\partial \theta_e}{\partial \beta} = -\left(\theta_e - \theta_l\right), \quad \frac{\partial \theta_l}{\partial \beta} = C\left(\theta_e - \theta_l\right); \quad \theta_e(0) = 1, \quad \theta_l(0) = 0 \tag{32}$$

Such a simple system based on the lumped formulation facilitates direction integrations to give

$$\theta_e(\beta) = \frac{C + \exp\left[-(1+C)\beta\right]}{1+C}, \quad \theta_l(\beta) = \frac{C\left\{1 - \exp\left[-(1+C)\beta\right]\right\}}{1+C}, \tag{33}$$

which are governed by a single parameter C, the heat capacity ratio between electrons and phonons. Since the value of C_e is smaller than that of C_l by approximately two orders of magnitude, for $C = 0.01$, the temperature response is shown in Fig. 4. While the electron temperature continues to decrease and the phonon temperature continues to increase due to the energy/power exchange between the two, the electron and phonon temperatures come to thermal equilibrium after a certain period. Strictly speaking, due to the exponential functions involved, the electron temperature and the phonon temperature become exactly identical as $\beta \to \infty$, when $\theta_e = \theta_l = C/(1+C) \cong C$ according to Eq. (33). In parallel to the definition for the laminar boundary layer thickness, where the local velocity of the fluid flow reaches 99 percent of the free stream velocity, however, thermal equilibrium could be defined as a stage where the difference between the electron temperature and the phonon temperature is less than a certain percentage of the electron temperature:

$$\frac{T_e - T_l}{T_e} < \varepsilon, \quad \text{or} \quad \frac{\theta_l}{\theta_e} > 1 - \varepsilon \tag{34}$$

In correspondence with the 99 percent threshold used in defining the boundary layer of the fluid flow, the value of ε is one percent or 0.01. Substituting Eq. (33) into Eq. (34) and noting also that C (the heat capacity ratio) is a small number ($C = 0.01$), it results in the time for achieving thermal equilibrium between electrons and phonons:

$$\beta_{\text{eq}} = \frac{\ln\left(\frac{1+C-\varepsilon}{C\varepsilon}\right)}{1+C} \cong \ln\left(\frac{1}{C}\right) - \ln(\varepsilon) \tag{35}$$

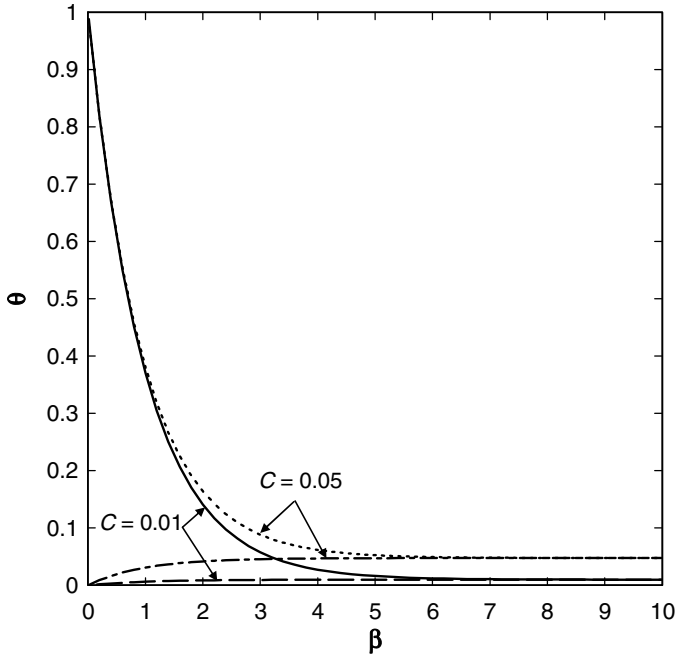

Fig. 4 Thermalization between electrons and phonons: Lumped parabolic two-step model: $C = 0.01$ and 0.05

Under the same values of C and ε being 0.01, $\beta_{eq} \cong 9.2$, which coincide with but is more strict than that shown in Fig. 4. Both electron and phonon temperatures increase with the value of C, as illustrated in Fig. 4 for $C = 0.05$. The effect of C is more significant on the phonon temperature over the entire stage of nonequilibrium heating. The same effect on the electron temperature, on the other hand, starts to amplify after $\beta > 1$, or $t > (C_e/G)$. Thermal equilibrium between electrons and phonons occurs earlier for the case of a larger value of C. For $C = 0.05$, $\beta_{eq} \cong 7.6$ under the same 99 percent threshold. Effects of conduction and volumetric heating in the electron gas, which are not included in Eq. (32), will make the thermalization behavior much more complicated and the close forms shown in Eq. (33) infeasible. All salient features as those displayed in Fig. 4, including the involvement of the time constant, C_e/G, introduced in Eq. (31), however, remain the same. Such a time constant is termed the thermalization time in the two-step model which, in the context of thermal lagging, will appear as one of the two phase lags characterizing the ultrafast transient between electrons and phonons.

Equation (30) describes the nonequilibrium heating between electrons and phonons in the picosecond domain due to the negligence of the thermal relaxation of electrons in femtoseconds. To shorten the domain of descriptions to femtoseconds, effect of thermal relaxation needs to be instated in the electron gas,

which results in the hyperbolic two-step model reflecting the wave effect of heat propagation in the electron gas:

$$\begin{cases} C_e \dfrac{\partial T_e}{\partial t} = -\nabla \bullet \mathbf{q}_e - G\left(T_e - T_l\right) \\ \mathbf{q}_e + \tau_F \dfrac{\partial \mathbf{q}_e}{\partial t} = -k_e \nabla T_e \\ C_l \dfrac{\partial T_l}{\partial t} = G\left(T_e - T_l\right) \end{cases} \tag{36}$$

The relaxation behavior accommodated in the electron gas, the second expression in Eq. (36), is exactly the same as that in the *CV*-wave, with $\tau_F \sim 10$ fs being the relaxation time of electrons calculated at the Fermi surface. In the case of $\tau_F = 0$, the second equation in Eq. (36) reduces to Fourier's law and the parabolic two-step model shown by Eq. (30) is recovered. Focusing on thermal equilibrium between electrons and phonons in the simplest mathematical content, parallel to the previous treatment applied to Eq. (30), effect of conduction in electrons is temporarily removed and Eq. (32) evolves into a more complicated form:

$$\begin{gathered} z\frac{\partial^2 \theta_e}{\partial \beta^2} + (1+z)\frac{\partial \theta_e}{\partial \beta} - z\frac{\partial \theta_l}{\partial \beta} = -(\theta_e - \theta_l), \quad \frac{\partial \theta_l}{\partial \beta} = C(\theta_e - \theta_l) \quad \text{with} \quad z = \frac{\tau_F}{\left(\dfrac{C_e}{G}\right)}; \\ \theta_e(0) = 1, \quad \frac{\partial \theta_e}{\partial \beta}(0) = 0, \quad \theta_l(0) = 0 \end{gathered} \tag{37}$$

Thermal relaxation of electrons raises two additional features. First, the thermal response now depends on the ratio (z) of the electron relaxation time (τ_F) to the thermalization time (C_e/G). Since thermalization between electrons and phonons occurs later than thermal relaxation of electrons, $\tau_F < C_e/G$, the ratio of z is less than one ($z < 1$). Second, a second order derivative of θ_e with respect to time now arises, $\partial^2\theta_e/\partial\beta^2$, which allows us to specify the initial time-rate of change of the electron temperature, $\partial\theta_e/\partial\beta$ as $\beta = 0$, in addition to the initial temperature. The condition of $\partial\theta_e/\partial\beta = 0$ as $\beta = 0$ is imposed in Eq. (37) to simulate electron heating from a stationary state, to be followed by the phonon-electron interactions in femtoseconds. Close form solutions to Eq. (37) are feasible under such conditions,

$$\begin{gathered} \theta_e = \frac{C(1+z)}{1+C} - \frac{(Cz-1)\exp\left(-\dfrac{\beta}{z}\right)\left[z(1+C) - \exp\left(-\beta\left(1+C-\dfrac{1}{z}\right)\right)\right]}{(1+C)(Cz+z-1)}, \\ \theta_l = \frac{C\exp\left[-(1+C)\beta\right]\left\{1 - Cz - (1+C)z^2\exp\left[-\beta\left(\dfrac{1}{z} - 1 - C\right)\right] + (1+z)\left[z(C+1)-1\right]\exp\left[\beta(1+C)\right]\right\}}{(1+C)(Cz+z-1)}, \end{gathered} \tag{38}$$

for which the same nondimensional scheme shown by Eq. (31) is used. The way in which thermal equilibrium is achieved between electrons and phonons in this case is shown in Fig. 5, where the value of C is fixed at 0.01 while that of z is allowed

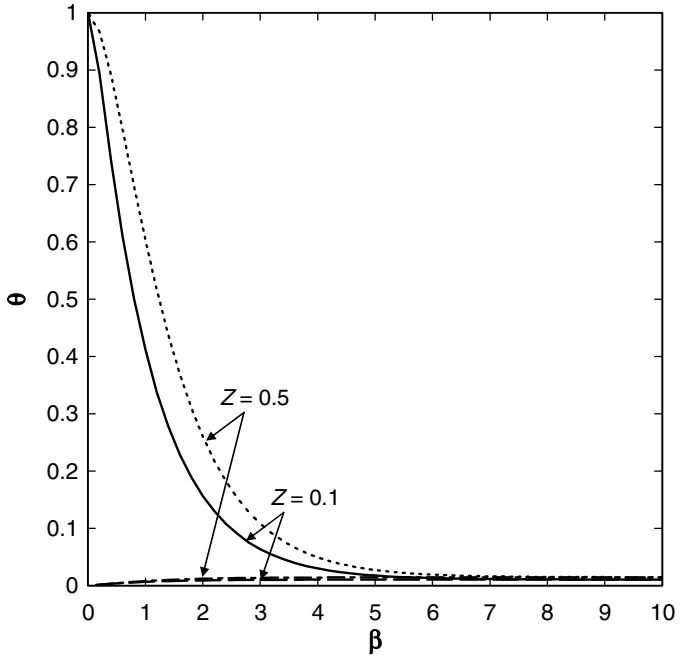

Fig. 5 Thermalization between electrons and phonons: Lumped hyperbolic two-step model: $C = 0.01$ and $z = 0.1$ and 0.5

to vary from 0.1 to 0.5 to show the effect of τ_F relative to C_e/G. The initial zero slope, $\partial\theta_e/\partial\beta = 0$ as $\beta = 0$, can only be seen in the domain of $\beta \in [0, 0.1]$, which is not clear in Fig. 5 due to the extended domain of $\beta \in [0, 10]$ chosen for illustrating the thermalization behavior. In addition to the heat capacity ratio (C), the thermalization behavior between electrons and phonons depends also on the parameter z, $\tau_F/(C_e/G)$. A larger value of z (stronger effect of thermal relaxation in electrons) results in a higher temperature for both electrons and phonons, which produces a much stronger effect on the electrons than phonons as seen in Fig. 5. As the conduction effect is further reinstated in the electron gas, in the context of thermal lagging to be developed later, the time ratio of z will evolve into the ratio between the two phase lags. All salient features in the electron-phonon interactions and their thermalization behaviors are preserved in the simple examples provided by Eqs. (32) and (37).

During the ultrafast transient, in times comparable to the relaxation time of energy carriers, explicit involvement of the relaxation time is a common feature in all microscale conduction models. Additional time constants characterizing the ultrafast transient, exemplified by the time constant (C_e/G) extracted from both the parabolic and hyperbolic two-step model above, however, seem to exit in companion. This is more obvious in the phonon scattering model and the

internal-energy relaxation model due to the explicit involvement of τ_R in Eq. (15) and τ_e in Eq. (28), but less obvious in the parabolic/hyperbolic two-step model where electron-phonon interactions are described through field coupling rather than the use of a specific constitutive equation. Apparently, this additional time constant will appear in different forms as different physical processes are described in different models.

3 Thermal Lagging

Regardless of different origins of the time constants characterizing the ultrafast response in small scales, the dual-phase-lag lumps the finite times required for accomplishing the various microstructural interactions in space onto the two phase lags in time. On top of the relaxation time of the energy carriers, recovery of the temporary loss of momentum in phonon scattering, additional relaxation of the internal energy in the context of irreversible thermodynamics, and the thermalization between electrons and phonons are microstructural interactions that will require a finite period of time to complete. In addition to the relaxation time that has commonly existed in all the microscale conduction models, it is necessary to find a way to implement another time constant to characterize the microstructural interaction effects.

The premise of the thermal lagging concept, and consequently the resulting dual-phase-lag (DPL) model, lies in the introduction of another time constant, termed phase lag in a more general sense [18], in the time series of the temperature gradient. Inheriting the same merit as that shown in Eq. (9) describing the general response with delays, another phase lag, τ_T, is introduced in relating the heat flux vector to the temperature gradient:

$$\mathbf{q}(\mathbf{r}, t+\tau_q) = -k\nabla T(\mathbf{r}, t+\tau_T)\,. \tag{39}$$

Building on the familiar Fourier's law, at least on the appearance, Eq. (39) was originally proposed as a constitutive equation that aims to extend what we have already been familiar with in macroscale to microscale heat transfer [18]. With the phase lag of the heat flux vector, τ_q, and the phase lag of the temperature gradient, τ_T, thus introduced, the overarching goal is to describe the finite times required for the various microstructural interactions to take place, in space, in terms of the two phase lags in time. Equation (39) needs to be coupled with the energy equation, Eq. (4), to determine the heat flux vector and the temperature. Due to the general delay described in Eq. (39), however, Eqs. (4) and (39) display a set of coupled partial differential equations where the physical quantities involved do not occur at the same instant of time. Instead of seeking for a solution to this type of partial differential equations with general delay, particularly in the 1980s when the DPL model was lack of either an experimental or a theoretical support, emphases were placed on the special conditions under which the degenerated forms of Eq. (39) could make a perfect contact with some experimentally verified and/or theoretically proven microscale conduction models. To this end, inheriting the first-order description made in Eq. (10), Eq. (39) can be expanded in terms of the

Taylor series. Assuming further that both phase lags are small in comparison with the process time, i.e., τ_T , τ_q << t, the Taylor series expansion of Eq. (39) containing the first order effects of τ_T and τ_q is

$$\mathbf{q}(\mathbf{r},t+\tau_q) = -k\nabla T(\mathbf{r},t+\tau_T) \quad \Rightarrow$$
$$\mathbf{q}(\mathbf{r},t) + \tau_q \frac{\partial \mathbf{q}}{\partial t}(\mathbf{r},t) + O\left(\tau_q^2\right) \cong -k\left[\nabla T(\mathbf{r},t) + \tau_T \frac{\partial}{\partial t}\nabla T(\mathbf{r},t) + O\left(\tau_T^2\right)\right] \tag{40}$$

With the effect of delays appearing in the coefficients, once again, the Taylor series expansion shows its use in casting all quantities into the same instant of time.

Elimination of the heat flux vector from Eqs. (4) and (40), for the purpose of obtaining an energy equation containing temperature alone, becomes more difficult due to the presence of the mixed-derivative term, $\partial(\nabla T)/\partial t$, in Eq. (40). A more general procedure is now introduced for this process. In terms of the operator form, Eqs. (4) and (40) can be expressed as

$$\begin{bmatrix} \nabla\bullet & C\dfrac{\partial}{\partial t} \\ \left(1+\tau_q \dfrac{\partial}{\partial t}\right) & k\left[\nabla\left(1+\tau_T \dfrac{\partial}{\partial t}\right)\right] \end{bmatrix} \begin{bmatrix} \mathbf{q} \\ T \end{bmatrix} = 0 \tag{41}$$

Solving for T, it results in

$$T = \frac{0}{\begin{vmatrix} \nabla\bullet & C\dfrac{\partial}{\partial t} \\ \left(1+\tau_q \dfrac{\partial}{\partial t}\right) & k\left[\nabla\left(1+\tau_T \dfrac{\partial}{\partial t}\right)\right] \end{vmatrix}} \quad \Rightarrow \quad \begin{vmatrix} \nabla\bullet & C\dfrac{\partial}{\partial t} \\ \left(1+\tau_q \dfrac{\partial}{\partial t}\right) & k\left[\nabla\left(1+\tau_T \dfrac{\partial}{\partial t}\right)\right] \end{vmatrix} T = 0 \tag{42}$$

Expanding the determinant (|•|) in Eq. (42),

$$k\left[\nabla^2\left(1+\tau_T \frac{\partial}{\partial t}\right)T\right] - C\frac{\partial}{\partial t}\left(1+\tau_q \frac{\partial}{\partial t}\right)T = 0, \quad \text{which gives}$$

$$\nabla^2 T + \tau_T \frac{\partial}{\partial t}\left(\nabla^2 T\right) = \frac{1}{\alpha}\frac{\partial T}{\partial t} + \left(\frac{\tau_q}{\alpha}\right)\frac{\partial^2 T}{\partial t^2} \tag{43}$$

Equation (43) has been the basis for the linear dual-phase-lag model due to the involvement of the first order effect of τ_T and τ_q. It has been studied extensively and rigorously from both mathematical and phenomenological points of view [70-79]. Note that Eq. (43) recovers the case of Fourier diffusion as $\tau_T = \tau_q = \tau$

including the special case of $\tau = 0$. Mathematically, this can be seen by casting Eq. (43) into the following form:

$$\left[\nabla^2 T - \frac{1}{\alpha}\frac{\partial T}{\partial t}\right] + \tau\frac{\partial}{\partial t}\left[\nabla^2 T - \frac{1}{\alpha}\frac{\partial T}{\partial t}\right] = 0, \tag{44}$$

which makes the expression in the bracket, $[\nabla^2 T - (1/\alpha)(\partial T/\partial t)] = 0$, as a general solution unless the initial distribution of temperature deviates from this condition. Physically, this is also perceivable because the condition $\tau_T = \tau_q = \tau$ provides a trivial shift of the time scale in Eq. (39), from the initial instant of $t = 0$ to $t = \tau$. Volumetric heating (Q) describing energy absorption in the electron gas in metals or metabolic heat generation in bio-heat transfer, can be instated in the energy equation,

$$-\nabla\bullet\mathbf{q}(\mathbf{r},t) + Q(\mathbf{r},t) = C\frac{\partial T}{\partial t}(\mathbf{r},t). \tag{45}$$

The same procedure can be applied to eliminate the heat flux vector from Eqs. (40) and (45), resulting in

$$\nabla^2 T + \tau_T\frac{\partial}{\partial t}\left(\nabla^2 T\right) + \frac{1}{k}\left(Q + \tau_q\frac{\partial Q}{\partial t}\right) = \frac{1}{\alpha}\frac{\partial T}{\partial t} + \left(\frac{\tau_q}{\alpha}\right)\frac{\partial^2 T}{\partial t^2} \tag{46}$$

For the case involving a rapid change of heating with time, such as material processing involving femtosecond laser pulses, the presence of apparent heating, $\tau_q(\partial Q/\partial t)$ in Eq. (46), is a byproduct that must be included along with the relaxation behavior of the energy carriers. The effect of apparent heating is among the central subjects in studying the thermal shock phenomena [34-40]. Since the heating terms do not alter the fundamental behavior of thermal lagging, however, they will be omitted in this chapter unless stated otherwise.

Like the *CV*-wave model, the temperature described by the dual-phase-lag model in Eq. (43)is nonequilibrium by nature. In the context of nonequilibrium thermodynamics, Eq. (10) can be viewed as the evolution equation describing the dynamic temperature (β) at a reference state (0):

$$\frac{d\beta_0}{dt}(t) \equiv \dot{\beta}_0 = \frac{1}{\tau}(\theta - \beta) \quad \Rightarrow \quad \dot{\beta}_0(\beta,\theta) \tag{47}$$

Based on such a reference state describing the *CV*-wave behavior, the evolution equation can be generalized to account for the time-rate of change of the nonequilibrium temperature, $\dot{\theta}$,

$$\dot{\beta}(\beta,\theta,\dot{\theta}) = \dot{\beta}_0 + \left(\frac{\partial\dot{\beta}}{\partial\dot{\theta}}\right)_0\dot{\theta} + \ldots \tag{48}$$

The corresponding equation to Eq. (12) is thus

$$\frac{\partial \mathbf{q}}{\partial t} = -k\nabla \overbrace{\frac{\partial \beta}{\partial t}}^{\frac{1}{\tau}(\theta-\beta)+\left(\frac{\partial \dot{\beta}}{\partial \dot{\theta}}\right)_0 \dot{\theta}} = -\frac{k}{\tau}\left(\nabla\theta - \overbrace{\nabla\beta}^{\frac{\mathbf{q}}{k}} + \tau\left(\frac{\partial \dot{\beta}}{\partial \dot{\theta}}\right)_0 \nabla\dot{\theta} \right) \Rightarrow$$

$$\mathbf{q} + \underbrace{\tau}_{\tau_q} \frac{\partial \mathbf{q}}{\partial t} = -k\left[\nabla\theta + \underbrace{\tau\left(\frac{\partial \dot{\beta}}{\partial \dot{\theta}}\right)_0}_{\tau_T} \frac{\partial}{\partial t}(\nabla\theta) \right]. \tag{49}$$

Equation (49) has exactly the same form as the dual-phase-lag equation shown by Eq. (40), with the coefficient in Eq. (48) representing the ratio of τ_T to τ_q, $\left(\frac{\partial \dot{\beta}}{\partial \dot{\theta}}\right)_0$ = (τ_T/τ_q). The semi-empirical temperature introduced phenomenologically earlier in Eq. (40), therefore, is a nonequilibrium temperature whose time evolution into the dynamic regime during the thermodynamic transition is described by Eq. (48). The entropy production rate, in correspondence with Eq. (13) for the *CV*-wave model, has been proven to be positive definite within the framework of extended irreversible thermodynamics [18].

Equation (43) results from the linear dual-phase-lag model that accounts for the linear terms of τ_T and τ_q in the Taylor's series expansion, as shown in Eq. (40). Continuing the expansion by retaining the first order term in τ_T but both the first- and second-order terms in τ_q results in

$$\mathbf{q}(\mathbf{r}, t+\tau_q) = -k\nabla T(\mathbf{r}, t+\tau_T) \Rightarrow$$
$$\mathbf{q}(\mathbf{r},t) + \tau_q \frac{\partial \mathbf{q}}{\partial t}(\mathbf{r},t) + \frac{\tau_q^2}{2}\frac{\partial^2 \mathbf{q}}{\partial t^2}(\mathbf{r},t) \cong -k\left[\nabla T(\mathbf{r},t) + \tau_T \frac{\partial}{\partial t}\nabla T(\mathbf{r},t) \right] \tag{50}$$

The same procedure applied in Eqs. (41) – (42) can be extended to eliminate the heat flux vector, and the result corresponding to Eq. (43) is

$$\nabla^2 T + \tau_T \frac{\partial}{\partial t}\left(\nabla^2 T\right) = \frac{1}{\alpha}\frac{\partial T}{\partial t} + \left(\frac{\tau_q}{\alpha}\right)\frac{\partial^2 T}{\partial t^2} + \left(\frac{\tau_q^2}{2\alpha}\right)\frac{\partial^3 T}{\partial t^3} \tag{51}$$

Likewise, the equations containing up to the second order effects in both τ_T and τ_q are

$$\mathbf{q}(\mathbf{r},t)+\tau_q\frac{\partial\mathbf{q}}{\partial t}(\mathbf{r},t)+\frac{\tau_q^2}{2}\frac{\partial^2\mathbf{q}}{\partial t^2}(\mathbf{r},t)\cong -k\left[\nabla T(\mathbf{r},t)+\tau_T\frac{\partial}{\partial t}\nabla T(\mathbf{r},t)+\left(\frac{\tau_T^2}{2}\right)\frac{\partial^2}{\partial t^2}\nabla T(\mathbf{r},t)\right], \tag{52}$$

$$\nabla^2 T+\tau_T\frac{\partial}{\partial t}\left(\nabla^2 T\right)+\left(\frac{\tau_T^2}{2}\right)\frac{\partial^2}{\partial t^2}\left(\nabla^2 T\right)=\frac{1}{\alpha}\frac{\partial T}{\partial t}+\left(\frac{\tau_q}{\alpha}\right)\frac{\partial^2 T}{\partial t^2}+\left(\frac{\tau_q^2}{2\alpha}\right)\frac{\partial^3 T}{\partial t^3}$$

The constitutive equation and the energy equation will continue to evolve as the higher order terms of τ_T and τ_q are taken into account. Rather than an endless expansion as such, however, a most important task is to realize the physical meanings of the two phase lags as well as the physical implications of their high order effects.

The high order effects shown by Eq. (52) can be accommodated in the general framework of nonequilibrium thermodynamics. First, incorporating the second order term of τ^2 in Eq. (10) in bridging the dynamic temperature with the nonequilibrium temperature,

$$\beta(t+\tau)\cong\beta(t)+\tau\frac{d\beta}{dt}(t)+\frac{\tau^2}{2}\frac{d^2\beta}{dt^2}(t)=\theta(t), \tag{53}$$

the evolution equation in correspondence with Eq. (47) becomes

$$\frac{d\beta_0}{dt}\equiv\dot{\beta}_0=\frac{1}{\tau}(\theta-\beta)-\left(\frac{\tau}{2}\right)\frac{d^2\beta}{dt^2} \tag{54}$$

In addition to θ and β in Eq. (47), the reference state of the evolution equation for the nonequilibrium temperature further depends on $\dot{\beta}$, the second order derivative of β with respect to time. Second, continuing the Taylor series expansion in Eq. (48) to include the $\dot{\theta}$-term,

$$\dot{\beta}(\beta,\theta,\dot{\theta},\ddot{\theta})\cong\dot{\beta}_0+\left(\frac{\partial\dot{\beta}}{\partial\dot{\theta}}\right)_0\dot{\theta}+\frac{1}{2}\left(\frac{\partial^2\dot{\beta}}{\partial\dot{\theta}^2}\right)_0\ddot{\theta}+\ldots, \tag{55}$$

Eq. (49) is cast into the following form:

$$\frac{\partial\mathbf{q}}{\partial t}=-k\nabla\overbrace{\frac{1}{\tau}(\theta-\beta)-\left(\frac{\tau}{2}\right)\ddot{\beta}+\left(\frac{\partial\dot{\beta}}{\partial\dot{\theta}}\right)_0\dot{\theta}+\frac{1}{2}\left(\frac{\partial^2\dot{\beta}}{\partial\dot{\theta}^2}\right)_0\ddot{\theta}}^{\frac{\partial\tilde{\beta}}{\partial t}}=-k\left[\frac{1}{\tau}\left(\nabla\theta-\overbrace{\frac{\mathbf{q}}{k}}^{\nabla\tilde{\beta}}\right)-\frac{\tau}{2}\overbrace{\frac{\ddot{\mathbf{q}}}{k}}^{\nabla\ddot{\beta}}+\left(\frac{\partial\dot{\beta}}{\partial\dot{\theta}}\right)_0\nabla\dot{\theta}+\frac{1}{2}\left(\frac{\partial^2\dot{\beta}}{\partial\dot{\theta}^2}\right)_0\nabla\ddot{\theta}\right]\Rightarrow \tag{56}$$

$$\mathbf{q}+\tau\frac{\partial\mathbf{q}}{\partial t}+\frac{\tau^2}{2}\frac{\partial^2\mathbf{q}}{\partial t^2}=-k\left[\nabla\theta+\tau\left(\frac{\partial\dot{\beta}}{\partial\ddot{\theta}}\right)_0\frac{\partial}{\partial t}(\nabla\theta)+\frac{\tau}{2}\left(\frac{\partial^2\dot{\beta}}{\partial\dot{\theta}^2}\right)_0\frac{\partial^2}{\partial t^2}(\nabla\theta)\right]$$

where $\left(\frac{\partial\dot{\beta}}{\partial\dot{\theta}}\right)_0$ and $\left(\frac{\partial^2\dot{\beta}}{\partial\dot{\theta}^2}\right)_0$ are two independent coefficients described by the initial slopes of $\dot{\beta}$ with respect to $\dot{\theta}$. With $\tau \equiv \tau_q$ and $\tau_T = \tau_q\left(\frac{\partial\dot{\beta}}{\partial\dot{\theta}}\right)_0$ defined earlier in Eq. (49), the last coefficient in Eq. (56) is

$$\left(\frac{\partial^2\dot{\beta}}{\partial\dot{\theta}^2}\right)_0 = \tau_q\left(\frac{\partial\dot{\beta}}{\partial\dot{\theta}}\right)_0^2 = \tau_T\left(\frac{\partial\dot{\beta}}{\partial\dot{\theta}}\right)_0, \tag{57}$$

which makes Eq. (56) exactly identical to the first equation in Eq. (52) containing the full second-order effects in τ_T and τ_q.

Admissibility of the dual-phase-lag model in general, Eq. (39), has been shown elegantly within the framework of the Boltzmann transport equation [80], which is an important milestone in the development of the phase-lag concept. Along with the second-law admissibility within the framework of the extended irreversible thermodynamics [18], the compatibility with the Boltzmann transport equation is one of the two guidelines that must be followed by any phenomenologically based constitutive equation. Boltzmann transport equation, in essence, describes the conservation of the distribution function $f(\mathbf{r}, \mathbf{v}, t)$ of energy carriers:

$$\frac{Df}{Dt} = -\left(\frac{\partial f}{\partial t}\right)_{\text{scattering}} \quad \Rightarrow \quad \frac{\partial f}{\partial t} + \mathbf{v}\bullet\nabla f = -\left(\frac{\partial f}{\partial t}\right)_{\text{scattering}} \tag{58}$$

where (D/Dt) represents the total derivative as that defined in fluid dynamics, $\mathbf{v}$ is the carrier velocity, and the change of the distribution function (f) results from scattering of the carriers. In the absence of the scattering term, $(\partial f/\partial t)_{\text{scattering}} = 0$, Eq. (58) reduces to the Liouville equation [81], which states that the number of energy carriers included in a hyper-spatial element ($d\mathbf{r}d\mathbf{v}$) is conserved in the absence of an external force. Dependence of f on $\mathbf{v}$ results from the observation made in the momentum space ($\mathbf{p}$). Consequently, $f(\mathbf{r}, \mathbf{v}, t) \equiv f(\mathbf{r}, \mathbf{p}(\mathbf{v}), t)$. Since the kinetic energy (ε) is proportional to the velocity squared, alternatively, such a functional dependence can also be expressed as $f(\mathbf{r}, \mathbf{v}, t) \equiv f(\mathbf{r}, \varepsilon(\mathbf{v}), t)$ in the energy space. Following Ref. [80], the energy space will be employed in this review. Should the distribution function be obtained from Eq. (58), the heat flux vector can be calculated in the energy space

$$\mathbf{q}(\mathbf{r},t) = \int_\varepsilon \mathbf{v}(\mathbf{r},t) f(\mathbf{r},\varepsilon,t)\varepsilon D(\varepsilon) d\varepsilon \tag{59}$$

where $D(\varepsilon)$ is the density of state of the carriers, $D(\varepsilon) = 4\pi m\sqrt{2m\varepsilon}$ for isotropic scattering in the absence of an external force. Accounting for the quantum effect, the coefficient (4π) in $D(\varepsilon)$ is replaced by $1/(\hbar^3\pi^2)$.

In the absence of an external force, the carrier's velocity and kinetic energy remain constant. As a result of mutual interactions and scattering of the energy carriers, the distribution function changes in the state space, from its value at ($\mathbf{r}$, ε, t) to that at ($\mathbf{r} + d\mathbf{r}$, ε, $t + dt$):

$$\frac{\partial f}{\partial t} \cong \frac{f(\mathbf{r}+d\mathbf{r},\varepsilon,t+dt)-f(\mathbf{r},\varepsilon,t)}{dt} = \left(\frac{\partial f}{\partial t}\right)_{\text{scattering}} \cong \frac{f_0(\varepsilon)-f(\mathbf{r},\varepsilon,t)}{\tau_q} \tag{60}$$

The first-order description has been applied to estimate the time-rate of change of the distribution function, $\partial f/\partial t$, and the relaxation-time approximation has been applied to estimate the scattering term, $(\partial f/\partial t)_{\text{scattering}}$. As clearly seen, the relaxation-time approximation estimates the scattering term by the change of the distribution function from its equilibrium state (f_0) over a period of the relaxation time, denoted by τ_q in Eq. (60). There are two incremental changes involved in Eq. (60), $d\mathbf{r}$ and dt. To differentiate their different origins, the left-hand side of the equation is decomposed into two components:

$$\frac{f(\mathbf{r}+d\mathbf{r},\varepsilon,t+dt)-f(\mathbf{r},\varepsilon,t+dt)}{dt} + \frac{f(\mathbf{r},\varepsilon,t+dt)-f(\mathbf{r},\varepsilon,t)}{dt} = \frac{f_0(\varepsilon)-f(\mathbf{r},\varepsilon,t)}{\tau_q} \tag{61}$$

A common term, $[f(\mathbf{r}, \varepsilon, t + dt)/dt]$, is subtracted in the first component and then added back in the second component. The first term on the left-hand side of Eq. (61) describes the change of the distribution function due to the change of the position of the energy carrier from $\mathbf{r}$ to ($\mathbf{r} + d\mathbf{r}$) at time ($t + dt$), whereas the second terms describes the change of the distribution function at $\mathbf{r}$ as time moves on from t to ($t + dt$). Since

$$f(\mathbf{r}+d\mathbf{r},\varepsilon,t+dt) \cong f(\mathbf{r},\varepsilon,t+dt) + d\mathbf{r}\bullet\nabla f(\mathbf{r},\varepsilon,t+dt), \tag{62}$$

according to the Taylor's series expansion with respect to $\mathbf{r}$, the first term in Eq. (61) can be expressed as

$$\frac{f(\mathbf{r}+d\mathbf{r},\varepsilon,t+dt)-f(\mathbf{r},\varepsilon,t+dt)}{dt} = \frac{d\mathbf{r}\bullet\nabla f(\mathbf{r},\varepsilon,t+dt)}{dt} = \mathbf{v}\bullet\nabla f(\mathbf{r},\varepsilon,t+dt) \equiv \mathbf{v}\bullet\nabla f(\mathbf{r},\varepsilon,t+\tau_T) \tag{63}$$

Note that Eq. (63) captures the advection term in Eq. (58) at time ($t + dt$). All distribution functions involved in Eq. (63) occur at a *later* time, ($t + dt$), as compared to the process time, t, described in the scattering term. For this reason, a time constant τ_T is introduced in Eq. (63) in place of (dt) to highlight such a *delayed* response, in time from t to ($t + \tau_T$), which is associated with the change of the distribution function in space, from $\mathbf{r}$ to ($\mathbf{r} + d\mathbf{r}$). The second expression in Eq. (61) can be treated the same by making the Taylor series expansion in time:

$$f(\mathbf{r},\varepsilon,t+dt) = f(\mathbf{r},\varepsilon,t) + (dt)\frac{\partial f}{\partial t}(\mathbf{r},\varepsilon,t) + \ldots \quad \Rightarrow \quad \frac{f(\mathbf{r},\varepsilon,t+dt)-f(\mathbf{r},\varepsilon,t)}{dt} = \frac{\partial f}{\partial t}(\mathbf{r},\varepsilon,t) \tag{64}$$

Substituting Eqs. (63) and (64) into Eq. (61), it results in

$$\begin{aligned} &\mathbf{v}\bullet\nabla f(\mathbf{r},\varepsilon,t+\tau_T)+\frac{\partial f}{\partial t}(\mathbf{r},\varepsilon,t)=\frac{f_0(\varepsilon)-f(\mathbf{r},\varepsilon,t)}{\tau_q} \quad \Rightarrow \\ &\tau_q\mathbf{v}\bullet\nabla f(\mathbf{r},\varepsilon,t+\tau_T)+\left[f(\mathbf{r},\varepsilon,t)+\tau_q\frac{\partial f}{\partial t}(\mathbf{r},\varepsilon,t)\right]=f_0(\varepsilon) \end{aligned} \tag{65}$$

The bracketed quantity in Eq. (65) is the first-order term in the Taylor series expansion of $f(\mathbf{r},\ t+\tau_q)$ with respect to t. In consistency with the first-order descriptions applied so far, therefore, Eq. (65) can be written as

$$\tau_q\mathbf{v}\bullet\nabla f(\mathbf{r},\varepsilon,t+\tau_T)+f(\mathbf{r},\varepsilon,t+\tau_q)=f_0(\varepsilon) \tag{66}$$

To recover the heat flux vector defined in Eq. (59), Eq. (66) is multiplied through by $(\varepsilon D(\varepsilon)\mathbf{v})$ and the result is integrated over the energy space:

$$\int_\varepsilon\tau_q\varepsilon D(\varepsilon)\mathbf{v}\left[\mathbf{v}\bullet\nabla f(\mathbf{r},\varepsilon,t+\tau_T)\right]d\varepsilon+\int_\varepsilon f(\mathbf{r},\varepsilon,t+\tau_q)\varepsilon D(\varepsilon)\mathbf{v}d\varepsilon=\int_\varepsilon f_0(\varepsilon)\varepsilon D(\varepsilon)\mathbf{v}d\varepsilon \tag{67}$$

The second term is $\mathbf{q}(\mathbf{r},\ t+\tau_q)$ according to Eq. (59). The last term vanishes since the equilibrium distribution, f_0, is an even function of $\mathbf{v}$ and the entire integrand is an odd function of $\mathbf{v}$ for either the Fermi-Dirac equilibrium function (for electrons) or the Bose-Einstein equilibrium function (for phonons). The gradient of the distribution function in the first term can be approximated by the chain rule, $\nabla f(\mathbf{r},\varepsilon,t+\tau_T)=\left(\frac{\partial f_0}{\partial T}(\varepsilon,T)\right)\nabla T(\mathbf{r},t+\tau_T)$. Consequently,

$$\begin{aligned} &\int_\varepsilon\tau_q\varepsilon D(\varepsilon)\mathbf{v}\left[\mathbf{v}\bullet\overbrace{\nabla f(\mathbf{r},\varepsilon,t+\tau_T)}^{\left(\frac{\partial f_0}{\partial T}(\varepsilon,T)\right)\nabla T(\mathbf{r},t+\tau_T)}\right]d\varepsilon=\left[\int_\varepsilon\tau_q\varepsilon D(\varepsilon)\left(\frac{df_0}{\partial T}(\varepsilon,T)\right)\mathbf{v}\mathbf{v}d\varepsilon\right]\bullet\nabla T(\mathbf{r},t+\tau_T)\equiv\mathbf{k}\bullet\nabla T(\mathbf{r},t+\tau_T) \\ &\text{with}\quad \mathbf{k}\equiv\int_\varepsilon\tau_q\varepsilon D(\varepsilon)\left(\frac{df_0}{\partial T}(\varepsilon,T)\right)\mathbf{v}\mathbf{v}d\varepsilon,\quad \mathbf{v}\mathbf{v}=\begin{bmatrix}v_1^2 & v_1v_2 & v_1v_3\\ v_2v_1 & v_2^2 & v_2v_3\\ v_3v_1 & v_3v_2 & v_3^2\end{bmatrix}. \end{aligned} \tag{68}$$

Equation (67) thus becomes

$$\mathbf{q}(\mathbf{r},t+\tau_q)=-\mathbf{k}\bullet\nabla T(\mathbf{r},t+\tau_T) \tag{69}$$

For isotropic scattering with $\mathbf{v}$ uniformly distributed in the state space, $\mathbf{k}=k\mathbf{I}$ with $\mathbf{I}$ being the unit matrix. Equation (69) reduces to

$$\mathbf{q}(\mathbf{r},t+\tau_q)=-k\nabla T(\mathbf{r},t+\tau_T), \tag{70}$$

which is the dual-phase-lag model shown by Eq. (39). The dual-phase-lag model in general has thus been established in the framework of the Boltzmann transport equation, with τ_q describing the relaxation time for carrier scattering (from the

relaxation-time approximation) and τ_T describing the lagging time due to the finite time required for the carrier to move from **r** to d**r**.

3.1 Correlations

The temperature representations shown by Eqs. (43), (51), and (52) serve as the common platform for examining the correlations between the dual-phase-lag model and the other microscale conduction models. Such cross examinations are critical to unveil the physical meanings of the two phase lags in relation to the finite times required for accomplishing the various microstructural interactions described in the microscale conduction models.

The phonon scattering model shown by Eqs. (4) and (15), first of all, can be combined by eliminating the heat flux vector. Taking the divergence of Eq. (15) and substituting Eq. (4) into the result for $\nabla \bullet \mathbf{q} = -C(\partial T/\partial t)$, it results in

$$\nabla^2 T + \left(\frac{9\tau_N}{5}\right)\frac{\partial}{\partial t}\left(\nabla^2 T\right) = \left(\frac{3}{\tau_R c^2}\right)\frac{\partial T}{\partial t} + \left(\frac{3}{c^2}\right)\frac{\partial^2 T}{\partial t^2} \tag{71}$$

The complicated structure of the heat flux vector involved in the phonon scattering model, evidently, results in an exactly identical form of the energy equation shown by Eq. (43) for the linear dual-phase-lag model. Comparing the coefficients in correspondence, specifically,

$$\alpha = \frac{\tau_R c^2}{3}, \quad \tau_T = \frac{9\tau_N}{5}, \quad \tau_q = \tau_R . \tag{72}$$

the phase lag of the heat flux vector (τ_q) is thus equivalent to the umklapp relaxation time (τ_R) in the phonon scattering model, while the phase lag of the temperature gradient (τ_T) stretches the normal relaxation time condenses by (9/5) times. In the context of thermal lagging, thermal diffusivity is bridged to the umklapp relaxation time and the mean phonon speed squared.

In the presence of free electrons in metals, the parabolic two-step model is another example that provides physical interpretations to the two phase lags. In parallel to Eq. (41), Eq. (30) can be arranged in an operator form

$$\begin{cases} C_e \dfrac{\partial T_e}{\partial t} = k_e \nabla^2 T_e - G\left(T_e - T_l\right) \\ C_l \dfrac{\partial T_l}{\partial t} = G\left(T_e - T_l\right) \end{cases} \Rightarrow \begin{bmatrix} G + C_e \dfrac{\partial}{\partial t} + k_e \nabla^2 & -G \\ -G & G + C_l \dfrac{\partial}{\partial t} \end{bmatrix} \begin{bmatrix} T_e \\ T_l \end{bmatrix} = 0\,, \tag{73}$$

which gives

$$\begin{vmatrix} G + C_e \dfrac{\partial}{\partial t} + k_e \nabla^2 & -G \\ -G & G + C_l \dfrac{\partial}{\partial t} \end{vmatrix} T = 0, \quad \text{or} \tag{74}$$

$$\nabla^2 T + \left(\frac{C_l}{G}\right)\frac{\partial}{\partial t}\left(\nabla^2 T\right) = \left(\frac{C_e + C_l}{k_e}\right)\frac{\partial T}{\partial t} + \left(\frac{C_e C_l}{k_e G}\right)\frac{\partial^2 T}{\partial t^2}, \quad T \equiv T_e, T_l$$

Heat transport in electrons (T_e) and phonons (T_l) is governed by the same equation, but T_e and T_l will be different due to different initial times involved in describing the individual behaviors of electrons and phonons. Comparing Eq. (74) with Eq. (43), once again,

$$\alpha = \frac{k_e}{C_e + C_l}, \quad \tau_T = \frac{C_l}{G}, \quad \tau_q = \frac{1}{G}\left(\frac{1}{C_e} + \frac{1}{C_l}\right)^{-1} \tag{75}$$

Even though the parabolic two-step model does not explicitly involve a different constitutive equation than Fourier's law, the energy/power coupling term between phonons and electrons results in a lagging response with two time constants characterizing the transient response. In the case of G approaching infinity, implying that electrons and phonons are able to exchange heat in *no* time as a result of either electrons or phonons are moving at an infinite speed, $\tau_T = 0$ and $\tau_q = 0$ from Eq. (75) and Eq. (74) recovers the diffusion equation employing Fourier's law. As compared to the thermalization time describing thermal equilibrium between electrons and phonons, (C_e/G) defined in Eq. (31), the expression of τ_T in Eq. (75) differs by the heat-capacity-ratio, $\tau_T = (C_e/G) \times (C_l/C_e)$. The phase lag of the temperature gradient is the thermalization time within the heat-capacity ratio. In the presence of both free electrons and phonons in metals, clearly, the lagging behavior (τ_T and τ_q) is due to the finite time required for the energy exchange between electrons and phonons characterized by G. Since

$$\frac{\tau_T}{\tau_q} = 1 + \frac{C_l}{C_e} > 1, \quad \text{which implies} \quad \tau_q < \tau_T \tag{76}$$

For metals, the ratio of τ_T to τ_q is of the order 10^2 since heat capacity of phonons is about two orders of magnitude greater than that of electrons, $C_l/C_e \sim 10^2$. The condition of $\tau_q < \tau_T$, according to Eq. (39), implies that heat flux vector occurs at an earlier time that the temperature gradient. Consequently, heat flux is the cause for heat flow while temperature gradient is the effect. The electron-phonon interaction in metals is thus an example for the flux-precedence type of heat flow in terms of thermal lagging. In this context, the presumed gradient-precedence

type of heat flow ($\tau_T < \tau_q$) in the *CV*-wave model, with $\tau_T = 0$ and $\tau_q = \tau > 0$ in comparing Eq. (7) with Eq. (39), is dubious when applied to describe the ultrafast transient in metals.

Equation (43) represents a general type of energy equation describing the lagging response. Regardless of the sources for delay, which could be the umklapp and normal relaxations of phonons in dielectric crystals or electron-phonon interactions in metals, the temperature distributions resulting from Eq. (43) are sketched in Fig. 6, in times (t) comparable to τ_T and τ_q. Since thermal lagging is a special behavior in time, to avoid unnecessary interference from the spatial effect, Fig. 6 represents the one-dimensional temperature distribution in a semi-infinite solid subjected to the excitation of a suddenly raised temperature at the surface at $x = 0$ [18]. Fourier diffusion, Fig. 6(a), displays a monotonically decaying temperature toward downstream, which is recovered by the solution to Eq. (43) with $\tau_T = \tau_q$, or (τ_T/τ_q) = 1. Response of the *CV*-wave is obtained by the same solution with $\tau_T = 0$, resulting in a sharp wavefront located at $x = ct$ with $c = \sqrt{(\alpha/\tau_q)}$. The temperature in the heat affected zone ($x < ct$) is higher than that predicted by Fourier diffusion, while that in thermally undisturbed zone ($x > ct$) is lower than that predicted by Fourier diffusion. As effect of τ_T comes into play on top of that of τ_q, the sharp wavefront is fully destroyed and the temperature distribution returns to diffusion-like. Having the same decaying pattern toward downstream, however, the temperature resulting from the dual-phase-lag (DPL) model is significantly higher than that from Fourier diffusion. The excessive amount over Fourier diffusion increases with the ratio of τ_T to τ_q, in the direction of the arrow head marked in Fig. 6(a). The significantly higher temperature due to thermal lagging, in times comparable to τ_T and τ_q, is critically important to prevent early-time thermal failure of the high power devices. While the phase lag of the heat flux vector (τ_q) introduces a finite speed of heat propagation, and consequently a sharp wavefront, the phase lag of the temperature gradient (τ_T) efficiently destroys the wavefront even for (τ_T/τ_q) ~ 10^{-3} – 10^{-2} as shown in Fig. 6(b). The temperature drop in transition from the heat affected zone to the thermally undisturbed zone is confined within a localized zone around $x = ct$, which is stretched wider as the ratio of (τ_T/τ_q) increases. Such a localized zone resembles the finite width of shock waves propagating in gases [82, 83].

The interwoven relaxations of international energy (τ_e) and heat flux vector (τ_q) are special features in the Gurtin-pipkin's relaxation model, as shown in Eq. (28). Unlike the previous cases with two unknowns to be determined in coupling with the energy equation, Eq. (28) involves three unknowns (e, T, and $\mathbf{q}$) to be determined:

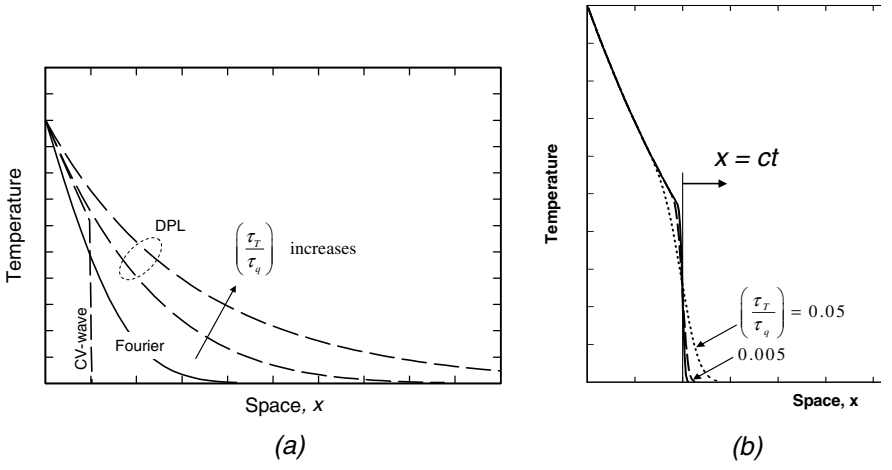

Fig. 6 Fourier diffusion, CV-wave ($\tau_T = 0$), and linear dual-phase-lag (DPL) models. (a) Elevated temperatures due to thermal lagging and (b) diminution of the wavefront at small values of (τ_T/τ_q).

$$\begin{bmatrix} \left(1+\tau_e\frac{\partial}{\partial t}\right) & -\left(\tau_e F_e + C\right) - \tau_e C\frac{\partial}{\partial t} & 0 \\ 0 & \tau F_q \nabla & \left(1+\tau\frac{\partial}{\partial t}\right) \\ \frac{\partial}{\partial t} & 0 & \nabla\bullet \end{bmatrix} \begin{bmatrix} e \\ T \\ \mathbf{q} \end{bmatrix} = 0 \tag{77}$$

Expanding the determinant like those in Eqs. (42) and (74), the energy equation containing temperature alone is

$$\nabla^2 T + \tau_e \frac{\partial}{\partial t}\nabla^2 T = \left(\frac{F_e\tau_e}{\tau F_q} + \frac{C_p}{\tau F_q}\right)\frac{\partial T}{\partial t} + \left[\tau_e\left(\frac{F_e}{F_q}\right) + \frac{C_p\tau_e}{\tau F_q} + \frac{C_p}{F_q}\right]\frac{\partial^2 T}{\partial t^2} + \left(\frac{C_p\tau_e}{F_q}\right)\frac{\partial^3 T}{\partial t^3} \tag{78}$$

In addition to the wave term, $\partial^2 T/\partial t^2$, the relaxation time of the internal energy (τ_e) not only gives rise to the mixed-derivative term, $\partial(\nabla T)/\partial t$, but also a jerk term, $\partial^3 T/\partial t^3$. The jerk term is a new feature that does not exist in the phonon scattering model (Eq. (71)) or the parabolic two-step model (Eq. (74)). It will alter the fundamental characteristics of heat transport since the jerk term represents the highest order derivative in Eq. (78). Nicely but not obviously, Eq. (78) has exactly the same form as Eq. (51) accounting for the linear effect of τ_T but up to the second order effect of τ_q in the dual-phase-lag model. Comparing the coefficients in correspondence, it results in

$$\alpha = \frac{\tau F_q}{\tau_e F_e + C}, \quad \tau_T = \tau_e, \quad \tau_q = \tau + \frac{\tau_e C}{\tau_e F_e + C} \tag{79}$$

In the framework of thermal lagging, the phase lag of the temperature gradient captures the relaxation time of the internal energy, whereas the phase lag of the heat flux vector captures the combined effect of τ (relaxation time of the heat flux vector in Eq. (28)) and τ_e (relaxation time of the internal energy).

The jerk term is not a prerogative of the Gurtin-Pipkin's model, however. Rooted on a different physical basis, the hyperbolic two-step model shown by Eq. (36) possesses the same feature:

$$\begin{cases} C_e \dfrac{\partial T_e}{\partial t} = -\nabla \cdot \mathbf{q}_e - G(T_e - T_l) \\ \mathbf{q}_e + \tau_F \dfrac{\partial \mathbf{q}_e}{\partial t} = -k_e \nabla T_e \\ C_l \dfrac{\partial T_l}{\partial t} = G(T_e - T_l) \end{cases} \Rightarrow \begin{bmatrix} \left(C_e \dfrac{\partial}{\partial t} + G\right) & -G & \nabla \cdot \\ k_e \nabla & 0 & \left(1 + \tau_F \dfrac{\partial}{\partial t}\right) \\ G & -\left(G + C_l \dfrac{\partial}{\partial t}\right) & 0 \end{bmatrix} \begin{bmatrix} T_e \\ T_l \\ \mathbf{q}_e \end{bmatrix} = 0. \tag{80}$$

Like the Gurtin-Pipkin's model, there are three unknowns involved: T_e, T_l, and $\mathbf{q}_e$ in Eq. (80) Expanding the determinant in correspondence, the energy equation is

$$\nabla^2 T_l + \left(\frac{C_l}{G}\right)\frac{\partial}{\partial t}\nabla^2 T_l = \left(\frac{C_l + C_e}{k_e}\right)\frac{\partial T}{\partial t} + \left(\frac{C_l C_e}{k_e G} + \frac{\tau_F (C_l + C_e)}{k_e}\right)\frac{\partial^2 T}{\partial t^2} + \tau_F \left(\frac{C_l C_e}{k_e G}\right)\frac{\partial^3 T}{\partial t^3} \tag{81}$$

where $T \equiv T_e$, T_l. The relaxation time of the electron gas, τ_F, gives rise to the jerk term, which is equivalent to the effect of τ_e in Eq. (78). Comparing Eq. (81) with Eq. (51), it results in

$$\alpha = \frac{k_e}{C_e + C_l}, \quad \tau_T = \frac{C_l}{G}, \quad \tau_q = \tau_F + \frac{1}{G}\left(\frac{1}{C_e} + \frac{1}{C_l}\right)^{-1} \tag{82}$$

While the expressions of α and τ_T remain the same as those in the parabolic two-step model, Eq. (75), τ_F (the relaxation time of the electron gas) appears as an added effect in τ_q.

The phonon scattering model and the parabolic two-step model have been described in the framework of the linear dual-phase-lag model containing the τ_T and τ_q effects. The internal energy relaxation model and the hyperbolic two-step model, on the other hand, are captured by an additional effect of τ_q^2. The general type of energy equation containing up to the second order effect of τ_q^2 is shown by Eq. (51), which can be degenerated into the various microscale conduction models as the three model parameters; thermal diffusivity (α), phase lag of the temperature gradient (τ_T), and phase lag of the heat flux vector (τ_q) assume the corresponding expressions summarized in Table 1. Jefferey's heat flux model is included without much elaboration because of the assumed dependence between the two time constants. The ratio of (τ_T/τ_q) is reduced to k_1 in correlation to this model.

Table 1 Correlations between the dual-phase-lag model and other microscale conduction models

DPL	Fourier Diffusion	Thermal Waves	Two-Step (parabolic)	Two-Step (hyperbolic)	Phonon Scattering	Jefferey's Heat Flux	Gurtin-Pipkin
α	α	α	$\frac{k_e}{C_e+C_l}$	$\frac{k_e}{C_e+C_l}$	$\frac{c^2\tau_R}{3}$	α	$\frac{\tau F_q}{\tau_e F_e+C_p}$
τ_T	0	0	$\frac{C_l}{G}$	$\frac{C_l}{G}$	$\frac{9\tau_N}{5}$	$k_1\tau$	τ_e
τ_q	0	τ	$\frac{C_eC_l}{G(C_e+C_l)}$	$\tau_F+\frac{C_eC_l}{G(C_e+C_l)}$	τ_R	τ	$\tau+\frac{\tau_e C_p}{\tau_e F_e+C_p}$

In passing, note that the linear dual-phase-lag model, Eq. (43), has been used to describe the anomalous diffusion in random media [18, 84] as well. The much slower rate of heat transfer at short times, before recovery of Fourier's law at long times, is preserved in the context of thermal lagging. Since the fractal and fracton models used to describe anomalous diffusion in discrete/random media do not have a specific form of the energy equation, their correlations to the dual-phase-lag cannot be included in Table 1. More detailed discussion on this correlation is postponed until the partial expansion technique is introduced in Section 3.2 for a more qualitative comparison.

3.2 Wavefront Expansions

While the effect of τ_T destroys the sharp wavefront introduced by the effect of τ_q in the linear dual-phase-lag model, the effect of τ_q^2 in Eq. (51) brings back thermal waves in heat propagation. This new type of wave, termed *T*-wave, is intrinsically different from the classical *CV*-wave resulting from the effect of τ_q alone. Since additional dimensions in space will only complicate the mathematics without altering the fundamental characteristics, the wave structure can be revealed by the one-dimensional form of Eq. (51):

$$\frac{\partial^2 T}{\partial x^2}+\tau_T\frac{\partial^3 T}{\partial t\partial x^2}=\frac{1}{\alpha}\frac{\partial T}{\partial t}+\left(\frac{\tau_q}{\alpha}\right)\frac{\partial^2 T}{\partial t^2}+\left(\frac{\tau_q^2}{2\alpha}\right)\frac{\partial^3 T}{\partial t^3} \tag{83}$$

Within the simplest mathematical content without any interference from the boundary effect and the initial time rate of change of temperature, Eq. (83) can be solved by the method of Laplace transform subjected to the initial/boundary conditions:

$$T(x,0)=0,\quad \frac{\partial T}{\partial t}(x,0)=0;\quad T(0,t)=T_w,\quad T\to 0\quad \text{as}\quad x\to\infty \tag{84}$$

Since thermal wave speed is a fundamental characteristic dictated by the equation governing the wave phenomenon, the thermal wave speed resulting from Eq. (84) will stay invariant even if different initial and boundary conditions are considered.

The Laplace transform solution to Eqs. (83) and (84) is

$$\overline{T}(x;p) = T_w \frac{\exp\left[-\sqrt{\dfrac{p}{\alpha}\left(\dfrac{1+\tau_q p+\dfrac{(\tau_q p)^2}{2}}{1+\tau_T p}\right)}\, x\right]}{p} \tag{85}$$

The limiting theorem in the Laplace transform supports that

$$\lim_{t\to 0} T(x,t) \sim \lim_{p\to\infty} \overline{T}(x;p) = \lim_{p\to\infty} \left\{ \exp\left[-\sqrt{\frac{p}{\alpha}\left(\frac{1+\tau_q p+\dfrac{(\tau_q p)^2}{2}}{1+\tau_T p}\right)}\, x\right] / p \right\} = \frac{\exp\left[-\left(\sqrt{\dfrac{\tau_q^2}{2\alpha\tau_T}}\right) px\right]}{p} \tag{86}$$

Under a large value of p, therefore, the short-time behavior of temperature is obtained by the Laplace inversion of Eq. (86),

$$\lim_{t\to 0} T(x,t) \sim L^{-1}\left[\exp\left(-\sqrt{\frac{\tau_q^2}{2\alpha\tau_T}}\, p\, x\right) / p\right] \sim H\left(t-\sqrt{\frac{\tau_q^2}{2\alpha\tau_T}}\, x\right) \tag{87}$$

where H represents the unit step function. Equation (87) clearly indicates a singularity at the wavefront, located at

$$x = c_T t, \quad \text{with} \quad c_T = \frac{\sqrt{2\alpha\tau_T}}{\tau_q}, \tag{88}$$

which separates the heat affected zone ($x < c_T t$) from the thermally undisturbed zone ($x > c_T t$). This approach employing the Laplace inversion of the transformed solution at a large value of p is termed partial expansion technique [18], which has been rigorously examined by nearly all the wave phenomena in heat transfer and solid mechanics. Obviously, its uniqueness lies in extracting the wave speed without solving the partial differential equations, which may become very much involved as shown by Eq. (83). As compared to the speed of *CV*-wave shown in Eq. (5), $c_{CV} = \sqrt{(\alpha/\tau_q)}$,

$$\frac{c_T}{c_{CV}} = \sqrt{2\left(\frac{\tau_T}{\tau_q}\right)}. \tag{89}$$

For metals in which $C_l/C_e \sim 10^2$, the ratio of (τ_T/τ_q) is of the order of 10^2 according to Eq. (76). Consequently, from Eq. (89), the speed of *T*-wave is faster than that of *CV*-wave by about one order of magnitude in metals.

Now that two types of thermal waves have been shown to exist in microscale heat conduction, it is worthwhile to revisit the pioneered work by Brorson et al. on electron-phonon heat transport in gold films [49]. For gold at room temperature [85], $C_e = 2.1 \times 10^4$ J/(m^{3}K), $C_l = 2.5 \times 10^6$ J/(m^{3}K), $\alpha = 1.27 \times 10^{-4}$ m/s, the use of $\tau = 40$ fs for the relaxation time of electrons in Eq. (5) gives $c_{CV} = \sqrt{(\alpha/\tau_q)} = 5.6 \times 10^4$ m/s. As compared to the reported value of 10^6 m/s [49], which is close to the Fermi speed, the speed of *CV*-wave (c_{CV}) is slower by nearly 18 times. According to Eq. (76), on the other hand, $(\tau_T/\tau_q) = 1 + (C_l/C_e) \cong 120$ and $c_T = 8.68 \times 10^5$ m/s calculated from the speed ratio given by Eq. (89). As compared to the experimentally determined value of 10^6 m/s, the speed of *T*-wave is close within the threshold of some uncertainties (such as the temperature dependence, effect of impurity, or defective lattices) of the physical properties. The thermal wave behavior observed in Ref. [49], therefore, is more likely attributed to the *T*-wave rather than the classical *CV*-wave. The term "Non-Fourier" used in the field of thermal wave propagation, in addition, may no longer be suitable due to the various types of diffusion and wave behaviors resulting from the effect of τ_T and τ_q of the various orders. All of them are non-Fourier, but such a generic term may imply intrinsically different behaviors in the general framework of thermal lagging.

Figure 7 sketches the responses of *CV*-wave (effect of τ_q, with $\tau_T = 0$ in Eq. (43)), linear DPL (effect of τ_T and τ_q, Eq. (43)), and *T*-wave (DPL including the effect of τ_q^2, Eq. (51)). Generally speaking, as the effect of τ_q, τ_T, and τ_q^2 is gradually taken into account in the lagging response, the *CV*-wave (τ_q-effect) to Fourier diffusion is the *T*-wave (DPL with τ_q^2-effect) to linear DPL (effect of τ_T and τ_q). The *T*-wave propagates faster than the *CV*-wave for $\tau_q < \tau_T$ (as in most metals), and consequently the heat affected zone produced by the *T*-wave is much wider than that produced by the *CV*-wave. Except for the thermally undisturbed zones in the wave phenomena, the temperature level is significantly higher as the higher order terms of τ_T and τ_q are taken into account in the dual-phase-lag model.

Based on the partial expansion technique illustrated in Eqs. (86) to (87), it is worthwhile to revisit the anomalous diffusion in random media that has been described by the linear DPL model shown by Eq. (40) [18, 84]. Instantaneous heating (as $t = 0$) applied at the surface ($x = 0$) of a semi-infinite medium has been modeled by the use of two Dirac-delta functions in Eq. (4) as the energy absorption rate. The surface temperature at $x = 0$, which decays with time in general, was obtained in the Laplace transform domain,

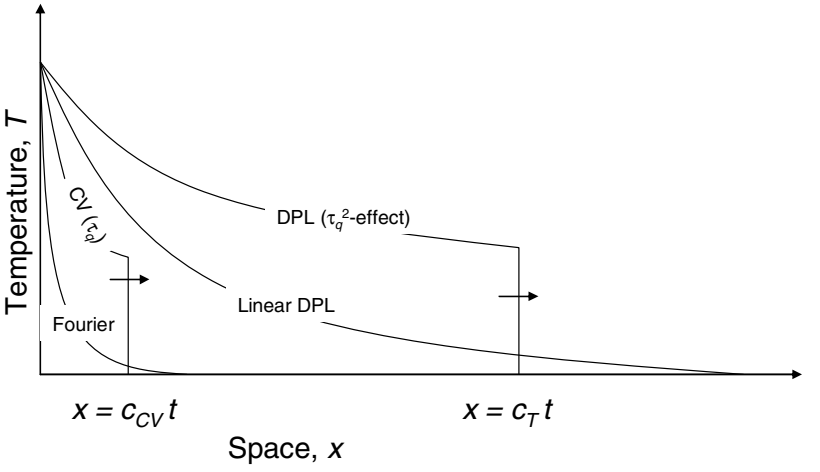

Fig. 7 Effects of τ_q (*CV*-wave), τ_T and τ_q (linear DPL) and τ_q^2 (*T*-wave)

$$\overline{\theta}(0;p) = \left(\frac{Q_0}{2}\right)\sqrt{\frac{1+p}{p(1+Zp)}}, \tag{90}$$

where Q_0 is the nondimensional intensity of surface heating, z is the ratio of τ_T to τ_q as before, $\overline{\theta}(0;p)$ is the Laplace transform of the normalized surface temperature, $\theta(0,t) \equiv (T(0,t)-T_0)/T_0$ with T_0 being the initial temperature of the medium, and p is the Laplace transform variable of the nondimensional time, t/τ_q. Focusing on the short-time behavior, as $t \to 0$, Eqs. (86) and (87) result in

$$\lim_{t\to 0}\theta(0,t) \sim L^{-1}\left[\lim_{p\to\infty}\overline{\theta}(0;p)\right] = L^{-1}\left[\left(\frac{Q_0}{2}\right)\sqrt{\frac{p}{zp^2}}\right] \sim \left(\frac{1}{\sqrt{\pi z}}\right)\frac{1}{\sqrt{t}}, \tag{91}$$

which shows a surface temperature calibrated by z. For the long-time behavior, as $t \to \infty$, similarly, Eqs. (86) and (87) give

$$\lim_{t\to\infty}\theta(0,t) \sim L^{-1}\left[\lim_{p\to 0}\overline{\theta}(0;p)\right] = L^{-1}\left[\left(\frac{Q_0}{2}\right)\sqrt{\frac{1}{p}}\right] \sim \left(\frac{1}{\sqrt{\pi}}\right)\frac{1}{\sqrt{t}} \tag{92}$$

The asymptotic behavior shown by Eq. (92), as $t \to \infty$, is the well-known quasi-stationary behavior of Fourier diffusion, which displays a straight line of a slope being (−1/2) on a logarithmic plot. The asymptotic behavior shown by Eq. (91), as $t \to 0$, on the other hand, displays *the same* $1/\sqrt{t}$-behavior but the surface temperature is inversely proportional to $\sqrt{z}$. Both asymptotic behaviors, a straight line with a slope being (−1/2) as $t \to \infty$ and $t \to 0$, have been observed in the

experiments for ultrafast heating on amorphous media [50, 86]. The Laplace inversion for Eq. (90) can be obtained by the Riemann-sum approximation [18], which is summarized in Fig. 8 at the various values of z. On the logarithmic scales, the short- and long-time responses in terms of a straight line of the same slope, $m = -1/2$, are clearly seen. Anomalous diffusion occurs at intermediate times between the two extremes, where the index m is significantly smaller than one-half, implying a slower rate of heat transfer as compared to Fourier diffusion. The temperature level established at short times (left of the curves) decreases with the value of z, in the manner of $T_{\text{surface}} \sim 1/\sqrt{z}$ as proven explicitly in Eq. (91), while the temperature level approaches that of Fourier diffusion from above at long times. The resulting overshooting of temperature, as marked in Fig. 8 on the logarithmic scale, could be over seventy percent of the temperature predicted by Fourier's law when recovered on the real scale. With all salient features thus captured in the framework of the linear DPL model, Fig. 8 has been used to determine the values of τ_T and τ_q for a number of random/discrete media. They are $\tau_T = 0.45$ μs and $\tau_q = 9$ ns for silica aerogels, $\tau_T = 27$ μs and $\tau_q = 2.5$ μs for rough carbon surfaces, and $\tau_T = 25$ ms and $\tau_q = 7$ ms for weakly bonded copper spheres (of a mean diameter 100 μm). The values of τ_T and τ_q in random media are much larger than those in condensed matters, which is an attractive feature in using this type of "slow" media for the further explorations of the lagging behavior in nonequilibrium heat transport.

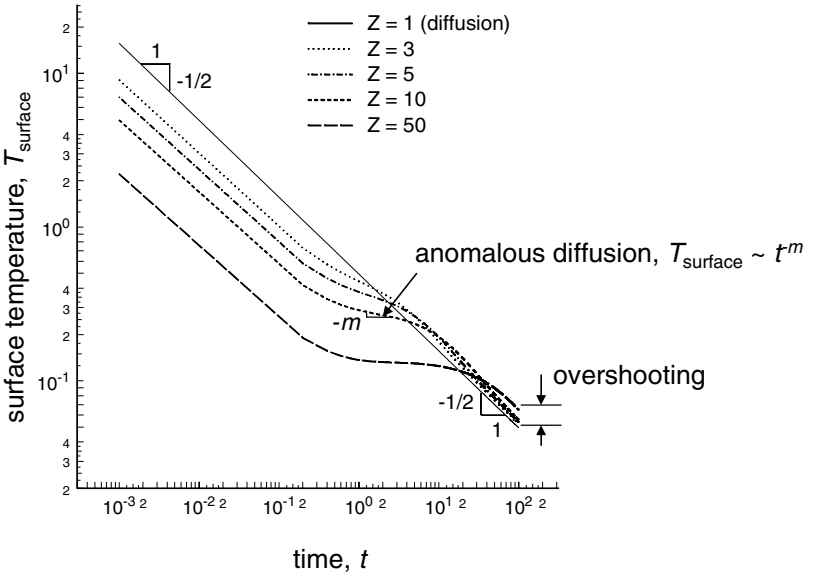

Fig. 8 Correlation of the dual-phase-lag model with anomalous diffusion in random media: Asymptotic behaviors of the surface temperature, $\ln(T_{\text{surface}}) \sim (-1/2)\ln(t)$ as $t \to 0$ and $t \to \infty$, and the slower rate of heat transport during intermediate times ($T_{\text{surface}} \sim t^{-m}$ with $m < 1/2$)

Anomalous diffusion shown in Fig. 8 is governed by a single parameter, $z = \tau_T / \tau_q$, which is not always possible especially for bio-systems where heat generation and/or a finite domain in heat/mass transport are present. The lagging response does depend on the individual values of the two phase lags in general, but the problem that can be characterized by a single ratio between τ_T and τ_q (such as Fig. 8) is valuable in revealing the scaling rule characterizing the lagging response. Anomalous diffusion obtained from the experiment on slow materials, for example an assembly of weakly bounded copper spheres during the *millisecond* transient, could be extended directly to interpret the anomalous behavior in fast materials, such as silicon dioxide in picoseconds, as long as the value of z stays the same. Thermal instrumentation on silicon dioxide for anomalous diffusion may be nontrivial due to the picosecond transient involved, resulting from its correlation length in nanometers. The scaling rule based on a single parameter z, however, facilitates interpretation of the same anomalous diffusion for a wide range of materials based on the simpler instrumentation made on slow materials.

3.3 Temperature and Mixed Formulation

Temperature distributions can be obtained from the temperature formulation shown by Eq. (43) or the mixed formulation that joins Eqs. (40) and (45) together without further combination. The result, however, may be different due to different initial conditions involved. For Eq. (43), the temperature formulation, two initial conditions are needed to make the formulation mathematically well-posed,

$$T(\mathbf{r},0) = T_0(\mathbf{r}), \quad \frac{\partial T}{\partial t}(\mathbf{r},0) = \dot{T}_0(\mathbf{r}) \qquad \text{(Temperature formulation).} \qquad (93)$$

For Eqs. (40) and (45), the mixed formulation, on the other hand, one initial condition for the heat flux vector and another for the temperature will be required:

$$\mathbf{q}(\mathbf{r},0) = \mathbf{q}_0(\mathbf{r}), \quad T(\mathbf{r},0) = T_0(\mathbf{r}) \qquad \text{(Mixed formulation).} \qquad (94)$$

The initial temperature, $T_0(\mathbf{r})$, the initial time-rate of change of temperature, $\dot{T}_0(\mathbf{r})$, and the initial heat flux vector, $\mathbf{q}_0(\mathbf{r})$, are functions of space in general, which can be prescribed independently according to the formulation being used. Generally speaking, due to the complicated relation between the heat flux vector and the temperature gradient as shown in Eq. (8), the temperature formulation is more convenient to use for problems involving temperature-specified boundary conditions. The mixed formulation, on the other hand, is more convenient to use for problems involving heat-flux and/or temperature specified boundary conditions.

Extreme caution has to be exercised as the solutions obtained from the temperature and the mixed formulations are compared. It can be shown that the initial heat flux (the initial condition specified in the mixed formulation) and

the initial time-rate of change of temperature (the initial condition specified in the temperature formulation) must follow Eq. (45) (the energy equation) to assure the same expression obtained for temperature:

$$-\nabla\bullet\mathbf{q}(\mathbf{r},0)+Q(\mathbf{r},0)=C\frac{\partial T}{\partial t}(\mathbf{r},0),\quad \text{or}\quad -\nabla\bullet\mathbf{q}_0(\mathbf{r})+Q_0(\mathbf{r})=C\dot{T}_0(\mathbf{r}) \tag{95}$$

where $Q_0(\mathbf{r}) \equiv Q(\mathbf{r}, 0)$. For a conductor disturbed from a stationary state with a zero initial time-rate of change of temperature assumed in the temperature formulation, $\dot{T}_0(\mathbf{r}) = 0$, for example, a fair comparison with the mixed formulation can only be assured as the initial heat flux vector specified in the mixed formulation satisfies the condition of $\nabla\bullet\mathbf{q}_0(\mathbf{r})=Q_0(\mathbf{r})$. A constant initial heat flux (including zero) can be assumed for problems without the heating term, $Q_0(\mathbf{r}) = 0$. For problems involving initial volumetric heating, alternatively, the initial heat flux specified in the mixed formulation must be checked against the condition $\nabla\bullet\mathbf{q}_0(\mathbf{r})=Q_0(\mathbf{r})$ to avoid any discrepancy between the temperature and the mixed formulations. In the presence of initial heating, $Q_0(\mathbf{r}) \neq 0$, note that the initial conditions shown by Eq. (93) (the temperature formulation) leaves no room for specifying the initial heat flux vector. Consequently, even for conductors disturbed from a stationary state, $\dot{T}_0(\mathbf{r}) = 0$, the initial heat flux ($\mathbf{q}_0(\mathbf{r})$) may be present and significant. Similarly, in the use of mixed formulation shown by Eq. (94), the initial time-rate of change of temperature ($\dot{T}_0(\mathbf{r})$) may be preset and significant even in the absence of the initial heat flux vector ($\mathbf{q}_0(\mathbf{r}) = \mathbf{0}$). For comparisons with the experimental results, therefore, the formulation must be carefully chosen that preserves the most important experimental conditions as reflected in the experimental data.

In addition to the intrinsic effect on bridging the temperature and mixed formulations together, the volumetric heating term in Eq. (46) plays a critical role in interpreting the experimental data [5, 18, 85]. For problems involving a know distribution of heating intensity, such as a modulated heat source with prescribed exciting frequencies [87], the heating intensity can be directly substituted into Eq. (46) for simulation. For ultrafast heating on metals by femtosecond lasers where the heating intensity is not known [5, 18], the admissible form of the heating intensity in Eq. (46) must be determined from the experimental result of the laser-light intensity, called the autocorrelation of the laser pulse [85]:

$$I_s(\tau)=C_0\int_{-\infty}^{\infty} I(t)I(t+\tau)dt \tag{96}$$

where C_0 is a crystal constant and τ is the delayed times between the preceding (for heating) and delayed (for probing) beams. The temporal profile of the light intensity, $I(t)$, cannot be determined experimentally due to the ultrafast transient in the femtosecond domain. By varying the delayed times between the heating and probing beams, on the other hand, the autocorrelation function, $I_s(\tau)$ as defined in Eq. (96),

can be measured experimentally [85]. The admissible form of $I(t)$ must be chosen to preserve the experimentally measured values of $I_s(\tau)$. The Gaussian profile used for simulating the ultrafast absorption (volumetric heating) of the femtosecond pulse in the microscopic two-step model [85], for example, is confirmed by the normalized autocorrelation of the laser pulse before its use in Eq. (46):

$$\frac{I_s(\tau)}{I_s(0)} = \exp\left[-\frac{\psi}{2}\left(\frac{\tau}{t_p}\right)^2\right], \quad \text{based on} \quad I(t) = I_0 \exp\left[-\psi\left(\frac{\tau}{t_p}\right)^2\right] \text{(Gaussian)} \cdot \tag{97}$$

For a pulse duration of t_p = 100 fs, the parameter ψ is fitted to be approximately 2.77 (4 ln(2)) as compared to the experimental result of the normalized autocorrelation of the laser pulse, $I_s(\tau)/I_s(0)$, from –200 fs to 200 fs. The alternative form of the light intensity introduced for facilitating the semi-analytical solution [18],

$$\frac{I_s(\tau)}{I_s(0)} = \left(1 + a\left|\frac{\tau}{t_p}\right|\right)\exp\left[-a\left|\frac{\tau}{t_p}\right|\right] \quad \text{with} \quad a \cong 1.88, \quad \text{based on} \quad I(t) = I_0 \exp\left[-a\left|\frac{\tau}{t_p}\right|\right], \tag{98}$$

as another example, fits the experimental result of the normalized autocorrelation of the laser pulse from –400 fs to 400 fs. With the experimentally verified results of $I_s(\tau)/I_s(0)$, the same temporal profile of $I(t)$ is then used in the volumetric heating term in Eq. (46),

$$Q(x,t) = 0.94J\left(\frac{1-R}{t_p\delta}\right)\exp\left(-\frac{x}{\delta}\right)I(t) \tag{99}$$

with J being the laser fluence, R the reflectivity of the heated surface (0.93 for visible light), δ the optical depth of penetration (15.3 nm for gold), and $I(t)$ inherited from either Eq. (97) or Eq. (98). A suitable form for the laser light intensity, $I(t)$ in Eq. (99), therefore, cannot be determined by a simplt fit of the Gaussian profile in the duration of the laser pulse. Instead, the presumed profile for $I(t)$ must be substituted into the integral shown by Eq. (96) for obtaining the autocorrelation $I_s(\tau)$, and the resulting normalized autocorrelation of the laser pulse, $I_s(\tau)/I_s(0)$, must match the experimental result in the full domain of time [18, 85]. There are articles in which the heating intensity is determined from fitting the sinusoidal fuinctions to the Gaussian profile without examining the autocorrelation. Since sinusoidal functions are not even integrable in the time domain of $t \in [-\infty, \infty]$, any form of $I(t)$ involving sinusoidal functions must be exercised with extreme caution, no matter how close it is to the Gaussian profile in the targeted domain of time.

3.4 Multiple Energy Carriers

Effects of τ_T, τ_q, and τ_q^2 have been accommodated in the framework of thermal lagging to capture the various mechanisms described in the various microscale

conduction models. As more high order terms in τ_T and τ_q are gradually included in the Taylor series expansion, a most important task is to identify the physical mechanisms in correspondence with such high order terms. The τ_T^2-term included in Eq. (52) is an example. This term was included in Eq. (52) purely on the basis of mathematical extension, continuing the previous attempts of including the τ_q^2-effect in bridging the DPL model with the hyperbolic two-step model and the internal energy relaxation model. The physics in correspondence with the τ_T^2-effect remains unclear.

To assess a possible cause for the τ_T^2-effect in thermal lagging, a system containing *three* energy carriers was formulated in a way similar to the phonon-electron interaction model [88]:

$$\begin{aligned} C_1\frac{\partial T_1}{\partial t} &= k_1\nabla^2 T_1 - G_{12}\left(T_1 - T_2\right) - G_{13}\left(T_1 - T_3\right);\\ C_2\frac{\partial T_2}{\partial t} &= k_2\nabla^2 T_2 + G_{12}\left(T_1 - T_2\right) - G_{23}\left(T_2 - T_3\right);\\ C_3\frac{\partial T_3}{\partial t} &= k_3\nabla^2 T_3 + G_{13}\left(T_1 - T_3\right) + G_{23}\left(T_2 - T_3\right). \end{aligned} \tag{100}$$

where, for $i, j = 1, 2$, and 3, T_i, C_i, and k_i are temperature, volumetric heat capacity, and thermal conductivity of the i^{th} carrier, respectively, and G_{ij} represent the energy coupling factor between the i^{th} and the j^{th} carriers, as sketched in Fig. 9(a). Equation (100), and its correspondence in general for N carriers as shown in Fig. 9(b), is an important step toward applications of the DPL model to interfacial/bioheat transfer where multiple energy carriers exist in more complicated settings. For heat transport across the interfacial region between dissimilar materials, for example, the two materials in contact and the interstitial air serve as the three energy carriers. For femtosecond laser processing on tooth, on the other hand, collagen, hydroxyapatite, and water could all be energy carriers that exchange heat during the ultrafast transient. To illustrate the τ_T^2-effect in the simplest content of mathematics, once again, effects of conduction in carriers 2 and 3 are neglected, $k_2 = 0$ and $k_3 = 0$, which correspond to the energy carriers with a small physical domain (like the lattices in thin metal films). Equation (100), in correspondence with the operator form shown by Eq. (73), is

$$\begin{bmatrix} C_1\dfrac{\partial}{\partial t} - k_1\nabla^2 + G_{12} + G_{13} & -G_{12} & -G_{13} \\ -G_{12} & C_2\dfrac{\partial}{\partial t} + G_{12} + G_{23} & -G_{23} \\ -G_{13} & -G_{23} & C_3\dfrac{\partial}{\partial t} + G_{13} + G_{23} \end{bmatrix} \begin{bmatrix} T_1 \\ T_2 \\ T_3 \end{bmatrix} = 0, \tag{101}$$

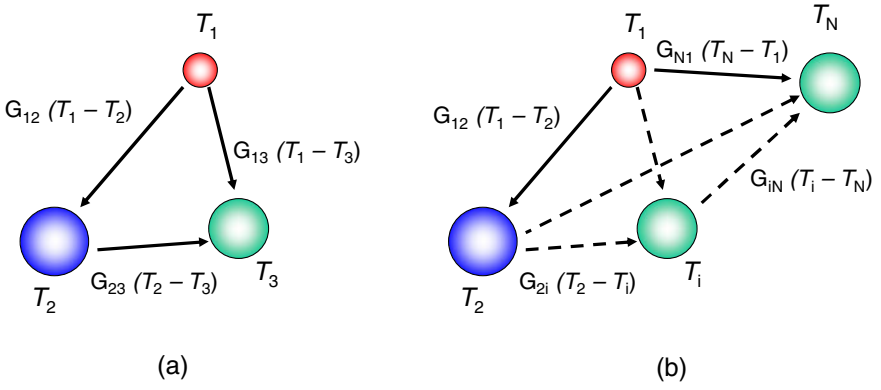

Fig. 9 Thermal energy exchange among N carriers

which can be expanded to give

$$\nabla^2 T_1 + D_{21}\frac{\partial}{\partial t}\left(\nabla^2 T_1\right) + D_{22}\frac{\partial^2}{\partial t^2}\left(\nabla^2 T_1\right) = D_1\frac{\partial T_1}{\partial t} + D_2\frac{\partial^2 T_1}{\partial t^2} + D_3\frac{\partial^3 T_1}{\partial t^3}, \quad \text{with}$$

$$\begin{aligned} D_{21} &= \frac{C_2\left(G_{13}+G_{23}\right)+C_3\left(G_{12}+G_{23}\right)}{G_{13}G_{23}+G_{12}G_{13}+G_{12}G_{23}}, \quad D_{22} = \frac{C_2C_3}{G_{13}G_{23}+G_{12}G_{13}+G_{12}G_{23}}, \\ D_1 &= \frac{C_1+C_2+C_3}{k_1}, \quad D_2 = \frac{C_1C_2\left(G_{13}+G_{23}\right)+C_1C_3\left(G_{12}+G_{23}\right)+C_2C_3\left(G_{12}+G_{13}\right)}{k_1\left(G_{13}G_{23}+G_{12}G_{13}+G_{12}G_{23}\right)}, \\ D_3 &= \frac{C_1C_2C_3}{k_1\left(G_{13}G_{23}+G_{12}G_{13}+G_{12}G_{23}\right)} \end{aligned} \tag{102}$$

The corresponding equations for T_2 and T_3 are of the same form, except for the different coefficients of Ds' as a result of setting $k_1 = 0$ and $k_3 = 0$ for T_2 and $k_1 = 0$ and $k_2 = 0$ for T_3. An additional mixed-derivative term, $D_{22}[\partial^2(\nabla^2 T_1)/\partial t^2]$, exists in Eq. (102), which corresponds to the τ_T^2-effect described in Eq. (52). Effect of τ_T^2, therefore, results from the energy exchange with the additional carrier in a three-carrier system described in Fig. 9(a). Comparing Eqs. (102) and (52), from the coefficients of D_{21}, D_1, and D_2, it results in

$$\begin{aligned} \alpha &= \frac{k_1}{C_1+C_2+C_3}, \quad \tau_T = \frac{C_2\left(G_{13}+G_{23}\right)+C_3\left(G_{12}+G_{23}\right)}{G_{13}G_{23}+G_{12}G_{13}+G_{12}G_{23}} \sim \left[\frac{CG}{G^2}\right] \sim O\left[\frac{C}{G}\right] \\ \tau_q &= \frac{C_1C_2\left(G_{13}+G_{23}\right)+C_1C_3\left(G_{12}+G_{23}\right)+C_2C_3\left(G_{12}+G_{13}\right)}{\left(C_1+C_2+C_3\right)\left(G_{13}G_{23}+G_{12}G_{13}+G_{12}G_{23}\right)} \sim \left[\frac{C^2G}{CG^2}\right] \sim O\left[\frac{C}{G}\right] \end{aligned} \tag{103}$$

Estimated on the order of magnitudes, it can be readily seen that τ_T and τ_q are of the order of (C/G). The coefficients of τ_T^2 and τ_q^2, from the coefficients of D_{22} and D_3 in Eq. (102), result in

$$\tau_T^2 = \frac{2C_2C_3}{G_{13}G_{23}+G_{12}G_{13}+G_{12}G_{23}} \sim \left[\frac{C^2}{G^2}\right] \sim O\left(\frac{C}{G}\right)^2$$
$$\tau_q^2 = \frac{2C_1C_2C_3}{\left(C_1+C_2+C_3\right)\left(G_{13}G_{23}+G_{12}G_{13}+G_{12}G_{23}\right)} \sim \left[\frac{C^3}{CG^2}\right] \sim O\left(\frac{C}{G}\right)^2, \tag{104}$$

which indicates that τ_T^2 and τ_q^2 are indeed of the order of $(C/G)^2$. With τ_T and τ_q of the order of (C/G) shown in Eq. (103), in other words, the mixed-derivative term, $D_{22}[\partial^2(\nabla^2 T_1)/\partial t^2]$, and the jerk term, $D_3(\partial^3 T_1/\partial t^3)$, are indeed their second-order effects.

In terms of the number of energy carriers, the high order effects of τ_T and τ_q can thus be concluded by examining Eqs. (43) and (52) with their correlations in Eqs. (74) and (102). Equation (43) containing the *linear* effect of τ_T and τ_q describes the energy exchange between *two* energy carriers, electrons and phonons. With reference to Eq. (74), the electrons correspond to carrier 1 and the phonons correspond to carrier 2. Equation (43) containing the *second-order* effect of τ_T and τ_q, with reference to Eq. (102), on the other hand, describes the energy exchange between *three* energy carriers. Should more energy carriers be present in the transport process, by the method of deduction, it is conceivable that a system containing N carriers will give rise to the lagging response of the order of $\tau_T^{(N-1)}$ and $\tau_q^{(N-1)}$. For the phonon-electron interaction model involving two carriers, $N = 2$, the lagging response is thus of the order of τ_T and τ_q, as shown in Eqs. (43) and (74). For the system involving three carriers, $N = 3$, the lagging response is of the order of τ_T^2 and τ_q^2, which is shown in Eqs. (52) and (102). As the number of energy carriers increases, the energy equation employing the DPL model will include more high-order terms in τ_T and τ_q, but the lagging response remains to be governed by two phase lags, τ_T and τ_q. Effects of conduction in carriers, when reinstated, will raise the order of Laplacian (∇^2) to biharmonic (∇^4) and higher, which are spatial effects that do not affect the fundamental characteristics of thermal lagging, in time [18].

The energy equation can be generalized to describe energy coupling in a system containing N carriers, as sketched in Fig. 9(b). Equation (100) involving energy coupling among N carriers becomes

$$C_1\frac{\partial T_1}{\partial t} = k_1\nabla^2 T_1 - \sum_{i=2}^{N} G_{1i}\left(T_1 - T_i\right);$$
$$C_m\frac{\partial T_m}{\partial t} = k_m\nabla^2 T_m + \sum_{j=1}^{m-1} G_{jm}\left(T_j - T_m\right) - \sum_{i=m+1}^{N} G_{mi}\left(T_m - T_i\right), \quad m = 2,3,...,(N-1); \tag{105}$$
$$C_N\frac{\partial T_N}{\partial t} = k_N\nabla^2 T_N + \sum_{i=1}^{N-1} G_{iN}\left(T_i - T_N\right).$$

This form will require the Taylor series expansion of Eq. (39) up to the terms of $\tau_T^{(N-1)}$ and $\tau_q^{(N-1)}$, but a general form of the energy equation corresponding to Eq. (102) will be difficult to obtain due to the high-order determinant to be expanded.

For the case of $N = 4$, to describes how fast such high-order terms could evolve, the energy equation containing the third-order effect of τ_T and τ_q is

$$\mathbf{q}(\mathbf{r},t)+\tau_q\frac{\partial\mathbf{q}}{\partial t}(\mathbf{r},t)+\frac{\tau_q^2}{2}\frac{\partial^2\mathbf{q}}{\partial t^2}(\mathbf{r},t)+\frac{\tau_q^3}{6}\frac{\partial^3\mathbf{q}}{\partial t^3}(\mathbf{r},t)\cong$$
$$-k\left[\nabla T(\mathbf{r},t)+\tau_T\frac{\partial}{\partial t}\nabla T(\mathbf{r},t)+\left(\frac{\tau_T^2}{2}\right)\frac{\partial^2}{\partial t^2}\nabla T(\mathbf{r},t)+\left(\frac{\tau_T^3}{6}\right)\frac{\partial^3}{\partial t^3}\nabla T(\mathbf{r},t)\right], \tag{106}$$

$$\nabla^2 T+\tau_T\frac{\partial}{\partial t}\left(\nabla^2 T\right)+\left(\frac{\tau_T^2}{2}\right)\frac{\partial^2}{\partial t^2}\left(\nabla^2 T\right)+\left(\frac{\tau_T^3}{6}\right)\frac{\partial^3}{\partial t^3}\left(\nabla^2 T\right)=$$
$$\frac{1}{\alpha}\frac{\partial T}{\partial t}+\left(\frac{\tau_q}{\alpha}\right)\frac{\partial^2 T}{\partial t^2}+\left(\frac{\tau_q^2}{2\alpha}\right)\frac{\partial^3 T}{\partial t^3}+\left(\frac{\tau_q^3}{6\alpha}\right)\frac{\partial^4 T}{\partial t^4}.$$

While the mixed-derivative terms continue to raise their order of derivatives with respect to time, the snap term, $\partial^4 T/\partial t^4$ from the τ_q^3-effect, now follows the jerk term (from the τ_q^2-effect) and appear in the energy equation. Continuing on, for systems involving five or six energy carriers that are not many in view of the complicated microstructures of human tissues, the crackle ($\partial^5 T/\partial t^5$) and pop ($\partial^6 T/\partial t^6$) terms will enter the scene and the resulting energy equation describing the lagging response will soon evolve into the most complicated we have ever seen.

The mixed-derivative terms containing high-order derivatives of $\nabla^2 T$ with respect to time is a special feature in Eqs. (52) or Eq. (102). The number of carriers is a possible source for such terms describing the lagging behavior in τ_T, but it by no means the only source for such unusual terms to appear in the energy equation. The conductive temperature (ψ) and the thermodynamic temperature (T) in the two-temperature model [89-91], which is shown admissible in the framework of the second law of thermodynamics, gives the same form of the energy equation while preserving the linear effect of τ_q as that in the *CV*-wave model. The two-temperature model employs Eq. (3) for the conductive temperature, ψ,

$$\mathbf{q}(\mathbf{r},t)+\tau\frac{\partial\mathbf{q}}{\partial t}(\mathbf{r},t)=-k\nabla\psi(\mathbf{r},t)\,, \tag{107}$$

while Eq. (4) stays the same for describing the thermodynamic temperature, T, without a heat source.[1] Equations (4) and (107) are to be solved for three unknowns; T, ψ, and $\mathbf{q}$, supplemented by the relation between ψ and T:

[1] The results shown in Eqs. (109) and (110) are valid in the absence of volumetric heating. In the presence of volumetric heating, Eq. (45) should be used in place of Eq. (4), which will introduce both heating and apparent heating terms in Eqs. (109) and (110). Consequently, the conductive and thermodynamic temperatures will differ by a volumetric heat source term even in steady state.

$$\psi(\mathbf{r},t) - T(\mathbf{r},t) = l^2 \nabla^2 \psi(\mathbf{r},t) \tag{108}$$

where l^2 is the square of a length parameter (l) describing the discrepancy between T and ψ.[2] Its role is parallel to the length parameter in Eq. (17) describing phonon scattering. In the case of $l = 0$, the conductive temperature reduces to the thermodynamic temperature and Eqs. (4) and (107) are reduced to the *CV*-wave model. In the general case with $l \neq 0$, Eqs. (4) and (107) can be first combined by eliminating **q** to give

$$\frac{1}{\alpha}\frac{\partial T}{\partial t} + \frac{\tau}{\alpha}\frac{\partial^2 T}{\partial t^2} = \nabla^2 \psi \quad \text{with} \quad \alpha \equiv \frac{k}{C}. \tag{109}$$

In steady state where the thermodynamic temperature is no longer a function of time, the left-hand side of Eq. (109) vanishes and the condition $\nabla^2 \psi = 0$ prevails. According to Eq. (108), the conductive temperature and thermodynamic temperature collapses onto each other in steady state, showing that the difference between two temperatures only exists during the transient process. Substituting the expression of T from Eq. (108) into Eq. (109), it gives an energy equation containing the conductive temperature alone,

$$\nabla^2 \psi + \overbrace{\left(\frac{l^2}{\alpha}\right)}^{\tau_T} \frac{\partial}{\partial t}\left(\nabla^2 \psi\right) + \overbrace{\left(\frac{l^2 \tau}{\alpha}\right)}^{\tau_T \tau_q = \frac{\tau_T^2}{z}} \frac{\partial^2}{\partial t^2}\left(\nabla^2 \psi\right) = \frac{1}{\alpha}\frac{\partial \psi}{\partial t} + \overbrace{\left(\frac{\tau}{\alpha}\right)}^{\tau_q} \frac{\partial^2 \psi}{\partial t^2}. \tag{110}$$

Comparing Eq. (110) with (52), clearly, $\tau_T = l^2/\alpha$, $\tau_q = \tau$, and $\tau_T \tau_q = \tau_T^2/z$, with $z = \tau_T/\tau_q$. In correlation with the two-temperature model, the finite time required to the energy carrier travelling through the correlation length (l) results in the phase lag of the temperature gradient, τ_T, where as the coefficient ($a\tau/\alpha$) is the product between τ_T and τ_q, which is indeed in τ_T^2 scaled by z. Equation (110) is thus of the same form as Eq. (52) without incorporating the τ_q^2 term in the Taylor series expansion. In passing, note that the conductive and thermodynamic temperatures

[2] Once again, the physical essence of Eq. (108) can be revealed by heat conduction in a one-dimensional fin, with $\nabla^2 \equiv \partial^2/\partial x^2$: $\frac{d^2T}{dx^2} - \left(\frac{hP}{kA_c}\right)(T - T_\infty) = 0$, or $\frac{d^2T}{dx^2} - \left(\frac{hP}{kA_c}\right)T = -\left(\frac{hP}{kA_c}\right)T_\infty$, where P and A_c are the perimeter and cross section of the fin, respectively, and h is the heat transfer coefficient. With (hP/kA_c) equivalent to $1/l^2$, clearly, the temperature of the fin (T) is equivalent to the conductive temperature (ψ) and the ambient temperature (T_∞) is equivalent to the thermodynamic temperature (T). Equation (108) thus describes the nonlocal response between the fin and the ambient as the energy exchange between them continues.

defined in the two-temperature model are similar to the dynamic and nonequilibrium temperatures defined in the gradient extension method.

3.5 Wave-Diffusion Duality

Whether heat propagation is driven by diffusion or wave has long been an obsession, which may have become even more exaggerated in view of different versions of diffusion (Fourier and linear DPL) and wave (*CV*- and *T*-wave) behaviors generated from the high order terms of τ_T and τ_q during the lagging response. Should the effects of τ_T^2 (which has already been absorbed in Eq. (52)), τ_q^3, τ_T^3, τ_q^4 and so forth be continuously accommodated in the DPL model, diffusion and wave will continue to alternate in the history of heat propagation. It is thus critical to establish a criterion that governs the alternations between diffusion and wave during the ultrafast transient.

A criterion based on the time-rate of change of temperature has already been established for the dominance of *CV*-waves over Fourier diffusion [33, 40]. Such a criterion, however, is implicit by nature because the temperature, and hence the time-rate of change of temperature, is the response of the thermal system that may not be known beforehand. A more explicit approach may be on the evaluation of the response time, with Fourier diffusion serving as the basis for the transient response. Equation (5) for the *CV*-wave is first revisited to illustrate the fundamental principles in weighing the relative contributions from the diffusion and wave behaviors in time. Under constant thermophysical properties, the coefficients can be moved into the derivatives with respect to time, which is an exercise already performed in Eq. (6) when weighing the relative importance of the heat flux vector and its time rate of change. In view of finite differencing, derivatives involve temperature differences in the numerators, which are all on the same orders of magnitude. The equation of Fourier diffusion,

$$\nabla^2 T = \frac{1}{\alpha}\frac{\partial T}{\partial t} \quad \sim \quad \frac{\partial^2 T}{\partial x^2} = \frac{\partial T}{\partial(\alpha t)} \quad \Rightarrow \quad t \sim \frac{x^2}{\alpha}, \tag{111}$$

therefore, implies equal contributions from the steady-state term ($\partial^2 T/\partial x^2$, effect of conduction) and the diffusion term ($\partial T/\partial(\alpha t)$) as their denominators are comparable in the physical domain where $x^2 \sim \alpha t$. For conductors with a characteristic dimension L, such as the thickness of a thin film, that means the transient effect of Fourier diffusion becomes as important as the conduction (steady-state) effect as $x^2 \sim \alpha t$ or $t \sim L^2/\alpha$. The first time scale on the regime map, as shown in Fig. 10 from right, is thus (L^2/α), which is also the characteristic time for Fourier diffusion. For the process time in the domain of $t >> (L^2/\alpha)$, the denominator of the diffusion term in Eq. (111) is much greater than that of the conduction term and Eq. (111) becomes the Laplace equation governing heat conduction in steady state. As effect of τ_q comes into play, along the same line, Eq. (5) can be rewritten as

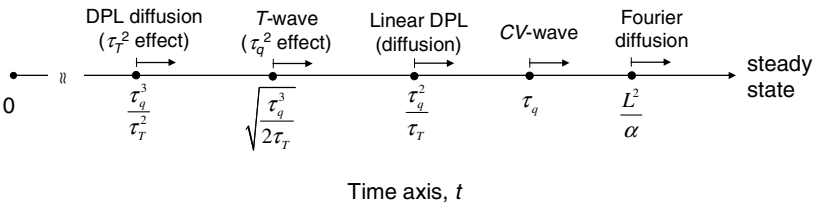

Fig. 10 Regime map for the alternation between diffusion and wave behaviors in heat propagation

$$\nabla^2 T = \frac{1}{\alpha}\frac{\partial T}{\partial t} + \frac{1}{c^2}\frac{\partial^2 T}{\partial t^2} = \frac{\partial T}{\partial(\alpha t)} + \frac{\partial^2 T}{\partial(ct)^2}, \quad c = \sqrt{\frac{\alpha}{\tau_q}} \tag{112}$$

Comparing the denominators, (αt) and $(ct)^2$, the *CV*-wave behavior becomes as important as

Fourier diffusion as

$$(ct)^2 \sim \alpha t \quad \text{or} \quad t \sim \tau_q . \tag{113}$$

On the regime map shown in Fig. 10, therefore, the relaxation time, τ_q, appears as the next time scale. Continuing on, shortening time further from Eq. (43) including the effect of τ_T to Eq. (51) including the additional effect of τ_q^2, two more time scales, (τ_q^2/τ_T) and $\sqrt{(\tau_q^3/(2\tau_T))}$, are resulted from weighing the successive terms and are placed on the time axis. More time scales can be generated in the same manner and incorporated on the regime map, including the last scale (τ_q^3/τ_T^2) resulting from Eq. (52) containing the τ_T^2 effect from systems with three energy carriers. As time starts from zero (left of the axis) and gradually increases, wave and diffusion will start to alternate in the time series. Whether heat behaves like diffusion or wave in the transport process depends on the time scale in which physical observations are made. This is the essence of the wave-diffusion *duality* for heat propagation in microscale [92, 93]. As compared to the previous criterion employing the time-rate of change of temperature, the criterion based on the response time shown in Fig. 10 is explicit because all time scales involved are functions of the two phase lags, which are treated as material constants characterizing the ultrafast transient in view of thermal lagging. The criterion based on the process time is necessary but may not be as sufficient as the implicit criterion based on the time-rate of change of temperature. Particularly for materials with closer time scales on the time axis, the wave behavior can still be active in the neighborhood of a time scale for diffusion if an excessive temperature is established thereby. This is a situation to be noticed for material processing employing high-power heat sources such as femtosecond lasers in tera- to petawatts.

Like other thermophysical properties, such as thermal conductivity, the phase lags can vary sensitively with temperature during thermal lagging. The energy equation will become highly nonlinear as the effect of temperature dependency is taken into account, making it more convenient to solve the DPL constitutive equation in direct coupling with the energy equation without combining them together. Numerical methods have contributed significantly in providing finer resolutions for the lagging response, but new finite difference schemes have continuously arisen to solve the DPL heat equations in multi-dimensions under the various conditions [94-105]. The basic Neumann stability analysis, for example, has been reformed to account for the tangling behaviors of the two phase lags [94, 95] in a consistent discretization scheme. Based on the fundamental understandings developed under constant thermophysical properties, these numerical methods are well ready to carry out more sophisticated but more realistic simulations for the lagging response.

4 Interdiffusion of Mass

Extension of the DPL model to nonequilibrium mass transport is intuitive in view of the analogy between Fourier's laws in heat conduction and Fick's law in mass transport. Particular emphases have been placed on the growth of ultrathin films [106] and intermetallic compound layers in metal based composites and solder joints [107, 108]. This branch of extension is particularly meaningful due to the existence of a vast amount of experimental data in the open literature, including not only different types of materials but also the film/layer growth data under different processing conditions. As compared to the time scales in heat transport, film growth is a much slower process that could occur in hours to days. The significantly larger values of the phase lags characterizing the growing process, however, make such prolonged times "ultrafast" due to the active and pronounced lagging behavior that occurs in the same domain of time. Growths of films and intermetallic compounds both involve interdiffusion for one substance into another and chemical reactions between them to form the third substance near their interface. Rapid thermal oxidation of silicon [109], as sketched in Fig. 11, is an example. Material A in this example is oxygen, which diffuses into the silicon lattices, material B, heated to 950-1150°C. Silicon dioxide is formed in the interfacial layer, which grows with time, resulting from the chemical reaction of $Si + O_2 \rightarrow SiO_2$ after interdiffusion. During the formation of intermetallic compound, as another example, material A may be Bismuth-Tin (Bi-Sn) solder and material B may be copper [110], and the interfacial layer is a result of interdiffusion and chemical reactions between the Bi-Sn solder and copper. The interface is zigzagging by nature, due to the interdiffusion and chemical reactions that are difficult to maintain uniform as they occur. This is particularly the case during the early-time growth when the thickness of the interfacial layer is only a few tens nanometers, which is comparable to the roughness and waviness of the interface. The thickness of the oxidation layer or the intermetallic compound, therefore, is more appropriately viewed as the topological means as illustrated in Fig. 11. The

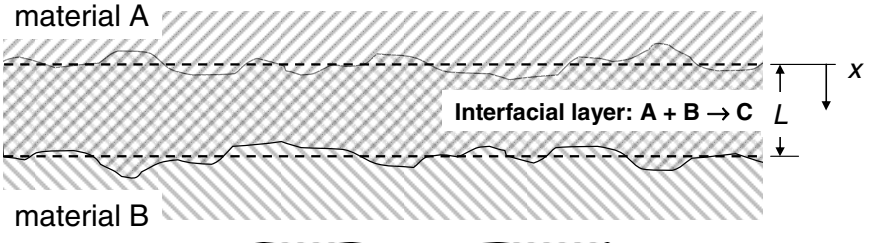

Fig. 11 Growth of an interfacial layer between dissimilar materials

interfacial layer grows with time, $L \equiv L(t)$, which is measured from the original interface between materials A and B before the interdiffusion and chemical reactions take place.

4.1 Film Growth

The linear-parabolic model [111] has long been used for predicting the thickness of silicon-dioxide (SiO_2) film during the rapid thermal oxidation:

$$L^2 + AL = B(t + C) \tag{114}$$

where L is the thickness of the SiO_2 film at time t, with A, B, and C being the material constants depending on the reaction rates (A and A/B) and the delay time (C) due to the preexisting oxides in the silicon wafer before the oxidation process. During the first 30 nm of the thermal oxidation of silicon in dry oxygen (O_2), however, Eq. (114) was found to significantly underestimate the thickness of the SiO_2 film [112, 113]. A further examination of the experimental data for the measured film thickness versus time (less than 30 nm) on a logarithmic scale, like those done in Fig. 8, shows that the growth rate of the SiO_2 film is significantly less than that predicted by Fick's law at short times [106]. The growth rate of Fickean diffusion is recovered as the process time lengthens, which is exactly the same behavior of anomalous diffusion described in Fig. 8 [18, 84]. Because of the shortcomings of Eq. (114) in predicting the growth of ultrathin films, in the range of a few tens nanometers, various attempts have been made to accommodate additional mechanisms into the phenomenological model, including effects of stress, strain, space charge/electric fields, oxide microstructures, silicon surface and substrate, and parallel oxidations [114, 115].

Rather than a phonological model shown in Eq. (114), even thought it is palatable to use, the linear DPL model has been extended to describe the film growth of SiO_2, in the full range from nanometers and above [106]. Parallel to Eqs. (4) and (40), with one-dimensional film growth in the x-direction as shown in Fig. 11, the equation describing the conservation of mass and the DPL equation describing the oxygen diffusion into the silicon lattices are

$$-\frac{\partial j}{\partial x}=\frac{\partial \rho}{\partial t},\quad j+\tau_j\frac{\partial j}{\partial t}=-D\left(\frac{\partial \rho}{\partial x}+\tau_\rho\frac{\partial^2\rho}{\partial t\partial x}\right) \tag{115}$$

where ρ is the mass density, j is the relative mass flux, and D is the diffusivity between oxygen and silicon. The two phase lags, τ_j and τ_ρ in equivalence to τ_T and τ_q in heat transport, measure the finite time required for the interfacial chemical reactions to take place in forming the oxides (τ_j) and the finite time required for the efficient diffusion of the atomic oxygen into the silicon lattices (τ_ρ). In terms of τ_ρ and τ_j, involvement of all possible parallel oxidations, different surface and substrate conditions, and the various mechanical/electrical effects are lumped onto the resulting delayed response in time. As the silicon lattices are strained during the thermal oxidation, for example, it would take more time for the oxygen to diffuse through effectively and the resulting value of τ_ρ would be larger than the normal value. In the presence of parallel oxidation at the Si/SiO_2 interface and of the silicon fragments that control the initial oxidation rate [116], as another example, the resulting value of τ_j would be smaller as compared to that involving one chemical reaction alone. Inheriting the phase lag concept in heat transport, therefore, τ_ρ and τ_j describe the finite times required for the completion of all microstructural processes involved, which reflect the microscale effect in space in terms of their greater (smaller) values for more (less) complicated processes. Eliminating the mass flux j from Eq. (115), parallel to Eq. (43) with $\nabla^2 \to \partial^2/\partial x^2$ to simulate the one-dimensional process, the mass conservation equation containing density along is

$$\nabla^2\rho+\tau_\rho\frac{\partial^3\rho}{\partial t\partial x^2}=\frac{1}{D}\frac{\partial \rho}{\partial t}+\left(\frac{\tau_j}{D}\right)\frac{\partial^2\rho}{\partial t^2}. \tag{116}$$

Designating material A as oxygen and material B as silicon, according to the coordinate system described in Fig. 11, the growth kinetics is described by

$$\frac{d\left(\rho_0 L\right)}{\partial t}=-D\frac{\partial \rho}{\partial x}\quad \text{at}\quad x=0;\quad \rho=\rho_s\quad \text{at}\quad x=L \tag{117}$$

where ρ_0 and ρ_s are the density of oxygen and silicon, respectively. The first condition in Eq. (117) is the surface recession rate that balances the mass flux of oxygen at the surface ($x = 0$) with the internal diffusion of oxygen (through the silicon lattices) right next to the surface. Along with the initial and boundary conditions,

$$\rho=0,\quad \frac{\partial \rho}{\partial t}=0\quad \text{as}\quad t=0;\quad \rho=\rho_s\quad \text{at}\quad x=L,\quad \rho\to 0\quad \text{as}\quad x\to\infty, \tag{118}$$

Eqs. (116) to (118) have been solved by the method of Laplace transform [106]. The growth rate of the SiO_2 layer was obtained as

$$\overline{l}(p)=\frac{\sqrt{\dfrac{p(1+p)}{1+zp}}}{p^2} \quad \text{with} \quad z=\frac{\tau_\rho}{\tau_j}, \tag{119}$$

where $\overline{l}$ is the Laplace transform of the nondimensional thickness, $L/[(\rho_s/\rho_0)\sqrt{(D\tau_j)}]$ and p is the Laplace transform parameter in correspondence with the nondimensional time, (t/τ_j).

It is remarkable to note that Eq. (119) gives rise to the same asymptotic behaviors as Eq. (90), except for the replacement of $1/\sqrt{t}$ (for the surface-temperature decay with time) by $\sqrt{t}$ (for the film growth with time). To prove this analogy, the partial expansion technique in Eqs. (91) and (92) is applied to yield

$$\lim_{t\to 0}\left[l(t)\right]\sim L^{-1}\left[\lim_{p\to\infty}\overline{l}(p)\right]=L^{-1}\left[\frac{1}{p^2}\sqrt{\frac{p}{z}}\right]=\left(\frac{2}{\sqrt{\pi z}}\right)\sqrt{\frac{t}{\tau_j}};$$

$$\lim_{t\to\infty}\left[l(t)\right]\sim L^{-1}\left[\lim_{p\to 0}\overline{l}(p)\right]=L^{-1}\left[\frac{1}{p^2}\sqrt{p}\right]\sim\left(\frac{2}{\sqrt{\pi}}\right)\sqrt{\frac{t}{\tau_j}} \tag{120}$$

The film thickness increases with $\sqrt{t}$ at both ends, as $t \to 0$ and $t \to \infty$ (Fick's law). Anomalous diffusion shown in Fig. 8 on the logarithmic scale, including the much slower film-growth rate during the intermediate times, therefore, remains the same except for the reversal of the response curves for the film thickness increasing with time. The Deal-Grove model shown by Eq. (114) does not have the same behavior as $t \to 0$. This is also the regime where the Deal-Grove model significantly underestimates the thickness of the SiO_2 film during the first 30 nm. Solving Eq. (114) for the film thickness (L) and applying the Taylor series expansion with respect to time (t), it results in

$$L=\frac{-A+\sqrt{A^2+4B(t+C)}}{2} \quad \Rightarrow \quad \lim_{t\to 0}L=\left(\frac{-A+\sqrt{A^2+4BC}}{2}\right)+\left(\frac{B}{\sqrt{A^2+4BC}}\right)t+\ldots \tag{121}$$

As $t \to 0$, Eq. (121) gives a constant, which implies *no* film growth in small times. In the limiting case that $(B/A) << 1$ and/or $(C/A) << 1$, the constant term in Eq. (121) is vanishingly small and the resulting film thickness increases *linearly* with time. As compared to the parabolic, $\sqrt{t}$-behavior as shown in Eq. (120) obtained from the DPL model, evidently, the linear growth with time resulting from the Deal-Grove model would significantly underestimate the film thickness during the initial stage of thermal oxidation of silicon.

The linear DPL model is by far the most superior as compared to other models in interpreting the experimental data on the film growth [106]. The values of τ_ρ and τ_j determined from the inverse method based on the linear DPL model and the

Table 2 The values of τ_j and τ_ρ modeling the rapid thermal oxidations

Oxidation Conditions	τ_j Hours	τ_ρ Hours
SiO_2 at 800°C and 2.03 MPa	0.1	2.8
SiO_2 at 900°C and 2.03 MPa	0.06	1.62
SiO_2 at 1000°C and 2.03 MPa	0.025	0.65
Dry oxidation of Silicon-Germanium alloy	0.033	1.03
Wet oxidation of Silicon-Germanium alloy	0.05	1.3
Oxidation of (HgCd)Te (junction depth)	0.85	5.95

experimental data are listed in Table 2. First, the two phase lags are now on the order of minutes/hours due to the slow processes of interdiffusion and chemical reactions. The oxidation process in minutes/hours is now considered ultrafast due to the values of τ_j and τ_ρ in the same domain of time. The processes in times comparable to the values of τ_j and τ_ρ, as those shown in Table 2, will see the pronounced lagging behavior represented by the mixed-derivate and the wave terms in Eq. (116). Second, because the ultrafast response is now stretched into minutes/hours, environmental conditions, such as the oxidation temperature described in the first three rows in Table 2, will have more pronounced effects on the thermal oxidation process. Both τ_T and τ_q values decrease as the oxidation temperature increases. The ratio of $z = \tau_\rho/\tau_j$, however, stays almost the same (around 27) as the oxidation temperature increases from 800 – 1000°C. Once again, the ratio of (τ_ρ/τ_j) is a dominating parameter in the process of film growth, even though the process of heat/mass transport depends on the individual values of the phase lags in general. Film growth in rapid thermal oxidation is an active field of research by itself. Rather than a rigorous survey on this rapidly evolving field of research, the intent here is to demonstrate the robustness of the DPL model in terms of the use of a mere three parameters; τ_ρ, τ_j, and D, in describing the film growth, in the ultrathin range from 22.36 nm all the way up to microns. Although all cases shown in Table 2 fall into the category of the flux-precedence type of mass transport with $\tau_j < \tau_\rho$ ($z > 1$), there are a few exceptions that are of the density-gradient precedence type, $\tau_\rho < \tau_j$ or $z < 1$ [106].

With the complicated microstructural interaction effects, in space, lumped onto the resulting delayed response in time, growth of intermetallic compounds can be interpreted in exactly the same way as the film growth in rapid thermal oxidation. The cases examined include the thickness of the interfacial Cu_3Sn and Cu_6Sn_5 compounds between Copper (Cu) and Tin (Sn), as well as the growth of the

γ-phase (Ag_5Zn_8) in the β-ε diffusion couples in silver-Zinc (Ag-Zn) alloys [107, 108]. Once again, the linear DPL model is much more superior to other models predicting the intermetallic layer growth. For the case of Cu_3Sn and Cu_6Sn_5 compounds between Cu and Sn, τ_j = 50 days, τ_ρ = 17.5 days, and z = 0.35. The characteristic times governing the growth behavior are now further stretched into days, which are typical for the interdiffusion between metals and the effective chemical reactions to take place between them.

Minutes and hours (for the thermal oxidation of silicon and other semiconductor materials) and days (for the formation and growth of intermetallic compound) are now considered ultrafast due to the comparable values of τ_ρ and τ_j in the corresponding domains of time. Mathematically, effects from the mixed-derivative term led by τ_ρ and the wave term led by τ_j will be pronounced until Fickean behavior recovers as $t >> \tau_\rho$ and τ_j. The overshooting phenomenon as described in Fig. 8, however, has not yet been reported in the open literature.

5 Bio-heat and Mass Transfer

Bioheat transfer often involves thermal energy exchange among different tissues/biological species. It has been a rapidly evolving field of research, particularly the fast transient processes that have become more active in recent years [117-123]. Continuing the applications of the DPL model, this section is to confirm the lagging behavior in bioheat/mass transport, with emphasis on deriving the analytical expressions of the two phase lags, τ_T and τ_q or τ_c and τ_j, in correlations with several bioheat/mass transfer models. In bioheat transfer, the two- and three-equation models describing the energy exchange between blood flows and tissues will be revisited [124]. For drug delivery in tumor cells [125] involving nonequilibrium transport of drug concentrations in living tissues, the lagging behavior will be demonstrated by identifying the sources for delay in relation to the various biological parameters.

5.1 Two-Equation Model

Heat transport between tissue and blood is nonequilibrium by nature, evidenced by the energy exchange rates described by the two-equation model [124]:

$$\varphi C_b\left(\frac{\partial T_b}{\partial t}+u\frac{\partial T_b}{\partial x}\right)=\varphi k_b\nabla^2 T_b+h\left(T_s-T_b\right)$$
$$\left(1-\varphi\right)C_s\frac{\partial T_s}{\partial t}=\left(1-\varphi\right)k_s\nabla^2 T_s-h\left(T_s-T_b\right) \tag{122}$$

where the subscripts b and s represent blood and tissue, respectively, u is the blood flow velocity, φ is the volume fraction of blood, and h is the energy coupling factor in W/(m^3K). The blood flow is assumed one-dimensional due to the small dimension of blood vessels. Equal in magnitude but opposite in sense, Eq. (122)

states that the amount of heat lost from tissue is equal to the amount of heat gained by blood. Except for the presence of the blood flow and the conduction effect placed in tissue, Eq. (122) is in close resemblance to Eq. (30) describing the electron-phonon interactions, with h between blood and tissue in place of G between electrons and phonons. The nonequilibrium feature between T_e and T_l described in Figs. 4 and 5 thus remain. Equation (122) is a step forward as compared to the Pennes' bioheat equation [126] since the blood temperature is allowed to vary in both space and time. The blood perfusion rate in the Pennes' model differs from the energy coupling factor (h) by the specific heat.

To extract the lagging behavior in the simplest mathematical content, parallel to the previous treatment applied to Eq. (30), conduction effect in blood is removed for the time being to minimize the interference from the spatial effect. Setting k_b = 0 and casting Eq. (122) into the operator form as illustrated in Eqs. (41) to (42), the energy equation containing the blood/tissue temperature alone is

$$\nabla^2 T + \left(\frac{\varphi C_b}{h}\right)\frac{\partial}{\partial t}\left(\nabla^2 T\right) + u\left[\left(\frac{C_b \varphi}{h}\right)\frac{\partial}{\partial x}\nabla^2 T - \left(\frac{C_b C_s \varphi}{h k_s}\right)\frac{\partial^2 T}{\partial t \partial x} - \left(\frac{C_b \varphi}{(1-\varphi)k_s}\right)\frac{\partial T}{\partial x}\right] = \left[\frac{C_s(1-\varphi)+C_b\varphi}{(1-\varphi)k_s}\right]\frac{\partial T}{\partial t} + \left(\frac{C_b C_s \varphi}{h k_s}\right)\frac{\partial^2 T}{\partial t^2} \tag{123}$$

where $T \equiv T_b$ or T_s. Except for the additional effect of convection led by the blood flow velocity (u), the remainder of Eq. (123) is exactly the same as the linear DPL model containing the effect of τ_T and τ_q. Comparing Eqs. (43) and (123), it results in

$$\alpha = \frac{(1-\varphi)k_s}{\varphi C_b + (1-\varphi)C_s}, \quad \tau_T = \frac{\varphi C_b}{h}, \quad \tau_q = \frac{1}{h}\left[\frac{1}{(1-\varphi)C_s} + \frac{1}{\varphi C_b}\right]^{-1} \quad \text{(two-equation model).} \tag{124}$$

The ratio of τ_T to τ_q is thus

$$\frac{\tau_T}{\tau_q} \equiv z = 1 + \frac{\varphi C_b}{(1-\varphi)C_s} \quad \text{(two-equation model)} \tag{125}$$

Since $0 < \varphi < 1$ and $C_{b,s} > 0$, Eq. (125) shows that $z > 1$, or $\tau_q < \tau_T$, which implies a flux-precedence type of heat flow. The values of α, τ_T, and τ_q shown by Eq. (125) are in the range of 10^{-7} m^2/s (α), 5 – 50 s (τ_T), and 3 – 25 s (τ_q), from the biological data reported in the open literature. Consequently, the value of z is between one and two ($1 < z < 2$) for nonequilibrium heat transport between blood and tissue.

With the lagging behavior thus confirmed in the two-equation model, the conduction effect in blood flow can now be reinstated, $k_b \neq 0$, which will give rise to an additional biharmonic term, $\nabla^4 T$, in Eq. (123). The coefficients in the resulting equation will become more complicated due to the involvement of the additional term, φk_b, but all terms in Eq. (123) remain the same. This is the same

result as the conduction effect is reinstated in the metal lattices in Eq. (30) [18]. The biharmonic term does provide finer resolutions in the spatial response, but it will not alter the lagging behavior, in time, as we have discussed so far. Metabolic heat generation is another effect to be incorporated for a more realistic simulation. Since the heat source term does not alter the fundamental structure of thermal lagging, such heating effect is temporarily removed in deriving Eq. (123). The convection effect due to the blood flow in Eq. (123) is, however, a salient feature in the dual-phase-lag model when applied to bioheat transfer. When normalizing Eq. (123) by α, τ_T and τ_q shown in Eq. (124) [117], the convection term transforms into the thermal Mach number [40], $u/\sqrt{(\alpha/\tau_q)}$, which measures the blood flow velocity (u) relative to the thermal wave speed, $c_{bs} = \sqrt{(\alpha/\tau_q)}$. According to Eq. (124), the thermal wave speed in the blood-tissue (two-equation) system is

$$c_{bs} = \sqrt{\frac{\alpha}{\tau_q}} = \sqrt{\frac{hk_s}{\varphi C_b C_s}} \tag{126}$$

With the value of α of the order of 10^{-7} m^2/s and that of τ_q of 10 s, the thermal wave speed (c_{bs}) is of the order of 10^{-4} m/s. Blood flow easily exceeds the thermal wave speed and enters the supersonic region due to such a small value of c_{bs}. The temperature described by Eq. (123) increases with the thermal Mach number [117] during the nonequilibrium stage of heat transport between blood and tissue.

5.2 Three-Equation Model

The two-equation model represented by Eq. (122) involves blood and tissue as two energy carriers during the nonequilibrium heat transport. A more refined treatment further splits the blood flow into arterial (subscript a) and venous (subscript v) components [124],

$$\begin{aligned}
\varphi_a C_a\left(\frac{\partial T_a}{\partial t} + u_a \frac{\partial T_a}{\partial x}\right) &= \varphi_a k_a \nabla^2 T_a + h_a\left(T_s - T_a\right) \\
\varphi_v C_v\left(\frac{\partial T_v}{\partial t} - u_v \frac{\partial T_v}{\partial x}\right) &= \varphi_v k_v \nabla^2 T_v + h_v\left(T_s - T_v\right) \\
\left(1-\varphi\right) C_s \frac{\partial T_s}{\partial t} &= \left(1-\varphi\right) k_s \nabla^2 T_s - h_a\left(T_s - T_a\right) - h_v\left(T_s - T_v\right)
\end{aligned} \tag{127}$$

where $\varphi = \varphi_a + \varphi_v$, resulting from mass conservation in the blood-tissue system. There are several features to be noticed in Eq. (127). First, there are three energy carriers, arterial blood, venous blood, and tissue, as compared to two carriers (blood and tissue) in the two-equation model. Second, arterial blood and venous blood flow in an opposite direction, as reflected by the opposite signs in front of u_a and u_v in the convective terms. This is alleged the countercurrent effect [124]. Third, the energy exchange described in Eq. (127) is not in the most general form

as compared to Eq. (100). Instead, heat loss from tissue is equal to the total received in arterial and venous blood. Besides, there is no energy exchange between the arterial and venous blood due to close temperatures in the arterial and venous vessels.

To demonstrate the lagging behavior in the simplest possible mathematical content, once again, conduction effects in the arterial and venous blood are neglected, $k_a = 0$ and $k_v = 0$.[3] Eliminating any two temperatures from T_a, T_v, and T_s, likewise, the energy equation corresponding to Eq. (123) is

$$\begin{aligned}
&\nabla^2 T + \left(\frac{\varphi_v C_v h_a + \varphi_a C_a h_v}{h_a h_v}\right)\frac{\partial}{\partial t}\left(\nabla^2 T\right) + \left(\frac{\varphi_a \varphi_v C_a C_v}{h_a h_v}\right)\frac{\partial^2}{\partial t^2}\left(\nabla^2 T\right) - \\
&u_a\left[\left(\frac{\varphi_a C_a C_s}{h_a k_s}\right)\frac{\partial^2 T}{\partial t \partial x} + \left(\frac{\varphi_a C_a}{(1-\varphi)k_s}\right)\frac{\partial T}{\partial x} - \left(\frac{\varphi_a C_a}{h_a}\right)\frac{\partial}{\partial x}\left(\nabla^2 T\right)\right] + \\
&u_v\left[\left(\frac{\varphi_v C_s C_v}{h_v k_s}\right)\frac{\partial^2 T}{\partial t \partial x} + \left(\frac{\varphi_v C_v}{(1-\varphi)k_s}\right)\frac{\partial T}{\partial x} - \left(\frac{\varphi_v C_v}{h_v}\right)\frac{\partial}{\partial x}\left(\nabla^2 T\right)\right] - \\
&(u_a - u_v)\left[\left(\frac{\varphi_v \varphi_a C_a C_s C_v}{h_a h_v k_s}\right)\frac{\partial^3 T}{\partial t^2 \partial x} + \left(\frac{\varphi_v \varphi_a C_a C_v (h_a + h_v)}{(1-\varphi)h_a h_v k_s}\right)\frac{\partial^2 T}{\partial t \partial x} - \left(\frac{\varphi_v \varphi_a C_a C_v}{h_a h_v}\right)\frac{\partial^2}{\partial t \partial x}\left(\nabla^2 T\right)\right] + \\
&u_a u_v\left[\left(\frac{\varphi_v \varphi_a C_a C_s C_v}{h_a h_v k_s}\right)\frac{\partial^3 T}{\partial t \partial x^2} + \left(\frac{\varphi_v \varphi_a C_a C_v (h_a + h_v)}{(1-\varphi)h_a h_v k_s}\right)\frac{\partial^2 T}{\partial x^2} - \left(\frac{\varphi_v C_a C_v}{h_a h_v}\right)\frac{\partial^2}{\partial x^2}\left(\nabla^2 T\right)\right] = \\
&\left(\frac{\varphi_v C_a C_s C_v}{h_a h_v k_s}\right)\frac{\partial^3 T}{\partial t^3} + \left[\frac{\varphi_v \varphi_a C_a C_v (h_a + h_v) + C_s(1-\varphi)(\varphi_v C_v h_a + \varphi_a C_a h_v)}{h_a h_v k_s}\right]\frac{\partial^2 T}{\partial t^2} + \\
&\left[\frac{C_s(1-\varphi) + \varphi_v C_v + \varphi_a C_a}{(1-\varphi)k_s}\right]\frac{\partial T}{\partial t}.
\end{aligned} \tag{128}$$

where $T \equiv T_a$, T_v, or T_s. In addition to the individual effects of convection from u_a and u_v as before, effects from the relative velocity $(u_a - u_v)$ and the cross velocity $(u_a u_v)$ are also present in Eq. (128). Excluding these terms containing the blood flow velocities, which are spatial effects by nature, the remainder of Eq. (128) is exactly the same as Eq. (52) that contains the full second-order effects in τ_T^2 and τ_q^2. Comparing the coefficients in correspondence, it results in

$$\begin{aligned}
&\alpha = \frac{(1-\varphi)k_s}{\varphi_a C_a + \varphi_v C_v + (1-\varphi)C_s}, \quad \tau_T = \frac{\varphi_a C_a h_v + \varphi_v C_v h_a}{h_a h_v}, \\
&\tau_q = \frac{(1-\varphi)\left[\varphi_a \varphi_v C_a C_v (h_a + h_v) + C_s(1-\varphi)(\varphi_a C_a h_v + \varphi_v C_v h_a)\right]}{h_a h_v \left[C_s(1-\varphi) + \varphi_a C_a + \varphi_v C_v\right]} \quad \text{(three-equation model)}
\end{aligned} \tag{129}$$

Thermophysical properties and flow velocities are very close for arterial and venous bloods; $k_a \cong k_v$, $C_a \cong C_v$, and $u_a \cong u_v$ [124], which will help simplify Eq. (129).

[3] Effect of conduction has been neglected in some components in a multi-carrier system in this chapter, for the purpose of demonstrating the lagging behavior, in time, under the least interference with the microstructural effect in space. This approach, however, becomes almost exact in nanofluids due to the small physical domain taken by the nanoparticle [127, 128].

With the phase lags derived analytically in Eqs. (124) for the two-equation model and (129) for the three-equation model, the lagging behavior becomes clear in bioheat transfer. It is important to note that Eq. (124) containing the *linear* effect of τ_T and τ_q results from the involvement of two energy carriers ($N = 2$) in the blood-tissue system. In the presence of three energy carriers in the three-equation model, $N = 3$, the order of thermal lagging is raised to the *second* order as shown by Eq. (128). This coincides with the conclusion made in Section 3.4, that thermal lagging is of the order of $\tau_T^{(N-1)}$ and $\tau_q^{(N-1)}$ for a system involving N carriers. Equation (128) is a complicated partial differential equation describing the second-order response in thermal lagging. The general response including all the velocity terms, particularly the time derivatives involved in the convective terms and their effects on the lagging behavior during the nonequilibrium heat transport, will be a focal point in future studies. Sine such velocity terms appear in the low-order derivatives in Eq. (128), however, they will not affect the fundamental behaviors of thermal lagging.

5.3 Liposome Drug Delivery

The full second-order effect of τ_T^2 and τ_q^2 in thermal lagging should be a common feature for any system containing three energy carriers. The three-equation model shown by Eq. (128) has well demonstrated this trend. To further examine the same behavior in biosystems, with ties to nonequilibrium mass transport this time, thermally targeted liposomal drug delivery in tumor is revisited [125]. The transport process involves interdiffusion among three drug concentrations: The free drug concentration in the extracellular space, c_E, the drug concentration in liposome form in the extracellular space, c_L, and the intracellular bound drug concentration, c_I. Drug concentration c_E and c_L are measured in milligrams per millimeter of total tumor volume, whereas drug concentration c_I is measured in milligrams per millimeter of intracellular volume. The coupled transport process is described by

$$\begin{cases} \dfrac{\partial c_E}{\partial t} = D_D \nabla^2 c_E + \dfrac{c_L}{t_0} - (1-\phi)\dfrac{\partial c_I}{\partial t} \\ \dfrac{c_L}{t_0} = D_L \nabla^2 c_L + P_L A_L \left(\cancel{c_V} - c_L \right) - \dfrac{\partial c_L}{\partial t} = D_L \nabla^2 c_L - P_L A_L c_L - \dfrac{\partial c_L}{\partial t} \\ \dfrac{\partial c_I}{\partial t} = a\left(\dfrac{c_E}{c_E + k_E} - \dfrac{c_I}{c_I + k_I} \right) \cong a\left(\dfrac{c_E}{k_E} - \dfrac{c_I}{k_I} \right) \end{cases} \tag{130}$$

where ϕ stands for the porosity of the tumor cell, D_D is the apparent diffusivity of free antitumor drug, D_L is the apparent diffusivity of liposome drug in tumor tissue, P_L represents the apparent permeability of the vasculature, A_L is the effective surface area if the vasculature per unit tumor volume, t_0 is the decaying

time constant describing the first-order kinetics during the liposome ruptures and free antitumor drug release, $k_{E(I)}$ is pharmacodynamics parameters (in milligrams per milliliter), and a is the maximum cellular uptake rate, in milligrams per milliliter per minute. Their values for biological tissues were summarized in Ref. [125], with an excellent discussion of all terms involved in Eq. (130). To extract the lagging behavior behind Eq. (130) under the least interference from the spatial effects, the liposome concentration in plasma, c_V, which is a known source term decaying exponentially with time, is dropped from Eq. (130). To minimize the mathematical complexity involved, in addition, the last expression in Eq. (130) has been linearized by remaining the first-order terms in $c_{E(I)}/k_{E(I)}$.

Proceeding for eliminating two of the three unknowns (c_E, c_L, and c_I) from Eq. (130), as before, the transport equation governing the remaining unknown is

$$\nabla^2 c - \left(\frac{D_L t_0}{1+P_L A t_0}\right)\nabla^4 c + \left[\frac{\left(\frac{k_I}{a}\right)(1+P_L A t_0) + t_0\left(1+\frac{D_L}{D_D}\right) + t_0\left(\frac{D_L}{D_D}\right)\left(\frac{k_I}{k_E}\right)(1-\phi)}{1+P_L A t_0}\right]\frac{\partial}{\partial t}\left(\nabla^2 c\right) + t_0\left(\frac{k_I}{a}\right)\left[\frac{1+\left(\frac{D_L}{D_D}\right)}{1+P_L A t_0}\right]\frac{\partial^2}{\partial t^2}\left(\nabla^2 c\right) - \left(\frac{k_I}{a}\right)\left(\frac{D_L t_0}{1+P_L A t_0}\right)\frac{\partial}{\partial t}\left(\nabla^4 c\right) = \left[\frac{1+(1-\phi)\left(\frac{k_I}{k_E}\right)}{D_D}\right]\frac{\partial c}{\partial t} + \left[\frac{\left(\frac{k_I}{a}\right)(1+P_L A t_0) + t_0\left[1+(1-\phi)\left(\frac{k_I}{k_E}\right)\right]}{D_D(1+P_L A t_0)}\right]\frac{\partial^2 c}{\partial t^2} + \left(\frac{k_I}{a}\right)\left[\frac{t_0}{D_D(1+P_L A t_0)}\right]\frac{\partial^3 c}{\partial t^3} = 0 \tag{131}$$

where $c \equiv c_E$, c_L, or c_I. The biharmonic terms containing $(\nabla^4 c)$ result from the conduction effects in the first two expressions (for c_E and c_L), which are kept intentionally here to demonstrate their effects in space, as repeated claimed. These terms are led by $\sqrt{D_L t_0}$, the length of drug diffusion. Focusing on the lagging behavior, in time, therefore, these terms reflecting the spatial effects can indeed be dropped to give

$$\nabla^2 C + \left[\frac{\left(\frac{k_I}{a}\right)(1+P_L A t_0) + t_0}{1+P_L A t_0}\right]\frac{\partial}{\partial t}\left(\nabla^2 C\right) + t_0\left(\frac{k_I}{a}\right)\left[\frac{1}{1+P_L A t_0}\right]\frac{\partial^2}{\partial t^2}\left(\nabla^2 C\right) = \left[\frac{1+(1-\phi)\left(\frac{k_I}{k_E}\right)}{D_D}\right]\frac{\partial C}{\partial t} + \left[\frac{\left(\frac{k_I}{a}\right)(1+P_L A t_0) + t_0\left[1+(1-\phi)\left(\frac{k_I}{k_E}\right)\right]}{D_D(1+P_L A t_0)}\right]\frac{\partial^2 C}{\partial t^2} + \left(\frac{k_I}{a}\right)\left[\frac{t_0}{D_D(1+P_L A t_0)}\right]\frac{\partial^3 C}{\partial t^3}. \tag{132}$$

Equation (132) is the same result by neglecting the conduction effect of liposome drug diffusion in tumor, i.e., $k_L \to 0$ and consequently $D_L \to 0$, in Eq. (130).

Equation (52) can be extended to mass transport by a simple replacement of the transport variables: $T \to c$, $q \to j$, $\alpha \to D$, $\tau_T \to \tau_c$, and $\tau_q \to \tau_j$:

$$\nabla^2 c + \tau_c \frac{\partial}{\partial t}\left(\nabla^2 c\right) + \frac{\tau_c^2}{2}\frac{\partial^2}{\partial t^2}\left(\nabla^2 c\right) = \frac{1}{D}\frac{\partial c}{\partial t} + \frac{\tau_j}{D}\frac{\partial^2 c}{\partial t^2} + \frac{\tau_j^2}{2D}\frac{\partial^3 c}{\partial t^3}. \tag{133}$$

Omitting the second order effects in τ_c and τ_j, in fact, Eq. (133) reduces to linear DPL that already appeared earlier in Eq. (116), with mass density replaced by concentration, $\rho \to c$ and $\tau_\rho \to \tau_c$. Equation (133) has exactly the same form as Eq. (132), resulting in the following correlations by comparing the coefficients in correspondence:

$$D = \frac{D_D}{1+(1-\phi)\left(\dfrac{k_I}{k_E}\right)}, \quad \tau_c = \frac{k_I}{a} + \frac{t_0}{1+P_L A t_0}, \quad \tau_j = \frac{\left(\dfrac{k_I}{a}\right)}{1+(1-\phi)\left(\dfrac{k_I}{k_E}\right)} + \frac{t_0}{1+P_L A t_0}. \tag{134}$$

Having the dimension of time, t_0 and (k_I/a) are common factors in τ_c and τ_j. The lagging behavior, and consequently the phase lags characterizing the delayed response in this case, thus results from the finite time required for the liposome rupture (t_0) and the finite time required for the effective absorption of antitumor drug (a). Assuming that liposome bursts in no time, $t_0 \to 0$, and the antitumor drug is absorb instantaneously by the tumor tissue, $a \to \infty$, both τ_j and τ_c approach zero and Eq. (133) recovers the familiar diffusion equation employing Fick's law. The difference between τ_j and τ_c lies in the scaling factor $[1+(1-\phi)(k_I/k_E)]$ on the time constant, k_I/a. Since porosity $\phi < 1$, and consequently $(1-\phi)(k_I/k_E) > 0$, it is evident that $\tau_j < \tau_c$, which implies the flux precedence type of mass transport as liposome drug penetrates through the cellular membranes. In terms of the lagging behavior, the mass flux (j) is the cause of the mass flow while the concentration gradient (∇c) is the effect.

Equation (133) containing the effect of τ_c^2 in mass transport has the same form as Eq. (52) containing the effect of τ_T^2 in heat transport. All discussions based on Eq. (52) thus apply to Eq. (133) as well. Effect of τ_T^2 further elevates the temperature level of the T-wave, as sketched in Fig. 12. By destroying the wavefront of the T-wave from the τ_q^2-effect, the second-order effect of τ_T evolves into diffusion of the higher order, which is active as the process time enters the threshold of the left-most time scale placed on the regime map, (τ_q^3/τ_T^2) in Fig. 10. The time scales will continue to shrink toward zero as the higher order terms in τ_T and τ_q are further taken into account, making the temperature higher and more uniformly distributed in the physical domain as the wave and diffusion behaviors continue to alternate in small times. Such frequent alterations between diffusion and wave give rise to a dual representation of heat propagation during nonequilibrium transport, depending on the time scale in which a physical observation is made.

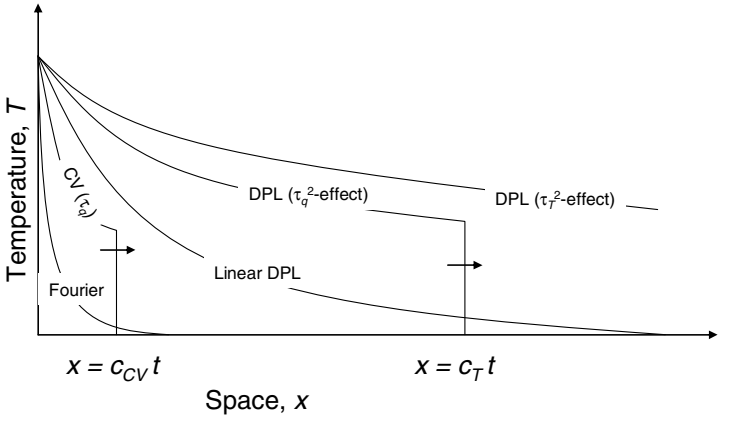

Fig. 12 High-order diffusion induced by the τ_T^2 effect in thermal lagging

6 Nonlocal Behavior

The phonon scattering model outlined in Section 2.2 has already revealed some lights on the nonlocal response between the heat flux vector and the temperature gradient. As shown in Eqs. (71), (72) and Table 1, the umklapp (τ_R) and normal (τ_N) relaxation times in the phonon scattering model in Eq. (15) can indeed be interpreted as the phase lags in the lagging response, in time, but the coefficient $(\tau_R c)(\tau_N c)/5 \sim l^2$ in Eq. (15) can also be viewed as a characteristic length (l) squared. At a given instant of time, more explicitly, should the heat flux be represented by

$$\mathbf{q}(\mathbf{r}+\mathbf{L},t) = \mathbf{q}(\mathbf{r},t) + (\mathbf{L}\bullet\nabla)\mathbf{q}(\mathbf{r},t) + \frac{1}{2}(\mathbf{L}\bullet\nabla)(\mathbf{L}\bullet\nabla)\mathbf{q}(\mathbf{r},t) + \ldots, \qquad (135)$$

the case of isotropic nonlocality with identical values of l in all three directions in the Cartesian space, $\mathbf{L} = (l)\mathbf{e}_{11} + (l)\mathbf{e}_{22} + (l)\mathbf{e}_{33}$, will gives rise to $(l^2\nabla^2\mathbf{q})$ as the third term in Eq. (135) is expanded. The phonon scattering model can thus be viewed as a subset of the nonlocal response, in space [18], which only includes the second order effect in l^2. The same effect of nonlocality is also reflected in the two-temperature model, Eq. (108), where the same behavior of nonlocality is reflected by $(l^2\nabla^2\psi)$ without the first-order term in l.

Nonlocal effect in space can be extended from the concept of thermal lagging in time, which has become evident in comparing the analogy between Eqs. (7) (for the lagging behavior in time) and (135) (nonlocal behavior in space). In addition to the signatures of nonlocality in the phonon scattering model and the two-temperature model, this extension of the lagging concept, from time to space, is further prompted by the recent development on the thermomass model [129-131].

6.1 Thermomass Model

As compared to others, most distinguishable feature of the thermomass (TM) model lies in its recognizing a finite mass for the phonon gas, the assumed energy carrier for microscale heat transport in dielectric materials [129, 130]. As a result, the thermal and mechanical fields become mutually implied, and are no longer independent. The process of heat transport is modeled by the phonon gas flow through the porous lattices in the TM model. Major quantities involved are the thermomass density of the phonon gas (ρ_h), the drift velocity (u_h), the phonon gas pressure (p_h) induced by the thermal vibration of the lattice, and the resistance force (f_h measured per unit volume) experienced by the phonon gas as it flows through the porous lattices [129, 130]:

$$\rho_h = \frac{CT}{c^2}, \quad u_h = \frac{q}{CT}, \quad p_h = \frac{\gamma c^2 \rho_h^2}{\rho}, \quad \text{and} \quad f_h = \beta u_h \tag{136}$$

The thermomass density (ρ_h) is calculated from the volumetric average of the thermomass (m_h) of the lattice, $m_h = E/c^2$, resulting from the Einstein's mass-energy relation with $E = m_R c_p T$ representing the thermal vibration energy stored in the lattice at rest, c the speed of light in vacuum, C the volumetric heat capacity of the lattice as before, $C = \rho c_p$, and m_R the rest mass of the lattice. Heat flux (q) is carried with the drift velocity (u_h) of the phonon gas in which the volumetric energy density is CT. The phonon gas pressure (p_h) is derived from the Debye's equation of state, which is the origin for the Grüneisen constant (γ) involved in Eq. (136). By the use of the first expression in Eq. (136) for ρ_h, it can be readily seen that the phonon gas pressure is proportional to its temperature squared, which is exactly the same behavior as that in the electron gas in metals [21]. The resistance force results from the gradient of the phonon gas pressure, $f_h = -dp_h/dx$, and the Darcy's law describing phonon scattering through the porous dielectrics. The resistance coefficient (β) is the proportional constant between f_h and u_h, $\beta = 2\gamma C^3 T^2/(\rho k c^2)$ with ρ being the mass density of the lattice at rest and k the thermal conductivity. The phonon drift velocity (u_h) is of the order of 10^{-5} m/s, based on a temperature difference of 10°K and a heat flux of 10^4 W/m^2.

Resulting from the finite mass of the phonon gas, most strikingly, the mechanical and thermal fields become mutually implied in the TM model. In the case of one-dimensional heat conduction, from Eq. (136), the continuity equation gives rise to the energy equation in the phonon gas,

$$\frac{\partial \overbrace{\rho_h}^{\frac{CT}{c^2}}}{\partial t} + \frac{\partial}{\partial x}\left(\rho_h \overbrace{u_h}^{\frac{q}{CT}} \right) = 0 \quad \Rightarrow \quad -\frac{\partial q}{\partial x} = C\frac{\partial T}{\partial t} \tag{137}$$

The momentum equation, on the other hand, gives rise to the constitutive equation for the phonon gas,

$$\rho_h\left(\frac{\partial u_h}{\partial t}+u_h\frac{\partial u_h}{\partial x}\right)+\frac{\partial \overbrace{p_h}^{\gamma c^2\rho_h^2/\rho}}{\partial x}+\overbrace{f_h}^{\beta u_h}=0 \quad \Rightarrow$$

$$\tau_{\mathrm{TM}}\frac{\partial q}{\partial t}-lC\frac{\partial T}{\partial t}+l\frac{\partial q}{\partial x}-M^2k\frac{\partial T}{\partial x}+k\frac{\partial T}{\partial x}+q=0 \quad \text{with} \tag{138}$$

$$\tau_{\mathrm{TM}}=\frac{\rho k}{2\gamma C^2T}, \quad l=\frac{\rho kq}{2\gamma C(CT)^2}, \quad M^2=\frac{\rho q^2}{2\gamma(CT)^3}=\overbrace{\frac{\rho}{2\gamma CT}}^{\tau_{\mathrm{TM}}/\alpha_{\mathrm{TM}}}\overbrace{\left(\frac{q}{CT}\right)^2}^{u_h^2}=\left(\frac{u_h}{c_{\mathrm{TM}}}\right)^2$$

where τ_{TM} is the lagging time of the phonon gas in the thermomass model, which is about two orders of magnitude larger than the relaxation time of the lattices calculated from the *CV*-wave model, l is a length parameter, and M is the thermal Mach number of the phonon drift velocity relative to the thermal wave speed defined as $c_{\mathrm{TM}} = \sqrt{(\alpha_{\mathrm{TM}}/\tau_{\mathrm{TM}})}$, with $\alpha_{\mathrm{TM}} = k/C$ being the thermal diffusivity of the phonon gas. In the second expression in Eq. (138), the first four terms on the left-hand side results from the inertia effect, $\rho_h(Du_h/Dt)$. The fifth term results from the pressure gradient of the phonon gas, and the last term results from the resistance force since $f_h = \beta u_h = \beta q/(CT)$ from Eq. (136). The continuity and momentum equations for the phonon gas flow, which belong to the mechanical field by nature, therefore, directly give the energy and constitutive equation in heat transport without a separate consideration of the thermal field. Fourier made a statement in 1822 that the principles of motion and equilibrium in mechanical theories do not apply to the effects of heat. Equations (137) and (138), however, show that "the effects of heat" (energy and constitutive equations for heat transport) is indeed derivable from mechanical theories (conservation equations of mass and momentum), and one may imply the other based on the finite mass of the phonon gas.

Involvement of the term containing the time-rate of change of temperature, $\partial T/\partial t$, warrants more explorations for the nature of Eq. (138). Eliminating heat flux (q) from Eqs. (137) and (138), the energy equation containing temperature (T) alone is:

$$\left[\frac{k(1-M^2)}{C\tau_{\mathrm{TM}}}\right]\frac{\partial^2 T}{\partial x^2}=\left(\frac{1}{\tau_{\mathrm{TM}}}\right)\frac{\partial T}{\partial t}+\left(\frac{2l}{\tau_{\mathrm{TM}}}\right)\frac{\partial^2 T}{\partial x\partial t}+\frac{\partial^2 T}{\partial t^2} \tag{139}$$

In addition to the wave behavior described by the second order derivative with respect to time, $\partial T^2/\partial t^2$, Eq. (139) contains a mixed derivative term, $\partial T^2/\partial x\partial t$, which has not appeared in any microscale conduction model. As compared to the linear DPL model shown in Eq. (43), the order of the mixed-derivative term in the TM model in space, $\partial T^2/\partial x\partial t$, is lower than that in the DPL model ($\partial T^3/\partial x^2\partial t$) by

one. Note that the length parameter (l) is in the same direction of heat flux (q) as shown in Eq. (138). As the heat flux changes its sign due to reversal of the coordinate system, the length parameter switches its sign accordingly and the principle of spherical symmetry for any constitutive equation to satisfy follows [18].

6.2 Nonlocal Response with Lagging

Involvement of a length parameter in Eq. (138) is enlightening for us to include the nonlocal behavior in space along with the lagging behavior in time:

$$q(x+\lambda_q, t+\tau_q) = -K\frac{\partial T}{\partial x}(x,t)\,. \tag{140}$$

Physically, in addition to the lagging response between the temperature gradient established at time t and the delayed heat flux at (t + τ_q), Eq. (140) further correlates the temperature gradient established at a location x to the heat flux at (x + λ_q) in the neighborhood. The correlation length, λ_q, thus draws a radius for the region of influence between q and $\partial T/\partial x$. Aimed toward the correlation with the TM model, the phase lag of the heat flux (τ_q) is assumed small in comparison with the process time (t), and the correlation length (λ_q) is assumed small in comparison with the space dimension (x). The Taylor series expansion of Eq. (140) containing the first-order effects of τ_q and λ_q then yields

$$q(x,t) + \lambda_q\frac{\partial q(x,t)}{\partial x} + \tau_q\frac{\partial q(x,t)}{\partial t} \cong -K\frac{\partial T}{\partial x}(x,t). \tag{141}$$

Eliminating heat flux (q) from Eq. (141) and the one-dimensional form of Eq. (4), the energy equation,

$$-\frac{\partial q}{\partial x} = C\frac{\partial T}{\partial t}\,, \tag{142}$$

It results in

$$\begin{vmatrix} 1+\lambda_q\dfrac{\partial}{\partial x}+\tau_q\dfrac{\partial}{\partial t} & K\dfrac{\partial}{\partial x} \\ \dfrac{\partial}{\partial x} & C\dfrac{\partial}{\partial t} \end{vmatrix} T = 0 \;\Rightarrow\; \left(\frac{K}{C\tau_q}\right)\frac{\partial^2 T}{\partial x^2} = \frac{1}{\tau_q}\frac{\partial T}{\partial t} + \left(\frac{\lambda_q}{\tau_q}\right)\frac{\partial^2 T}{\partial x \partial t} + \frac{\partial^2 T}{\partial t^2}\,. \tag{143}$$

Equation (143) obtained from the nonlocal response with thermal lagging (the NL model) has exactly the same form as Eq. (139) obtained from the TM model, resulting in the correlations

$$K = k(1-M^2), \quad \tau_q = \tau_{\mathrm{TM}}, \quad \lambda_q = 2l\,. \tag{144}$$

While the phase lag of the heat flux (τ_q) is equivalent to the lagging time (τ_{TM}) in the TM model, the correlation length (λ_q) in the NL model simply stretches the length parameter (l) in the TM model by two times. With the perfect correlation thus established, clearly, the NL model is equivalent to the TM model in capturing the effect of heat mass for heat transport in dielectrics. In addition to the thermal conductivity of nanowires calculated from the nonlocal effect in Section 2.2, the perfect correlation with the TM model is another support for the nonlocal behavior in the presence of thermal lagging. The phase lag of the temperature gradient, τ_T, can be instated as done in Section 3. The equations governing the nonlocal response with higher order effects in both τ_T and τ_q will become much more complicated, but further correlations will be postponed until new phenomena/models warrant such an extension.

The presence of the mixed-derivative term in Eq. (143) does not alter the fundamental characteristics since the highest order derivative remains to reside in the wave term. The wave speed, however, may be altered due to the additional derivative with respect to time carried in the mixed-derivative term. Equation (143) can be rearranged into a standard form:

$$\frac{\partial^2 T}{\partial x^2} = \frac{1}{\alpha}\frac{\partial T}{\partial t} + \left(\frac{\lambda_q}{\alpha}\right)\frac{\partial^2 T}{\partial x \partial t} + \left(\frac{\tau_q}{\alpha}\right)\frac{\partial^2 T}{\partial t^2} \tag{145}$$

Taking the Laplace transform of Eq. (145) under zero initial conditions and extracting the component that vanishes as x approaches infinity, the result corresponding to Eq. (85) is

$$\frac{\overline{T}(x;p)}{T_w} = \frac{\exp\left[\dfrac{\left(\lambda_q p - \sqrt{\left(\lambda_q p\right)^2 + 4\alpha p + 4\alpha\tau_q p^2}\right)x}{2\alpha}\right]}{p} \tag{146}$$

The partial expansion technique shown by Eqs. (86) and (87) then yields

$$\lim_{t\to 0} T(x,t) \sim L^{-1}\left[\lim_{p\to\infty}\overline{T}(x;p)\right] = L^{-1}\left\{\lim_{p\to\infty}\left\{\exp\left[\frac{\left(\lambda_q p - \sqrt{\left(\lambda_q p\right)^2 + 4\alpha p + 4\alpha\tau_q p^2}\right)x}{2\alpha}\right]/p\right\}\right\} =$$

$$L^{-1}\left\{\frac{\exp\left[-\left(\dfrac{\sqrt{\lambda_q^2 + 4\alpha\tau_q} - \lambda_q}{2\alpha}\right)px\right]}{p}\right\} = H\left(t - \left(\frac{\sqrt{\lambda_q^2 + 4\alpha\tau_q} - \lambda_q}{2\alpha}\right)x\right), \tag{147}$$

which possesses a discontinuity at the wavefront of the nonlocal-lagging (*NL*) wave:

$$x = c_{\rm NL} t \quad \text{with} \quad c_{\rm NL} = \frac{2\alpha}{\sqrt{\lambda_q^2 + 4\alpha\tau_q} - \lambda_q} = \frac{2c_{\rm CV}^2}{\sqrt{c_q^2 + 4c_{\rm CV}^2} - c_q} = \sqrt{c_{\rm CV}^2 + \left(\frac{c_q}{2}\right)^2} + \frac{c_q}{2}, \quad (148)$$

where $c_{\rm CV} = \sqrt{(\alpha/\tau_q)}$ and $c_q = (\lambda_q/\tau_q)$ is the averaged wave speed travelling across the correlation length over the relaxation time. The *NL*-wave propagates faster than the *CV*-wave, $c_{\rm NL} > c_{\rm CV}$. In view of the TM model, from Eqs. (144), (138), and (136),

$$c_q = \frac{\lambda_q}{\tau_q} = \frac{2l}{\tau_{\rm TM}} = \frac{2q}{CT} = 2u_h. \quad (149)$$

The wave speed c_q is thus twice of the drift velocity of the phone gas in correlation with the TM model. Since $u_h << c_{\rm CV}$, by substituting Eq. (149) into Eq. (148),

$$c_{\rm NL} = \sqrt{c_{\rm CV}^2 + u_h^2} + u_h \cong c_{\rm CV} + u_h, \quad (150)$$

which explicitly shows the difference between the *NL*- and *CV*-wave speed by u_h.

The *NL*-wave obtained from the solution to Eq. (145) is sketched in Fig. 13. The wave structure is extracted from a simple system for heat propagation in a semi-infinite solid, driven by a suddenly raised temperature (T_w) at the surface at

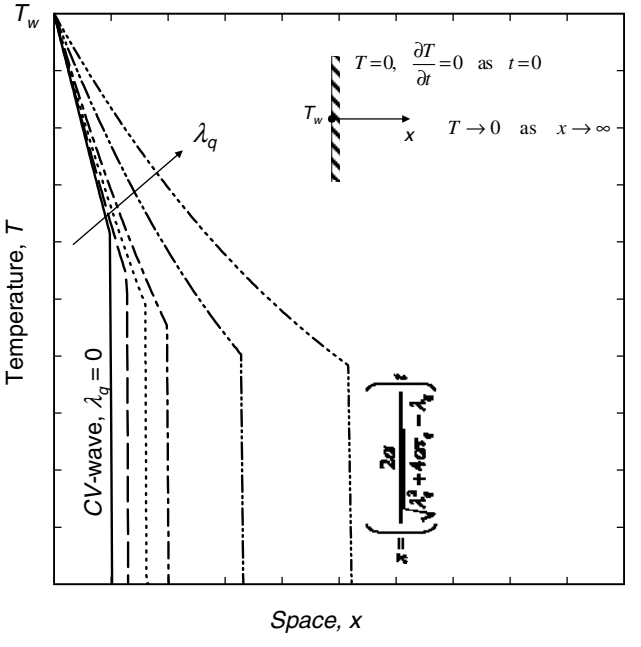

Fig. 13 Nonlocal behavior in thermal lagging – The wave behavior

$x = 0$ [131]. The *NL*-wave speed, heat affected zone, and the temperature within the heat affected zone all increases with the value of λ_q due to the enlarged domain of influence. From Eq. (145), returning to the regime map, the nonlocal term becomes as important as the wave term as the process time enter the threshold of $t \sim \tau_q(L/\lambda_q)$, with L being the characteristic dimension of the conductor. Depending on the ratio of L to λ_q, this time scale can either be on the left ($L < \lambda_q$) or right ($\lambda_q < L$) of τ_q. The nonlocal response in space, particularly as more high-order terms of λ_q are taken into account, thus adds another dimension of complexity to the regime map established in time.

The nonlocal behavior with thermal lagging is admissible within the framework of nonequilibrium thermodynamics. Based on the same reference (0) state, Eq. (47), gradient of the dynamic temperature (a vector) can be implemented as an additional internal state variable in the evolution equation:

$$\dot{\beta}(\theta,\beta,\nabla\beta) = \overbrace{\dot{\beta}_0(\theta,\beta)}^{\frac{1}{\tau}(\theta-\beta)} + \left[\frac{\partial\dot{\beta}}{\partial(\nabla\beta)}\right]_0 \bullet \nabla\beta + \ldots \tag{151}$$

where, in consistency with the linear expansion adopted so far as in Eq. (48), the deviation of $\nabla\beta$ from the reference state ($\dot{\beta}_0(\theta,\beta)$) is assumed so small that only the first-order term needs to be included in the Taylor series expansion. Therefore, from Eq. (11),

$$\dot{\mathbf{q}} = -k\nabla\dot{\beta} = -\frac{k}{\tau}\left(\nabla\theta - \overbrace{\nabla\beta}^{-\frac{\mathbf{q}}{k}}\right) - k\left\{\left[\frac{\partial\dot{\beta}}{\partial(\nabla\beta)}\right]_0 \bullet \nabla\right\}\overbrace{\nabla\beta}^{-\frac{\mathbf{q}}{k}} \tag{152}$$

Multiplying throughout by τ, it results in

$$\mathbf{q} + \tau\dot{\mathbf{q}} - \tau\left\{\left[\frac{\partial\dot{\beta}}{\partial(\nabla\beta)}\right]_0 \bullet \nabla\right\}\mathbf{q} = -k\nabla\theta \tag{153}$$

In the case of one-dimensional response, $\mathbf{q} \equiv q\mathbf{e}_x$, $\nabla \equiv \partial/\partial x$, $\left[\partial\dot{\beta}/\partial(\nabla\beta)\right]_0 \equiv \left[\partial\dot{\beta}/\partial(\partial\beta/\partial x)\right]_0$, and Eq. (153) reduces to

$$q + \tau\frac{\partial q}{\partial t} - \tau\left[\frac{\partial\dot{\beta}}{\partial(\partial\beta/\partial x)}\right]_0\frac{\partial q}{\partial x} = -k\nabla\theta \tag{154}$$

With the substitutions of $k \equiv K$, $\tau \equiv \tau_q$, and $\left[\partial\dot{\beta}/\partial(\partial\beta/\partial x)\right]_0 \equiv -\left(\lambda_q/\tau_q\right)$, Eq. (154) has exactly an identical form to Eq. (141) describing the nonlocal behavior

with thermal lagging. In the representation made in the state space of $\dot{\beta}$ versus $\nabla\beta$, the *slope* of the reference state, $\left[\partial\dot{\beta}/\partial(\partial\beta/\partial x)\right]_0$, refers to the mean speed $c_q = \lambda_q/\tau_q$ as defined in Eq. (149). It can either be positive or negative depending on the direction of the nonlocal response. In correlation with Eq. (141), the negative sign in front of the nonlocal term ($\partial q/\partial x$) in Eq. (154) implies a negative slope, $\left[\partial\dot{\beta}/\partial(\partial\beta/\partial x)\right]_0 < 0$; meaning that the temperate-rate ($\dot{\beta}$) decreases as the temperature gradient ($\partial\beta/\partial x$) increases in departure from the reference state. Equivalently, in terms of the mean speed c_q in the nonlocal response, this implies the nonlocal response in the opposite direction of the coordinate system, $c_q < 0$, which has already been seen in Fig. 3 as the phonons are backscattered from the nanowire surface. Unlike thermal lagging in time, which involves scalars in describing the phase lags, the nonlocal response is direction dependent in space, which will involve a careful adjustment of the sign of c_q according to the physical event being described.

7 Conclusion

Lagging behavior in time and nonlocal behavior in space are natural consequences during nonequilibrium transport. The thermodynamic state transits at a fast pace during nonequilibrium transport, resulting in many phenomena that cannot be described by the conventional approaches assuming a quasi-stationary transition. The various wave behaviors, while alternating with the high-order diffusion in times comparable to the phase lags characterizing the lagging response, are noteworthy. Depending on the sources for lagging, the phase lags can be from femto- to picoseconds for heat transport by electrons and electron-phonon coupling in metals. The phase lags could be stretched into days, on the other hand, during the intermetallic compound growth due to the prolonged processes of mass interdiffusion and chemical reactions involved. Any process taking place in times comparable to the phase lags is ultrafast, even though for some seemingly slow processes in minutes and days, because the lagging/nonlocal behaviors will be pronounced in the same domain of time. The nonequilibrium temperature resulting from the lagging/nonlocal response can be many times higher than the equilibrium temperature in general. As the process time enters the physical domain of phase lags, the excessive temperature induced by the effect of τ_T and the large temperature gradient induced by the effect of τ_q near the wavefront are important causes for the thermal and mechanical damage. The regime map in terms of the process time has been established to help avoid their incidences.

Employing two phase lags, in time, the DPL model is a phenomenological approach targeted toward lumping the various microstructural interactions effects in space into the resulting delayed response in time. The two phase lags absorbs the finite times required for the microstructural interactions to accomplish, regardless of their different nature in microscale. The relaxation time of electrons

and the thermalization time for the phonons and electrons to come to thermal equilibrium and the umklapp and normal relaxation times in dielectric crystals, for example, describe the lagging behavior without following detailed mechanical traces of electrons and phonons in microscale. Continuing on to the nonequilibrium mass transport, based on the same premise, the finite times required for the effective interdiffusion and chemical reaction to take place during the thin-film/interfacial-layer growth and the finite times required for the liposome rupture and the effective antitumor drug absorption identify the same lagging behavior with intrinsically different origins of delay. In transition from one type of medium to another with fundamentally different compositions in microscale, development of the DPL model has closely followed the guidelines from mathematical analogy. The exactly identical forms of the transport equations describing lagging/nonlocality, which has spun from the linear effect of the phase lag of the heat/mass flux vector to the inclusion of the full second-order effects including the phase lag of the temperature/concentration/density gradient as well, not only highlight the lagging/nonlocal effects during the nonequilibrium transport but also facilitate the interpretations of the two phases lags/correlation length in terms of the various microstructural parameters involved in different types of media. The correlations shown in Table 1, which relate the DPL model to the various microscale conduction models with different sources of delay, as well as the lagging behaviors derived from the bioheat equations, ultrathin film/interfacial layer growth, drug delivery in tumors and inclusion of the nonlocal behavior in thermal lagging, are explicit efforts with the same merit. With the lagging behaviors thus confirmed, continued efforts for the determination of the phase lags/correlation length in the laboratories should be promising.

The number of phase lags sufficient to describe the lagging response in general is an important philosophical question to be answered. Sine any physical process involves cause and effect, it has been shown that two phase lags, one for the cause and another for the effect, are sufficient to cover a wide variety of materials. This has been evident in the use of one phase lag for the heat/mass flux vector and another for the temperature/concentration/density gradient. As new phenomena continuously arise in nonequilibrium transport during the ultrafast transient, exemplified by those from biological systems with multiple carriers, high order effects of the same phase lags will appear and continue to evolve. As the nonequilibrium process in microscale continuously advances due to the creation of new technologies, this is an observation to be examined over time.

Tangling of the two phase lags during the nonequilibrium transport in ultrafast transient results is by far the most complicated equations in any discipline of engineering and science. They give rise to the various wave and high-order diffusion in heat and mass transport, activating/diminishing at different times during the transport process. Depending on the sources of lagging and/or nonlocality, the number of microstructural parameters involved can be overwhelmed as seen in the biological systems covered in Section 5. By introducing the phase lags in characterizing the lagging response, all microstructural parameters are absorbed in the three parameters in DPL, the two phase lags and the effective thermal diffusivity. There are special cases where the

lagging response is governed by the ratio between the two phase lags, such as the anomalous diffusion in amorphous media or the growth of ultrathin films or intermetallic compounds. The number of dominating parameters in these cases is further reduced from three to one, but they are demonstrations for the scaling rule in thermal lagging and cannot be viewed as a general result. This is particularly the case for problems involving a heat source or a finite boundary, which are typical in bioheat and mass transfer.

Relative to the decade-long development of the dual-phase-lag model, nonlocal effect in thermal lagging is a new direction. The phonon scattering model and the two-temperature model have addressed, in part, the second-order effect of nonlocality, but recently developed thermomass model provides an incidence to formally and rigorously introduce the nonlocal behavior in the same framework of thermal lagging. Nonlocality in space has been accommodated in the same way as thermal lagging in time, both appearing as discrete parameters in the general response between the heat flux vector and the temperature gradient. For heat transport in dielectric crystals, all salient features resulting from the finite mass of the phonon gas are nicely captured by a simple accommodation of the first-order effect in nonlocality and the first-order effect of the phase lag of the heat flux vector in thermal lagging. Like evolution of the DPL model from the linear version to the inclusion of the full second-order effects, however, further accommodation of the high order terms in nonlocality should wait until more experimental/theoretical developments appear, which could also include another correlation length to be introduced in the temperature gradient.

References

1. Momma, C., Chichkov, B.N., Nolte, S., Alvensleben, F.V., Tunnermann, A., Welling, H., Wellegehausen, B.: Short-pulse laser ablation of solid targets. Optics Communications 129, 134–142 (1996)
2. Shirk, M.D., Molian, P.A.: A review of ultrashort pulsed laser ablation of materials. J. Laser Applications 10, 18–28 (1998)
3. Hopkins, J.M., Sibbett, W.: Ultrashort-pulse lasers: big payoffs in a flash. Scientific American 283, 72–79 (2000)
4. Perry, M.D., Staurt, B.C., Banks, P.S., Feit, M.D., Yanovsky, V., Rubenchik, A.M.: Ultrashort-pulse laser micro-machining of dielectric materials. J. Appl. Phys. 85, 6803–6810 (1999)
5. Qiu, T.Q., Tien, C.L.: Short-pulse laser heating on metals. Int. J. Heat and Mass Transfer 35, 719–726 (1992)
6. Qiu, T.Q., Tien, C.L.: Heat transfer mechanisms during short-pulse laser heating of metals. J. Heat Transfer 115, 835–841 (1993)
7. Russo, R.E., Mao, X., Gonzalez, J.J., Mao, S.S.: Femtosecond laser ablation ICP-MS. Analytical Atomic Spectrometry 17, 1072–1075 (2002)
8. Nolte, S., Chichkov, B.N., Welling, H., Shani, Y., Lieberman, K., Terkel, H.: Nanostructuring with spatially localized femtosecond laser pulses. Optics Lett. 24, 914–916 (1999)

9. Wang, Z.B., Guo, W., Pena, A., Whitehead, D.J., Luk'yanchuk, B.S., Li, L., Liu, Z., Zhou, Y., Hong, M.H.: Laser micro/nano fabrication in glass with tunable-focus particle lens array. Optics Express 16, 19706–19711 (2008)
10. Rizvi, N.H.: Femtosecond laser micromachining: Current status and applications. RIKEN Review 50, 107–112 (2003)
11. Perrie, W., Gill, M., Robinson, G., Fox, P., O'Neill, W.: Femtosecond laser microstructuring of aluminium under helium. Appl. Surf. Sci. 230, 50–59 (2004)
12. Feng, Q., Picard, Y.N., Liu, H., Yalisove, S.M., Mourou, G., Pollock, T.M.: Femtosecond laser micromachining of a single-crystal superalloy. Scripta Materialia 53, 511–516 (2005)
13. Kam, D.H., Mazumder, J.: Three-dimensional biomimetic microchannel network by laser direct writing. J. Laser Appl. 20, 185–191 (2008)
14. Bovatsek, J.M., Arai, A.Y., Yoshino, F., Uehara, Y.: Ultrashort pulse micromachining with the 10-μJ FCPA fiber laser. In: Proc. SPIE, vol. 6102, pp. 1–11 (2006)
15. Moreno, P., Méndez, C., García, A., Arias, I., Conejero, E., Roso, L.: Micromecanizado de materiales cerámicos mediante láser de femtosegundo. Boletin de la Sociedad Española de Cerámica y Vidrio 44, 9–12 (2005)
16. Wang, Y., Dai, N., Li, Y., Wang, X., Lu, P.: Ablation and cutting of silicon wafer and micro-mold fabrication using femtosecond laser pulses. J. Laser Appl. 19, 240–244 (2007)
17. Sudheer, S.K., Kothwala, D., Prathibha, S.: Laser microfabrication of L605 cobalt-chromium cardiovascular stent implants with modulated pulsed Nd:YAG laser. J. Micro/Nanolithography, MEMS, and MOEMS 7, 33012 (2008)
18. Tzou, D.Y.: Macro- to Microscale Heat Transfer: The Lagging Behavior. Taylor & Francis, Washington (1997)
19. Tzou, D.Y., Beraun, J.E., Chen, J.K.: Ultrafast deformation in femtosecond laser heating. J. Heat Transfer: Special Issue in Micro/Nanoscale Heat Transfer 124, 284–292 (2002)
20. Tzou, D.Y., Chen, J.K., Beraun, J.E.: Hot-electron blast induced by ultrashort-pulsed lasers in layered media. Int. J. Heat Mass Transfer 45, 3369–3382 (2002)
21. Tzou, D.Y., Chen, J.K., Beraun, J.E.: Recent development on ultrafast thermoelasticity. J. Thermal Stresses 28, 563–594 (2005)
22. Chen, J.K., Beraun, J.E., Grimes, L.E., Tzou, D.Y.: Modeling of femtosecond laser-induced non-equilibrium deformation in metal films. Int. J. Solids Structures 39, 3199–3216 (2002)
23. Chen, J.K., Beraun, J.E., Tzou, D.Y.: Thermomechanical response of metals heated by ultrashort-pulsed lasers. J. Thermal Stresses 25, 539–558 (2002)
24. Chen, J.K., Beraun, J.E., Grimes, L.E., Tzou, D.Y.: Short-time thermal effects on thermomechanical response caused by pulsed lasers. J. Thermophysics Heat Transfer 17, 35–42 (2003)
25. Chen, J.K., Tzou, D.Y., Beraun, J.E.: Numerical investigation of ultrashort laser damage in semiconductors. Int. J. Heat Mass Transfer 48, 501–509 (2005)
26. Chen, J.K., Beraun, J.E., Tzou, D.Y.: Investigation of ultrafast laser ablation using a semiclassical two-temperature model. J. Directed Energy 1, 261–274 (2005)
27. Chen, J.K., Tzou, D.Y., Beraun, J.E.: A semiclassical two-temperature model for ultrafast laser heating. Int. J. Heat Mass Transfer 49, 307–316 (2006)
28. Cattaneo, C.: A form of heat conduction equation which eliminates the paradox of instantaneous propagation. Compte Rendus 247, 431–433 (1958)

29. Vernotte, P.: Les paradoxes de la théorie continue de l'équation de la chaleur. Compte Rendus 246, 3154–3155 (1958)
30. Vernotte, P.: Some possible complications in the phenomena of thermal conduction. Compte Rendus 252, 2190–2191 (1961)
31. Joseph, D.D., Preziosi, L.: Heat waves. Rev. Modern Phys. 61, 41–73 (1989)
32. Joseph, D.D., Preziosi, L.: Addendum to the paper on heat waves. Rev. Modern Phys. 62, 375–391 (1990)
33. Özisik, M.N., Tzou, D.Y.: On the wave theory in heat conduction. J. Heat Transfer 116, 526–535 (1994)
34. Tzou, D.Y.: On the thermal shock wave induced by a moving heat source. J. Heat Transfer 111, 232–238 (1989)
35. Tzou, D.Y.: Shock wave formation around a moving heat source in a solid with finite speed of heat propagation. Int. J. Heat Mass Transfer 32, 1979–1987 (1989)
36. Tzou, D.Y.: The effects of thermal shock waves on the crack initiation around a moving heat source. J. Eng. Fracture Mechs. 34, 1109–1118 (1989)
37. Tzou, D.Y.: Thermal shock waves induced by a moving crack. J. Heat Transfer 112, 21–27 (1990)
38. Tzou, D.Y.: Thermal shock waves induced by a moving crack - A heat flux formulation. Int. J. Heat Mass Transfer 33, 877–885 (1990)
39. Tzou, D.Y.: Thermal shock formation in a three dimensional solid due to a rapidly moving heat source. J. Heat Transfer 113, 242–244 (1991)
40. Tzou, D.Y.: Thermal shock phenomena under high-rate response in solids. In: Tien, C.L. (ed.) Annual Review of Heat Transfer, ch. 3, vol. IV, pp. 111–185. Hemisphere Publishing Inc., Washington (1992)
41. Tzou, D.Y.: Fracture path emanating from a rapidly moving heat source - The effects of thermal shock waves under high rate response. J. Eng. Fracture Mechs., 111–125 (1992)
42. Tzou, D.Y.: Experimental evidence for the temperature waves around a rapidly propagating crack tip. J. Heat Transfer 114, 1042–1045 (1992)
43. Tzou, D.Y.: Reflection and refraction of thermal waves from a surface or an interface between dissimilar materials. Int. J. Heat Mass Transfer 36, 401–410 (1993)
44. Tzou, D.Y.: Thermal resonance under frequency excitations. J. Heat Transfer 114, 310–316 (1992)
45. Tzou, D.Y.: Damping and resonance phenomena of thermal waves. J. Appl. Mechs. 59, 862–867 (1992)
46. Cimmelli, V.A., Sellitto, A., Jou, D.: Nonlocal effects and second sound in a nonequilibrium steady state. Phys. Rev. B 79, 14303 (2009)
47. Majumdar, A.: Microscale heat conduction in dielectric thin films. J. Heat Transfer 115, 7–16 (1993)
48. Jou, D., Casas-Vázquez, J., Lebon, G.: Extended irreversible thermodynamics. Rep. Prog. Phys. 51, 1105–1179 (1988)
49. Brorson, S.D., Fujimoto, J.G., Ippen, E.P.: Femtosecond electron heat transport dynamics in thin gold films. Phys. Rev. Lett. 59, 1962–1965 (1987)
50. Fournier, D., Boccara, A.C.: Heterogeneous media with rough surfaces: A fractal approach for heat diffusion studies. Physica A 157, 587–592 (1989)
51. Wang, L.Q., Zhou, X.S., Wei, X.H.: Heat Conduction: Mathematical Models and Analytical Solutions. Springer, Heidelberg (2007)
52. Haji-Sheikh, A., Minkowycz, W.J., Sparrow, E.M.: Certain anomalies in the analysis of hyperbolic heat conduction. J. Heat Transfer 124, 307–319 (2002)

53. Tisza, L.: Sur la supraconductibilite thermique de l'helium II liquide et la statistique de Bose-Einstein. C. R. Acad. Sci. 207, 1035 (1938)
54. Peshkov, V.: Second sound in helium II. USSR J. Phys. 8, 381 (1944)
55. Bertman, B., Sandiford, D.J.: Second in solid helium. Sci. Ameri. 222, 92–101 (1970)
56. Taitel, Y.: On the parabolic, hyperbolic, and discrete formulations of the heat conduction equation. Int. J. Heat Mass Transfer 15, 369–371 (1972)
57. Guyer, R.A., Krumhansl, J.A.: Solution of the linearized Boltzmann equation. Phys. Rev. 148, 766–778 (1966)
58. Tzou, D.Y.: Nonlocal behavior in heat propagation. Int. J. Heat Mass Transfer (in press)
59. Asheghi, M., Leung, Y.K., Wong, S.S., Goodson, K.E.: Phonon-boundary scattering in thin silicon layers. Appl. Phys. Lett. 71, 1798–1800 (1997)
60. Li, D., Wu, Y., Kim, P., Shi, L., Yang, P., Majumdar, A.: Thermal conductivity of individual silicon nanowires. Appl. Phys. Lett. 83, 2934–2936 (2003)
61. Liu, W., Asheghi, M.: Phonon boundary scattering in ultra thin single crystal silicon layers. Appl. Phys. Lett. 84, 3819–3821 (2004)
62. Zhang, Z.M.: Nano/Microscale Heat Transfer. McGraw-Hill, New York (2007)
63. Gad-el-Hak, M.: The fluid mechanics of microdevices – The freeman scholar lecture. J. Fluids Eng. 121, 5–33 (1999)
64. Sondheimer, E.H.: The mean free path of electrons in metals. Adv. Phys. 50, 499–537 (2001)
65. Ziman, J.M.: Electrons and Phonons. Oxford University Press, Oxford (2001)
66. Dingle, R.B.: The electrical conductivity of thin wires. Proc. R. Soc. 201, 545–560 (1950)
67. Gurtin, M.E., Pipkin, A.C.: A general theory of heat conduction with finite wave speeds. Arch. Ration. Mech. Anal. 31, 113–126 (1968)
68. Kaganov, M.I., Lifshitz, I.M., Tanatarov, M.V.: Relaxation between electrons and crystalline lattices. Soviet Phys. JETP 4, 173–178 (1957)
69. Anisimov, S.I., Kapeliovich, B.L., Perel'man, T.L.: Electron emission from metal surfaces exposed to ultra-short laser pulses. Soviet Phys. JETP 39, 375–377 (1974)
70. Wang, L.Q., Xu, M.T., Zhou, X.S.: Well-posedness and solution structure of dual-phase-lagging heat equation. Int. J. Heat Mass Transfer 44, 1659–1669 (2001)
71. Wang, L.Q., Xu, M.T.: Well-posedness and solution structure of dual-phase-lagging heat equation: higher dimensions. Int. J. Heat Mass Transfer 45, 1165–1171 (2002)
72. Antaki, P.J.: Solution for non-Fourier dual phase lag heat conduction in a semi-infinite solid with surface heat flux. Int. J. Heat Mass Transfer 41, 2253–2258 (1998)
73. Jou, D., Criado-Sancho, M.: Thermodynamic stability and temperature overshooting in dual-phase-lag heat transfer. Phys. Lett. A 248, 172–178 (1998)
74. Al-Huniti, N.S., Al-Nimr, M.A.: Thermoelastic behavior of a composite slab under rapid dual-phase-lag heating. J. Thermal Stress 27, 607–623 (2004)
75. Hader, M.A., Al-Nimr, M.A., Abu Nabah, B.A.: The dual-phase-lag heat conduction model in thin slabs under a fluctuating volumetric thermal disturbance. Int. J. Thermophys. 23, 1669–1680 (2002)
76. Quintanilla, R., Racke, R.: A note on stability in dual-phase-lag heat conduction. Int. J. Heat Mass Transfer 49, 1209–1213 (2006)
77. Su, S., Dai, W., Jordan, P.M., Mickens, R.E.: Comparison of the solutions of a phase-lagging heat transport equation and damped wave equation. Int. J. Heat Mass Transfer 48, 2233–2241 (2005)

78. Tang, D.W., Araki, N.: Non-Fourier heat conduction behavior in finite mediums under pulse surface heating. Mat. Sci. Eng. A 292, 173–178 (2000)
79. Tang, D.W., Arakia, N.: Wavy, wavelike, diffusive thermal responses of finite rigid slabs to high-speed heating of laser-pulses. Int. J. Heat Mass Transfer 42, 855–860 (1999)
80. Xu, M., Wang, L.Q.: Dual-phase-lagging heat conduction based on Boltzmann transport equation. Int. J. Heat Mass Transfer 48, 5616–5624 (2005)
81. Carey Van, P.: Statistical Thermodynamics and Microscale Thermophysics. Cambridge University Press, Cambridge (1999)
82. Stupochenko, E.V.: Estimation of the width of the front of strong shock waves in gases. J. Appl. Mech. Tech. Phys. 6, 81–82 (1965)
83. Raitza, T., Reinholz, H., Röpke, G., Mintsev, V., Wierling, A.: Reflectivity in shock wave fronts of xenon. J. Phys. A 39, 4393–4399 (2006)
84. Tzou, D.Y., Chen, J.K.: Thermal lagging in random media. AIAA J. Thermophysics Heat Transfer 12, 567–574 (1998)
85. Qiu, T.Q., Tien, C.L.: Femtosecond laser heating of multi-layer metals – I. Analysis. Int. J. Heat Mass Transfer 37, 2789–2797 (1994)
86. Goldman, C.H., Norris, P.M., Tien, C.L.: Picosecond energy transport by fractons in amorphous materials. In: ASME National Heat Transfer Conference, Portland, Oregon (1995)
87. Ordóñez-Miranda, J., Alvarado-Gil, J.J.: Determination of time-delay parameters in the dual-phase lagging heat conduction model. J. Heat Transfer 132, 061302 1-9 (2010)
88. Tzou, D.Y., Dai, W.: Thermal lagging in multi-carrier systems. Int. J. Heat Mass Transfer 52, 1206–1213 (2009)
89. Chen, P.J., Gurtin, M.E.: On a theory of heat conduction involving two temperatures. Z. Angew. Math. Phys. 19, 614–627 (1968)
90. Chen, P.J., Gurtin, M.E., Williams, W.O.: A note on non-simple heat conduction. Z. Angew. Math. Phys. 19, 969–970 (1968)
91. Youssef, H.M.: Theory of two-temperature-generalized thermoelasticity. IMA J. Appl. Math. 71, 383–390 (2006)
92. Tzou, D.Y.: Heat propagation: Duality of diffusion and waves. In: Panel on Dual-Phase-Lagging Heat Conduction, 1st ASME International Conference on Micro/Nanoscale Heat Transfer, Tainan, Taiwan, January 6-9 (2008)
93. Tzou, D.Y.: Thermal lagging: duality of diffusion and wave in ultrafast transient. In: The 7th International Symposium on Heat Transfer, Beijing, China, October 26-29 (2008)
94. Tzou, D.Y., Chiu, K.S.: Temperature-dependent thermal lagging in ultrafast laser heating. Int. J. Heat Mass Transfer 44, 1725–1734 (2001)
95. Tzou, D.Y.: Computational Techniques for Microscale Heat Transfer. In: Minkowycz, W.J., Sparrow, E.M., Murthy, J.Y. (eds.) Handbook of Numerical Heat Transfer, 2nd edn., pp. 623–657. Wiley, New York (2006)
96. Zhang, J., Zhao, J.J.: High accuracy stable numerical solution of 1D microscale heat transport equation. Comm. Numer. Meth. Eng. 17, 821–832 (2001)
97. Zhang, J., Zhao, J.J.: Unconditionally stable finite difference scheme and iterative solution of 2D microscale heat transport equation. J. Comp. Phys. 170, 261–257 (2001)
98. Zhang, J., Zhao, J.J.: Iterative solution and finite difference approximations to 3D microscale heat transport equation. Math. Comput. Simul. 57, 387–404 (2001)

99. Dai, W., Nassar, R.: A compact finite difference scheme for solving a three-dimensional heat transport equation in a thin film. Numer. Meth. Partial Diff. Eqns. 16, 441–458 (2000)
100. Dai, W., Nassar, R.: A compact finite difference scheme for solving a one-dimensional heat transport equation in microscale. J. Comp. Appl. Math. 130, 431–441 (2001)
101. Dai, W., Shen, L., Nassar, R., Zhu, T.: A stable and convergent three-level finite difference scheme for solving a dual-phase-lagging heat transport equation in spherical coordinates. Int. J. Heat Mass Transfer 47, 1817–1825 (2004)
102. Dai, W., Tzou, D.Y.: A stable finite difference scheme for thermal analysis in an N-carrier system. Int. J. Thermal Sci. 48, 1530–1541 (2009)
103. Dai, W.: A hyperbolic microscopic model and its numerical scheme for thermal analysis in an N-carrier system. Int. J. Heat Mass Transfer 52, 2379–2389 (2009)
104. Chou, Y., Yang, R.-J.: Two-dimensional dual-phase-lag thermal behavior in single-/multi-layer structures using CESE method. Int. J. Heat Mass Transfer 52, 239–249 (2009)
105. McDonough, J.M., Kunadian, I., Kumar, R.R., Yang, T.: An alternative discretization and solution procedure for the dual phase-lag equation. J. Comput. Phys. 219, 163–171 (2006)
106. Chen, J.K., Beraun, J.E., Tzou, D.Y.: A dual-phase-lag diffusion model for predicting thin film growth. Semicond. Sci. Technol. 15, 235–241 (2000)
107. Chen, J.K., Beraun, J.E., Tzou, D.Y.: A dual-phase-lag diffusion model for interfacial layer growth in metal matrix composites. J. Mater. Sci. 34, 6183–6187 (1999)
108. Chen, J.K., Beraun, J.E., Tzou, D.Y.: A dual-phase-lag diffusion model for predicting intermetallic compound layer growth in solder joints. ASME J. Electron. Packag. 123, 52–57 (2001)
109. Helms, C., Deal, B.E. (eds.): The physics and Chemistry of SiO_2 and the Si-SiO_2 Interface. Plenum, New York (1988)
110. Vianco, P.T., Killgo, A.C., Grant, R.: Intermetallic Compound Layer growth by solid state reactions between 58Bi-42Sn solder and copper. J. Electron. Mater. 24, 1493–1505 (1995)
111. Deal, B.E., Grove, S.: General relationship for the thermal oxidation of silicon. J. Appl. Phys. 36, 3770–3778 (1965)
112. Nulman, J.: In-situ processing of silicon dielectrics by rapid thermal processing: Cleaning, growth and annealing. Mater. Res. Soc. Symp. Proc. 92, 141–146 (1987)
113. Blanc, J.: The oxidation of silicon by dry oxygen – Can we distinguish between models? Phil. Mag. B 55, 685–710 (1987)
114. Bjorkman, C.H., Lucovsky, G.L.: Strain Dependent Diffusion During Dry Thermal Oxidation of Crystalline Si. In: Helms, C.R., Deal, B.E. (eds.) The Physics and Chemistry of SiO_2 and the Si-SiO_2 Interface, 2nd edn., pp. 15–21. Plenum, New York (1993)
115. Watanabe, T., Tatsumura, K., Ohdomari, I.: New linear-parabolic rate equation for thermal oxidation of silicon. Phys. Rev. Lett. 96, 196102 (2006)
116. Ganem, J.J., Rigo, S., Trimaille, I.: Modellization of the silicon rapid thermal oxidation in the initial stages according to the silicon fragments model. Microelectronic Eng. 22, 35–38 (1993)
117. Tzou, D.Y.: Lagging behavior in biological systems, Keynote Lecture. In: 2nd ASME International Conference on Micro/Nanoscale Heat Transfer, Shanghai, China, December 18-22 (2009)

118. Liu, K.C., Chen, H.T.: Analysis for the dual-phase-lag bio-heat transfer during magnetic hyperthermia treatment. Int. J. Heat Mass Transfer 52, 1185–1192 (2009)
119. Xu, F., Lu, T.J., Seffen, K.A., Ng, E.Y.K.: Mathematical modeling of skin bioheat transfer. Appl. Mech. Rev. 62, 050801(1-35) (2009)
120. Zhou, J., Chen, J.K., Zhang, Y.W.: Dual-phase lag effects on thermal damage to biological tissues caused by laser irradiation. Computers in Biology and Medicine 39, 286–293 (2009)
121. Zhou, J., Zhang, Y.W., Chen, J.K.: An axisymmetric dual-phase-lag bioheat model for laser heating of living tissues. Int. J. Thermal Sci. 48, 1477–1485 (2009)
122. Xu, F., Seffen, K.A., Lu, T.J.: Non-Fourier analysis of skin biothermomechanics. Int. J. Heat Mass Transfer 51, 2237–2259 (2008)
123. Xu, L.X., Liu, J.: Discussion of non-equilibrium heat transfer in biological systems. In: Clegg, S. (ed.) Advances in Heat and Mass Transfer in Biotechnology, ASME HTD, Vol. 362/BED-Vol. 40 pp. 13–17 (1998)
124. Roetzel, W., Xuan, Y.: Transient response of the human limb to an external stimulus. Int. J. Heat Mass Transfer 41, 229–239 (1998)
125. Zhang, A., Mi, X., Yang, G., Xu, L.X.: Numerical study of thermally targeted liposomal drug delivery in tumor. J. Heat Transfer 131, 043209 (1–10) (2009)
126. Pennes, H.H.: Analysis of tissue and arterial blood temperature in the resting human forearm. J. Appl. Physiol. 1, 93–122 (1948)
127. Vadasz, P.: Heat conduction in nanofluid suspensions. J. Heat Transfer 128, 465–477 (2006)
128. Wang, L.Q., Wei, X.H.: Nanofluids: Synthesis, heat conduction, and extension. J. Heat Transfer 131, 033102 (1-7) (2009)
129. Cao, B.Y., Guo, Z.Y.: Equation of motion of a phonon gas and non-Fourier heat conduction. J. Appl. Phys. 102, 535031–535036 (2007)
130. Guo, Z.Y., Hou, Q.W.: Thermal Wave Based on the Thermomass Model. J. Heat Transfer 132, 072403 (1-6) (2010)
131. Tzou, D.Y., Guo, Z.Y.: Nonlocal behavior in thermal lagging. Int. J. Thermal Sci. 49, 1133–1137 (2010)

Microfluidics: Fabrication, Droplets, Bubbles and Nanofluids Synthesis

Yuxiang Zhang and Liqiu Wang*

Abstract. Present studies include a series of investigations on microfluidics from fabrication to application. In the application this study focuses on some fundamental problems regarding the manipulation of droplets and bubbles inside microfluidics, including the size control during generation, the critical condition for breaking droplets, chaotic mixing inside moving droplets and nanofluids synthesis.

A low-cost fabrication method for manufacturing glass-based microfluidic devices is developed in a routine laboratory without the requirement of a clean room. Direct bonding of glass material is realized without using any additives. The fabrication method is very reliable and the yield is larger than 90%. Channel surface modification from hydrophilic to hydrophobic is realized inside the microfluidic devices after fabrication. With the help of the surface modification, both of the two types of droplets, oil-in-water and water-in-oil, can be generated inside glass-based microfluidic devices.

Droplet formation under controlled flow rates and bubble formation under controlled pressures in confined T-shaped junctions are experimentally investigated by changing thermophysical properties of continuous phases and by changing the controlled dynamic parameters. A pressure-driven mechanism of droplet/bubble formation is experimentally discovered. The influence of the continuous phase thermophysical properties and the controlled dynamic parameters on droplet/bubble volume and formation time is systematically investigated. Empirical correlations are obtained for predicting the droplet volume and formation time.

Droplet breakup in either symmetrically or asymmetrically confined T-shaped junctions is experimentally studied. The critical condition with which microfluidic droplets will break equally is theoretically analyzed based on the pressure-driven mechanism. A semi-empirical correlation is obtained for predicting the equal breakup in symmetric T-shaped junctions. Besides the equal breakup, a new droplet

Yuxiang Zhang · Liqiu Wang
Department of Mechanical Engineering, The University of Hong Kong,
Pokfulam Road, Hong Kong
e-mail: lqwang@hku.hk

* Corresponding author.

L.Q. Wang (Ed.): Advances in Transport Phenomena, ADVTRANS 2, pp. 171–294.
springerlink.com

breakup pattern, unequal breakup, is observed in the symmetric T-shaped junction. In asymmetric T-shaped junctions the droplet breakup is found to be very difficult.

Scaling analysis of the chaotic mixing inside moving droplets is conducted based on the idealized recirculating flow and the Baker's transformation. Experimental investigations on the mixing efficiency inside the droplets moving in curved microchannels are performed with the help of the micro visualization system. It is found that the mixing efficiency is significantly enhanced by the chaotic advection inside the moving droplets and the full mixing time can be reasonably estimated by the scaling analysis. A significant mixing enhancement during the droplet formation process is observed, which is not so frequently reported by others. An effective microstructure is designed for mixing two or more individual droplets after their formation.

Synthesis of copper nanofluids is realized in microfluidic reactors. In contrast to the traditional method, the copper nanofluids synthesized in the microfluidic reactors have a narrower size distribution. The synthesis time is also reduced by one order of magnitude. It is also found that the particle size and size distribution are insensitive to the flow rate of reactants, the reactants concentration and the surfactant concentration.

1 Introduction

1.1 Background

Microfluidics refers to devices where precise control and manipulation of fluids are geometrically constrained to a small scale, typically larger than one micron but less than one millimeter [1]. From historical point of view, microfluidics can be regarded as a branch of micro-electrical-mechanical system (MEMS) because the fabrication method of microfluidics is borrowed from MEMS industry in the early days and both of them function at the microscale [2-4]. Microfluidics has been remarkably developed since 1980s, triggered by the generalization of ink jet printing because of the high demand on fast and cheap portable devices able to perform chemical and biological analysis [5]. When microfluidics is combined with electric, magnetic, optic or acoustic elements, it will build up an even more powerful microsystem which is called Lab-On-a-Chip (LOC) or micro-Total-Analysis-System (μ-TAS) by researchers in chemical society [6]. Microfluidic technologies hold great promise as it can perform typical laboratory reactions using a fraction of reagents in significantly reduced time. Compared to conventional techniques, the use of microfluidics has many advantages, such as the significantly reduced consumption of samples and reagents, fast screening time and narrow distribution of residence time due to the fast and uniform mixing, and decreased risk of the manipulation of toxic and harmful reagents [7]. One subcategory of microfluidics is droplet/bubble-based microfluidics involving manipulation of discrete droplets and bubbles inside microfluidics. Microfluidics has the natural superiority to generate uniform droplets and bubbles in a controllable way because of its microscale dimensions and the easily controlled

laminar flow inside. Different from continuous flow systems, droplet-based microfluidics allows for independent control of individual droplets, so that the droplets and bubbles can be individually transported, mixed, and analyzed as microreactors [8-12]. The diameter of bubbles and droplets generated in microfluidics ranges from several micrometers to hundreds of micrometers, resulting in the volume ranging from femtoliters to nanoliters. In such small volume, the reagents consumption is even reduced and the mixing efficiency is further enhanced, which facilitates fast reactions and examinations in chemical synthesis and biochemical analysis [9, 13-18].

1.2 Microfluidics Fabrication

Fabrication methods of microfluidic devices depend on the selected materials. In general, all fabrication methods include two steps: fabricating the desirable microstructures and sealing the opened structures fabricated with proper covers, which is normally called bonding. Microfluidic devices in the earliest reports have relied on quartz material, e.g. silicon and glass, as the mature micromachining technology borrowed from the well developed semiconductor industry [19-21]. Micromachining of silicon and glass are mainly relied on photolithography, wet or dry etching, and a variety of other techniques, all of which require the use of clean-room facilities and equipments [22]. Recently, polymer materials tend to be popular for fabricating disposable microfluidic devices as their potentially low manufacturing cost and the ease of mass production for chemical and biochemical applications. The most widely used polymers are polydimethylsiloxane (PDMS) [23-25], SU-8 [26-29] and poly(methylmethacrylate) (PMMA) [30-32]. Microstructure fabrication of polymer usually needs a mold to replicate the designed microstructures by either casting (e.g. PDMS) or hot embossing (e.g. PMMA), but for photosensitive polymers (e.g. SU-8) the mold is not necessary as microstructures can be fabricated by photolithography [33-35]. In the following sub-sections we generally outline the fabrication methods for quartz material and different polymers. Three most reported polymers, PDMS, PMMA and SU-8, are taken as examples to illustrate the fabrication methods of polymer materials.

1.2.1 Photolithography Technology for Processing Quartz Material

The general procedure of photolithography for processing quartz material is outlined in Fig. 1. A clean and polished substrate can be a silicon or glass wafer (Fig. 1 (a)). A layer of photoresist is first coated on the flat surface of the substrate and then exposed to UV light (or electron beams) through a photo-mask with desirable microstructures (Figs. 1 (b) and (c)). Under UV light, the exposed photoresist changes its solubility in the following development process, compared to the unexposed part. After development, the desirable microstructures are revealed, where the substrate material is ready for etching (Fig. 1 (d)). The remained photoresist material will protect the uncovered area of the substrate from etching

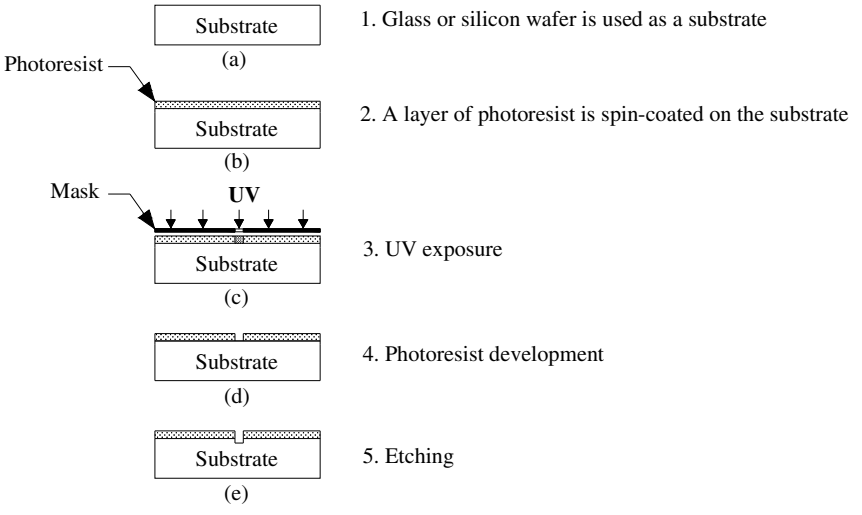

Fig. 1 General procedures of photolithography for processing quartz material

(Fig. 1 (e)). Etching process can be either dry etching using plasma or wet etching using chemical solutions (HF solution) depending on the requirement of the accuracy of the microstructure. Dry etching usually gives a higher resolution and straight sidewalls of the microchannels fabricated, and the smallest micro-feature can be on the scale of nanometer, but the cost is high and the expensive etching machine is necessary [22]. Wet etching in chemical solution usually gives a relatively low resolution and curved sidewalls. The smallest micro-feature can be only on the scale of micrometer, but the cost is pretty low [36-38].

1.2.2 Casting

Casting is the most widely reported method for fabricating polymer microfluidics, which is also referred as soft lithography, a term coined by Whitesides and coworkers [39-43]. PDMS microstructures are normally fabricated by using this method. A typical fabrication process is shown in Fig. 2. PDMS is a kind of elastomer, on which if an external force is acted the polymer will have an elastic deformation and will return to its original shape as soon as the external force is withdrawn [34]. Before casting, PDMS prepolymer is mixed with its curing agent at a certain volume ratio according to its operation manual. At this stage, the mixture is still liquid because the curing effect is slow at room temperature (thorough curing is normally finished in about 48 hours in room temperature), but in elevated temperature the curing is much faster, for instance 2 hours at 60°C and 30 minutes at 115 °C (Becker and Gartner 2008). The mixture is then simply poured over a master and cured in a furnace in a temperature range of 40-80 °C [25, 44, 45].

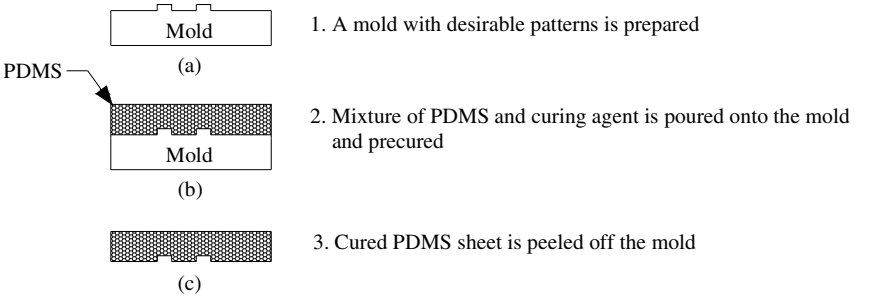

Fig. 2 Schematic illustration of PDMS casting

The stiffness of PDMS microfluidic devices is controlled by the curing temperature and the ratio of the curing agent to PDMS prepolymer. After curing, the PDMS sheet is peeled off the master. Channel inlets and outlet can simply be realized by punching into the cured material at proper locations with a suitable needle. With this method, three-dimensional microstructures can be built up by bonding such two-dimensional sheets layer by layer [23, 25, 42].

1.2.3 Hot Embossing

Hot embossing is a technique that involves the use of thermoplastic materials, typically in a format of flat sheets which are patterned against a master (stamp) by using pressure and heat [30, 46]. PMMA is a representative of thermoplastic materials (one kind of polymer) that can be structured using hot embossing [32]. Figure 3 shows a schematic diagram of a hot embossing machine. The process consists of the following steps: (1) the master and the polymer substrate (sheet material) are placed in the system and heated in vacuum to a temperature just above the glass transition temperature of the polymer material; (2) the master is then pressed into the polymer substrate under some pressure which is depended on channel design, polymer properties and master material; (3) the Master and the substrate are isothermally cooled to a temperature just below the glass transition temperature and then separated.

1.2.4 Injection Molding

Injection molding is a process widely used in the plastics industry to produce a variety of everyday objects [46-49]. Figure 4 schematically shows a diagram of an injection molding machine. The polymer material is fed as pre-dried granules into the hopper. In the heated barrel, a screw transports the material towards the injection port, during which the thermoplastic (e.g., PMMA, PC) are melted (200–350 °C) and injected under high pressure (typically between 600 and 1,000 bar) into the heated mold cavity of the molding tool. For accurate microstructure

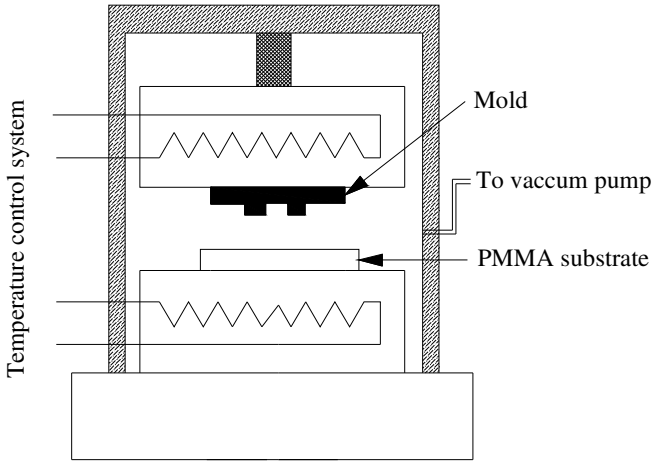

Fig. 3 Schematic diagram of a hot embossing machine

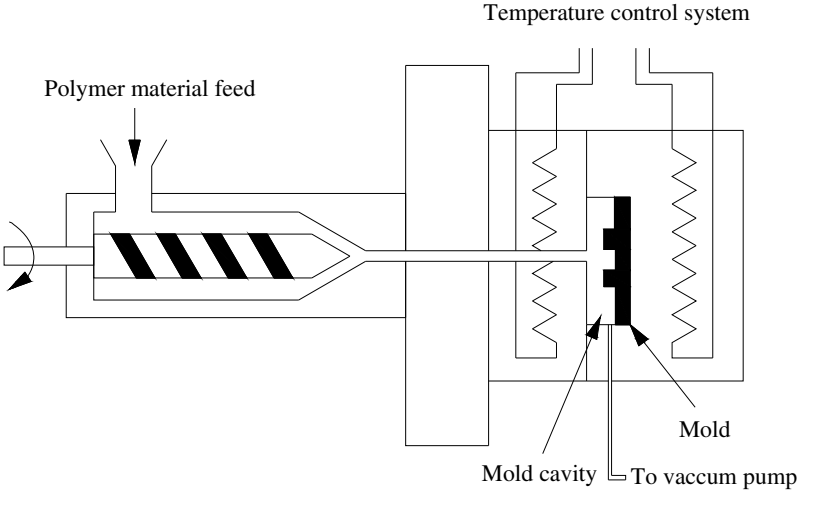

Fig. 4 Schematic diagram of an injection molding machine

replication, the mold cavity has to be vacuumed to achieve a good filling of the mold and to prevent the formation of air bubbles. The injected pieces are then cooled below glass transformation temperature of the material and separated from the mold.

1.2.5 Photolithography for SU-8

Photolithography is frequently used to manufacture SU-8 microfluidic devices. SU-8 is a relatively new photosensitive material capable of developing thick photoresist structures in a single photolithographic step [27, 28, 50-52]. The aspect ratio of the microchannels fabricated by SU-8 can be over 25 [53, 54] and the sheet depth is up to 1.5 mm in a single coating step [55]. When it is exposed to UV light, very strong cross-linking takes place in a process of cationic polymerization, which offers high mechanical strength and excellent thermal and chemical stabilities. Figure 5 schematically illustrates a typical fabrication process using SU-8. First, a layer of SU-8 is spin-coated onto a substrate (Figs. 5 (a) and (b)), silicon or glass wafer. The layer thickness is controlled by the spinning velocity. The coated wafer is then transferred to a hot plate or an oven for soft baking at around 90 °C for

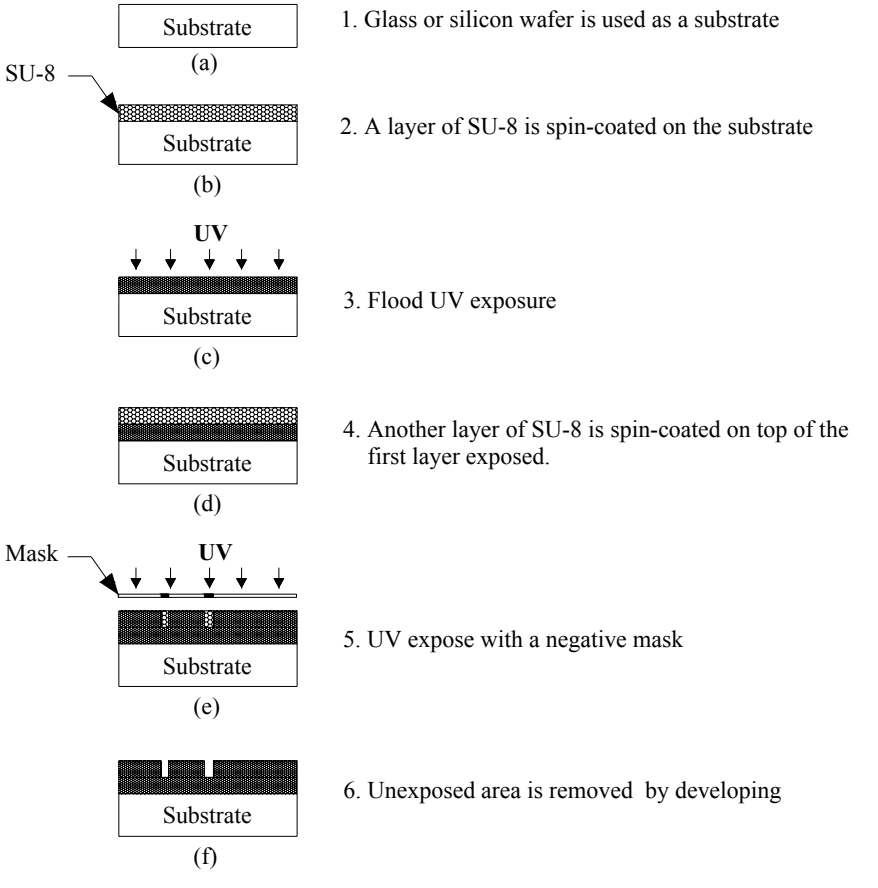

Fig. 5 General procedures of photolithography for processing SU-8

several minutes, depending on SU-8 species, aiming to increase its stiffness and get ready for the next step–flood UV exposure (Fig. 5 (c)). After flood UV exposure, the exposed SU-8 becomes cross-linked and hardened and will be remained after development. In the next step, another SU-8 layer is spin-coated on the top of the previous exposed one, followed by the same soft baking as the previous one (Fig. 5 (d)). The second coated SU-8 layer is then exposed to UV light under a mask with designed microstructures (Fig. 5 (e)), where the exposed SU-8 will be cross-linked and hardened. One more baking, post baking, is employed for further increasing SU-8 layers' stiffness. Finally, the two layers are developed in SU-8 developer in order to remove the unexposed part and uncover the microstructure features (Fig. 5 (f)). The developed SU-8 microstructures can be simply peel off the base wafer.

1.2.6 Microfluidics Bonding

No mater what kinds of material are used, the fabricated microstructures have to be sealed to a cover in order to close the channels for fluid flow, which is called bonding [3, 4, 6, 32, 56]. Bonding methods can be clarified into two catalogues: direct bonding and adhesive bonding. In the direct bonding, the substrate with microstructure and the cover are directly bonded together, and no other material is introduced between them. The direct bonding can be realized by either self stickiness for polymers [23, 24, 45, 57] or thermal bonding [31, 58] and anodic bonding for quartz material with the help of electric field [22]. In the adhesive bonding, a third layer of material is introduced between the microstructure substrate and the cover plate. The third layer material can be glues [37, 59], or other curable polymer materials that can bond the two plates after being cured [60, 61].

1.3 Microfluidic Droplet Manipulations

In microfliudics, droplet manipulation has attracted much more attention compared with bubble manipulation. In fact, the manipulation methods for droplets and bubbles are quite similar. The following discussion on droplets is also applicable to bubbles. Droplet manipulation inside microfluidics mainly involves droplet generation, droplet fission and droplet fusion [62, 63]. The droplet generation means generating droplets inside microfluidics [64-67]. The droplet fission, also called droplet breakup, means splitting one mother droplet into two or more daughter droplets with smaller sizes [68-70]. The droplet fusion stands for controlled coalescence of droplets inside microfluidics at desirable locations [15, 71]. All those manipulations can be realized in either active or passive ways. By the active ways, the droplet manipulation is realized under the external forces induced by piezoelectric transducer, pneumatics, electric field, etc. By the passive ways, there are no movable parts or actuators inside microfluidics, and the droplet manipulation is fully controlled by droplet size, channel geometry and local flow field. In present studies, we focus on using the passive ways to realize some

manipulation of droplets and bubbles inside microfluidics. For active manipulation readers can refer to several reviews and books [5, 62, 63].

1.3.1 Droplet Generation

In droplet generation, the fluid used to be dispersed is commonly named as dispersed phase, and the fluid carrying droplets is named as continuous phase. The introduction of the dispersed phase and the continuous phase relies on pressure-driven flow accomplished by syringe pumps or other high pressurized sources. Droplets are formed under the influence of the local flow field that highly depends on the local geometrical structures of the microfluidics. Many microfluidic structures have been demonstrated in generating droplets effectively, including straight microchannel arrays [72-75], flow focusing devices [65, 71, 76], microcapillary tubes [77-80], and microchannel T-shaped junctions [66, 67, 81-85]. Depending on the flow field at the location where the two phases meet, those structures can be categorized into three groups: (1) co-flowing configuration (Fig. 6 (a)), (2) flow focusing configuration (Fig. 6 (b)) and (3) cross-flowing configuration (Fig. 6 (c)).

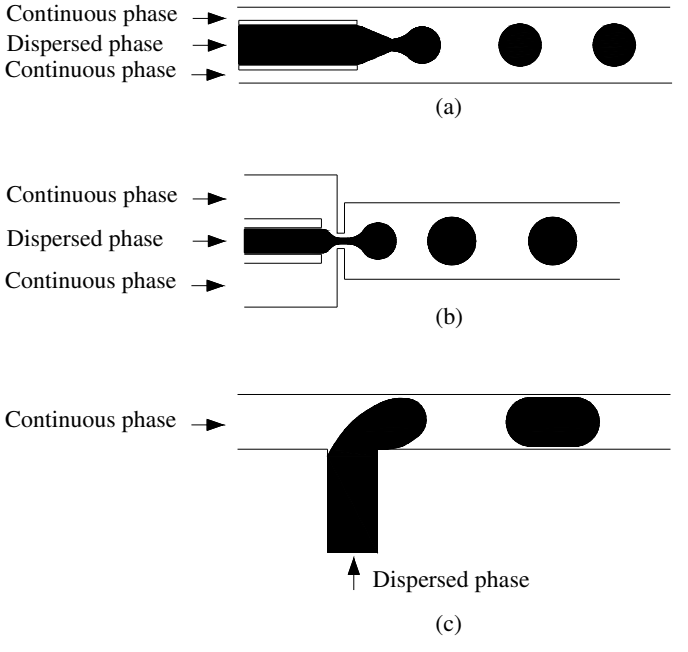

Fig. 6 Flow configurations for generating droplets and bubbles in microfluidics: (a) co-flowing configuration, (b) flow focusing configuration and (c) cross-flowing configuration.

Although all the structures have been demonstrated to be capable of generating uniform droplets, the understanding of controlling parameters regarding droplet size and formation time is quite limited. In general, the droplet formation is characterized by the competition between the local stresses acting to detach the forming interface and the capillary pressure acting to stabilize the forming interface. Due to the confinement of the local structure, a dramatic increase of the upstream pressure is usually reported as a driving stress to detach the forming interface. In the co-flowing and flow focusing structures, two different regimes of droplet formation–dripping and jetting–have been discovered depending on the continuous phase velocity [86-89]. When the continuous phase velocity is low, the forming droplet will be released near the outlet tip of the inner channel and the droplet size is relatively big. As the continuous phase velocity increases, the forming droplet will be released at a long distance downstream to the mouse of the inner channel and the droplet size is relatively small. Cramer et al. (2004) performed experimental investigation on the effect of flow rates, fluid viscosities and interfacial tensions on the droplet size in the dripping regime by using a capillary tip immersed in a continuous co-flowing liquid [86]. In the experiments, they found the droplet size decreased monotonically with increased continuous phase velocity, and increased with decreasing interfacial tension. The viscosity of the dispersed phase had little influence on the droplet size in a wide range of continuous phase velocity. Umbanhowar et al. (2000) conducted a similar experiment, and proposed a scaling analysis of droplet size by taking the whole forming droplet as the investigating object on which a force balance model was applied [64]. Based on their scaling model, the predicted droplet size was independent of the dispersed phase viscosity and decreased as the interfacial tension decreased. It is seen that this result agrees to the result reported by Cramer et al. (2004) [86] on the influence of the dispersed phase viscosity, but conflicts with the influence of the interfacial tension.

The microfluidic flow-focusing configuration is first proposed by Anna et al. (2003) [65], and then widely employed to generate droplets [71, 76, 90-92] and bubbles [93, 94]. At present time, no simple model has been reported on predicting either droplet or bubble size, as a function of controlling parameters such as flow rate ratio, fluid viscosity and interfacial tensions. Additionally, in the work reported by Ward et al. (2005), the droplet size was found to be significantly influenced by the control manner of the dispersed phase and the continuous phase, under controlled flow rates or under controlled pressures [91]. In either control manner, the droplet size cannot be simply predicted by the pressure ratio or flow rate ratio of the dispersed phase to the continuous phase. Bubble size was experimentally investigated by Garstecki et al. (2004) in the flow-focusing configuration [93]. The bubble volume was found to be proportional to the gas driven pressure and inversely proportional to the product of flow rate and viscosity of the continuous phase. The authors proposed a bubble formation mechanism that the bubble detachment is fully driven by the pressure increase in the continuous phase before the orifice, resulting from the blockage of the orifice by the forming interface.

T-shaped junction is the most frequently reported structure for utilizing cross-flowing configuration. Most microfluidic T-shaped junctions can be classified into two groups according to their geometrical characteristics: unconfined T-shaped junctions and confined T-shaped junctions [95]. In the unconfined T-shaped junctions, the main channel size is much larger than the lateral channel size such that the growing droplets can freely develop before detaching, whereas in the confined T-shaped junctions the main channel size is comparable with the lateral channel size and the forming droplets will be seriously confined by the main channel walls. In unconfined T-shaped junctions, a force or torque balance model is frequently mentioned to predict droplet volume, which states that the droplet will detach when all possible forces exerted on it reach equilibrium [83, 85]. Husnty et al. (2006) argued that the droplet detachment will occur when the drag force exerted on the forming droplet by the continuous phase flow overcomes the interfacial tension force resisting the detachment [85]. According to their results the droplet size wholly depends on the capillary number and the hydraulic diameter of the main channel. Xu et al. (2005) argued that another two forces, dynamic lift force and buoyancy force, should be included as the detaching forces that facilitate the droplet detachment, and a torque balance model was adopted to predict the droplet size in their work [83]. The droplet size predicted by either the force balance or the torque balance model agreed well with their experimental results, respectively. In the confined T-shaped junctions, however, the force balance model is not applicable any more, which has been noted by many researchers recently [82, 84, 96, 97]. Experimental investigation of droplet size in confined T-shaped junction was first implemented by Thorsen et al. (2001) under controlled-pressure driven of the dispersed and continuous phases [81]. They proposed a simple analysis of the droplet diameter based on the assumption that droplets should detach when the viscous stresses exerted on the forming droplet overcome the interfacial tension, resulting in the droplet diameter inversely proportional to the capillary number. Garstecki et al. (2006) argued that a significant pressure increase would occur in the upstream continuous phase flow as the forming droplet blocked the continuous phase flow at low capillary number, and the droplet detachment was mainly induced by the pressure increase rather than viscous stresses [84]. Such pressure increase was verified in a recent numerical simulation [97]. In the work reported by Garstecki et al. (2006), the droplet size was depended on the flow rate ratio of dispersed phase to continuous phase and on the main channel width. The fluid properties of either dispersed phase or continuous phase did not influence the droplet size. But in the simulation work it was found that both the increased pressure and the continuous phase properties played an important role on determining the droplet size [97]. Van der Graaf et al. proposed an empirical model based on the numerical simulation and experiments [82, 96, 98]. They experimentally observed that the droplet volume consists of two parts, a critical volume coming from the initial expansion of the forming droplet and a necking volume coming from the detaching process. By using the two reference values from

simulation, reference volume and reference necking time, an empirical correlation was proposed to predict the droplet volume [96].

1.3.2 Droplet Fission and Droplet Fusion

Droplet fission, shown in Fig. 7, has been realized inside microfluidics by using either symmetric or asymmetric T-shaped junctions [68, 70]. They found that not all mother droplets would break up in the symmetric T-shaped junction. Only when the deformation of the mother droplet is large enough, the droplet breakup occurs. Such critical condition was discussed by Link et al. (2004) based on the competition between shear stresses and interfacial tensions on the deforming droplet according to the Rayleigh-Plateau instability in which a cylindrical liquid thread can reduce its total surface area by breaking when its length exceeds its circumference [68]. Theoretical studies of the critical condition in two-dimensional T-shaped junctions were conducted based on lubrication analysis with a simple geometrical construction by Leshansky and Pismen (2009) [99].

Droplet fusion inside microfluidics has been accomplished in a sudden expansion or in a gradual expansion in the channels where droplets are translated [15, 100, 101]. Figure 8 schematically shows the fusion process in the sudden expansion and in the gradual expansion. In the expansions the upstream droplet move faster than the downstream droplet, making the upstream droplet catch up and finally fuse with the downstream one after certain time. The fusion process is quite complex and is totally determined by the changing local flow field. The quantitative investigation of such fusion process is very limited.

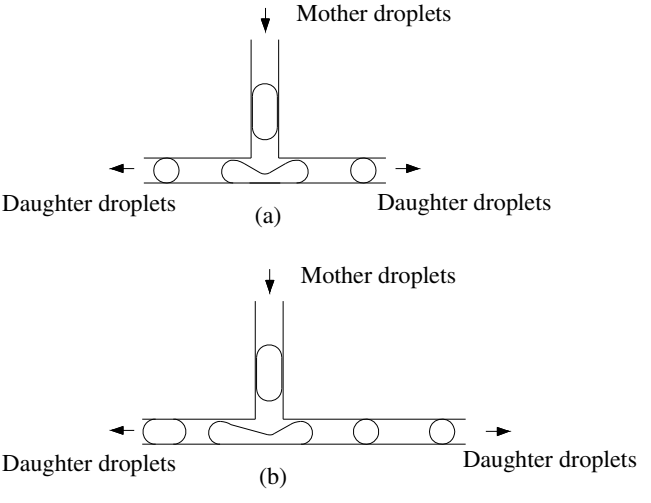

Fig. 7 Droplet fission in T-shaped junctions: (a) equal breakup in a symmetric junction and (b) unequal breakup in an asymmetric junction

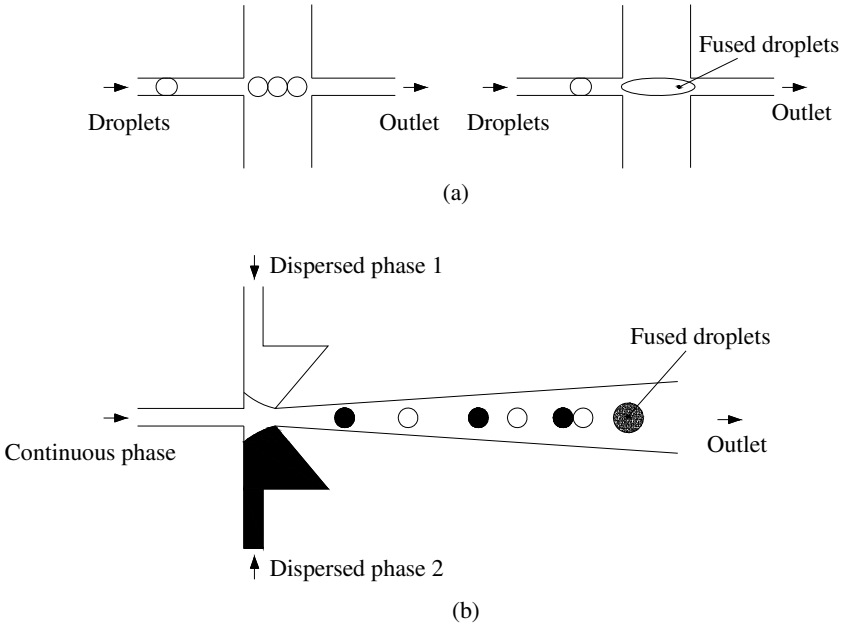

Fig. 8 Droplet fusion in expansions: (a) a sudden expansion and (b) a gradual expansion

1.4 Microfluidics Application

Microfluidics has been widely used in the bio-/chemical society for fast reactions and high resolution screenings [7]. In microfluidics, reactions occur in an environment of controllable laminar flow over microscale dimensions. The molecular diffusion over such small scale is much faster than in conventional reactors (e.g. beakers), and the temperature variation and unequal mixing over such small scale is dramatically reduced. Almost all the reactions conducted in microfluidics take the advantage of the fast and uniform mixing over such microscale dimension. In microflulidic droplets, the reaction scale is further reduced and the mixing efficiency and uniformity are further enhanced due to the chaotic advection inside moving droplets. The other benefits of microfluidic droplets for conducting reactions include the confinement of the interfaces preventing the material inside from possible contaminations outside, narrow residence time distribution, transport and manipulation of each individual droplet-reactor, and tiny reagents consumption [7, 62, 102]. Tens of thousands chemical reactions and biochemical assays have been reported by using microfluidic methods in either single phase flow or moving droplets, including enzyme assays [103], biological screening [17, 104], protein crystallization [105, 106] and many others [62, 107, 108]. Recently microfluidic reactors have been successfully used to manufacture new materials such as micro/nano-particles with

desirable shapes [8, 109-113] and uniform nanocrystals [114-118]. Besides bio-/chemical applications, microfluidic droplets have also been successfully used to fabricate monodispersed emulsions that are widely used in cosmetic, pharmaceutical and food industries [72, 119, 120]. The polydispersity of the droplets generated by microfluidics, defined as the standard deviation of the size distribution divided by the mean size, can be as small as 1%, which significantly increases the emulsion's stability.

1.5 Organization of Present Work

From the above introduction to the manipulation of droplets inside microfluidics, it is seen that there are many arguments over the mechanism of the droplet formation and breakup in microfluidics. In addition, though many applications have been successfully demonstrated relying on the fast mixing inside droplets, the quantitative investigation of the mixing efficiency inside droplets seems inadequate. In present work we try to answer some fundamental questions regarding the droplet formation and breakup (i.e. fission) in microfluidic T-shaped junctions, as well as chaotic mixing inside moving droplets, with the help of micro visualization system. In order to generate and observe the droplets and bubbles inside microfluidics, a low-cost fabrication method for manufacturing transparent glass-based microfluidics is developed in a routine laboratory without clean-room requirement. Besides the fundamental studies regarding droplets and bubbles, the application of microfluidic reactors in synthesizing nanofluids is also studied. The influences of the reaction conditions on the nanoparticles dispersed in the nanofluids are systematically investigated.

Present work consists of seven parts: introduction, glass-based microfluidics fabrication, droplet and bubble formation in confined T-shaped junctions, droplet breakup in confined T-shaped junctions, chaotic mixing in moving droplets, nanofluids synthesis in microfluidics, and conclusion.

In part 1, some background information regarding microfulidics fabrication, droplet manipulation and microfluidics application is presented. Finally, contents of present studies are outlined.

In part 2, glass-based microfluidics fabrication is discussed in more detail. A low-cost and efficient fabrication method for fabricating glass-based microfluidics is developed in a routine laboratory without clean-room requirement. Transparent glass-based microfluidic devices with high chemical and mechanical resistance are fabricated out. Channel surface modification from hydrophilic to hydrophobic is realized inside the microfluidic devices after fabrication.

In part 3, droplet formation under controlled flow rates of dispersed phase and continuous phase is experimentally investigated in a confined T-shaped junction. Bubble formation under controlled gas inlet pressures and controlled flow rates of continuous phase is experimentally studied. The influences of continuous phase viscosities and interfacial tensions on droplet/bubble volume and formation time are systematically investigated. The relationship between droplet volume and droplet

formation time is developed and experimentally confirmed. Two empirical correlations are obtained for predicting the droplet volume and droplet formation time, respectively. The influences of the controlling parameters on the bubble formation regime, bubble volume and bubble formation time are also studied.

In part 4, droplet breakup in either symmetrically or asymmetrically confined T-shaped junctions is experimentally studied. Scaling analysis of the critical condition where mother droplets can break is performed based on a pressure-driven-breakup mechanism, which is also experimentally verified. A new droplet breakup pattern is found in the symmetrically confined T-shaped junction.

In part 5, chaotic mixing inside moving droplets in curved channels is experimentally studied. Scaling analysis of the full mixing time based on idealized recirculating flow is performed and can give a reasonable estimation of the full mixing time inside moving droplets. An effective microstructure for mixing two individual droplets (i.e. droplet fusion) is proposed and experimentally tested within a wide range of flow conditions.

In part 6, copper nanofluids synthesis is realized in microfluidic reactors and is compared with the ones synthesized in beakers by traditional methods. Some new features of the copper nanoparticles are found. The particle size synthesized in the microfluidic reactors is quite stable and uniform, and is insensitive to the flow rates of reagents, reagents concentration and surfactant concentration.

In part 7, conclusion of present studies is presented.

2 Glass-Based Microfluidics Fabrication

2.1 Introduction

Glass-based microfluidic devices have many advantages compared with polymer microfluidic devices when exposed to extreme operating conditions. Glass material has excellent performance in chemical resistance, thermal resistance and mechanical strength. Moreover, glass material is inert to most organic/inorganic solutions, while polymers (e.g. PMMA, PDMS and PC) will be swollen when exposed to organic solutions. The bonding strength of glass material at high temperature is up to 12 MPa [121]. The bonding strength of polymer is much lower, which limits its application to the hydrodynamic field where the pressure is normally very large compared with the polymers bonding strength. In addition, PDMS microstructure will have large deformation when exposed to high pressure due to its high elasticity. Additionally, the mold involved in many fabrication methods of polymer microfluidics is usually made of glass/silicon by using traditionally photolithographic technology [46, 122, 123]. In our studies, we mainly focus on investigating the manipulation of droplets and bubbles, chaotic mixing inside droplets and nanofluids synthesis in microfluidic devices by utilizing micro visualization technology, which requires the microfluidic devices to have such properties that they must be transparent to visible light and resistant to high pressure

(maximum pressure is about 7 bars in our experiments) for long time running. Therefore glass-based microfluidic devices are much more suitable for our research considering its excellent transparency, mechanical strength and chemical resistance.

2.2 Glass-Based Microfluidics Fabrication

Figure 9 shows the protocols developed in our laboratory for fabricating glass-based microfluidic devices. The main steps involve substrate preparation (Fig. 9 (a)), mask fabrication (Fig. 9 (b)), UV exposure, developing and chrome removing (Figs. 9 (b)-(d)), wet etching and channel characterization (Figs. 9 (e) and (f)), thermal bonding (Fig. 9 (g)), and connectors adhesion (Fig. 9 (h)). In addition,

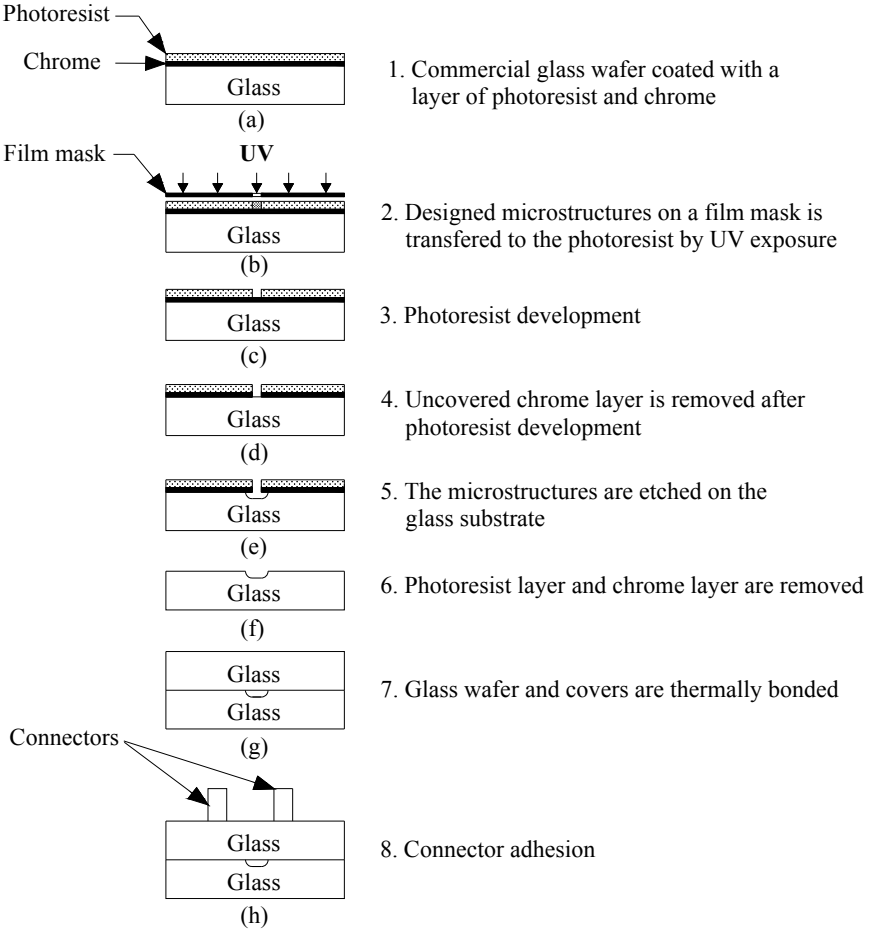

Fig. 9 Protocols for fabricating glass-based microfluidic devices

to generate aqueous droplets inside glass-based microfluidic devices, modification of the wetting ability of channel walls must be applied. In the following sections, we will discuss each step in detail for a better understanding of the device fabrication.

2.2.1 Chemicals

Chemicals used in the fabrication process of glass-based microfluidic devices include hydrofluoric acid (HF), ammonia fluoride (NH_4F), perchloric acid (HCl), perchoric acid ($HClO_4$), ammonium cerium nitrate ($(NH_4)_2Ce(NO_3)_6$), sodium hydroxide (NaOH), acetone (C_3H_6O) and ethanol (C_2H_6O). All chemicals are analytical grade and bought from Tianjin Damao Chemical Reagent factory, China.

2.2.2 Substrate Preparation

In order to do selective etching, a layer of photoresist must be coated on glass substrate to protect the undesirable glass area from etching. To further increase the adhesion force and protect the designed microstructure, a thin metal layer, such as chrome, is normally deposited between glass substrate and photoresist layer before coating photoresist [22, 35], because any shedding of photoresist will cause deathful damage to the designed microstructure in wet etching process. Those preparation processes need expensive facilities such as spinner for coating photoresist and vacuum evaporator for metal deposition.

In our studies, we use commercial glass wafers on which chrome and photoresist have already been coated. Therefore the complex preparation procedures and expensive facilities are not necessary any more. Such commercial glass wafers (SG2506) are bought from Shaoguang Chrome Blank Co. Ltd., China, and are shown in Fig. 10 (a). On the top of the glass wafer, a layer of 145 nm chromium and a layer of 570 nm positive photoresist AZ-1805 have already been deposited uniformly. The commercial glass wafers have an identical length and width of 62 mm, and the thickness is 1.7 mm. Glass wafers without any coating will be served as covers to seal the etched microchannels and are also bought from this company, shown in Fig. 10 (b).

2.2.3 Mask Fabrication

Masks used in our studies are provided by Shenzhen New Way electronics Co. Ltd and are shown in Fig. 11. The masks are made of transparent plastic films, measuring 60×60 mm^2, on which microstructure design is printed by using high resolution photo-plotter. As the photoresist (AZ-1805) coated on the glass wafer is positive photoresist, positive film mask must be used. When the film mask is exposed to UV light, therefore, the light can only penetrate though the designed microstructure and in other places the light will be blocked. Figure 12 explains the final etched channels at the different combinations between the positive and negative mask and the positive and negative photoresist. In our design, the minimum channel width on the film mask is always larger than 10 μm which is

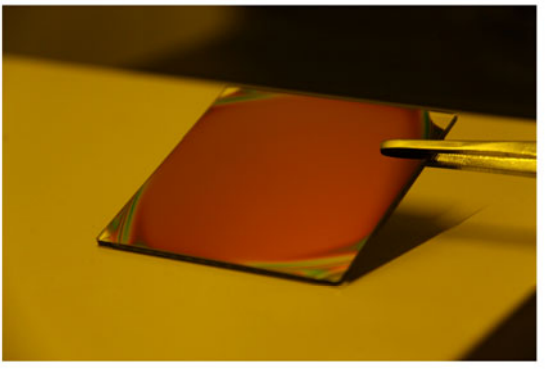

(a) coated glass wafer (substrate)

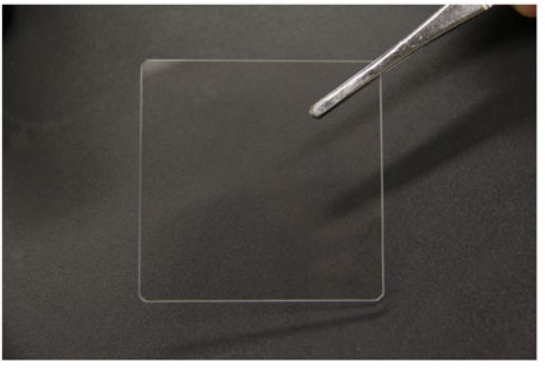

(b) uncoated glass wafer (cover)

Fig. 10 Coated and uncoated glass wafers

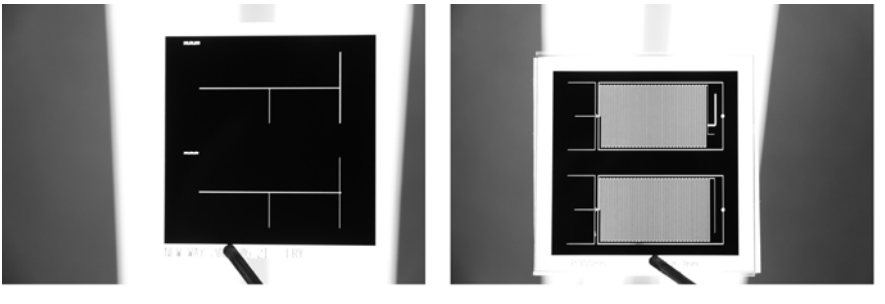

Fig. 11 Film masks

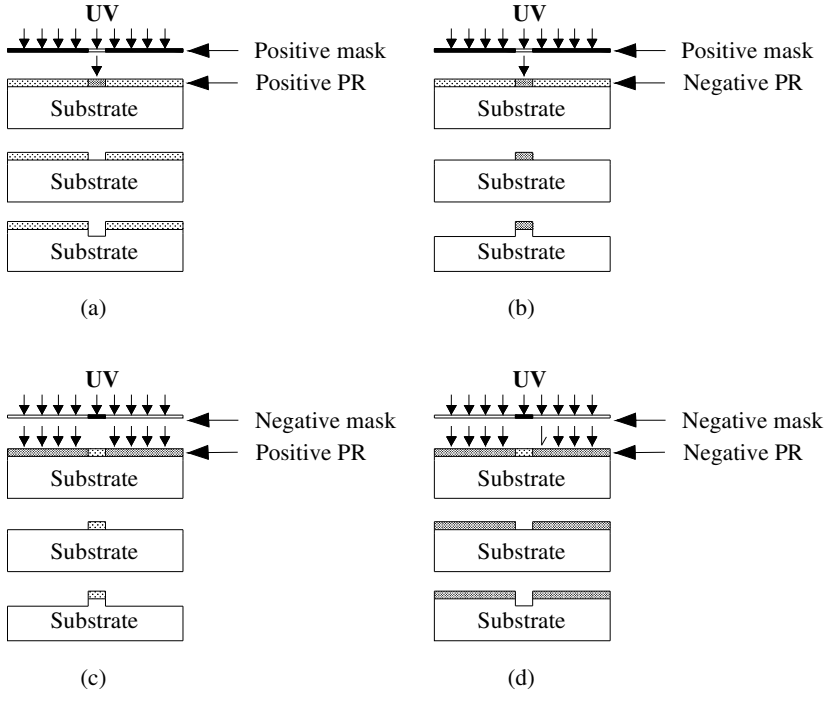

Fig. 12 Microstructures etched at different combinations of mask and photoresist: (a) positive mask and positive photoresist; (b) positive mask and negative photoresist; (c) negative mask and positive photoresist; (d) negative mask and negative photoresist

constrained by two limitations. The first one is the limitation of the photo-plotter resolution (3000 dpi). By examining the provided film mask, it is found that when the channel width is 10 μm the channel quality is not stable and channel blockage is found in some cases as shown in Fig. 13. This problem can be resolved by using a photo-plotter with even higher resolution, but the cost will be much higher. The second constrain is the exposing efficiency. It is found that when the channel width on film masks is 10 μm failure of exposure can happen in some cases. This may be resulted from inadequate dose of UV light, probably caused by the diffraction or interference when the UV lights pass through such narrow channel.

2.2.4 UV Exposure, Developing and Chrome Removing

A contact exposure is employed in an UV exposure unit (LV204, Mega Electronics Ltd., UK), the expensive mask aligner is not necessary. Since the photoresist is sensitive to UV light, this step and the following fabrication steps until preparation of inlets and outlets must be conducted in a dark room (under yellow light). During

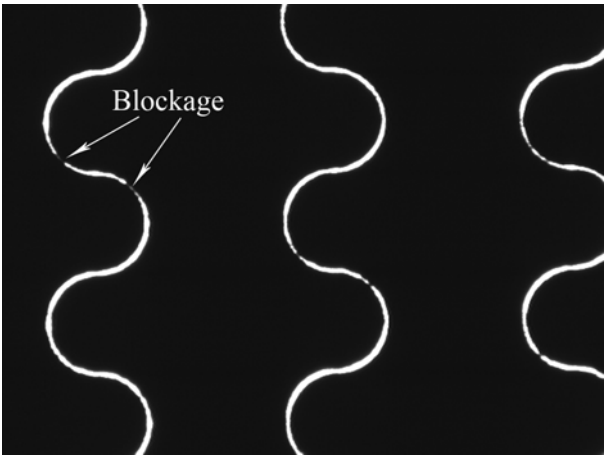

Fig. 13 Channel blockage on film mask

UV exposure, we make the film mask surface on which ink is printed contact with photoresist layer closely in order to transfer designed microstructures and channel width as accurate as possible (Fig. 14 (a)). The exposure time is an important parameter depended on the intensity of the UV light and the photoresist properties. For the exposure unit used here the UV intensity is 650 W/m^2, and the suitable exposure time is experimentally found to be around 20 seconds for AZ-1805. Inadequate exposure will result in incomplete chemical reaction in photoresit and cause the following development to fail, whereas over exposure will cause enlarged transfer of channel width due to the possible reflection and refraction of unparallel UV light between the film mask and the photoresit layer. Although the UV expose unit is designed to shine parallel light, small amount of unparallel light cannot be totally avoided in practice. When the small amount UV light exposes onto the film mask for long time, enlarged transfer of channel width will be induced. Figures 14 (b)-(c) graphically illustrates the reason why the unparallel light will cause enlarged transfer of channel width. By comparing Fig. 14 (b) with Fig. 14 (c), it is found that when the ink-printed surface of the film mask is attached to the photoresist the enlarged area (red color in Fig. 14 (c)) is smaller than in Fig. 14 (b). That is why we always keep ink-printed surface attached to the photoresist layer (Fig. 14 (a)).

After UV exposure, the glass wafer is developed in 0.7 wt % NaOH solution in which the exposed photoresist has a much faster dissolving speed than the unexposed area. The developing process is conducted in a 500 mL plastic beaker for 40 seconds under a gentle hand-shaking. The developing time has to be controlled preciously. Because if the develop time is too short the exposed microstructure pattern may not be totally dissolved, which will cause the followed chrome removing to fail and in turn wet etching to fail. On the other hand, if the developing time is too long the unexposed photoresist on the edges of the exposed pattern may

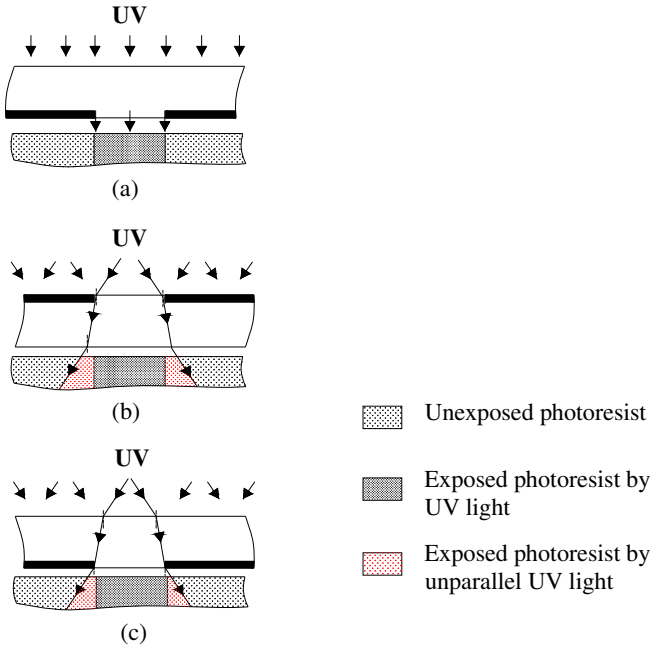

Fig. 14 Mask aligning manners and unexpected UV exposure: (a) idea UV exposure, (b) unexpected UV exposure when ink-printed surface is up, (c) unexpected UV exposure when ink-printed surface is down

be partially dissolved unexpectedly, which will result in large channel width after chrome removing and wet etching.

The next step is to remove the chromium layer uncovered in the photoresist development step stated above. The solution used to remove the chromium layer is a mixture of $HClO_4$ (70%, 6 mL) and $(NH_4)_2Ce(NO_3)_6$ (25g) dissolved in 150 mL deionized water [56]. The glass wafer developed in the last step is immediately washed using deionized water and put into the removal solution for 20 seconds. For similar reason as stated in the photoresist development step, much attention should be paid on the time control. If the time is too long the chrome under the unexposed photoresist near the area of the developed area may be dissolved and result in enlarged channel width after wet etching.

The total resolution loss caused by the steps stated above is estimated to be 20μm based on our experience

$$W_{be} \approx W_{fm} + 20 \tag{1}$$

where W_{be} (μm) is the channel width after removing the chrome layer but before wet etching and W_{fm} (μm) is the designed channel width on the film mask. The enlarged

transfer of channel width is a result of unparallel UV expose, partial dissolve of photoresist and chrome in the developing and removing steps. This resolution loss (~20 μm) must be considered when designing the desirable microchannel width.

2.2.5 Wet etching and Channel Characterization

After removing chrome, the glass wafer is immediately washed using deionized water to flush away the removing solution. Then the glass wafer is dried and baked in a vacuum oven (DZF-6020, Shanghai Shengxin Scientific Instrument Factory, China) at 100 °C for 15 minutes in order to harden the photoresist and improve its resistance in the etching step. A mixing solution of HF (1 mol/L) and NH_4F (1 mol/L) is used for etching glass wafer, according to the following chemical formula,

$$SiO_2+4HF=SiF_4+2H_2O. \quad (2)$$

Here NH_4F is used as a buffer solution to supply HF smoothly and continuously to maintain a constant concentration of HF in the etching solution

$$NH_4F=NH_3+HF. \quad (3)$$

The etching solution is contained in a 500 mL plastic baker placed in an ultrasonic cleaner (Cole-Parmer® 8893, Cole-Parmer Instrument Company, USA). The developed glass wafer is soaked in the etching solution and is etched under ultrasonic environment (f=44 KHz) at room temperature. During the etching process, the revealed microstructure where glass is exposed to HF solution will be etched and the other place will be protected by both photoresist layer and chromium layer. After etching, the etched glass wafer is washed by deionized water, followed by removing the left photoresist layer and chromium layer using ethanol and chrome removing solution, respectively. The cross section of the microchannel etched on glass material has a bowl-like shape (Fig. 15); the curved sidewalls are resulted from the isotropic property of glass material in the wet etching process. Channel width and depth are controlled by chemicals concentration, etching time, etching temperature and ultrasonic intensity [36, 37, 124]. In our studies, we always conduct etching by using 1 mol/L etching solution under the same ultrasonic intensity (f=44 KHz) at room temperature. Given all those conditions unchanged, we have experimentally obtained the relation between the etching time and channel depth measured by using a surface roughness tester (SV-3000S4, Mitutoyo Corporation, Japan). It is found that under our experimental conditions the channel depth is linearly proportional to the etching time, shown in Fig. 16, and the correlation is experimentally fitted as

$$H=1.2t \quad (4)$$

where H (μm) is channel depth, and t (minute) is etching time. This correlation provides us the ability to get the desirable channel depth according to the etching time which is the easiest parameter to be controlled. The upper (wider) channel width can then be estimated by

$$W = W_{be} + 2H \,. \tag{5}$$

Substituting Eqs. (1) and (4) into Eq. (5), the upper channel width (μm) reads,

$$W \approx W_{fm} + 2.4t + 20 \,. \tag{6}$$

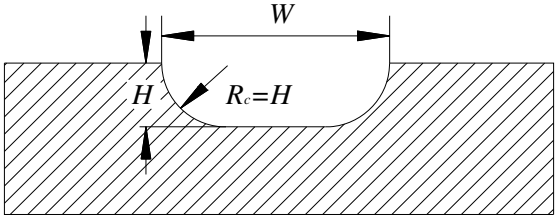

Fig. 15 Cross section of etched microchannel

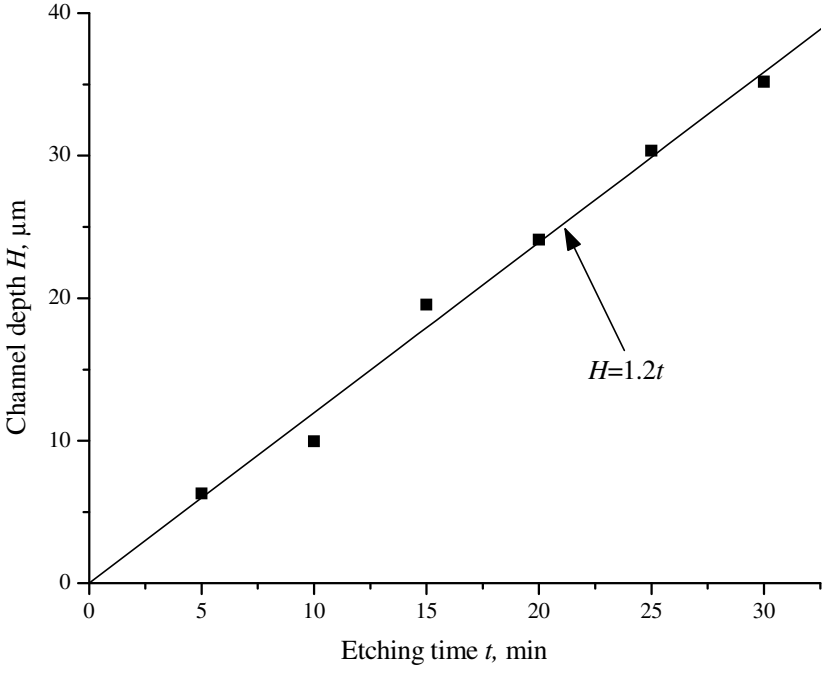

Fig. 16 Correlation between channel depth and etching time

Equations (4) and (6) are used to roughly estimate the final channel width based on the value on the film mask and the etching time. In practice, the accurate channel width after etching is measured by using a vision measuring machine with an error of ±0.1 μm (Quick Vision Pro 202, Mitutoyo Corporation, Japan). The cross section area of the etched microchannels can be estimated as

$$A = (W - 2H)H + \frac{\pi H^2}{2} \tag{7}$$

2.2.6 Thermal Bonding

Before thermal bonding, inlets and outlets for fluids flow are drilled on the etched substrate using a 1.5 mm diamond driller (Metabo, Germany). Then the etched substrate is tailored to small pieces according to the microstructure designed on the film mask. Those small pieces are cleaned using a brush with home detergent and flushed with tap water, flowing at a high speed, in order to flush away glass debris brought in during inlet and outlet drilling. Uncoated glass wafers tailored to pieces with the same size as the etched ones are used as covers to seal the channels. Thorough cleaning of the tailored cover pieces is necessary in order to remove dusts introduced during tailoring. Deep cleaning must be conducted in order to remove tiny and invisible contaminations on glass surfaces of both substrate and cover pieces because such kind of tiny contamination may cause serious problem to thermal bonding and results in low bonding yield. Those glass pieces, in our studies, are cleaned in detergent solution, acetone, ethanol and deionized-water, sequentially, under ultrasonic environment for 20 minutes. Finally the substrate pieces and the cover pieces are put together in pairs in deionized water. Each pair is then tightly tied up by using PTFE tape and put into the vacuum oven for desiccation and pre-hydrolysis at 200 ºC for 2 hours. After desiccation, the glass pairs are already bonded together but the bonding strength is weak. They can be easily separated from each other during handling. Therefore the pre-bonded glass pairs are transferred to a programmable muffle furnace (Vulcan® 3-550, DENTSPLY Ceramco, USA) where thermal bonding at high temperature will be conducted. The temperature program employed here is similar to that reported by Xiao et al. (1999) [58] and Liu et al. (2006) [122]. There are four stages in the temperature program as shown in Fig. 17: (1) Stage 1, the temperature is raised to 150 ºC with a raising ratio of 10 ºC/min and kept at 150 ºC for 1 hour, aiming to eliminate the internal thermal stresses; (2) Stage 2, the temperature is raised from 150 to 300 ºC and kept at 300 ºC for 1 hours, where fast hydrolysis reaction between glass interfaces will start; (3) Stage 3, the temperature is further raised from 300 to 580 ºC and then kept at 580 ºC for 3 hours, where the hydrolysis reaction will be finished and glass surfaces will be fused together; (4) Stage 4, the temperature is naturally cooled down to room temperature, taking more than 6 hours, in order to

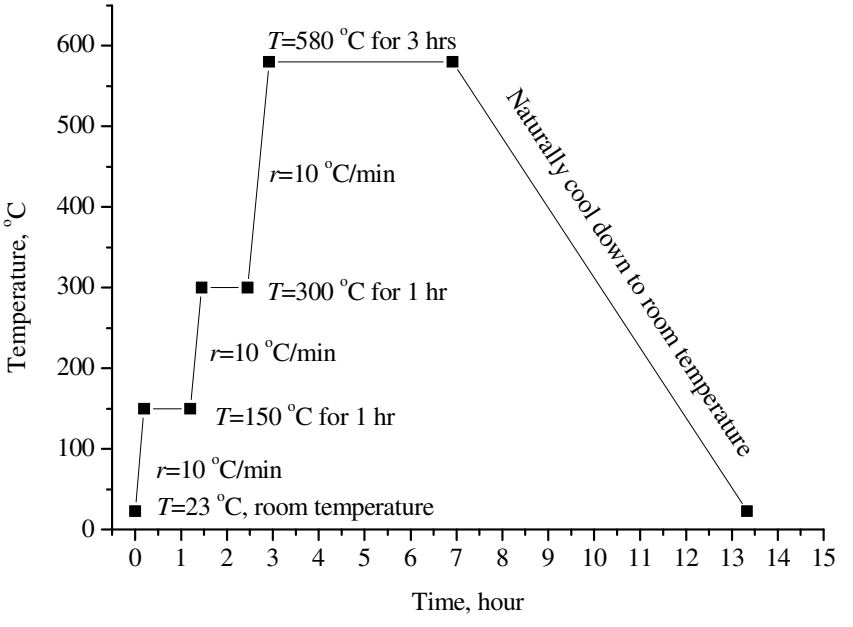

Fig. 17 Temperature program in the thermal bonding process

minimize the thermal stresses inside the microfluidic devices. The total time consumption is around 11 hours for one cycle of such thermal bonding.

Using this method the product yield is found to be larger than 90%. Some failure cases are found when the unbounded area locates near or within the designed microstructures. The unbounded area can be easily examined by Newton Rings resulted from light interference. In the center of the Newton Ring there are probably some residual tiny dusts after cleaning processes or introduced from air during operation.

2.2.7 Connectors

The microfluidic devices after thermal bonding cannot be connected into experimental systems until interfaces are provided to the inlets and outlets. Luer-Lock fittings (1/16", Nylon, cole-parmer, USA) are found to be very suitable for playing such a role as they can be connected or disconnected quickly and repeatedly without linkage at all within our experimental range. Female Luer-Lock fittings are glued to the microfluidic devices at the inlets and outlet by using transparent epoxy glue. Figure 18 shows several microfluidic devices after providing the connectors, which are ready to be used.

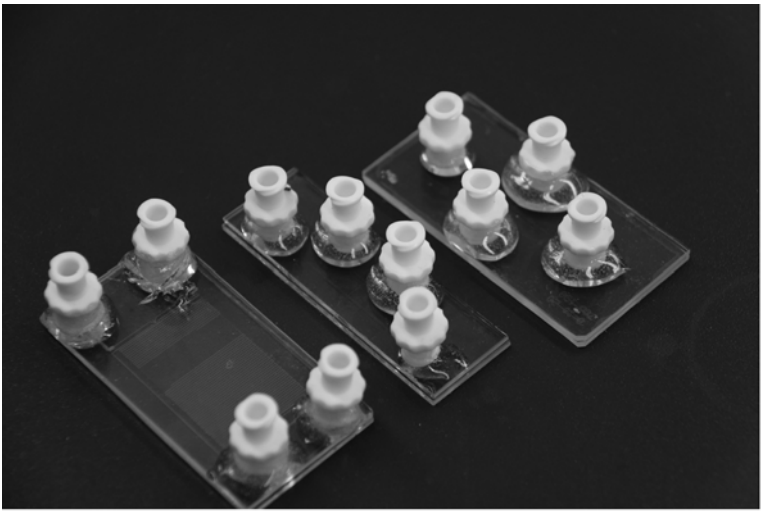

Fig. 18 Glass-based microfluidic devices fabricated in our lab

2.2.8 Wetting Ability Modification

To generate droplets or bubbles, the main channel walls must have such a property that on the wall surfaces continuous phase have much stronger wetting abilities than dispersed phase, i.e. the contact angle of continuous phase must be less than the dispersed phase. Figure 19 graphically demonstrates the definition of contact angle θ by taking water and glass surface as examples. When $\theta<90°$ the solid surface is hydrophilic, whereas when $\theta>90°$ the solid surface is hydrophobic. The freshly fabricated channel walls are totally hydrophilic surfaces, contact angle $\theta=0$, meaning water can spread all over the channel walls and form a thin film. Therefore when water is used as the continuous phase, the glass-based microfluidic devices can be used directly after fabrication to generate oil-in-water droplets and bubbles, without any wetting ability modification. But if water is used as the dispersed phase to generate water-in-oil droplets, the fabricated channel walls have to be modified from hydrophilic to hydrophobic. Octadecyltrichlorosilane (ODS, $CH_3(CH_2)_{17}SiCl_3$, Sigma, USA) is a hydrophobic molecule that is widely used for self-assembled monolayers (SAMs) on hydroxylated surfaces such as silica glasses [125-128]. In our fabrication method, ODS is used to alter the channel surface from hydrophilic to hydrophobic. ODS solution is prepared in toluene with a concentration of 0.1wt%. Since ODS is easily hydrolyzed under the influence of atmospheric humidity and oxygen, the ODS toluene solution is always freshly prepared and used within 30 minutes after preparation. When a drop of ODS solution is dipped into one inlet of the channel network of the microstructure, the ODS solution will quickly spread the whole channel network spontaneously under the effect of capillary force, normally in less than 10 seconds. As soon as ODS solution fills the

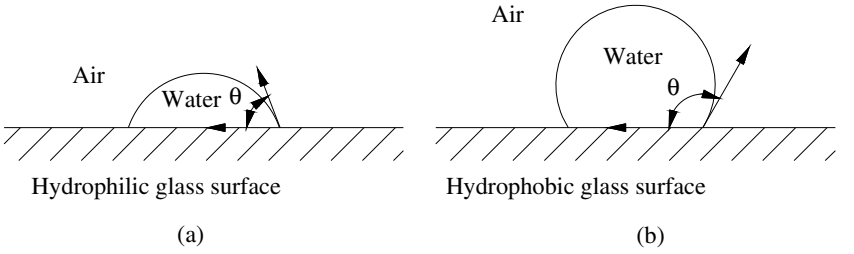

Fig. 19 Contact angle on (a) hydrophilic glass surface (θ<90°) and (b) hydrophobic glass surface (θ>90°)

whole channel network, it is flushed with toluene several times to drain the surplus ODS solution and then dried using nitrogen gas. Finally the microfluidic devices will be cured in the muffle furnace at 100 °C for 30 minutes to further enhance siloxane effect. After ODS treatment, the contact angle of water on glass surface changes from 0 to between 104° and 115° as reported by Srinivasan et al. (1998), Maboudian et al. (2000) and Kirkpatrick and Muhstein (2007) [127, 129, 130].

The surface modification mechanism is schematically illustrated in Fig. 20. The trichlorosilane polar head-groups hydrolyze and convert the Si–Cl bonds to Si–OH (silanol) groups. The silanol groups, which are strongly attracted to the oxidized hydrophilic channel surfaces, condense with the OH^- groups on the surface to form Si–O–Si (siloxane) links. The siloxane groups condense with other and similar groups on precursor molecules, producing covalent siloxane bonds [129, 130]. The result is a monolayer in which the molecules are connected to each other and to the surface by strong chemical bonds. Curing at 100 °C can further enhance those cross linking between chains. Finally, the hydrophobic tail-group of the precursor molecule is at the outside while the head group is firmly attached to the channel surfaces, and then the channel surface is changed from hydrophilic to hydrophobic.

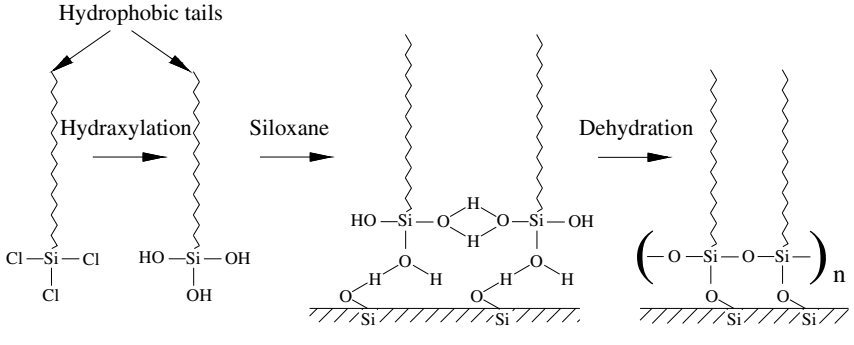

Fig. 20 Chemical fundamentals of ODS silanization

2.3 Concluding Remarks

Glass-based microfluidic devices have been successfully fabricated out in a routine laboratory without the requirement of clean room. The fabrication method is very reliable and the product output is larger than 90%. The relationship between etching speed and etching time and the relationship between designed channel width and etched channel width are studied, offering us the ability to predetermine the channel dimensions before etching. Wetting ability modification of glass material is realized inside the microfluidic devices after fabrication. With the help of such modification, either oil-in-water or water-in-oil type droplets can be generated in glass-based microfluidic devices.

3 Droplet and Bubble Formation in T-Shaped Junctions

3.1 Introduction

Most microfluidic T-shaped junctions can be classified into two groups according to their geometrical characteristics: unconfined T-shaped junctions and confined T-shaped junctions [95]. In an unconfined T-shaped junction, the main channel is much larger than the lateral channel such that the forming bubbles/droplets can freely develop before detaching, similar to the droplet formation process in the membrane emulsification [131-135]. A force balance model is normally adopted to predict the droplet/bubble size. The force balance model states that the bubble/droplet will detach when all possible forces exerted on it reach equilibrium [83, 85]. In confined T-shaped junctions, however, the forming droplets/bubbles are seriously confined by the main channel walls and the force balance model is quite inaccurate to predict the droplet/bubble volume, which has been noted by many researchers [82, 84, 96, 97]. The failure may be resulted from the inaccurate estimation of the forces involved in the droplet formation process that is seriously influenced by the confinement of main channel walls. There are many arguments over here regarding which parameters contribute to the formation process most and how those parameters influence the droplet/bubble size. Some researchers believe that, in confined T-shaped junctions, fluids properties have little impact on droplet/bubble volume when the capillary number is less than 0.01, and the flow rate ratio of dispersed phase to continuous phase is the only factor affecting the droplet/bubble size for a specified T-shaped junction [84, 97]. In contrast, the capillary number representing the influence of fluids properties is found playing an important role on determining droplet/bubble size, but the influence of flow rate ratio is not indicated [82, 96]. In addition, few studies on the formation time in such confined T-shaped junctions are available. Most works on droplet/bubble formation in microfluidic T-shaped junctions are focusing on the size rather than the formation time. In fact, the droplet/bubble size and the formation time are always coupled together because, intuitively, the droplet/bubble volume (i.e. size) is equal

to the volume of the dispersed phase pumped into the forming droplets/bubbles within the formation time. Therefore a further examination of the formation process in such confined T-shaped junctions is necessary for better utilization and manipulation of droplets and bubbles. In this study, droplet formation under controlled flow rates and bubble formation under controlled pressures in confined T-shaped junctions are experimentally investigated. The influence of fluids properties on the droplet/bubble volume and the formation time is systematically studied.

3.2 Reexamination of Force Balance in Confined T-Shaped Junctions

As the formation process and the force analysis of droplets and bubbles are quite similar, we take droplets as an example to do the force analysis, but it is also applicable for bubbles. In unconfined T-shaped junctions, the dispersed phase grows, deforms and detaches under a series of forces all of which can be clarified as two groups depending on the effect of the forces on droplet detachment: (1) resisting forces, trying to stabilize the forming droplet, including the force caused by interfacial tension only; (2) driving forces, tending to detach the forming droplet, including buoyancy force caused by density difference and gravity, viscous force exerted by continuous phase flow on the forming interfaces, and inertial forces caused by continuous and dispersed phase flow and inflation [85, 136-138]. When the unconfined T-shaped junction is placed in the vertical plane, the gravity may play some role, and another driving force, buoyancy force, caused by density difference between the continuous and the dispersed phases is considered [83]. The droplet size derived from the force balance model was reported to be capable of giving a reasonable estimation of droplet size.

Force analysis in confined T-shaped junctions is much more difficult than in unconfined T-shaped junctions because of the highly disturbed flow field of the continuous phase around the forming droplet. In confined T-shaped junctions, the forming droplet is always confined by channel walls; therefore the buoyancy force will be balanced by the opposite force from channel walls at any time, which does not contribute to the detachment. The inertial forces involved in the droplet formation in the confined T-shaped junctions are usually omitted because the Reynolds numbers of either continuous or dispersed phase are quite small [68, 84]. The buoyancy force which plays an important role on bubble formation in unconfined flow is always balanced in confined T-shaped junctions, and the inertial forces of gas phase is much smaller compared with dispersed liquid phase, which can be neglected. Therefore the formation process of and the force analysis on droplets should be also applicable for bubbles. Hereafter droplets will be used as an example to do the force analysis. In addition to the driving forces in unconfined T-shaped junctions there is another driving force that arises from the pressure increase in the continuous phase flow, in the upstream of the forming droplet. Then the main forces involved during droplet

formation process are the interfacial force caused by interfacial tension, the force caused by pressure drop in the continuous phase flow over the forming droplet and the viscous force exerted on the forming interface [84]. Figure 21 shows a typical intermediate process of a droplet formation in a confined T-shaped junction. The whole forming droplet is usually taken as an investigating object. The interfacial force is taken as a resisting force; and the viscous force and the force caused by pressure drop are the two driving forces. The interfacial force results from the different interfacial curvatures at the two tips of the forming droplet. At the front forming tip, the interface is confined by both channel depth H and width W_c, then the two principal radius of curvature are $R_1 \approx W_c/2$ and $R_2 \approx H/2$ (Figs. 21 (a) and (b)), whereas at the rear tip the interface is regarded as being confined only by the channel depth, $R_2 \approx H/2$, because the principal radius in the horizontal plan is very large compared with channel width, i.e. $R_1 \sim \infty$. The pressure inside the forming droplet is assumed to be constant and equal to P_0 everywhere. Taken the droplet formation as a quasi-static process and based on Young-Laplace equation, the capillary pressure at the front tip $\Delta P_{\sigma 2}=P_0-P_{c2} \approx 2\sigma(1/W_c+1/H)$, and at the rear tip $\Delta P_{\sigma 1}=P_0-P_{c1} \approx 2\sigma/H$, then the total capillary pressure difference, pointing upstream, is $\Delta P_\sigma=\Delta P_{\sigma 2}-\Delta P_{\sigma 1}=-(P_{c1}-P_{c2}) \approx 2\sigma/W$. The pressure drop in the continuous phase flow over the forming droplet can be found at the same time, $P_{c1}-P_{c2} \approx -2\sigma/W$. The force caused by pressure difference in the continuous phase is regarded as resulting from the increased pressure at P_{c1} when the droplet partially blocks the main channel where the flow resistance of the continuous phase is dramatically increased. It was argued that the viscous force was resulted from the continuous phase flow in the thin film between the interfaces and the channel walls and was regarded as a driving force.

Although the force balance model is attractive and frequently mentioned in many reported works, it seems that no one has obtained a reliable and accurate correlation for predicting droplet volume [84, 97]. We believed that this results from the inaccuracy and difficulty of the force estimation in confined T-shaped junctions. From the above deduction of the total capillary pressure drop ΔP_σ, it is seen that the pressure drop $P_{c1}-P_{c2}$ will always be balanced by the total capillary pressure drop if taking the whole forming droplet as the investigating object. Then the pressure increase at P_{c1} will not influence the droplet detachment, which conflicts with many reported works where the pressure increase plays an important role in droplet detachment [84, 97, 139]. In addition, the total viscous force exerted on the forming interfaces by the continuous phase is really hard to be judged regarding whether it is a driving force or a resisting force as the serious confinement from channel walls. Here we separate the whole forming interface into three parts. Two partial interfaces close to the upper and lower walls of the main channel are named to be upper and lower interfaces (Fig. 21 (b)), respectively, and the left part is named to be lateral interface. During the whole droplet formation process, the forming droplet is always confined by the channel depth, surrounded by thin films of continuous phase existing between the forming interfaces and channel walls. The flow velocity in the thin films between the upper and lower interfaces and channel

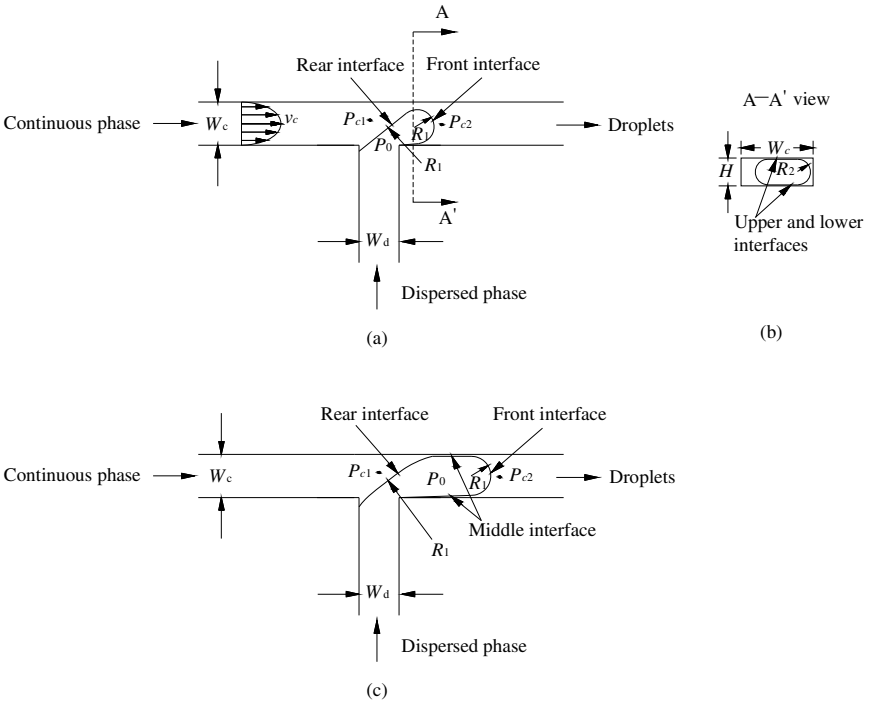

Fig. 21 Schematic diagram of droplet shape in a confined T-shaped junction during generation

walls is probably much lower than inside the forming droplet due to the wall effects, and the viscous forces on these two interfaces are resisting forces. The viscous force on the lateral interface is much more complex depending on the size of the forming droplet. When the forming droplet is sufficiently large the lateral interface can be distinguished into three sections (Fig. 21 (c)): (1) the rear interface opposing to the main flow stream of continuous phase in the up steam direction, (2) the front interface opposing to the main flow stream of the continuous phase in the down stream direction, and (3) the middle interface between the rear and the front lateral interface. When the forming droplet is not so big, the middle interface will disappear (Fig. 21 (b)). On the rear interface the viscous force is probably a driving force, pointing downstream, because it is very close to the mouse of the T-shaped junction where the dispersed phase flow inside the forming droplet is mainly in the direction along the lateral channel, perpendicular to the flow direction of the continuous phase in the main channel. The dispersed phase flow inside the forming droplet will be changed direction under the viscous stresses exerted on the rear interface by the continuous phase flow. The viscous force on the middle interface is probably a resisting force due to the wall effects (Fig. 21 (c)). The viscous force on

the front interface is very hard to be judged because it is depended on the developing flow field inside the forming droplet and in the continuous phase flow.

To summarize, taking the whole forming droplet as an investigating object to apply force balance model to predict droplet volume is not easy to make. The total viscous force exerted on the forming interfaces is extremely difficult to determine due to the confinement of channel walls. Sometimes, even the direction of the viscous force cannot be determined easily.

3.3 Experiments

3.3.1 Characterization of Microfluidic T-Shaped Junctions

Two microfluidic T-shaped junctions are fabricated for investigating droplet and bubble formation processes, respectively. Figure 22 shows the dimensions of the two T-shaped junctions. The two T-shaped junctions have the same length for the main channel and the lateral channel. The lateral channel is located in the middle point of the main channel. The T-shaped junction used for investigating bubble

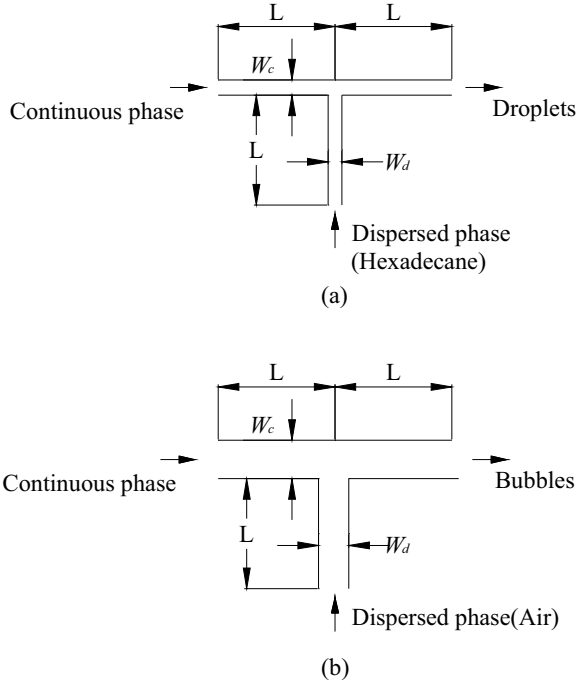

Fig. 22 Schematic diagram of the T-shaped junctions for studying droplet and bubble formation

formation has a wider channel width than the one used for investigating droplet formation. As stated in Part 2, microchannels manufactured by wet etching have curved sidewalls and their cross section area can be calculated by Eq. (7). Then the following two equations are used for calculating the cross section area of the lateral channel and the main channel, respectively.

$$A_d = (W_d - 2H)H + \frac{\pi H^2}{2} \tag{8}$$

and

$$A_c = (W_c - 2H)H + \frac{\pi H^2}{2}, \tag{9}$$

where W_d is the lateral channel width, W_c is the main channel width and H is the channel depth. For the T-shaped junction used for investigating droplet formation, W_d=86.5 μm, W_c=101.3 μm, H=35.4 μm, A_d=2.52×10^{-9} m^2 and A_c=3.05×10^{-9} m^2. For the T-shaped junction used for investigating bubble formation, W_d=364.1 μm, W_c=430.0 μm, H=36.0 μm, A_d=1.25×10^{-8} m^2 and A_c=1.49×10^{-8} m^2. For both T-shaped junctions the lateral channel length is L=20 mm, and the main channel length is 2L=40 mm.

3.3.2 Fluids Selection

Deionized water is used as continuous phase; hexadecane and air are used as dispersed phases to generate droplets and bubbles, respectively. The deionzied water is prepared by using a home-made water purification system. The hexadecane is bought from Sigma-Aldrich Inc., USA. To investigate the influence of continuous phase viscosity on droplet/bubble volume and formation time, different amount of glycerin (Tianjin Damao Chemical Reagent Factory, China) is added into the deionzied water to change continuous phase viscosity. To investigate the influence of interfacial tension, surfactant Tween 20 (Sigma-Aldrich Inc., USA) and Sodium dodecyl sulfate (SDS) (Tianjin Damao Chemical Reagent Factory, China) are used to alter the interfacial tension between dispersed phases and continuous phases. Continuous phase viscosities are measured by using a viscometer (SCHOTT-GERATE GmbH, Germany) with an accuracy of 0.65%, and interfacial tensions between dispersed phases and continuous phases are measured by using a tensiometer (Cole-Parmer® Surface Tension Meter 20, Cole-Parmer Instrument Company, USA) with a measurement error of ±0.25 mN/m. Table 1 lists the measured values of the viscosity and interfacial tension at room temperature. Each value is an average over three measurements.

3.3.3 Experimental Setups

Two experimental setups are built up for investigating the formation process of droplets and bubbles respectively. The only difference between the two experimental systems is the injection methods of the dispersed phase. When

Table 1 Measured viscosities and interfacial tensions at room temperature (23℃)

Dispersed phase-Continuous phase	μ_c mPa·s	σ mN/m
Hexadecane-Deionized water	1.0	44.0
Hexadecane-30wt.% glycerin aqueous solution	2.4	29.7
Hexadecane-60wt.% glycerin aqueous solution	10.5	28.0
Hexadecane-0.0001wt.% Tween 20 aqueous solution	1.0	28.0
Hexadecane-0.1wt.% Tween 20 aqueous solution	1.0	10.0
Air-Deionized water	1.0	72.8
Air-60wt.% glycerin aqueous solution	10.0	68.0
Air-0.3wt.% SDS solution	1.0	9.0

hexadecane is used as the dispersed phase, a syringe pump is used to inject the hexadecane, while when air is used as the dispersed phase a pressurized air tank is used to drive it into the microfluidic T-shaped junction. In other words, the hexadecane is fed in under controlled volumetric flow rates, and the air is fed in under controlled pressure.

Figure 23(a) is the schematic diagram of the experimental system for investigating droplet formation. The dispersed phase and the continuous phase are injected into the T-shaped junction by two syringe pumps via flexible PTFE tubings (Cole-Parmer Instrument Company, USA). The flow rate of either phase is automatically controlled by the syringe pumps with an accuracy of 0.5%. When the two flow streams meet at the T-shaped junction, droplets will be formed as a result of instabilities between the two phases. An inversed microscope is used for micro visualization purpose (XD101, Nanjing Jiangnan Novel Optics Co. Ltd., China), with which a high speed camera is integrated for recording the droplet formation process in terms of imagines and videos (MotionPro® X4, IDT, Taiwan). Nominal speed of the high speed camera is 5000 fps (frame per second) for capturing 512×512 pixels photos. The capturing speed used in our studies ranges from 100 to 4000 fps, depending on the droplet formation time (frequency) at different flow conditions. The droplet formation time is directly measured from the consecutive images by utilizing the software provided with the high speed camera. We usually measure five consecutive droplet formation processes and calculate the average value of the formation time. The droplet volume can be derived from the droplet dimensions in the images in Adobe Photoshop. We will discuss the method for determining droplet volume in detail later on. To insure the collected information of the droplet formation is under a steady state, we check out the number of droplets formed within a specific time period at least three times with a time interval at least five minutes after every change of the flow rate of either dispersed phase or

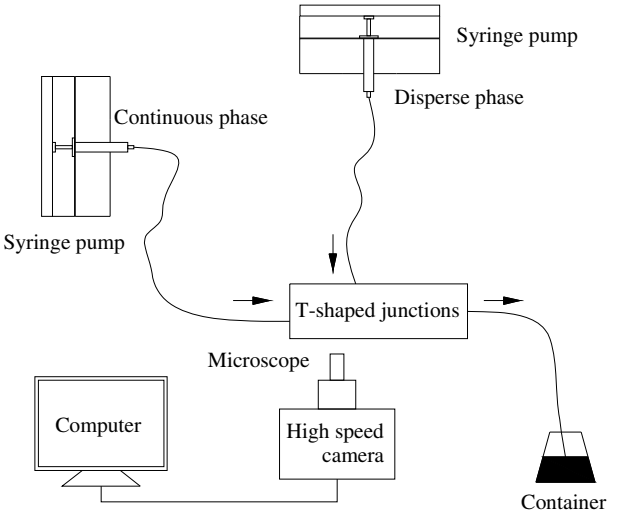

(a)

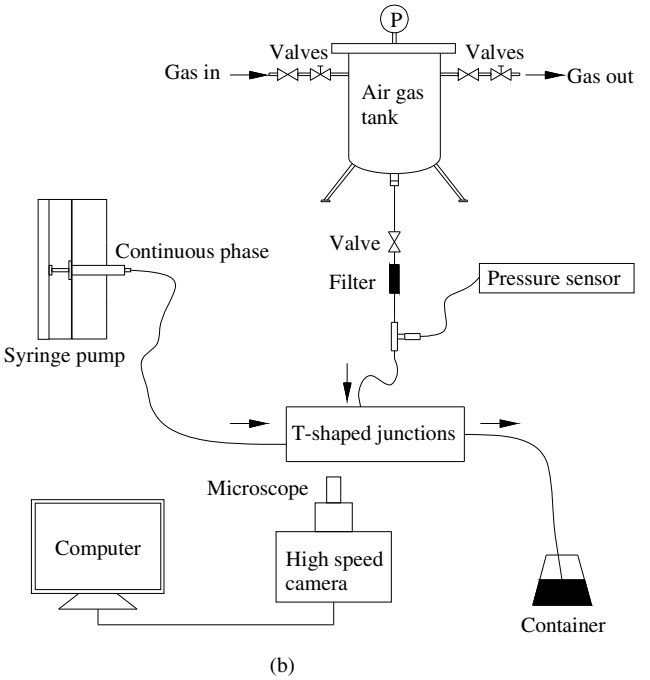

(b)

Fig. 23 Experimental setups: (a) for studying droplets and (b) for studying bubbles

continuous phase. The pictures and videos are collected only when the number does not change for the last two measurements.

Figure 23(b) is a schematic diagram of the experimental setup for investigating bubble formation. The only difference with the system used for investigating droplet formation, as stated above, is the injection method of the dispersed phase. Here the dispersed phase, air, is injected into the T-shaped junction via an adjustable pressurized air tank monitored by a pressure sensor with an accuracy of 0.2% (ZFBY3803, Xi'an Zhongfei Aero Sensors Technology Co. Ltd., China). To avoid any possible dusts or contaminations entering the T-shaped junction, a micro-filter (Beijing satellite manufacturing factory, Beijing, China) is placed in the gas loop.

3.4 Results and Discussion

3.4.1 Droplet Formation Process

Two stages have been experimentally identified during a typical droplet formation process: (1) growing stage—when the two streams meet at the T-shaped junction, the dispersed phase gradually intrudes and inflates into the continuous phase (Figs. 24 (a) and (b)) and reaches a critical position after which the rear interface of forming droplet tip starts traveling downstream (Fig. 24 (b)); (2) necking stage—after reaching the critical position, the rear interface travels downstream in the continuous phase, and the neck connecting the forming droplet and the main stream of the dispersed phase becomes thinner and thinner until it breaks near the downstream corner of the T-shaped junction (Figs. 24 (c)-(e)). Within the two stages, the forming droplet is always confined by the main channel, but it does not wet main channel walls due to the higher interfacial energy between water and glass than between hexadecane and glass.

Based on the experimental observations of the droplet formation process, it is seen that the movement of the rear interface determines the droplet formation time and in turn determines the droplet volume after generation. The droplet formation time is equal to the time consumed by the rear interface traveling from the very beginning position to near downstream corner of the T-shaped junction. This inspires us to take the rear interface rather than the whole forming droplet as the investigating object, and then it is not necessary to consider the total force exerted on the whole forming interface. We only pay attention to the rear interface, where the viscous force is probably a driving force due to the cross-flowing configuration at the T-shaped junction.

3.4.2 Determination of Droplet Volume

Droplet volume, after detachment, is determined from image analysis of micrographs captured by the high speed camera. In the micrographs the main channel width is

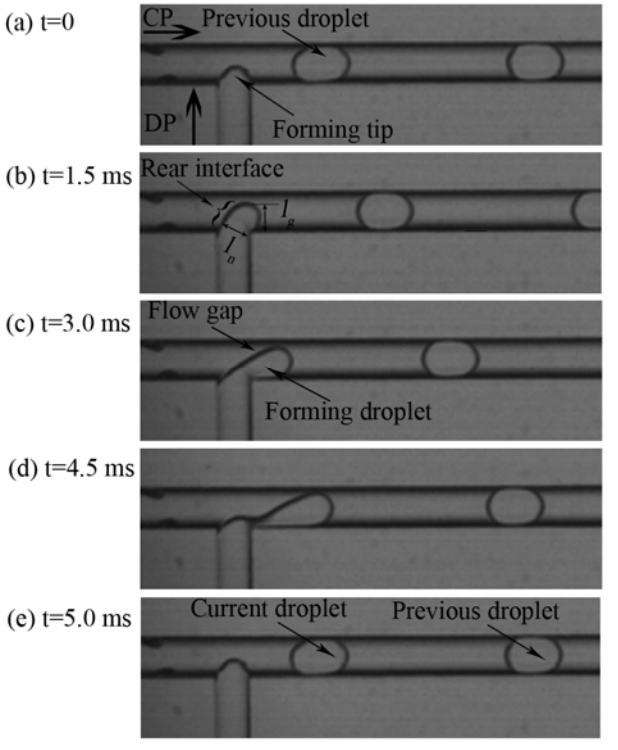

Fig. 24 A typical droplet formation process (CP: continuous phase, 0.1wt% Tween 20 aqueous solution, Q_c=16μL/min; DP: dispersed phase, hexadecane, Q_d=6 μL/min)

measured in terms of pixels and compared with the real channel width measured from the vision measuring machine (Quick Vision Pro 202, Mitutoyo Corporation, Japan), and then the represented length of one pixel is obtained. Square of this represented length is the represented area of one pixel. Based on the represented length and area, the measured droplet dimensions in micrographs can be easily transformed to its real size. The main channel width in the micrograph is about 25 pixels and the measurement error is about 2 pixels, thus the relative error of the represented length and area of one pixel is about 8% and 16% respectively. The main error of droplet volume determination results from those two errors because the measured channel width by using the vision measuring machine can be neglected (less than 0.1%). The curved sidewalls of microchannels, however, make the determination of droplet volume not so intuitive. We measure droplet length, width and area in Adobe Photoshop, and find most droplets generated in our study have a longer length than the main channel width, and even for smaller droplets the length is still comparable with the main channel width. It is reasonable to assume that the middle section of a long droplet fully occupies the cross

section of the main channel and its two tips have the same shape in both horizontal and vertical planes (Fig. 25). Each tip can be treated as a semicircle with a diameter of the main channel width in the horizontal plane. The curved tip in the vertical plane, confined in the channel depth direction, can be regarded as a body of rotation by rotating half cross-section of the main channel from A to B along O-O′ (Fig. 25). With the above postulations, the droplet volume is a sum of the volume in the middle part and the volume of the two tips,

$$V_d = H\left(L_d - W_c\right)\left(W_c - \frac{H(4-\pi)}{2}\right) + \pi H\left(H\left(\frac{W_c - 2H}{4} + \frac{2}{3}\right) + \frac{\left(W_c - 2H\right)^2}{4}\right) \tag{10}$$

where L_d is droplet length between the two ends. Note that Eq. (10) is only valid for the case $L_d \geq W_c$. When $L_d < W_c$, the droplet will have a circle shape in the horizontal plane and we assume that the droplet has a "cylindrical" shape confined by the main channel depth. V_d is thus calculated by

$$V_d = \kappa A H\,, \tag{11}$$

where k is a correction coefficient used to modify the assumption of cylindrical shape. A is droplet area in the horizontal plane. When $L_d = W_c$, the value of k=0.83 can be derived from Eq. (10). For the case of $L_d < W_c$ we estimate that the k value does not vary too much because the droplet generated in our experiment is not so small that letting itself have a spherical shape between the up and bottom channel walls. In fact, the droplet volume should be slightly smaller than the value of a cylinder considering its curved lateral interface in reality. Then a constant value k=0.80 is employed in Eq. (11) for calculating droplet volume when $L_d < W_c$.

For the long droplets, $L_d \geq W_c$, the measurement error of droplet length L_d in micrographs decreases from 8% to 2% as their sizes increase in our experiment.

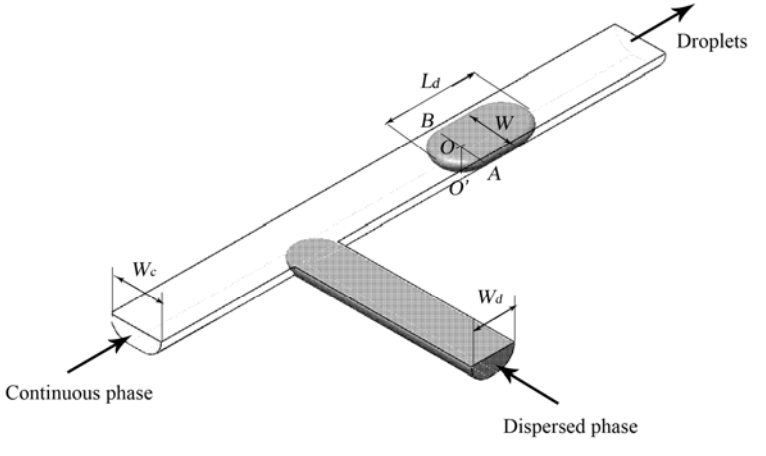

Fig. 25 Schematic illustration of droplet volume calculation

Considering the error introduced by the represented pixel length, the error of droplet volume calculated by Eq. (10) is less than 16% and will decrease as droplet volume increase. For the small droplets, $L_d<W_c$, the measurement error of droplet area in micrographs is estimated less than 5% and will decrease as droplet volume increases. Considering the error introduced by the represented pixel area, the error of droplet volume calculated by Eq. (11) is less than 21%, and will decreases as droplet volume increases. Droplet volume generated in our experiment ranges from 0.10 to 1.32 nL (nano Liter) at different flow conditions, calculated by Eqs. (10) and (11). Under each specific condition, the droplet volume is quite uniform, the polydispersity defined as the ratio of volume variation to the mean volume is about 2%.

3.4.3 Relationship between Droplet Volume and Droplet Formation Time

For incompressible dispersed phases, droplet volume should be equal to the volume of the dispersed phase pumped into the forming droplet within droplet formation time. In our experiment the dispersed phase is pumped at controlled flow rates, the droplet volume should satisfy

$$V_d = t_d \cdot Q_d \,, \tag{12}$$

where t_d represents the droplet formation time, Q_d is the flow rate of the dispersed phase. After measuring the droplet formation time, we have conducted a comparison of the droplet volume determined by Eqs. (10) and (11) with the values calculated by Eq. (12). Figure 26 shows the comparison results in a dimensionless format, where the droplet volume V_d is normalized by $W_c W_d H$. A good agreement of the droplet volume calculated by the two methods can be seen, implying that Eqs. (10) and (11) are effective and accurate for estimating droplet volume generated in confined microfluidic T-shaped junctions. It also confirms that the relationship between droplet volume and droplet formation time, Eq. (12), does exist.

3.4.4 Analysis of Droplet Volume and Droplet Formation Time

Equation (12) has demonstrated the relationship between the droplet volume and the droplet formation time. The droplet volume equals the dispersed phase volume flowed into the forming droplet within the formation time. From the analysis of the droplet formation process stated above, the droplet formation time consists of two parts: the time consumed in the growing stage and the time consumed in the necking stage. The former can be estimated by

$$t_g = \frac{l_g}{\bar{v}_g} \,, \tag{13}$$

where l_g is the distance of the forming droplet tip intruding into the continuous phase in the growing stage (Fig. 24 (b)). $\bar{v}_g$ is the average intrusion speed of the

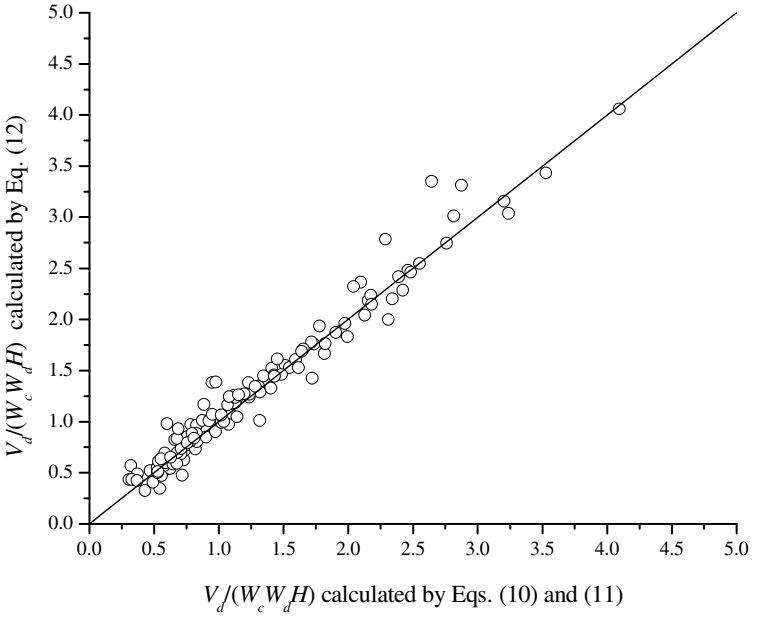

Fig. 26 Validation of the droplet volume

forming tip. In the growing stage, the dispersed phase tip does not inflate downstream too much, which leads $\overline{v}_g$ could be approximated by the average velocity of the dispersed phase flowing in the lateral channel, $v_d=Q_d/A_d$. The penetration length l_g is always less than but comparable with W_c as being found by experimental visualization of the droplet formation process. Therefore l_g and $\overline{v}_g$ in Eq. (13) can be further estimated as W_c and v_d, respectively. We note that using W_c instead of l_g will overvalue t_g since the dispersed phase can hardly block the entire main channel width in the growing stage, resulting in $l_g<W_c$; using v_d instead of $\overline{v}_g$ will underestimate t_g because in the growing stage the front interface does inflate downstream some distance, resulting in $\overline{v}_g < v_d$. Due to such two-side effect, W_c/v_d should give a reasonable estimation of t_g. To increase the accuracy of the estimation, a correction coefficient a should be introduced. Then t_g becomes

$$t_g = a\frac{W_c}{v_d}, \tag{14}$$

where a is a dimensionless correction coefficient depending on fluids properties and the local flow field at the T-shaped junction, and should be on the order of one.

The time consumed in the necking stage is estimated as

$$t_n = \frac{l_n}{\bar{v}_n}, \tag{15}$$

where l_n is the distance of the rear interface traveling from the critical position to the breakup point in the necking stage (Fig. 24 (b)). $\bar{v}_n$ is the average speed of the rear interface traveling downstream in the continuous phase. From the analysis of the droplet formation process, we note that l_n can be approximated by W_d since the breakup always happens at the downstream corner of the T-shaped junction. The average traveling speed $\bar{v}_n$ should have a same magnitude of the average velocity of the continuous phase in the main channel, $v_c=Q_c/A_c$, where Q_c is the flow rate of continuous phase. Therefore l_n and $\bar{v}_n$ in Eq. (15) can be further estimated by W_d and v_c, respectively. It is notable that using W_d instead of l_n will overestimate t_n because $W_d>l_n$, and using v_c in stead of $\bar{v}_n$ will underestimate t_n because $v_c>\bar{v}_n$ due to the leakage of continuous phase in the flow gap between the forming droplet and channel walls. Because of this two-side effect, W_d/v_c should give a reasonable estimation of t_n. Similar to the estimation of t_g, a correction coefficient b is adopted here, and t_n reduces to

$$t_n = b\frac{W_d}{v_c}, \tag{16}$$

where b is a dimensionless correction coefficient depending on fluids properties and the local flow field at the T-shaped junction, and should be on the order of one. Then the droplet formation time is calculated by

$$t_d = a\frac{w_c}{v_d} + b\frac{w_d}{v_c}. \tag{17}$$

Based on Eq. (12), the droplet volume is obtained

$$V_d = a\frac{W_c Q_d}{v_d} + b\frac{W_d Q_d}{v_c}. \tag{18}$$

Substituting $Q_d=v_d A_d$ and $v_c=Q_c/A_c$ into Eq. (18), we have

$$V_d = aW_c A_d + bW_d A_c \frac{Q_d}{Q_c}. \tag{19}$$

We take the characteristic volume of the T-shaped microchannel as $W_c W_d H$ and normalize Eq. (19) by this value, and then a dimensionless expression of the droplet volume can be obtained

$$\tilde{V}_d = a\frac{A_d}{W_d H} + b\frac{A_c}{W_c H}\frac{Q_d}{Q_c}, \tag{20}$$

where $\tilde{V}_d = V_d/(W_c W_d H)$. We note that the value of $A_d/(W_d H)$ and $A_c/(W_c H)$ are solely depending on the shape and dimensions of the microchannels cross section. For the lateral channel and the main channel in our experiment, $A_d/(W_d H)$=0.82 and $A_c/(W_c H)$=0.85.

3.4.5 Determination of Correction Coefficients

Equation (20) shows that the droplet volume may be linearly proportional to the flow rate ratio of the dispersed phase to the continuous phase. Here we plot the relationship between the dimensionless droplet volume and the flow rate ratio at two typical flow rates of continuous phase in Fig. 27. In Fig. 27 it is seen that the droplet volume formed in all investigated continuous phases, changing viscosity or changing interfacial tension or both, always linearly increases as the flow rate ratio Q_d/Q_c increases at different flow rates of continuous phase. We also note that the minimum droplet volume and the increasing rate of the droplet volume with respect to the flow rate ratio changes as either the continuous phase viscosity or the interfacial tension or the flow rate of continuous phase changes. In other words, the slope of V_d vs. Q_d/Q_c as well as the minimum droplet volume, $V_{d,min}$, is a function of μ_c, σ and v_c, where μ_c is the viscosity of continuous phase and σ is the interfacial tension. Under each flow rate of continuous phase, the influences of the continuous phase viscosity and the interfacial tension on the droplet volume are investigated. Figure 28 shows the influence of the continuous phase viscosity on the droplet volume at the two typical flow rates of continuous phase. We can see that the minimum droplet volume and the slope of V_d vs. Q_d/Q_c decrease as the continuous phase viscosity increases. Figure 29 shows the influence of the interfacial tension on the droplet volume at the two typical flow rates of continuous phase. We can see that the minimum droplet volume and the slope of V_d vs. Q_d/Q_c increase as the interfacial tension increases. Figure 30 shows the influence of the average velocity of the continuous phase on the minimum droplet volume for all the tested continuous phases at a constant flow rate of dispersed phase. It can be seen that the minimum droplet volume decreases as the average velocity of the continuous phase decreases. From Eq. (20) we note that the minimum droplet volume is represented by the correction coefficient a, while the slope is represented by the correction coefficient b, for fixed microfluidic T-shaped junctions. Based on the above analysis of the influences of μ_c, σ and v_c on droplet volume, we note that the correction coefficients a and b will increase as σ increases and will decrease as either μ_c or v_c increases. The main stresses involved in the formation process are viscous stress, interfacial stress and inertial stress. For most of our experimental results, the inertial stress has the weakest influences on the formation process because the Reynolds numbers, $Re=\rho_c v_c W_c/\mu_c$, representing the relative importance of inertial stress to viscous stress, are on the order of 0.1. Therefore the correction coefficients are mainly dependent on the competition between the two most important stresses, the viscous stress and the interfacial stress,

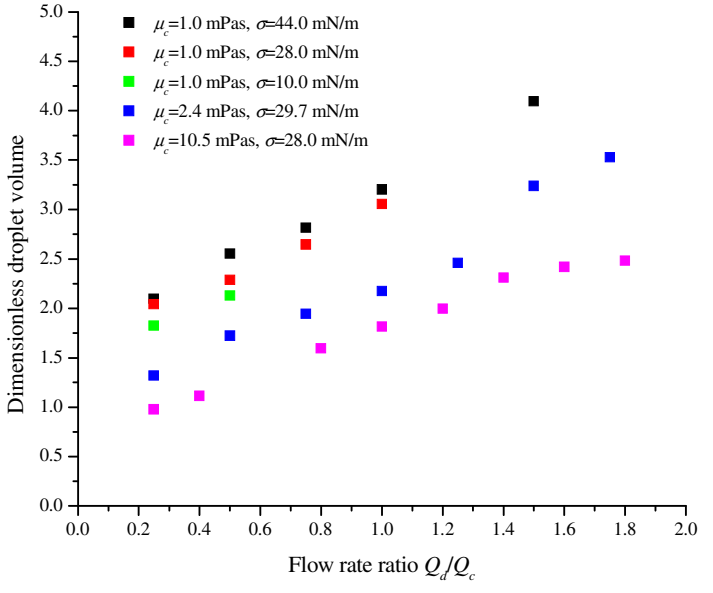

(a)

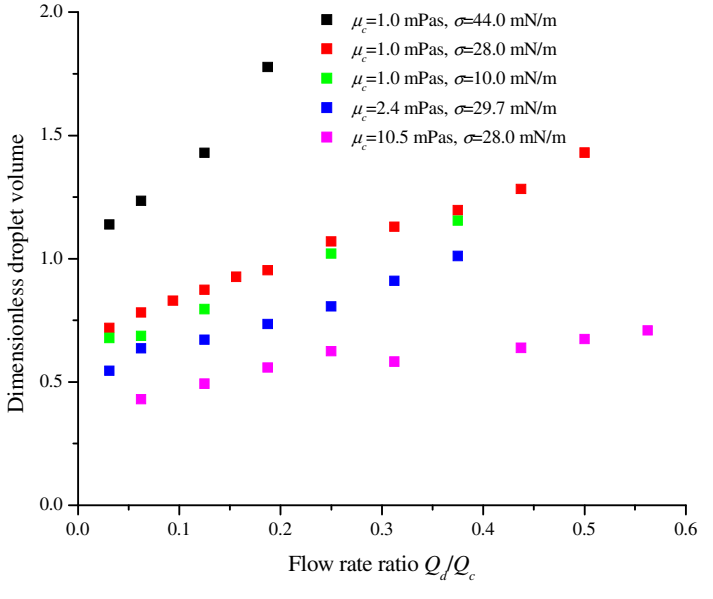

(b)

Fig. 27 Linear relationship between droplet volume and flow rate ratio at typical experimental conditions (a) Q_c=2 μL/min and (b) Q_c=16 μL/min

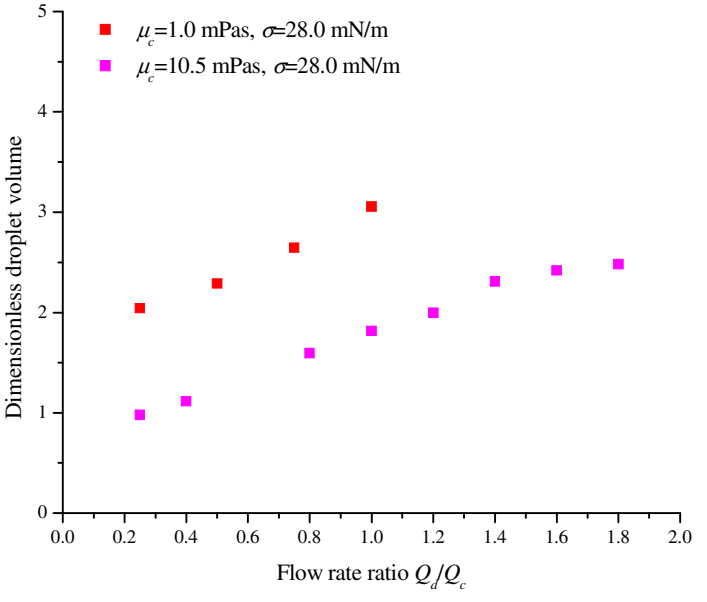

(a)

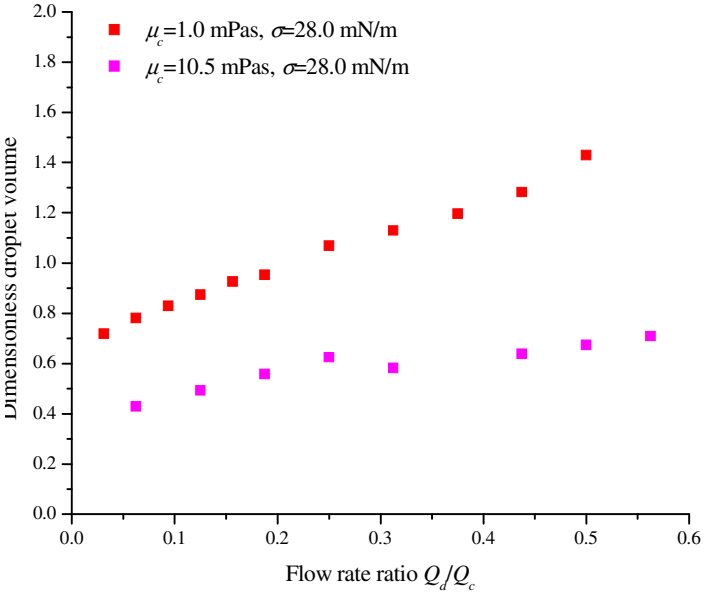

(b)

Fig. 28 Influences of continuous phase viscosity on droplet volume at typical experimental conditions (a) Q_c=2 μL/min and (b) Q_c=16 μL/min

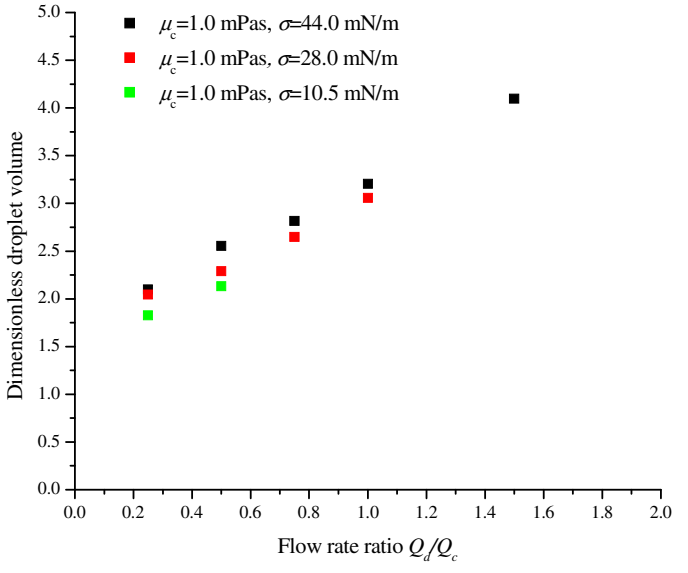

(a)

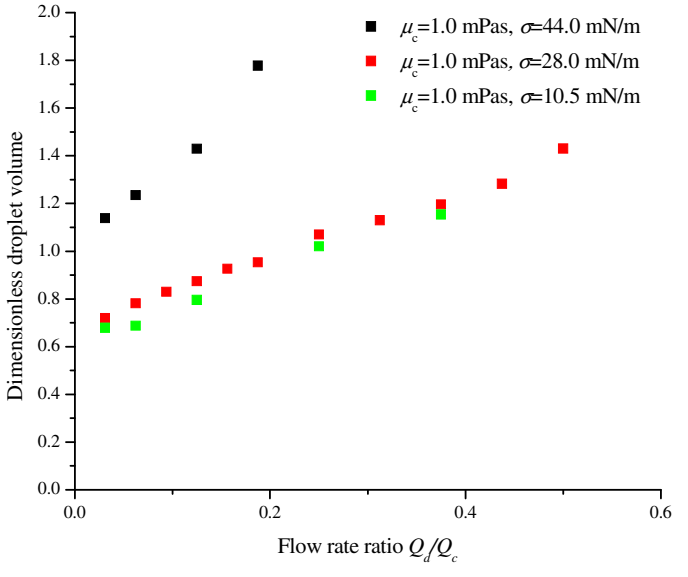

(b)

Fig. 29 Influences of interfacial tension on droplet volume at typical experimental conditions (a) Q_c=2 μL/min and (b) Q_c=16 μL/min

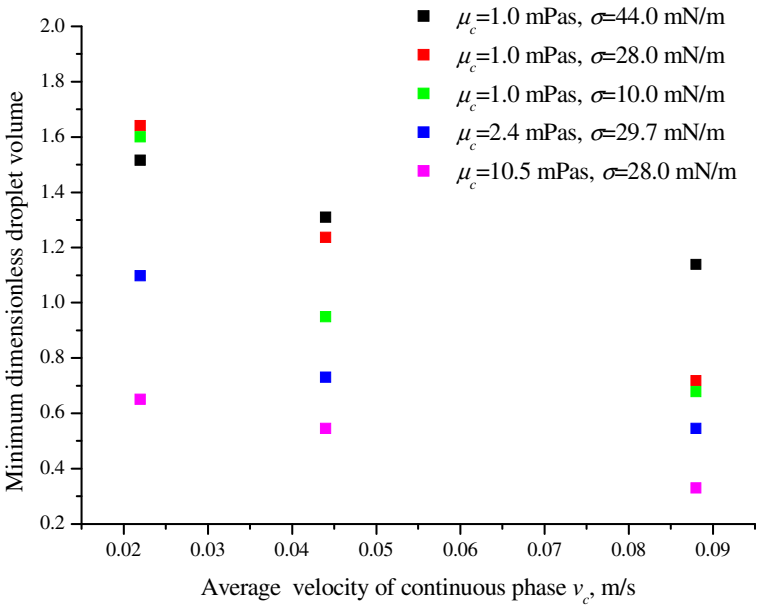

Fig. 30 Influences of the average velocity of the continuous phase on the minimum droplet volume (Q_d=1 μL/min)

which can be represented by the Capillary number $Ca=\mu_c v_c/\sigma$. Inspired by the work reported in [96], an exponential correlation is adopted for relating the correction coefficients to Ca,

$$a = C_1 Ca^{\alpha_1}, \tag{21}$$

$$b = C_2 Ca^{\alpha_2}, \tag{22}$$

where C_1, α_1, C_2 and α_2 are dimensionless numbers depending on the geometrical characteristics of the T-shaped junction. Combining Eqs. (20)-(22), the dimensionless droplet volume is formulated as

$$\tilde{V}_d = C_1 Ca^{\alpha_1} \frac{A_d}{W_d H} + C_2 Ca^{\alpha_2} \frac{A_c}{W_c H} \frac{Q_d}{Q_c}. \tag{23}$$

By fitting our experimental data, it is found C_1=0.147, α_1=-0.344, C_2=0.535 and α_2=-0.141 for the T-shaped junction used in this study.

Substituting the expressions of a and b into Eq. (17), the droplet formation time is also obtained

$$t_d = C_1 \cdot Ca^{\alpha_1} \frac{w_c}{v_d} + C_2 \cdot Ca^{\alpha_2} \frac{w_d}{v_c}. \tag{24}$$

Figure 31 shows a comparison of the measured droplet volume and the calculated droplet volume by Eq. (23). A very good agreement is presented in Fig. 31, where most of the points are located on the line $\tilde{V}_d$ (measured)=$\tilde{V}_d$ (calculated). Since the fitted dimensionless numbers C_1, α_1, C_2, and α_1 are fitted by using Eq. (23) on the droplet volume, they are double checked by using the droplet formation time, Eq. (24), shown in Fig. 32. The measured droplet formation time and that predicted by Eq. (24) are also compared as a function of Ca and v_d in Figs. 33 and 34, respectively. The good consistencies confirm our understanding of the droplet formation process and the validity of the relationship between droplet volume and droplet formation time. In our study, the Capillary number is in the range of 5.0×10^{-4}–3.3×10^{-2}. In Eq. (23) the first item on the right side $C_1Ca^{\alpha1}A_d/(W_dH)$ varies from 2.10 to 0.39, and the coefficient of Q_d/Q_c in the second item, $C_2Ca^{\alpha2}A_c/(W_cH)$, varies from 1.46 to 0.74 when Ca increases from 5.0×10^{-4} to 3.3×10^{-2}.

For long droplets, the ratio L_d/W_c is an alternative expression of droplet size. When droplets are relatively large, droplet volume V_d can be estimated by treating droplets as cuboids with a height of H, a length of L_d and a width of W_c, resulting in an

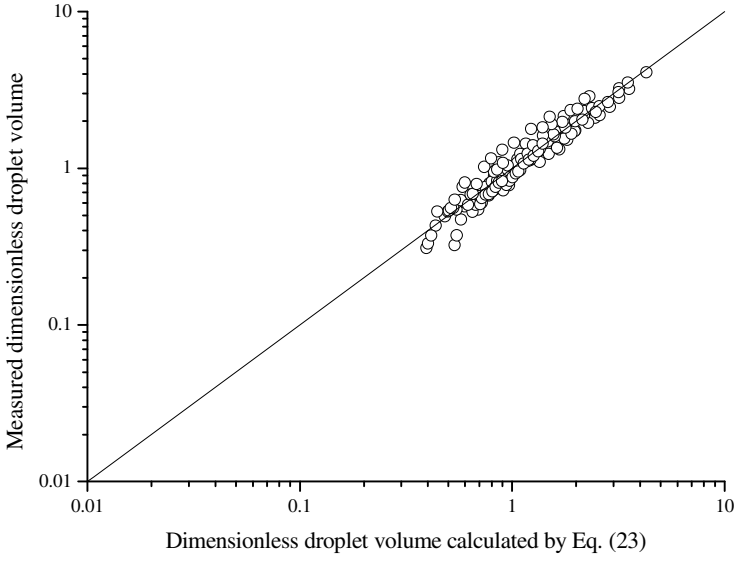

Fig. 31 Comparison of droplet volume between the values calculated and experimentally measured

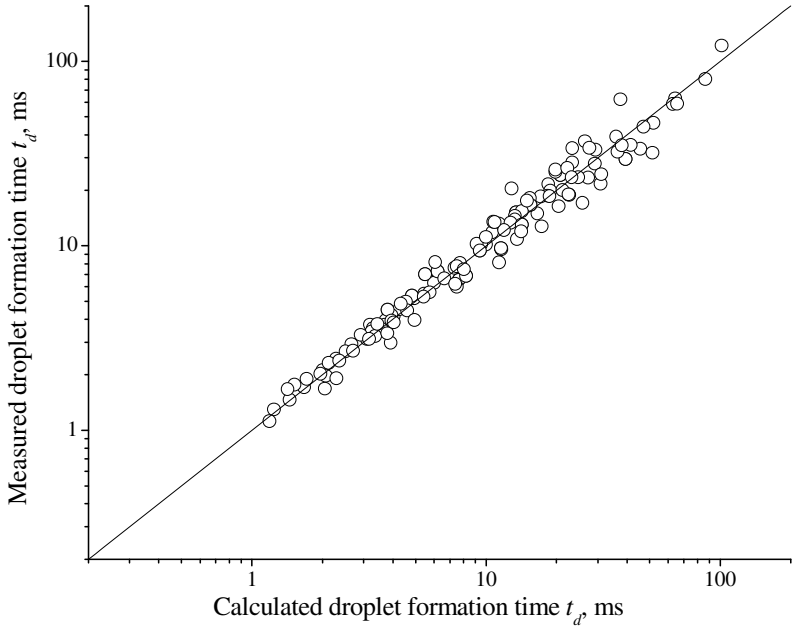

Fig. 32 Comparison of droplet formation time between the values calculated and experimentally measured

estimation of $V_d \approx L_d W_c H$. After substituting this estimation into Eq. (23) and doing some rearrangement, we have

$$\frac{L_d}{W_c} = C_1 \cdot Ca^{\alpha_1} \frac{A_d}{W_c H} + C_2 \cdot Ca^{\alpha_2} \frac{A_c W_d}{W^2{}_c H} \frac{Q_d}{Q_c}, \tag{25}$$

which can be further reformed to

$$\frac{L_d}{W_c} = C_1 \cdot Ca^{\alpha_1} \frac{A_d}{W_c H} \left(1 + \lambda \frac{Q_d}{Q_c}\right), \tag{26}$$

where $\lambda = Ca^{\alpha_2 - \alpha_1} \dfrac{C_2 A_c W_d}{C_1 A_d W_c}$.

Substituting the fitted value of C_1=0.147, C_2=0.535, α_1=-0.344, α_2=-0.141, W_d, W_c, A_d and A_c into Eq. (26), it is found the value of $C_1 Ca^{\alpha 1} A_d/(W_c H)$ varies from 1.79 to 0.33 and λ varies from 0.72 to 1.9 when Ca increases from 5.0×10^{-4} to 3.3×10^{-2}. The unity order of these two items in Eq. (26) exhibits the consistency of our result with

the reported scaling analysis on droplet size formed in confined T-shaped junctions by Garstecki et al. (2006) [84] and De Menech et al. (2008) [97],

$$\frac{L_d}{W_c} = 1 + \lambda \frac{Q_d}{Q_c} \tag{27}$$

where λ is a constant on the order of unity and depends only on the geometrical characteristics of T-shaped junctions. However, according to our experiments the value of λ changes a lot even for a specific T-shaped junction, 171% increase from 0.72 to 1.9, meaning both Ca and Q_d/Q_c have strong influences on determining droplet size. The influence of Ca on droplet volume is also reported by van der Graaf et al. (2006) [96],

$$V_d = V_{crit,ref} Ca^m + t_{neck,ref} Ca^n Q_d \tag{28}$$

where $V_{crit,\ ref}$ and $t_{neck,\ ref}$ are the critical volume and the necking time at Ca=1, respectively. The exponents m and n depend on the geometrical characteristics of T-shaped junctions, and are taken to be m=n=-0.75 for the T-shaped junction in [96]. Unfortunately Eq. (28) did not capture the linear influence of the flow rate ratio on the droplet volume.

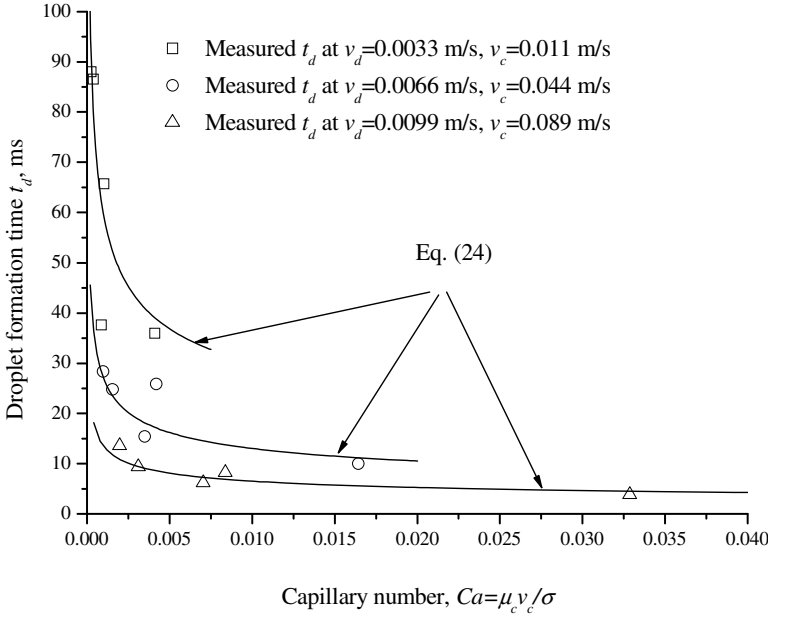

Fig. 33 Comparison of droplet formation time between the values calculated and experimentally measured at different capillary numbers

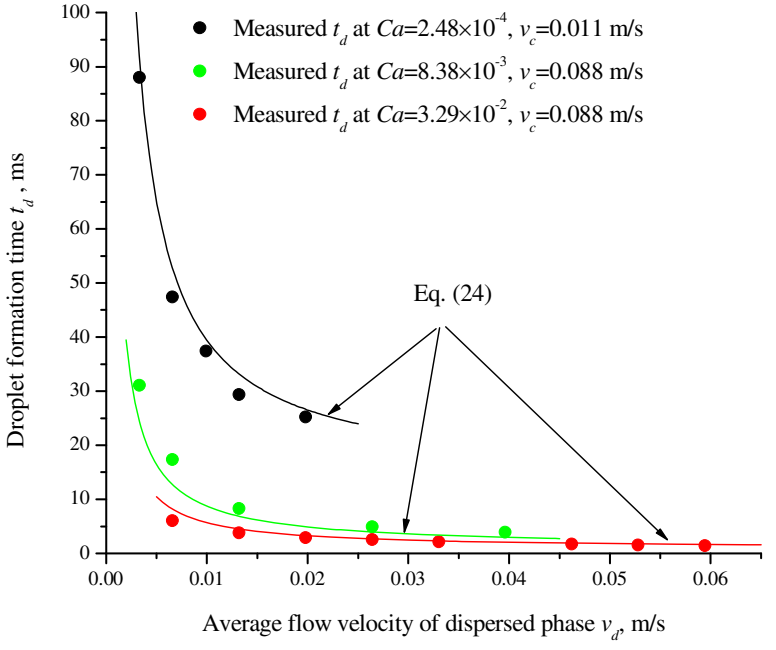

Fig. 34 Comparison of droplet formation time between the values calculated and experimentally measured at different dispersed phase velocity

3.4.6 Bubble Formation Process

In addition to the growing and the necking stages observed in droplet formation process, a third stage is observed in the bubble formation process. We name this stage as the flowing stage. At the end of the flowing stage, the bubble formation process enters the growing stage and then the necking stage. Figure 35 shows the three stages in a typical bubble formation process: (1) flowing stage—the air stream tip recoils back some distance in the lateral channel after the last bubble released and then starts to move toward the main channel (Figs. 35 (a) and (b)); (2) growing stage—the forming bubble tip intrudes into the continuous phase in the main channel (Figs. 35 (b) and (c)) and gradually reaches the critical position at which the rear interface of air tip starts to travel downstream (Fig. 35 (c)); (3) necking stage—the rear interface travels downstream until it touches the downstream corner of the T-shaped junction and releases a bubble, during which the forming bubble is still linked to the main air stream but the connecting neck becomes thinner continuously (Figs. 35 (c)-(e)).

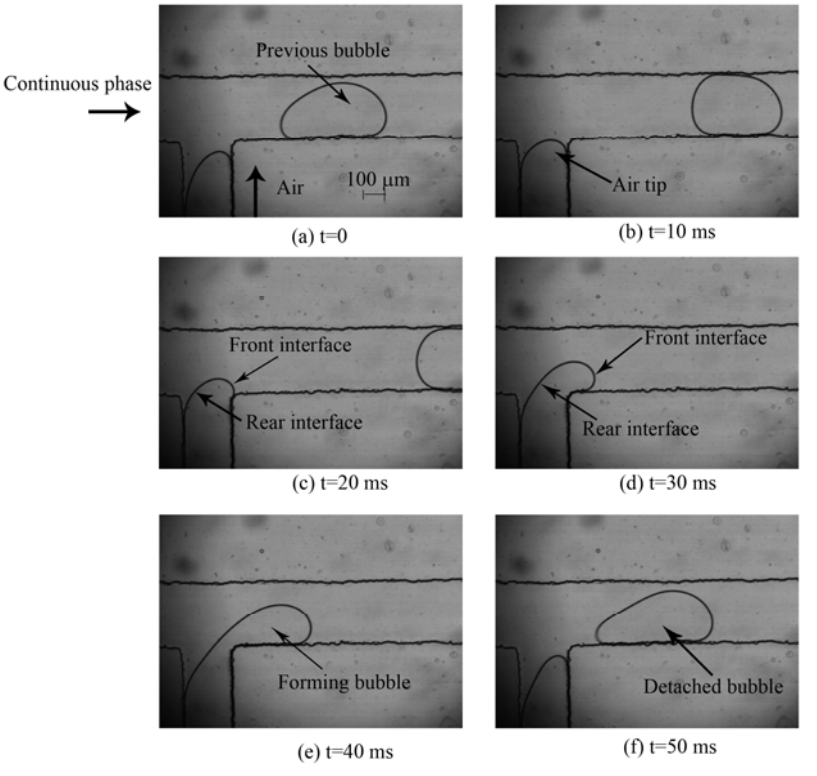

Fig. 35 Typical bubble formation process in the T-shaped junction (μ_c=1 mPa·s, σ=72.8 mN/m, Q_c=20 μL/min and P_g=26 kPa)

3.4.7 Bubble Formation Regime

In the study of bubble formation, the flow rate of continuous phase is changed from 1 to 10 μL/min for 60wt% glycerin aqueous solution and changed from 10 to 100 μL/min for 0.3wt% SDS aqueous solution and deionized water. The concentration of SDS is above the Critical Micelle Concentration (CMC), which is about 0.2%. At such high concentrations, surfactant transport between the continuous phase and the forming interfaces is fast, which can suppress the Marangoni effect caused by interfacial tension gradient [140]. When we gradually increase the air inlet pressure P_g under each flow rate of continuous phase, we find that there exists a certain range of air inlet pressure outside which bubbles cannot be formed. The minimum and maximum inlet pressures are denoted as $P_{g,min}$ and $P_{g,max}$ respectively. To determine $P_{g,min}$ and $P_{g,max}$ with a high accuracy, the air inlet pressure P_g is increased successively with a step of 1 kPa which is the minimum value limited by the accuracy of the pressure sensor. Under this pressure increment, the uncertainty of

$P_{g,min}$ and $P_{g,max}$ is found to be less than 6.3%. When $P_g<P_{g,min}$, the air stream in the lateral channel cannot intrude into the continuous phase and will be pushed back to the lateral channel as shown in Fig. 36 (a), while if $P_g>P_{g,max}$ the air stream does not release bubbles anymore but changes to a layer of air flow in the main channel as shown in Fig. 36 (b). The air inlet pressure is actually equal to the pressure inside the forming bubbles because of the negligible air pressure drop in the lateral channel, resulted from the extremely low flow rate (~10 μm/min) and air viscosity (~10^{-5} Pas). We experimentally examined the air pressure drop in the lateral channel and found that the pressured drop was less than 1% of the air inlet pressure. Considering the forming bubble and based on the Young-Laplace equation, the air inlet pressure is related to the pressure drop in the main channel from the T-shaped junction to the outlet

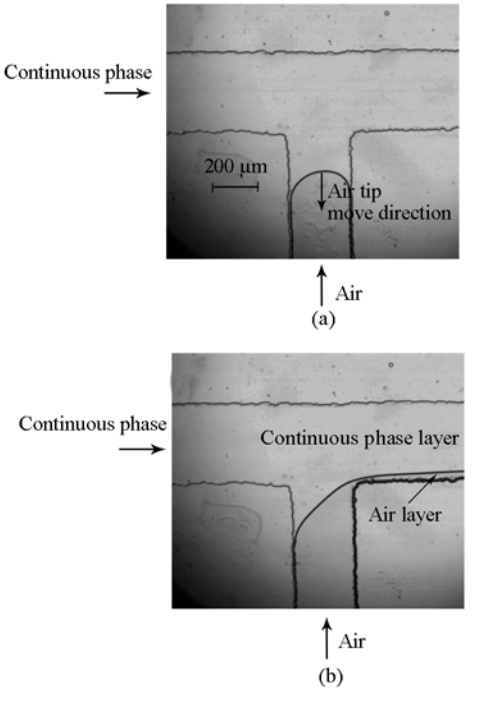

Fig. 36 Typical flow situations beyond the bubble formation regime: (a) the air tip flows back to the lateral channel (Q_c=4 μL/min, P_g=38 kPa); (b) parallel flow of air and continuous phase in the main channel (Q_c=4 μL/min, P_g=43 kPa)

$$P_g - \Delta P_\sigma = \Delta P_c \tag{29}$$

where ΔP_σ is the capillary pressure caused by interfacial tension and ΔP_c is the pressure drop in the main channel from the T-shaped junction to the outlet. Here we define the value of P_g-ΔP_σ as an effective inlet pressure P_e, because only when P_g-ΔP_σ>0 the air-liquid interface in the lateral channel has the possibility to flow toward the main channel. Equation (29) establishes the physical relationship between the dispersed phase and the continuous phase. In this T-shaped junction the channel depth is much smaller than the main channel width (H/W_c=0.084), the capillary pressure is mainly resulted from the shorter principal radius of the curvature confined by the channel depth. It is thus reasonable to estimate

$$\Delta P_\sigma = 2\sigma/H \tag{30}$$

The pressure drop ΔP_c in the main channel from the T-shaped junction to the outlet should be the pressure drop of bubbly flow. However, the pressure drop of bubbly flow in microchannels is very complicated, depending on many factors including the number of bubbles, bubble size, the additives types and channel wall properties [125, 141-143]. In this study, we do not focus on the pressure drop of bubbly flow. Then we simply use the single-phase continuous phase flow to estimate ΔP_c. The pressure drop of the continuous phase flow is calculated by using the analytical result for calculating pressure drop of single phase laminar flow in rectangular channels [144, 145],

$$\Delta P_c = \frac{4\mu_c Q_c L}{H^3 W_c}\left[\frac{1}{3} - \frac{64H}{\pi^5 W_c}\tanh\left(\frac{\pi W_c}{2H}\right)\right]^{-1}. \tag{31}$$

Figure 37 shows the minimum effective inlet pressure at different values of the pressure drop of continuous phase flow. We can see that the minimum effective inlet pressure $P_{e,min}$ linearly increases as the pressure drop ΔP_c increases and can be fitted as

$$P_{e,\min} = P_{g,\min} - \Delta P_\sigma = 4.2\Delta P_c. \tag{32}$$

Equation (32) offers much more information than just describing the minimum effective inlet pressure needed to form bubbles at the T-shaped junction. It partially reveals the mechanism of the bubble formation. At the very beginning of the bubble formation regime, the bubble number generated from the T-shaped junction is relative small and the minimum effective inlet pressure is an indicator of the average pressure in the continuous phase around the forming bubbles. From Eq. (32) we can see that the continuous phase pressure in the upstream near the forming tip must be increased in order to balance the pressure inside the forming tip. In other words, the pressure inside the continuous phase at the T-shaped junction increases from ΔP_c to $4.2\Delta P_c$ as the dispersed phase enters the T-shaped junction at the very begging of the bubble formation regime. This pressure increase is resulted from the

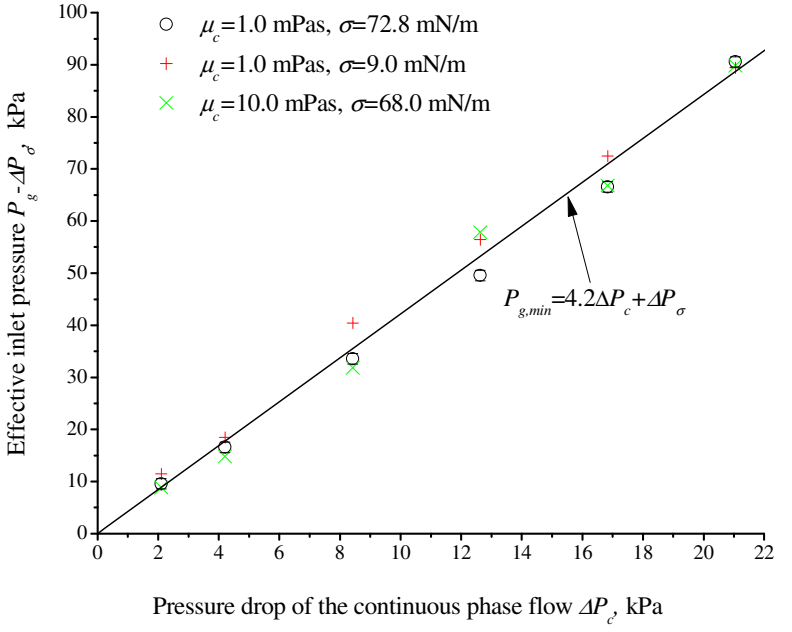

Fig. 37 The minimum effective inlet pressure

partial blockage of the main channel by the forming bubbles. Such pressure increase is also found by numerical simulations using phase-field methods [97]. By examining their figures, we find that the ratio of pressure increase is about 2.5, which is comparable with the value of 4.2 found in this work.

For the maximum effective inlet pressure, shown in Fig. 38, similar linear trends are presented, but the influence of the interfacial tension appears. When the interfacial tension is reduced from σ=72.8 to σ=9.0 mN/m, the maximum effective inlet pressure increases a lot and the increasing speed becomes much faster. For the interfacial tensions σ=72.8 and σ=68.0 mN/m, no obvious difference can be detected between the maximum effective inlet pressure due to the small difference of the interfacial tension. By fitting our experimental data, it is found that the maximum effective inlet pressure for 0.3wt% SDS aqueous solution (σ=9.0 mN/m) is

$$P_{e,\max} = P_{g,\max} - \Delta P_\sigma = 6.0\Delta P_c + 11, \tag{33}$$

and for distilled water (μ_c=1.0 mPas and σ=72.8 mN/m) and 60wt% glycerin aqueous solution (μ_c=10.0 mPas and σ=68.0 mN/m),

$$P_{e,\max} = P_{g,\max} - \Delta P_\sigma = 4.9\Delta P_c. \tag{34}$$

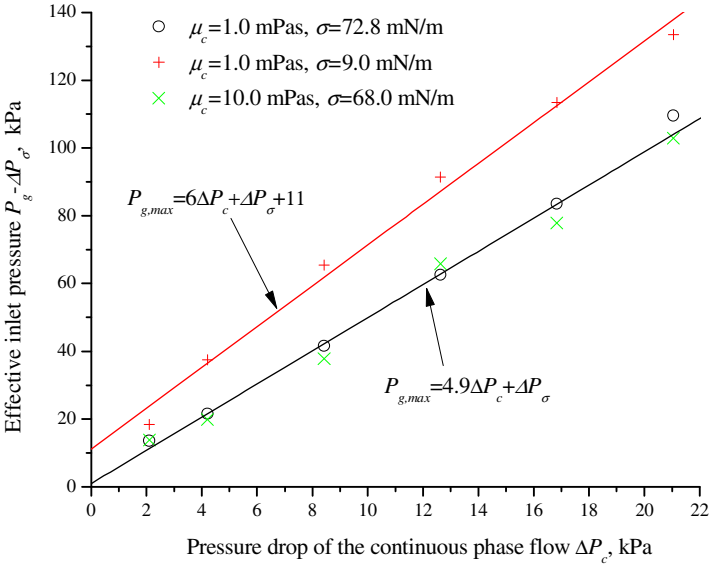

Fig. 38 The maximum effective inlet pressure

Figure 39 plots the bubble formation regime represented by the minimum and the maximum effective inlet pressures. It is seen that the bubble formation regime in 0.3wt% SDS solution is much larger than the other two continuous phases. The wider range of bubble formation regime, $P_{e,max}$-$P_{e,min}$, in 0.3wt% SDS solution may be resulted from three reasons. The most important one is the stabilization effect of surfactant additive (SDS) which will reduce the system's instability and facilitate bubble formation. The second one is the significant increase of the pressure drop of the bubbly flow in the main channel. As a result of the stabilization effect of the surfactant additive, large amount of bubbles will be generated and flow inside the main channel, which significantly increases the pressure drop in the main channel. The third possible reason is the large flow resistance in the main channel in the presence of surfactant additive. The presence of surfactant on interfaces of flowing bubbles may make the stationary liquid films between gas-liquid interface and channel walls to move at a speed of bubble velocity, which increases the viscous dissipation and results in a high flow resistance [84, 142, 143].

3.4.8 Bubble Volume and Formation Time

Bubble volume, V_b, is determined by using Eq. (11) where the coefficient k=1 is adopted. Because the main channel width of the T-shaped junction used for investigating bubbles is W_c=430 μm that is much larger than the channel depth H=36 μm, the effect of the curved sidewalls on bubble volume is quite small. In last section, we have pointed out that bubbles will be formed only when the inlet

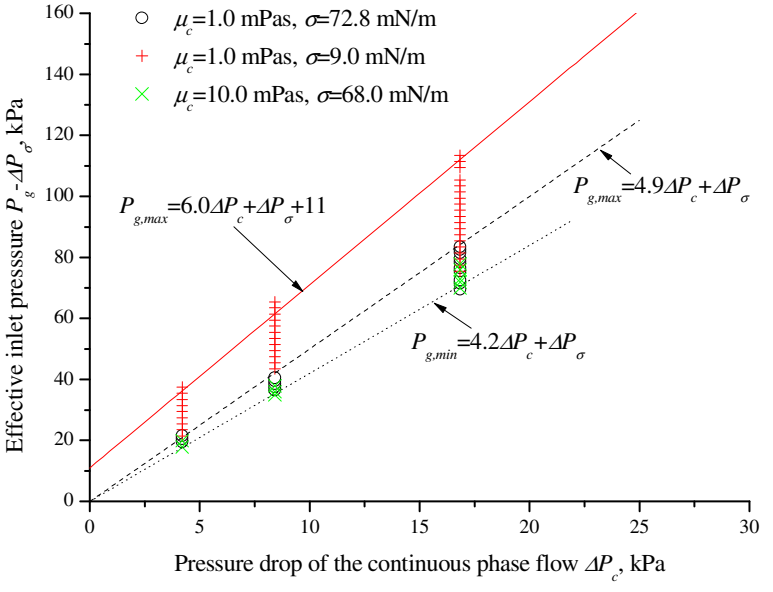

Fig. 39 Bubble formation regime

pressure is larger than the minimum inlet pressure. Figure 40 shows the plot of the variation of bubble volume as changing effective inlet pressures at three typical pressure drops of continuous phase flow. It is noted that the bubble volume almost linearly increases as the effective inlet pressure increases under each pressure drop of continuous phase flow, i.e. $V_b \propto (P_g - \Delta P_\sigma)/\Delta P_c$. Under constant effective inlet pressure and constant pressure drop of continuous phase flow, it is found that the bubble volume is almost the same for the continuous phases with similar interfacial tension (σ=72.8 mN/m and σ=68.0 mN/m), but for the continuous phase with surfactant SDS (σ=9.0 mN/m) the bubble volume significantly decreases. Figure 41 shows the variation of bubble formation time, t_b, as changing effective inlet pressures under the three typical pressure drops of continuous phase flow. It is found that the formation time exponentially decreases as the pressure ratio $(P_g - \Delta P_\sigma)/\Delta P_c$ increases. Under constant effective inlet pressure and constant pressure drop of continuous phase flow, it is found that the formation time decreases as viscosity decreases (i.e. increasing average velocity of the continuous phase flow) at similar interfacial tension (μ_c=10.0 mPas, σ=68.0 mN/m and μ_c=1.0 mPas, σ=72.8 mN/m), and decreases as the interfacial tension increases at the same viscosity (μ_c=1.0 mPas, σ=9.0 mN/m and μ_c=1.0 mPas, σ=72.8 mN/m).

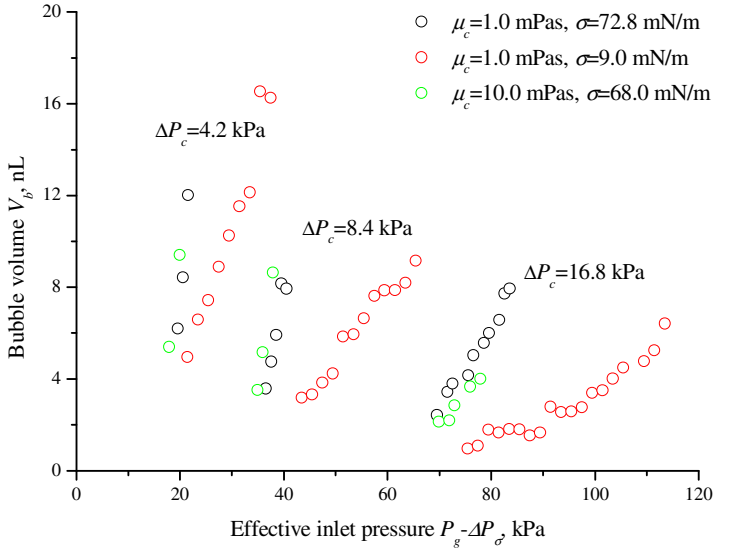

Fig. 40 Variation of bubble volume with the effective inlet pressure and the pressure drop of continuous phase flow

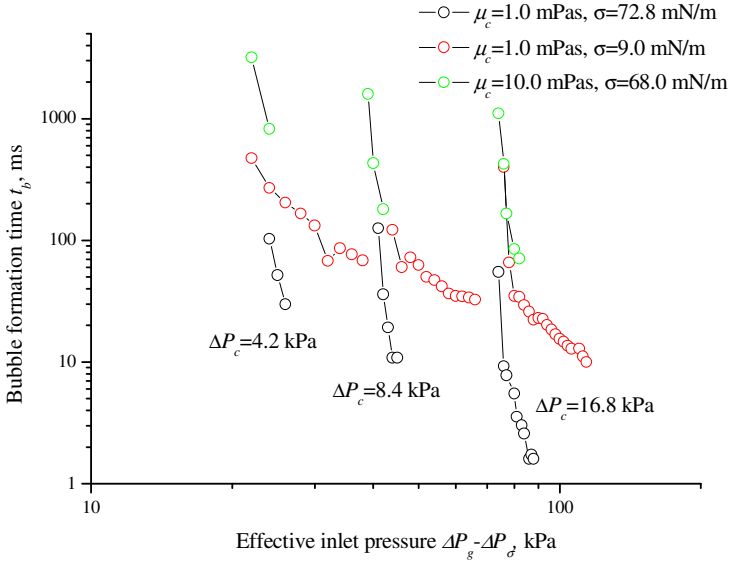

Fig. 41 Variation of bubble formation time with the effective inlet pressure and the pressure drop of continuous phase flow

3.5 Concluding Remarks

Droplet and bubble formation in confined T-shaped junctions are experimentally analyzed. The movement of the rear interface of the forming tip of dispersed phase plays a very important role in determining formation time and volume. Based on the similar formation processes of droplet and bubble and the existence of the minimum inlet pressure in the bubble formation process, the formation process of either bubbles or droplet can be generalized as follows: (1) the dispersed phase tip with a higher pressure gradually intrudes into the continuous phase and the pressure behind the rear interface of the forming tip gradually increases in order to balance the pressure inside the forming droplet/bubble. During this process the rear interface does not move downstream, while the front interface moves downstream within this stage because the initial pressure inside the growing tip is higher than the pressure in the downstream; (2) when the pressure behind the rear interface is increased to a critical value, the rear interface starts to move downstream under the effects of the increased pressure, as well as the viscous force exerted on the rear interface, until touching the downstream corner of the T-shaped junction.

It is experimentally confirmed that the droplet volume is equal to the volume of dispersed phase flowed into the forming tip within droplet formation time. Two empirical correlations for predicting droplet volume and formation time have been developed. When the dispersed phase is liquid and driven under controlled flow rates, the droplet volume linearly increases as the flow rate ratio increases. Influences of continuous phase viscosity, interfacial tension and average velocity of continuous phase can be characterized by capillary number as a correction coefficient to modify the correlations. When the dispersed phase is gas and driven under controlled pressures, it is found that the bubble volume is almost linearly proportional to the ratio of the effective inlet pressure to the pressure drop of continuous phase flow from the T-shaped junction to the outlet. The bubble formation time exponentially decreases as the ratio increases.

4 Droplet Breakup in T-Shaped Junctions

4.1 Introduction

As interests grow in the field of droplet-based microfluidics, more technologies have been developed to control and manipulate droplet size. Inside a droplet, the fast mixing and uniform reaction environment mainly benefits from the small length scale of the droplet. Further reducing the droplet size will even facilitate the mixing and reactions inside the droplet. Droplet breakup after the droplet formation (i.e. droplet fission) is one way to realize such purpose. After breakup, mother droplets will be separated into multiple daughter droplets with either identical or different sizes which can be used to realize parallel reactions simultaneously at different locations inside microfluidics. In Part 3 we have demonstrated the ability

of microfluidic T-shaped junctions in generating uniform droplets and bubbles. Beside the controllable generation ability, microfluidic T-shaped junctions have been also demonstrated to be able of droplet breakup in a controllable manner [68, 70]. It is found that the mother droplets could be broken into smaller daughter droplets in either symmetric or asymmetric T-shaped junctions when the flow condition and droplet size reach a critical condition. Link et al. (2004) proposed a scaling analysis on the critical condition in the symmetric T-shaped junction based on shear-driven-breakup mechanism according to the Rayleigh-Plateau instability in which a cylindrical liquid thread can reduce its total surface area by breaking when its length exceeds its circumference in order to minimize the interfacial energy to get a steady state [68]. The critical condition has also been studied theoretically by using the lubrication theory with a geometrical construction in simplified 2-D symmetric T-shaped junctions [99]. In Part 3, we have studied the droplet formation where the upstream pressure increase significantly influences the droplet formation process due to the confinement. In fact, droplet breakup in a confined T-shaped junction experiences a similar confinement where the upstream pressure should also increase dramatically. We believe such pressure increase will play an important role in determining the droplet breakup. Therefore further examination of droplet breakup in confined T-shaped junctions is necessary for a better understanding of the breakup mechanism.

4.2 Pressure Analysis around Breaking Droplets

To understand the mechanism of droplet breakup, it is critical to understand the driving forces that make the interface deform and move. A perfectly symmetric T-shaped junction is employed to make such analysis of driving forces exerted on the deforming interface. Suppose that a mother droplet is moving in the main channel at a velocity of U_d and has an initial length of L^0_d before entering the T-shaped junction, shown in Fig. 42 (a). The moving speed U_d is actually almost equal to the superficial velocity in the main channel $J=(Q_c+Q_d)/A_c$ due to the negligible slip velocity between dispersed phase and continuous phase [2, 146]. The stage when the mother droplet just fully enters the T-shaped junction is named to be the initial stage of droplet breakup, shown as Fig. 42 (a). At the initial stage the mother droplet has an almost flat interface at the end of the main channel. We focus on the analysis of pressure field around the mother droplet after it fully enters the T-shaped junction. Three pressure points are defined in the continuous phase around the mother droplet and the locations are indicated in Fig. 42 (b). Point P1 is set at the end of the centerline of the main channel, point P2 is near the mother droplet tip, and point Ps is near the curved interface in the middle part of the mother droplet. The average pressure at the defined points is represented by P_1, P_2 and P_s respectively. And the pressure P_1 and P_2 are named to be upstream pressure and downstream pressure, respectively, relative to the breaking droplet. Pressure inside the mother droplet is assumed to be uniform and is equal to P_0. Obviously we can find $P_1>P_s>P_2$ along the flow direction in the continuous phase.

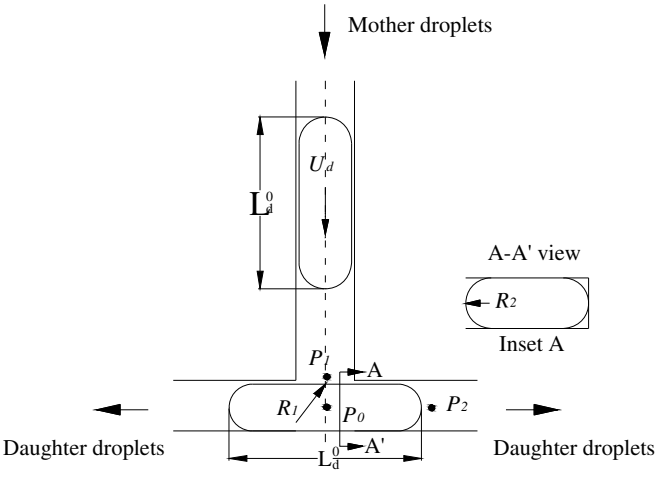

(a)

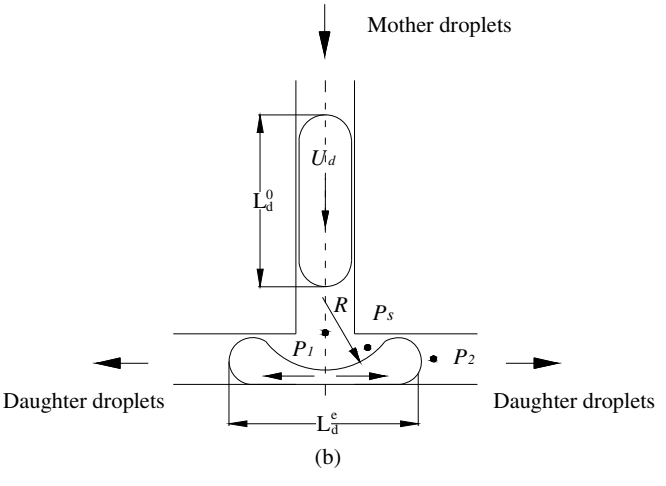

(b)

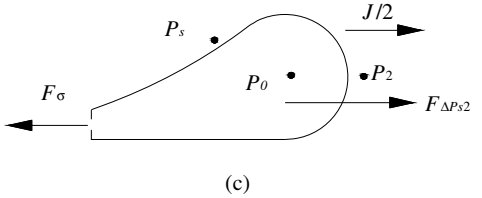

(c)

Fig. 42 Schematic illustration of the mother droplet deformation in a symmetric T-shaped junction

At the initial stage, the principal radius R_1, shown in Fig. 42 (a), of the interface at the end of the main channel has an infinite value, and the principal radius R_2, shown in the Inset A in Fig. 42 (a), is still confined by channel depth, H. According to Young-Laplace equation, assuming the interface motion is quasi-static, the upstream pressure at point P1 is

$$P_1=P_0-2\sigma/H \tag{35}$$

The mother droplet can be treated as blocking the main channel due to the small capillary number that represents the relative weak strength of viscous stresses to interfacial stresses. Therefore the shear stresses exerted on the interface by the continuous phase are not strong enough to deform the interface significantly away from an area-minimizing shape [97]. As a result, the continuous phase is confined to a thin film between the interface and the outlet channel walls. Then the continuous phase flow in the thin film is subject to an increased viscous resistance, which leads to a build-up of the upstream pressure P_1, similar to the pressure increase in a T-shaped junction where a droplet is generated rather than broken up [84, 97, 139, 147].

The pressure build-up of P_1 during deformation can be confirmed by examining the pressure P_s on the curved interface. Again using Young-Laplace equation, the pressure P_s is estimated to be

$$P_s=P_0-2\sigma/H+2\sigma/R, \tag{36}$$

where R is the radius of the curved interface in the middle part of the mother droplet (Fig. 42 (b)). It is clearly shown that the pressure P_s during deformation is already larger than the value of P_1 in the initial stage. Thus the upstream pressure P_1 at the end of the main channel is obviously built up, and this pressure build-up causes the movement of the interfaces until breakup. Similar to that specified by De Menech et al. (2008) [97] for the droplet generation case, we conclude here that the droplet breakup is also fundamentally different from the breakup in unbounded creeping flow because the pressure effects are never negligible, unless the radius of the droplet is much smaller than the channel width [97, 148].

From the above analysis we describe the interface dynamics as the following: after the mother droplet fully enters the T-shaped junction, the interface near the end of the main channel will be deformed due to the pressure build-up in the continuous phase, and the dispersed phase inside the mother droplet will be squeezed downstream, where two droplet tips will be formed (Fig. 42 (b)). The two droplet tips then move downstream in the two outlet channels at the same velocity under the force, $F_{\Delta Ps2}$, caused by pressure difference ΔP_{s2} between points Ps and P2. At this time the two tips are still connected via a thinning column in between them, the resultant force exerted on one tip by the other one can be represented by the interfacial force, F_σ, exerted on the perimeter of the thin column, shown in Fig. 42 (c). Once the upstream pressure P_1 is built up to a critical value that makes $F_{\Delta Ps2}$ large enough to overcome the hinder of the interfacial force and possible viscous forces exerted on the interfaces close to channel walls, the droplet tips will move downstream continuously until breakup. In other words, the critical condition can be expressed as the following: the pressure drop over half of the breaking droplet,

ΔP_{12}, must be larger than the pressure drop, ΔP_{s2}, in order to provide enough energy for the droplet tips to overcome the interfacial energy of the connecting column of the dispersed phase. If $\Delta P_{12}<\Delta P_{s2}$ the droplet tips do not have enough energy and the breakup will not happen.

By treating each droplet tip as a moving droplet, the pressure drop, ΔP_{s2}, can be estimated by the classic Bretheton correlation that describes the pressure drop over a moving droplet/bubble flowing in capillary tubes [2, 149]. Bretherton points out that for droplets moving at a speed of U, the pressure drop across the whole droplet is estimated as $10\sigma Ca^{2/3}/r$, where $Ca=\mu_c U/\sigma$ and r is the radius of capillary tube. In our study the moving velocity of each droplet tip is estimated to be the same as the superficial velocity in each outlet channel, $J/2$, half of the superficial velocity in the main channel, where $J=(Q_d+Q_c)/A_c$. Because, based on our pressure analysis, the movement of tips is mainly driven by pressure where the shear stress is relatively weak, which implies that the slip between interfaces and channel walls is not serious. Then the pressure drop across each droplet tip is estimated to be on the order of

$$\Delta P_{s2} \sim \frac{10\sigma Ca^{2/3}}{H}, \tag{37}$$

where $Ca=\mu_c J/\sigma$. We chose channel depth H as the characteristic length for estimating ΔP_{s2} because the channel depth is smaller than the channel width, meaning that the channel depth has a stronger influence because ΔP_{s2} is inversely proportional to the characteristic dimension. The pressure drop ΔP_{12} over half of the breaking droplet is estimated by the equation describing pressure drop for single phase laminar flow in rectangular channels [143, 145]

$$\Delta P_{12} \sim \frac{12\mu_c (J/2)(L^e_d/2)}{H^2}. \tag{38}$$

The only unknown parameter in Eq. (38) is the length of the extended mother droplet, L^e_d. In fact, this value can be estimated as the value of L^0_d without introducing serious errors because the deformation of the mother droplet is assumed to be driven mainly by pressure where the stretching effect of shear stress is not so strong. By replacing L^e_d with L^0_d and after some simple rearrangement, Eq. (38) becomes

$$\Delta P_{12} \sim \frac{3\mu_c J L^0_d}{H^2}. \tag{39}$$

Balancing Eqs. (37) and (39) with a modification coefficient ψ, we have the critical conditions where breakup of the mother droplet is achievable,

$$\frac{L^0_d}{H} = 3\psi Ca^{-1/3}, \tag{40}$$

In order to get a more concise expression, another dimensionless parameter, $\chi=3\psi$, is used to further simplify Eq. (40) to

$$\frac{L^0_d}{H} = \chi Ca^{-1/3}, \tag{41}$$

where χ is a dimensionless coefficient modifying the estimation of the two pressure drops. From Eq. (41) we can see that at the critical condition the initial droplet length rescaled by channel depth is proportional to the $Ca^{-1/3}$, i.e. $L^0_d/H \propto Ca^{-1/3}$.

4.3 Experiments

4.3.1 Characterization of T-Shaped Functions

Three different designs of microfluidic T-shaped junctions are employed to investigate droplet breakup and are schematically shown in Fig. 43. In each design there are two T-shaped junctions placed along the main channel. The first one locating in the middle point of the main channel is used to generate droplets, and the second one locating at the end of the main channel is used to break up the droplets generated at the first one. The second T-shaped junction in design A is a symmetric structure having two identical outlet channels (Fig. 43 (a)), whereas in design B and C asymmetric T-shaped junctions are adopted (Figs. 43 (b) and (c)). In the designs B and C, the length ratios of two outlet channels are 1:2 and 1:3, respectively. In this Part we do not focus on droplet formation in the first T-shaped junction but focus on droplet breakup at the second T-shaped junction induced by either symmetric or asymmetric outlet channels. The asymmetric influence on the droplet breakup is designed to be realized by asymmetric length of the outlet channels only. In order to eliminate possible influences caused by other geometrical differences, all the other geometrical dimensions in the three designs are the same, including channel width, channel depth and channel length. In any design, the main channel width W_c, the lateral channel width W_d and the outlet channel width W_o are designed to be of 120 μm, i.e. $W_c=W_d=W_o=120$ μm, and the uniform channel depth is designed to be of 35 μm i.e. $H=35$ μm. All the channel dimensions are measured after fabrication and listed in Table 2. The slight difference of channel width in Table 2 is introduced during the fabrication process.

4.3.2 Fluids Selection

Deionized water is selected as dispersed phase, hexadecane and silicon oils with different viscosities are used as continuous phases. The deionzied water is prepared by using a home-made water purification system. The hexadecane and silicon oil are bought from Sigma-Aldrich Inc., USA. Different from the experiments in Part 3, no surfactants are used in the investigation of droplet breakup. The continuous phase viscosities are measured by using a viscometer (SCHOTT-GERATE GmbH, Germany)

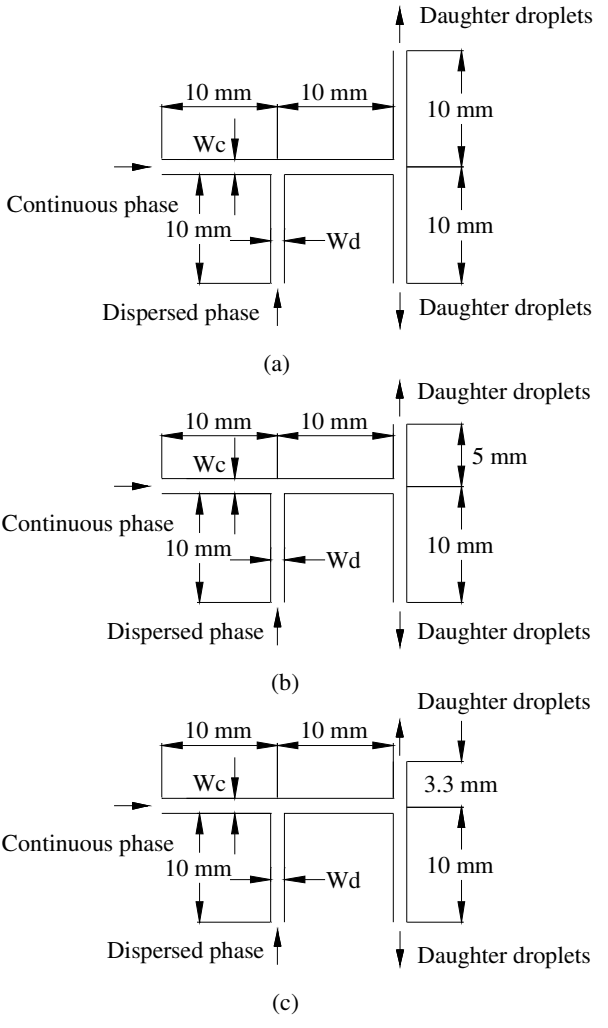

Fig. 43 Channel configurations and dimensions of the T-shaped junctions used for investigating droplet breakup: (a) Design A, length ratio of the outlet channel is 1:1; (b) Design B, length ratio of the outlet channel is 1:2; (c) Design C, length ratio of the outlet channel is 1:3

with an accuracy of 0.65%, and interfacial tensions between the dispersed phases and the continuous phases are measured by using a tensiometer (Cole-Parmer® Surface Tension Meter 20, Cole-Parmer Instrument Company, USA) with an accuracy of 0.25mN/m. Table 3 lists the measured values of the viscosity and interfacial tension at room temperature. Each value is an average over three measurements.

Table 2 Channel dimensions

	W_c=W_d=W_o, μm	H, μm	L, mm
Design A	122.1	36.2	10
Design B	120.7	35.1	10
Design C	125.3	37.3	10

Table 3 Measured viscosities and interfacial tensions at room temperature (23°C)

Dispersed phase-Continuous phase	μ_c / mPa·s	σ / mN/m
Deionized water-Hexadecane	3.0	44.0
Deionized water-Silicon oil (10 mPa·s)	10.0	31.2
Deionized water-Silicon oil (50 mPa·s)	50.0	31.6

4.3.3 Experimental Setup

The experimental setup used in this study is exactly the same as used in the droplet formation investigation in Part 3. For the completeness of this part we simply outline the key steps here. Please refer to Part 3 for more details of the experimental system. The dispersed phase and the continuous phase are injected into the first T-shaped junction by two syringe pumps via flexible PTFE tubings (Cole-Parmer Instrument Company, USA). The flow rate of either phase is automatically controlled by the syringe pumps with an accuracy of 0.5%. An inversed microscope is used for micro visualization purpose (XD101, Nanjing Jiangnan Novel Optics Co. Ltd., China), with which a high speed camera is integrated for recording the droplet breakup process in terms of imagines and videos (MotionPro® X4, IDT, Taiwan). The droplet length is obtained by measuring the micrographs captured by the high speed camera in Adobe Photoshop. To insure the collected information of the droplet breakup is under a steady state, we check out the number of droplets formed within a specific time period at least three times with a time interval at least five minutes after every change of either flow rate of the dispersed or the continuous phase. The pictures and videos are collected only when the number does not change for the last two measurements.

4.4 Results and Discussion

4.4.1 Droplet Breakup in Symmetric T-Shaped Junction

As expected, the mother droplet does not always break in the symmetric T-shaped junction, non-breakup case is also experimentally observed. In the non-breakup cases, mother droplets will flow out the T-shaped junction, without breaking, via the two outlet channels alternatively. More interestingly, besides non-breakup and equal breakup, a third breakup pattern—unequal breakup—is also observed in the symmetric T-shaped junction. We conclude that the unequal breakup is resulted from the asymmetrically geometrical characteristics of the two outlet channels, introduced during the channel fabrication process, which will be discussed in detail later. After measuring the initial length of mother droplet, a pattern diagram of the droplet breakup is plotted in terms of L^0_d/H and Ca, shown in Fig. 44. It is found that there exist three droplet breakup patterns, zone A to C from lower left to upper right in the pattern diagram (Fig. 44). Zone A is the area below the boundary A0-A1-A2, where no droplet breakup occurs. Zone B is constructed by boundary A2-A1-B1-B2, where the mother droplet always breaks into two daughter droplets with identical sizes. Zone C is the area above the boundary A0-A1-B1-B2, where the mother droplet always breaks into two daughter droplets with unequal sizes. Points A0, A1 and B1 locate on the line L^0_d/H=13.3. Boundary A1-A2, the critical condition where the mother droplet can just break up, is experimentally fitted by using Eq. (41) and is shown in Fig. 45. A very good agreement between the experimental values and the estimation of Eq. (41) can be seen and the coefficient χ is found to be χ=1.2.

Figure 46 shows a typical non-breakup situation in zone A. In this zone $L^0_d/H<1.2Ca^{-1/3}$, the pressure difference in the continuous phase over half the deforming mother droplet is not large enough to provide sufficiently large force to overcome the interfacial force due to the relatively short droplet length. Additionally, it is found that the mother droplet will always flow out through the two outlet channels alternatively, shown as the droplets labeled 0, 1 and 2 in Fig. 46. This can be explained by the alternative increment of flow resistance of the two outlet channels and the unbalanced shear forces exerted on each half-droplet. Before reaching the critical condition, the mother droplets size is relatively small, and when they enter the T-shaped junction, the blocking effect is not so serious and the shear forces exerted on the interface cannot be neglected. In Fig. 46 (a) the last previous mother droplet is moving into the outlet channel A (OCA), the flow resistance in this outlet channel will be increased because more energy is needed to overcome the viscous dissipation between droplet interfaces and channel walls. Since pressure drop from the T-shaped junction to either outlet of the two outlet channels is the same, the superficial velocity in the outlet channel A (OCA) will be lower than in the outlet channel B (OCB). When the next mother droplet (droplet 1) arrives at the T-shaped junction, the shear forces exerted on the two halves of droplet 1 are not balanced any more, the relatively larger shear force will drag the

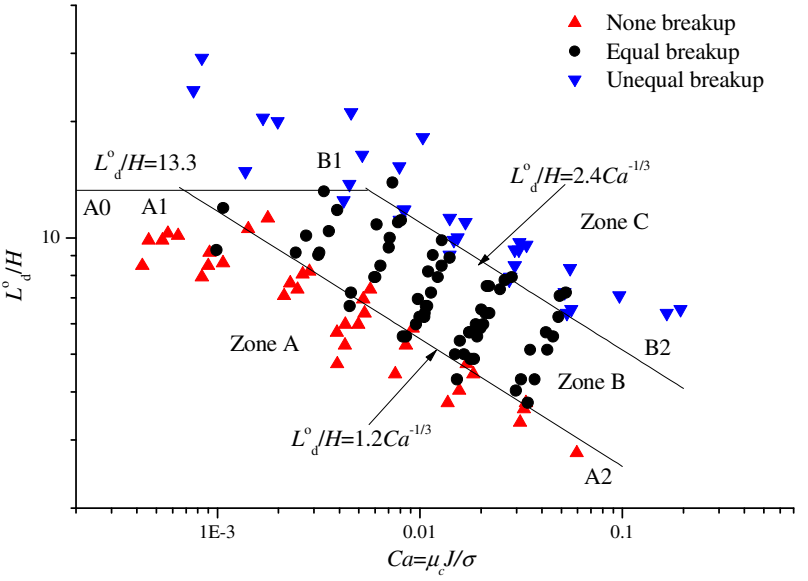

Fig. 44 Droplet breakup pattern in the symmetric T-shaped junction

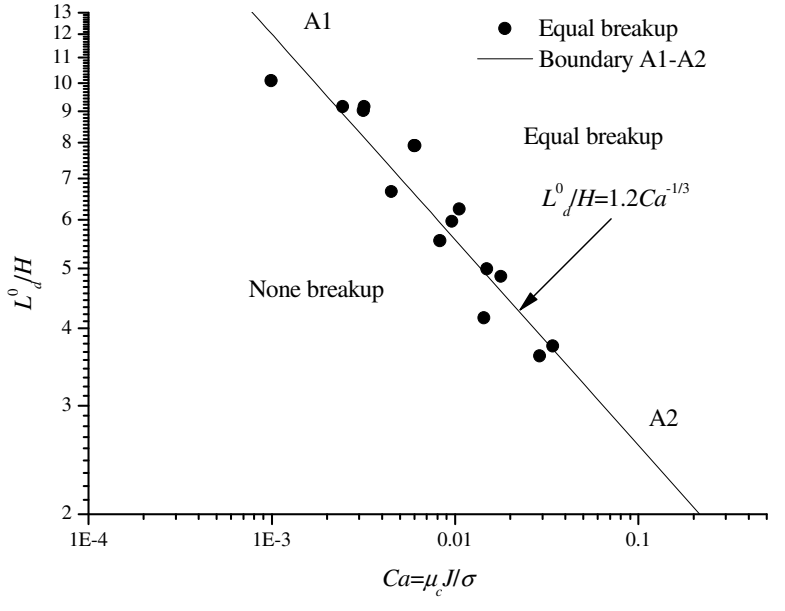

Fig. 45 The critical condition of droplet breakup in the symmetric T-shaped junction

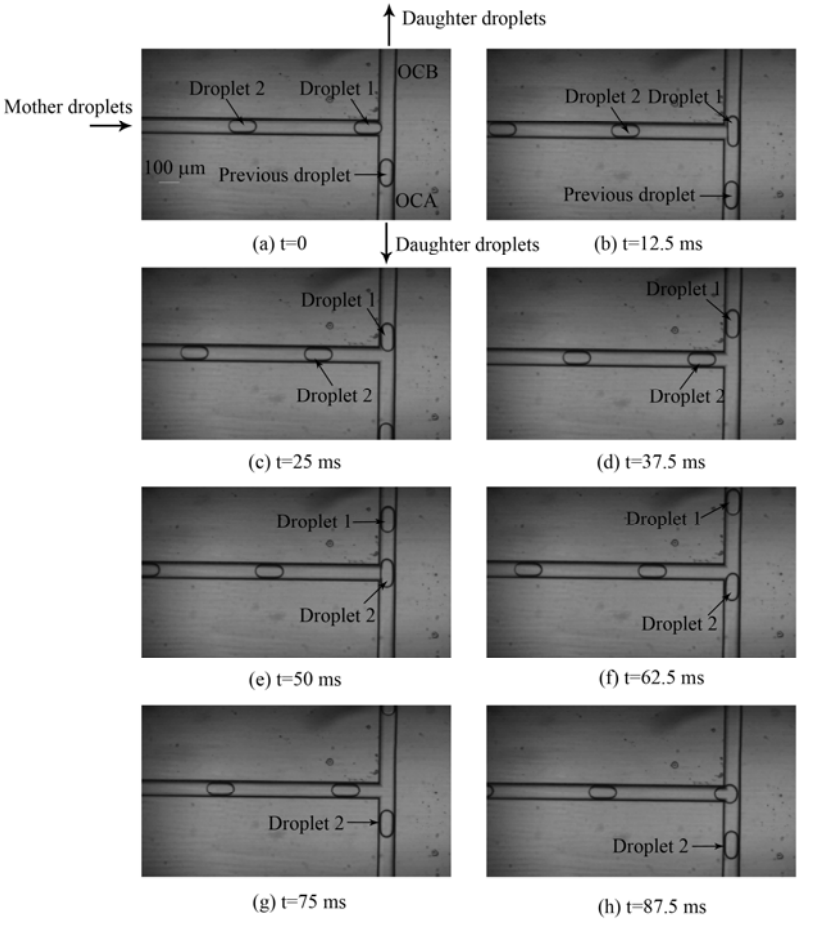

Fig. 46 Typical non-breakup pattern in the symmetric T-shaped junction (L^0_d/H=6.1, Ca=4.3×10^{-3})

mother droplet into the outlet channel B (OCB) where the superficial velocity is higher. The flow resistance now in OCB is higher than OCA because some droplets in OCA have already flowed out and its flow resistance returns to previous level. So the following mother droplet (droplet 2) will flow out through OCA as the similar reason for droplet 1 in OCB. Such alternating cycle will be repeated when the following droplets arrive at the T-shaped junction.

Figure 47 shows a typical process of equal breakup in zone B $1.2Ca^{-1/3}<L^0_d/H<2.4Ca^{-1/3}$. Mother droplets moving in this zone will always equally break into two daughter droplets and flow out through two outlet channels simultaneously.

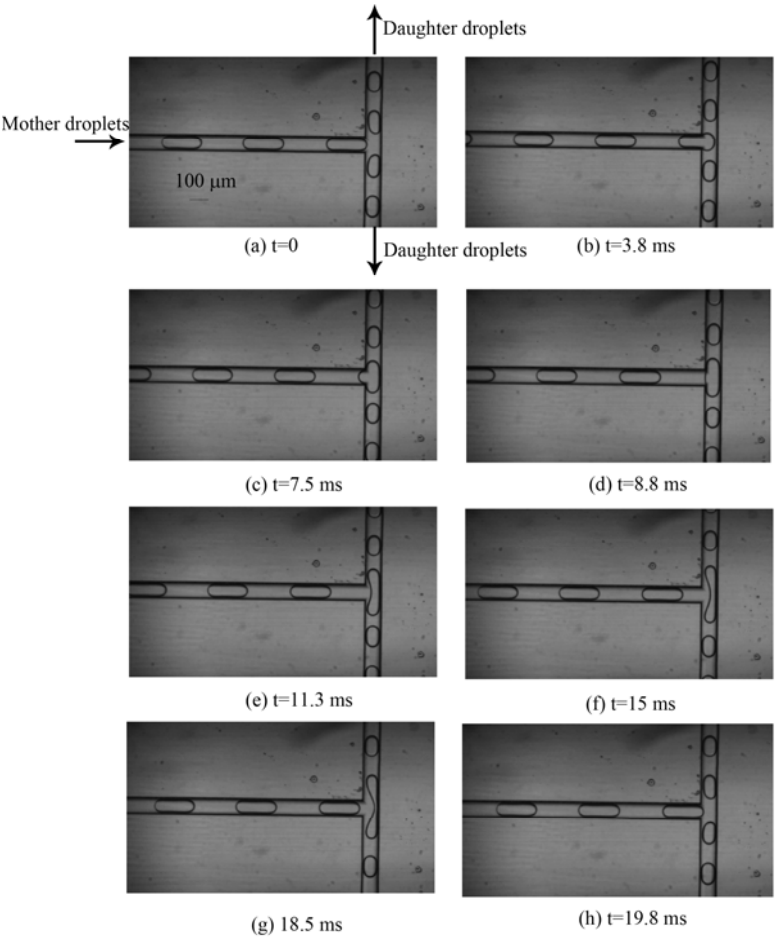

Fig. 47 Typical equal-breakup pattern in the symmetric T-shaped junction (L^0_d/H=8.4, Ca=6.0×10^{-3})

The critical condition described by boundary A1-A2 has been theoretically investigated by Leshansky and Pismen (2009) [99] for 2D T-shaped junctions where the channel depth H was regarded as infinite compared with the channel width W_c. The critical condition was reported to be dependent on the droplet extension and capillary number by combining a geometric construction for the interface and with lubrication analysis in the narrow gap between the breaking mother droplet and channel walls. By using our notation, the analytical solution is

$$L^e_d/W_c \approx 1.3Ca^{-0.2}, \tag{42}$$

where L^e_d is the extended length of mother droplet at the critical condition. Leshansky and Pismen (2009) did not show the explicit relation between L^e_d and the

initial droplet length L^0_d. To do the comparison, we use the initial droplet length L^0_d and H in stead of L^e_d and W_c in Eq. (42), respectively. Link et al. (2004) reported another correlation based on experimental observation combined with the classical Rayleigh-Plateau instability in which a cylindrical liquid thread can reduce its total surface area by breaking when its length exceeds its circumference under the effect of shear stress [68, 150]. By using volume conservation before and after the mother droplet deformation, a correlation describing the critical condition of droplet breakup was proposed

$$Ca = \alpha\left[L^0_d/(\pi H)\right]\left[\left[L^0_d/(\pi H)\right]^{-2/3} - 1\right]^2, \tag{43}$$

where α was a dimensionless constant depending on viscosity contrast of dispersed phase to continuous phase and on the geometry of junction. Its value was experimentally fitted to be 1 in their study. This correlation was examined by numerical simulations by using a phase-field method conducted by De Menech (2006) [151]. Figure 48 shows the comparison of the critical condition between our results Eq. (41) and the two reported correlations, Eqs. (42) and (43), by plotting Ca as a function of L^0_d/H in order to get a uniform format with Eq. (43) where L^0_d cannot be expressed by Ca explicitly. It is found that a large discrepancy exists between our correlation and the two reported ones. We conclude that the large discrepancy is resulted from different reasons for the two reported correlations. The correlation, Eq. (42), is derived from a 2-D simplification where the channel depth is regarded as infinite and the influence of channel geometry is only from the channel width. We consider that such assumption may not be suitable for determining the influence of channel geometry in real microchannels, especially rectangular ones. In rectangular microchannels the depth is usually comparable or less than the width, therefore the influence of channel depth cannot be neglected. The difference between our correlation and that reported by Link et al. (2004) [68], Eq. (43), is resulted from the different understanding of the mechanism behind the droplet breakup. Their correlation is proposed based on the consideration of a shear-driven breakup rather than pressure driven. This kind of consideration is reasonable for their experiments because in their experiment the capillary number is relatively high, Ca>0.1, and the droplet length is relatively small, L^0_d/H<4, which will result in a relative larger shear stress than the increased pressure exerted on the interface of the deforming mother droplet. In our experiments, the capillary number is much smaller, Ca~10^{-3}-10^{-1}, and the droplet length is relatively large, L^0_d/H>4, which makes the breakup dominated by the pressure driven rather than the shear driven. From this kind of comparison we can see that for mother droplets with different sizes and flowing at different capillary numbers, different mechanisms of droplet breakup, either the shear driven or the pressure driven or both, should be considered.

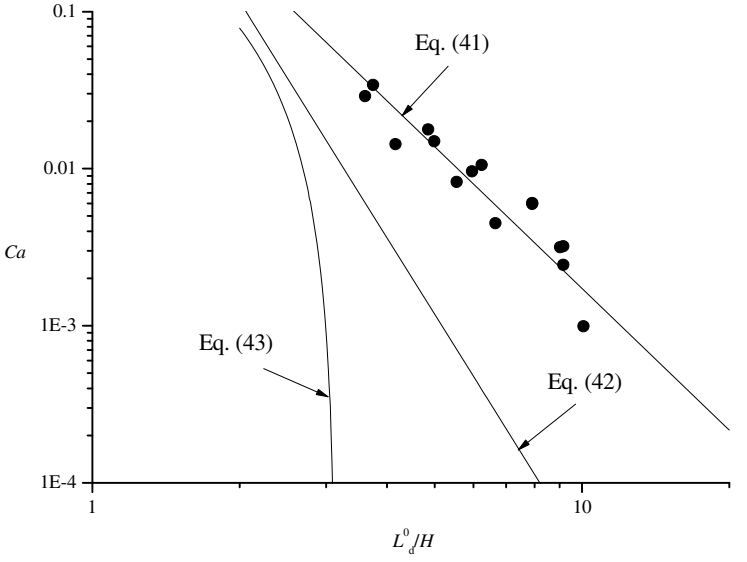

Fig. 48 Comparison of the critical condition with the reported ones

Theoretically all the mother droplets locating above the critical boundary $L^0_d/H=1.2Ca^{-1/3}$ should break into two equal-sized daughter droplets. However we find when $L^0_d/H>2.4Ca^{-1/3}$ or $L^0_d/H>13.3$ (zone C in Fig. 44), the mother droplet will not break up equally any more. Figure 49 shows a typical process of the unequal breakup. This asymmetric breakup is probably caused by the asymmetry of the two outlet channels introduced in the channel fabrication process. For a perfectly symmetric T-shaped junction, the flow field at the T-shaped junction is always symmetric to the center line of the main channel. However fabricating a perfectly symmetric T-shaped junction seems impossible in practice. In our channel fabrication process, asymmetric features of outlet channels may be resulted from non-uniform strength of wet etching induced by possible non-uniform ultrasonic strength. Then, when mother droplets enter the T-shaped junction, different amount of dispersed phase will be squeezed into the outlet channels (Fig. 49 (e)) and the mother droplets finally break into two daughter droplets unequally due to the asymmetric flow resistance. It is interesting to note that the influence of geometrical asymmetry on droplet breakup does not appear in Zone B, equal breakup zone. Such breakup difference means that the asymmetric influence is quite sensitive to droplet size and flow conditions in the T-shaped junction. In Zone B the influence of geometrical asymmetry is weak and unequal breakup cannot be observed. However, the influence will become strong enough to make mother droplets break up unequally for the combinations of droplet sizes and flow conditions in Zone C.

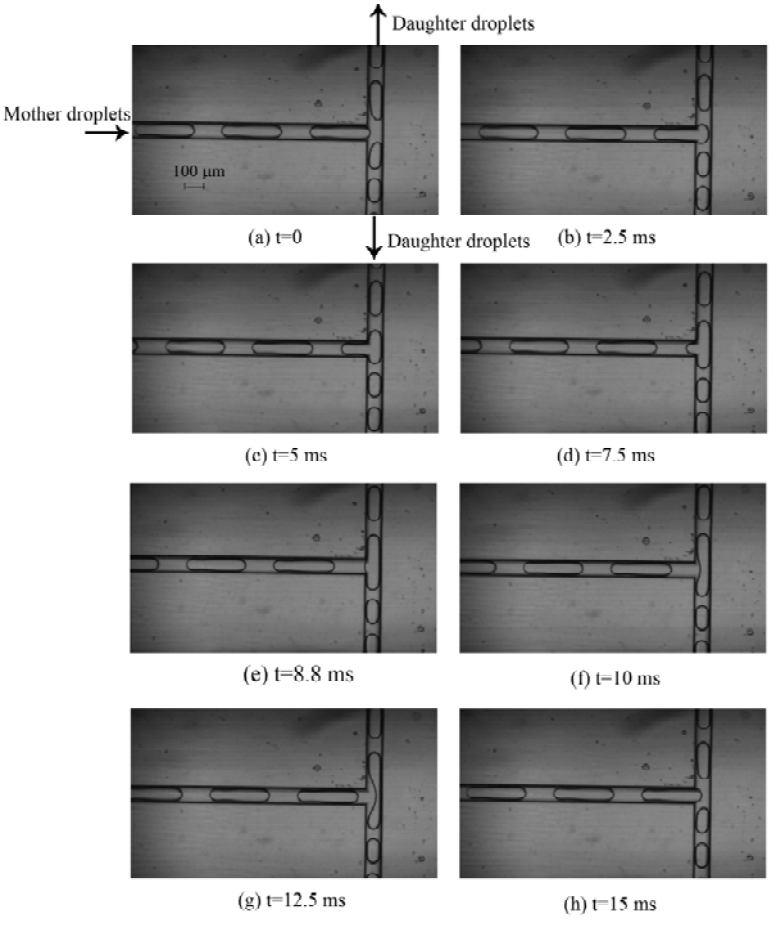

Fig. 49 Typical unequal-breakup pattern in the symmetric T-shaped junction (L^0_d/H=12.3, Ca=5.7×10^{-3})

4.4.2 Droplet Breakup in Asymmetric T-Shaped Junctions

Figure 50 shows our experimental results on droplet breakup in the asymmetric T-shaped junctions. It is found that the droplet breakup in the asymmetric T-shaped junctions is quite difficult. As we change the capillary number three orders of magnitude ($10^{-4}<Ca<10^{-1}$), only several points are found in the T-shaped junction with 1:2 outlet channel ratio (Design B), where the mother droplets can break up, shown as the black dots in Fig. 50. In the T-shaped junction with 1:3 outlet channel ratio (Design C), we do not find any breakup within our experimental range. Even at the several breakup points in Design B, we find that the droplet breakup at the second T-shaped junction is not stable any more. Figure 51 shows the two typically

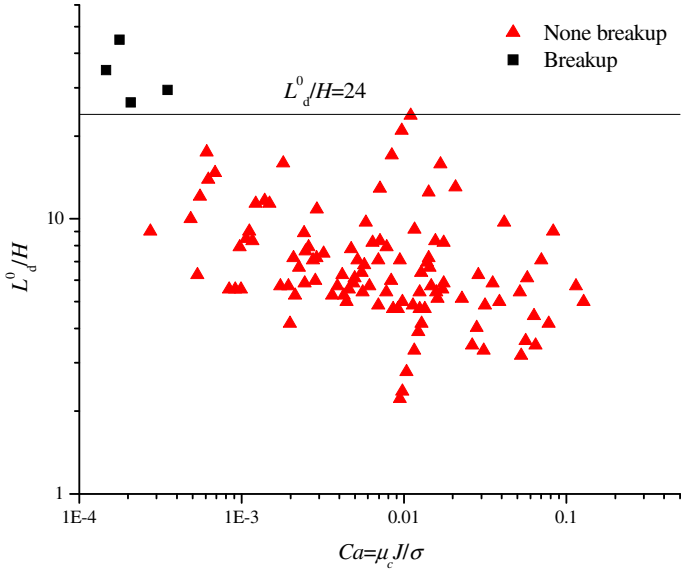

Fig. 50 Droplet breakup pattern in asymmetric T-shaped junctions

unstable breakup situations. The length ratio of the daughter droplets changes from case to case.

In asymmetric T-shaped junctions, it is found that mother droplets always flow out via the shorter outlet channel and no droplets flow out through the longer one, shown in Fig. 52. As mother droplets enter the asymmetric T-shaped junctions, the moving droplet tip in the short outlet channel always moves at a much higher speed than the tip in the longer channel due to the lower flow resistance in the shorter outlet channel (Fig. 52 (b)). After mother droplets fully enter the T-shaped junction, a smaller half will be formed in the longer outlet channel, and a longer half will be formed in the shorter outlet channel (Fig. 52 (c)). The blockage effect of the short half droplet is much weaker than the longer half, and the deformation of the short half droplet in the longer channel at this time is mainly driven by viscous forces (Figs. 52 (d)-(f)). In the longer channel the superficial velocity is much lower; the resulted viscous forces are not large enough to overcome the interfacial forces exerted on the perimeter of the dispersed phase column connecting the two halves. Then the short half droplet will be pulled into the shorter channel and flow out (Figs. 52 (g) and (h)).

Droplet breakup in asymmetric T-shaped junctions was also investigated by Link et al. (2004) [68]. They mentioned that mother droplets will break into two different-sized daughter droplets with a length ratio inversely proportional to the length ratio of the outlet channels. But they did not mention the conditions where

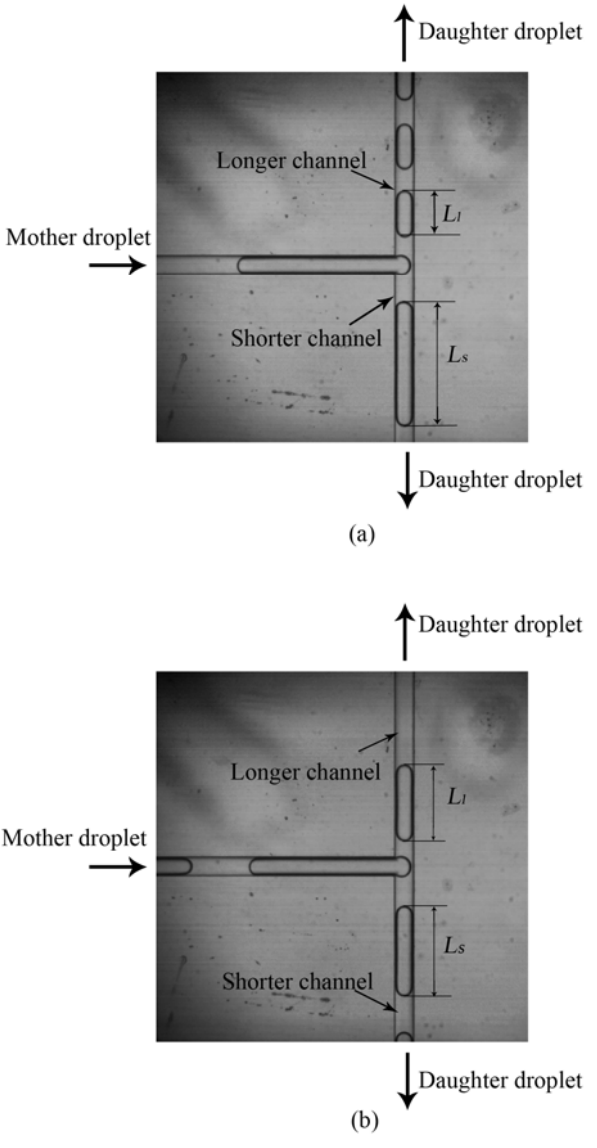

Fig. 51 Unstable droplet breakup in the asymmetric T-shaped junction with the outlet channel length ratio of 1:2 (Design B) (L^0_d/H=32.0, Ca=1.5×10^{-4}): (a) L_l:L_s=0.36 (b) L_l:L_s=0.86

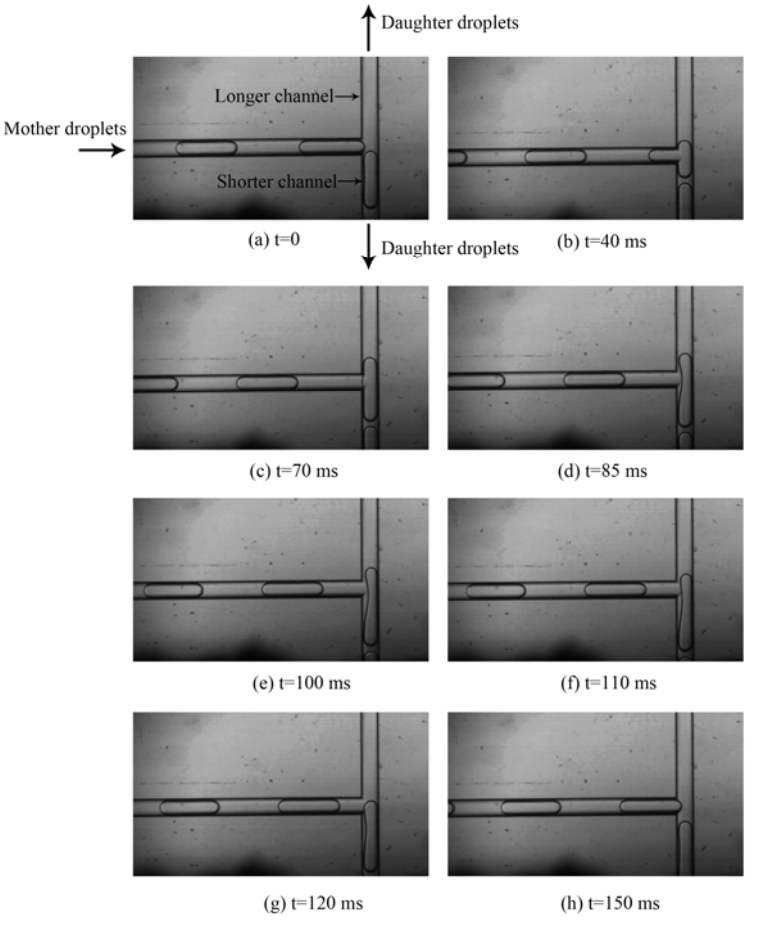

Fig. 52 Typical non-breakup pattern in asymmetric T-shaped junctions (L^0_d/H=10.7, Ca=2.1×10^{-4})

this breakup can be realized and if the breakup was stable or not. In our work, we find that the droplet breakup in asymmetric T-shaped junctions is quite difficult. Only when the mother droplets are sufficiently long and the capillary number are sufficiently small several unstable breakup cases can be observed (L^0_d/H>24 and Ca<3×10^{-4}). We consider that such big difference between our study and that reported by Link et al. (2004) [68] is resulted from the large difference of interfacial tension. In their work, they used surfactant (Span 80) to stabilize the droplets against coalescence, which will also decrease the interfacial tension significantly. The interfacial tension in their study is about σ=5 mN/m, whereas it is σ=44 mN/m in our works without any surfactant. Droplets with lower interfacial tension will facilitate the breakup because the interfacial tension force is easier to overcome.

4.5 Concluding Remarks

Scaling analysis of the critical condition for droplet breakup in symmetric T-shaped junctions is conducted based on the analysis of the pressure field during droplet breakup. The scaling analysis is experimentally confirmed, implying that the droplet breakup in a confined T-shaped junction is a pressure-driven process when the capillary number is less than ~0.1. After mother droplets fully enter the T-shaped junction, the upstream pressure will be increased significantly and such pressure increase is the main driven force yielding the droplet breakup. The critical condition where mother droplets can breakup is found to be dependent on the initial droplet length, channel depth and capillary number, which can be formulated as $L^0_d/H \propto Ca^{-1/3}$. A new droplet breakup pattern, unequal breakup, is found in the symmetric T-shaped junction. Such unequal breakup is resulted from the slightly asymmetric properties of the T-shaped junction introduced in the fabrication process. In other words, slight asymmetry of T-shaped junctions will influence the breakup significantly under some flow conditions. In practical operation of droplet breakup, flow conditions should be controlled within proper ranges where the influence of the asymmetry does not appear. In asymmetric T-shaped junctions it is found that the droplet breakup is quite difficult, and reducing interfacial tension may benefit the droplet breakup.

5 Chaotic Mixing in Microfluidic Droplets

5.1 Introduction

Microfluidic reactors have been widely used for performing chemical reactions because the reactions can be more precisely controlled at microscale than at conventional macroscale due to the laminar flow of low Reynolds number. Although diffusion mixing over the microscale is already much faster than at traditional macrosacle, the mixing efficiency is still seriously limited by diffusion and sometimes it cannot satisfy our requirement. Thus, efficient mixing of reagents requires a stirring mechanism, such as chaotic advection that stretches and folds fluid elements throughout the entire volume of the flow. In single phase flow, various channel structures and obstacles have been designed to introduce chaotic advection in order to increase the mixing efficiency, including C-shaped channel [152], L-shaped channel [153, 154], X-shaped channel [155] and some other geometries [156, 157]. However, those complex structures are not easy to fabricate and the cost is quite high. More recently microfluidic droplets are widely reported as effective reactors where the mixing is significantly enhanced due to the naturally chaotic advection inside the droplets moving in the Stokes flow [10, 158-164]. The residence time distribution is also narrowed down as a result of confined dispersion inside the droplets, compared with reactions in the single phase flow.

The mechanism of chaotic mixing inside moving droplets is normally studied by idealizing the chaotic advection as the recirculating flow and is explained by the Baker's transformation. In this part we will discuss the scaling of the full mixing time of chaotic mixing based on the work reported by Bringer et al. (2004) [165], and compare with our experimental results.

5.2 Recirculating Flow Inside Moving Droplets

Suppose that the velocity of a moving droplet is U_d and the absolute velocity field inside the moving droplet is u. Then near the front and back interfaces inside the moving droplet $u \approx U_d$ as the continuity requirement and in the areas far from the front and back interfaces the velocity profile is parabolic due to the viscous stress exerted on the moving interfaces induced by channel walls. Figure 53 (a) shows a schematic illustration of the flow field inside the moving droplet. For the parabolic type flow far away from the front and back interfaces, the internal velocity is largest in the center-plane of the microchannel and decreases to a smallest value on the interfaces close to channel walls. When we examine the relative velocity field, u-U_d, inside the moving droplet, a pair of symmetric vortices will be presented, resulted from the symmetric influences of channel walls. The relative velocity field can be understood as the fluid velocity observed from inside the droplet (droplet frame of reference), which means that the observer is moving at the same velocity as the droplet. Such symmetric vortices pair has already been confirmed by many researchers in either numerical or experimental studies [146, 166-170]. In curved channels the two vortices are not symmetric any more due to the asymmetry of flow field inside the moving droplet and the asymmetric influence of channel walls. It is found that a big vortex always locates near the outer wall side and a small vortex always locates near the inner wall side [146, 171-174]. Figure 53 (c) schematically shows the two asymmetric vortices.

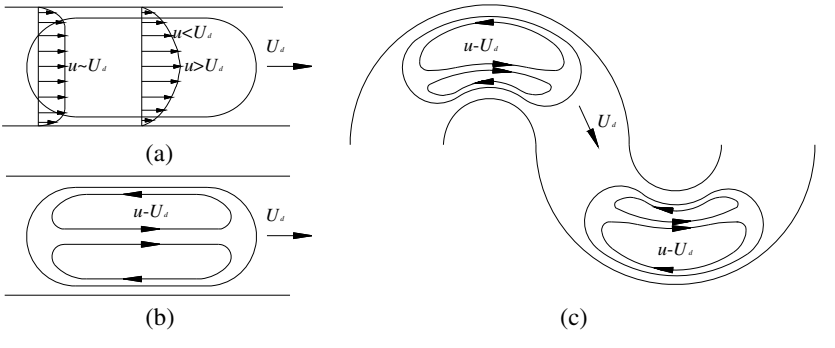

Fig. 53 Schematic illustration of recirculating flow in moving droplets

The mixing rate inside moving droplets depends on the relative fluid velocity. The recirculating flow inside each vortex will significantly enhance the mixing efficiency, and such rapid mixing is usually referred to chaotic mixing in microfluidics area [35, 160, 163, 165, 174, 175]. In general, there are two arrangements of the reagents to be mixed inside a moving droplet, relative to the center-plane of the moving droplet. In the first arrangement the two reagents can be located along the center-plane, shown in Fig. 54 (a), and in the other one the two reagents can be located perpendicularly to the center-plane, shown in Fig. 54 (b). It is intuitively seen that for the first arrangement the internal recirculating flow will result in chaotic mixing in either straight channels or curved channels. For the second arrangement, the recirculating flow cannot benefit the mixing of reagents in straight microchannels because the two vortices totally locate within the two reagents respectively and the recirculating flow in each vortex can only induce recirculation inside the reagent where it is located (Fig. 54 (b)). The mixing between the two reagents can only rely on diffusion through the "interface" of the two vortices, i.e. the center plane of the moving droplets. In curved channels, however,

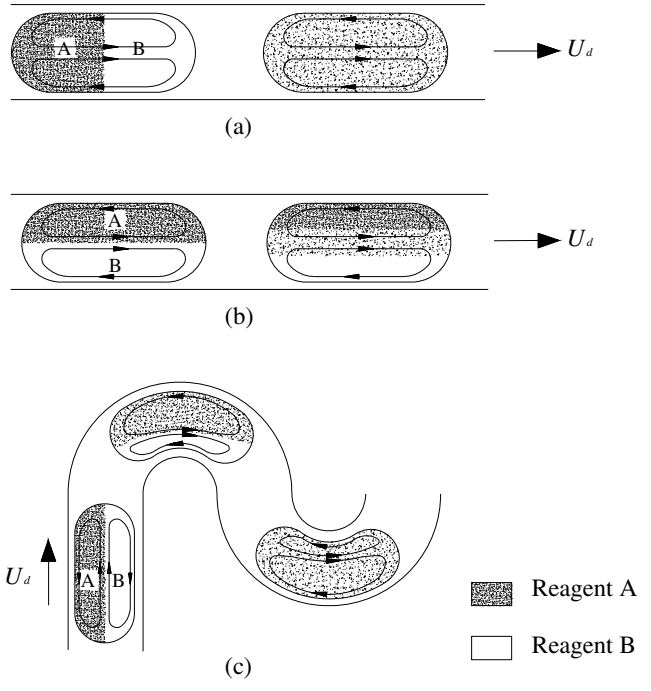

Fig. 54 Mixing situation at different initial distribution of the two reagents: (a) the two reagents distributed along droplets center plane in straight channels, (b) the two reagents distributed perpendicular to droplets center plane in straight channels, and (c) the two reagents distributed along droplets center plane in curved channels

chaotic mixing inside droplets can still happen due to the asymmetric feature of the two vortices. Figure 54 (c) schematically illustrates the process how the asymmetric vortices facilitate the mixing of reagents A and B. Before the droplet enters the curved microchannels, the two reagents are equally distributed perpendicularly to the center-plane of the moving droplet. In the first curved section, the bigger vortex will bring an amount of reagent B exposed to the inner wall into vortex A. When the channel curvature reverses in the following section the original smaller vortex evolves into the relatively bigger one and takes an amount of reagent A. As such alternative exchange is repeated, the chaotic mixing of the two reagents will be realized under the effects of the recirculation within each vortex and under the advection of the "interface" between the two vortices.

5.3 Baker's Transformation

Baker's transformation is usually employed to explain the chaotic mixing inside moving droplets [159, 165, 176-178]. The Baker's transformation can be geometrically explained in Figs. 55 (a)-(c): a unit square is stretched to a rectangle which is twice as wide and half as tall, and then this rectangle is cut along the center plane, and then place the right-hand part above the left to reform a square. After one time Baker's transformation the number of interfaces between reagents A and B increases from 1 to 2. Figures 55 (a)-(g) demonstrates the interface increment after three times Baker's transformation. The interface number increases from 1 to 8. From the Baker's transformation it is seen that the interface number is increased by a factor of two for each cycle of stretching and folding, and as the cycles are repeated the interfaces between the two reagents increase exponentially according to

$$N = 2^n , \tag{44}$$

where N is the interface number after n cycles of Baker's transformation.

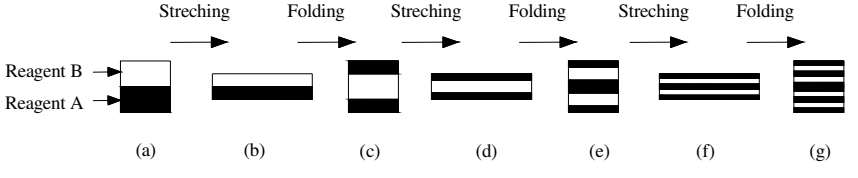

Fig. 55 Schematic illustration of the Baker's transformation

5.4 Scaling Analysis of Chaotic Mixing

Microfluidic mixing normally operates at low Reynolds number and over small length scale where turbulence cannot happen. Therefore the diffusive mixing in

laminar streams is the most significant feature inside either droplets or continuous streams. The time consumed by diffusion to reach full mixing, t_{fdif}, is proportional to the square of the striation thickness and inversely proportional to the diffusion coefficient

$$t_{fdif} = \frac{S_t^{\,2}}{2D}, \tag{45}$$

where S_t is the striation thickness, the distance that reagents must diffuse to mix with each other [179]. D is the diffusion coefficient. The striation thickness is defined as

$$S_t = \frac{V_{total}}{A_{ti}/2}, \tag{46}$$

where V_{total} is the total volume involving interfaces, and A_{ti} is the total interfacial surface area involved in the total volume. When there is only one interface between the two reagents, this stage is defined as the initial stage. At the initial stage, by treating the droplet to be a cuboid, the droplet volume is estimated to be $V_{total} \approx L_d W_c H$ and the total interfacial surface area $A_{ti} = A_0 \approx 2L_d H$ (Noting that one interface has two interfacial surfaces), where L_d is the droplet length, W_c is the channel width and H is the channel depth. Therefore the initial striation thickness is $S_0 \approx W_c$. When chaotic mixing happens, the recirculation inside droplets is reasonably treated as repeatedly stretching and folding that can be idealized by the Baker's transformation. Figure 56 schematically shows the increased interface number, as well as interfacial surface area, between reagent streams in each vortex after a number of recirculation cycles. As a result the total interfacial surface area increases to, according to Eq. (44),

$$A_{ti}(n) = N \cdot A_0 = 2^n A_0, \tag{47}$$

where A_0 is the initial interfacial surface area before the recirculation occurs and n is the number of recirculating cycles. During the mixing process, the two reagents are confined in the droplet and the total volume is not changed. Then the striation thickness will decrease exponentially based on Eq. (46)

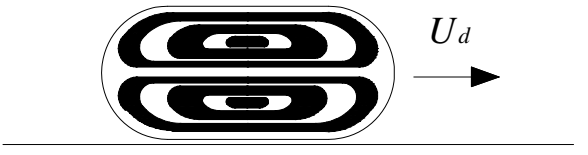

Fig. 56 Schematic illustration of the increased interfaces inside a moving droplet

$$S_t(n) = \frac{V_{total}}{2^n A_0/2} = \frac{S_0}{2^n}, \tag{48}$$

where S_t (n) is the striation thickness after n cycles recirculation. Substituting Eq. (48) into Eq. (45) leads to

$$t_{fdif}(n) = \frac{1}{2^{2n}} \frac{S_0^{\,2}}{2D} = \frac{t_0}{2^{2n}}, \tag{49}$$

where t_0 is the initial diffusion time, t_0=S_0^2/(2D). Equation (49) presents the mechanism behind the chaotic mixing in moving droplets: recirculating flow inside the moving droplets results in exponential decrease of the striation thickness, where full mixing by diffusion happens not necessarily on the droplet width scale but on the scale of the decreased striation thickness, and then the diffusion time over the striation thickness is exponentially decreased. Note that the initial striation thickness $S_0 \approx W_c$. The initial diffusion time to reach full mixing is estimated to be

$$t_0 \approx \frac{W_c^{\,2}}{2D}. \tag{50}$$

Substituting Eq. (50) into Eq. (49), the diffusion time after n cycles recirculation, $t_{fdif}(n)$, is obtained

$$t_{fdif}(n) \approx \frac{W_c^{\,2}}{2^{2n+1} D}. \tag{51}$$

We estimate that the recirculation velocity, u-U_d, is on the scale of 0.5U_d [168]. The time taken by one cycle recirculation inside the droplet is then estimated to be on the scale of

$$t_{conv}(1) \sim \frac{2L_d}{0.5U_d}, \tag{52}$$

and the time consumed by n cycles recirculation is estimated to be

$$t_{conv}(n) \sim \frac{4nL_d}{U_d}. \tag{53}$$

where t_{conv}(1) and t_{conv}(n) is the time consumed by one cycle and n cycles recirculation flow by convection inside the droplet, respectively.

It is generally assumed that the full mixing time is approximately the time when the diffusion time on the striation thickness scale and the convective transport time inside droplets are matched [159, 160, 165, 180]. In other words, after n cycles recirculation the diffusion time over the striation thickness will be equal to or much

smaller than the total time collapsed already [165]. Based on this assumption, we can balance the time consumed by diffusion over the striation thickness with the time consumed by the convection,

$$t_{fdif}(n) \sim t_{conv}(n). \tag{54}$$

Substituting Eqs. (51) and (53) into Eq. (54), we have

$$\frac{W_c^{\,2}}{2^{2n+1}D} \sim \frac{4nL_d}{U_d}. \tag{55}$$

Rescaling the droplet length by the channel width, $L_d=mW_c$, results in

$$\frac{W_c^{\,2}}{2^{2n+1}D} \sim \frac{4nmW_c}{U_d}, \tag{56}$$

where m is the dimensionless droplet length rescaled by channel width.

After some rearrangement, Eq. (56) becomes

$$2^{2n+3}mn \sim \frac{W_c U_d}{D} = Pe \tag{57}$$

where Pe is the Peclet number defined by $Pe=W_cU_d/D$.

The value of n (the number of recirculation) can be determined by taking logarithm operation on both sides of Eq. (57),

$$n \sim \frac{\log(Pe)-\log(mn)}{2\log 2} - \frac{3}{2}. \tag{58}$$

Given that Pe and m are known values, the value of n can be numerically solved from Eq. (58), and substituting the value of n into the express Eq. (53), the full mixing time scale by diffusion is then estimated to be,

$$t_{fdif} \sim t_{conv}(n) \sim \frac{4nL_d}{U_d} \tag{59}$$

5.5 Experiments

5.5.1 Fluids Selection

Silicon oil with the viscosity of 10^{-2} mPas is used as continuous phase. Two reagents to be mixed are Parker ink solution (Parker Quink black) and deionized water (colorless). The Parker ink solution is used as a dye solution to evaluate the mixing efficiency. The reagents chosen should satisfy the following requirements:

(1) the two reagents must be miscible to each other; (2) the two reagents must have a strong black and white contrast under the illuminating light, limited by the monochrome color of the high speed camera used in our experiment. The dye solution in this investigation is prepared by diluting black Parker ink with deionized water at a volume ratio of 1:10.

5.5.2 Channel Design and Characterization

Figure 57 schematically shows the channel configuration in this study. Two inlet channels for introducing ink solution and deionized water are merged into a very short channel before entering the main channel, where a T-shaped junction is constructed. Droplets containing the reagents to be mixed will be generated at the T-shaped junction. The curved channel consists of a series of S-shaped sections connected sequentially, shown in Fig. 57 (b). The total channel length from the T-shaped junction to the outlet is L=103 mm, the channel width is W_c=122.1 μm, and the radius of curvature of the channel centerline is R=120 μm. Wetting ability modification of the microchannel walls has to be applied in order to get hydrophobic surfaces that are necessary for aqueous droplets formation in the T-shaped junction.

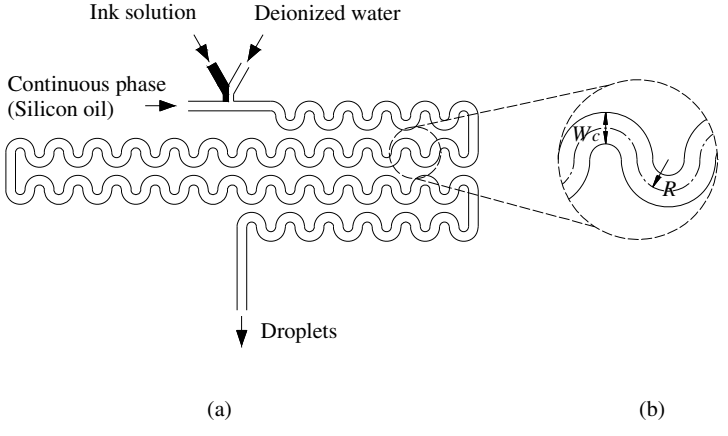

Fig. 57 Schematic diagram of the channel design

5.5.3 Experimental Setup

Figure 58 presents the schematic diagram of the experimental system. The ink solution and the deionized water are preloaded in two identical syringes (2.5 mL, Gastight 1001, Hamilton Co., USA) and are injected into the inlet channels at the same volumetric flow rate controlled by the same syringe pump (Cole-Parmer® 74900, Cole-Parmer Instrument Company, USA). Such arrangement of one syringe

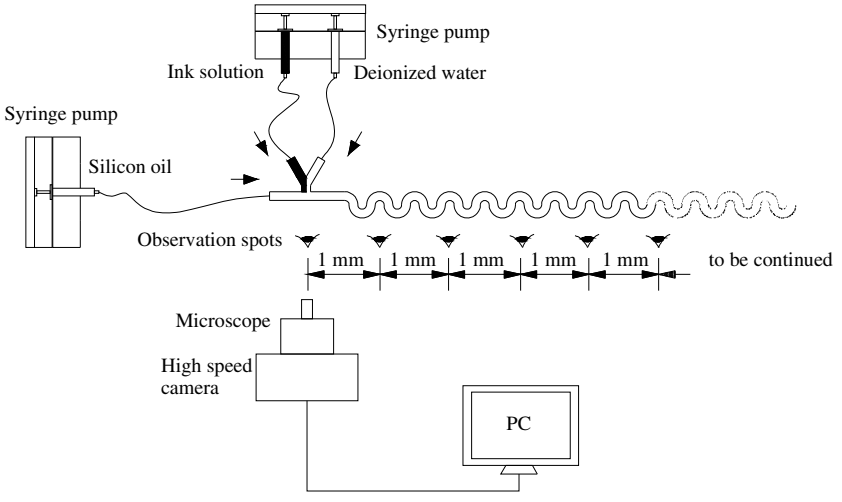

Fig. 58 Experimental setup for investigating chaotic mixing inside droplets

pump propelling two identical syringes secures that the feed of the two reagents is always at a same flow rate, where equal volume distribution in the droplets is realized. Another syringe pump with the same model is used for introducing the continuous phase, silicon oil. All the flow rates are automatically controlled by the syringe pumps. An inversed microscope is used for visualization purpose (XD101, Nanjing Jiangnan Novel Optics Co. Ltd., China), with which a high speed camera is integrated for recording the mixing process in droplets in terms of imagines and videos (MotionPro® X4, IDT, Taiwan). We note that the images recorded in our experiment give an average mixing situation in the channel depth direction, which is limited by the microscope used in this study. A full scale 3-D mixing visualization in microscale is still a challenging problem. The lens used in this experiment is either 4×, tracking droplets location along the main channels, or 10×, evaluating the chaotic mixing efficiency inside the droplets. Because the 4× lens gives a wider field of view (view diameter is about 1.5 mm) in the digital micrographs captured by the high speed camera but with a lower resolution, whereas the 10× lens gives a narrower field of view but with a higher resolution (view diameter is about 0.5 mm). Therefore the 4× lens is used for finding the full mixing location primarily and quickly, and then the 10× lens is used near that location for further evaluating the chaotic mixing efficiency with a higher resolution. Droplet traveling time is directly measured from the consecutive images by utilizing the software provided with the high speed camera. Droplet length and channel width in micrographs are measured in ImagJ (Rasband, W.S., ImageJ, U. S. National Institutes of Health, Bethesda, Maryland, USA, http://rsb.info.nih.gov/ij/, 1997-2009). To insure the droplet formation and the mixing inside are under a

stable state, we check out the number of droplets as well as the volume distribution of the two reagents within a specific time period at least three times after every change of either flow rate of dispersed phase or continuous phase. We collect the data including droplet length, droplet formation time and full mixing time only when the number does not change for the last two measurements.

5.5.4 Time-Distance Relationship

Note that as the chaotic mixing takes place inside a droplet, the droplet travels in microchannels at the same time. Therefore the time consumed by chaotic mixing is equal to the time consumed by the droplet traveling along the channel. The traveling time can be estimated by the distance the droplet travels over the droplet moving speed. Then the time-distance relationship is established,

$$t_{mix}=L_{tr}/U_d, \tag{60}$$

where t_{mix} is the time consumed by chaotic mixing inside the droplet. L_{tr} is the distance the droplet travels.

Equation (60) relates the mixing time collapsed inside the droplet and the distance the droplet travels from the T-shaped junction to the measuring positions. One distinct characteristics of droplet formation in a single T-shaped junction is the extremely high stability in terms of droplet formation time and droplet volume, meaning that at a specific observation spot droplets always appear at the same time interval with the same droplet size. This is quite useful when conducting CCD micro visualization experiment because the observation field in the microscope is quite narrow within which the full mixing by diffusion is probably not reached, then tracking the droplet in the downstream observation spots is necessary. But tracking a specific droplet in the following spots is quite difficult because the droplet probably flows downstream far away within the time for shifting the observation spots. Fortunately the high stability of droplet generation in microfluidic T-shaped junctions together with the time-distance relationship, Eq. (60), offers us the ability not necessarily tracking one specific droplet but observing any droplet in a desirable location.

5.5.5 Estimation of Ink Diffusion Coefficient

In order to calculate the full mixing time via Eq. (48) the diffusion coefficient of Parker ink must be provided. However this value cannot be found in either literature or from the product provider. Parker ink is a kind of complex colloid, consisting of carbon nanoparticles, colored ionize (Fe^{2+} and Cu^{+}), surfactants, and some other materials. For such complex mixture, Einstein relation describing the diffusivity of particles is not applicable any more [181]. Therefore we have designed a simple experiment to estimate the diffusion coefficient of the Park ink solution used in this study. A Y-shaped straight microchannel, shown in Fig. 59, is designed for estimating the diffusion coefficient of the ink solution. The ink solution and deionized water are simultaneously pumped into the straight channel via the

Fig. 59 Y-shaped straight channel for determining the diffusion coefficient of ink solution

Y-shaped inlets at a very low flow rate in order to eliminate possible convection in channel width direction. In this diffusivity estimation experiment, the two reagents are pumped at a total flow rate of 0.02 μL/min, and the resulted Reynolds number is on the order of 10^{-3}. At such small Reynolds number, convection in channel width direction can be effectively neglected. As reagents flow in the straight channel, diffusion mixing occurs in channel width direction and convection occurs in channel length direction simultaneously. Considering the influence of parabolic profile velocity inside the channel, the diffusion coefficient can be estimated from the concentration diffusion in Hagen-Poiseuille flow [7],

$$D = \frac{8W_c^{\,2}v}{L_{tr}} \tag{61}$$

where L_{tr} is the distance from the meeting point of two reagents to the location where the full mixing by diffusion is achieved. v is the average flow velocity of the two reagents in the straight microchannel, $v=(Q_{ink}+Q_w)/A_c$.

It is seen from Eq. (61) that finding the distance where the full mixing of the two reagents is achieved is crucial to estimate the diffusion coefficient since the other parameters can be easily obtained from either measurement or calculation. Micrograph analysis based on evaluating gray values of pixels is used here to judge where the full mixing is reached. Figure 60 shows the method for determining L_{tr}. Starting from the meeting point, we place a series of cross line in the flow direction with a distance interval of the channel width. Then the gray value on each cross line is measured and plotted in Fig. 61. At the first cross section x=0 (Fig. 61 (a)) a sharp gray value difference within channel width means that the diffusion mixing has not started yet. As the diffusion takes place, the gray value difference within channel width becomes smoother and smoother, standing for the increasing mixing efficiency along channel direction. In the last two insets (Figs. 61 (g) and (h)), no obvious difference of gray value can be detected, which means that the full mixing is achieved at $x=6W_c$. The small fluctuation of gray value within channel width, shown in Fig. 61 (g), is probably induced by the non-uniform background illumination. The full mixing length is then estimated to be between $x=5W_c$ and $x=6W_c$, and a middle value $x=5.5W_c$ is accepted in this estimation. Substituting

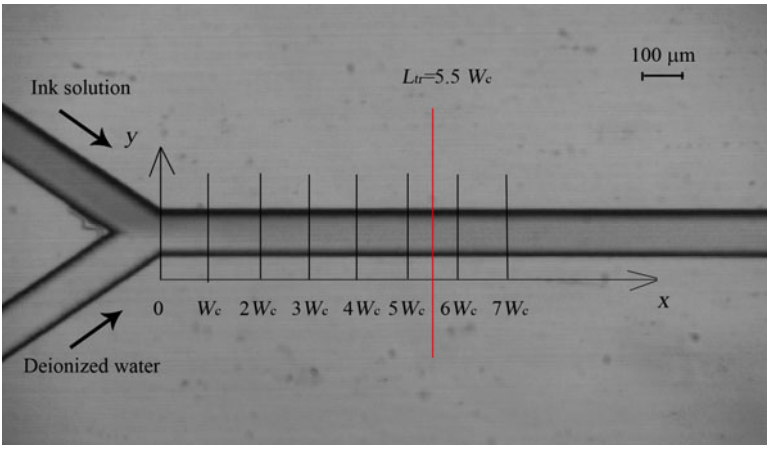

Fig. 60 Graphical instruction of the method to find the full mixing location

W_c=112 μm, Q_{ink}=Q_w=0.01 μL/min, A_c=3.39×10^{-9} m^2, and L_{tr}=5.5W_c into Eq. (61), the diffusion coefficient of ink solution is estimated to be D=2.9×10^{-9} m^2/s.

5.5.6 Full Mixing Determination Inside Moving Droplets

In the estimation of ink diffusion coefficient, we have already used some basic techniques of micrograph analysis based on the gray values of pixels. Here we will discuss much more in detail because the determination of full mixing inside the droplet is much more complicated.

When the transparent deionized water is exposed to illumination, much more light will be penetrated and captured by the CCD sensor and results in bright areas in the micrographs. When the ink solution is exposed to illumination, much more light will be absorbed by the ink solution, resulting in weak exposure of the CCD sensor and dark areas in the micrographs. Moreover, the ink solution with different concentrations will exhibit different abilities of absorbing light and in turn results in dark areas with different gray values in the micrographs. The denser the ink solution is, the darker the area in micrographs is. As the mixing inside the droplet takes place, the local ink concentrations decrease from the initial values at different speeds due to the recirculation. Therefore, the gray value of each pixel inside the droplet is not uniform until the full mixing is achieved. This provides us a powerful tool to determine the full mixing by using micrograph analysis based on analyzing the homogeneity of the pixel gray values within the drops in micrographs, given that the background illumination is absolutely uniform everywhere. The standard deviation of the gray values of the pixel inside the mixing droplet can be accepted as an index of mixing efficiency. The standard deviation should decrease from a

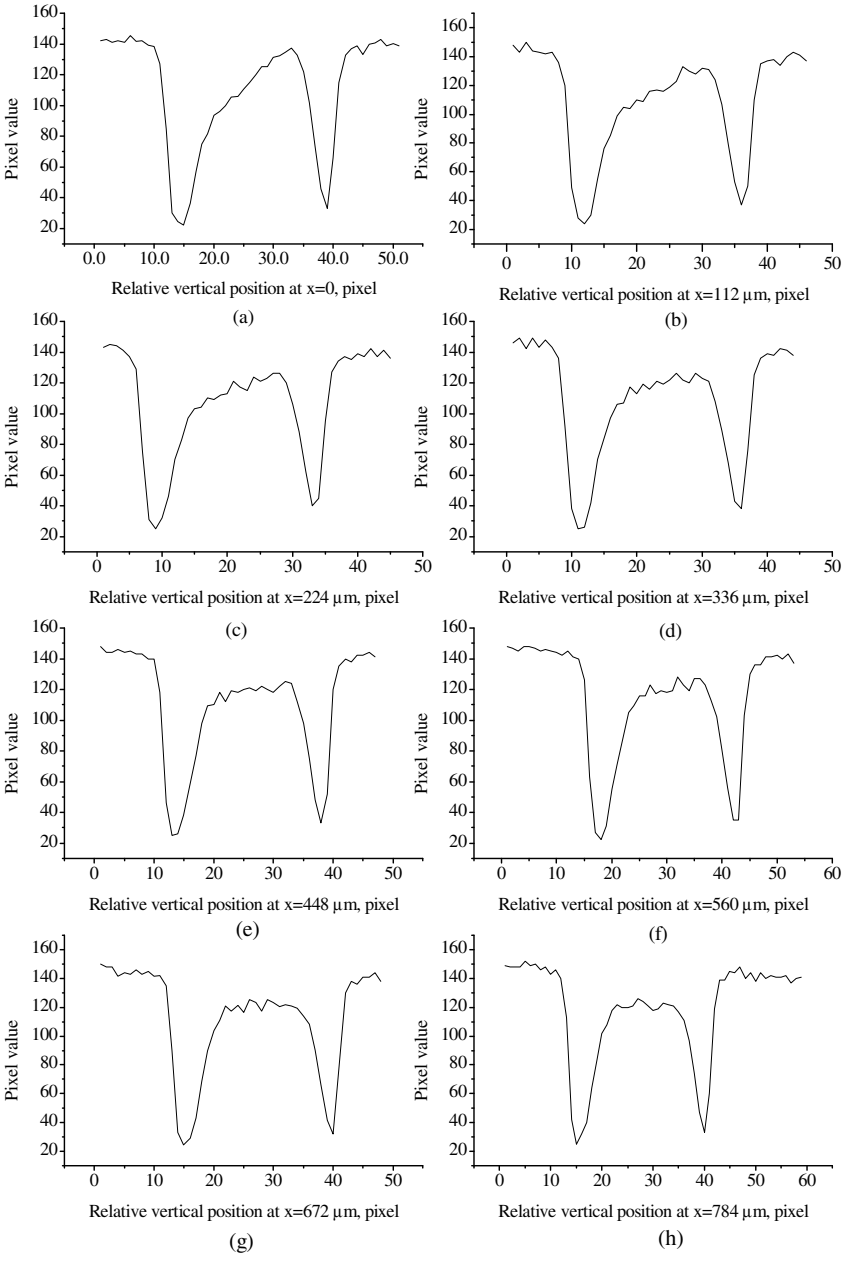

Fig. 61 Pixel values variation in channel length direction

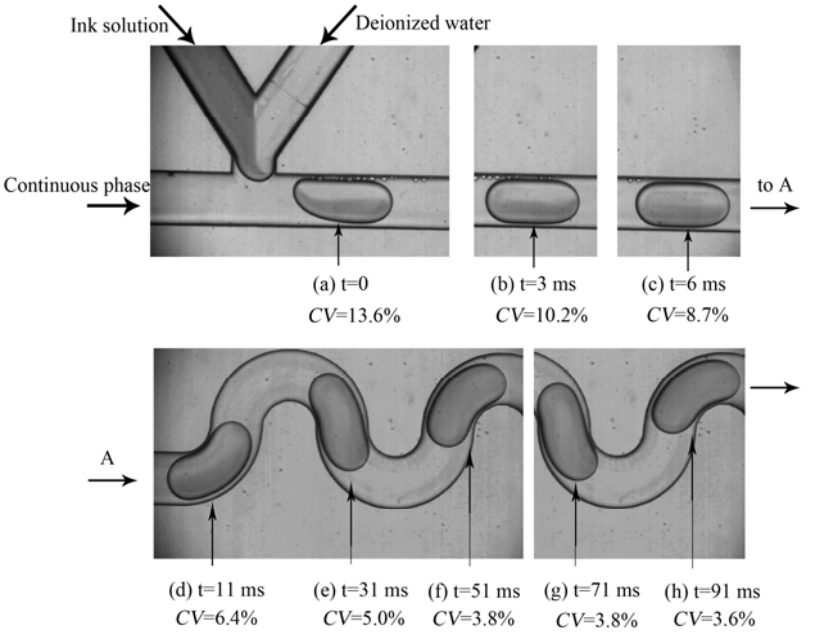

Fig. 62 Coefficient of variation at different time instant (Q_c=4.0 μL/min, Q_w=Q_{ink}=2.0 μL/min)

certain value to zero as mixing undergoes until full mixing is achieved. In any real experiment, however, absolutely uniform background illumination seems not possible due to the non-uniform light strength from light source, unequal light loss during light transport, and unequal light absorbing resulted from non-uniformity of internal structure of microfluidic devices through which light passes. Any such possible influence will result in a nonzero value of the standard deviation when full mixing is achieved. To overcome this problem, we track the change of coefficient of variation of pixel values instead of the standard deviation, which will eliminate the influence of the non-uniform background illumination. The coefficient of variation, *CV*, is defined as the standard deviation over the mean value,

$$CV = \sqrt{\frac{1}{N}\sum_{i=1}^{N}\left(\frac{G_i}{G}-1\right)^2} \times 100\%, \tag{62}$$

where $G = \frac{1}{N}\sum_{i=1}^{N} G_i$ is the mean gray value of N pixels. N is the number of pixel selected inside the droplet in the micrograph. G_i is the gray value of each pixel.

In ImageJ we set the gray value of absolute white as 255 and absolute black value as 0, then any gray value of pixels locates within 0–255. As mixing takes place, *CV* value will decrease to a certain value and keep unchanged when the full mixing is achieved. Figure 62 shows a typical mixing process inside a moving droplet and the change of coefficient of variation at different time instant. When the *CV* value measured at different mixing time does not change any more, the full mixing is regarded to be achieved and the time collapsed is the full mixing time.

5.6 Results and Discussion

5.6.1 Chaotic Mixing during Droplet Formation

Much effort has been made on the influence of the chaotic mixing inside the droplet that are already moving in microchannels, not much attention has been on the mixing process during the droplet formation. However, we experimentally observe that the chaotic mixing inside the droplet has already started during the droplet formation especially when the forming droplet is relatively small, L_d/W_c~1, shown as the vortex in Fig. 63 (e). According to the scaling analysis of droplet size in Part 3, the droplet size $L_d/W_c \propto (Q_{ink}+Q_w)/Q_c$. Therefore smaller droplet size corresponds to larger velocity difference between silicon oil and reagents stream, where larger viscous stresses will be exposed on the forming droplet as it just intrudes into the continuous stream. A thin layer of ink solution is stretched from the main stream of the ink solution to the front of the forming tip under the viscous stresses resulted from the velocity difference between silicon oil and reagents flow can be seen in Figs. 63 (a) and (b). The vortex will be formed inside the front part of the forming droplet under the viscous stresses. It is seen that for smaller droplet size the vortex can be sustained and occupy almost the whole forming droplet due to the higher viscous stresses and smaller droplet size, shown in Figs. 63 (c)-(h). The mixing within formation process is already highly enhanced by the chaotic advection inside the forming droplet. It is experimentally observed that the full mixing inside small droplets is nearly achieved at the moment of the droplet detachment. For larger droplets, the chaotic advection is relatively low because the velocity difference is small and the viscous stresses are relatively weak. The vortex cannot be sustained inside the whole forming droplets but evolves to a weak vortex inside the front tip. Figure 64 shows a typical mixing process for a relatively large droplet (L_d/W_c~3) during the droplet formation process. In Figs. 64 (a)-(c) we can see that there is also a thin layer of ink solution brought from the main stream of the ink solution to the front of the emerging droplet tip under the viscous stresses. When the droplet tip almost blocks the main channel, however, the droplet will be squeezed downstream mainly under the increased pressure behind the rear interface (Fig. 64 (d)). The viscous stresses exerted on the interfaces are not strong enough to sustain the vortex

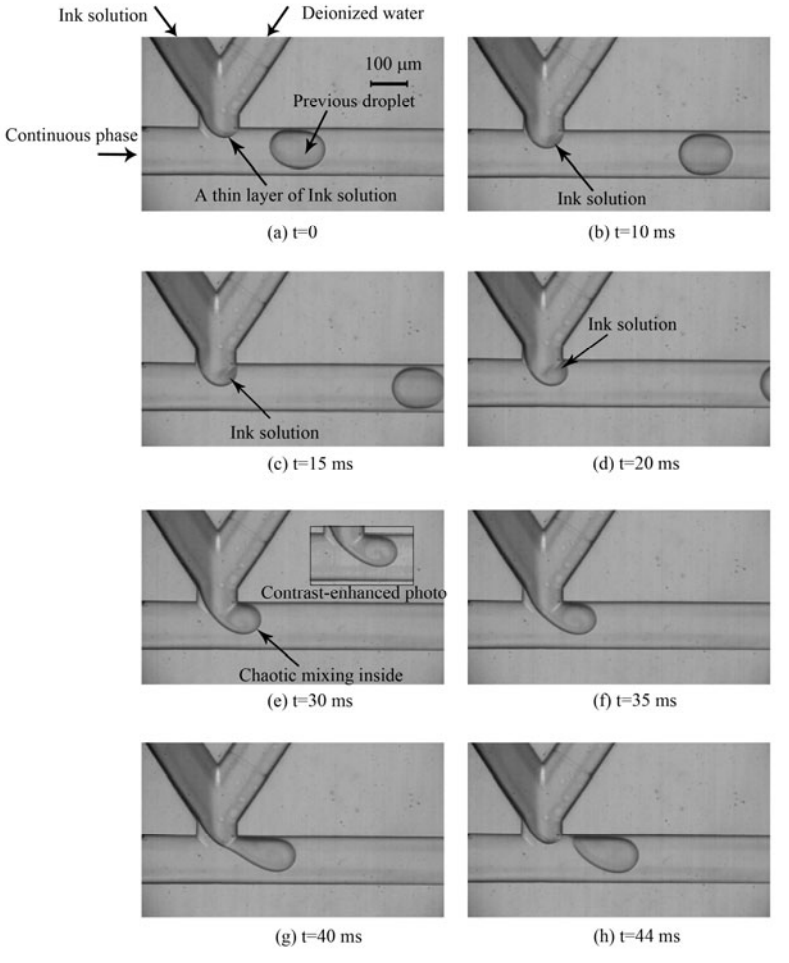

Fig. 63 Chaotic mixing inside a small droplet during its generation (Q_c=4.0 μL/min, Q_w=Q_{ink}=0.25 μL/min)

in the entire forming droplet. The weak vortex generated at the beginning of the droplet formation will be quickly smoothed and propagated downstream (Figs. 64(e)-(h)).

In this study, the recirculating flow inside droplets, after generation, moving in the curved microchannels, is hard to be observed clearly due to the limited resolution of the high speed camera and the smoothed contrast between the ink solution and the deionized water. However, the enhanced efficiency of chaotic

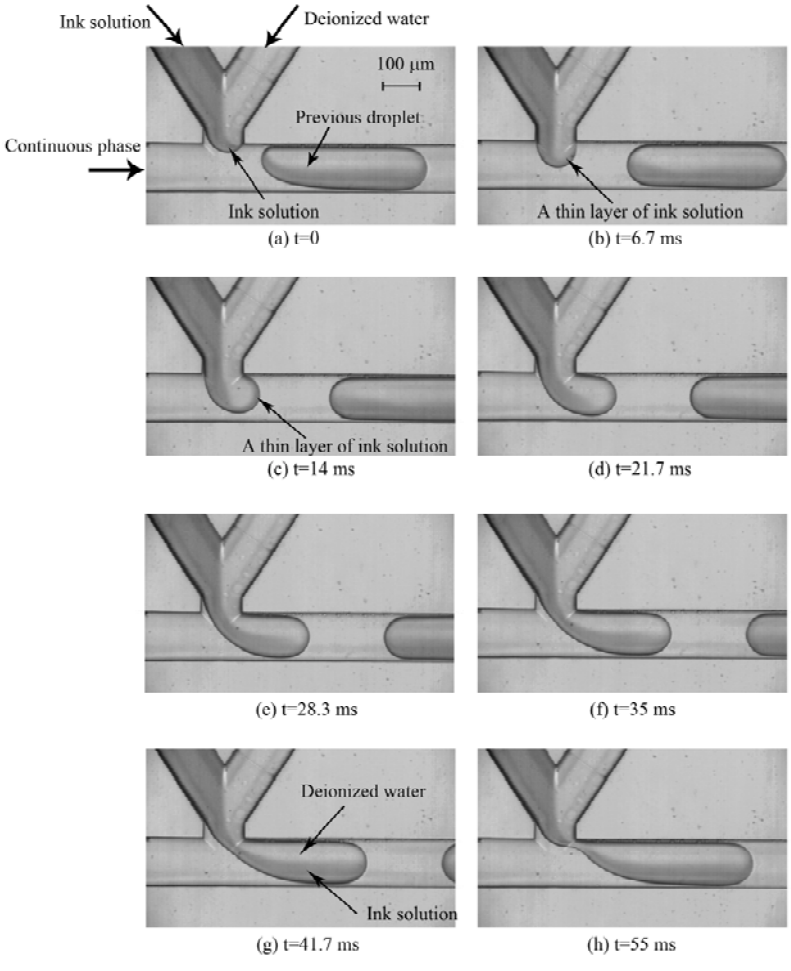

Fig. 64 Mixing inside a big droplet during its generation (Q_c=0.5 μL/min, Q_w=Q_{ink}=0.25 μL/min)

mixing inside moving droplets is indeed confirmed by measuring the full mixing time, which will be discussed in the next section.

5.6.2 Full Mixing Time

Since the chaotic mixing during the droplet formation process is already started, the total full mixing time must include the time used during the droplet formation. After measuring the full mixing time, it is found that the full mixing time inside moving droplets is usually less than 0.4 s which is one order smaller than the full mixing time by pure diffusion without chaotic advection. According to Eq. (50),

$t_0=W_c^2/(2D)$, the full mixing time by pure diffusion over the channel width is estimated to be 2.5 s. For smaller droplets in which the chaotic mixing dominates during the formation process, the full mixing time is reduced as much as two orders, from 2.5 s to 0.04s.

Since no serious slippery flow occurs between the moving droplet and the continuous phase, the droplet moving speed is estimated to be the superficial velocity in the curved microchannels, $U_d=J=(Q_{ink}+Q_w+Q_c)/A_c$. Actually the slip velocity between the droplet and the continuous phase can be neglected based on the classic Bretherton correlation [2, 149]. It points out that the droplet moving in microchannels will travel at a little higher speed than the average velocity of the continuous phase, and the relative excess velocity is estimated to be $1.29(3Ca)^{2/3}$, where $Ca=\mu_c J/\sigma$. In our experiments, the capillary number is in the range of 10^{-3} to 10^{-2}, thus the relative exceeding velocity is less than 5% which can be neglected without introducing serious errors. The negligible slip velocity is also confirmed by the experimental PIV measurement by Tung et al. (2009) [146]. After measuring the droplet length, the value of n in Eq. (58) can be numerically solved and finally the full mixing time by chaotic mixing inside the droplet can be calculated according to Eq. (59). Figures 65 and 66 show the comparison of the full mixing time between the values calculated by Eq. (59) and that experimentally measured. From Figs. 65 and 66 we can see that the scaling analysis of Eq. (59) can give us a reasonable estimation of the full mixing time inside moving droplets.

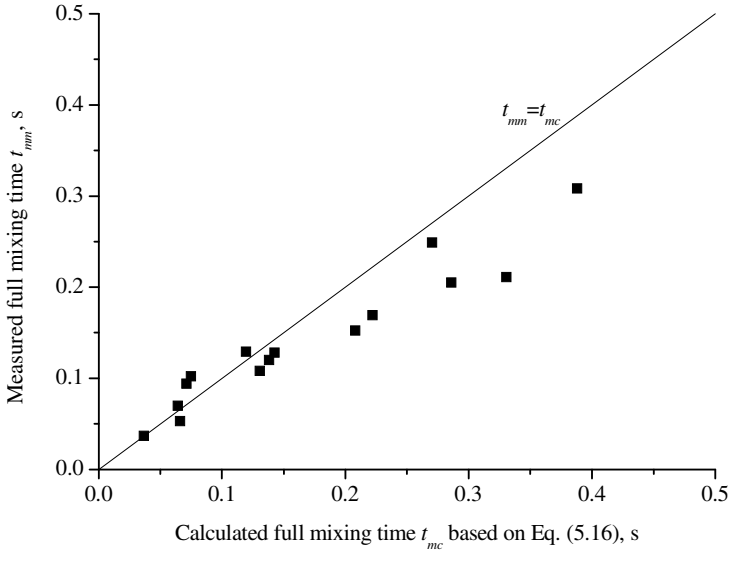

Fig. 65 Comparison of the full mixing time between the values measured and calculated

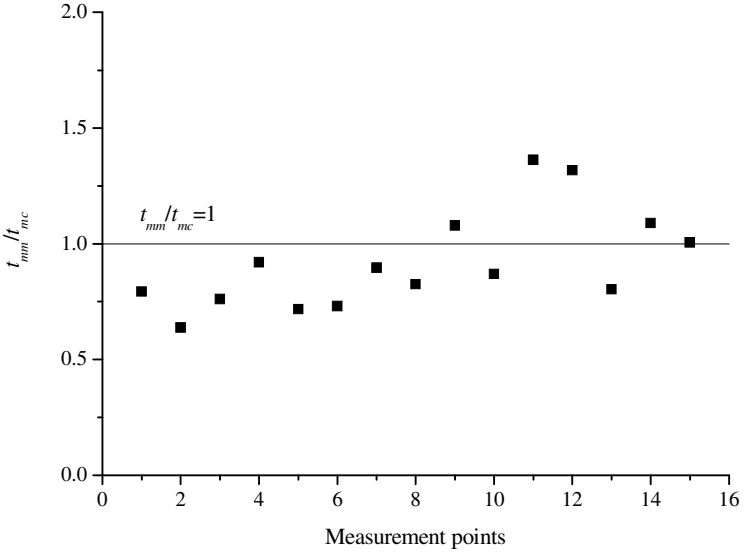

Fig. 66 Comparison of the full mixing time between the values measured and calculated

5.7 An Effective Microstructure Designed for Droplet Fusion

In last section we note that the ink solution and the deionized water are always distributed perpendicularly to the center-plane inside the droplets after generation. In order to get the better arrangement of the two reagents, distributed along the center-plane (Fig. 54 (a)), an effective microstructure for getting such initial distribution is crucial. A possible way is generating two droplets of the reagents, ink droplet and water droplet, respectively, and making them fused in channel length direction. In a channel with identical width, droplets will never be fused without external forces (e.g. electrical field) since they move at the same velocity and are always separated by slugs of continuous phase. In a channel where channel width varies in channel length direction, the velocity field and the pressure field inside the channel will vary in the channel length direction, and the droplets moving at different locations will have different velocities, which provides the possibility of droplets merge somewhere inside the channel [15, 71, 101]. Inspired by the work reported by Hung et al. (2006), a divergent nozzle is designed for the fusion purpose [15]. Figure 67 shows the microstructure and its dimensions designed for realizing such purposes. Two T-shaped junctions along the main microchannel are placed on the opposite sides, where ink droplets and deionized water droplets will be generated respectively, followed with a divergent nozzle where the fusion will be realized due to the reduced droplet velocity. We name the T-shaped junction where the ink droplets are generated as ink junction and the T-shaped junction where the

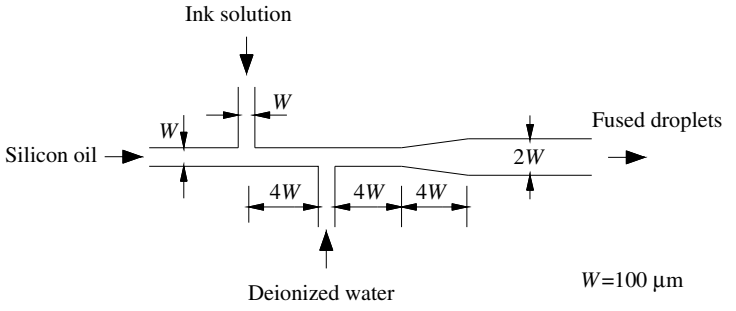

Fig. 67 Channel dimensions of the microstructure designed for droplet fusion

deionized water droplets are generated as water junction for making a clear reference in the following text. Different flow rate combinations of the continuous phase and the dispersed phase are employed for testing the generation and fusion ability of the microstructure. The flow rate of silicon oil is tested from Q_c=0.5 μL/min to Q_c=4 μL/min with a twofold increment. Under each flow rate of the continuous phase, the flow rate ratio of deionized water to ink solution, Q_w/Q_{ink}, is tested at 2:1, 1:1 and 1:2, respectively. All the testing conditions are outlined in Table 4.

Table 4 Testing conditions for the microstructure designed for droplet fusion

Q_w/Q_{ink}	Q_c=0.5, μL/min		Q_c=1.0, μL/min		Q_c=2.0, μL/min		Q_c=4.0, μL/min	
	Q_w μL/min	Q_{ink} μL/min	Q_w μL/min	Q_{ink} μL/min	Q_w μL/min	Q_{ink} μL/min	Q_w μL/min	Q_{ink} μL/min
2:1	0.25	0.125	0.50	0.25	0.50	0.25	1.00	0.50
	0.50	0.25	1.00	0.50	1.00	0.50	2.00	1.00
1:1	0.125	0.125	0.25	0.25	0.50	0.50	0.50	0.50
	0.25	0.25	0.50	0.50	1.00	1.00	1.00	1.00
	0.50	0.50	1.00	1.00	2.00	2.00	2.00	2.00
1:2	0.125	0.25	0.25	0.50	0.25	0.50	0.50	1.00
	0.25	0.50	0.50	1.00	0.50	1.00	1.00	2.00

It is found that stable fusion at all the tested flow conditions is reliable, but the fusion situation is different and depends on the flow rate ratio of Q_w/Q_{ink}. When $Q_w/Q_{ink}\geq 1$, droplet fusion happens at the ink junction, in other words the ink solution is injected into the deionized water droplets as the deionized water droplets flow pass the ink junction. Figure 68 shows a typical fusion process at $Q_w/Q_{ink}\geq 1$. In Fig. 68 (a), a previous fusion, injection of ink solution into a deionized water droplet, has been finished and the fused droplet has detached the ink junction. At this time, the water droplet tip is already formed at the water junction. But the ink droplet tip grows very slowly compared with the water droplet tip (Figs. 68 (b) and (c)) because the growth of the ink droplet tip is suppressed by the increased pressure in the continuous phase at the ink junction locating downstream to the water junction. When the water droplet arrives at the ink junction, it will merge with the growing ink droplet tip (Figs. 68 (c)-(f)). Within this stage it is seen that only little

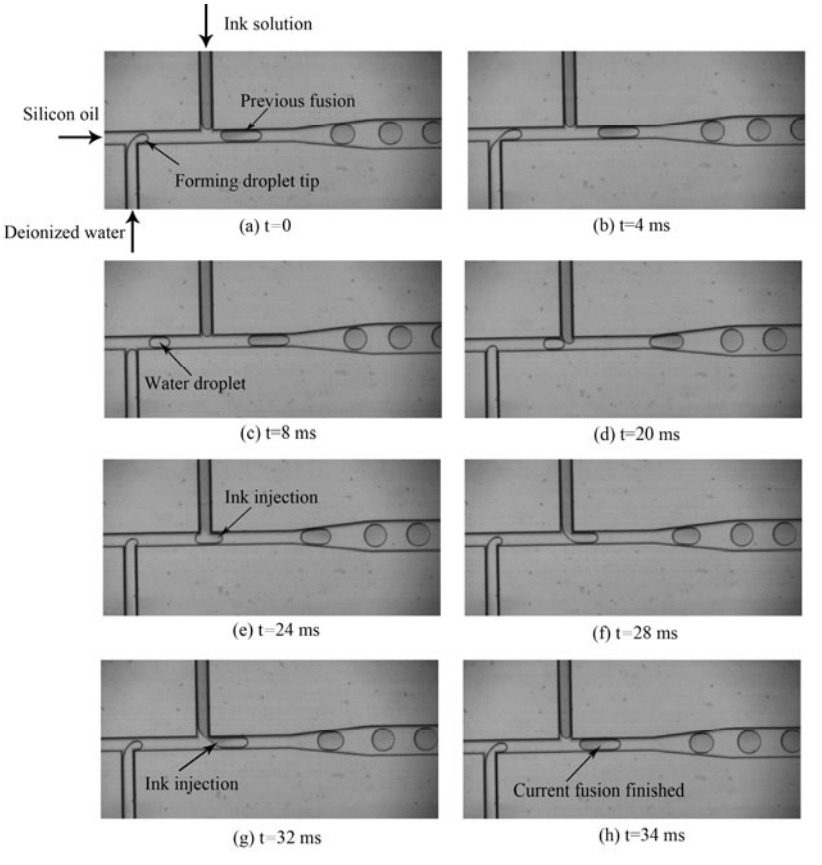

Fig. 68 A typical fusion process at $Q_w/Q_{ink}=1$ (Q_c=2.0 μL/min, $Q_w=Q_{ink}$=0.5 μL/min)

ink solution is injected into the front part of the water droplet (Fig. 68 (e)). The water droplet fused with ink solution continuously moves downstream and finally detaches the ink junction (Figs. 68 (g) and (h)). At the end stage of detaching, we can see that large amount of ink solution is injected into the back half of the water droplet (Fig. 68 (g)), resulted from the quick release of the accumulated pressure in the ink stream.

When $Q_w/Q_{ink}<1$, droplet fusion situation is much more complicated than that described above because the generation frequency of the water droplet and the ink droplet is not the same any more. Two droplets will be released from the ink stream and only one droplet is released from the water stream within the same time interval. Figure 69 shows a typical fusion process when $Q_w/Q_{ink}<1$. In Fig. 69 (a),

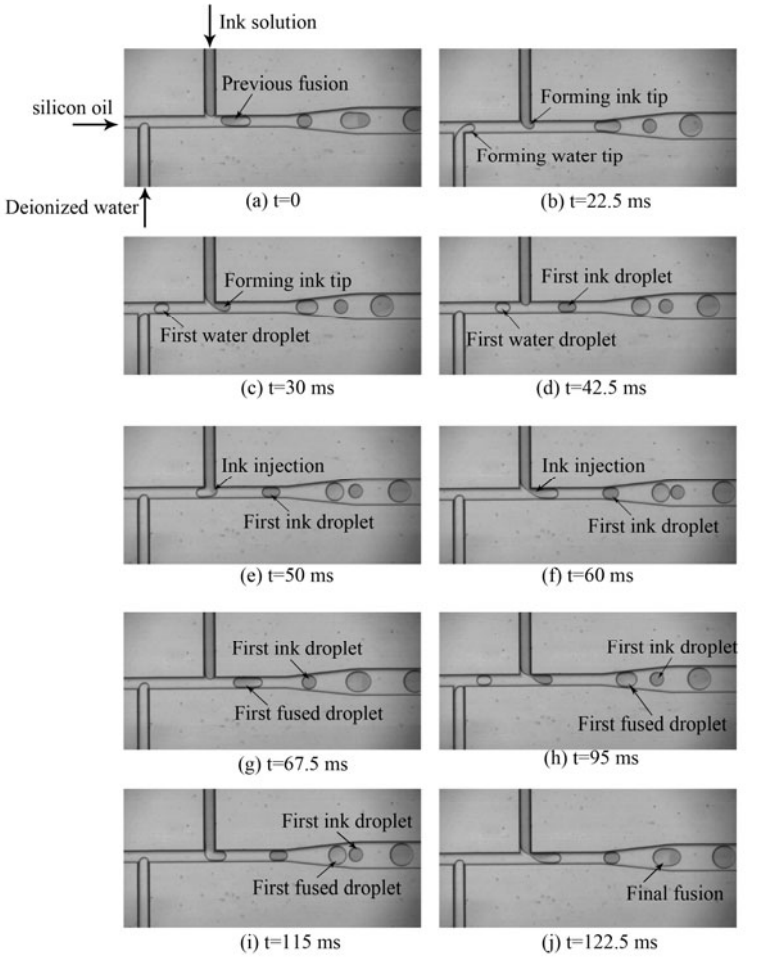

Fig. 69 A typical fusion process at Q_w/Q_{ink}=0.5 (Q_c=2.0 μL/min, Q_w= 0.25 μL/min and Q_{ink}=0.5 μL/min)

the previous water droplet fused with the ink droplet tip has just detached from the ink junction, and a small water droplet tip has already been formed at the water junction. In the growing process followed, the ink droplet tip grows at a speed slightly slower than the water droplet tip (Fig. 69 (b)). After certain time the water droplet has already detached, but the first ink droplet is still under growth (Fig. 69 (c)). As the water droplet approaches to the ink junction, the first ink droplet detaches and moves downstream (Fig. 69 (d)). When the water droplet arrives at the ink junction, the water droplet will be fused with the reforming ink droplet tip (Fig. 69 (e)). Within this stage, the fusion process is similar to that described above for $Q_w/Q_{ink} \geq 1$ (Figs. 69 (e) and (f)). In Figs. 69 (g) and (h), the water droplet fused with the reformed ink tip detaches from the ink junction and moves downstream at a higher velocity than the first ink droplet because at this moment the first ink droplet has already entered the divergent nozzle where its velocity is reduced. After certain time, the fused water droplet will catch up the first ink droplet within the nozzle area and final fusion is realized (Figs. 69 (i) and (j)).

5.8 Concluding Remarks

Chaotic mixing inside droplets is experimentally investigated by using a micro visualization system. It is experimentally observed that the chaotic mixing is already started during droplet formation. For small droplets, the chaotic mixing during generation is very strong and the full mixing can almost be achieved after droplet detachment. For large droplets, the chaotic mixing during generation is not as strong as inside small droplets, but it still enhances the mixing significantly at the initial stage of droplet formation. To evaluate the full mixing, the chaotic mixing during the formation process must be considered. The determination of full mixing is accomplished with the help of micrograph analysis based on the gray values of pixels. It is found that the mixing efficiency inside moving droplets can be significantly increased by the chaotic advection and the full mixing time can be reduced as much as two orders of magnitude compared with the pure diffusion in single phase laminar flow. The scaling analysis of the chaotic mixing based on the idealized recirculating flow and Baker's transformation can give a reasonable estimation of the full mixing time. An effective microstructure is designed for mixing two or more individual droplets. The good performance of the microstructure is experimentally confirmed at different flow conditions.

6 Microfluidic Synthesis of Copper Nanofluids

6.1 Introduction

Nanofluids are stably dilute suspensions of nanomaterials including nanoparticles, nanotubes, and nanofibers. After first proposed by Choi (1995) [182], nanofluids

have attracted intensive effort from thermal society due to their excellent performance in heat transfer [183-186]. In clinical studies, magnetic nanofluids have been successfully applied to treat patients with cancers [187, 188]. In general, there are two methods to produce nanofluids: two-step method and one-step method. In the two-step method nanoparticles are first fabricated out and then separated and redispersed in base fluids [189-191]. In this method the aggregation of nanoparticles, resulted from the separation process, usually causes poor stability of nanofluids after redispersion. In the one-step method nanoparticles are fabricated out in based fluids directly, no redispersion process needed, by Vacuum Evaporation onto a Running Oil Substrate (VEROS) [191, 193], Submerged Arc Nanoparticle synthesis system (SANSS) [194-196], or chemical synthesis in flasks [185, 197, 198]. Nanoparticle size produced by the methods mentioned above is normally hard to be controlled and the size distribution is relatively broad.

More recently microfluidic method as a promising technology has been reported superior to traditional methods for producing high quality nanoparticles due to the advantage of eliminating local variations in reaction conditions such as concentration and temperature variations. Many kinds of nanopartilces have been synthesized by using microfluidic methods in continuous stream or inside droplets, which involve semiconductor quantum dots [13, 14, 199-202], metallic nanoparticles [115, 203-209], composite nanoparticles [114, 117], and polymeric nanoparticles [210, 211]. However, a systematic investigation on the influence of involving parameters, like flow rates of reactants, reactants concentration and surfactants concentration, is still limited. In present work copper nanofluids synthesized in microfluidic reactors and in traditional flasks are studied. In microfluidic reactors, the influence of flow rates of reactants, reactant concentration and surfactant concentration on copper particle size and size distribution is systematically investigated.

6.2 Experiments

6.2.1 Chemicals and Materials

Hydrazine hydrate (98%) and copper hydroxide (99.9%) are purchased from Sigma Aldrich Inc. (USA). Sodium dodecylbenzenesulfonate (DBS), Chloride acid, and Trisodium phosphate (Tris) are purchased from Tianjin Damao Chemical Reagent Co., Ltd. (China). Ammonia solution (25%) is bought from Tianjin Fuyu Fine Chemical Industry Co., Ltd. (China). Deionized water is prepared by an in-house ion exchange system with ultrasonic treatment before use to dispel the dissolved air. All reagents are of reagent grade and used as received without further purification.

6.2.2 Preparation of Stock Solutions

A typical synthesis procedure involves the preparation of two stock solutions: a dilute $[Cu(NH_3)_4]\cdot(OH)_2$ solution and a dilute hydrazine hydrate solution containing

stabilizer DBS. Stock solution $[Cu(NH_3)_4]\cdot(OH)_2$ is freshly prepared by dissolving 0.195 g copper hydroxide into 40 mL dense ammonia solution (25%) followed by being diluted to 100 mL with diluted ammonia solution (1 M (mol/L)), resulting in the final concentration of $[Cu(NH_3)_4]\cdot(OH)_2$ to be 20 mM (mmol/L). Different concentrations of $[Cu(NH_3)_4]\cdot(OH)_2$ solution used in the experiment, from 0.5 mM to 8 mM, are obtained by diluting corresponding amount of stock solution with deionized water to a total volume of 20 mL. The reducing solutions are prepared by dissolving corresponding amount of hydrazine hydrate in 20 mL deionized water such that the molar concentration ratio of hydrazine to copper complex $[Cu(NH_3)_4]\cdot(OH)_2$ is always kept at 30:1. Different amount of DBS is added into the reducing solution before synthesis in order to stabilize the resulted nanofluids. A buffer solution, pH=8.5, is prepared by mixing 50 mL Tris solution (0.1 M) and 14.7 mL HCl solution (0.1 M), and then diluted with deionized water to 100 mL.

6.2.3 Design and Characterization of Microfluidic Reactors

Two microfluidic reactors are designed for synthesizing copper nanofluids, which are schematically depicted in Fig. 70. The only difference between the two microfluidic reactors was the number of inlets for introducing reactant streams. There are two inlets for $[Cu(NH_3)_4]\cdot(OH)_2$ and N_2H_4 in the two-inlet design shown as inset A in Fig. 70(a), whereas an additional inlet for introducing the buffer solution was added in the three-inlet design shown as inset B in Fig. 70(b). Due to the extremely low flow rate in the microfluidic reactors, ~μL/min, the compressibility of aqueous solution and the flexibility of tubings connecting syringes and microfluidic reactors extend the time the flow system requires to get equilibrated significantly. A blind channel, "indicating channel" shown as inset C, is designed to monitor whether the flow system reaches a stable state or not. The air spontaneously constrained in the "indicating channel" will be compressed after the solutions are pumped. The motion of the air-liquid interface can be treated as a signal reflecting flow situations inside the microfluidic reactors. When the flow situation inside the microfluidic reactors reaches a steady state, the interface will have a fixed position corresponding to the total flow rate. Channel dimensions are shown in Fig. 70(c): channel width W_c=122.2 μm, channel depth H=40.1 μm and curved radius R=120 μm. The cross-section area A_c and perimeter L_p of the curved channels can be calculated by

$$A_c = (W_c - 2H)H + \frac{\pi H^2}{2}, \tag{63}$$

$$L_P = 2(W_c - H) + \pi H . \tag{64}$$

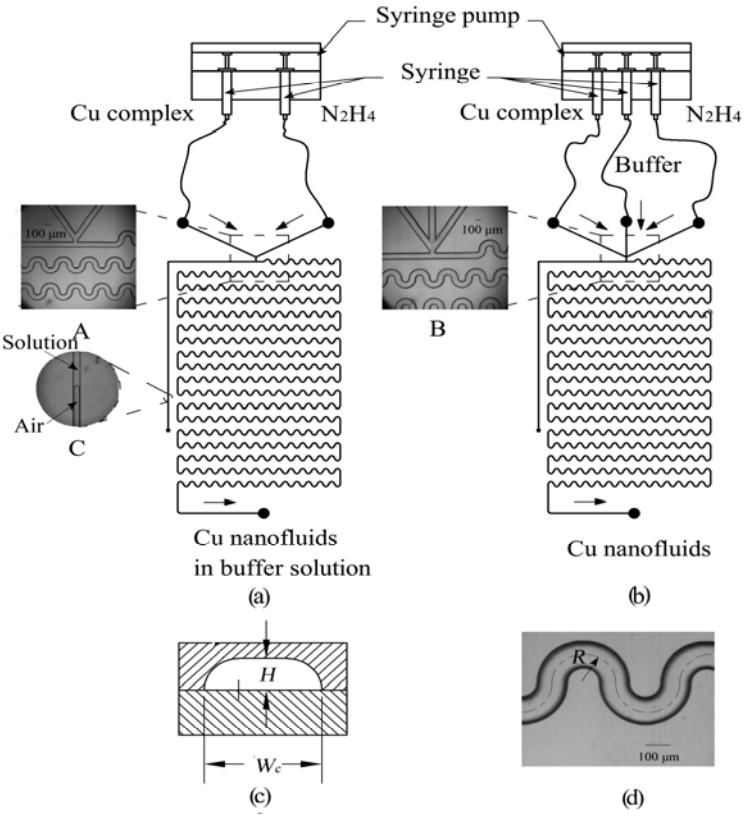

Fig. 70 Schematics of microfluidic reactors: (a) two-inlet design; (b) three-inlet design; (c) cross section of curved channels; (d) micrograph of curved channels (Inset A: micrograph of the two-inlet design; Inset B: micrograph of the three-inlet design; Inset C: micrograph of air-liquid interface in the indicating channel)

The total length of the curved channel was L=2304 mm. The volumetric capacity V_{mr} of the microfluidic reactors is 9.5 μL calculated from

$$V_{mr} = L \cdot A_c . \tag{65}$$

In our studies, chemical synthesis of copper nanofluids is normally found to be finished within ten-minute scale by using traditional method in a 50 mL boiling three –neck flask. To insure nanoparticles are fully synthesized in microfluidic reactors, the long reaction channel is necessary for providing sufficient residence time. Curved channels with a total length of more than two meters are designed to do so. Another purpose of the utilization of curved channel is to introduce Dean vortices to provide an even efficient mixing for nanoparticles nucleation and growth. When a fluid flows through a curved channel, the counter-rotating Dean vortices on the cross-section plane will arise

from the interaction among viscous, inertial and centrifugal forces [212-216]. The strength of Dean vortices is evaluated by the Dean number,

$$Dn = Re\sqrt{\frac{D_h}{R}}, \tag{66}$$

where Re is Reynolds number. $D_h=4A_c/L_P$ is the hydraulic diameter of reaction channels. Reynolds number indicates the relative ratio of inertial force to viscous force,

$$Re = \frac{\rho v D_h}{\mu}, \tag{67}$$

where ρ is copper nanofluid density. μ is copper nanofluid viscosity. $v=Q/A_c$ is the average velocity of copper nanofluid in the curved channels, where Q is the total volumetric flow rate of all the reagents. In fact, it is quite accurate to use the density and viscosity of the base fluid (deionized water) instead of the copper nanofluids in Eqs. (66) and (67) because the influence of copper nanoparticles on the density and viscosity of deionized water is negligible at very low volume fraction. The classic theoretical model to describe the effective viscosity of nanofluids with a low concentration of rigid spherical particles is developed by Einstein [217, 218]

$$\mu_{eff} = \mu_{bf}\left(1 + 2.5\Phi\right), \tag{68}$$

where μ_{eff} is the effective viscosity of nanofluids. μ_{bf} is the viscosity of base fluids. Φ is the particle volume fraction in base fluids. In our experiment, the highest molar concentration of copper hydroxide is 4 mM, and the resulted volume fraction and mass fraction of copper nanoparticles is about 0.0029% and 0.026% respectively. Therefore the error of using base fluids density and viscosity to calculate Re and Dn can be omitted.

6.2.4 Copper Nanofluids Synthesis in Flasks

Diluted N_2H_4 solution (20 mL) containing surfactant DBS is first placed in a boiling three-neck flask with a capacity of 50 mL. Diluted stock solution $[Cu(NH_3)_4]\cdot(OH)_2$ (20 mL) is then added into the flask under a magnetic stirring at 400 round/min at room temperature. The mixed solution turns into light yellow immediately, implying a very fast reduction rate from $Cu^{2+}\rightarrow Cu$, and the color of the reacting solution becomes denser gradually until no further color changes after about 10 to 30 minutes depending on the reagents concentration.

6.2.5 Copper Nanofluids Synthesis in Microfluidic Reactors

In the process of microfluidic synthesis, reagent solutions are preloaded in 1mL Gastight syringes (Gastight 1001, Hamilton Co., USA) to which microfluidic reactors are connected using Luer-Lock fittings and 1/16" PTFE tubing (Cole-Parmer, USA). The preloaded stock solutions were introduced into

microfluidic reactors at the same volumetric flow rates propelled by a syringe pump (Cole-Parmer® 74900, Cole-Parmer Instrument Company, USA). The motion of the air-liquid interface in the "indicating channel" and the flow situation inside microfluidic reactors were monitored by an inversed microscope (XD101, Nanjing Jiangnan Novel Optics Co. Ltd., China) interfaced with a high-speed camera (MotionPro X4, IDT, Taiwan). Due to the ease of oxidization of copper nanoparticles, copper nanofluids are collected in the buffer solution to slow down the oxidization rate in the two-inlet design (Fig. 70(a)).

6.2.6 Nanoparticles Characterization

Particle morphology, size, and size distribution are determined from image analysis of micrographs taken by a Transition Electron Microscope (Philips Tecnai G2 20 S-TWIN TEM microscope, FEI Co., USA), and the open software ImageJ is used to do so (Rasband WS, U. S. National Institutes of Health, Bethesda, Maryland, USA, 1997-2009). Observation of 150 to 300 particles for each sample is used in the calculation of average size (diameter), d, and the size distribution, CV, defined as the ratio of standard deviation to the average diameter. Measurement error in micrographs by using ImageJ was estimated to be less than 0.3 nm. To do TEM measurement, samples are first dripped onto a 400-mesh carbon-coated copper grid (G400 Square Mesh, SPI supplies, USA), followed by washing with absolute alcohol, and then dried in ambient atmosphere. Typical micrographs of copper nanoparticles synthesized in either the flask or the microfluidic reactors are shown in Figs. 71 (a)-(c). Element of the nanoparticles is confirmed by doing Selected Area Electron Diffraction (SAED) measurement on 400-mesh carbon-coated nickel grids (G400 Square Mesh, SPI supplies, USA). By comparing the lattice spacing, rings in the SAED micrograph (Fig. 71 (d)), with the standard atomic spacing along their characteristic *hkl* index documented in the Powder Diffraction File (PDF), the nanoparticles synthesized by chemical method in present study are verified as copper nanocrystal.

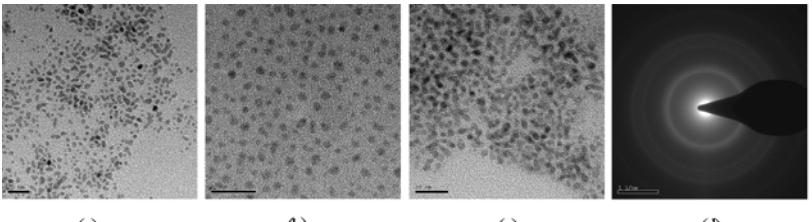

Fig. 71 TEM micrographs of copper nanoparticles synthesized by: (a) flask method; (b) two-inlet microfluidic reactor; (c) three-inlet microfluidic reactor; (d) SAED image of copper nanoparticles (4 mM $[Cu(NH_3)_4]\cdot(OH)_2$, 120 mM N_2H_4, and 1 mM DBS)

6.3 Results and Discussion

6.3.1 Influence of Total Flow Rate on Particle Size

During the experiment, it is found that the syringe pump could not be operated at very high flow rates. When the total flow rate is over 30 μL/min, the syringe pump would be stalled because the frictional resistance inside the microfluidic reactors is too high to be overcome by the syringe pump thrust. On the other hand, the total flow rate cannot be too low. It is noted that the experimental system needs at least 10 minutes, sometimes hours, to reach a steady state after every change of flow rate, judged from the air-liquid interface motion in the "indicating channel" (inset C in Fig. 70). The lower the flow rate is, the longer time the system needs. When the total flow rate is too low, the waiting time could be extremely long and sometimes even no nanoparticles could be detected in the nanofluids.

To investigate the influence of flow rate on nanoparticle size and size distribution, we synchronously change both flow rates of the two stock solutions from 1.25 to 10 μL/min, resulting in the total flow rate variation from 2.5 to 20 μL/min in the two-inlet microfluidic reactor (Fig. 70(a)). Hereafter without special specification the microfluidic reactor used to investigate the influence of flow rate, reactants concentration and DBS concentration is the two-inlet microfluidic reactor. The concentration of $[Cu(NH_3)_4]\cdot(OH)_2$ solution is set at 4 mM, and the reducing solution N_2H_4 containing 1 mM DBS is retained at 120 mM. Average residence time of the two precursors is directly related to the volume of the microfluidic reactor and the total flow rate,

$$t_r = \frac{V_{mr}}{Q}. \tag{69}$$

where t_r is the average residence time.

As the total flow rate increases from 2.5 to 20 μL/min, the average residence time decreases from 227 to 28 s. Since the average residence time at Q=20 μL/min is much shorter than the synthesis time observed in the flask method, nanoparticle synthesis might still be in progress in the receiving container if it is not fully conducted inside the microfluidic reactor. To testify that the copper nanoparticles are fully synthesized in the microfluidic reactor for those cases, a comparison of the nanoparticles taken from the collecting container and collected at the moment when nanoparticles just flow out the outlet. It is found that the particle size and size distribution are almost the same, and no distinct difference was detected. Moreover, such comparison reveals that by using the microfluidic reactor the synthesis time of copper nanoparticles is drastically decreased as much as one order of magnitude, compared with the traditional flask method that usually takes 10 to 30 minutes to fully finish the synthesis.

Figure 72 depicts that the total flow rate has little influence on particle size as it is changed from 2.5 to 20 μL/min. The average size is around 3.3 nm, and the

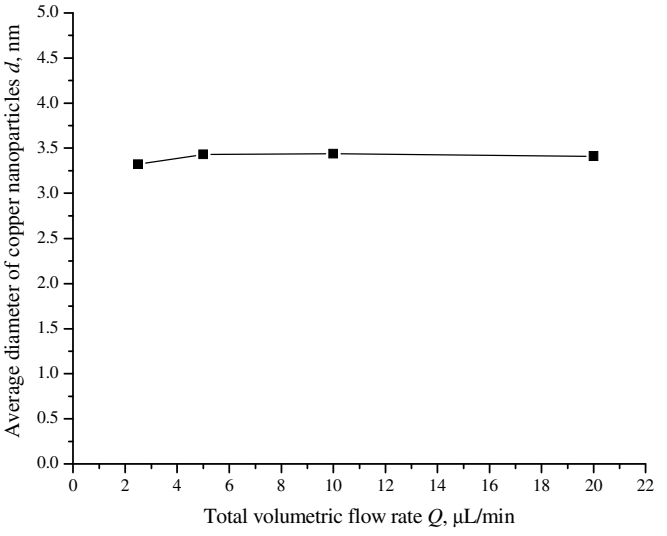

Fig. 72 Dependence of the average particle size on the total volumetric flow rate in the two-inlet microfluidic reactor (4 mM $[Cu(NH_3)_4]\cdot(OH)_2$, 120 mM N_2H_4, and 1 mM DBS)

coefficient of variation is about 22% for all the samples collected at different flow rates. The insensitivity of particle size and size distribution to the change of the total flow rate may be explained by the same mixing mechanism for copper nucleation. In the range of the total flow rate studied, mixing for copper nucleation in the microfluidic reactor is mainly dominated by the mass diffusion because of the extremely low *Re* and *Dn*, where the Dean vortices are not strong enough to induce intensive transverse convections and cause large discrepancies in mixing efficiency at different flow rates. Numerical studies of mixing in curved square/circular ducts have shown that fluid mixing is hardly influenced by the Dean vortices when *Re* is on the order of unity, and the mixing is primarily diffusion driven [219]. A detailed comparison between numerical and experimental investigation of fluid mixing in a 200 μm square curved channel has also revealed that for low Dean number (~10) no chaotic mixing occurs, and the inter-diffusion area approximately moves back to its original position when channel curvature is reversed [213]. In present study, as the total flow rate increases from 2.5 to 20 μL/min, *Re* increases from 0.6 to 4.7 and *Dn* number increases from 0.4 to 3.2. Both *Re* and *Dn* are below their threshold (*Re*~5 or *Dn*~10) for Dean vortices to significantly enhance the mixing in curved microchannels.

In common with other colloidal formation by chemical synthesis, copper nanoparticles are formed starting from an initial homogenous nucleation in which tiny nuclei precipitate spontaneously from solutions and entering a subsequent growth phase in which the freshly formed nuclei capture dissolved atoms or molecules by diffusion [220, 221]. Particle size and size distribution are strongly

influenced by the quality of nuclei formed in the nucleation phase which is significantly influenced by the mixing efficiency of precursors. In the inter-diffusion area between the two reactant streams, large amount of copper atoms appear because of the high reduction rate, and then a quick nucleation process arises. After fully mixed, a similar number of copper nuclei form at different flow rates due to the same mixing mechanism–mass diffusion. The formed copper nuclei absorb copper atoms generated from chemical reaction to further increase the particle size until all copper atoms are consumed. Therefore the copper nanoparticles finally grow up to a similar size regardless of the changes of the total flow rate.

6.3.2 Influence of Reactants Concentration on Particle Size

The influence of reactants concentration on particle size is investigated in both the microfluidic reactor and the flask by altering the concentration of $[Cu(NH_3)_4]\cdot(OH)_2$ from 0.5 to 8 mM while keeping a fixed concentration ratio at 4: 120: 1 for $[Cu(NH_3)_4]\cdot(OH)_2$: N_2H_4: DBS. Figure 73 shows the results that reactants concentration has little influence on copper nanoparticle size synthesized in the microfluidic reactor. The average particle diameter is around 3.4 nm, and the variation of coefficient is about 22%. The insensitivity of particle size and size distribution to the reactants concentration may be interpreted as a result of the fast and efficient mass diffusion in the microfluidic reactor. The full mixing time, t_{fdif}, in the microfluidic reactor by diffusion can be estimated as

$$t_{fdif} \approx \frac{W_c^{\,2}}{2D}, \tag{70}$$

where D is the mass diffusivity of Cu/N_2H_4 in water. Given that D is on the order of 10^{-9} m^2/s, t_{fdif} is estimated to be around only 7.2 seconds. With the help of fast and efficient mixing, copper atoms have an equal opportunity to aggregate to form copper nuclei in the nucleation phase. At a higher concentration, larger amount of copper nuclei will arise from a single or multiple nucleation and many more copper atoms are consumed in the nucleation phase. At a lower concentration, less amount copper nuclei will be formed and less copper atoms are consumed. Therefore at the end of the growth phase of copper nanoparticles synthesized at either higher or lower reactants concentration, the particles will have a similar average size and size distribution. However, in the flask method copper nanoparticle size exhibits an unpredictable dependency on reactants concentration, which could be resulted from the un-equilibrated balance between mixing efficiency and copper nucleation rate, resulted from the non-uniform mixing inside the flask. The average particle size varies from 2.7 to 4.9 nm with a broad size distribution, larger than 30%, as shown in Fig. 73.

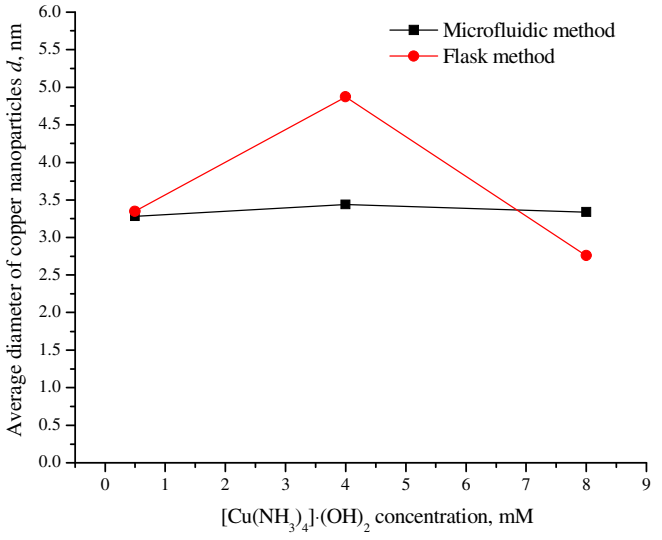

Fig. 73 Dependence of the average nanoparticle size on the concentration of copper complex in the two-inlet microfluidic reactor (C($[Cu(NH_3)_4]\cdot(OH)_2$): C(N_2H_4): C(DBS)= 4: 120: 1)

6.3.3 Influence of DBS Concentration on Particle Size

The concentration of DBS in N_2H_4 solution is changed from 0 to 1 mM while keeping the concentration of $[Cu(NH_3)_4]\cdot(OH)_2$ and N_2H_4 at 4 and 120 mM, respectively. It is found that, shown in Fig. 74, the DBS concentration has little influence on nanoparticle size synthesized in the microfluidic reactor; the average particle size is around 3.4 nm with a coefficient of variation (CV) about 23%. However, the average size of particles synthesized in the flask increases from 3.3 to 4.9 nm as DBS concentration increases, and the CV-value is larger than 30%. The large discrepancy of the influence of DBS concentration on particle size is probably resulted from the different mixing mechanism for copper nucleation and growth in these two methods. In the microfluidic reactor, mixing for nucleation is mainly dominated by mass diffusion, while in the flask, mixing is mainly dominated by convection. In the limit of low *Re*, for spherical particles, the diffusivity of particles can be estimated by Einstein correlation [222]

$$D = \frac{K_B T}{6\pi\mu r}, \tag{71}$$

where K_B is the Boltzmann constant. T is the absolute temperature. r is the diameter of particles, including molecules or atoms. For a copper atom the diameter is on the order of 10^{-10} m, and the diffusivity is on the order of 10^{-9} m^2/s in water. In aqueous solutions, surfactant DBS ($C_{18}H_{29}SO_3Na$) dissociates a long chain group with

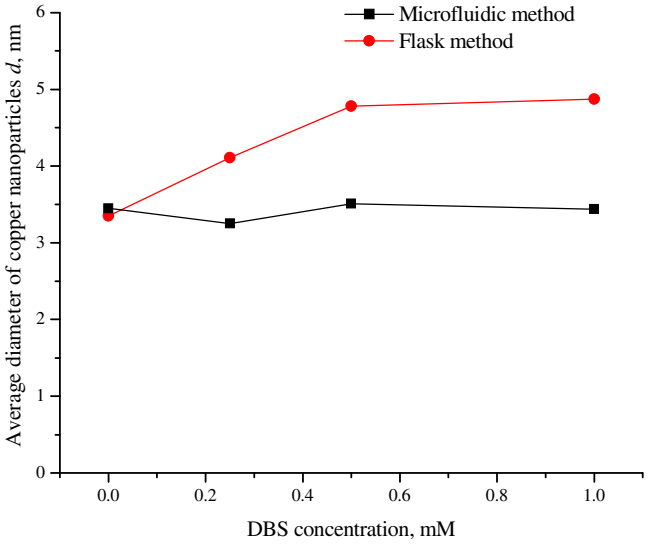

Fig. 74 Dependence of the average nanoparticle size on the concentration of surfactant DBS in the two-inlet microfluidic reactor ($C([Cu(NH_3)_4]\cdot(OH)_2)$=4 mM, $C(N_2H_4)$=120 mM)

surface activity $C_{18}H_{29}SO_3^-$ of which the equivalent diameter is at least one order higher than the copper atom. According to Eq. (71), the diffusivity of $C_{18}H_{29}SO_3^-$ is on the order of 10^{-10} m^2/s that is one order smaller than the copper atom. The higher the diffusivity is, the faster the particles transport in liquid by diffusion. Therefore in the microfluidic reactor, copper atoms aggregate to form nuclei and are further absorbed onto already formed nuclei at a much higher speed than the $C_{18}H_{29}SO_3^-$ by diffusion. The large discrepancy of diffusivity between the copper atoms and $C_{18}H_{29}SO_3^-$ weakens the influence of DBS on the size of copper nanoparticles in the microfluidic reactor. In the flask, however, precursors are under a strong stirring where the mixing is dominated by fluid convection. The intensive convection will promote the motion of both $C_{18}H_{29}SO_3^-$ and copper atoms and relatively reduce the difference of the aggregation rate between copper atoms and $C_{18}H_{29}SO_3^-$ such that the influence of DBS on particle size is visible.

6.3.4 Stability Improvement of Copper Nanofluids

Copper nanofluids synthesized by chemical reduction without pH adjustment are found to have a poor stability due to the oxidization of copper nanoparticles, where the freshly synthesized copper nanofluids can only stand for ~2 hrs without obvious oxidization or precipitation in open air at room temperature. It has been found that pH adjustment of copper nanofluids would effectively slow down the oxidization rate and the effective pH range is located between 8.45 and 8.65 [223]. Therefore, a

Tris-HCl buffer solution with a pH =8.5 is used to collect copper nanofluids in this study. After pH adjustment, the copper nanofluids can normally stand for 5 hours including the time consumed in the collection process without obvious oxidization or precipitation. The three-inlet microfluidic reactor (Fig. 70(b)) is designed to do so by introducing the buffer solution between $[Cu(NH_3)_4]\cdot(OH)_2$ and N_2H_4 during chemical reaction rather than after the reaction finished. It is found in such a flow configuration the copper nanofluids have a similar stability as that synthesized without but collected in the buffer solution.

6.3.5 Aggregation of Nanoparticles on Channel Walls

Nanoparticle agglomeration on channel surfaces is found in our experiments in either two- or three-inlet design. Figure 75 shows a typical agglomeration of copper nanoparticles on microchannel walls. At present time it seems that effective methods to prevent nanoparticles from aggregating on channel walls are still unavailable for such continuous synthesis in microfluidic reactors. Particle agglomeration on channel surfaces is affected by many parameters among which the running time and the reactants concentration are found to be the most important ones. Severe aggregation normally appears after a long time running of chemical reaction at a high concentration. For 4 mM $[Cu(NH_3)_4]\cdot(OH)_2$, agglomeration of copper nanoparticles would be found after ~3 hours running at the total flow rate of 10 μL/min (Fig. 75 (a)), and severe agglomeration is found after ~5 hours running (Fig. 75 (b)). The agglomeration in the three-inlet microfluidic reactor is also found, shown in Fig. 75 (c), after running at the total flow rate of 10 μL/m for 4 hours.

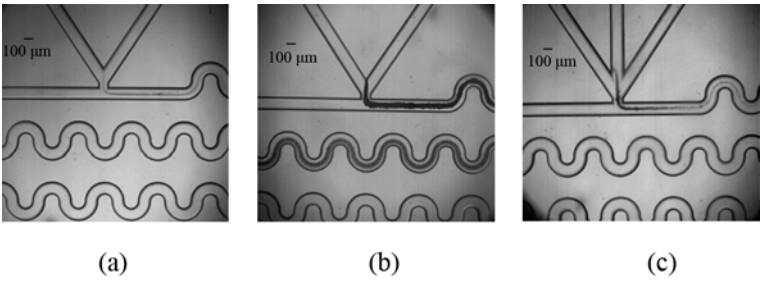

Fig. 75 Aggregation of copper nanoparticles on channel walls at the total flow rate of 10 μL/min for: (a) 3 hours; (b) 5 hours; (c) 4 hours ($C([Cu(NH_3)_4]\cdot(OH)_2)$=4 mM, $C(N_2H_4)$=120 mM and C(DBS)=1 mM)

6.4 Concluding Remarks

Synthesis of copper nanofluids is realized in microfluidic reactors. Although agglomeration of nanoparticle on channel walls is still a challenge, a variety of benefits arising from the fast and efficient mixing have been demonstrated,

including the insensitivity of nanoparticle size and size distribution to the flow rate of reactants, reactants concentration and surfactant concentration. In comparison with the flask method, copper nanofluids containing nanoparticles with a uniform size distribution can be achieved by using microfluidic reactors. Copper nanoparticles synthesized in the microfluidic reactors have an average size around 3.4 nm with a coefficient of variation of about 22%, whereas the average size of copper nanoparticles synthesized in the flask changes from 2.7 to 4.9 nm with a coefficient of variation larger than 30%. By using microfluidic reactors, the synthesis time of copper nanofluids is reduced one order of magnitude, from ~10 minutes to ~28 seconds.

Dean vortices effectively used in micromixing technology have limited application in enhancing the mixing efficiency for nanofluid synthesis because of the extremely low *Re* and *Dn*, normally on the order of unity. Unlike pure micromixers, microfluidic reactors designed for nanofluids synthesis must have such a feature that provides long enough residence time for nanoparticles nucleation and growth. That can be realized by slowing down flow velocity in the reaction channel or by increasing the length of the reaction channel. However, low flow velocity directly causes low *Re* and *Dn* and negligible transverse convection, whereas long reaction channel will result in operational difficulties due to the high flow resistance and the manufacture of long microfluidic reactors.

7 Conclusion

A low-cost fabrication method for producing glass-based microfluidic devices has been developed in a routine laboratory without the requirement of a clean room. The fabrication method is very reliable and the product output is larger than 90%. Wetting ability modification of glass material, from hydrophilic to hydrophobic, has been realized inside the microfluidic devices after fabrication. With the help of such modification, either oil-in-water or water-in-oil type droplets can be generated in glass-based microfluidic devices.

Droplet and bubble formation in confined T-shaped junctions has been experimentally examined. The movement of the rear interface of the forming tip of dispersed phase is found to have a very important role in determining formation time and volume. The formation process of either droplets or bubbles can be generalized as follows: (1) the dispersed phase tip with a higher pressure gradually intrudes into the continuous phase and the pressure behind the rear interface of the forming tip gradually increases in order to balance the pressure inside the forming droplet/bubble. During this process the rear interface does not move downstream, while the front interface moves downstream within this stage because the initial pressure inside the growing tip is higher than the pressure in the downstream; (2) when the pressure behind the rear interface is increased to a critical value, the rear interface starts to move downstream under the effects of the increased pressure, as well as the viscous force, exerted on the rear interface until the rear interface touches the downstream corner of the T-shaped junction. It has been experimentally

confirmed that droplet volume is equal to the volume of dispersed phase flowed into the forming tip within the droplet formation time. Two empirical correlations for predicting droplet volume and formation time have been developed. When the dispersed phase is liquid and is driven under controlled flow rates, the droplet volume increases linearly as the flow rate ratio increases. Influences of continuous phase viscosity, interfacial tension and average velocity of continuous phase can be characterized by capillary number as a correction coefficient to modify the correlations. When the dispersed phase is gas and driven under controlled pressures, it has been found that the bubble volume is almost linearly proportional to the ratio of the effective inlet pressure to the pressure drop of continuous phase flow from the T-shaped junction to the outlet. The bubble formation time exponentially decreases as the ratio increases.

Scaling analysis of the critical condition where mother droplets can break up in symmetric T-shaped junctions has been made based on the pressure-driven mechanism and has been experimentally confirmed. After mother droplets fully enter the T-shaped junction, the upstream pressure will be increased significantly and such pressure increase is the main driven force responsible for the droplet breakup. The critical condition has been found to be dependent on the initial droplet length, channel depth and capillary number, which can be formulated as $L^0_d/H \propto Ca^{-1/3}$. A new droplet breakup pattern, unequal breakup, has been found in the symmetric T-shaped junction. Such unequal breakup is resulted from the slightly asymmetric properties of the T-shaped junction introduced in the fabrication process. In other words, slight asymmetry of T-shaped junctions will influence the breakup significantly under some flow conditions. In practical operation of droplet breakup, flow conditions should be controlled within proper ranges where the influence of the asymmetry does not appear. In asymmetric T-shaped junctions it has been found that the droplet breakup is quite difficult.

Chaotic mixing inside droplets has been experimentally investigated by using a micro visualization system. It has been experimentally observed that chaotic mixing has already started during the droplet formation. For small droplets, the chaotic mixing during generation is very strong and the full mixing can almost be achieved after the droplet detachment. For large droplets, the chaotic mixing during generation is not as strong as inside small droplets, but still enhances the mixing significantly. To evaluate the full mixing, the chaotic mixing during the formation process must be considered. It has been found that the mixing efficiency inside moving droplets can be significantly increased by the chaotic advection and the full mixing time can be reduced as much as two orders of magnitude compared with the pure diffusion in single phase laminar flow. The scaling analysis of the chaotic mixing based on the idealized recirculating flow and the Baker's transformation can give a reasonable estimation of the full mixing time. An effective microstructure is designed for mixing two or more individual droplets. The good performance of the microstructure has been experimentally verified at different flow conditions.

Synthesis of copper nanofluids has been realized in microfluidic reactors. Although agglomeration of nanoparticles on channel walls is still a challenging

issue, a variety of benefits arising from the fast and efficient mixing have been demonstrated, including the insensitivity of nanoparticle size and size distribution to the flow rate of reactants, reactants concentration and surfactant concentration. In contrast to the flask method, the copper nanofluids synthesized in microfluidic reactor have a narrow size distribution, and the synthesis time is reduced by one order of magnitude, from ~ 10 minutes to ~28 seconds.

Acknowledgement. The financial support from the Research Grants Council of Hong Kong (GRF718009 and GRF704906) is gratefully acknowledged.

References

1. Stone, H.A., Stroock, A.D., Ajdari, A.: Engineering flows in small devices: Microfluidics toward a lab-on-a-chip. Annual Review of Fluid Mechanics 36, 381–411 (2004)
2. Gad-el-Hak, M.: The MEMS handbook. CRC Press, Boca Raton (2002)
3. Velten, T., Ruf, H.H., Barrow, D., Aspragathos, N., Lazarou, P., Jung, E., Malek, C.K., Richter, M., Kruckow, J.: Packaging of bio-mems: Strategies, technologies, and applications. IEEE Transactions on Advanced Packaging 28, 533–546 (2005)
4. Baharudin, L.: Microfluidics: Fabrications and applications. Instrumentation Science & Technology 36, 222–230 (2008)
5. Berthier, J.: Microdroplets and digital microfluidics. William Andrew Inc., New York (2008)
6. Abgrall, P., Gue, A.M.: Lab-on-chip technologies: Making a microfluidic network and coupling it into a complete microsystem - a review. Journal of Micromechanics and Microengineering 17, R15–R49 (2007)
7. Jean, B., Pascal, S.: Microfluidics for biotechnology. Artech house Inc., MA (2005)
8. Ikkai, F., Iwamoto, S., Adachi, E., Nakajima, M.: New method of producing mono-sized polymer gel particles using microchannel emulsification and uv irradiation. Colloid and Polymer Science 283, 1149–1153 (2005)
9. Henares, T.G., Mizutani, F., Sekizawa, R., Hisamoto, H.: Single-drop analysis of various proteases in a cancer cell lysate using a capillary-assembled microchip. Analytical and Bioanalytical Chemistry 391, 2507–2512 (2008)
10. Kai, Z., Ping, H., Qiong-Lin, L., Guo-An, L.: Control and application of microdroplet in microfluidic chip. Chinese Journal of Analytical Chemistry 36, 556–562 (2008)
11. Sassa, F., Fukuda, J., Suzuki, H.: Microprocessing of liquid plugs for bio/chemical analyses. Analytical Chemistry 80, 6206–6213 (2008)
12. Xu, J., Attinger, D.: Drop on demand in a microfluidic chip. Journal of Micromechanics and Microengineering 18, 65020 (2008)
13. Shestopalov, I., Tice, J.D., Ismagilov, R.F.: Multi-step synthesis of nanoparticles performed on millisecond time scale in a microfluidic droplet-based system. Lab on a Chip 4, 316–321 (2004)
14. Chan, E.M., Alivisatos, A.P., Mathies, R.A.: High-temperature microfluidic synthesis of cdse nanocrystals in nanoliter droplets. Journal of the American Chemical Society 127, 13854–13861 (2005)

15. Hung, L.H., Choi, K.M., Tseng, W.Y., Tan, Y.C., Shea, K.J., Lee, A.P.: Alternating droplet generation and controlled dynamic droplet fusion in microfluidic device for cds nanoparticle synthesis. Lab on a Chip 6, 174–178 (2006)
16. Song, H., Chen, D.L., Ismagilov, R.F.: Reactions in droplets in microflulidic channels. Angewandte Chemie-International Edition 45, 7336–7356 (2006)
17. Clausell-Tormos, J., Lieber, D., Baret, J.C., El-Harrak, A., Miller, O.J., Frenz, L., Blouwolff, J., Humphry, K.J., Koster, S., Duan, H., Holtze, C., Weitz, D.A., Griffiths, A.D., Merten, C.A.: Droplet-based microfluidic platforms for the encapsulation and screening of mammalian cells and multicellular organisms. Chemistry & Biology 15, 427–437 (2008)
18. Song, Y.J., Hormes, J., Kumar, C.: Microfluidic synthesis of nanomaterials. Small 4, 698–711 (2008)
19. Terry, S.C., Jerman, J.H., Angell, J.B.: Gas-chromatographic air analyzer fabricated on a silicon-wafer. IEEE Transactions on Electron Devices 26, 1880–1886 (1979)
20. Harrison, D.J., Manz, A., Fan, Z.H., Ludi, H., Widmer, H.M.: Capillary electrophoresis and sample injection systems integrated on a planar glass chip. Analytical Chemistry 64, 1926–1932 (1992)
21. Jacobson, S.C., Hergenroder, R., Koutny, L.B., Ramsey, J.M.: High-speed separations on a microchip. Analytical Chemistry 66, 1114–1118 (1994)
22. Tai-Ran, H.: MEMS & Microsystems design and manufacture. McGraw-Hill, New York (2002)
23. Cha, J., Kim, J., Ryu, S.K., Park, J., Jeong, Y., Park, S., Kim, H.C., Chun, K.: A highly efficient 3d micromixer using soft PDMS bonding. Journal of Micromechanics and Microengineering 16, 1778–1782 (2006)
24. Yoo, J.C., La, G.S., Kang, C.J., Kim, Y.S.: Microfabricated polydimethylsiloxane microfluidic system including micropump and microvalve for integrated biosensor. In: Nano Korea 2006 Symposium, Ilsan, South Korea (2006)
25. Yun, K.S., Yoon, E.: Fabrication of complex multilevel microchannels in pdms by using three-dimensional photoresist masters. Lab on a Chip 8, 245–250 (2008)
26. Yu, H., Balogun, O., Li, B., Murray, T.W., Zhang, X.: Fabrication of three-dimensional microstructures based on singled-layered SU-8 for lab-on-chip applications. In: 18th IEEE International Conference on Micro Electro Mechanical Systems (MEMS), Miami Beach, FL (2005)
27. Mata, A., Fleischman, A.J., Roy, S.: Fabrication of multi-layer SU-8 microstructures. Journal of Micromechanics and Microengineering 16, 276–284 (2006)
28. Koller, D.M., Hohenau, A., Ditlbacher, H., Galler, N., Baudrion, A.L., Reil, F., Schausberger, S., Aussenegg, F.R., Leitner, A., Krenn, J.R.: Three-dimensional su-8 sub-micrometer structuring by electron beam lithography. Microelectronic Engineering 85, 1639–1641 (2008)
29. Steigert, J., Brett, O., Muller, C., Strasser, M., Wangler, N., Reinecke, H., Daub, M., Zengerle, R.: A versatile and flexible low-temperature full-wafer bonding process of monolithic 3d microfluidic structures in SU-8. Journal of Micromechanics and Microengineering 18, 095013 (2008)
30. Singh, V., Desta, Y., Datta, P., Guy, J., Clarke, M., Feedback, D.L., Weimert, J., Goettert, J.: A hybrid approach for fabrication of polymeric biomems devices. In: 6th Biennial International Workshop on High Aspect Ratio Micro Structure Technology, Gyenogju, South Korea (2005)

31. Zhu, X.L., Liu, G., Guo, Y.H., Tian, Y.C.: Study of pmma thermal bonding. In: 6th Biennial International Workshop on High Aspect Ratio Micro Structure Technology, Gyenogju, South Korea (2005)
32. Chen, Y., Zhang, L.Y., Chen, G.: Fabrication, modification, and application of department of analytical poly(methyl methacrylate) microfluidic chips. Electrophoresis 29, 1801–1814 (2008)
33. Fiorini, G.S., Chiu, D.T.: Disposable microfluidic devices: Fabrication, function, and application. Biotechniques 38, 429–446 (2005)
34. Becker, H., Gartner, C.: Polymer microfabrication technologies for microfluidic systems. Analytical and Bioanalytical Chemistry 390, 89–111 (2008)
35. Nguyen, N.T.: Micromixers: Fundamentals, design and fabrication. William Andrew Inc., New York (2008)
36. Iliescu, C., Tay, F.E.: Ieee: Wet etching of glass. In: International Semiconductor Conference, Sinaia, Romania (2005)
37. Chen, Q., Li, G., Jin, Q.H., Zhao, J.L., Ren, Q.S., Xu, Y.S.: A rapid and low-cost procedure for fabrication of glass microfluidic devices. Journal of Microelectromechanical Systems 16, 1193–1200 (2007)
38. Sorouraddin, M.H., Amjadi, M., Safi-Shalamzari, M.: Simple and rapid methods for the fabrication of polymeric and glass chips for using in analytical chemistry. Analytica Chimica Acta 589, 84–88 (2007)
39. McDonald, J.C., Duffy, D.C., Anderson, J.R., Chiu, D.T., Wu, H.K., Schueller, O.J.A., Whitesides, G.M.: Fabrication of microfluidic systems in poly(dimethylsiloxane). Electrophoresis 21, 27–40 (2000)
40. Whitesides, G.M., Ostuni, E., Takayama, S., Jiang, X.Y., Ingber, D.E.: Soft lithography in biology and biochemistry. Annual Review of Biomedical Engineering 3, 335–373 (2001)
41. Gates, B.D., Xu, Q.B., Stewart, M., Ryan, D., Willson, C.G., Whitesides, G.M.: New approaches to nanofabrication: Molding, printing, and other techniques. Chemical Reviews 105, 1171–1196 (2005)
42. Lee, K., Kim, C., Shin, K.S., Lee, J., Ju, B.K., Kim, T.S., Lee, S.K., Kang, J.Y.: Fabrication of round channels using the surface tension of pdms and its application to a 3d serpentine mixer. Journal of Micromechanics and Microengineering 17, 1533–1541 (2007)
43. Thian, S.C.H., Fuh, J.Y.H., Wong, Y.S., Loh, H.T., Gian, P.W., Tang, Y.: Fabrication of microfluidic channel utilizing silicone rubber with vacuum casting. Microsystem Technologies-Micro-and Nanosystems-Information Storage and Processing Systems 14, 1125–1135 (2008)
44. Fleger, M., Neyer, A.: Pdms microfluidic chip with integrated waveguides for optical detection. In: 31st International Conference on Micro- and Nano-Engineering, Vienna, Austria (2005)
45. Bubendorfer, A., Liu, X.M., Ellis, A.V.: Microfabrication of pdms microchannels using su-8/pmma moldings and their sealing to polystyrene substrates. Smart Materials & Structures 16, 367–371 (2007)
46. Koerner, T., Brown, L., Xie, R.X., Oleschuk, R.D.: Epoxy resins as stamps for hot embossing of microstructures and microfluidic channels. Sensors and Actuators B-Chemical 107, 632–639 (2005)
47. McCormick, R.M., Nelson, R.J., AlonsoAmigo, M.G., Benvegnu, J., Hooper, H.H.: Microchannel electrophoretic separations of DNA in injection-molded plastic substrates. Analytical Chemistry 69, 2626–2630 (1997)

48. Li, J.M., Liu, C., Qiao, H.C., Zhu, L.Y., Chen, G., Dai, X.D.: Hot embossing/bonding of a poly(ethylene terephthalate) (pet) microfluidic chip. Journal of Micromechanics and Microengineering 18, 015008 (2008)
49. Li, S.G., Xu, Z.G., Mazzeo, A., Burns, D.J., Fu, G., Dirckx, M., Shilpiekandula, V., Chen, X., Nayak, N.C., Wong, E., Yoon, S.F., Fang, Z.P., Youcef-Toumi, K., Hardt, D., Tor, S.B., Yue, C.Y., Chun, J.H.: Review of production of microfluidic devices: Material, manufacturing and metrology - art. No. 69930f. In: Conference on MEMS, MOEMS and Micromachining III, Strasbourg, France (2008)
50. Burns, M.A., Johnson, B.N., Brahmasandra, S.N., Handique, K., Webster, J.R., Krishnan, M., Sammarco, T.S., Man, P.M., Jones, D., Heldsinger, D., Mastrangelo, C.H., Burke, D.T.: An integrated nanoliter DNA analysis device. Science 282, 484–487 (1998)
51. Kirby, B.J., Hasselbrink, E.F.: Zeta potential of microfluidic substrates: 2. Data for polymers. Electrophoresis 25, 203–213 (2004)
52. Patel, J.N., Kaminska, B., Gray, B.L., Gates, B.D.: PDMS as a sacrificial substrate for SU-8-based biomedical and microfluidic applications. Journal of Micromechanics and Microengineering 18, 095028 (2008)
53. Sikanen, T., Tuomikoski, S., Ketola, R.A., Kostiainen, R., Franssila, S., Kotiaho, T.: Characterization of su-8 for electrokinetic microfluidic applications. Lab on a Chip 5, 888–896 (2005)
54. Tuomikoski, S., Sikanen, T., Ketola, R.A., Kostiainen, R., Kotiaho, T., Franssila, S.: Fabrication of enclosed su-8 tips for electrospray ionization-mass spectrometry. Electrophoresis 26, 4691–4702 (2005)
55. Madou, M.: Fundamentals of microfabrication. CRE, New York (2002)
56. Fang, Z.: Manufacture and applications of microfluidic chips. Chemical Industry Press, Beijing (2005)
57. Vullev, V.I., Wan, J.D., Heinrich, V., Landsman, P., Bower, P.E., Xia, B., Millare, B., Jones, G.: Nonlithographic fabrication of microfluidic devices. Journal of the American Chemical Society 128, 16062–16072 (2006)
58. Xiao, Z.X., Wu, G.Y., Li, Z.H., Zhang, C.B., Hao, Y.L., Wang, Y.Y.: Silicon-glass wafer bonding with silicon hydrophilic fusion bonding technology. Sensors and Actuators a-Physical 72, 46–48 (1999)
59. Niklaus, F., Stemme, G., Lu, J.Q., Gutmann, R.J.: Adhesive wafer bonding. Journal of Applied Physics 99, 031101 (2006)
60. Pan, Y.J., Yang, R.J.: A glass microfluidic chip adhesive bonding method at room temperature. Journal of Micromechanics and Microengineering 16, 2666–2672 (2006)
61. Chen, Y.T., Lee, D.: A bonding technique using hydrophilic su-8. Journal of Micromechanics and Microengineering 17, 1978–1984 (2007)
62. Teh, S.Y., Lin, R., Hung, L.H., Lee, A.P.: Droplet microfluidics. Lab on a Chip 8, 198–220 (2008)
63. Yang, C.G., Xu, Z.R., Wang, J.H.: Manipulation of droplets in microfluidic systems. Trac-Trends in Analytical Chemistry 29, 141–157 (2010)
64. Umbanhowar, P.B., Prasad, V., Weitz, D.A.: Monodisperse emulsion generation via drop break off in a coflowing stream. Langmuir 16, 347–351 (2000)
65. Anna, S.L., Bontoux, N., Stone, H.A.: Formation of dispersions using “Flow focusing” In microchannels. Applied Physics Letters 82, 364–366 (2003)
66. Xu, J.H., Li, S.W., Tan, J., Wang, Y.J., Luo, G.S.: Preparation of highly monodisperse droplet in a t-junction microfluidic device. Aiche Journal 52, 3005–3010 (2006)

67. Xu, J.H., Li, S.W., Tan, J., Wang, Y.J., Luo, G.S.: Controllable preparation of monodisperse o/w and w/o emulsions in the same microfluidic device. Langmuir 22, 7943–7946 (2006)
68. Link, D.R., Anna, S.L., Weitz, D.A., Stone, H.A.: Geometrically mediated breakup of drops in microfluidic devices. Physical Review Letters 92 (2004)
69. Menetrier-Deremble, L., Tabeling, P.: Droplet breakup in microfluidic junctions of arbitrary angles. Physical Review E 74, 035303 (2006)
70. Jullien, M.C., Ching, M., Cohen, C., Menetrier, L., Tabeling, P.: Droplet breakup in microfluidic t-junctions at small capillary numbers. Physics of Fluids 21, 072001 (2009)
71. Liu, K., Ding, H.J., Chen, Y., Zhao, X.Z.: Droplet-based synthetic method using microflow focusing and droplet fusion. Microfluidics and Nanofluidics 3, 239–243 (2007)
72. Kawakatsu, T., Komori, H., Nakajima, M., Kikuchi, Y., Yonemoto, T.: Production of monodispersed oil-in-water emulsion using crossflow-type silicon microchannel plate. Journal of Chemical Engineering of Japan 32, 241–244 (1999)
73. Kobayashi, I., Mukataka, S., Nakajima, M.: Production of monodisperse oil-in-water emulsions using a large silicon straight-through microchannel plate. Industrial & Engineering Chemistry Research 44, 5852–5856 (2005)
74. Saito, M., Yin, L.J., Kobayashi, I., Nakajima, M.: Preparation characteristics of monodispersed oil-in-water emulsions with large particles stabilized by proteins in straight-through microchannel emulsification. Food Hydrocolloids 19, 745–751 (2005)
75. Xu, Q.Y., Nakajima, M., Binks, B.P.: Preparation of particle-stabilized oil-in-water emulsions with the microchannel emulsification method. Colloids and Surfaces a-Physicochemical and Engineering Aspects 262, 94–100 (2005)
76. Seo, M., Paquet, C., Nie, Z.H., Xu, S.Q., Kumacheva, E.: Microfluidic consecutive flow-focusing droplet generators. Soft Matter 3, 986–992 (2007)
77. Ganan-Calvo, A.M., Gordillo, J.M.: Perfectly monodisperse microbubbling by capillary flow focusing. Physical Review Letters 87, 274501 (2001)
78. Utada, A.S., Lorenceau, E., Link, D.R., Kaplan, P.D., Stone, H.A., Weitz, D.A.: Monodisperse double emulsions generated from a microcapillary device. Science 308, 537–541 (2005)
79. Chu, L.Y., Utada, A.S., Shah, R.K., Kim, J.W., Weitz, D.A.: Controllable monodisperse multiple emulsions. Angewandte Chemie-International Edition 46, 8970–8974 (2007)
80. Shah, R.K., Shum, H.C., Rowat, A.C., Lee, D., Agresti, J.J., Utada, A.S., Chu, L.Y., Kim, J.W., Fernandez-Nieves, A., Martinez, C.J., Weitz, D.A.: Designer emulsions using microfluidics. Materials Today 11, 18–27 (2008)
81. Thorsen, T., Roberts, R.W., Arnold, F.H., Quake, S.R.: Dynamic pattern formation in a vesicle-generating microfluidic device. Physical Review Letters 86, 4163–4166 (2001)
82. van der Graaf, S., Steegmans, M.L.J., van der Sman, R.G.M., Schroen, C., Boom, R.M.: Droplet formation in a t-shaped microchannel junction: A model system for membrane emulsification. Colloids and Surfaces a-Physicochemical and Engineering Aspects 266, 106–116 (2005)
83. Xu, J.H., Luo, G.S., Chen, G.G., Wang, J.D.: Experimental and theoretical approaches on droplet formation from a micrometer screen hole. Journal of Membrane Science 266, 121–131 (2005)

84. Garstecki, P., Fuerstman, M.J., Stone, H.A., Whitesides, G.M.: Formation of droplets and bubbles in a microfluidic T-junction - scaling and mechanism of break-up. Lab on a Chip 6, 437–446 (2006)
85. Husny, J., Cooper-White, J.J.: The effect of elasticity on drop creation in t-shaped microchannels. Journal of Non-Newtonian Fluid Mechanics 137, 121–136 (2006)
86. Cramer, C., Fischer, P., Windhab, E.J.: Drop formation in a co-flowing ambient fluid. Chemical Engineering Science 59, 3045–3058 (2004)
87. Utada, A.S., Fernandez-Nieves, A., Stone, H.A., Weitz, D.A.: Dripping to jetting transitions in coflowing liquid streams. Physical Review Letters 99, 094502 (2007)
88. Utada, A.S., Chu, L.Y., Fernandez-Nieves, A., Link, D.R., Holtze, C., Weitz, D.A.: Dripping, jetting, drops, and wetting: The magic of microfluidics. Mrs Bulletin 32, 702–708 (2007)
89. Marre, S., Aymonier, C., Subra, P., Mignard, E.: Dripping to jetting transitions observed from supercritical fluid in liquid microcoflows. Applied Physics Letters 95, 134105 (2009)
90. Garstecki, P., Stone, H.A., Whitesides, G.M.: Mechanism for flow-rate controlled breakup in confined geometries: A route to monodisperse emulsions. Physical Review Letters 94, 164501 (2005)
91. Ward, T., Faivre, M., Abkarian, M., Stone, H.A.: Microfluidic flow focusing: Drop size and scaling in pressure versus flow-rate-driven pumping. Electrophoresis 26, 3716–3724 (2005)
92. Lee, C.Y., Lin, Y.H., Lee, G.B.: A droplet-based microfluidic system capable of droplet formation and manipulation. Microfluidics and Nanofluidics 6, 599–610 (2009)
93. Garstecki, P., Gitlin, I., DiLuzio, W., Whitesides, G.M., Kumacheva, E., Stone, H.A.: Formation of monodisperse bubbles in a microfluidic flow-focusing device. Applied Physics Letters 85, 2649–2651 (2004)
94. Cubaud, T., Tatineni, M., Zhong, X.L., Ho, C.M.: Bubble dispenser in microfluidic devices. Physical Review E 72, 037302 (2005)
95. Christopher, G.F., Anna, S.L.: Microfluidic methods for generating continuous droplet streams. Journal of Physics D-Applied Physics 40, R319–R336 (2007)
96. van der Graaf, S., Nisisako, T., Schroen, C., van der Sman, R.G.M., Boom, R.M.: Lattice boltzmann simulations of droplet formation in a T-shaped microchannel. Langmuir 22, 4144–4152 (2006)
97. De Menech, M., Garstecki, P., Jousse, F., Stone, H.A.: Transition from squeezing to dripping in a microfluidic t-shaped junction. Journal of Fluid Mechanics 595, 141–161 (2008)
98. van der Graaf, S., Schroen, C., Boom, R.M.: Preparation of double emulsions by membrane emulsification - a review. Journal of Membrane Science 251, 7–15 (2005)
99. Leshansky, A.M., Pismen, L.M.: Breakup of drops in a microfluidic t junction. Physics of Fluids 21, 023303 (2009)
100. Tan, Y.C., Fisher, J.S., Lee, A.I., Cristini, V., Lee, A.P.: Design of microfluidic channel geometries for the control of droplet volume, chemical concentration, and sorting. Lab on a Chip 4, 292–298 (2004)
101. Tan, Y.C., Ho, Y.L., Lee, A.P.: Droplet coalescence by geometrically mediated flow in microfluidic channels. Microfluidics and Nanofluidics 3, 495–499 (2007)
102. Niu, X.Z., Zhang, M.Y., Peng, S.L., Wen, W.J., Sheng, P.: Real-time detection, control, and sorting of microfluidic droplets. Biomicrofluidics 1, 044101 (2007)

103. Burke, B.J., Regnier, F.E.: Stopped-flow enzyme assays on a chip using a microfabricated mixer. Analytical Chemistry 75, 1786–1791 (2003)
104. Koster, S., Angile, F.E., Duan, H., Agresti, J.J., Wintner, A., Schmitz, C., Rowat, A.C., Merten, C.A., Pisignano, D., Griffiths, A.D., Weitz, D.A.: Drop-based microfluidic devices for encapsulation of single cells. Lab on a Chip 8, 1110–1115 (2008)
105. Zheng, B., Gerdts, C.J., Ismagilov, R.F.: Using nanoliter plugs in microfluidics to facilitate and understand protein crystallization. Current Opinion in Structural Biology 15, 548–555 (2005)
106. Zheng, B., Roach, L.S., Tice, J.D., Gerdts, C.J., Chen, D., Ismagilov, R.F.: A microfluidic system for screening protein crystallization conditions inside nanoliter droplets with on-chip x-ray diffraction. In: Micro Total Analysis Systems 2004, pp. 145–147 (2005)
107. William, B.J.: Microfluidics: history, theory and applications. Springer, New York (2006)
108. Jeong, G.S., Chung, S., Kim, C.B., Lee, S.H.: Applications of micromixing technology. Analyst 135, 460–473 (2010)
109. Boleininger, J., Kurz, A., Reuss, V., Sonnichsen, C.: Microfluidic continuous flow synthesis of rod-shaped gold and silver nanocrystals. Physical Chemistry Chemical Physics 8, 3824–3827 (2006)
110. Champion, J.A., Katare, Y.K., Mitragotri, S.: Making polymeric micro- and nanoparticles of complex shapes. Proceedings of the National Academy of Sciences of the United States of America 104, 11901–11904 (2007)
111. Gross, G.A., Hamann, C., Gunther, M., Kohler, J.M.: Formation of polymer and nanoparticle doped polymer minirods by use of the microsegmented flow principle. Chemical Engineering & Technology 30, 341–346 (2007)
112. Hwang, D.K., Dendukuri, D., Doyle, P.S.: Microfluidic-based synthesis of non-spherical magnetic hydrogel microparticles. Lab on a Chip 8, 1640–1647 (2008)
113. Weng, C.H., Huang, C.C., Yeh, C.S., Lei, H.Y., Lee, G.B.: Synthesis of hollow, magnetic fe/ga-based oxide nanospheres using a bubble templating method in a microfluidic system. Microfluidics and Nanofluidics 7, 841–848 (2009)
114. Wang, H.Z., Li, X.Y., Uehara, M., Yamaguchi, Y., Nakamura, H., Miyazaki, M.P., Shimizu, H., Maeda, H.: Continuous synthesis of cdse-zns composite nanoparticles in a microfluidic reactor. Chemical Communications, 48–49 (2004)
115. Wagner, J., Kohler, J.M.: Continuous synthesis of gold nanoparticles in a microreactor. Nano Letters 5, 685–691 (2005)
116. Jahn, A., Reiner, J.E., Vreeland, W.N., DeVoe, D.L., Locascio, L.E., Gaitan, M.: Preparation of nanoparticles by continuous-flow microfluidics. Journal of Nanoparticle Research 10, 925–934 (2008)
117. Kohler, J.M., Abahmane, L., Wagner, J., Albert, J., Mayer, G.: Preparation of metal nanoparticles with varied composition for catalytical applications in microreactors. Chemical Engineering Science 63, 5048–5055 (2008)
118. Li, S.W., Xu, H.H., Wang, Y.J., Luo, G.S.: Controllable preparation of nanoparticles by drops and plugs flow in a microchannel device. Langmuir 24, 4194–4199 (2008)
119. Kobayashi, I., Lou, X.F., Mukataka, S., Nakajima, M.: Preparation of monodisperse water-in-oil-in-water emulsions using microfluidization and straight-through microchannel emulsification. Journal of the American Oil Chemists Society 82, 65–71 (2005)

120. Kobayashi, I., Nakajima, M.: Microchannel emulsification technology: Formulation and application of monodisperse emulsions. Journal of the Japanese Society for Food Science and Technology-Nippon Shokuhin Kagaku Kogaku Kaishi 53, 317–326 (2006)
121. Chen, L.X., Luo, G.A., Liu, K.H., Ma, J.P., Yao, B., Yan, Y.C., Wang, Y.M.: Bonding of glass-based microfluidic chips at low- or room-temperature in routine laboratory. Sensors and Actuators B-Chemical 119, 335–344 (2006)
122. Liu, J.S., Liu, C., Guo, J.H., Wang, L.D.: Electrostatic bonding of a silicon master to a glass wafer for plastic microchannel fabrication. Journal of Materials Processing Technology 178, 278–282 (2006)
123. Wang, Q.D., Duan, Y.G., Lu, B.H., Ding, Y.C., Tang, Y.P.: Imprint template fabrication based on glass wet etching using a soft etching mask. Journal of Micromechanics and Microengineering 16, 564–570 (2006)
124. Castano-Alvarez, M., Ayuso, D.F.P., Granda, M.G., Fernandez-Abedul, M.T., Garcia, J.R., Costa-Garcia, A.: Critical points in the fabrication of microfluidic devices on glass substrates. Sensors and Actuators B-Chemical 130, 436–448 (2008)
125. Hibara, A., Iwayama, S., Matsuoka, S., Ueno, M., Kikutani, Y., Tokeshi, M., Kitamori, T.: Surface modification method of microchannels for gas-liquid two-phase flow in microchips. Analytical Chemistry 77, 943–947 (2005)
126. Hibara, A., Nonaka, M., Hisamoto, H., Uchiyama, K., Kikutani, Y., Tokeshi, M., Kitamori, T.: Stabilization of liquid interface and control of two-phase confluence and separation in glass microchips by utilizing octadecylsilane modification of microchannels. Analytical Chemistry 74, 1724–1728 (2002)
127. Kirkpatrick, R., Muhstein, C.L.: Performance and durability of octadecyltrichlorosilane coated borosilicate glass. Journal of Non-Crystalline Solids 353, 2624–2637 (2007)
128. Takei, G., Nonogi, M., Hibara, A., Kitamori, T., Kim, H.B.: Tuning microchannel wettability and fabrication of multiple-step laplace valves. Lab on a Chip 7, 596–602 (2007)
129. Srinivasan, U., Houston, M.R., Howe, R.T., Maboudian, R.: Alkyltrichlorosilane-based self-assembled monolayer films for stiction reduction in silicon micromachines. Journal of Microelectromechanical Systems 7, 252–260 (1998)
130. Maboudian, R., Ashurst, W.R., Carraro, C.: Self-assembled monolayers as anti-stiction coatings for mems: Characteristics and recent developments. Sensors and Actuators a-Physical 82, 219–223 (2000)
131. Jing, W.H., Wu, J., Jin, W.Q., Xing, W.H., Xu, N.P.: Monodispersed w/o emulsion prepared by hydrophilic ceramic membrane emulsification. Desalination 191, 219–222 (2006)
132. Bao, D.C., Zhang, H.A., Liu, X.D., Zhao, Y.J., Ma, X.J., Yuan, Q.: Preparation of monodispersed polymer microspheres by spg membrane emulsification-solvent evaporation technology. Journal of Dispersion Science and Technology 28, 485–490 (2007)
133. Christov, N.C., Danov, K.D., Danova, D.K., Kralchevsky, P.A.: The drop size in membrane emulsification determined from the balance of capillary and hydrodynamic forces. Langmuir 24, 1397–1410 (2008)

134. Egidi, E., Gasparini, G., Holdich, R.G., Vladisavljevic, G.T., Kosvintsev, S.R.: Membrane emulsification using membranes of regular pore spacing: Droplet size and uniformity in the presence of surface shear. Journal of Membrane Science 323, 414–420 (2008)
135. Yuan, Q.C., Aryanti, N., Gutierrez, G., Williams, R.A.: Enhancing the throughput of membrane emulsification techniques to manufacture functional particles. Industrial & Engineering Chemistry Research 48, 8872–8880 (2009)
136. Wang, Z., Wang, S.C., Schroeder, V., Schubert, H.: Effect of continuous phase viscosity on membrane emulsification. Chinese Journal of Chemical Engineering 8, 108–112 (2000)
137. De Luca, G., Drioli, E.: Force balance conditions for droplet formation in cross-flow membrane emulsifications. Journal of Colloid and Interface Science 294, 436–448 (2006)
138. De Luca, G., Sindona, A., Giorno, L., Drioli, E.: Quantitative analysis of coupling effects in cross-flow membrane emulsification. Journal of Membrane Science 229, 199–209 (2004)
139. Christopher, G.F., Noharuddin, N.N., Taylor, J.A., Anna, S.L.: Experimental observations of the squeezing-to-dripping transition in t-shaped microfluidic junctions. Physical Review E 78, 036317 (2008)
140. Scheid, B., Delacotte, J., Dollet, B., Rio, E., Restagno, F., van Nierop, E.A., Cantat, I., Langevin, D., Stone, H.A.: The role of surface rheology in liquid film formation. EPL 90(2), 24002 (2010)
141. Hu, Y.D., Werner, C., Li, D.Q.: Influence of three-dimensional roughness on pressure-driven flow through microchannels. Journal of Fluids Engineering-Transactions of the Asme 125, 871–879 (2003)
142. English, N.J., Kandlikar, S.G.: An experimental investigation into the effect of surfactants on air-water two-phase flow in minichannels. Heat Transfer Engineering 27, 99–109 (2006)
143. Fuerstman, M.J., Lai, A., Thurlow, M.E., Shevkoplyas, S.S., Stone, H.A., Whitesides, G.M.: The pressure drop along rectangular microchannels containing bubbles. Lab on a Chip 7, 1479–1489 (2007)
144. Spurks, J.H., Aksel, N.: Fluid mechanics. Springer, Berlin (2008)
145. Constantinescu, V.N.: Laminar viscous flow. Springer, New York (1995)
146. Tung, K.Y., Li, C.C., Yang, J.T.: Mixing and hydrodynamic analysis of a droplet in a planar serpentine micromixer. Microfluidics and Nanofluidics 7, 545–557 (2009)
147. Stone, H.A.: On lubrication flows in geometries with zero local curvature. Chemical Engineering Science 60, 4838–4845 (2005)
148. Xi, H.W., Duncan, C.: Lattice boltzmann simulations of three-dimensional single droplet deformation and breakup under simple shear flow. Physical Review E 59, 3022–3026 (1999)
149. Bretherton, F.P.: The montion of bubbles in tubes. Journal of Fluid Mechanics 10, 166–188 (1961)
150. Guillot, P., Colin, A., Ajdari, A.: Stability of a jet in confined pressure-driven biphasic flows at low reynolds number in various geometries. Physical Review E 78, 016307 (2008)
151. De Menech, M.: Modeling of droplet breakup in a microfluidic t-shaped junction with a phase-field model. Physical Review E73, 031505 (2006)

152. Liu, R.H., Stremler, M.A., Sharp, K.V., Olsen, M.G., Santiago, J.G., Adrian, R.J., Aref, H., Beebe, D.J.: Passive mixing in a three-dimensional serpentine microchannel. Journal of Microelectromechanical Systems 9, 190–197 (2000)
153. Vijayendran, R.A., Motsegood, K.M., Beebe, D.J., Leckband, D.E.: Evaluation of a three-dimensional micromixer in a surface-based biosensor. Langmuir 19, 1824–1828 (2003)
154. Chen, H., Meiners, J.C.: Topologic mixing on a microfluidic chip. Applied Physics Letters 84, 2193–2195 (2004)
155. Xia, H.M., Wan, S.Y.M., Shu, C., Chew, Y.T.: Chaotic micromixers using two-layer crossing channels to exhibit fast mixing at low reynolds numbers. Lab on a Chip 5, 748–755 (2005)
156. Hong, C.C., Choi, J.W., Ahn, C.H.: A novel in-plane passive microfluidic mixer with modified tesla structures. Lab on a Chip 4, 109–113 (2004)
157. Jeon, M.K., Kim, J.H., Noh, J., Kim, S.H., Park, H.G., Woo, S.I.: Design and characterization of a passive recycle micromixer. Journal of Micromechanics and Microengineering 15, 346–350 (2005)
158. Stone, H.A., Nadim, A., Strogatz, S.H.: Chaotic streamlines inside drops immersed in steady stokes flows. Journal of Fluid Mechanics 232, 629–646 (1991)
159. Song, H., Bringer, M.R., Tice, J.D., Gerdts, C.J., Ismagilov, R.F.: Experimental test of scaling of mixing by chaotic advection in droplets moving through microfluidic channels. Applied Physics Letters 83, 4664–4666 (2003)
160. Grigoriev, R.O., Schatz, M.F., Sharma, V.: Chaotic mixing in microdroplets. Lab on a Chip 6, 1369–1372 (2006)
161. King, C., Walsh, E., Grimes, R.: Piv measurements of flow within plugs in a microchannel. Microfluidics and Nanofluidics 3, 463–472 (2007)
162. Sarrazin, F., Prat, L., Di Miceli, N., Cristobal, G., Link, D.R., Weitz, D.A.: Mixing characterization inside microdroplets engineered on a microcoalescer. Chemical Engineering Science 62, 1042–1048 (2007)
163. Rhee, M., Burns, M.A.: Drop mixing in a microchannel for lab-on-a-chip platforms. Langmuir 24, 590–601 (2008)
164. Sivasamy, J., Chim, Y.C., Wong, T.N., Nguyen, N.T., Yobas, L.: Reliable addition of reagents into microfluidic droplets. Microfluidics and Nanofluidics 8, 409–416 (2010)
165. Bringer, M.R., Gerdts, C.J., Song, H., Tice, J.D., Ismagilov, R.F.: Microfluidic systems for chemical kinetics that rely on chaotic mixing in droplets. Philosophical Transactions of the Royal Society of London Series a-Mathematical Physical and Engineering Sciences 362, 1087–1104 (2004)
166. Taha, T., Cui, Z.F.: Hydrodynamics of slug flow inside capillaries. Chemical Engineering Science 59, 1181–1190 (2004)
167. Kashid, M.N., Gerlach, I., Goetz, S., Franzke, J., Acker, J.F., Platte, F., Agar, D.W., Turek, S.: Internal circulation within the liquid slugs of a liquid-liquid slug-flow capillary microreactor. Industrial & Engineering Chemistry Research 44, 5003–5010 (2005)
168. Tanthapanichakoon, W., Aoki, N., Matsuyama, K., Mae, K.: Design of mixing in microfluidic liquid slugs based on a new dimensionless number for precise reaction and mixing operations. Chemical Engineering Science 61, 4220–4232 (2006)
169. Kinoshita, H., Kaneda, S., Fujii, T., Oshima, M.: Three-dimensional measurement and visualization of internal flow of a moving droplet using confocal micro-piv. Lab on a Chip 7, 338–346 (2007)

170. Galusinski, C., Vigneaux, P.: On stability condition for bifluid flows with surface tension: Application to microfluidics. Journal of Computational Physics 227, 6140–6164 (2008)
171. Stone, Z.B., Stone, H.A.: Imaging and quantifying mixing in a model droplet micromixer. Physics of Fluids 17, 063103 (2005)
172. Fries, D.A., Waelchli, S., Von Rohr, P.R.: Gas-liquid two-phase flow in meandering microchannels. Chemical Engineering Journal 135, S37–S45 (2008)
173. Fries, D.M., von Rohr, P.R.: Liquid mixing in gas-liquid two-phase flow by meandering microchannels. Chemical Engineering Science 64, 1326–1335 (2009)
174. Che, Z.Z., Wong, T.N., Nguyen, N.T.: An analytical model for a liquid plug moving in curved microchannels. International Journal of Heat and Mass Transfer 53, 1977–1985 (2010)
175. Tabeling, P.: A brief introduction to slippage, droplets and mixing in microfluidic systems. Lab on a Chip 9, 2428–2436 (2009)
176. Ottino, J.M., Wiggins, S.: Applied physics - designing optimal micromixers. Science 305, 485–486 (2004)
177. Ottino, J.M., Wiggins, S.: Introduction: Mixing in microfluidics. Philosophical Transactions of the Royal Society of London Series a-Mathematical Physical and Engineering Sciences 362, 923–935 (2004)
178. Wiggins, S., Ottino, J.M.: Foundations of chaotic mixing. Philosophical Transactions of the Royal Society of London Series a-Mathematical Physical and Engineering Sciences 362, 937–970 (2004)
179. Chris, R.: Polymer extrusion. Hanser Gardner Publication Inc., CA (2001)
180. Song, H., Ismagilov, R.F.: Millisecond kinetics on a microfluidic chip using nanoliters of reagents. Journal of the American Chemical Society 125, 14613–14619 (2003)
181. Khan, S.A., Gunther, A., Schmidt, M.A., Jensen, K.F.: Microfluidic synthesis of colloidal silica. Langmuir 20, 8604–8611 (2004)
182. Choi, S.: Enhancing thermal conductivity of fluids with nanoparticles. In: Proceedings of the 1995 ASME International Mechanical Engineering Congress and Exposition, San Francisco, USA (1995)
183. Das, S.K., Choi, S.U.S., Patel, H.E.: Heat transfer in nanofluids - a review. Heat Transfer Engineering 27, 3–19 (2006)
184. Trisaksri, V., Wongwises, S.: Critical review of heat transfer characteristics of nanofluids. Renewable & Sustainable Energy Reviews 11, 512–523 (2007)
185. Wei, X.H., Zhu, H.T., Wang, L.Q.: $CePO_4$ nanofluids: Synthesis and thermal conductivity. Journal of Thermophysics and Heat Transfer 23, 219–222 (2009)
186. Wen, D.S., Lin, G.P., Vafaei, S., Zhang, K.: Review of nanofluids for heat transfer applications. Particuology 7, 141–150 (2009)
187. Cashion, L.M., Bare, L.A., Harvey, S., Trinh, Q., Zhu, Y., Devlin, J.J.: Use of enhanced green fluorescent protein to optimize and quantitate infection of target cells with recombinant retroviruses. Biotechniques 26, 924 (1999)
188. Chen, D.H., Liao, M.H.: Preparation and characterization of yadh-bound magnetic nanoparticles. Journal of Molecular Catalysis B-Enzymatic 16, 283–291 (2002)
189. Lee, S., Choi, S.U.S., Li, S., Eastman, J.A.: Measuring thermal conductivity of fluids containing oxide nanoparticles. Journal of Heat Transfer-Transactions of the Asme 121, 280–289 (1999)
190. Xuan, Y.M., Li, Q.: Heat transfer enhancement of nanofluids. International Journal of Heat and Fluid Flow 21, 58–64 (2000)

191. Wang, X.Q., Mujumdar, A.S.: A review on nanofluids - part ii: Experiments and applications. Brazilian Journal of Chemical Engineering 25, 631–648 (2008)
192. Yatsuya, S., Hayashi, T., Akoh, H., Nakamura, E., Tasaki, A.: Magnetic-properties of extremely fine particles of iron prepared by vacuum evaporation on running oil substrate. Japanese Journal of Applied Physics 17, 355–359 (1978)
193. Yatsuya, S., Tsukasaki, Y., Yamauchi, K., Mihama, K.: Ultrafine particles produced by vacuum evaporation onto a running oil substrate (VEROS) and the modified method. Journal of Crystal Growth 70, 533–535 (1984)
194. Chang, H., Tsung, T.T., Chen, L.C., Yang, Y.C., Lin, H.M., Han, L.L., Lin, C.K.: Tio2 nanoparticle suspension preparation using ultrasonic vibration-assisted arc-submerged nanoparticle synthesis system (ASNSS). Materials Transactions 45, 806–811 (2004)
195. Lo, C.H., Tsung, T.T., Chen, L.C.: Shape-controlled synthesis of cu-based nanofluid using submerged arc nanoparticle synthesis system (SANSS). Journal of Crystal Growth 277, 636–642 (2005)
196. Lo, C.H., Tsung, T.T., Lin, H.M.: Preparation of silver nanofluid by the submerged arc nanoparticle synthesis system (SANSS). In: 12th International Symposium on Metastable and Nano-Materials (ISMANAM 2005), Paris, France (2005)
197. Zhu, H.T., Lin, Y.S., Yin, Y.S.: A novel one-step chemical method for preparation of copper nanofluids. Journal of Colloid and Interface Science 277, 100–103 (2004)
198. Liu, M.S., Lin, M.C.C., Tsai, C.Y., Wang, C.C.: Enhancement of thermal conductivity with cu for nanofluids using chemical reduction method. International Journal of Heat and Mass Transfer 49, 3028–3033 (2006)
199. Jackman, R.J., Floyd, T.M., Ghodssi, R., Schmidt, M.A., Jensen, K.F.: Microfluidic systems with on-line uv detection fabricated in photodefinable epoxy. Journal of Micromechanics and Microengineering 11, 263–269 (2001)
200. Edel, J.B., Fortt, R., de Mello, J.C., de Mello, A.J.: Microfluidic routes to the controlled production of nanoparticles. Chemical Communications, 1136–1137 (2002)
201. Chan, E.M., Mathies, R.A., Alivisatos, A.P.: Size-controlled growth of cdse nanocrystals in microfluidic reactors. Nano Letters 3, 199–201 (2003)
202. Krishnadasan, S., Tovilla, J., Vilar, R., de Mello, A.J., de Mello, J.C.: On-line analysis of cdse nanoparticle formation in a continuous flow chip-based microreactor. Journal of Materials Chemistry 14, 2655–2660 (2004)
203. Shalom, D., Wootton, R.C.R., Winkle, R.F., Cottam, B.F., Vilar, R., de Mello, A.J., Wilde, C.P.: Synthesis of thiol functionalized gold nanoparticles using a continuous flow microfluidic reactor. Materials Letters 61, 1146–1150 (2007)
204. Song, Y.J., Doomes, E.E., Prindle, J., Tittsworth, R., Hormes, J., Kumar, C.: Investigations into sulfobetaine-stabilized cu nanoparticle formation: Toward development of a microfluidic synthesis. Journal of Physical Chemistry B 109, 9330–9338 (2005)
205. Song, Y.J., Kumar, C., Hormes, J.: Synthesis of palladium nanoparticles using a continuous flow polymeric micro reactor. Journal of Nanoscience and Nanotechnology 4, 788–793 (2004)
206. Song, Y.J., Modrow, H., Henry, L.L., Saw, C.K., Doomes, E.E., Palshin, V., Hormes, J., Kumar, C.: Microfluidic synthesis of cobalt nanoparticles. Chemistry of Materials 18, 2817–2827 (2006)
207. Wagner, J., Kirner, T., Mayer, G., Albert, J., Kohler, J.M.: Generation of metal nanoparticles in a microchannel reactor. In: 7th International Conference on Microreaction Technology (IMRET 7), Lausanne, Switzerland (2003)

208. Wang, H.Z., Nakamura, H., Uehara, M., Miyazaki, M., Maeda, H.: Preparation of titania particles utilizing the insoluble phase interface in a microchannel reactor. Chemical Communications, 1462–1463 (2002)
209. Xue, Z.L., Terepka, A.D., Hong, Y.: Synthesis of silver nanoparticles in a continuous flow tubular microreactor. Nano Letters 4, 2227–2232 (2004)
210. Karnik, R., Gu, F., Basto, P., Cannizzaro, C., Dean, L., Kyei-Manu, W., Langer, R., Farokhzad, O.C.: Microfluidic platform for controlled synthesis of polymeric nanoparticles. Nano Letters 8, 2906–2912 (2008)
211. Laulicht, B., Cheifetz, P., Mathiowitz, E., Tripathi, A.: Evaluation of continuous flow nanosphere formation by controlled microfluidic transport. Langmuir 24, 9717–9726 (2008)
212. Jiang, F., Drese, K.S., Hardt, S., Kupper, M., Schonfeld, F.: Helical flows and chaotic mixing in curved micro channels. Aiche Journal 50, 2297–2305 (2004)
213. Yamaguchi, Y., Takagi, F., Watari, T., Yamashita, K., Nakamura, H., Shimizu, H., Maeda, H.: Interface configuration of the two layered laminar flow in a curved microchannel. Chemical Engineering Journal 101, 367–372 (2004)
214. Sudarsan, A.P., Ugaz, V.M.: Fluid mixing in planar spiral microchannels. Lab on a Chip 6, 74–82 (2006)
215. Sudarsan, A.P., Ugaz, V.M.: Multivortex micromixing. Proceedings of the National Academy of Sciences of the United States of America 103, 7228–7233 (2006)
216. Ahn, Y.C., Jung, W.G., Chen, Z.P.: Optical sectioning for microfluidics: Secondary flow and mixing in a meandering microchannel. Lab on a Chip 8, 125–133 (2008)
217. Toda, K., Furuse, H.: Extension of einstein's viscosity equation to that for concentrated dispersions of solutes and particles. Journal of Bioscience and Bioengineering 102, 524–528 (2006)
218. Ren, Z.Q., Han, Y.P., Hong, R.Y., Ding, H.M., Li, H.Z.: On the viscosity of magnetic fluid with low and moderate solid fraction. Particuology 6, 191–198 (2008)
219. Kumar, V., Aggarwal, M., Nigam, K.D.P.: Mixing in curved tubes. Chemical Engineering Science 61, 5742–5753 (2006)
220. LaMer, V.K., Dinegar, R.H.: Theory, production and mechanism of formation of monodispersed hydrosols. Journal of the American Chemical Society 72, 4847–4854 (1950)
221. Hosokawa, M., Nogi, K., Naito, M., Yokoyama, T.: Nanoparticle technology handbook. Elsevier, Amsterdam (2007)
222. Einstein, A.: Investigations on the theory of the brownian movement. Dover Publications Inc., New York (1956)
223. Jiang, W., Wang, L.Q.: Copper nanofluids: Synthesis and thermal conductivity. Current Nanoscience 6, 512–519 (2010)

Multi-scale Modelling of Liquid Suspensions of Micron Particles in the Presence of Nanoparticles

Chane-Yuan Yang and Yulong Ding*

Abstract. A combined continuous, discrete, and statistic mechanics (CCDS) method is proposed to model micron particle dynamics in the presence of nanoparticles – a highly asymmetric system. The CCDS method treats the liquid medium as a continuum and the micron particles as a discrete phase, whereas the statistics mechanics method is used to treat the nanoparticles. The treatment of the nanoparticles involves the use of the Ornstein-Zernike equation with Percus-Yevick approximation based on the hard-sphere interaction. Such an approach enables the effective coupling between different length scales. Sedimentation of micron particles in the presence of nanoparticles is used as a case study for the CCDS method. It is shown that, at a high salt concentration where electrostatic repulsive force is significantly screened, the structural force induced by both monodisperse and bidisperse nanoparticles could overcome the van der Waals attractive force between the micron particles and thus prevent particle flocculation. It is also shown that the introduction of disparity in the system complicates the effective interactions between the micron particles and consequently the particle dynamics.

Keywords: Multi-scale modelling; Micron particles, Nanoparticles; Structural interaction; Stabilisation of colloidal suspensions; CCDS method.

1 Introduction

Liquid suspensions of colloid particles are relevant to numerous industrial applications including surface coatings, personal care, healthcare, homecare, energy, food and drink, and pigment. One of the key aspects for such suspensions

Chane-Yuan Yang · Yulong Ding
Institute of Particle Science and Engineering, University of Leeds,
Leeds LS2 9JT, UK
e-mail: Y.Ding@leeds.ac.uk

* Corresponding author.

L.Q. Wang (Ed.): Advances in Transport Phenomena, ADVTRANS 2, pp. 295–331.
springerlink.com

is their physical stability, particularly when the particles have a density very different from the liquid medium. Such density difference can lead to creaming if the particles are lighter than the liquid medium or sedimentation if the particles are heavier. Apart from particle density, the creaming or sedimentation behaviour is affected by many other factors such as size, shape, concentration and solution chemistry. If particles are very small, interparticle forces such as van der Waals (attraction) and electrostatic (repulsion) forces may affect the suspension behaviour. For example, the attractive van der Waals force may cause particles to aggregate and hence to accelerate the suspension destabilisation (Russel et al., 1991; Larson, 1999). As a consequence, stabilization of colloidal suspensions has long been the centre of concern for both industrial and academic communities.

Conventionally, suspension stability is achieved through either or both of steric and electrostatic stabilisations (Hunter, 2001). The strategy of the steric stabilisation involves grafting a layer of polymers onto the surface of the particles, resulting in repulsive brushes that prevent the colloidal particles from contacting. The charge stabilisation method makes use of the repulsive interaction between particles carrying like surface charges due to the overlapping of the electric double layer of microscopic co-ions and counter-ions. The combination of the van der Waals attraction and the electrostatic double layer repulsion gives the well-known DLVO theory (Derjaguin and Landau 1941, Verwey and Overbeek 1948). Over the past decade, another mechanism for stabilising micron particle suspensions has been proposed, which makes use of structural interactions due to the presence of small nonadsorbed species including macromolecules, micelles, and nanoparticles. Such a stabilisation mechanism is interpreted by the so-called 'haloing' structure of nanoparticles around micro particle surfaces. The 'haloing' effect is hypothesised to generate the Coulombic interactions between the small particles, leading to a repulsive barrier preventing the microparticles from approaching each other (Tohver et al. 2001a & 2001b).

This work aims to investigate numerically the structural stabilisation of dilute liquid suspensions of micron particles in the presence of nanoparticles. Two of the biggest challenges for doing this are (i) the system contains multi-components with relevant length scales differing by many orders of magnitudes, and (ii) the number of discrete components particularly those with smaller sizes is astronomical. Such challenges imply that the use of direct numerical simulation method is prohibitively expensive even with today's computing power. The challenges could be tackled by the concept of coarse-graining, whereby the degrees of freedom of the microscopic species are traced out. In this way, suspensions of micron colloids can be viewed as a system of Brownian colloidal particles, which interact with each other through an effective interaction potential and interact with the host liquid (Ermak, 1975). Numerically, the modelling can be achieved by using the so-called combined continuous and discrete approaches (Tsuji et al., 1992; Xu and Yu, 1997; Zeidan et al., 2007; Yang et al., 2008). In such a combined scheme, the dynamics of particles is treated individually using

Newton's second law of motion, which is more commonly known as the Distinct Element Method (DEM) originated by Cundall and Strack (1979), whereas the flow field of the liquid medium is treated as a continuum using the computational fluid dynamics (CFD) method. Numerous studies have been reported in the literature on modelling suspensions with asymmetric time and length scales. However, most of these studies are limited to binary systems with small size ratios; see for example Boublik (1970), Fries and Hansen (1983), Malijevsky et al. (1997), Dickman et al. (1997) and Yau et al. (1997) for a size ratio smaller than 10, and Malherbe and Amokrane (1999) and Largo and Wilding (2006) for size rations up to 20. There are a few reports on systems with an asymmetrical ratio up to 100; see Liu and Luijten, (2004a, 2004b, 2005a, 2005b & 2006), and Martinez et al. (2005). However, these authors used a variant of the geometric cluster algorithm for the simulation. Such a method was originally introduced by Dress and Krauth (1995), which facilitates the rejection-free simulations of highly size-asymmetric mixtures via large-scale collective updates that move whole group of particles, rather than individual particles, in a single step.

This work uses the combined continuous, discrete and statistic mechanics (CCDS) method to deal with large size disparities in liquid suspensions (Yang 2008). In such a method, nanoparticles in a colloidal mixture are taken as a microscopic species similar to ions in suspensions. This implies that the multi-component mixtures of micron particles and nanoparticles are mapped onto an effective one-component system, in which the degrees of freedom of the small constituents including liquid molecules, ions and nanoparticles are integrated out. The CCDS treats the solvent as the continuous phase and the microparticles as the discrete phase, whereas the nanoparticles are treated by using the statistics mechanics approach involving the use of the Ornstein-Zernike equation with Percus-Yevick approximation (Yang, 2008). Such a method enables the effective coupling between different length scales. The paper is organised in the following manner. In Section2, CCDS model formulation and numerical solution to the model are presented. The results of the numerical simulations are discussed in Section 3 using a case study to how the model reveals the effect of the presence of nanoparticles on the dynamics of microparticle suspensions. Section 4 summaries the conclusion.

2 CCDS Model Formulation and Numerical Solutions

The CCDS model involves the treatments of microparticles, nanoparticles and the base liquid. Section 2.1 presents the model of microparticle dynamics, the dynamics of the fluid phase is dealt with in Section 2.2, and the detailed methodology for the treatment of nanoparticles is given in Section 2.3. Finally, numerical method for solving the CCDS model is briefly descried in Section 2.4, where the conditions for the case studies are also given.

2.1 Dynamics of Micron Particles – Discrete Method

Consider a liquid suspension containing spherical micron particles, the dynamics of the micron particles is governed by the Newton's second law of motion:

$$m_i \frac{d\mathbf{u}_{p,i}}{dt} = \mathbf{F}_{G,i} + \mathbf{F}_{D,i} + \mathbf{F}_{Br,i} + \mathbf{F}_{vdw,i} + \mathbf{F}_{edlr,i} + \mathbf{F}_{str,i} + \sum_{j=1}^{k_i} (\mathrm{f}_{c,ij} + \mathrm{f}_{d,ij}) \tag{1}$$

where m_i is the mass of the i^{th} particle, $\mathbf{u}_{p,i}$ is the velocity vector of the i^{th} particle, t is the time, $\mathbf{F}$s are various forces acting on the particle to be detailed in the following, $\sum_{j=1}^{k_i} (\mathrm{f}_{c,ij} + \mathrm{f}_{d,ij})$ is the summation of the contact forces ($\mathbf{f}_{c,ij}$) and viscous contact damping forces ($\mathbf{f}_{d,ij}$) acting on the i^{th} particle in both normal and tangential directions by other particles, and k_i is the number of particles in contact with the i^{th} particle. The contact forces can be modelled by using the spring and dash pot models; see Cundall and Strack (1979) and Xu and Yu (1997) for details.

$\mathbf{F}_{vdw,i}$ in Equation (1) is the total of the van der Waals force acting on i^{th} particle by all the other particles. For two spherical particles with radius a separated by a centre-to-centre distance r, the van der Waals force takes the following form (Russel et al., 1991):

$$F_{vdw}(r) = -\frac{A_{PMP}}{6}\left[-\frac{2a^2 \cdot 2r}{\left(r^2-4a^2\right)^2} - \frac{2a^2}{r^3} + \frac{8a^2}{\left(r^2-4a^2\right)r}\right] \tag{2}$$

where A_{pmp} is the Hamaker constant for the two particles in the liquid medium. According to the Lifshitz theory, A_{pmp} is positive for two identical particles so the van der Waals force is always attractive (Israelachvili 1997). $\mathbf{F}_{vdw,i}$ can be obtained by considering all pair interactions as given by Equation (2) in the vector's form. $\mathbf{F}_{edlr,i}$ in Equation (1) represents the total of the electrostatic force acting on i^{th} particle due to overlapping of the electrical double layer of the particles. For any pair of particles the electrostatic force is given by the following Debye-Huckel equation (Hunter 2001):

$$F_{edlr}(h) = \frac{4\pi}{\varepsilon\varepsilon_0}\left(\frac{\sigma_1 a_1^2}{1+\kappa a_1}\right)\left(\frac{\sigma_2 a_2^2}{1+\kappa a_2}\right)\cdot\frac{[\kappa r+1]\cdot\exp(-\kappa h)}{r^2} \tag{3}$$

where σ_i is the surface charge density, $\varepsilon\varepsilon_0$ is the dielectric permittivity of the bulk liquid, r is the interparticle surface separation, κ is the inverse of the Debye screening length given by:

$$\kappa^{-1} = \left(\frac{2z^2 e^2 n_0}{\varepsilon_0 \varepsilon k_B T} \right)^{-1/2} \tag{4}$$

where z is the ionic valence, n_0 is the number density of ions in the bulk solution, e is the electronic charge, k_B is the Boltzmann constant, and T the absolute temperature. Like $\mathbf{F}_{vdw,i}$, $\mathbf{F}_{edlr,\,i}$ can be obtained by considering all pair interactions as given by Equation (3). $\mathbf{F}_{G,i}$ in Equation (1) represents the combination of the gravitational and buoyancy forces acting on the i^{th} particle given by:

$$\mathbf{F}_{G,i} = \frac{4}{3}\pi a_i^3 \left(\rho_p - \rho_f\right)\mathbf{g} \tag{5}$$

where ρ_p and ρ_f are the densities of the i^{th} particle and the fluid, respectively, and **g** the gravitational acceleration. $\mathbf{F}_{Br,i}$ in Equation (1) represents the stochastic force giving rise to the Brownian motion, which satisfies:

$$\left\langle \mathbf{F}_{\mathrm{Br}} \right\rangle = 0 \text{ and } \left\langle \mathbf{F}_{Br}(0)\mathbf{F}_{Br}(t) \right\rangle = 2k_B T \left(6\pi\mu_f a_i\right)\mathbf{I}\delta(t) \tag{6}$$

where the brackets, $\langle\ \rangle$, represent the time average, μ_f is the effective suspension viscosity, and **I** and δ(t) are respectively the dyadic unit tensor and delta function. $\mathbf{F}_{D,i}$ in Equation (1) is the hydrodynamic drag force from the fluid, which can be calculated by:

$$\mathbf{F}_{D,i} = 6\pi\mu_f a_i \left(\mathbf{u}_f - \mathbf{u}_{p,i}\right) \tag{7}$$

where $\mathbf{u}_f$ is the local fluid velocity vector and a_i is the micron particle. Equation (7) is the so-called Stokes law which is applicable for cases with relatively a small liquid-particle slip velocity, and can be easily extended to more complicated cases. $\mathbf{F}_{str,i}$ in Equation (1) is the structural force induced by the nanoparticles and will be detailed in Section 2.3.

Note that Equation (1) contains two main assumptions: (a) all the forces considered are additive to give the total force, and (b) the van der Waals, electrostatic and structural forces can be obtained by summation of pair interactions. The validity of these assumptions needs further investigation but is expected to apply for dilute suspensions of micron particles.

Among the forces detailed above, the non-contact forces, e.g. the gravitational and fluid drag forces, act on the mass centre of the particle *i*, while the contact forces act at the contact point between particles *i* and *j*. This inter-particle contact forces will generate a torque, $\mathbf{T}_{ij}$, causing particle *i* to rotate. For a spherical particle, $\mathbf{T}_{ij}$ can be given by:

$$\mathbf{T}_{ij} = \mathbf{R}_{\mathrm{i}} \times \left(\mathbf{f}_{c,ij} + \mathbf{f}_{d,ij} \right) \tag{8}$$

where $\mathbf{R}_{\mathrm{i}}$ is a vector running from the centre of the particle i to the contact point. The equation governing the rotational motion of the particle i is:

$$I_i \frac{d\boldsymbol{\omega}_i}{dt} = \sum_{j=1}^{k_i} \mathbf{T}_{ij} \tag{9}$$

where $\boldsymbol{\omega}_i$ is the angular velocity, and I_i is the moment of inertia of particle i, given as $I_i = \frac{2}{5} m_i a_i^2$ for a spherical particle.

2.2 Fluid Dynamics – Continuum Based Method

As detailed in Section 2.1, solving the equations governing particle motion requires the information of the fluid dynamics. This is obtained by solving the continuity equation and the locally averaged Navier-Stokes equation (Anderson and Jackson, 1967):

$$\frac{\partial \varepsilon_p}{\partial t} + \nabla \cdot \left(\varepsilon_p \mathbf{u}_f \right) = 0 \tag{10}$$

and

$$\frac{\partial \left(\rho_f \varepsilon_p \mathbf{u}_f \right)}{\partial t} + \nabla \cdot \left(\rho_f \varepsilon_p \mathbf{u}_f \mathbf{u}_f \right) = -\varepsilon_p \nabla p - \mathbf{F}_{pf} + \nabla \cdot \left(\varepsilon_p \boldsymbol{\Gamma} \right) + \rho_f \varepsilon_p \mathbf{g} \tag{11}$$

where ε_p, p, $\mathbf{F}_{pf}$ and $\boldsymbol{\Gamma}$ are respectively porosity, fluid phase pressure, fluid-particle interaction force and viscous stress tensor, and ρ_f is the fluid density. The porosity ε_p in a computational cell is defined as the ratio of the void volume to the cell volume:

$$\varepsilon_p = 1 - \frac{\sum_{i=1}^{n_i} V_{P,i}}{\Delta V} \tag{12}$$

where ΔV is the volume of a local computational cell, $V_{p,i}$ the volume of particle i and n_i the number of particles in ΔV. The fluid-particle interaction force can be obtained by using the Newton's third law of motion over a fluid cell:

$$\mathbf{F}_{pf} = \frac{\sum_{i=1}^{n_i} \mathbf{F}_{D,i}}{\Delta V} \tag{13}$$

where $\mathbf{F}_{D,i}$ is the hydrodynamic drag force acting on particle *i* and has been discussed in Section 2.1. Equation (13) acts as a linkage between the discrete phase of micron particles and the continuous fluid phase. The viscous stress tensor in Equation (11) is given by (Bird et al., 1960):

$$\mathbf{\Gamma} = \left[(\mu_f' - \frac{2}{3}\mu_f)\nabla \cdot \mathbf{u}_f \right] \boldsymbol{\delta}_K + \mu_f \left[\left(\nabla \mathbf{u}_f\right) + \left(\nabla \mathbf{u}_f\right)^{-1} \right] \tag{14}$$

where $\boldsymbol{\delta}_k$ is the Kronecker delta, and μ_f' is the bulk viscosity. Equation (14) contains two suspension viscosities, μ_f' and μ_f . For liquids under normal conditions, they can be regarded as incompressible and hence the bulk viscosity is zero. The shear viscosity, μ_f , usually increases with increasing particle concentration and the following polynomial expression is often used to describe the dependence of the shear viscosity on particle volume fraction:

$$\mu_f = \mu_0 \left(1 + k_1\phi_p + k_2\phi_p^2 + k_3\phi_p^3 + ...\right) \tag{15}$$

where μ_0 is the viscosity of the base liquid, k_1, k_2, k_3, … are constants and ϕ_p is particle volume fraction in the suspension. Equation (15) is truncated to different orders for different suspensions. For example, for very dilute suspensions containing non-interacting particles, a first order approximation is sufficient, and for suspensions containing interacting particles, higher order approximation is needed; see for example Batchelor (1972), Larson (1999), Cheng and Law (2003) and Ding and Wen (2005) for more discussion. In this work, the following expression proposed by Cheng and Law (2003) will be used:

$$\mu_f = \mu_0 \left(1 + \frac{5}{2}\phi_p + \frac{35}{8}\phi_p^2 + \frac{105}{16}\phi_p^3 \right) \tag{16}$$

Clearly, Equation (16) can be easily replaced by other appropriate expression such as the famous empirical expression proposed by Krieger and Dougherty (1959), which can also account for the effect of particle aggregation (Chen et al., 2007).

2.3 Nanoparticle-Induced Structural Interaction – Statistic Mechanics Method

Apart from the fluid hydrodynamic information, solving the dynamics of micron particles also requires information of the structural interaction between micron particles due to the presence nanoparticles (Section 2.1). This is discussed in this section. Assuming that only pair interactions occur in the suspensions, then, within the framework of statistical mechanics, the Boltzmann equation provides an exact expression relating the pair radial distribution function, *g(r)*, to the potential of mean force between a pair of micron particles immersed in a fluid (Hanson and McDonald, 1989):

$$w(r) = -k_B T \cdot ln[g(r)] \tag{17}$$

where $w(r)$ is the potential of the mean force, k_B is the Boltzmann constant and T is the absolute temperature. The radial distribution function, $g(r)$, measures the probability that, given a particle at the origin, another particle in the system can be found at a distance of r from it. Differentiation of Equation (17) gives the interaction mean force between two micron particles:

$$F(r) = -\nabla w(r) = k_B T \cdot \nabla g(r) \tag{18}$$

To obtain the functional form of $g(r)$ on the distance between two particles, r, a seemingly universal route is by solving the Orstein-Zernike (OZ) integral equation (IE), which reads:

$$g_{ij}(r) - 1 = c_{ij}(r) + \sum_k \rho_k \int dr' [g_{ik}(r') - 1] \cdot c_{kj}(|\mathbf{r} - \mathbf{r}'|) \tag{19}$$

where $c_{ij}(r)$ is the direction correlation function between species i and j, ρ_k the number density of particle species k, and r the centre-to-centre distance between the particles. Equation (19) shows that solution to the OZ equation requires a mathematical closure and there are many of them (Hansen and McDonald, 1989). Among the mathematical closures, the most popular one is the so-called Percus-Yevick (PY) approximation (Percus and Yevick, 1958):

$$c(r) = \{1 - \exp[v(r)/k_B T]\} g(r) \tag{20}$$

where $v(r)$ is the pair interaction potential and the simplest model for $v(r)$ is the hard-sphere (HS) interaction model for which the particles interact only through infinite repulsion at contact. The HS model for particles of diameter d is expressed by:

$$v(r) = \begin{cases} \infty, & r < d \\ 0, & r > d \end{cases} \tag{21}$$

Numerous efforts have been devoted to the solution of OZ/PY equations by using the above HS model. Henderson and Locada-Cassou (1986) obtained an analytical expression of the Laplace Transformation (LT) of $g(r)$ by using an algorithm developed by Perram (1975) in a single-component i.e., monodispersed, hard-sphere fluid, which is able to account for the oscillatory profiles in both the depletion potential and the force. Subsequently, Henderson (1988) obtained the LT of the interaction energy and force from Lebowitz's expression (1964) for the LTs of the radial distribution function for a one-component hard-sphere mixture. More recently, Henderson et al (2004a), extending the approach for one-component hard-sphere liquid to a two-component hard-sphere fluid and propose a more generalized approximation of the correlation function for a pair of

macrospheres immersed in a background fluid. In the limit of extremely large size of colloids compared with fluid particles, the expression reads:

$$L[g(r)] = s\frac{3\left(\phi_2 e^{sd_1} + \phi_1 e^{sd_2}\right) - \left(\frac{3}{2}\delta_2 s^2 - 3\delta_1 s + 3\delta_0\right)e^{s(d_1+d_2)}}{D(s)}d \tag{22}$$

where s is the Laplace variable, $\phi_i = \frac{\pi}{6}\rho_i$ with $\rho_i = N_i / V$ being the number density of species i, N_i is the number of hard spheres of species i, $\delta_n = \sum_{i=1}^{m}\phi_i d_i^n$ with n=0, 1, 2, 3, m is the number of species and d_i is the diameter of species i. D(s) in Equation (22) is:

$$D(s) = h' - L_1(s)e^{sd_2} - L_2(s)e^{sd_1} + S(s)e^{s(d_1+d_2)} \tag{23}$$

where

$$L_1(s) = 12\phi_1\left[1 + \frac{1}{2}\delta_3 + \frac{3}{2}\phi_2 d_2^2(d_1 - d_2)\right]d_1 s^2 + \left[12\phi_1(1 + 2\delta_3) - h'd_2\right]s + h' \tag{24}$$

$$L_2(s) = 12\phi_2\left[1 + \frac{1}{2}\delta_3 + \frac{3}{2}\phi_1 d_1^2(d_2 - d_1)\right]d_2 s^2 + \left[12\phi_2(1 + 2\delta_3) - h'd_1\right]s + h' \tag{25}$$

$$S(s) = h' + \left[12\delta_0(1 + 2\delta_3) - h'(d_1 + d_2)\right]s - 18\delta_2^2 s^2 - 6\delta_2(1 - \delta_3)s^3 - (1 - \delta_3)^2 s^4 \tag{26}$$

with

$$h' = 36\phi_1\phi_2(d_1 - d_2)^2 \tag{27}$$

From the above, one can see that an analytical radial distribution function of the Laplace transformation is obtained. The use of Laplace transformation has two important advantages. First, the Laplace transform of the force is easily obtained from the LT of the energy, eliminating the difficulty in the subsequent numerical differentiation. Second, the analytic results are obtained in Laplace space and the results in real space can be obtained by simple integration, thus avoiding the time consuming iterations (Henderson et al., 2004a).

After obtaining the Laplace transform, the *g(r)* in the real space can be obtained via the inverse Laplace transform of the Equation (22). Three methods could be used for the inverse transformation. The first is the so-called zonal method (Henderson, 1988), which works for monodisperse systems or for binary systems with small size ratios. If the size ratio is large, then the procedure is very cumbersome as a large number of zones are needed. The second method is the linear integral method, which is highly time-consuming. The third method is through Fourier transformation (Henderson et al., 2004a). The third method has been found to be convenient and will be used in this work. This method involves inserting $s = \pm ik$ into the LT of *g(r)* to obtain the following expression:

$$\tilde{g}(k) = \int_0^\infty g(x) \cdot \sin kx dx = \frac{1}{2i}\left(L[g(r)]_{s=-ik} - L[g(r)]_{s=ik}\right) \tag{28}$$

where i is the imaginary number and k the Fourier transform variable. Integration of Equation (28) gives the radial distribution function:

$$g(x) = \frac{2}{\pi}\int_0^\infty \tilde{g}(k) \cdot \sin kx dx \tag{29}$$

Equation (29) requires a numerical integration. Once $g(x)$ is obtained, Equation (18) can be solved for the interaction force. To avoid difficulties in the direct differentiation of the radial distribution function, this work takes the real space derivative of the radial distribution function through numerical inverse Fourier transformation (Henderson et al., 2004a).

Note that the above treatment follows the methodology proposed by Henderson et al. (2004a), which contains an assumption of very large size ratios and hence is specifically suitable for the systems considered in this work – the effect of the presence of nanoparticles on the stability of micro particles. Note also that the stabilisation of micron particles using nanoparticles is a dynamic process as the nanoparticles can move between bulk phase and confined regions (between micron particles) rapidly due to small sizes of nanoparticles and large nano-to-micro particle size ratios. As a consequence, it would be reasonable to assume that distribution of nanoparticles around the surfaces of the microparticles reach their thermodynamic equilibrium with the bulk solution quickly and is within the time step that is suitable for dynamics of microparticles.

Coming back to the real space derivative for obtaining the interaction force as mentioned above, the real space expression of Fourier transform can be given as (Henderson et al., 2004a):

$$\tilde{g}_s(k) = -k\frac{a(k)c(k) + b(k)d(k)}{c^2(k) + d^2(k)}d \tag{30}$$

where

$$\begin{aligned} a(k) = {} & 3\phi_1 \cos kd_2 + 3\phi_2 \cos kd_1 - \\ & 3\delta_1 k \cdot \sin k(d_1 + d_2) - 3\left[\delta_0 - \frac{1}{2}\delta_2 k^2\right] \cdot \cos k(d_1 + d_2) \end{aligned} \tag{31}$$

$$\begin{aligned} b(k) = {} & -3\phi_1 \sin kd_2 - 3\phi_2 \sin kd_1 - \\ & 3\delta_1 k \cdot \sin k(d_1 + d_2) + 3\left[\delta_0 - \frac{1}{2}\delta_2 k^2\right] \cdot \sin k(d_1 + d_2) \end{aligned} \tag{32}$$

$$
\begin{aligned}
c(k) = h' - &\left\{h' - 12\phi_1 \cdot \left[\left(1+\frac{1}{2}\delta_3\right) + \frac{3}{2}\phi_2 d_2^2 (d_1 - d_2)\right] d_1 k^2\right\} \cdot \cos kd_2 - \\
&\left\{h' - 12\phi_2 \cdot \left[\left(1+\frac{1}{2}\delta_3\right) + \frac{3}{2}\phi_1 d_1^2 (d_2 - d_1)\right] d_2 k^2\right\} \cdot \cos kd_1 + \\
&k\left[12\phi_1(1+2\delta_3) - h' d_2\right] \cdot \sin kd_2 + k\left[12\phi_2(1+2\delta_3) - h' d_1\right] \cdot \sin kd_1 + \\
&\left[h' + 18\delta_2^2 k^2 - (1-\delta_3)^2 k^4\right] \cdot \cos k(d_1 + d_2) - \\
&\left\{\left[12\delta_0(1+2\delta_3) - h'(d_1 + d_2)\right]k + 6\delta_2(1-\delta_3)k^3\right\} \cdot \sin k(d_1 + d_2)
\end{aligned}
\tag{33}
$$

$$
\begin{aligned}
d(k) = &\left\{h' - 12\phi_1 \cdot \left[\left(1+\frac{1}{2}\delta_3\right) + \frac{3}{2}\phi_2 d_2^2 (d_1 - d_2)\right] d_1 k^2\right\} \cdot \sin kd_2 + \\
&\left\{h' - 12\phi_2 \cdot \left[\left(1+\frac{1}{2}\delta_3\right) + \frac{3}{2}\phi_1 d_1^2 (d_2 - d_1)\right] d_2 k^2\right\} \cdot \sin kd_1 + \\
&k\left[12\phi_1(1+2\delta_3) - h' d_2\right] \cdot \cos kd_2 + k\left[12\phi_2(1+2\delta_3) - h' d_1\right] \cdot \cos kd_1 - \\
&\left[h' + 18\delta_2^2 k^2 - (1-\delta_3)^2 k^4\right] \cdot \sin k(d_1 + d_2) - \\
&\left\{\left[12\delta_0(1+2\delta_3) - h'(d_1 + d_2)\right]k + 6\delta_2(1-\delta_3)k^3\right\} \cdot \cos k(d_1 + d_2)
\end{aligned}
\tag{34}
$$

The parameters in the above equations have all been defined before. By analogy and using the relationship between the Laplace transforms and the Fourier transform of *g(r)* in the form of Equation (29), the Fourier transform of the interaction force or the real space Fourier transform of the derivative, $\partial g(x)/\partial x$, is:

$$
\tilde{g}_s'(k) = k^2 \frac{a(k)dd(k) - b(k)c(k)}{c^2(k) + d^2(k)} d \tag{35}
$$

As the Fourier transforms of *g(x)* and $\partial g(x)/\partial x$ are not monotonic functions and they converge very slowly to zero, a direct inverse transform requires a large number of integration points. To resolve this issue, Henderson et al. (2004a) proposed the following difference functions:

$$
\delta\tilde{g}_s(k) = \tilde{g}_s(k) - g(d)\frac{k}{\lambda^2 + k^2} \tag{36}
$$

and

$$
\delta\tilde{g}_s'(k) = \tilde{g}_s'(k) - g'(d)\frac{k}{\lambda^2 + k^2} \tag{37}
$$

where *g(d)* is the so-called contact value given as:

$$g(d) = \lim_{s\to\infty} s \cdot L[g(r)] = \frac{3}{2}\frac{\delta_2}{(1-\delta_3)^2} d \tag{38}$$

and the corresponding derivative is:

$$g'(d) = -\beta \frac{\partial w(r)}{\partial r} = -\frac{3\delta_1(1-\delta_3)+9\delta_2}{(1-\delta_3)^2} d \tag{39}$$

The advantage of using the difference functions, Equations (38) and (39), is that they go to zero more rapidly, and is therefore more efficient than direct inverse Fourier transform. Since the expressions of *g(r)* and its derivative are obtained, the real space functions of the radial distribution and its derivative can be calculated respectively as follows:

$$g(x) = \delta g(x) + g(d) e^{-\lambda x} \tag{40}$$

$$\frac{\partial g(x)}{\partial x} = \delta g'(x) + g'(d) e^{-\lambda x} \tag{41}$$

where $\delta g(x)$ and $\delta g'(x)$ are respectively the results of the inverse Fourier transforms of $\delta \tilde{g}_s(k)$ and $\delta \tilde{g}'_s(k)$ using Equations (29).

From above, the radial distribution function, *g(r)*, and its derivative, *g'(r)*, are obtained, which, upon inserting into the Boltzmann equation (Equation 17), gives the interaction potential and hence the effective interaction force by using Equation (18). The interaction force induced by nanoparticle can be directly employed in the discrete particle simulation for dynamics of microparticles; see Section 2.2.

2.4 Numerical Solution to the CCDS Model

An in-house code has been developed for the CCDS method. The code was written in FORTRAN environment and run in Dell dual core workstations. In the following, a brief account is given on the discretisation of the governing equations, the methodology for solving the discretised equations, the initial and boundary conditions, and the convergence criteria.

2.4.1 Discretisation and Solution to the Governing Equations

The finite difference method is used in this work to discretise the governing equations. Using such a method, the continuous derivatives in the partial differential equations are replaced by a truncated Taylor series expansion to an order appropriate to the problem (Fletcher, 1991). This gives a system of algebraic

equations, which is the conservative form of the discretised equations. For performing the discretisation, the simulation domain is discretised first to give the so-called control volumes (also called computational cells). In this work, the concept of finite volume is employed to generate the control volumes. These treatments imply that the original continuous variables throughout the simulation domain are now defined at the discrete positions located at the centre or the surface of the control volumes.

There are two approaches to construct the computational cells. One is the non-staggered grid method, which involves building the grids first and then constructing the cells by positioning their faces at the middle between neighbouring grids. In this method, all the flow variables such as velocities, pressure and volume fractions are stored at the same grid points, which, despite being successfully applied to incompressible single-phase flows (Armfield and Debler, 1993), fails to converge when applied to multi-phase flow problems (Xu, 1997). This work uses the second approach - the staggered grid method. Such a method was first employed by Harlow and Welch (1956) (with a name of Marker and Cell – MAC method), and then adopted by Patankar (1980) in the well-known SIMPLE (Semi-Implicitly Modified Pressure Equations) algorithm. The staggered grid method involves building the cell boundaries first and then placing a grid point at the geometric centre of each cell so that different variables are evaluated at different grid points.

Discretisation of the governing equations using the method briefly discussed above will lead to a system of coupled algebraic equations. These equations were solved by using the SIMPLE method first developed by Patankar and Spalding (1972) and elaborated by Patankar (1980).

2.4.2 Initial and Boundary Conditions

The computational domain employed in the case study is a rectangular box of size $0.02\times0.02\times0.04$ m^3 with the side wall surfaces in parallel to the gravitational direction. Both the micron particles and the fluid phase are taken as stationary at time zero. At the wall surfaces (boundaries), the no-slip condition is specified for the velocity components. For the voidage and pressure, a zero gradient in the normal direction applies along all the boundaries. Note that, for specifying the boundary conditions, the computational domain is surrounded by a layer of dummy cells. These dummy cells are virtual ones although there are also geometrical quantities like volume or face vector associated with them. The purpose of the use of dummy cells is to simplify the computation of fluxes, gradients and dissipation, etc. along the boundaries.

2.4.3 Convergence Criterion

As mentioned above, discretisation of the governing equations gives the algebraic equations, which have to be solved using the iteration approach. The convergence criterion is therefore defined as following Patankar (1980):

$$\sum_{\text{Cells}} \left| bb_{i,j,k} \right| \le e' \tag{42}$$

where $bb_{i,j,k}$ is the mass residual for individual cells and the summation is over all the cells. e' is the tolerance of the mass residual, which is set as 1.56×10^{-8}.

3 Results and Discussion

The case study in this work considers two identical micron particles with 2.85μm diameter. The micron particles are spherical and have a density of 1400 ke/m^3. They are submerged in an aqueous electrolyte solution containing nanoparticles; see Figure 1 for a schematic diagram. The colloidal mixture is placed within the 3-dimensional rectangular box. Both monodisperse nanoparticles with a diameter of 26nm and bidisperse nanoparticles with diameters of 26nm and 50nm are considered. For the bidispersed case, the 26nm particles is denoted as nanoparticle 1 ($d_{np,1} = 26\text{nm}$) and the 50nm particles as nanoparticle 2 ($d_{np,2} = 50\text{nm}$). To investigate the stabilising / destabilising effect induced by the nanoparticles, the micron particles are initially set to separate at specific surface-to-surface distance, which are scaled by the physical diameter of nanoparticles 1. A typical simulation lasts about 7-10 days. The results of the simulations are presented in the following subsections.

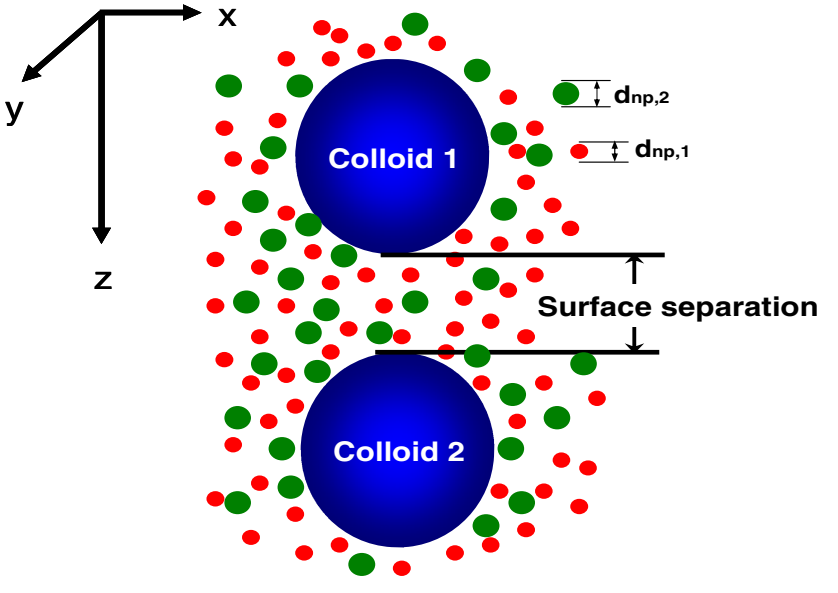

Fig. 1 A schematic representation of the simulation system: diameters of nanoparticle are $d_{np,1}$=26 nm and $d_{np,2}$=50nm. The initial surface separations between the two colloidal micron particles are scaled by $d_{np,1}$.

3.1 Monodisperse Nanoparticles

3.1.1 Force Profiles between Micron Particles

Figure 2 shows the force profiles between two micron particles for various volume fractions of monodisperse nanoparticles with 26nm diameter. For comparison, the DLVO interaction forces are also shown in the figure for two mono-valence salt concentrations of 0.02M (DLVO-1) and 0.002M (DLVO-2). One can see that the presence of nanoparticles leads to the oscillatory dependence of the interaction force on the separation between the micron particles and the magnitude of the peaks/troughs depends on both the separation between the micron particles and the nanoparticle concentration. A smaller separation between the micron particles gives a higher peak / deeper trough, whereas a higher nanoparticle concentration gives a higher peak / deeper trough. The presence of nanoparticles is also seen to affect the effective range of interaction between the micron particles. For example, the interaction force between the micron particles (also called the structural/depletion force) at a nanoparticle volume fraction of 20% is larger than that of the DLVO forces at the higher salt concentration of 0.02 M. Figure 2 also shows that the profile of mean force becomes more oscillatory at higher nanoparticle concentrations. The peaks in the force profiles represent repulsive energy barriers, whereas the troughs denote the attractive depletion energy wells. The results shown in Figure 2 suggest that the magnitude of the repulsive barrier be higher enough to overcome the van der Waals attractive interaction, and thus help stabilisation of micron particle suspensions. In the meantime, at high nanoparticle concentrations, the preceding attractive energy well could also be deeper enough to favour flocculation of micron particles.

3.1.2 Dynamics of Micron Particles in the Presence of Nanoparticles

As discussed above, the structural interaction force between micron colloidal particles due to the presence of nanoparticles depends on both nanoparticle concentration and surface separation between the micron particles. Simulations were therefore performed to investigate the effects of initial separations between the micron particles and nanoparticle concentration on the micron particle dynamics. Such an exercise may provide a mean to assess colloidal stability as destabilisation of micron particle suspensions often happens when colloids approach one another due to the attractive interaction between them, leading to flocculation of and hence acceleration of sedimentation (if micron particles are heavier than the suspending medium). The results of the simulations are presented in Figures 3-10, where Figures 3, 5, 7 and 9 show respectively the time evolution of the surface separation between the micron particles at an initial separation of 1, 2, 3, and 5 times the nanoparticle diameter, and Figures 4, 6, 8 and 10 illustrate the corresponding sedimentation velocities of the micron particles as a function of time. These results are discussed in the following.

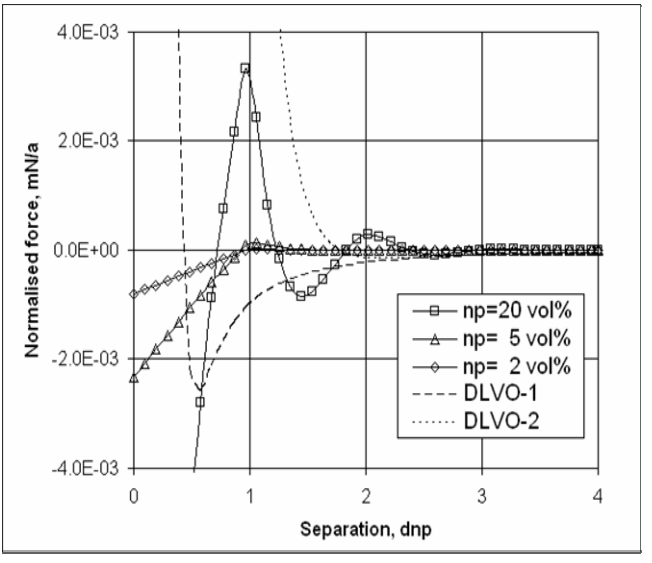

2(a)

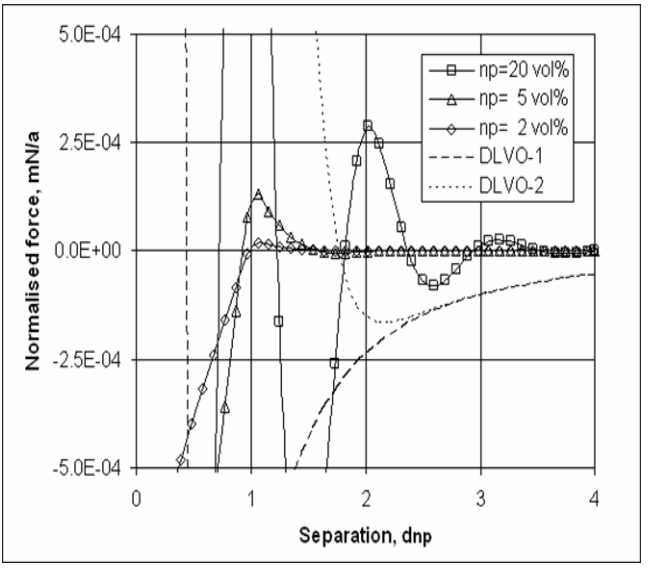

2(b)

Fig. 2 Effective interaction force between two microparticles (a) and enlargement of part of force profiles to show the magnitudes of the structural forces (b). The surface separation between micron particles is scaled by the diameter of nanoparticle 1. DLVO-1 and DLVO-2 represent respectively the DLVO interaction force at a mono-valance salt concentration of 0.02M and 0.002 M.

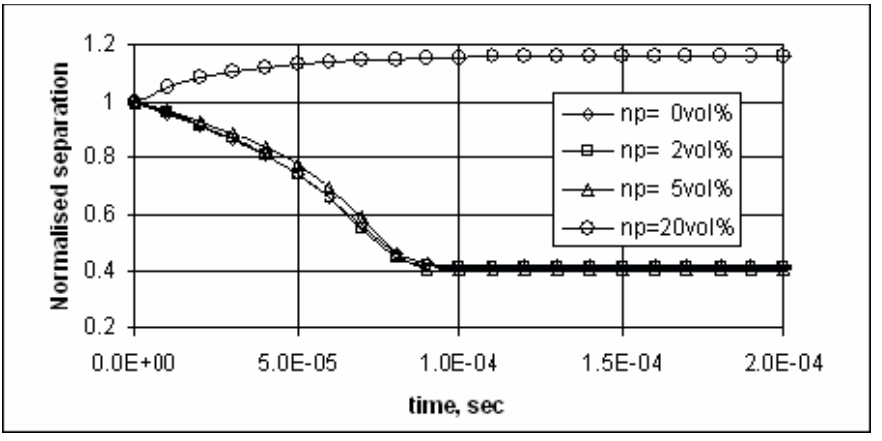

3(a)

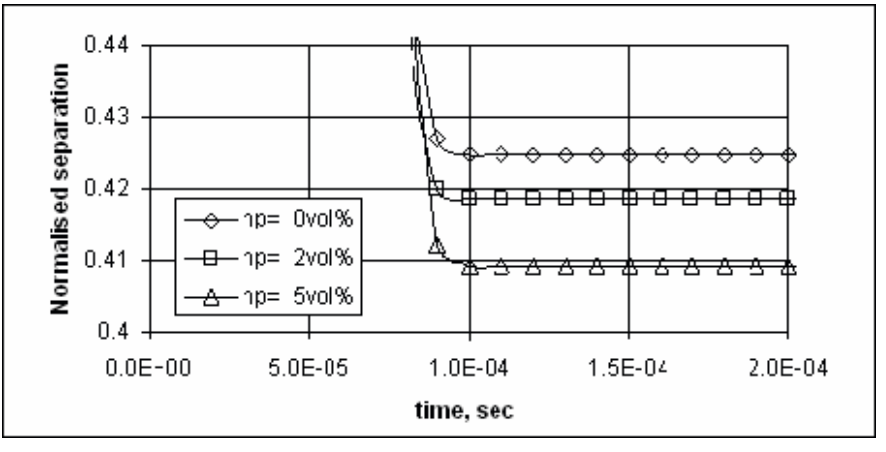

3(b)

Fig. 3 Interparticle surface separation as a function time for an initial normalised separation of 1 in the presence of different concentrations of monodisperse nanoparticles (a) and enlarged view of the profiles for nanoparticle concentrations of 0, 2, and 5% by volume

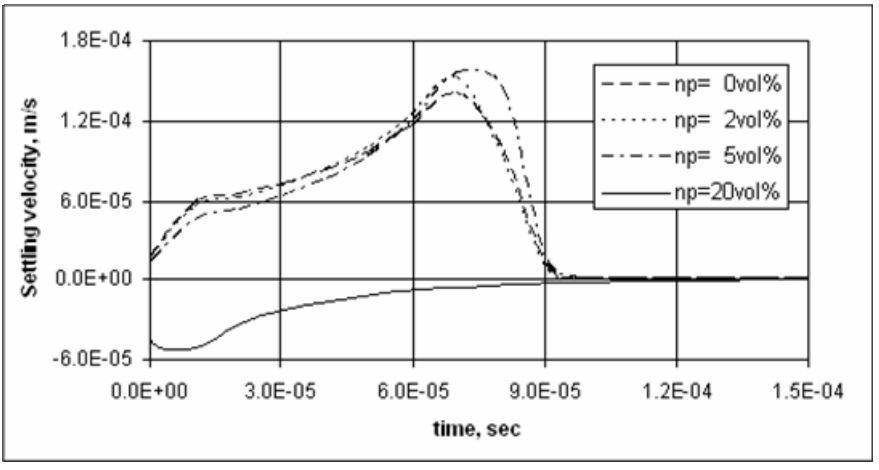

4(a)

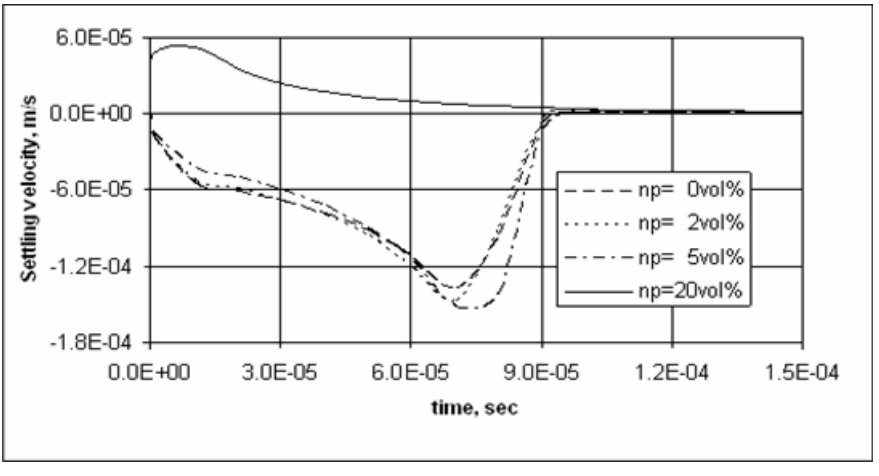

4(b)

Fig. 4 Time evolution of sedimentation velocity of micron particles at various nanoparticle concentrations for micron particle 1 (a) and micron particle 2 (b). The initial normalised micron particle separation is 1.

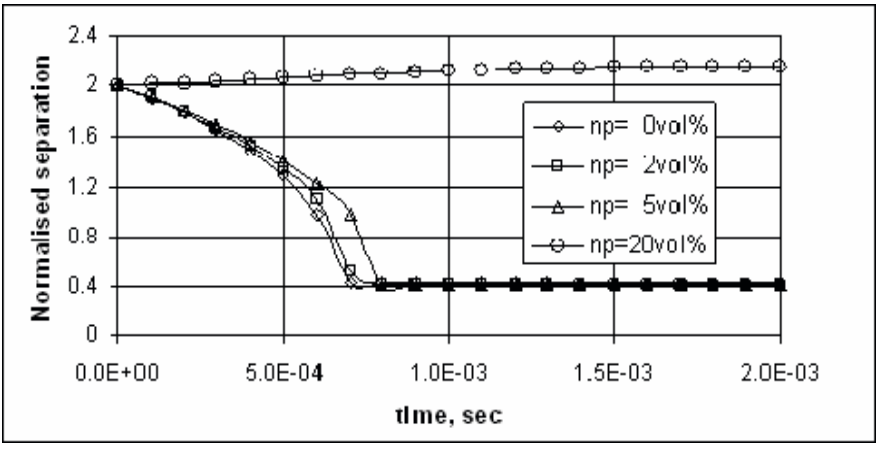

5(a)

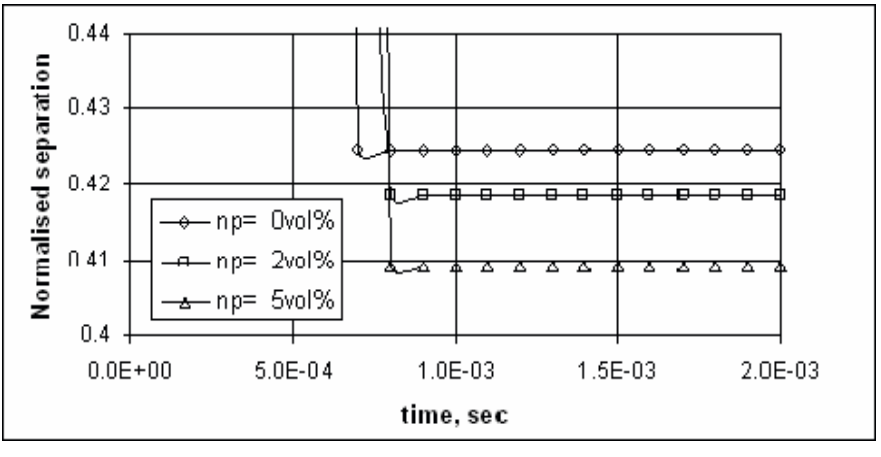

5(b)

Fig. 5 Interparticle surface separation as a function time for an initial normalised separation of 2 in the presence of different concentrations of monodisperse nanoparticles (a) and enlarged view of the profiles for nanoparticle concentrations of 0, 2, and 5% by volume

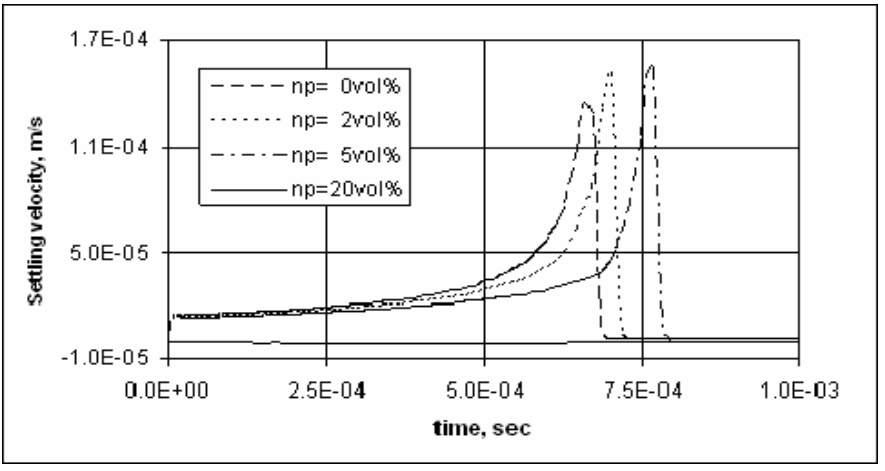

6(a)

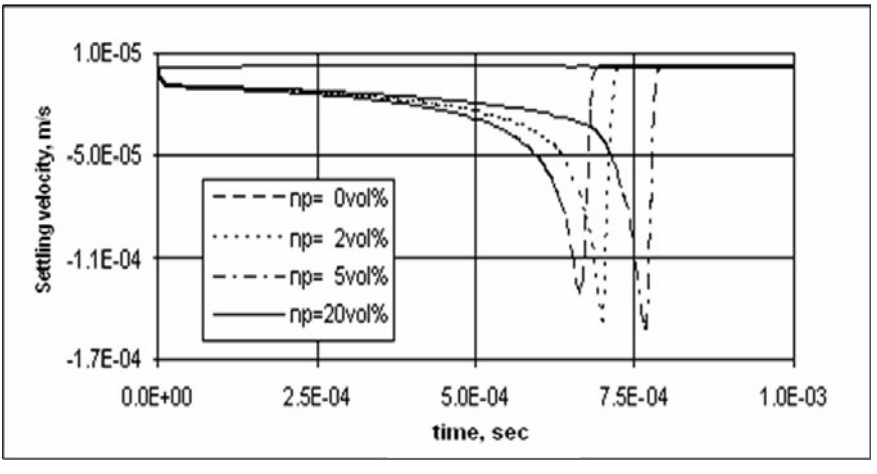

6(b)

Fig. 6 Time evolution of sedimentation velocity of micron particles at various nanoparticle concentrations for micron particle 1 (a) and micron particle 2 (b). The initial normalised micron particle separation is 2.

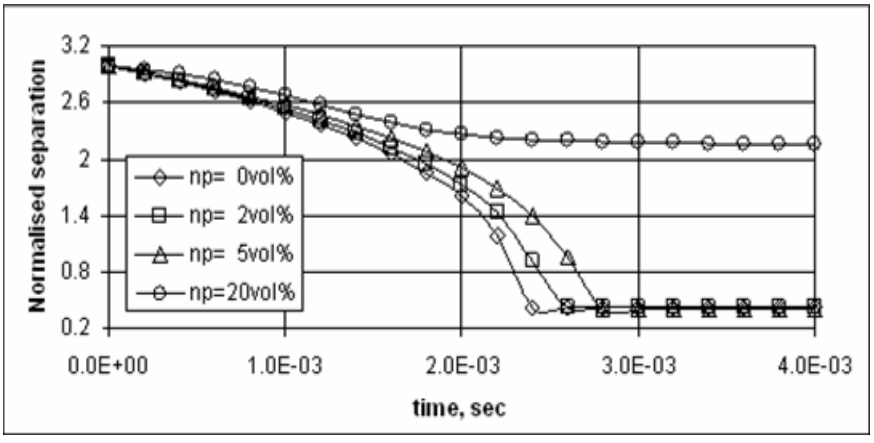

7(a)

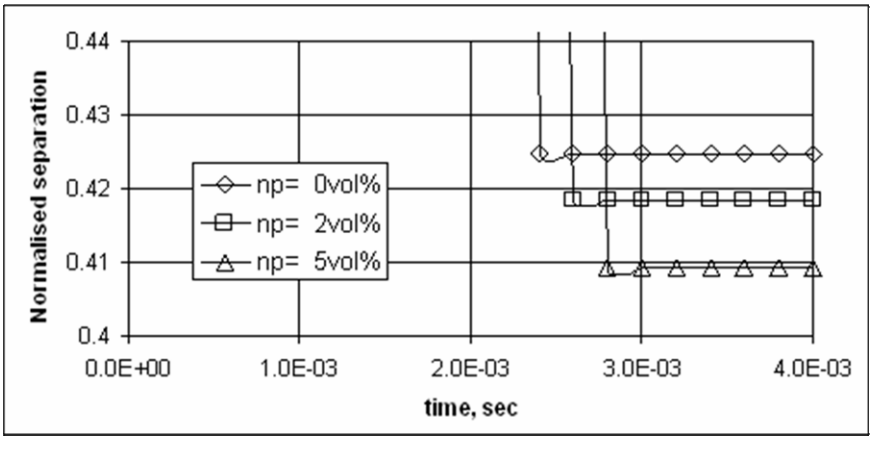

7(b)

Fig. 7 Interparticle surface separation as a function time for an initial normalised separation of 3 in the presence of different concentrations of monodisperse nanoparticles (a) and enlarged view of the profiles for nanoparticle concentrations of 0, 2, and 5% by volume (b).

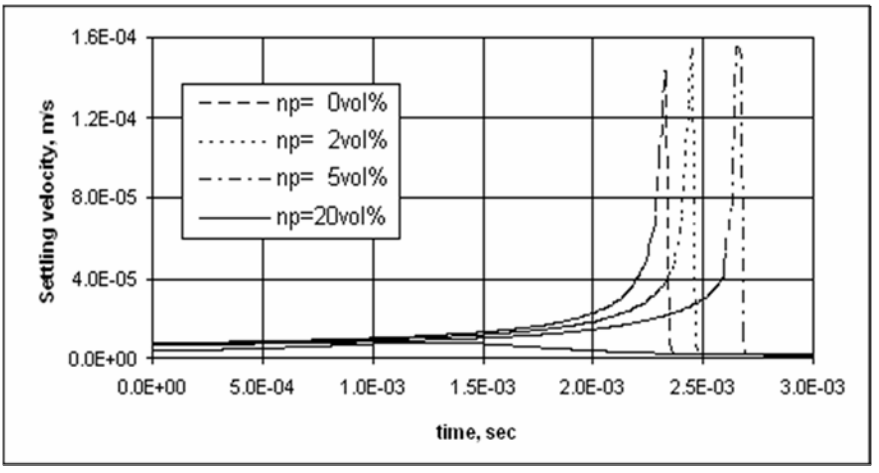

8(a)

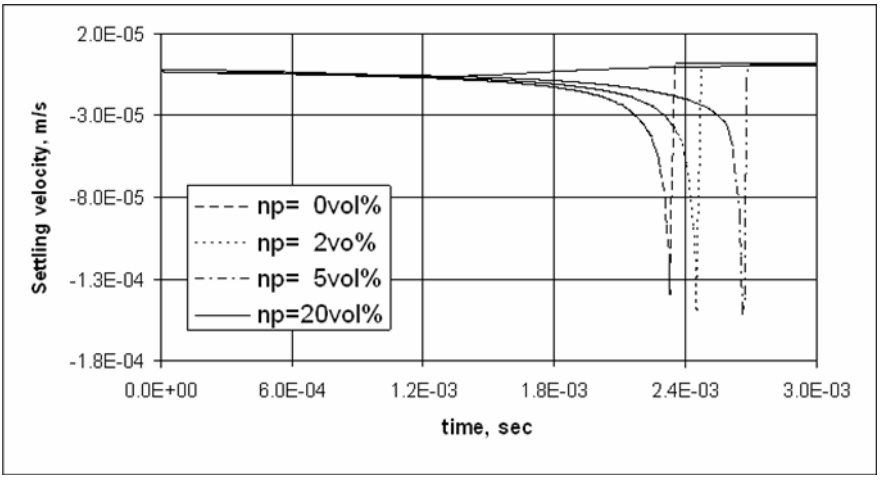

8(b)

Fig. 8 Time evolution of sedimentation velocity of micron particles at various nanoparticle concentrations for micron particle 1 (a) and micron particle 2 (b). The initial normalised micron particle separation is 3.

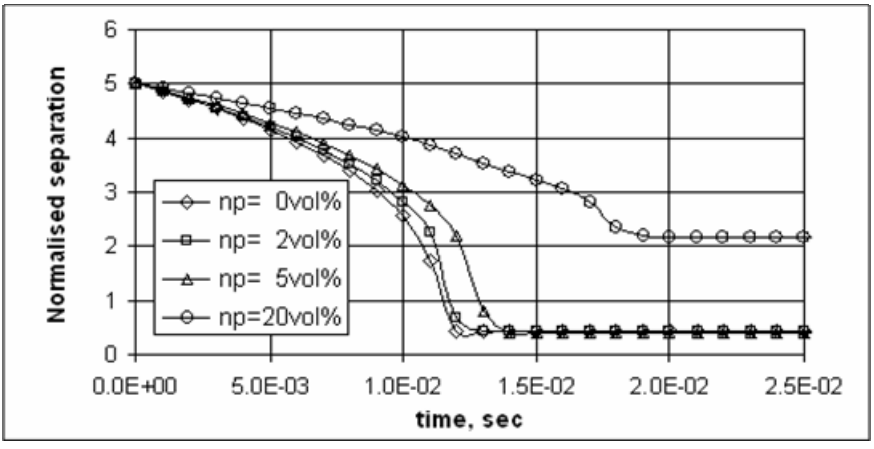

9(a)

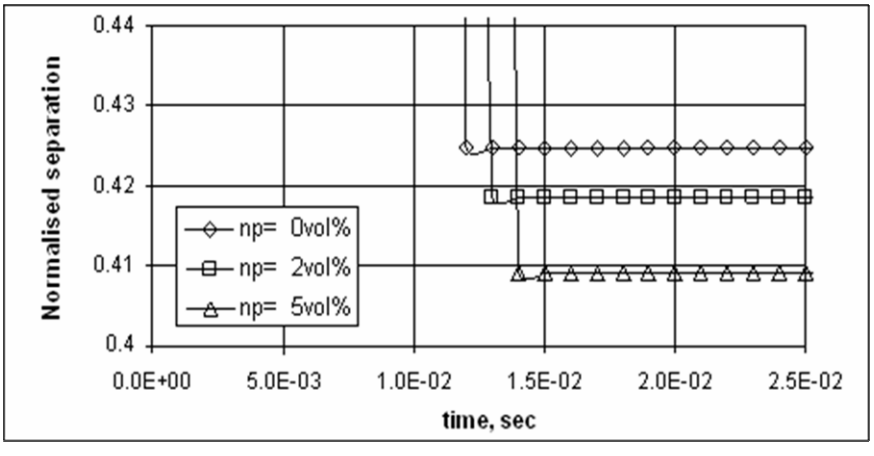

9(b)

Fig. 9 Interparticle surface separation as a function time for an initial normalised separation of 5 in the presence of different concentrations of monodisperse nanoparticles (a) and enlarged view of the profiles for nanoparticle concentrations of 0, 2, and 5% by volume (b).

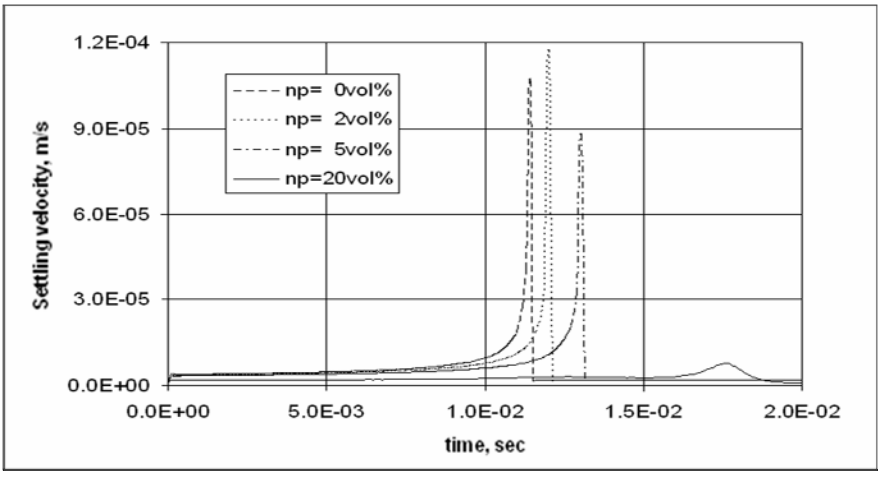

10(a)

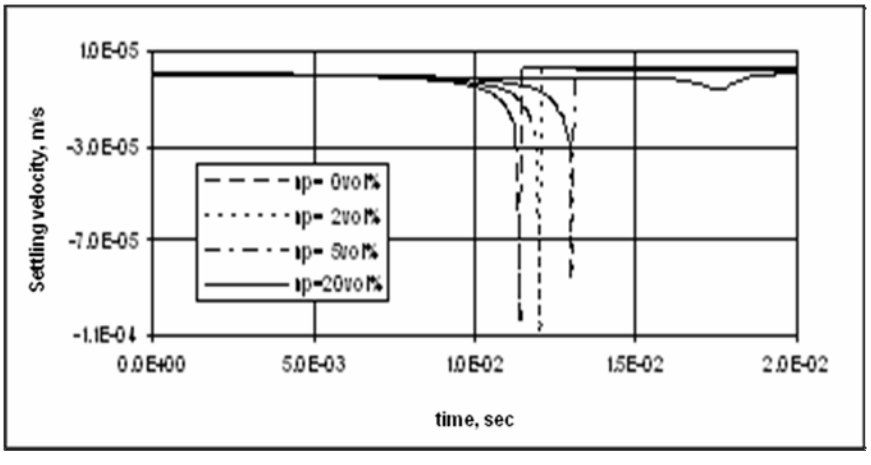

10(b)

Fig. 10 Time evolution of sedimentation velocity of micron particles at various nanoparticle concentrations for micron particle 1 (a) and micron particle 2 (b). The initial normalised micron particle separation is 5.

Look at the time evolution of the interparticle separation of the micron particles first (Figures 3, 5, 7 and 9). For all the initial surface separations considered in this work, only the presence of 20% nanoparticles could give a sufficient level of structural force to overcome the van der Waals attraction, and hence to prevent the micron particles from approaching each other (the final separation between micron particles is larger than that initial separation). At lower nanoparticle concentrations, i.e. 0, 2 and 5%, the structural forces are insufficient to counteract the inherent van der Waals attraction between micron particles, and hence the final equilibrium separation between the micron particles is smaller than the initial values. An inspection of Figures 3, 5, 7 and 9 shows that the interparticle distances decrease rapidly with time at low nanoparticle concentrations. This agrees with the force profile shown in Figure 2, where significant repulsive forces appear at a normalised separation distances being integers. Once the interparticle distance is away from these positions, the structural potential could be attractive – the so-called depletion potential (Asakura and Oosawa, 1954 & 1958). Such a depletion attraction combines with the inherent van der Waals attractive interaction, leading to the rapid approaching of micron particles. This implies that, under certain conditions, the addition of nanoparticles is not only able to stabilise micron particle suspensions, but also to cause destabilisation.

The sedimentation velocities of the micron particles are shown in Figures 4, 6, 8 and 10 as a function of time. In these figures, the negative values represent the upward velocity due to the coordinate system designed in the simulation (Figure 1). From the velocity profiles, one can examine the sedimentation behaviour of the micron particles in the presence of nanoparticles. Take Figure 4 as an example, at low nanoparticle concentrations of 0, 2, and 5%, the velocity of particle 1 is positive for about 90 ms (meaning a downward motion, while the velocity of particle 2 is negative during the initial ~90 ms (implying an upward movement). This implies the two particles approach each other over the initial period of ~ 90 ms at these low nanoparticle concentrations. After ~90 ms, velocities of the micron particles approach zero, implying a very slow settling process. At the high nanoparticle concentration of 20 vol%, on the other hand, the velocity of particle 1 is negative and velocity of particle 2 is positive in the initial 90 ms. This implies that particle 1 moves upward as a result of structural force effect and particle 2 settles due to a combined effect of gravitational action and the structural repulsion and the high nanoparticle concentration has a stabilisation effect on the micron particles, i.e. preventing them to approach each other. Similar analyses can be made on Figures 6, 8 and 10.

3.2 Bidisperse Nanoparticles

Although monodisperse nanoparticle suspensions can be excellent model systems for the theoretical studies, binary nanoparticle mixtures are more realistic models since, in practice, nanoparticles are not monodisperse. It has been observed both experimentally (Bindal et al, 2002) and theoretically (Henderson et al, 2003;

2004b) that, when the size disparity of fine particles is introduced, the effective structural interaction is deteriorated. As a consequence, the effect of size disparity of nanoparticles is investigated by using 26 and 50 nm nanoparticles. In this set of simulations, the volume fraction of 50 nm nanoparticle are taken as 5, 10 or 15% by volume and the corresponding concentration of the 26 nm nanoparticles are 15, 10 or 5%. The overall nanoparticle concentration is therefore maintained at 20%.

3.2.1 Force Profiles between Micron Particles

Figure 11 shows the interaction force between the micron particles in the presence of bidispersed nanoparticles, where V1 and V2 denote concentrations of nanoparticle 1 (26nm) and 2 (50nm), respectively. For comparison, the DLVO forces at two salt concentrations of 0.02 M and 0.002 M and the interaction force induced by monodisperse nanoparticles at 20% (V2=0) are also shown in the figure. One can see that the magnitude of the structural/depletion forces induced by nanoparticles decreases with increasing concentration of 50 nm nanoparticles at a surface separation of one diameter of nanoparticle 1 ($d_{np,1}$ = 26nm). When the concentration of the nanoparticle 2 is comparable to that of nanoparticle 1, a second repulsive barrier occurs at a surface separation of one diameter of nanoparticle 2 ($d_{np,2}$ = 50 nm), while the main peak at the surface separation of $d_{np,1}$ decreases. In addition, with an increase in the concentration of nanoparticle 2, an extra potential barrier occurring at surface separation of $2d_{np,1}$, which corresponds to approximately the diameter of nanoparticle 2. The force profiles of the micron particles in the presence of bidisperse nanoparticles are much more complicated than that of the monodisperse nanoparticles, which also provide more opportunities (and challenges) for engineering micron particle suspensions.

3.2.2 Dynamics of Micron Particles in Bidisperse Suspensions of Nanoparticles

The sedimentation behaviour of microparticles in the presence of binary nanoparticle suspensions are illustrated in Figures 12-15, where Figures 12 and 14 show respectively the time evolution of the surface separation between the micron particles at an initial separation of 1 and 3 times the diameter of nanoparticle 1, and Figures 13 and 15 are the corresponding sedimentation velocities of the micron particles as a function of time. These results are discussed in the following.

From Figure 12, one can see that the surface separation between the micron particles increases with time at concentrations of nanoparticle 2 (V2) of 0, 5 and 10% and an initial normalised separation of micron particles of 1, indicating the presence of the nanoparticles gives a stabilising effect on the micron particles. However, the surface separation of the micron particles decreases with time at V2=15%, indicating an effect of destabilisation. This agrees with the force profiles as shown in Figure 11. At an initial micron particle surface separation of 26 nm and V2=15%, the structural potential is mainly induced by the 26nm nanoparticles, which, at a volume concentration of 5%, is smaller than the van der Waals attraction.

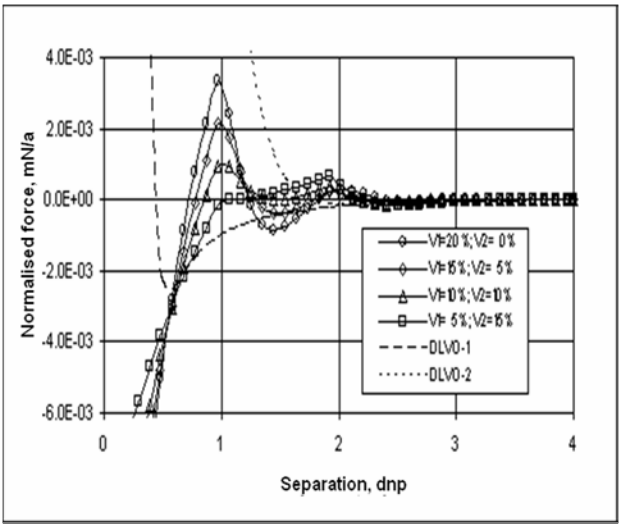

11(a)

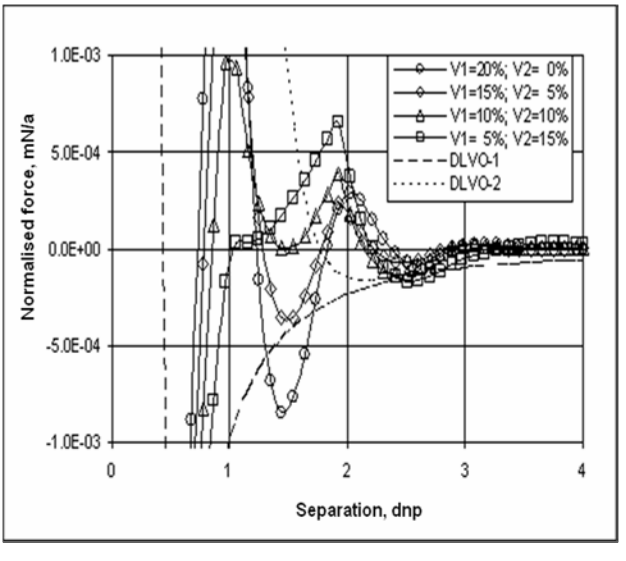

11(b)

Fig. 11 Interaction force induced by the presence of bidisperse nanoparticles (a) and enlarged view of the force profiles (b). V1 denotes the volume fraction of nanoparticle 1 (26nm); V2 denotes the volume fraction of nanoparticle 2 (50nm). DLVO-1 represents DLVO force at a salt concentration of 0.02M. DLVO-2 represents DLVO force at a salt concentration of 0.002M.

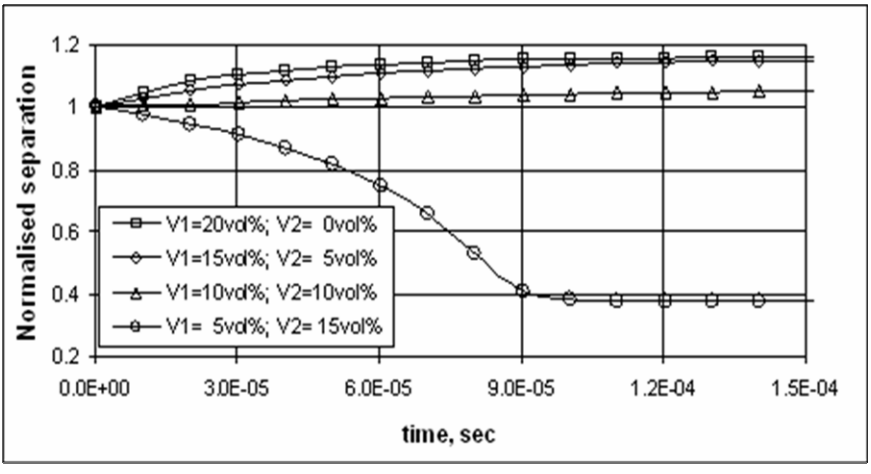

12(a)

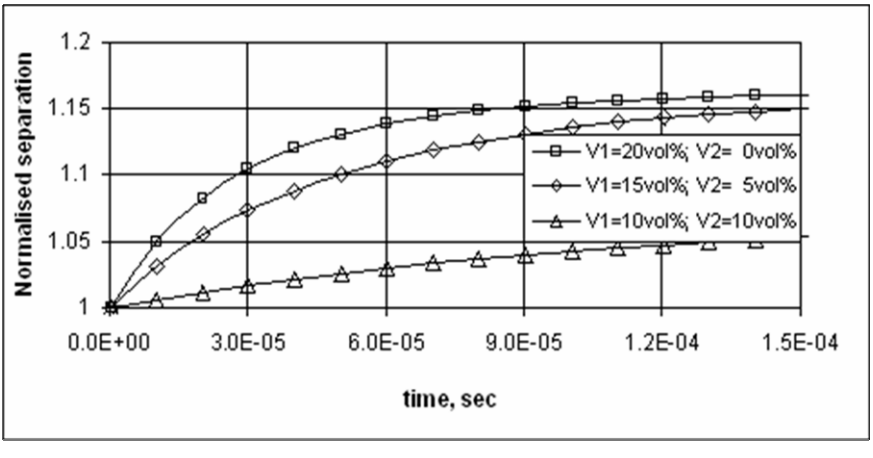

12(b)

Fig. 12 Interparticle surface separation as function of time for an initial normalised separation of 1 in binary nanoparticle suspensions (a) and enlarged view of the profiles (b).

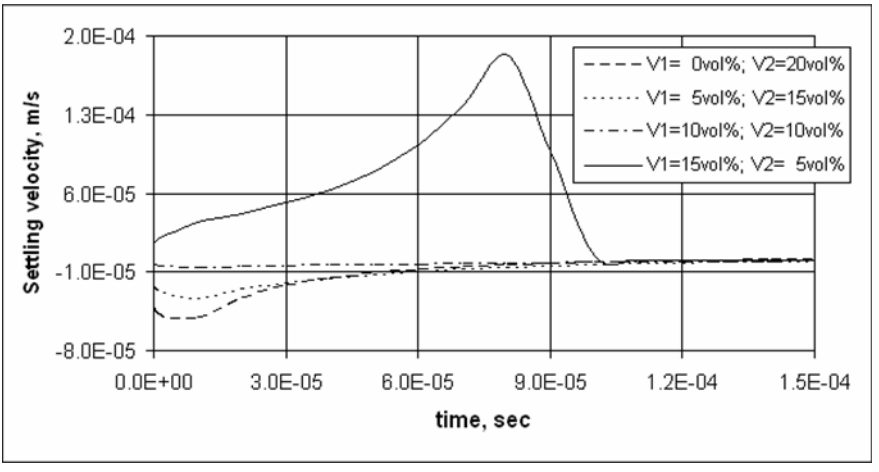

13(a)

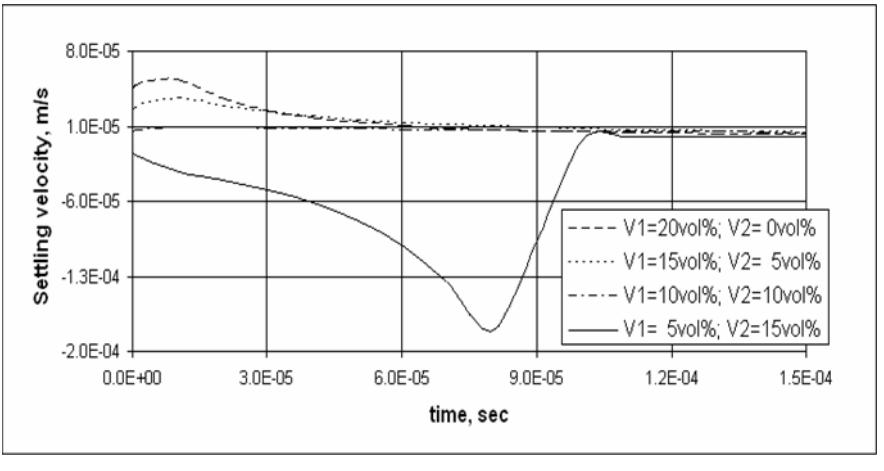

13(b)

Fig. 13 Time evolution of the sedimentation velocity of the micron particles at various combinations of binary nanoparticle concentration for an initial normalised separation of 1: (a) micron particle 1; (b) micron particle 2.

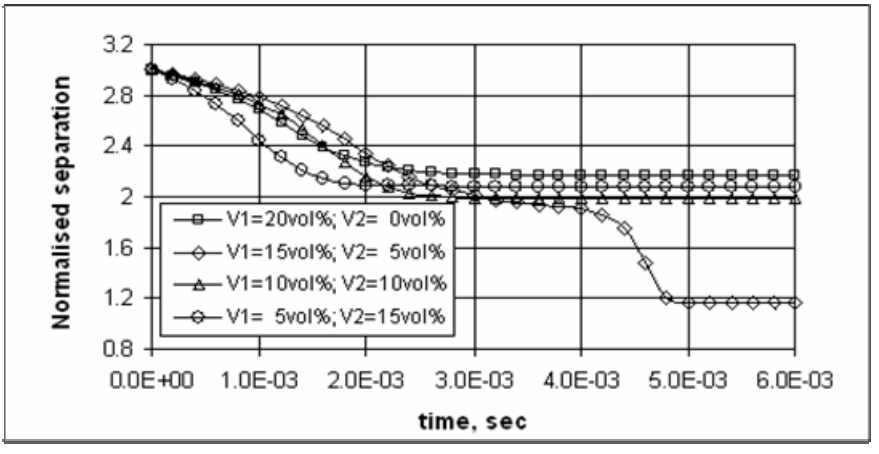

14(a)

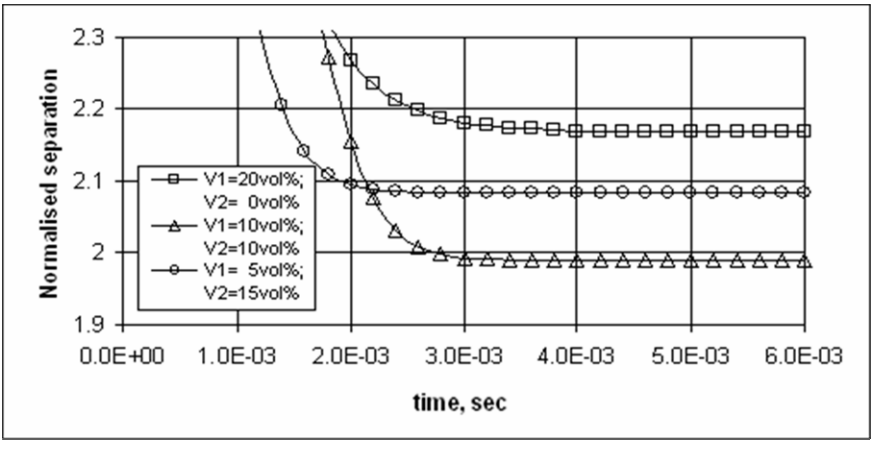

14(b)

Fig. 14 Interparticle surface separation as function of time for an initial normalised separation of 3 in binary nanoparticle suspensions (a) and enlarged view of the profiles (b).

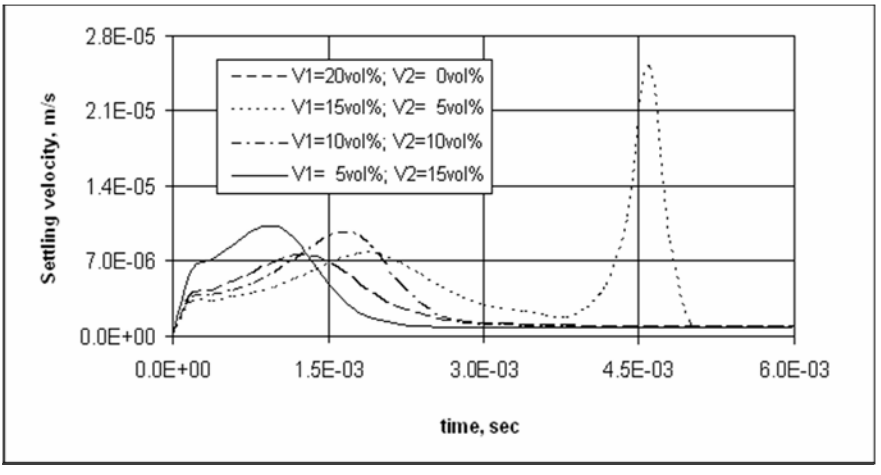

15(a)

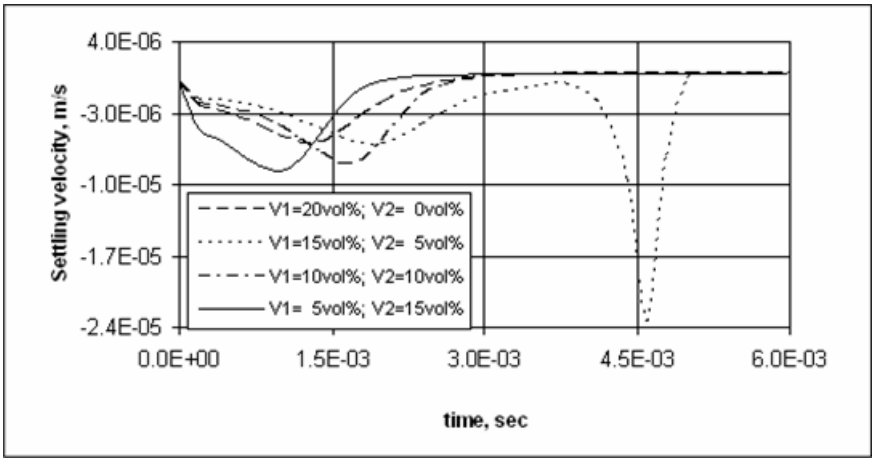

15(b)

Fig. 15 Time evolution of the sedimentation velocity of the micron particles at various combinations of binary nanoparticle concentration for an initial normalised separation of 3: (a) micron particle 1; (b) micron particle 2.

Physically, these 26nm nanoparticles cannot enlarge the gap between micron particles to let the 50nm nanoparticles enter the confined region, and as a result, the micron particles become closer with time. This can also be seen from the sedimentation velocity of micron particles shown in Figure 13, where a higher approach velocity of the micron particles is seen at V2=15%.

The results shown in Figure 14 are for an initial normalised separation of micron particles of 3, which differ considerably from that shown in Figure 12 for the initial particle separation of 1. First, the normalised separation of the micron particles for all combinations of V1 and V2 decreases with time until time = ~2.5ms. After 2.5ms, the normalised separation becomes constant for V2=0, 10 and 15% and ranges between ~2 and ~2.2, whereas that for V2=5% decreases further with time and eventually reaches ~1.2. This can also be explained from the force files as shown in Figure 11. At an initial normalised separation of 3, the repulsive forces induced by these four combinations of V1 and V2 are lower than the van der Waals attractive forces. As a result, the separation of the micron particles decreases. When the separation approaches ~2, three combinations of V1 and V2 (20 and 0, 10 and 10, and 5 and 15) give a sufficient potential barrier to overcome the van der Waals attraction and as consequence, the separation becomes constant.

As discussed above and shown in Figure 14, the final (equilibrium) separation is about 2.2 for V2=0. This results from the second peak of potential induced entirely by 26nm nanoparticles. At V2=10 and 15%, nanoparticles 2 ($d_{np,2} = 50\text{nm}$) produce potential barriers around a separation of 50nm i.e. 2 times diameter of nanoparticle 1 ($d_{np,1} = 26\text{nm}$). At V2=5%, although the 50nm nanoparticles also induce a significant barrier at a surface separation of 50 nm, it is less than the van der Waals attraction at such a position and as a result, microparticles approach each other to the final separation of ~1.2. The surface separation results agree with the particle sedimentation data shown in Figure 15 where a sharp peak appears for the micron particles at V2=5%.

4 Concluding Remarks

This paper introduces a new combined continuous, discrete and statistical mechanics (CCDS) method for modelling suspensions of highly asymmetric particles. The CCDS method treats the liquid medium as a continuum and the micron particles as a discrete phase, whereas the statistics mechanics method is used to treat the nanoparticles. The treatment of the nanoparticles involves the use of the Ornstein-Zernike equation with Percus-Yevick approximation based on the hard-sphere interaction. Such an approach enables the effective coupling between different length scales. The sedimentation behaviour of two micron particles submerged in both monodisperse and bidisperse nanoparticles suspensions nanoparticles is used as a case study for the CCDS method. The results show that, at a high salt concentration where electrostatic repulsive force is significantly screened, the structural force induced by both monodisperse and bidisperse nanoparticles could

overcome the van der Waals attractive force between the micron particles and thus prevent them from flocculation. The results also show that the introduction of disparity in the system complicates the effective interactions between the micron particles and consequently the particle dynamics.

Although the case study considers only two micron particles, it is straight forward to extend the modelling to multi-micron particles systems. Currently, the limitation for modelling the multi-micron particle systems is the computer power. As a consequence, we are in a process of developing the code further to enable parallel computing, which, together with increasing computer power, is able to deal with large number of micron particles.

Acknowledgements

This work is partially supported by UK Engineering and Physical Sciences Research Council (EPSRC) under grants EP/F000464/1 and EP/F023014/1.

Symbols

Alphabets

a	radius of micron particle
A_{pmp}	Hamaker constant for two particles through medium
bb	mass residual for individual cells in CFD
$c(r)$	direct correlation function
d	diameter of microparticle
e	electronic charge
e'	tolerance of the mass residual in continuum equation
$g(r)$	radial distribution function
h	surface-to-surface distance between two particles
$h(r)$	total correlation function
i	imaginary number
I_i	momentum of inertia of i^{th} particle
k	Fourier variable
k_B	Boltzmann constant
$L[\ ]$	notation of Laplace transform
m_i	mass of i^{th} particle
n_0	number density of ions in the bulk solution
p	fluid pressure in a computational cell
r	centre-to-centre distance between two particles
s	Laplace variable
t	time

T	absolute temperature
$v(r)$	the pair interaction potential
$V_{p,i}$	volume of ith particle
$w(r)$	potential of mean force
z	ionic valence

Vectors and tensors

$\mathbf{F}_{Br}$	Brownian force
$\mathbf{F}_{D,i}$	drag force
$\mathbf{F}_{g,i}$	gravitational force
$\mathbf{F}_{pf}$	volumetric fluid-particle interaction force
$\mathbf{F}_{vdW,i}$	van der Waals attractive force
$\mathbf{F}_{edlr,i}$	electrical double layer repulsive force
$\mathbf{F}_{str,i}$	structural force due to nanoparticles in suspension
$\mathbf{f}_{c,ij}$	contact force due to collision between particle *i* and *j*
$\mathbf{f}_{d,ij}$	viscous contact force due to collision between particle *i* and *j*
$\mathbf{g}$	gravitational acceleration
$\mathbf{u}_f$	velocity of fluid
$\mathbf{u}_{p,i}$	velocity of particle *i*
$\mathbf{I}$	unit tensor
$\boldsymbol{\delta}_k$	Kronecker delta tensor
$\boldsymbol{\Gamma}$	viscous stress tensor

Greeks

ΔV	volume of a computational cell
σ	surface charge density
$\delta(t)$	Delta function
ε	permittivity of medium
ε_0	permittivity of vacuum
ε_p	porosity of computational cell
ϕ_p	volume fraction of nanoparticles in the suspension
κ^{-1}	Debye screening length
μ_0	viscosity of water

μ_f	viscosity of solution
μ'_f	viscosity of bulk solvent
ρ_f	density of fluid
ρ_k	number density of fluid component k
ρ_p	density of solid particle

References

Anderson, T.B., Jackson, R.: Fluid mechanical description of fluidised beds. Equation of motion. Industrial and Engineering Chemistry Fundamentals 6, 527–539 (1967)

Armfield, S.W., Debler, W.: Purging of density stabilized basins. International Journal of Heat and Mass Transfer 36, 519–530 (1993)

Asakura, S., Oosawa, F.: On interaction between two bodies immersed on a solution of macromolecules. Journal of Chemical Physics 22, 1255–1256 (1954)

Asakura, S., Oosawa, F.: Interaction between particles suspended. I. Solutions of macromolecules. Journal of Polymer Science 33, 183–194 (1958)

Batchelor, G.K.: Sedimentation in a dilute dispersion of spheres. Journal of Fluid Mechanics 52, 245–268 (1972)

Bindal, S.K., Sethumadhavan, G., Nikolov, A.D., Wasan, D.T.: Foaming mechanisms in surfactant free particle suspensions. AIChE Journal 48, 2307–2314 (2002)

Bird, R.B., Warren, E.S., Edwin, E.L.: Transport Phenomena. Wiley, New York (1960)

Boublik, T.: Hard-sphere equation of state. Journal of Chemical Physics 53, 471–472 (1970)

Chen, H.S., Ding, Y.L., Tan, C.Q.: Rheological behaviour of Nanofluids. New Journal of Physics 9, 1–25 (2007)

Cheng, N.S., Law, A.W.K.: Exponential formula for computing effective viscosity. Powder Technology 129, 156–160 (2003)

Cundall, P.A., Strack, O.D.L.: A discrete numerical model for granular assemblies. Geotechnique 29, 47–65 (1979)

Derjaguin, B.V., Landau, L.: Theory of the stability of strongly charged lyophobic sols and of the adhesion of strongly charged particles in solutions of electrolytes. Acta Physicochem. USRR 14, 633–662 (1941)

Dickman, R., Attard, P., Simonian, V.: Entropic forces in binary hard sphere mixtures: Theory and simulation. Journal of Chemical Physics 107, 205–213 (1997)

Ding, Y.L., Wen, D.S.: Particle migration in a flow of nanoparticle suspensions. Powder Technology 149, 84–92 (2005)

Dress, C., Krauth, W.: Cluster algorithm for hard spheres and related systems. Journal of Physics A: Mathematical and General 28, L597–L601 (1995)

Ermak, D.L.: A computer simulation of charged particles in solution I. Technique and equilibrium properties. Journal of Chemical Physics 62, 4189–4196 (1975)

Fletcher, C.A.J.: Computational Techniques for Fluid Dynamics, 2nd edn. Springer Series in Computational Physics. Springer, Berlin (1991)

Fries, P., Hansen, J.P.: A Monte Carlo study of semi-dilute hard sphere mixtures. Molecular Physics 48, 891–901 (1983)

Hansen, J.-P., McDonald, J.R.: Theory of Simple Fluids. Academic Press, London (1989)
Harlow, F.H., Welch, J.E.: Numerical calculation of time-dependent viscous incompressible flow fluid with free surface. Physics of Fluids 8, 2182–2189 (1965)
Henderson, D.: An explicit expression for the solvent contribution to the force between colloidal particles using a hard sphere model. Journal of Colloidal Interface Science 121, 486–490 (1988)
Henderson, D., Lozada-Cassou, M.: A simple theory for spheres immersed in a fluid. Journal of Colloidal Interface Science 114, 180–183 (1986)
Henderson, D., Wasan, D.T., Trokhymchuk, A.D.: Effective interaction between large spheres immersed into a multicomponent hard-sphere fluid. Journal of Chemical Physics 19, 11989–11997 (2003)
Henderson, D., Trokhymchuk, A.D., Wasan, D.T.: Interaction energy and force for a pair of colloidal particles in a bidisperse hard-sphere solvent. Journal of Molecular Liquid 112, 21–28 (2004a)
Henderson, D., Wasan, D.T., Trokhymchuk, A.: Effective interaction between two giant spheres in a size polydisperse hard-sphere fluid. Molecular Physics 102, 2081–2090 (2004b)
Hunter, R.J.: Foundations of Colloidal Science. Oxford University Press, Oxford (2001)
Israelachvili, J.: Intermolecular and Surface Forces, 3rd edn. Academic Press, London (1997)
Krieger, I.M., Dougherty, T.J.: A mechanism for non-Newtonian flow in suspensions of rigid spheres. Transactions of the Society of Rheology 3, 137–152 (1959)
Largo, J., Wilding, N.: Influence of polydispersity on the critical parameters of an effective-potential model for asymmetric hard-sphere mixtures. Physical Review E 73, 036115 (2006)
Larson, R.G.: The Structure and Rheology of Complex Fluids. Oxford University Press, New York (1999)
Lebowitz, J.L.: Exact solution of generalized Percus-Yevick equation for a mixture of hard spheres. Physical Review 133, A895 (1964)
Liu, J., Luijten, E.: Rejection-free geometric cluster algorithm for complex fluids. Physical Review Letter 92, 035504 (2004a)
Liu, J., Luijten, E.: Stabilization of colloidal suspensions by means of highly charged nanoparticles. Physical Review Letter 93, 247802 (2004b)
Liu, J., Luijten, E.: Generalized geometric cluster algorithm for fluid simulation. Physical Review E 71, 066701 (2005a)
Liu, J., Luijten, E.: Colloidal stabilization via nanoparticle halo formation. Physical Review E 72, 061401 (2005b)
Liu, J., Luijten, E.: Geometric Cluster Algorithm for Interacting Fluids, in. Computer Simulation Studies in Condensed-Matter Physics XVI 103, 109–121 (2006)
Malherbe, J.G., Amokrane, S.: Asymmetric mixture of hard particles with Yukawa attraction between unlike ones: a cluster algorithm simulation study. Molecular Physics 97, 677–683 (1999)
Malijevsky, A., Barosova, M.: Integral equation and computer simulation study of the structure of additive hard-sphere mixtures. Molecular Physics 91, 65–74 (1997)
Martinez, C.J., Liu, J.W., Rhodes, S.K., Luijten, E., Weeks, E.R., Lewis, J.A.: Interparticle interactions and direct imaging of colloidal phases assembled from microsphere-nanoparticle mixtures. Langmuir 21, 9978–9989 (2005)
Patankar, S.V.: Numerical heat transfer and fluid flow. Hemisphere, New York (1980)

Patankar, S.V., Spalding, D.B.: A calculation procedure for heat, mass and momentum transfer in three-dimensional parabolic flows. Int. J. Heat Mass Transfer 15, 1787–1806 (1972)

Percus, J.K., Yevick, G.J.: Analysis of classical statistical mechanics by means of collective coordinates. Physical Review 110, 1–13 (1958)

Perram, J.W.: Hard sphere correlation functions in the Percus-Yevick approximation. Molecular Physics 30, 505–1509 (1975)

Russel, W.B., Saville, D.A., Schowalter, W.R.: Colloidal Dispersions, 2nd edn. Cambridge University Press, Cambridge (1991)

Tohver, V., Smay, J.E., Braem, A., Braun, P.V., Lewis, J.A.: Nanoparticle halos: A new colloid stabilization mechanism. Proceedings of the National Academy of Sciences 98, 8950–8954 (2001a)

Tohver, V., Chan, A., Sakurada, O., Lewis, J.A.: Nanoparticle engineering of complex fluid behaviour. Langmuir 17, 8414–8421 (2001b)

Tsuji, Y., Tanaka, T., Ishida, T.: Lagrangian numerical simulation of plug flow of cohesionless particles in a horizontal pipe. Powder Technology 71, 239–250 (1992)

Verwey, E.J.W., Overbeek, J.T.G.: Theory of the Stability of Lyophobic Colloids—The Interaction of Soil Particle Having an Electrical Double Layer. Elsevier, Amsterdam (1948)

Xu, B.H.: PhD Thesis, Numerical Simulation of the Gas-Solid Flow in Fluidized Beds. The University of New South Wales, Australia (1997)

Xu, B.H., Yu, A.B.: Numerical simulation of the gas-solid flow in a fluidised bed by combining discrete particles method with computational fluid dynamics. Chemical Engineering Science 52, 2785–2809 (1997)

Yang, C.Y.: PhD Thesis, Simulations of colloidal suspensions: sedimentation and stabilisation, University of Leeds (2008)

Yang, C.Y., Ding, Y.D., York, D., Broeckx, W.: Numerical simulation of sedimentation of microparticles using the discrete particle method. Particuology 6, 38–49 (2008)

Yau, D.H.L., Chan, K.-Y., Henderson, D.: Pair correlation functions for a hard sphere mixture in the colloidal limit. Molecular Physics 91, 1137–1142 (1997)

Zeidan, M., Xu, B.H., Jia, X., Williams, R.A.: Simulation of aggregate deformation and breakup in simple shear flows using a combined continuum and discrete model. Transactions of IChemE, Part A: Chemical Engineering Research and Design 85, 1645–1654 (2007)

Author Index

Ding, Yulong 295

Guo, Zeng-Yuan 1

Li, Zhi-Xin 1

Tzou, D.Y. 93

Wang, Liqiu 171

Xu, Jinliang 93

Yang, Chane-Yuan 295

Zhang, Yuxiang 171